Finite Element Method based
Electro- and Magnetoencephalography
Source Analysis in the Human Brain

Finite Element Method based Electro- and Magnetoencephalography Source Analysis in the Human Brain

Am Fachbereich Mathematik und Informatik
der Universität Münster
eingereichte

K U M U L A T I V E   H A B I L I T A T I O N S S C H R I F T

zur Erlangung der Venia Legendi
für

M A T H E M A T I K

vorgelegt von

Dr.rer.nat. Carsten Hermann Wolters

im Januar 2008

Finite Element Method based Electro- and Magnetoencephalography Source Analysis in the Human Brain

Wolters, Carsten Hermann

Abstract

Electro- and magneto-encephalography (EEG/MEG) based source analysis has risen to a promising brain imaging tool in the field of neuroscience and in medical research and diagnosis. In this work, it is shown to what extent spatial resolution of both EEG and MEG source analysis is dependent on the modeling accuracy of the embedded forward problem, i.e., the simulation of EEG and MEG fields for a given dipolar source in the brain using a volume conduction model of the head. Multimodal magnetic resonance imaging (MRI) and computed tomography registration and segmentation techniques are presented for the generation of realistically shaped head volume conductor models. A low resolution conductivity estimation method is developed and a technique based on diffusion-tensor MRI is used to individually estimate head tissue conductivity inhomogeneity and anisotropy. The finite element (FE) method is proposed for the forward problem. A key component in FE based source analysis is the numerical modeling of the singularity introduced into the differential equation by the current dipole and its interplay with the conductivity inhomogeneity and anisotropy. For a subtraction potential approach, a proof for existence and uniqueness of a weak solution in the function space of zero-mean potential functions and convergence properties of the FE method for the numerical solution to the correction potential are given. A combination of a full subtraction approach with high quality constrained Delaunay tetrahedralization FE meshes is shown to lead to forward modeling accuracies which, so far as the author knows, have not yet been presented before. A transfer matrix approach for both EEG and MEG is derived and its combination with algebraic multigrid preconditioned conjugate gradient solver techniques is shown to yield huge speedup factors and to enable mesh resolutions which seemed to be impossible before. An FE approach in a geometry-adapted hexahedral model is shown to outperform a collocation double layer boundary element approach with regard to both accuracy and computational speed. A new and fast spatio-temporal regularization procedure for an improved current density reconstruction is presented. Sensitivity studies show the importance of realistic volume conductor modeling. Using modern EEG and MEG inverse approaches, the developed methods are then successfully applied in the fields of evoked responses and in presurgical epilepsy diagnosis.

Contents

Chapter 1

Introduction

1.1 Brain imaging techniques

Important research in the neurosciences is devoted to the question, how the human brain processes information (M.S.Gazzaniga et al. [2002]; Andrä and Nowak [2002]). The brain's activity involves a complex interplay of electrical, chemical and mechanical processes, extending over both space and time. This vast diversity of phenomena carrying information on brain functions naturally leads to a great variety of possible means by which this information can be extracted. Brain imaging techniques are characterized by the brain process that they monitor, by their degree of invasiveness, and by their spatial and temporal resolutions. Methods relying on metabolic and hemodynamic changes in the brain tissue indirectly reflect neuronal activity, as for example positron emission tomography (PET) and functional magnetic resonance imaging (fMRI). These represent different degrees of invasiveness (radioactive substances, large magnetic fields), and good spatial and poor temporal resolution. Much more direct and completely non-invasive measure of the activity of nerve cells is delivered by *electroencephalography* (EEG) and *magnetoencephalography* (MEG) to which this work is dedicated.

1.2 EEG and MEG

EEG and MEG are based on the fact, that electric currents in the dimension of a few nAm are flowing in the active cortical areas. These so-called *primary currents* produce electric potentials on the surface and magnetic fields outside the head. The first measurement of a human EEG was carried out in 1929 by Berger [1929]. Around forty years later, Cohen [1968] for the first time recorded the magnetic fields produced by the brain, the MEG. The sensitivity of the MEG and therefore its importance was increased when superconducting quantum interference devices (SQUIDs) were invented. Cohen [1972] reported about the first MEG measurement using SQUIDs. In contrast to fMRI and PET, EEG and MEG can be recorded with a high temporal resolution of less than one millisecond, which is a further advantage of EEG and MEG methods. The question of spatial resolution, where especially the EEG is often considered to be rather poor, is treated in detail below.

1.3 Relevant application fields of EEG and MEG to this work

EEG and MEG methods have many important clinical applications. The reasons for this stem from the fact that there are predictable EEG and MEG signatures associated with different behavioral states. For example, in deep sleep, EEG and MEG are characterized by slow, high-amplitude oscillations, presumably resulting from rhythmic changes in the activity states of large groups of neurons. In other phases of sleep and during wakeful states, this pattern changes, but in a predictable manner. Since the normal EEG and MEG patterns are well-established and consistent among individuals, EEG and MEG recordings can detect abnormalities in brain function such as for example in the assessment and treatment of *epilepsy*.

1.3.1 Presurgical epilepsy diagnosis

About 0.5%-1% of the world population has epilepsy and in 70-80% a drug therapy is successful (P.Kwan and M.J.Brodie [2000]). For those patients who are still pharma-resistent after the administration of two up to three different drugs, the probability of a success of a further drug is only 5-10% (P.Kwan and M.J.Brodie [2000]). Surgical resection of epileptogenic cortical tissue in pharmaco-resistant epilepsy patients was shown to safely and effectively control seizures, recover function, improve quality of life and even save lives, but epilepsy surgery is still underused in developed countries and non-existent in most developing countries (Wiebe et al. [2001]). Of the many forms of epileptic seizures, generalized seizures have no known locus of origin and appear bilaterally symmetrical in EEG and MEG records. *Focal seizures*, in contrast, begin in a restricted area and spread throughout the brain (Stefan et al. [2003]). Focal seizures frequently produce the first hint of a neurological abnormality. They can result from congenital abnormalities such as a vascular malformation or can develop as a result of a local infection, enlargement of a tumor, or residual damage from a stroke or traumatic event. Because of the movements of the patient and the rigid MEG helmet, most tonic-clonic seizures can only be registered by the

EEG. However, quite often, the damaged brain areas produce *inter-ictal* (occurring between seizures) *spikes* without body movements which can be measured by both EEG and MEG (Stefan et al. [2003]).

The precise localization of the epileptogenic areas in the brain, preferably with non-invasive methods, is the major goal of the presurgical evaluation (Rosenow and Luders [2001]; Waberski et al. [1998]). It will be discussed in detail in Chapter 2.17 how surface EEG measurements can be exploited for this task.

1.3.2 Evoked responses

Besides focal seizures in epilepsy, which might lead to considerable current flows in the brain and resulting EEG potentials and MEG fields extracted at the head surface, the raw EEG and MEG signal is otherwise limited in providing insight to brain processes because the recordings tend to reflect the brain's global electrical activity. A more powerful approach used by many neuroscientists focuses on how brain activity is modulated in response to a particular task. The method requires extracting an *evoked response* from the global EEG and MEG signals. The procedure is the following: EEG and MEG measurements from a series of trials are averaged together by aligning the records according to an external event such as the onset of a stimulus (*trigger*). The averaging procedure decreases variations in the brain's electrical activity that are unrelated to the trigger and extracts the signal of interest which might be related to sensory (somatosensory evoked potentials or fields, SEP/SEF) (Buchner et al. [1996]), auditory (auditory evoked potentials or fields, AEP/AEF) (Pantev et al. [1989]), visual (visually evoked potentials or fields, VEP/VEF) (Makeig et al. [2002]) or cognitive events (Friederici et al. [2000]). Besides of the general usefulness of evoked responses in the field of neuroscience, the reconstruction of the underlying sources can also have clinical importance. This has, e.g., been shown by Roberts et al. [1998], where analysis of SEF sources in a patient with a brain tumor near the central sulcus revealed that somatosensory cortex was anterior to the lesion, so that the motor area could not be affected since it is anterior to the somatosensory cortex. If the tumor extends into the precentral sulcus, surgery might be avoided as it is likely to damage motor cortex and leave the patient with partial paralysis.

The localization of the sources underlying simultaneously measured tactile SEP and SEF data will be discussed in detail in Chapters 2.11 and 2.16.

1.4 EEG and MEG source analysis

The question for spatial resolution of EEG and MEG necessitates a deeper insight into the methodology of source analysis. The activity that is measured in EEG and MEG is the result of movements of ions, the so-called *impressed* or *primary currents*, within mainly the apical dendrites of the large pyramidal cells (Murakami and Okada [2006]). The impressed currents are generally formulated as a mathematical point current dipole (Brazier [1949]; de Munck et al. [1988]; Sarvas [1987]), which is a convenient representation in the case of synchronous polarization of a small patch of cortical tissue (Hämäläinen and Sarvas [1989]; Bertrand et al. [1991]; de Munck and Peters [1993]; Yvert et al. [1995]; Zanow and Peters [1995]; van den Broek [1997]; Awada et al. [1997]; Marin et al. [1998]; Fuchs et al. [1998]). The current dipole causes ohmic *return* or *secondary currents* to flow through the surrounding medium. The EEG measures the potential differences from the return currents at the scalp surface, whereas the MEG measures the magnetic flux of both impressed and return currents. The reconstruction of the dipole sources is called the EEG and MEG *inverse problem*. A critical component of the inverse problem is the numerical approximation method used to reach an accurate solution of the associated EEG and MEG *forward problem*, i.e., the simulation of potentials and fields at measurement sensors for a known dipole source in the brain.

1.4.1 The forward problem

For the forward problem, the electrical conduction properties of the human head (the *volume conductor*) have to be modeled. It is obvious that a completely realistic volume conductor model currently cannot be accomplished in routine source analysis, but it is important to specify those characteristics of the system which play a dominant role.

Head tissue geometries

Magnetic resonance imaging (MRI) or computed tomography (CT) provides the geometry information for the brain, the cerebrospinal fluid (CSF), the skull, and the scalp ([Pham and Prince, 1999; Huiskamp et al., 1999; Wolters, 2003; Ramon et al., 2004]). MRI has the advantage of being a safe and quasi-noninvasive method for imaging the head, while CT provides better definition of hard tissues such as bone. However, while CT can be used in clinical examinations, it is not justified for routine physiological studies in healthy human subjects. In this work, a combination of T1-weighted MRI, which is well suited for the identification of soft tissues (scalp, brain) and proton-density (PD) weighted MRI, enabling the segmentation of the inner skull surface, will be proposed. This approach leads to an improved modeling of the skull thickness over standard T1-MRI based approches.

Head tissue conductivities

Source analysis is sensitive to the conductivities of the head tissues, which vary across individuals and within the same individual due to variations in age, disease state, and environmental factors. First attempts to measure the conductivities of biological tissues were made in vitro, often using samples taken from animals (Geddes and Baker [1967]). Brain white matter was measured to have a direction dependent (*anisotropic*) conductivity with a ratio of about 1 to 9 normal to parallel to the fibers (Nicholson [1965]). The conductivity of human cerebrospinal fluid (CSF) was measured by Baumann et al. [1997] and that of skull by Akhtari et al. [2002]. The human skull consists of a soft bone layer (spongiosa) enclosed by two hard bone layers (compacta). Since the spongiosa has a much higher measured conductivity than the compacta (Akhtari et al. [2002]), the skull is often described by an anisotropic conductivity (Rush and Driscoll [1968]; de Munck [1988]; van den Broek [1997]; Marin et al. [1998]). Recently, it has been proposed to determine in vivo conductivities of head tissues by using an electrical impedance tomography (EIT) based approach (Gonçalves et al. [2003a]) or by estimating them from measured EEG data (Gutierrez et al. [2004]; Vallaghé et al. [2007]), EEG and simultaneous intra-cranial data (Lai et al. [2005]) or combined EEG and MEG data (Gonçalves et al. [2003b]). A deep insight into the EIT method is given in (Somersalo et al. [1992]). However, EIT is not likely to resolve the anisotropy of the intra-cranial tissues, instead, an indirect determination of the anisotropic brain conductivity through diffusion tensor magnetic resonance imaging (DT-MRI) was proposed (Basser et al. [1994]; Tuch et al. [1999, 2001]). The underlying assumption of these models is that the same structural features that result in anisotropic mobility of water molecules (detected by DT-MRI) also result in anisotropic conductivity. The quantitative expression for this assumption is that the eigenvectors of the conductivity tensor are the same as those from the water diffusion tensor (Basser et al. [1994]). Even more specifically, Tuch et al. [1999, 2001] have applied a differential effective medium approach to porous brain tissue and derived a linear relationship between the eigenvalues of the DT and the conductivity tensors.

Analytical and boundary element approaches

Different numerical approaches for the forward problem have been used. For the EEG, de Munck and Peters [1993] presented a quasi-analytical solution of a volume conductor model consisting of an arbitrary number of concentric/confocal anisotropic layers of different conductivities. For the MEG, an analytical formula has been derived for a spherically symmetric conductor by Sarvas [1987]. It appears that the magnetic field outside the sphere is completely independent of the conductivity profile, radial sources do not produce any magnetic field outside the sphere and return currents only contribute to tangential magnetometers, not at all to radial ones. Besides the fact that those models are still frequently used in source analysis routine, they also serve as validation tools for more realistic numeric modeling.

In order to better take into account the realistic shape of the scalp and skull surfaces, boundary element (BE) head models have been developed, being adequate for piecewise homogeneous isotropic compartments (Barnard et al. [1967]). Numerical accuracy of the BE approach could be improved through the *isolated skull approach* (ISA) (Hämäläinen and Sarvas [1989]; Meijs et al. [1989]), the use of linear basis functions with analytically integrated elements (de Munck [1992]), quadratic elements (Frijns et al. [2000]), local mesh refinement around the source (Yvert et al. [1995]; Zanow and Peters [1995]) and virtual mesh refinement techniques (Fuchs et al. [1998]). Most often, a collocation method for a double layer potential approach was used (Hämäläinen and Sarvas [1989]; Meijs et al. [1989]; de Munck [1992]; Yvert et al. [1995]; Zanow and Peters [1995]; Fuchs et al. [1998]), but it was shown by Mosher et al. [1999] and Kybic et al. [2005] that a Galerkin approach yields superior results. Finally, a very promising symmetric BE approach was presented by Kybic et al. [2005] where single layer and double layer potential approaches were combined and significantly higher accuracies were achieved than with the alternative methods.

Finite element approaches

Besides the finite difference (FD) (Saleheen and Kwong [1997]; Mohr [2004]; Hallez et al. [2005]) and the finite volume (FV) (Mohr [2004]; Cook and Koles [2006]) methods, finite element (FE) volume conductor modeling is able to treat both realistic geometries and inhomogeneous and anisotropic material parameters (Yan et al. [1991]; Bertrand et al. [1991]; Haueisen et al. [1995]; Awada et al. [1997]; Buchner et al. [1997]; van den Broek [1997]; Marin et al. [1998]; Ollikainen et al. [1999]; Weinstein et al. [2000]; Schimpf et al. [2002]; Uitert et al. [2003]; Gencer and Acar [2004]; Ramon et al. [2004]). Sensitivity studies have been carried out in realistic 3D models for the influence of skull anisotropy (van den Broek [1997]; Marin et al. [1998]) and realistic white matter anisotropy (Haueisen et al. [2002]) on EEG and MEG. Those studies support the hypothesis that modeling skull and white matter anisotropy is crucial for accurate EEG and EEG/MEG source reconstruction, respectively. It has furthermore been shown that skull conductivity inhomogeneities (Ollikainen et al. [1999]) such as skull sutures (Pohlmeier et al. [1997]) have a non-negligible effect on EEG source analysis, while they hardly influence the MEG (van den Broek [1997]). Local conductivity changes around the primary source (Haueisen et al. [2000]) as caused by especially brain lesions (van den Broek [1997]) or skull incisions from trepanation (van den Broek [1997]) have a non-negligible effect on both EEG and MEG.

A key component in FE-based source analysis is the numerical modeling of the singularity introduced into the equation by the current dipole and its interplay with the conductivity inhomogeneities and anisotropies. Different FE approaches for modeling the singularity are known from the literature: a *subtraction* approach (Bertrand et al. [1991]; van den Broek [1997]; Awada et al. [1997]; Marin et al. [1998]), a *partial integration* direct method (Yan et al. [1991]; Awada et al. [1997]), and a *Venant* direct method (Buchner et al. [1997]). The subtraction approach divides the total potential into the analytically known singularity potential and the singularity-free correction potential, which can then be approximated numerically using an FE approach. Both the partial integration and the Venant direct FE methods approximate the dipole through monopolar sources and sinks on neighboring FE nodes with the constraint to optimally match the given dipole moment vector.

From the mathematical perspective, a satisfying FE theory was not yet derived for any of the above approaches.

Validation of numerical forward approaches

Validation of numerical forward approaches in EEG and MEG source analysis is generally carried out in multilayer sphere models where analytical solutions exist (de Munck and Peters [1993]; Sarvas [1987]). For a given dipole source in the inner sphere (brain), the EEG or MEG is simulated numerically and this vector is validated against the analytically computed one.

Three error criteria are commonly evaluated in source analysis (Meijs et al. [1989]; Bertrand et al. [1991]; van den Broek [1997]; Marin et al. [1998]). The first is the relative Euclidian (RE) error(Bertrand et al. [1991]), which is generally well known for the evaluation of numerical algorithms. In order to distinguish between the topography (driven primarily by changes in dipole location and orientation) and the magnitude error (indicating changes in source strength), Meijs et al. [1989] introduced the relative difference measure (RDM) and the magnification factor (MAG), respectively.

A second important point in validation studies is the examined source *eccentricity*. The eccentricity is defined as the percent ratio of the distance between the source location and the model midpoint divided by the radius of the inner sphere (brain). It is well-known that with increasing eccentricity, the numerical accuracy in sphere model validations decreases. This is not only the case for the FE subtraction approach (Bertrand et al. [1991]; van den Broek [1997]; Awada et al. [1997]; Marin et al. [1998]), but also for the direct approach in FE modeling (Yan et al. [1991]; Buchner et al. [1997]) and in BE modeling (Hämäläinen and Sarvas [1989]; Meijs et al. [1989]; Yvert et al. [1995]; Zanow and Peters [1995]; Fuchs et al. [1998]; Mosher et al. [1999]; Kybic et al. [2005]). When considering a three-shell model (skin, skull, brain), the dipoles that are located in the cortex will have an eccentricity of maximally 92% as reported by Marin et al. [1998]. However, the three-compartment model ignores the CSF compartment between the cortex and the skull. The CSF has a much higher conductivity than the brain compartment (Baumann et al. [1997]). Additionally, it is shown to have a significant influence on the forward problem (Ramon et al. [2004]). In four-compartment models, this layer is taken into account, but source eccentricity then has to be determined with regard to the inner CSF surface, i.e., the most eccentric sources are only 1 or 2mm apart from the next conductivity discontinuity. Therefore, eccentricities of more than 98% have to be examined, a much harder numerical task.

The consideration of mesh resolutions is important when comparing numerical approaches. Due to the excessive computational burden created by previous FE techniques in source analysis (and surely also because of limited computational resources at the time of the examination), evaluation studies often only used sub-optimal numbers of nodes (Bertrand et al. [1991]; van den Broek [1997]; Marin et al. [1998]; Waberski et al. [1998]).

The following shortly summarizes the achieved accuracy of previous FE studies in source analysis. In a locally refined (around the source singularity) tetrahedral mesh with 12,500 nodes of a four layer sphere model with anisotropic skull, Bertrand et al. [1991] reported numerical accuracies up to a maximal eccentricity of 97.6%. A maximal RE of above 20% and a maximal MAG up to 70% were documented for the most eccentric source. van den Broek [1997] also used a locally refined (around the source singularity) tetrahedral mesh with 3,073 nodes of a three layer sphere model with anisotropic skull. For the maximal examined eccentricity of 94.2%, an RDM of up to 50% was given. It was mentioned in the conclusion that in some cases the accuracy could not further be improved by adding points globally as the numerical stability of the matrix equation that had to be solved was reduced. Marin et al. [1998] restricted the finest tetrahedral mesh of 87,907 nodes to eccentricities of 81% in order to reach a sufficient accuracy for radial dipole forward solutions in a three compartment sphere model with anisotropic skull. Schimpf et al. [2002] investigated an FE subtraction approach in a four layer sphere model with isotropic skull and sources up to 1mm below the CSF compartment. In their article, a regular 1mm hexahedral model was used and a maximal RDM of 7% and a maximal MAG of 25% was achieved. Papadopoulo and Vallaghé [2007] investigated a partial integration FE approach in a three layer sphere model with anisotropic skull and sources up to 3.5mm below the inner skull surface. In their article, a 1mm hexahedral approach was used. In order to avoid the stair-like approximation of the smooth tissue boundaries with regular hexahedra, the FE stiffness matrix was computed from levelset segmentations of the tissue boundaries, i.e., elements through which a levelset surface passed, were properly integrated for both participating tissues. For their approach, a maximal RDM of 2% was reported.

Computational complexity of the finite element approach

One impediment to using the FE method has been the high computational cost of carrying out the simulations, especially when many evaluations of the forward problem are needed, e.g., in source localization schemes. It was speculated that BEM models are less computationally intensive compared to FEM models, while providing improved computational accuracy relative to simple analytical models (Plis et al. [2007]). The state-of-the-art approach in FE based source analysis was to solve one FE equation system for each source (Bertrand et al. [1991]; Buchner et al. [1997]; Awada et al. [1997]; van den Broek [1997]; Waberski et al. [1998]; Schimpf et al. [2002]). Due to the excessive computational burden created by such FE-based techniques, evaluation studies often only used sub-optimal numbers of FE nodes and/or sub-optimal numbers of possible sources in the brain (Bertrand et al. [1991]; Buchner et al. [1997]; van den Broek [1997]; Waberski et al. [1998]). For example, Buchner et al. [1997] reported that the setup of a lead field matrix with 8,742 unknown dipole components in a tetrahedral FE approach with 18,322 nodes took roughly a week of computation time. Waberski et al. [1998] used a tetrahedral FE model with only 10,731 nodes and mentioned in the discussion that, for a general clinical use of FE source analysis, a finer FE discretization and parallel computing is needed.

With regard to FE solver techniques, a direct banded LU factorization for a 2D source analysis scenario (Awada et al. [1997]) or, for 3D scenarios, iterative solver techniques like the *conjugate gradient* (CG) method without preconditioning (Bertrand et al. [1991]), Jacobi-preconditioned CG (Zhukov et al. [2000]), *incomplete Cholesky* (IC) preconditioned CG (Buchner et al. [1997]) or the successive over-relaxation method (Schimpf et al. [2002]) were used. Therefore, specific symmetrical implementations were carried out which are only useful in a spherical volume conductor (Schimpf et al. [2002]) or local mesh refinement strategies around the source location were proposed to reduce the otherwise unacceptably large numerical errors for eccentric sources (Bertrand et al. [1991]; van den Broek [1997]). However, with regard to the inverse problem, the setup of source-location dependent locally refined meshes is difficult to implement and time-consuming to compute and thus might not be practicable for an inverse source analysis.

For the EEG, it was shown for the FD method (Vanrumste et al. [1998]) and later for the FE method (Weinstein et al. [2000]) how the principle of reciprocity can be used to reduce the number of large sparse linear equation systems that have to be solved to the number of measurement electrodes. This was a major step forward in the reduction of the computational complexity for FE- or FD-based EEG source analysis, but it was still unclear if a similar approach can be derived for the MEG.

Finite element mesh generation

Mesh generation in FE based EEG and MEG source analysis generally influences greatly the accuracy of the results. It is thus important to determine a meshing strategy well adopted to achieve both acceptable forward modeling accuracy and reasonable computation times and memory usage. The FE method is generally considered to be quite flexible with regard to an accurate modeling of the geometry, but the difficult construction of the volume discretization is often seen to be a major disadvantage of the FEM compared to the BEM which only requires the use of surface triangulation meshes (Kybic et al. [2005]). So far, surface-based *ordinary Delaunay tetrahedralizations* (ODT) were mainly used (Bertrand et al. [1991]; Awada et al. [1997]; van den Broek [1997]; Buchner et al. [1997]; Marin et al. [1998]; Wolters [2003]). However, three-dimensional *constrained Delaunay tetrahedralizations* (CDT) are known to perform better (Si [2004]; Si and Gärtner [2005]) and, so far as the author knows, were not yet applied to source analysis. Only few studies examined regular hexahedral elements exploiting the spatial discretization inherent in medical tomographic data (Schimpf et al. [2002]). The problematic stair-like approximation of curved boundaries with regular hexahedra has been addressed by Camacho et al. [1997] in a biomechanical context, where it was shown that a geometry-adaptation approach can significantly reduce errors in von Mises stress at the surface, in spite of detrimental effects of deformed elements.

1.4.2 The inverse problem

The non-uniqueness of the EEG and MEG inverse problem implies that assumptions on the source model, as well as anatomical and physiological a-priori knowledge about the source region and sometimes even results from other techniques like fMRI (Menon et al. [1997]; Opitz et al. [1999]; Dale et al. [2000]) should be taken into account to obtain a unique solution. Therefore, different inverse approaches for continuous and discrete source parameter space have been proposed.

Spatio-temporal dipole fit

The first class of inverse approaches that will be used in this work are the classical *spatio-temporal dipole modeling* approaches, where the number of possible dipoles is restricted to only some few (Scherg and von Cramon [1985]; Mosher et al. [1992]; Knösche [1997]; Wolters et al. [1999]). The spatio-temporal focal source models differ in the manner in which they describe the time dependence of the data. Generally, they are grouped into three classes, the unconstrained dipole model (moving dipole), a dipole with temporally fixed location (rotating dipole) and a dipole with fixed location and fixed orientation (fixed dipole) (Mosher et al. [1992]). Optimization of the resulting cost function (Mosher et al. [1992]) is most often performed with a Nelder-Mead simplex optimizer (Nelder and Mead [1965]) which is started from appropriate seed-points and finds the next local minimum of the cost function (Knösche [1997]). The *goodness of fit* (GOF) of the spatio-temporal dipole model to the data can then be used as an index of the models quality. The simplex optimizer needs a-priori chosen seed-points and, dependent on the seed dipoles, it can converge to local minima which are not identical to the global minimum. This was shown for brain-stem auditory evoked potentials by Gerson et al. [1994], where the optimizer produced significant errors for just a single dipole model. Huang et al. [1998] examined a multi-start simplex in order to imitate a global optimization technique for fitting multi-dipole, spatio-temporal MEG data. The method of *simulated annealing* (SA) utilizes concepts of combinatorial optimization for globally minimizing a given cost function in acceptable time and it was shown by (Gerson et al. [1994]; Haneishi et al. [1994]; Wolters et al. [1999]) that the SA optimization stabilizes the spatio-temporal dipole modeling.

The *independent component analysis* (ICA) has not only proven to be an effective method for removing eye and muscle activity artifacts from EEG data and thus increasing the effective *signal-to-noise ratio* (SNR) of subsequent analysis (Jung et al. [2000]), but it was also shown to enable the disentangling of multiple current generators (Kobayashi et al. [2001]; Makeig et al. [2002]) underlying the measured data, so that ICA topography patterns are generated that are most often dipolar or in some few cases bi-dipolar, i.e., two strongly time-correlated sources located near symmetrically in both brain hemispheres, possibly supported by dense connections via the corpus callosum (Makeig et al. [2002]). The ICA-driven inverse problem is thus reduced to spatio-temporal dipole fits of only one or two focal sources for the ICA spatial topography patterns of interest. This approach is used in Chapter 2.17.2.

Scanning method

This work will furthermore exploit a so-called least-squares scanning or *goal function scan* (GFS) inverse method (Mosher et al. [1992]; Knösche [1997]). The GFS scans systematically position by position of a predefined discrete source space. At each position, a least squares fit is performed to the chosen data samples, i.e., an optimal rotating dipole is computed for the considered location. As a result, the GOF at each position is displayed as a color map on cross-sections of the source space mesh. The GFS is not subject to pitfalls of non-linear search algorithms, such as being trapped in local minima or slow convergence. Additionally, if the underlying sources have distinct EEG and MEG topographies and comparable strength, areas of similar GOF can serve as confidence regions (Knösche [1997]) and GFS results can be used as seed-points for spatio-temporal dipole models. Since a single dipole at each source space mesh node is fitted to the data, this method will naturally work, if a single focal source is underlying the measured data. However, the GFS might fail, e.g., when there are multiple sources which are close to each other, sources that produce overlapping topographies or EEG and MEG's of greatly differing intensities (Mosher et al. [1992]).

Current density reconstruction

The last class of inverse approaches addressed in this work are the *current density reconstruction* (CDR) methods. The CDR methods act on a distributed source model, where the restriction to a limited number of focal sources is abolished, i.e., sources are allowed to be simultaneously active on all discrete mesh nodes of a predefined source space (e.g., all nodes of a cortical triangle mesh). The non-uniqueness of the resulting problem is compensated by the assumption that the dipole distribution should be minimal with regard to a specific norm. Different norms have been proposed, such as the L2-norm (Hämäläinen and Ilmoniemi [1984]; Knösche [1997]), which is often denoted as the *minimum norm least squares* (MNLS) or Tikhonov-regularization method. The MNLS leads to a smooth current distribution with minimal source energy. The choice of an L1-norm results in a more focal distribution as shown by (Wagner et al. [1996]; Fuchs et al. [1999]). It is well-known that a regularization without any depth-weighting gives preference to superficial sources (Fuchs et al. [1994]). Therefore, the use of a source weighting matrix with L2-norms of the corresponding lead field columns as diagonal entries was proposed by Fuchs et al. [1994]. However, as reported by Pascual-Marqui [2002], despite of all weighting efforts, linear solutions such as MNLS produced at best images with systematic non-zero localization errors. In contrast, in a large series of single test source simulations at arbitrary positions and depths in the volume conductor, a standardization of the MNLS as performed within the *standardized low resolution electromagnetic tomography* (sLORETA) was shown to produce zero-localization error (Pascual-Marqui [2002]). Most distributed source models are instantaneous models, i.e., they only make use of a spatial regularization with a single time sample of data. Recent developments, however, showed that spatio-temporal CDR approaches can help stabilizing the inverse reconstruction process (Schmitt et al. [2002]).

1.4.3 Spatial resolution of EEG versus MEG

As discussed above, the EEG is strongly dependent on accuracy aspects of volume conductor modeling with regard to both geometry and conductivity properties of the different head tissues. Moreover, the synchronous activity of large populations of cells is required to produce measurable extra-cranial signals. As a consequence, current EEG source analysis methods are often considered to have a rather poor spatial resolution (M.S.Gazzaniga et al. [2002]; Andrä and Nowak [2002]). MEG monitors the same electrical brain activity as EEG and shares many of its properties, but, as it will also be shown in this work, it is less disturbed by the complex conductivity profile of the head tissues, because mainly the primary currents are contributing to the typical MEG measurement sensors. Therefore, MEG source analysis is considered to have a higher spatial reconstructability of the brain processes (Hämäläinen et al. [1993]; M.S.Gazzaniga et al. [2002]; Andrä and Nowak [2002]). However, another typical trait of MEG in comparison to EEG is the different sensitivity profile, which largely excludes deep primary currents and those primary currents that flow perpendicular to the cranial surface (Sarvas [1987]; Hämäläinen et al. [1993]; Andrä and Nowak [2002]). Furthermore, in order to extract the extremely weak magnetic fields of the considered brain activity from environmental noise, techniques such as the passive shielding by means of measurements in a magnetically shielded chamber and active noise-cancellation such as gradiometer schemes (Hämäläinen et al. [1993]; Vrba [2000]; Vrba and Robinson [2001]) are needed for the MEG.

Spatial resolution aspects of MEG versus EEG will be covered in Chapters 2.5 and 2.16 of this work.

1.5 Scope of this habilitation

In light of the above discussion, this habilitation work will cover the following topics:

Chapter 2.1 Because of a lack of a satisfying FE theory in the FE source analysis literature, a proof for existence and uniqueness of a weak solution in the function space of zero-mean potential functions and convergence properties of the FE method for the numerical solution to the correction potential are given for the subtraction dipole approach. An FE *projected subtraction approach* is then implemented and validated in tetrahedral and hexahedral meshes.

Chapter 2.2 A *transfer matrix approach* (also called *lead field bases approach*) is derived for both EEG and MEG which limits the number of FE equation systems to be solved to the number of sensors and can be applied to both the direct potential approaches and the subtraction approach.

Chapter 2.3 It is shown that an algebraic multigrid preconditioned CG method with multiple right-hand side treatment can be used for an efficient computation of the EEG and MEG transfer matrices.

Chapter 2.4 For both the Venant and the subtraction dipole model and for EEG and MEG, the computational speed of the transfer matrix approach is compared to the state-of-the-art approach, i.e., solving one FE equation system for each source.

Chapter 2.5 is dedicated to a comparison of the projected subtraction approach and the Venant direct FE approach for the EEG and the MEG in ordinary tetrahedral and regular hexahedral meshes.

Chapter 2.6 The projected subtraction approach is compared to the direct FE approaches partial integration and Venant in a regular hexahedral model for the EEG.

Chapter 2.7 reports on the accuracy improvements of geometry-adapted versus regular hexahedral meshes for the Venant method and the projected subtraction approach.

Chapter 2.8 A *full subtraction approach* is developed which takes special care to appropriately evaluate the right-hand side integral with the objective of achieving highest possible convergence order for linear basis functions. The combination of the full subtraction approach with high quality CDT meshes leads to RDM and MAG accuracies below 0.4% for a maximal examined eccentricity of 98.7% in an anisotropic four-compartment sphere model.

Chapter 2.9 compares the efficiency of *algebraic multigrid* (AMG), IC and Jacobi preconditioners for the CG method for iteratively solving the FE based

EEG forward problem. The interplay of the three solvers with a full subtraction approach and the two direct potential approaches Venant and partial integration is examined in specifically-tuned CDT FE meshes. Additionally, inverse single dipole reconstruction errors are discussed that result from the numerical FE forward modeling errors for the full subtraction method and the Venant approach in specifically-tuned CDT FE meshes. Furthermore, a method is proposed for the treatment of forward modeling error oscillations of the direct FE potential approaches.

Chapter 2.10 will show that a double layer collocation BE approach using the ISA and linear basis functions with analytically integrated elements is outperformed by a Venant FE approach in a geometry-adapted hexahedral model with regard to both accuracy and computational speed.

Chapter 2.11 A *low resolution conductivity estimation* (LRCE) method using SA optimization on high-resolution FE models is proposed that individually optimizes a realistically-shaped volume conductor with regard to the tissue conductivities and likely produces a more robust estimate of source location.

Chapter 2.12 A new and fast spatio-temporal regularization procedure for current density reconstructions, STR, is proposed. It is shown in statistical tests that STR shows superior reconstruction results compared to the temporally uncoupled MNLS.

Chapter 2.13 reports on the influence of remote tissue conductivity anisotropy on EEG and MEG field and return current computation.

Chapter 2.14 is dedicated to the influence of local tissue conductivity anisotropy

Chapter 2.15 presents the influence of volume conduction effects on the EEG and MEG reconstruction of the sources of the *Early Left Anterior Negativity* (ELAN) using an L1-norm CDR approach.

Chapter 2.16 First, the MEG machine at the Institute for Biomagnetism and Biosignalanalysis of the University of Münster is presented. The Chapter introduces into the active noise cancellation with gradiometer schemes, since its modeling is necessary for proper MEG forward simulations. In the second part, simultaneously measured tactile somatosensory evoked potentials (SEP) and fields (SEF) will be analyzed. It will be shown that, with a proper realistic head model and a larger number of trials for the EEG than for the MEG, both EEG and MEG correctly localize in the primary somatosensory cortex.

Chapter 2.17 first evaluates whether non-invasive surface EEG (sEEG) source analysis based on 1mm anisotropic FE head modeling can provide additional information for presurgical epilepsy diagnosis. Therefore, GFS, MNLS, spatio-temporal current dipole modeling and sLORETA inverse approaches are applied to averaged ictal spikes of a medically-intractable epilepsy patient and the reconstruction results are successfully validated with the outcome of intra-cranial EEG (iEEG) recordings.

In the second part, an ICA based source reconstruction of surface (sEEG) and intra-cranial EEG (iEEG) data of a medically-intractable epilepsy patient is presented with a special focus on the FE modeling of the skull incision from trepanation and the iEEG silastic pads.

1.6 Listed publications

The following publications are part of this habilitation:

1. Wolters, C.H., Köstler, H., Möller, C., Härdtlein, J., Grasedyck, L., and Hackbusch, W.. Numerical mathematics of the subtraction approach for the modeling of a current dipole in EEG source reconstruction using finite element head models. *SIAM J. on Scientific Computing*, 30(1), pp. 24–45, 2007.

2. Wolters, C.H., Grasedyck, L. and Hackbusch, W., Efficient Computation of Lead Field Bases and Influence Matrix for the FEM-based EEG and MEG Inverse Problem. *Inverse Problems*, 20(4), pp. 1116–1099, 2004.

3. Wolters, C.H., Anwander, A., Reitzinger, S. and Haase, G., Algebraic Multigrid with Multiple Right-Hand Side Treatment for an Efficient Computation of EEG and MEG Lead Field Bases. In *Halgren, E., Ahlfors, S., Hämäläinen, M. and Cohen, D. (eds.): BIOMAG 2004, Proc. of the 14th Int. Conf. on Biomagnetism, Boston, USA*, pp. 465–466, 2004.

4. Wolters, C.H., Grasedyck, L., Anwander, A. and Hackbusch, W., Efficient Computation of Lead Field Bases and Influence Matrix for the FEM-based EEG and MEG Inverse Problem. In *Halgren, E., Ahlfors, S., Hämäläinen, M. and Cohen, D. (eds.): BIOMAG 2004, Proc. of the 14th Int. Conf. on Biomagnetism, Boston, USA*, http://www.biomag2004.org, pp. 104–107, 2004.

5. Lanfer, B., Wolters, C.H., Demokritov, S.O. and Pantev, C., Validating Finite Element Method Based EEG and MEG Forward Computations. In:

Proc. Biomedizinische Technik, Aachen, Germany, BMT, ISSN: 0939-4990, September 26–29, 2007.

6. Wolters, C.H., Köstler, H., Möller, C., Härdtlein, J. and Anwander, A.. Numerical approaches for dipole modeling in finite element based source analysis. *International Congress Series, ICS-07008*, Vol.1300, pp. 189–192, 2007.

7. Wolters, C.H., Anwander, A., Berti, G. and Hartmann, U.. Geometry-adapted hexahedral meshes improve accuracy of finite element method based EEG source analysis. *IEEE Trans. Biomed. Eng.*, 54(8), pp. 1446-1453, 2007.

8. Drechsler, F., Wolters, C. H., Dierkes, T., Si, H. and Grasedyck, L.. A highly accurate full subtraction approach for dipole modelling in EEG source analysis using the finite element method. submitted to *Applied Numerical Mathematics*, 2007.

9. Lew, S., Wolters C.H., Dierkes, T., Röer, C., MacLeod, R.S.. Accuracy and time comparison for different potential approaches and iterative solvers in finite element method based EEG source analysis. submitted to *Applied Numerical Mathematics*, 2008.

10. Lanfer, B., Wolters, C.H., Anwander, A., Dümpelmann, M., and Knösche, T.R.. Comparison of finite element and boundary element modeling in EEG source analysis with regard to accuracy and computational speed. submitted to *Phys.Med.Biol.*, 2007.

11. Lew, S., Wolters C.H., Anwander, A., Makeig, S. and MacLeod, R.S. Improved EEG source localization using low resolution conductivity estimation in a realistic head model. submitted to *NeuroImage*, 2007.

12. Schmitt, U., Wolters, C.H., Anwander, A. and Knösche, T., STR: A new Spatio-Temporal Approach for Accurate and Efficient Current Density Reconstruction In *Halgren, E., Ahlfors, S., Hämäläinen, M. and Cohen, D. (eds.): BIOMAG 2004, Proc. of the 14th Int. Conf. on Biomagnetism, Boston, USA*, http://www.biomag2004.org, pp. 591–592, 2004.

13. Wolters, C.H., Anwander, A., Tricoche, X., Weinstein, D., Koch, M.A., and MacLeod, R.S. Influence of Tissue Conductivity Anisotropy on EEG/MEG Field and Return Current Computation in a realistic Head Model: A Simulation and Visualization Study using High-Resolution Finite Element Modeling. *NeuroImage*, 30(3), pp. 813–826, 2006.
DOI: http://dx.doi.org/10.1016/j.neuroimage.2005.10.014,

14. Wolters, C.H., Anwander, A., Tricoche, X., Lew, S. and Johnson, C.R., Influence of Local and Remote White Matter Conductivity Anisotropy for a Thalamic Source on EEG/MEG Field and Return Current Computation *Int. Journal of Bioelectromagnetism*, 7(1), pp. 203–206, 2005.

15. Wolters, C.H., Anwander, A., Maess, B., MacLeod, R.S. and Friederici, A.D., The Influence of Volume Conduction Effects on the EEG/MEG Reconstruction of the Sources of the Early Left Anterior Negativity. In *Proc. of the 26th Annual Int. Conf. IEEE Engineering in Medicine and Biology Society, San Francisco, USA*, http://www.ucsfresno.edu/embs2004, September 1-5, pp. 3569–3572, 2004.

16. Lanfer, B., Wolters C.H., Pantev, C., and Demokritov, S.. Validation and Comparison of Realistic Head Modelling Techniques and Application to Tactile Somatosensory Evoked EEG and MEG Data. unpublished results, 2008.

17. Rullmann, M., Anwander, A., Warfield, S.,Duffy, F.H. and Wolters C.H.. EEG source analysis of epileptiform activity with a high resolution finite element head model. submitted to *NeuroImage*, 2008.

18. Wolters C.H., Makeig, S., Johnson, C., Röer, C. and Worrell, G.A.. Multiscale modeling of neuronal activity from simultaneous iEEG and sEEG data. unpublished results, 2008.

Chapter 2

Publications

2.1 Numerical mathematics of the subtraction method and the projected subtraction approach.

Numerical mathematics of the subtraction approach for the modeling of a current dipole in EEG source reconstruction using finite element head models
Wolters, C.H., Köstler, H., Möller, C., Härdtlein, J., Grasedyck, L., and Hackbusch, W.. *SIAM J. on Scientific Computing*, Vol. 30, No. 1, pp. 24-45 (2007).

Corresponding author: C.H. Wolters

SIAM J. SCI. COMPUT.
Vol. 30, No. 1, pp. 24–45

NUMERICAL MATHEMATICS OF THE SUBTRACTION METHOD FOR THE MODELING OF A CURRENT DIPOLE IN EEG SOURCE RECONSTRUCTION USING FINITE ELEMENT HEAD MODELS*

C. H. WOLTERS†, H. KÖSTLER‡, C. MÖLLER‡, J. HÄRDTLEIN‡, L. GRASEDYCK§, AND W. HACKBUSCH§

Abstract. In electroencephalography (EEG) source analysis, a dipole is widely used as the model of the current source. The dipole introduces a singularity on the right-hand side of the governing Poisson-type differential equation that has to be treated specifically when solving the equation toward the electric potential. In this paper, we give a proof for existence and uniqueness of the weak solution in the function space of zero-mean potential functions, using a subtraction approach. The method divides the total potential into a singularity and a correction potential. The singularity potential is due to a dipole in an infinite region of homogeneous conductivity. We then state convergence properties of the finite element (FE) method for the numerical solution to the correction potential. We validate our approach using tetrahedra and regular and geometry-conforming node-shifted hexahedra elements in an isotropic three-layer sphere model and a model with anisotropic middle compartment. Validation is carried out using sophisticated visualization techniques, correlation coefficient (CC), and magnification factor (MAG) for a comparison of the numerical results with analytical series expansion formulas at the surface and within the volume conductor. For the subtraction approach, with regard to the accuracy in the anisotropic three-layer sphere model (CC of 0.998 or better and MAG of 4.3% or better over the whole range of realistic eccentricities) and to the computational complexity, 2mm node-shifted hexahedra achieve the best results. A relative FE solver accuracy of 10^{-4} is sufficient for the used algebraic multigrid preconditioned conjugate gradient approach. Finally, we visualize the computed potentials of the subtraction method in realistically shaped FE head volume conductor models with anisotropic skull compartments.

Key words. source reconstruction, EEG, finite element method, dipole, subtraction method, algebraic multigrid, validation in three-layer sphere models, realistic head models, conductivity, anisotropy

AMS subject classifications. 35J25, 35Q80, 65N12, 65N21, 65N30, 65N50, 65N55, 65Y20, 68U20, 92C50

DOI. 10.1137/060659053

1. EEG source reconstruction.

Electroencephalography (EEG) based source reconstruction of cerebral activity (the EEG *inverse problem*) with respect to the individual anatomy is common practice in clinical routine and research and in cognitive neuroscience. The inverse methods are based on solutions to the corresponding

*Received by the editors May 5, 2006; accepted for publication (in revised form) April 5, 2007; published electronically November 7, 2007. This work was supported by the Deutsche Forschungsgemeinschaft (WO1425/1-1, GR3179/1-1), the IST-program of the European Community, project SIMBIO (http://www.simbio.de), and the NIH NCRR Center for Integrative Biomedical Computing (http://www.sci.utah.edu/cibc).

http://www.siam.org/journals/sisc/30-1/65905.html

†Corresponding author. Institut für Biomagnetismus und Biosignalanalyse, Westfälische Wilhelms-Universität Münster, Malmedyweg 15, 48149 Münster, Germany; Max-Planck-Institut für Mathematik in den Naturwissenschaften, Inselstrasse 22, 04103 Leipzig, Germany; Scientific Computing and Imaging Institute, University of Utah, Salt Lake City, UT 84112 (carsten.wolters@uni-muenster.de).

‡Institut für Informatik 10 (Systemsimulation), Universität Erlangen-Nürnberg, Cauerstrasse 6, D-91058 Erlangen, Germany (harald.koestler@informatik.uni-erlangen.de, chris_moeller@gmx.de, haerdtlein@ informatik.uni-erlangen.de).

§Max-Planck-Institut für Mathematik in den Naturwissenschaften, Inselstrasse 22, 04103 Leipzig, Germany (lgr@mis.mpg.de, wh@mis.mpg.de).

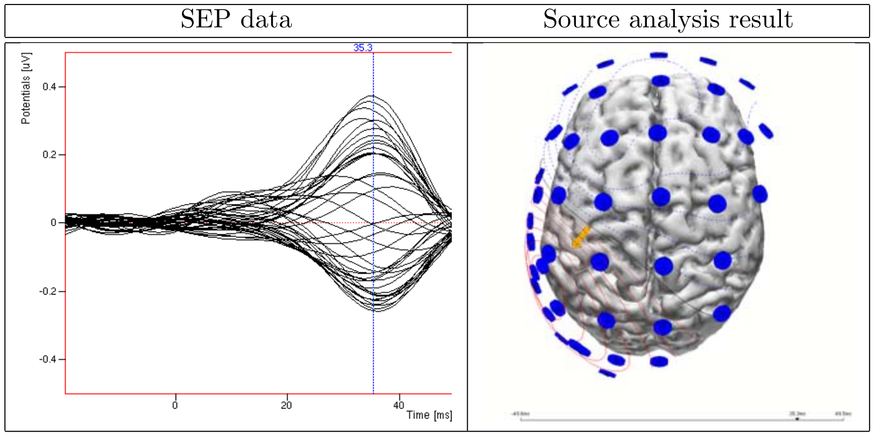

FIG. 1.1. *Left: Tactile somatosensory evoked potentials (SEP): Butterfly plot of the averaged EEG data. The peak of the SEP signal component of interest at* 35.3*ms is marked. Right: Reconstructed current dipole in somatosensory cortex (SI) with a remaining variance to the data of less than* 1%*.*

forward problem, i.e., the simulation of the electric potential in the head volume conductor for a *primary source*. The primary sources to be reconstructed in the inverse problem are electrolytic currents within the dendrites of the large pyramidal cells of activated neurons in the cortex sheet of the human brain. A primary source is generally formulated as an ideal or *mathematical point current dipole* [22, 24]. Such a focal brain activation can, e.g., be observed in epilepsy [29] (interictal spikes) or can be induced by a stimulus in neurophysiological or neuropsychological experiments, e.g., somatosensory or auditory evoked fields [20, 25]. Source analysis of individual somatosensory evoked potential (SEP) data is of high clinical interest for precise non-invasive localization of the central sulcus in the case of lesions lying in or adjacent to the sensorimotor region. This example from the wide application field of EEG source analysis will now be used to give a general motivation for this paper: Tactile stimuli were presented onto the right index finger tip of a 39 year old healthy male right-handed subject using balloon diaphragms driven by bursts of compressed air. Following [20], the optimal interstimulus interval of 1 sec. (± 10% variation) was used and 3 runs of 600 epochs each were recorded. After band-pass filtering and artifact rejection, the remaining epochs were averaged, resulting in a signal-to-noise ratio of more than 21. A butterfly plot of the measured SEP is shown in Figure 1.1 (left). A current dipole was then reconstructed at the peak of the early component at 35.3ms using a simulated annealing (SA) optimization procedure on a presegmented triangulated surface 2mm below the cortex surface. A finite element head model with anisotropic skull compartment was used to solve the corresponding forward problems. The remaining variance of the dipole solution to the data was less than 1%. The result, shown in Figure 1.1 (right), agrees well with a recent paper showing that the early tactile somatosensory component arises from area 3b of the primary somatosensory cortex (SI) contralateral to the side of stimulation [20].

2. Introduction. In addition to the finite difference method (see, e.g., [15]), the finite element (FE) method [36, 2, 1, 5, 6, 18, 30, 17, 27, 21, 34] has become popular to solve the forward problem because it allows a realistic representation of the head volume conductor with its various tissue geometries and conductivities. Improved mathematical algorithms, increased power of state-of-the-art computational platforms, and modern imaging methods allow today's use of the FE method for practical localization problems [30, 31, 11, 32]. In [5, 18, 34], the influence of conductivity anisotropy of the human skull, and in [17, 34], the influence of conductivity anisotropy of brain white matter were examined with regard to source reconstruction, motivating the use of three-dimensional (3D) methods when compared to spherical head models (see, e.g., [23]) or the boundary element method (see, e.g., [10]). In FE analysis, it is yet theoretically unclear how to treat *local* (in contrast to the above *remote*) anisotropy, i.e., tissue conductivity anisotropy in the direct environment of the source (cortical conductivity anisotropy). Because of its moderate anisotropy, the cortex is generally modeled as isotropic.

In the case of a point current dipole in the brain, the singularity of the potential at the source position can be treated with the so-called *subtraction method*, where the total potential is divided into the analytically known singularity potential and the singularity-free correction potential, which can then be approximated numerically using an FE approach [2, 1, 5, 18, 27]. In addition to the subtraction method, *direct approaches* to the total potential were developed, where either partial integration over the point source on the right-hand side of the weak FE formulation was used, approximating the source singularity by means of a projection in the function space of the FE trial-functions [30, 21], or the point dipole was approximated by a smoother monopolar primary source distribution [36, 6, 31, 27]. Even if it is known that the direct approaches perform reasonably well in locally isotropic spherical head model validation studies, it is impossible to formulate a satisfying FE theory if the mathematical dipole, being widely used in source reconstruction (especially also sphere and BE forward modeling) [22, 24], is used as the model for a primary source. Our study will therefore focus on the computationally more expensive (when compared to the direct approaches) FE subtraction method, where also, until now, no sufficient theory concerning existence and uniqueness of a solution and FE convergence properties was shown. Furthermore, the theory of the subtraction method was presented only for multicompartment models with an isotropic conductivity in the source environment. Either tetrahedra [2, 5, 18] or regular hexahedra [27] elements were used, but no comparison of different element types was found with regard to their numerical properties. The use of standard direct (banded LU factorization for a two-dimensional (2D) source analysis scenario [1]) or iterative (conjugate gradient (CG) without preconditioning [2] or successive overrelaxation (SOR) [27]) FE solver techniques limited the overall resolution. Therefore, local mesh refinement strategies around the source location were proposed to reduce the otherwise unacceptably large numerical errors for eccentric sources [2, 5], or specific symmetrical implementations were carried out which are useful only in a spherical volume conductor [27]. With regard to the inverse problem, local mesh refinement strategies around the source location are rather complicated to implement and time-consuming to compute and thus might not be appropriate for practical application.

In this paper, we formulate the theory of the subtraction approach for both locally isotropic and anisotropic conductivity and give a proof for existence and uniqueness of a weak solution in a zero-mean function space. We examine the FE convergence properties for the singularity-free correction potential and thus gain deep insight into the theory and practice of the method. The presented theory is valid for both EEG but also magnetoencephalography (MEG) source reconstruction. We examine the necessary accuracies of an algebraic multigrid preconditioned CG (AMG-CG) solver for the correction potential and describe how the subtraction approach is combined with our recent work on lead field bases [32]. This combination also allows sufficiently fast solutions to the EEG and MEG inverse problems. We then consider 3D three-layer sphere model scenarios to validate our approach in isotropic models and in models with an anisotropic skull compartment. The validation of other anisotropy types would exceed the scope of this paper. We use globally high mesh resolutions for both tetrahedra and hexahedra elements which results in a sufficient accuracy for the whole range of realistic source eccentricities. We show that regular hexahedra and especially geometry-conforming node-shifted hexahedra elements perform better than tetrahedra elements. We finally apply the method to three-compartment realistically shaped volume conductor models with anisotropic skull compartments obtained from MR images of the human head.

3. Forward problem formulation.

3.1. The Maxwell equations. Let us begin with the introduction of the necessary notation: let $\mathbf{E}$ and $\mathbf{D}$ be the electric field and electric displacement, respectively, ρ the electric free charge density, ϵ the electric permittivity, and $\mathbf{j}$ the electric current density. By μ we denote the magnetic permeability and by $\mathbf{H}$ and $\mathbf{B}$ the magnetic field and induction, respectively.

In the considered low frequency band (frequencies below 1000 Hz), the capacitive component of tissue impedance, the inductive effect, the electromagnetic propagation effect, and thus the temporal derivatives can be neglected in the Maxwell equations of electrodynamics [26]. It can be assumed that μ is constant over the whole volume and equal to the permeability of vacuum [26]. Therefore, the electric and magnetic fields can be described by the quasi-static Maxwell equations

$$\nabla \cdot \mathbf{D} = \rho,$$

$$\nabla \times \mathbf{E} = 0,$$

$$\nabla \times \mathbf{B} = \mu \mathbf{j}, \tag{3.1}$$

$$\nabla \cdot \mathbf{B} = 0 \tag{3.2}$$

with the material equations

$$\mathbf{D} = \epsilon \mathbf{E},$$

$$\mathbf{B} = \mu \mathbf{H},$$

since biological tissue mainly behaves as an electrolyte [26]: The electric field can be expressed as a negative gradient of a scalar potential:

$$\mathbf{E} = -\nabla \Phi. \tag{3.3}$$

In the field of bioelectromagnetism, the current density is divided into two parts [26], the primary or impressed current, $\mathbf{j}^p$, and the *secondary* or return currents, $\underline{\underline{\sigma}}\mathbf{E}$,

$$\mathbf{j} = \mathbf{j}^p + \underline{\underline{\sigma}}\mathbf{E}, \tag{3.4}$$

where $\underline{\underline{\sigma}} : \Omega \to \mathbb{R}^{3\times 3}$ denotes the 3×3 conductivity tensor.

3.2. The forward problem. Taking the divergence of (3.1) (divergence of a curl of a vector is zero) and using (3.3) and (3.4) give the Poisson equation

$$\nabla \cdot \left(\underline{\underline{\sigma}} \nabla \Phi\right) = \nabla \cdot \mathbf{j}^p = \mathrm{J}^p \quad \text{in } \Omega, \tag{3.5}$$

which describes the potential distribution in the head domain Ω due to a primary current $\mathbf{j}^p$ in the cortex sheet of the human brain. We find homogeneous Neumann boundary conditions on the head surface $\Gamma = \partial\Omega$,

$$\langle \underline{\underline{\sigma}} \nabla \Phi, \mathbf{n} \rangle \big|_{\Gamma} = 0, \tag{3.6}$$

with $\mathbf{n}$ the unit surface normal, and a reference electrode with given potential, i.e.,

$$\Phi(x_{\text{ref}}) = 0\,. \tag{3.7}$$

3.3. The primary currents. The primary currents are movements of ions within the dendrites of the large pyramidal cells of activated regions in the cortex sheet of the human brain and at already small distances equal to the size of the activated region only the dipolar moment of the source term is visible [24]. The mathematical dipole model at position $x_0 \in \mathbb{R}^3$ with the moment $\mathbf{M} \in \mathbb{R}^3$ can be formulated as [22]

$$\mathrm{J}^p(x) = \nabla \cdot \mathbf{j}^p\,(x) := \nabla \cdot \mathbf{M}\delta(x - x_0)\,. \tag{3.8}$$

3.4. The subtraction approach. In the following, it is assumed that we can find a nonempty subdomain $\Omega^\infty \subset \Omega$ around the source position x_0 with homogeneous constant conductivity $\underline{\underline{\sigma}}^\infty$, so that $x_0 \in \Omega^\infty \,/\, \partial\Omega^\infty$.

For the subtraction method, the conductivity $\underline{\underline{\sigma}}$ is then split into two parts,

$$\underline{\underline{\sigma}} = \underline{\underline{\sigma}}^\infty + \underline{\underline{\sigma}}^{\text{corr}}, \tag{3.9}$$

so that $\underline{\underline{\sigma}}^\infty$ is constant over the whole domain Ω and $\underline{\underline{\sigma}}^{\text{corr}}$ is zero in the subdomain Ω^∞: $\underline{\underline{\sigma}}^{\text{corr}}(x) = 0$ for all $x \in \Omega^\infty$. The total potential Φ can now be split into two parts,

$$\Phi = \Phi^\infty + \Phi^{\text{corr}}, \tag{3.10}$$

where the singularity potential Φ^∞ is defined as the solution for a dipole in an unbounded homogeneous conductor with constant conductivity $\underline{\underline{\sigma}}^\infty$. An analytic formula for Φ^∞ will be derived in the following. Let us first discuss the case of a homogeneous and isotropic conductivity $\underline{\underline{\sigma}}^\infty|_{\Omega^\infty} = \sigma^\infty\,\mathbf{Id}, \sigma^\infty \in \mathbb{R}$. In this case, the solution of Poisson's equation

$$\Delta\Phi^\infty = \mathrm{J}^p/\sigma^\infty \tag{3.11}$$

can be formed analytically by use of (3.8) [26]:

$$\Phi^\infty(x) = \frac{1}{4\pi\sigma^\infty} \frac{\langle \mathbf{M}, (x - x_0)\rangle}{|x - x_0|^3}. \tag{3.12}$$

In the case that the conductivity $\underline{\underline{\sigma}}^\infty$ is homogeneous and anisotropic in Ω^∞, we find [12]

$$\Phi^\infty(x) = \frac{1}{4\pi\sqrt{\det \underline{\underline{\sigma}}^\infty}} \frac{\langle \mathbf{M}, (\underline{\underline{\sigma}}^\infty)^{-1}(x - x_0)\rangle}{\langle (\underline{\underline{\sigma}}^\infty)^{-1}(x - x_0), (x - x_0)\rangle^{3/2}} \quad . \tag{3.13}$$

In both cases the potential Φ^∞ has a singularity at $x = x_0$ but is smooth everywhere else. Inserting (3.9)–(3.11) into (3.5) yields a Poisson equation for the correction potential

$$-\nabla \cdot \left(\underline{\underline{\sigma}} \nabla \Phi^{\text{corr}}\right) = f \quad \text{in } \Omega, \qquad f := \nabla \cdot \left(\underline{\underline{\sigma}}^{\text{corr}} \nabla \Phi^\infty\right), \tag{3.14}$$

with inhomogeneous Neumann boundary conditions at the surface:

$$\langle \underline{\underline{\sigma}} \nabla \Phi^{\text{corr}}, \mathbf{n} \rangle = g \quad \text{on } \Gamma, \qquad g := -\langle \underline{\underline{\sigma}} \nabla \Phi^\infty, \mathbf{n} \rangle. \tag{3.15}$$

After solving this numerically toward Φ^{corr}, the unknown scalar potential Φ can then be calculated using (3.10). The gain of the reformulation using the explicit representation of Φ^∞ is that the singularity on the right-hand side of (3.5) has been eliminated: let $\bar{\Phi}^\infty$ denote a smooth extension of $\Phi^\infty|_{\Omega \setminus \Omega^\infty}$ to Ω. Then $\bar{\Phi}^\infty$ is globally smooth and $\underline{\underline{\sigma}}^{\text{corr}} \nabla \Phi^\infty = \underline{\underline{\sigma}}^{\text{corr}} \nabla \bar{\Phi}^\infty$ ($\underline{\underline{\sigma}}^{\text{corr}}$ vanishes in Ω^∞), so that the right-hand side f is square-integrable over the whole domain Ω. For the given right-hand side f and the linear operator $\nabla \cdot \underline{\underline{\sigma}} \nabla$, we can apply a standard FE discretization and thus derive standard FE convergence results.

3.5. Existence and uniqueness of the solution. In the following, we use the definitions of the scalar products, norms, seminorms, function spaces, and weak derivatives as used in the FE standard literature (see, e.g., [4, 14]).

Equation (3.14) can only be understood in the classical sense under the condition $\underline{\underline{\sigma}} \in C^1\left(\Omega, \mathbb{R}^{3\times 3}\right)$. For the multilayer model with conductivity jumps between the compartments, we search for a weak solution in the Sobolev space $H^1(\Omega)$.

THEOREM 3.1 (variant of Friedrichs's inequality [4]). *Let Ω be a domain with volume $\mu(\Omega)$ that is contained in a cube with edge length s. We then find for all $u \in H^1(\Omega)$*

$$||u||_0 \leq |\overline{u}|\sqrt{\mu(\Omega)} + 2s|u|_1, \qquad \overline{u} := \int_\Omega u(x)dx/\mu(\Omega).$$

For existence and uniqueness of a solution for the correction potential, we will make use of the following specific subspace of $H^1(\Omega)$:

$$H^1_*(\Omega) := \left\{ v \in H^1(\Omega) \;\middle|\; \int_\Omega v(x)dx = 0 \right\}.$$

We now formulate the bilinear form $a : H^1(\Omega) \times H^1(\Omega) \to \mathbb{R}$ and the functional $l : H^1(\Omega) \to \mathbb{R}$ for our application:

$$a(u,v) := \int_\Omega \langle \underline{\underline{\sigma}}(x) \nabla u(x), \nabla v(x) \rangle dx, \quad l(v) := \int_\Omega f(x)v(x)dx + \int_\Gamma g v d\Gamma, \tag{3.16}$$

with f and g from (3.14) and (3.15).

DEFINITION 3.2 (continuous bilinear form). *Let H be a Hilbert space. A bilinear form $\mathcal{B} : H \times H \to \mathbb{R}$ is called continuous if there is a constant $C_{\text{cont}} > 0$, so that*

$$\forall u, v \in H : \quad |\mathcal{B}(u,v)| \leq C_{\text{cont}} ||u||_H ||v||_H.$$

LEMMA 3.3. *The bilinear form $a(\cdot,\cdot)$ from (3.16) is continuous on $H^1(\Omega) \times H^1(\Omega)$.*

Proof. Let σ_{max} be the largest eigenvalue of any conductivity tensor $\underline{\underline{\sigma}}(x), x \in \Omega$. Then the bilinear form is continuous,

$$|a(u,v)| \stackrel{(3.16)}{=} \left| \int_\Omega \langle \underline{\underline{\sigma}}(x)\nabla u(x), \nabla v(x)\rangle dx \right| \leq \sigma_{max} \int_\Omega \|\nabla u(x)\| \|\nabla v(x)\| dx$$

$$\stackrel{\text{Hölder}}{\leq} \sigma_{max}\|\nabla u\|_{L^2(\Omega)}\|\nabla v(x)\|_{L^2(\Omega)} \leq \sigma_{max}\|u\|_{H^1(\Omega)}\|v\|_{H^1(\Omega)},$$

with continuity constant $C_{\text{cont}} = \sigma_{max}$. ∎

DEFINITION 3.4 (H-ellipticity). *A symmetric, continuous bilinear form $\mathcal{B}$ is called H-elliptic if there is a constant $C_{\text{ell}} > 0$ so that*

$$\forall u \in H : \qquad \mathcal{B}(u,u) \geq C_{\text{ell}}||u||_H^2.$$

LEMMA 3.5. *The bilinear form $a(\cdot,\cdot)$ from* (3.16) *is $H^1_*(\Omega)$-elliptic.*

Proof. Let σ_{min} be the smallest eigenvalue of any conductivity tensor $\underline{\underline{\sigma}}(x), x \in \Omega$. Let $u \in H^1_*(\Omega)$, and let s be the constant from Friedrichs's inequality. Then the ellipticity

$$a(u,u) = \int_\Omega \langle \underline{\underline{\sigma}}(x)\nabla u(x), \nabla u(x)\rangle dx \geq \sigma_{min} \int_\Omega \langle \nabla u(x), \nabla u(x)\rangle dx = \sigma_{min}|u|_1^2$$

$$= \frac{\sigma_{min}}{1+4s^2}(|u|_1^2 + 4s^2|u|_1^2) \stackrel{|\bar{u}|=0}{=} \frac{\sigma_{min}}{1+4s^2}(|u|_1^2 + (|\bar{u}|\sqrt{\mu(\Omega)} + 2s|u|_1)^2)$$

$$\stackrel{\text{Th. 3.1}}{\geq} \frac{\sigma_{min}}{1+4s^2}(|u|_1^2 + \|u\|_0^2) = \frac{\sigma_{min}}{1+4s^2}\|u\|_1^2$$

holds with ellipticity constant $C_{\text{ell}} = \sigma_{min}/(1+4s^2)$. ∎

LEMMA 3.6. *The functional $l(\cdot)$ in* (3.16) *is well defined and bounded on $H^1(\Omega)$, particularly $l(\cdot) \in (H^1_*(\Omega))'$.*

THEOREM 3.7 (existence and uniqueness). *Let Ω be compact with piecewise smooth boundary (e.g., polygonal). Then the variational problem*

$$\textit{seek } u \in H^1_*(\Omega) : \quad \forall v \in H^1(\Omega), \quad a(u,v) = l(v)$$

has exactly one solution $u \in H^1_*(\Omega)$.

Proof. The bilinear form $a(\cdot,\cdot)$ is H^1-continuous (Lemma 3.3) and $H^1_*(\Omega)$-elliptic (Lemma 3.5) and the functional $l(\cdot)$ is bounded (Lemma 3.6). Due to Lax–Milgram we find exactly one $u \in H^1_*(\Omega)$ that solves the variational problem for all $v \in H^1_*(\Omega)$. For $\tilde{v} \in H^1(\Omega)$ we use the splitting $\tilde{v} = v + c \cdot 1, v \in H^1_*(\Omega)$, and find that first

$$a(u,\tilde{v}) = a(u,v) + c \cdot a(u,1) = a(u,v)$$

and, with $\Omega' := \Omega \setminus K(x_0,\epsilon)$ ($K(x_0,\epsilon)$ being a small ball with radius ϵ around the source position at x_0),

$$\begin{aligned} l(\tilde{v}) &= l(v) + c \cdot l(1) = l(v) + c \cdot \left(\int_\Omega f + \int_\Gamma g \right) \\ &= l(v) + c \cdot \left(\int_\Omega \nabla \cdot \left(\underline{\underline{\sigma}}^{\text{corr}} \nabla \Phi^\infty \right) - \int_\Gamma \langle \underline{\underline{\sigma}} \nabla \Phi^\infty, \mathbf{n} \rangle \right) \\ &\overset{\text{Gauß}}{=} l(v) + c \cdot \left(\int_\Gamma \langle \underline{\underline{\sigma}}^{\text{corr}} \nabla \Phi^\infty, \mathbf{n} \rangle - \int_\Gamma \langle \underline{\underline{\sigma}} \nabla \Phi^\infty, \mathbf{n} \rangle \right) \\ &= l(v) - c \int_\Gamma \langle \underline{\underline{\sigma}}^\infty \nabla \Phi^\infty, \mathbf{n} \rangle \\ &\overset{\text{Gauß}}{=} l(v) - c \left(\int_{\Omega'} \nabla \cdot \left(\underline{\underline{\sigma}}^\infty \nabla \Phi^\infty \right) - \int_{\partial K(x_0,\epsilon)} \langle \underline{\underline{\sigma}}^\infty \nabla \Phi^\infty, \mathbf{n} \rangle \right) \\ &= l(v). \end{aligned}$$

In the last step of the above equation, both integrals are zero: The volume integral is zero, because Φ^∞ defined in (3.12) or (3.13) is a solution of the homogeneous problem and $J^p(x) = 0$ for all $x \in \Omega'$. The surface integral is zero, because Φ^∞ is the potential for a dipole in the center of the spherical integration domain, and, when dividing the domain into two half-spheres, the surface integral over the one is exactly the negative of the other. $\square$

3.6. FE formulation and implementation issues. A numerical method is needed for the field simulation in a realistically shaped head volume conductor. We will use the FE method because of its ability to treat geometries of arbitrary shape and inhomogeneous and anisotropic material parameters. As a first step, we will use partial integration on the right-hand side of (3.14) (see (3.14), (3.15), and (3.16)):

$$l(v) = -\int_\Omega \langle \nabla v(x), \underline{\underline{\sigma}}^{\text{corr}}(x) \nabla \Phi^\infty(x) \rangle dx - \int_\Gamma \langle \underline{\underline{\sigma}}^\infty \nabla \Phi^\infty(x), \mathbf{n}(x) \rangle v(x) dx. \tag{3.17}$$

The linear space $H^1(\Omega)$ is discretized by the FE space

$$V_N := \operatorname{span}\{\varphi_i(x) \mid i = 1, \ldots, N\} \subset H^1(\Omega)$$

spanned by piecewise affine basis functions φ_i at nodes ξ_i, i.e., $\varphi_i(x) = 1$ for $x = \xi_i$ and $\varphi_j(x) = 0$ for all $j \neq i$. The singularity potential Φ^∞ can be projected into this FE space (required only in the smooth part $\Omega \setminus \Omega_\infty$):

$$\Phi^\infty(x) \approx \Phi_h^\infty(x) := \sum_{i=1}^N \varphi_i(x) u_i^\infty, \quad u_i^\infty := \Phi^\infty(\xi_i). \tag{3.18}$$

Now we seek coefficients u_j for the discrete approximation of $\Phi^{\text{corr}}(x) \approx \Phi_h^{\text{corr}}(x) := \sum_{j=1}^N \varphi_j(x) u_j$; i.e., we solve the problem

$$\text{find } u \in H^1(\Omega) \text{ so that } \forall v \in H^1(\Omega): \quad a(u,v) = l(v)$$

in the discrete space V_N:

$$\text{find } u \in V_N \text{ so that } \forall v \in V_N: \quad a(u,v) = l(v). \tag{3.19}$$

The coefficient vector $\underline{u} := (u_1, \ldots, u_N)$ solves the corresponding linear system

$$K\underline{u} = \underline{j}^\infty, \quad \underline{j}^\infty := -K^{\text{corr}}\underline{u}^\infty - S\underline{u}^\infty, \tag{3.20}$$

where $\underline{u}^\infty := (u_1^\infty, \ldots, u_N^\infty)$ is the coefficient vector for Φ_h^∞ and

$$K_{i,j} := \int_\Omega \langle \underline{\underline{\sigma}}(x)\nabla\varphi_i(x), \nabla\varphi_j(x)\rangle \, dx,$$

$$K_{i,j}^{\text{corr}} := \int_\Omega \langle \underline{\underline{\sigma}}^{\text{corr}}(x)\nabla\varphi_i(x), \nabla\varphi_j(x)\rangle \, dx,$$

$$S_{i,j} := \int_\Gamma \langle \underline{\underline{\sigma}}^\infty(x)\nabla\varphi_j(x), \mathbf{n}(x)\rangle\varphi_i(x) \, d_\Gamma x.$$

The computation of the matrix entries is simple, because the gradients of the basis functions are piecewise constant. We used the template C++ library COLSAMM described in detail in [8]. Additionally, the supports of the basis functions are small and local so that the number of entries in K, K^{corr}, S is $\mathcal{O}(N)$.

In the next section we will see that the L^2-error of the approximation

$$\varepsilon_N := \|\Phi_h^{\text{corr}} - \Phi^{\text{corr}}\|_{L^2(\Omega)}$$

behaves like $h^2 = N^{-2/3}$, so we have to use a finite dimensional but large space V_N. In order to solve the large linear system (3.20) for the correction potential, we apply an AMG-CG solver [13, 31]. For the special case of a homogeneous conductivity $\underline{\underline{\sigma}}^\infty$ in the source area (the cortex), it was shown in [32] that one can compute lead field bases for EEG and MEG which then strongly reduce the computational burden for the FE-based inverse problem in EEG and MEG.

3.7. Convergence analysis. For our FE approximation Φ_h^{corr}, we are interested in estimates of the form

$$||\Phi^{\text{corr}} - \Phi_h^{\text{corr}}|| \leq Ch^k \tag{3.21}$$

with the largest possible quantitative order k. h denotes the edge length of a finite element. In general, the order depends on the regularity of the solution, on the degree of the FE trial-functions, on the chosen Sobolev norm, and on the approximation properties of the triangulation to the geometry.

For a one-layer model with homogeneous conductivity, we have the following property.

THEOREM 3.8 (quantitative error estimate for one-layer model [14]). *Let us assume a sufficiently regular solution $\Phi^{\text{corr}} \in H^2(\Omega)$. For an appropriate triangulation (hexahedrization), linear (trilinear) FE trial-functions, and a continuous and elliptic bilinear form $a(\cdot,\cdot)$, we find a constant C_1 which is independent of Φ^{corr} and h with*

$$||\Phi^{\text{corr}} - \Phi_h^{\text{corr}}||_1 \leq C_1 h||\Phi^{\text{corr}}||_2.$$

The regularity assumption $\Phi^{\text{corr}} \in H^2(\Omega)$ is typically fulfilled because the boundary of the domain Ω is piecewise smooth.

LEMMA 3.9 (Aubin–Nitsche [14]). *Let us assume a sufficiently regular solution $\Phi^{\text{corr}} \in H^2(\Omega)$. For an appropriate triangulation (hexahedrization), linear (trilinear) FE trial-functions, and a continuous and elliptic bilinear form $a(\cdot,\cdot)$, we find a constant C_2 which is independent of Φ^{corr} and h with*

$$||\Phi^{\text{corr}} - \Phi_h^{\text{corr}}||_0 \leq C_2 h^2||\Phi^{\text{corr}}||_2.$$

For a multilayer model with different conductivities on each compartment, we can only assume $\Phi^{\mathrm{corr}} \in H^1(\Omega)$. Following Hackbusch [14], we can hope that the general error bounds $||\Phi^{\mathrm{corr}} - \Phi_h^{\mathrm{corr}}||_1 = \mathcal{O}(h)$ and $||\Phi^{\mathrm{corr}} - \Phi_h^{\mathrm{corr}}||_0 = \mathcal{O}(h^2)$ can be achieved by means of isoparametric, i.e., geometry conforming, finite elements.

With regard to our specific application, we can give a statement concerning the property of the constant C in (3.21), which will be of practical interest (see section 4).

LEMMA 3.10. *Let δ be the distance between the source position x_0 and the closest location of the next conductivity jump on $\partial\Omega^\infty$. If δ gets small, then the constant $C(\delta)$ in*

$$|l(v)| \leq C(\delta)||v||_{L_2(\Omega)} \quad \forall v \in H^1(\Omega),$$

with $l(v)$ from (3.17)*, is proportional to $\delta^{-5/2}$ ($c_1(\delta) \approx \delta^{-5/2}$).*

Proof. When defining $r := x - x_0$, we find $|\Delta\Phi^\infty| \approx 1/|r|^4$ and, with $\bar{\Omega} := \Omega \setminus \Omega^\infty$,

$$||\Delta\Phi^\infty||_{L_2(\bar{\Omega})} = \sqrt{\int_{\bar{\Omega}} (\Delta\Phi^\infty)^2\, dx} \approx \sqrt{\int_{|r|\geq\delta} 1/r^8 dr} \approx \sqrt{1/\delta^5} = \delta^{-5/2} =: c_1(\delta).$$

We then find constants $C(\delta)$ and c_2, so that

$$\begin{aligned}
|l(v)| &= \left| \int_\Omega \nabla \cdot \left(\underline{\underline{\sigma}}^{\mathrm{corr}} \nabla\Phi^\infty\right) v dx - \int_\Gamma \langle \underline{\underline{\sigma}} \nabla\Phi^\infty, \mathbf{n}\rangle v d\Gamma \right| \\
&\leq \int_\Omega \left|\nabla \cdot \left(\underline{\underline{\sigma}}^{\mathrm{corr}} \nabla\Phi^\infty\right) v\right| dx + c_2||v||_{L_2(\Omega)} \\
&\leq \sigma_{\max}^{\mathrm{corr}} \int_{\bar{\Omega}} ||\Delta\Phi^\infty||\ ||v||dx + c_2||v||_{L_2(\Omega)} \\
&\overset{\text{Hölder}}{\leq} \sigma_{\max}^{\mathrm{corr}} ||\Delta\Phi^\infty||_{L_2(\bar{\Omega})} ||v||_{L_2(\bar{\Omega})} + c_2||v||_{L_2(\Omega)} \\
&\leq \left(\sigma_{\max}^{\mathrm{corr}} c_1(\delta) + c_2\right) ||v||_{L_2(\Omega)} \leq C(\delta)||v||_{L_2(\Omega)}. \qquad \square
\end{aligned}$$

Lemma 3.10 has to be interpreted in the following way. If the source approaches a next conductivity jump, i.e., if δ goes to 0, then the constant for the upper estimation of the right-hand side functional l gets larger (with exponent 5/2). Because of the assumed H^2-regularity, we find [4]

$$||\Phi^{\mathrm{corr}} - \Phi_h^{\mathrm{corr}}||_0 \leq C_2 h^2 ||\Phi^{\mathrm{corr}}||_2 \leq C_2 h^2 ||l||_0 \leq C(\delta) C_2 h^2.$$

For sources close to the next conductivity jump (e.g., sources with high eccentricity; see section 4), we have to be aware of possibly larger numerical errors because of a strongly increasing constant $C(\delta)$.

4. Validation and numerical experiments.

4.1. Validation in multilayer sphere models.

4.1.1. Analytical solution. In [23], series expansion formulas were derived for a mathematical dipole in a multilayer sphere model, denoted now as "the analytical solution." A rough overview of the formulas will be given in this section. The model consists of shells S up to 1 with radii $r_S < r_{S-1} < \cdots < r_1$ and constant radial, $\sigma^{\mathrm{rad}}(r) = \sigma_j^{\mathrm{rad}} \in \mathbb{R}^+$, and constant tangential conductivity, $\sigma^{\mathrm{tang}}(r) = \sigma_j^{\mathrm{tang}} \in \mathbb{R}^+$, within each layer $r_{j+1} < r < r_j$. It is assumed that the source at position x_0 with radial coordinate $r_0 \in \mathbb{R}$ is in a more interior layer than the measurement electrode at position $x_e \in \mathbb{R}^3$ with radial coordinate $r_e = r_1 \in \mathbb{R}$. The spherical harmonics expansion for the mathematical dipole (3.8) was expressed in terms of the gradient of the monopole potential with respect to the source point, using an asymptotic approximation and an addition-subtraction method to speed up the series convergence [23]. This resulted in

$$\Phi(x_0, x_e) = \frac{1}{4\pi} \left\langle \mathbf{M}, S_0 \frac{x_e}{r_e} + (S_1 - \cos\omega_{0e} S_0) \frac{x_0}{r_0} \right\rangle$$

with ω_{0e} being the angular distance between source and electrode and with

$$S_0 = \frac{F_0}{r_0} \frac{\Lambda}{(1 - 2\Lambda\cos\omega_{0e} + \Lambda^2)^{3/2}} + \frac{1}{r_0} \sum_{n=1}^{\infty} \left\{(2n+1)R_n(r_0, r_e) - F_0\Lambda^n\right\} P_n'(\cos\omega_{0e}) \tag{4.1}$$

and

$$S_1 = F_1 \frac{\Lambda\cos\omega_{0e} - \Lambda^2}{(1 - 2\Lambda\cos\omega_{0e} + \Lambda^2)^{3/2}} + \sum_{n=1}^{\infty} \left\{(2n+1)R_n'(r_0, r_e) - F_1 n\Lambda^n\right\} P_n(\cos\omega_{0e}). \tag{4.2}$$

The coefficients R_n and their derivatives R_n' can be computed analytically and the derivative of the Legendre polynomial can be determined by means of a recursion formula. Refer to [23] for the derivation of the above series of differences and for the definition of F_0, F_1, and Λ.[1] Here, it is important only that the latter terms can be computed from the given radii and conductivities of layers between source and electrode and of the radial coordinate of the source and that they are independent of n. The computation of the series (4.1) and (4.2) are stopped after the k term if the following criterion is fulfilled:

$$\frac{t_k}{t_0} \le \upsilon, \qquad t_k := (2k+1)R_k' - F_1 k\Lambda^k. \tag{4.3}$$

In the following simulations, a value of 10^{-6} was chosen for υ. Using the asymptotic expansion, no more than 30 terms were then needed for the series computation for each electrode.

4.1.2. Model generation and error criteria. In source reconstruction, head modeling is generally based on segmented magnetic resonance (MR) data, where curved tissue boundaries have a stair-step representation. We therefore created a

[1] The following is a result of a discussion with J. C. de Munck: While constants in formulas (71) and (72) in the original paper [23] have to be flipped, our versions of S_0 and S_1 in (4.1) and (4.2) are correct.

three-compartment sphere model ($S = 3$ in section 4.1.1) in MR format with $1mm^3$ voxel resolution as a basis for our validation studies. Starting from the outside, the layers represent the compartments skin, skull, and brain with outer surfaces of radii $r_1 = 90$mm, $r_2 = 80$mm, and $r_3 = 70$mm, respectively. In the isotropic simulations, we chose conductivities of $\sigma_1 = 0.33$ S/m, $\sigma_2 = 0.0042$ S/m, and $\sigma_3 = 0.33$ S/m for the three compartments [27], while we chose $\sigma_2^{\text{rad}} = 0.0042$ S/m and $\sigma_2^{\text{tang}} = 0.042$ S/m for the simulations with a 1:10 anisotropic skull compartment [18].

Comparisons between the numeric and the analytic solutions were made for dipoles located on the y-axis at depths of 0% to 95% (in 1mm steps) of the inner layer (70mm radius) using both radial and tangential orientations. We defined *eccentricity* as the percent ratio of the distance between the source location and the model midpoint divided by the radius of the inner sphere. As reported in [18] and further explained in the discussion, the dipoles that are located in the cortex will have an eccentricity lower than 92%. Tangential sources were oriented in the $+z$-axis and radial dipoles in the $+y$-axis. The dipole moments were 1nAm. To achieve error measures which are independent of the specific choice of the sensor configuration, we distributed electrodes in a most regular way over a given sphere surface: we generated 134 electrode configurations on the surface of the outer sphere (90mm, surface-EEG *sEEG*) and under the skull (radius 70mm, internal-EEG *iEEG*).

We used two error criteria that are commonly used in source analysis [19, 2, 18, 27]—the correlation coefficient (CC) and the magnification factor (MAG). The CC is defined as

$$\text{CC} = \frac{\sum_{i=1}^{m} (\Phi_i^{\text{ana}} - \bar{\Phi}^{\text{ana}})(\Phi_i^{\text{num}} - \bar{\Phi}^{\text{num}})}{\sqrt{\sum_{i=1}^{m} \left(\Phi_i^{\text{ana}} - \bar{\Phi}^{\text{ana}}\right)^2} \sqrt{\sum_{i=1}^{m} \left(\Phi_i^{\text{num}} - \bar{\Phi}^{\text{num}}\right)^2}}, \tag{4.4}$$

where m denotes the number of sensors, $\underline{\Phi}_{\text{ana}} \in \mathbb{R}^m$ and $\underline{\Phi}_{\text{num}} \in \mathbb{R}^m$ the analytic or numeric solution vectors at the measurement positions, respectively, and $\bar{\Phi}^{\text{ana}}$ and $\bar{\Phi}^{\text{num}}$ the sample means. The CC is a measure for the topography error, driven primarily by changes in dipole location and orientation (minimal error: CC = 1). The second similarity measure, the MAG, is defined as

$$\text{MAG} = \frac{\sqrt{\sum_{i=1}^{m} (\Phi_i^{\text{num}})^2}}{\sqrt{\sum_{i=1}^{m} (\Phi_i^{\text{ana}})^2}}, \tag{4.5}$$

and indicates changes in the source strength (minimal error: MAG = 1).

4.1.3. Hexahedra mesh generation. Our hexahedra mesh generation approach takes advantage of the spatial discretization inherent in MR images. The voxel-based approach directly converts image voxels to eight-noded hexahedra elements, so that a $1mm^3$ FE hexahedra model (model `cube3130` in Table 4.1) exactly represents the segmented tissues. In order to keep the computation amount within a reasonable limit, our mesh generator allows a lower resolution with edge lengths of e times the edge length of a voxel-sized cube (e being an integer multiple). In this case, the generated cube is assigned the most frequent label of its e^3 interior voxels.

Table 4.1
Hexahedra models: Mesh description.

Model	Nodes	Elements	Mesh resolution (in mm)
cube3130	$3,130,496$	$3,053,617$	1.0 regular
cube398	$397,634$	$378,384$	2.0 regular
cube398ns	$397,634$	$378,384$	2.0 node-shift
cube52	$52,138$	$47,272$	4.0 regular

Table 4.2
Tetrahedra models: Mesh description. With increasing depth, the thinning distance was increased as indicated in the table for models tet57 *and* tet156.

Model	Nodes	Elements	Thinning	Erosions (in mm)		
			(mm)	skin	skull	brain
tet606	$605,959$	$3,680,234$	1.1	4×2.0	4×2.0	all 2.0
tet234	$234,314$	$1,412,813$	2.0	4×2.0	4×2.0	all 2.0
tet156	$156,074$	$930,175$	2.0-5.0	3.0, 4.0	3.0, 3.0, 2.0	2.0, 2.0, then 5.0
tet57	$57,033$	$328,511$	3.0-7.0	3.0, 4.0	3.0, 4.0	all 7.0

Material interfaces of regular hexahedra models are characterized by abrupt transitions and right angles. In [7], a node-shift approach was proposed for a biomechanical FE application in order to smooth the irregular boundaries, leading to a better representation of the interfaces between different tissue compartments. The node-shift hexahedra approach was used for mesh `cube398ns` in Table 4.1. The table summarizes the properties of all hexahedra models that we used for validation purposes in this study.

4.1.4. Tetrahedra mesh generation. For the tetrahedra meshing approach, we used the software CURRY [9] to create a surface-based tetrahedral tessellation of the segmented and auxiliary surfaces of the three-layer sphere model. The procedure exploits the Delaunay criterion, enabling the generation of compact and regular tetrahedra. In Table 4.2, we indicate the thinning-distance parameter, which is used for the computation of FE vertices on the segmented and auxiliary surfaces. Furthermore, the erosion parameters for defining intermediate auxiliary surfaces within each layer are shown. As an example, for model `tet156` in Table 4.2, we have used a thinning of 2mm for the compartments skin and skull and increased the thinning distance to maximally 5mm within the brain compartment. We furthermore used skin surface erosions of 3.0 and 4.0mm to generate auxiliary surfaces at 87 and 83mm for the skin compartment and auxiliary surfaces of 77, 74, and 72mm for the skull compartment before tetrahedra mesh generation.

4.1.5. Isotropic three-layer sphere modeling. Figure 4.1 plots CC and MAG for the total surface potentials at 134 sEEG measurement electrodes on the outer surface ($r_1 = 90$mm) for the different source eccentricities. The performance of the subtraction method is completely satisfying for model `cube3130` and `cube398ns`, with a CC of 0.999 or better and a MAG of 1.028 or better at all depths and for both source orientations. For high eccentricities, the errors begin to rise—a behavior which has also been observed in [27] in a regular 1mm hexahedra model. For the 2mm regular cube model `cube398`, we also get very satisfying CC results, while, due to the stair-step approximation of the compartment boundaries, we face about 10% MAG error over the whole range of eccentricities. This magnitude problem, which is a consequence of the rough geometry description, can be alleviated with the node-shift approach, where, with maximally 1.6% for model `cube398ns`, we achieve the smallest

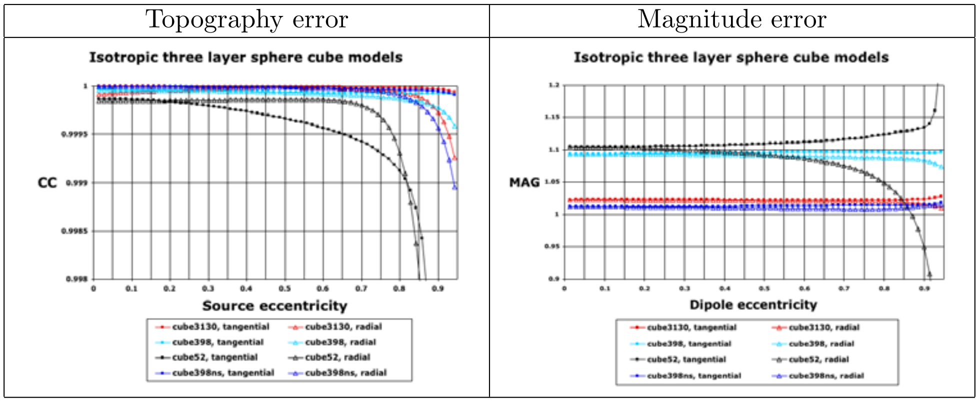

FIG. 4.1. *Isotropic three compartment sphere model: Numerical accuracy for hexahedra models at* 134 *sEEG electrodes.*

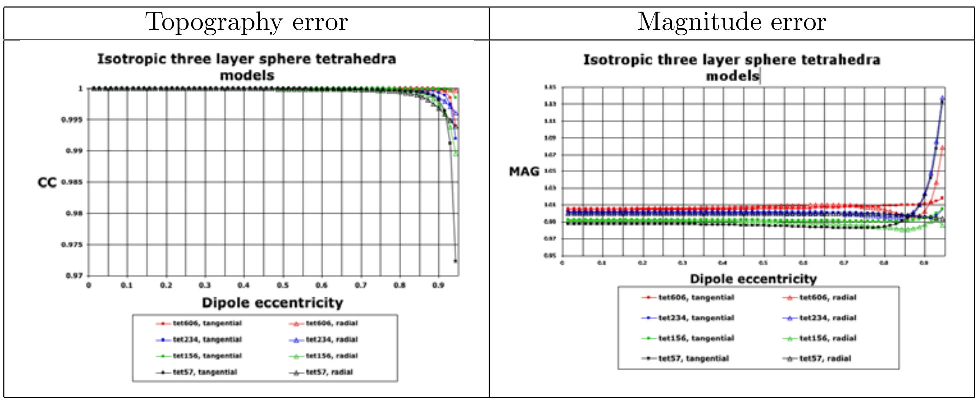

FIG. 4.2. *Isotropic three compartment sphere model: Numerical accuracy for tetrahedra models at* 134 *sEEG electrodes.*

MAG errors of all tested hexahedra models. Model `cube52` is too coarse to appropriately represent the volume conductor. Even if sufficient CC accuracies are achieved for eccentricities up to 90% and therefore for the vast majority of realistic source positions, the results for higher eccentricities fall below a CC of 0.99, and also the MAG is equipped with an error of up to 26%.

Figure 4.2 shows the sEEG ($r_1 = 90$mm) similarity measures CC and MAG for the tetrahedra models for the different source eccentricities. We observe larger topography errors and sharper declines at high eccentricities than for the best hexahedra models (note the different CC scalings in Figures 4.1 and 4.2), but with a CC of 0.99 or better, the performance of the subtraction method over the whole range of practically interesting eccentricities is still satisfying for most of the examined models. Even the coarsest model `tet57` gives sufficient CC accuracies for eccentricities up to 94%, but the CC then declines strongly below a value of 0.99 for the highest evaluated eccentricity. With regard to the potential magnitude, with a maximal MAG error of 1.9% over all eccentricities and for both source orientations, the best result is achieved with model `tet156`.

4.1.6. Three-layer sphere models with anisotropic skull compartment. The importance of well-defined skull conductivity tensor eigenvectors was already pointed out in [18]. For anisotropy modeling of the middle ("skull") compartment in a three-layer sphere model, the conductivity tensor eigenvector in a radial direction can be determined by means of normalizing the vector from an element barycenter to the midpoint of the sphere model, denoted now as the *optimal sphere procedure*. The vector product can then be used to define both tangential directions. With regard to a realistic head model, we also evaluated another procedure. We eroded the segmented outer surface of the middle "skull" compartment by half of the "skull's" thickness, strongly smoothed (important only in the case of a realistic head model) and triangulated it with an edge length of x mm (denoted now as the smooth surface model (SSM) *SSMx*). We then exploited the SSM surface normals for the definition of the radial tensor direction. Because the triangulated mesh is generated from a staircase-like surface, it is obvious that the edge length of the mesh should not be chosen too small. We evaluated CC and MAG in a model with 1 to 10 radial to tangential skull anisotropy when using SSM2, SSM5, SSM10, SSM20, and the optimal sphere procedure. In Figure 4.3, results are presented for SSM10, which, besides the optimal sphere procedure, led to the smallest errors. As the figure shows, the results are similar to the results in the isotropic volume conductor. Model `cube398ns` again overall performs best with a CC of more than 0.999 and a MAG of maximally 4.3%.

In a last examination, we plotted the exactness of the numerical approach versus the relative solver accuracy of the AMG-CG for the correction potential for different source eccentricities. The AMG-CG solver process was stopped if the relative error in the controllable $K_h C_h^{-1} K_h$-energy norm (with C_h^{-1} being one V-cycle of the AMG) was below the value indicated on the x-axis (for further information, see [31]). Errors at 134 sEEG (90mm) and at 134 iEEG (70mm) electrodes are shown in Figure 4.4. It can be observed that the higher the eccentricity of the source, the more important it is to accurately determine the correction potential. A relative solver accuracy of 10^{-4} was sufficient for the tested eccentricities; the solution exactness no longer increased with higher relative solver accuracies.

4.2. Validation in a realistic anisotropic head model. A three tissue realistic head model with compartments skin, skull, and brain and an isotropic voxel size of 1mm^3 was segmented from a T1- and proton-density-weighted MR dataset of a healthy 32 year old male subject. The bimodal MR approach allowed an improved modeling of the skullshape as described in detail in [34]. 71 electrodes were positioned on the model surface using the international 10/20 system.

The model was then meshed using the different mesh generation approaches described in sections 4.1.3 and 4.1.4. Table 4.3 summarizes the parametrization of the different meshes. For hexahedra model `cube386ns`, a node-shift was used at the compartment boundaries skin, outer skull, and inner skull. For tetrahedra model `tet265`, the following surfaces were included in the meshing procedure as also indicated in Table 4.3: skin, 2mm eroded skin, outer skull, 2mm eroded outer skull, inner skull, and continuous 2mm erosions into the depths. Following the results of section 4.1.6, a strongly smoothed triangular mesh with 10mm edge length (SSM10) from a 3mm eroded outer skull surface was used for the modeling of 1 to 10 quasi-radial to quasi-tangential skull conductivity anisotropy. While, in a multilayer sphere model, CC and MAG errors for the numerically computed potential distribution serve for indirect validation of the modeled skull conductivity tensors, those error metrics are not available in a realistic head model. It is therefore important to at least visualize the

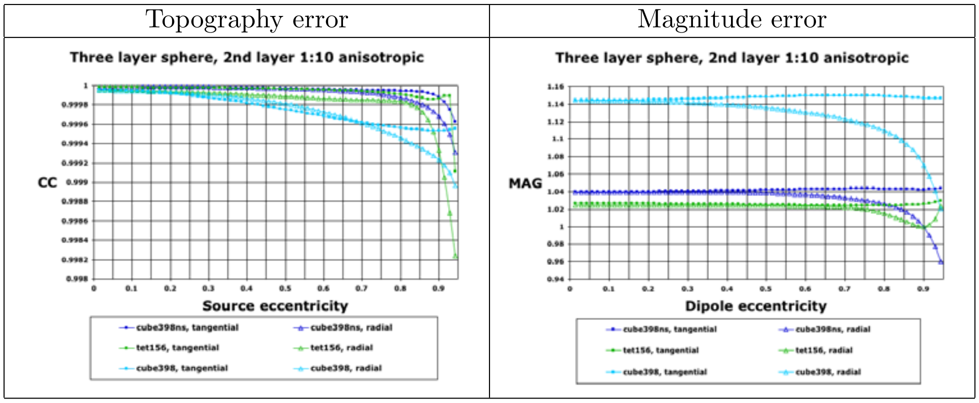

FIG. 4.3. *Three compartment sphere model with a* 1:10 *anisotropic middle ("skull") layer: Numerical accuracy at* 134 *sEEG electrodes for hexahedra models* cube398ns *and* cube398 *and tetrahedra model* tet156 *when using SSM*10 *for the determination of the "skull" conductivity tensor eigenvectors.*

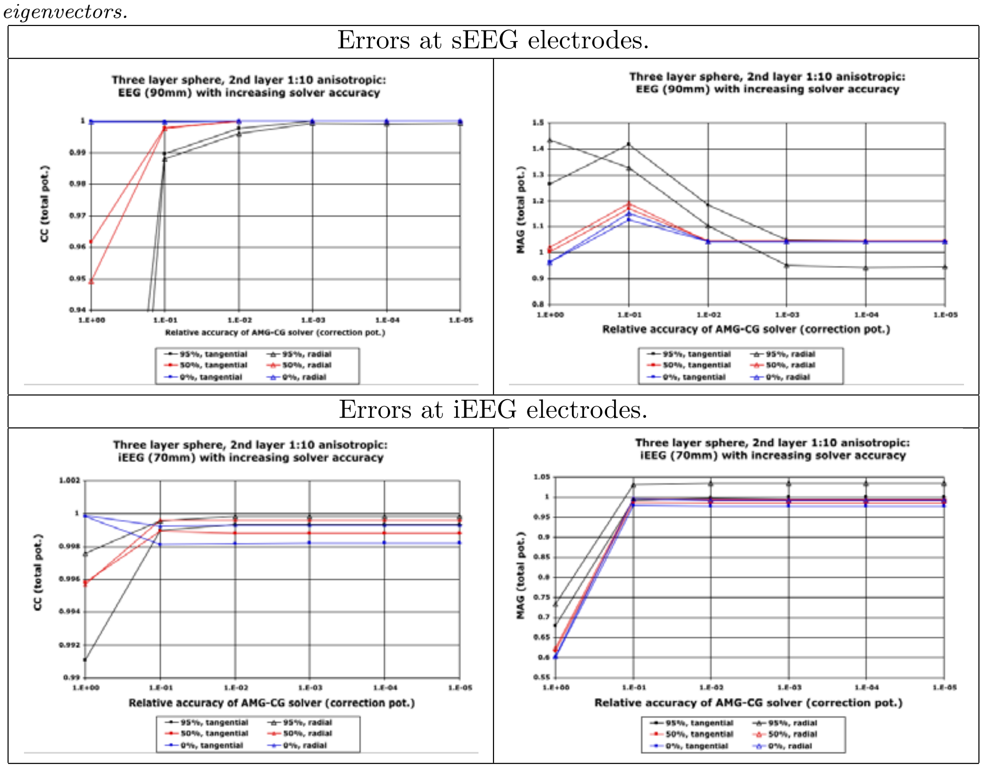

FIG. 4.4. *Three compartment sphere model with a* 1:10 *anisotropic middle ("skull") layer, FE model* cube398ns*: CC (left) and MAG (right) error at* 134 *sEEG electrodes on "skin" surface* $r_1 = 90mm$ *(top) and at* 134 *iEEG electrodes on "inner skull" surface* $r_3 = 70mm$ *(bottom) with increasing AMG-CG relative solver accuracy for sources at* 95%*,* 50%*, and* 0% *eccentricity.*

tensors in order to check for correct skull tensor registration and eigenvector directions. Figure 4.5 shows the anisotropic conductivity tensor ellipsoids of the human skull compartment with the underlying T1-MRI. The figure shows that the ellipsoids are oblate with minor axis in a quasi-radial direction through the skull compartment.

TABLE 4.3
Realistically shaped three compartment head models: Mesh description.

Model	Nodes	Elements	Thinning	Resolution (in mm)		
			(in mm)	skin	skull	brain
cube386ns	385,901	366,043	2.0	2.0ns	2.0ns	2.0ns
cube386	385,901	366,043	2.0	2.0	2.0	2.0
tet265	265,313	1,620,794	1.8	2.0, rest	2.0, rest	all 2.0

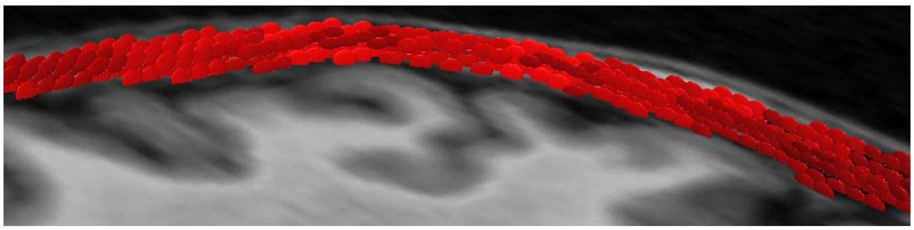

FIG. 4.5. 1:10 *(Quasi-radial to quasi-tangential) anisotropic conductivity tensor ellipsoids of the human skull compartment when using SSM*10 *with underlying T*1*-MRI. Visualization, carried out using BioPSE* [3]*, is important to validate if the ellipsoids are oblate with minor axis in a quasi-radial direction through the skull compartment.*

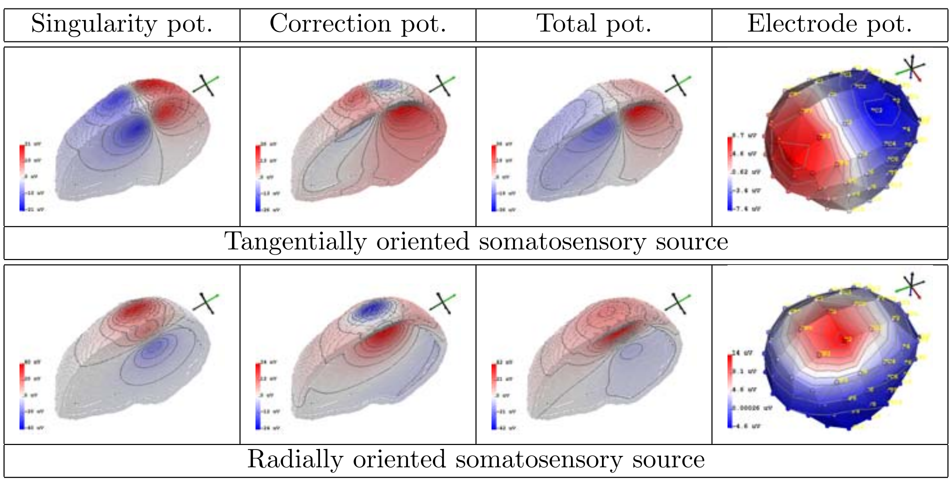

FIG. 4.6. *Realistically shaped head model* cube386ns *with* 1 *to* 10 *quasi-radial to quasi-tangential anisotropic skull compartment: Visualization results for the singularity potential, the correction potential, and the total potential in the volume conductor and at the* 71 *surface electrodes for a quasi-tangentially and a quasi-radially oriented source in the somatosensory cortex. Visualization was carried out using BioPSE* [3].

In a first study, we computed the singularity, the correction, and the total potential in model `cube386ns` for a radially and a tangentially oriented source at an eccentric location in the somatosensory cortex. Figure 4.6 presents the visualization results.

We then compared the results for the different mesh generation techniques. As the node-shifted hexahedra model showed the best accuracies in the three-layer sphere validations, we chose this model as a reference. In Table 4.4 we present the differences from the solutions in other models. With a CC above 0.998 and a maximal MAG of 6.9%, the differences among the three models are fairly small. Again, the regular

TABLE 4.4

Realistic three compartment head models, comparison of results using different meshing techniques: Differences between the forward computations at 71 *electrodes using the subtraction approach for an eccentric source in the somatosensory cortex. The reference results are the ones in the node-shifted* 2mm *cube model, because this model performed best in the sphere validation studies.*

	Differences for somatosensory source			
	Tangential		Radial	
Model	CC	MAG	CC	MAG
cube386	0.9989	1.0643	0.9982	1.0689
tet265	0.9997	1.0009	0.9997	0.9849

TABLE 4.5

Realistic volume conductor modeling: Computation times (see (3.20)*) and maximal memory usage.* (a) *Has to be done once per head geometry.* (b) *Following* [32]*, this has to be done* max(nb_sour,nb_sens) *times.* (c) *Has to be done* nb_sour *times.*

Model	Computation times (in sec.)					Max. mem.
	(a)			(b)	(c)	
	K, K^{corr}	S	AMG setup	$K\underline{u} = \underline{j}^{\infty}$	$\underline{u}^{\infty}$	
cube386ns	17.2	14.8	16.6	6.2	0.3	795MB
tet265	28.1	40.3	8.2	3.6	0.14	675MB

2mm hexahedra model `cube386` exhibits the highest magnitude difference because of its rough approximation of the interfaces.

In a final study, the computation times and the maximal amount of memory in our current implementation were measured for models `cube386ns` and `tet265` (Table 4.5). In Table 4.5, `nb_sour` is the number of sources and `nb_sens` the number of measurement sensors. The experiment was run on a Linux-PC with an Intel Pentium 4 processor (3GHz). The computation time for S contains the times for finding the source element (determination of $\underline{\underline{\sigma}}^{\infty}$), for determining surface finite elements, and for computing the integration over all surface elements. For the determination of a surface element, the property was used that it has at least one face that is not a face to any other element. A list structure was therefore built up where, for each mesh node, all neighboring finite elements were administered. A face of an element is then a face of the surface of the volume conductor if the intersection of the finite elements of all face nodes is just a single finite element. For the AMG-CG, the relative solver accuracy was chosen to be 10^{-4}. The multiplication of a sparse matrix times a fully populated vector as for $-(K^{\text{corr}} + S)\underline{u}^{\infty}$ in (3.20) can be neglected (0.03 sec. for `cube386ns` and 0.02 sec. for `tet265`).

With regard to the inverse problem, the computation of K, K^{corr}, and S and the setup of the AMG preconditioner have to be carried out only once per head geometry. `nb_sour` is generally by far larger than `nb_sens` and the lead-field basis approach should be applied [32]. It reduces the necessary computation to mainly `nb_sens` times the solution of an equation system of the form $K\underline{o} = \underline{p}$ with a fully populated right-hand side vector $\underline{p}$ (Table 4.5 (b)) to built the lead-field basis B^{∞}_{eeg}, a fully populated matrix with `nb_sens`-1 rows and N columns. Each forward computation then involves only the computation of $\underline{u}^{\infty}$ (Table 4.5 (c)) and its multiplication with the lead-field basis, i.e., $B^{\infty}_{eeg}\underline{u}^{\infty}$ (0.68 sec. for model `cube386ns` and 0.47 sec. for model `tet265`).

5. Discussion. In this paper, we presented the theory of the subtraction approach to model a point dipole in the finite element (FE) method based electroencephalography (EEG) source reconstruction for isotropic and anisotropic volume conductors. We proved existence and uniqueness of a weak solution for the potential in zero-mean function space. We embedded our numerical approach for the correction potential in the general FE convergence theory and showed that the constant in the FE convergence proof largely depends on the distance of the source to the next conductivity jump. Therefore, higher FE trial-functions or, if linear trial-functions are used, a higher integration order and/or multiple element layers are needed between the source and the next conductivity jump; otherwise one would have to be aware of probably larger and unacceptable numerical errors. Since the magnetoencephalography (MEG) forward problem is also based on the computed electric potential (see, e.g., [32]), our results are also applicable to MEG source reconstruction. Besides the presented clear mathematical theory, a further important advantage of the subtraction approach is the fact that, as soon as the corresponding singularity potential function is known, the implementation of any other primary source model is straightforward. Our theoretical statements are thus valid for any such primary source model. Despite the fact that the bioelectric primary current sources in EEG and MEG are naturally continuous throughout the cortical tissue (which would also reduce numerical errors), they are usually modeled with a mathematical point dipole [22, 24].

The main aim of our study was therefore to validate the subtraction approach for the usual model, i.e., a point current dipole in a three-layer sphere with piecewise homogeneous conductivity, for which series expansion formulas are available [23]. As a measure of similarity, we used two common criteria [19, 6]: The first and by far more important one, the correlation coefficient (CC), indicates defects in the topography of the potential distribution and therefore, with regard to the inverse solution, defects in the localization and orientation of the sources. Another frequently used topography error measure is the relative difference measure (RDM), introduced in [19]. For the used zero-mean data, CC and RDM can be related through $RDM = \sqrt{2(1 - CC)}$, and a CC above 0.99 has been associated with a localization error of no more than 1mm, while a CC of 0.98 led to dipole localization errors of 5–8mm on average, maximally 1.5cm [27]. In source localization practice, an accuracy of 1mm is more than satisfactory because main limitations are then due to other sources of error such as the limited data signal-to-noise ratio, segmentation errors, inaccuracies in the determination of the conductivities, etc. The second error measure, the magnification factor (MAG), indicates changes in the potential amplitude and thus in the source strength. In our sphere validation studies, we placed dipole sources at positions along the y-axes from the center of the model in 1mm steps toward the inner skull surface up to an eccentricity of 95%. As reported in [18], the dipoles that are located in the cortex will have an eccentricity lower than 92%. The reasons are that first, compartments such as the arachnoid cavity, the subdural cavity, and the dura mater, whose conductivities are generally approximated with the conductivity of the brain compartment [5, 6, 18], are located between the cortex and the inner skull surface, and second, the dipoles are located some millimeters below the cortical surface (see, e.g., [24]). Our validation has been carried out for two different classes of elements, FE hexahedra and tetrahedra. In the class of hexahedra, we examined regular and geometry-conforming node-shifted elements.

With a CC of 0.998 or better over the whole range of realistic eccentricities at the 134 regularly distributed surface or depths electrodes, we achieved completely satisfying results for all tested 1mm and 2mm isotropic and anisotropic hexahedra models. The node-shift reduced the maximal MAG error for the 2mm anisotropic model from about 15% to only 4.3%. For the tetrahedra models, we observed larger topography errors and sharper declines at high eccentricities, but with minimal CC values of 0.99 for the whole range of tested eccentricities, the three models with higher resolutions still perform sufficiently well. In summary, with regard to the accuracy and computational complexity, the 2mm node-shifted hexahedra model achieved the best results. We found that with increasing eccentricity, a higher relative solver accuracy is needed for the correction potential, a relative accuracy of 10^{-4} being sufficient for the used AMG-CG approach. Using eccentric sources in human somatosensory cortex in a realistically shaped three-compartment head model with anisotropic skull compartment, we computed the potential distributions within the volume conductor. Validation was carried out by visually inspecting and comparing the results when using the different meshing techniques.

It is well known (and, in this paper, we have given a theoretical reasoning for this fact), that with increasing eccentricity, the numerical accuracy in sphere model validations decreases, especially with regard to radially oriented dipoles [2, 5, 18]. This is the case not only for the subtraction approach in FE modeling, but also for the direct approach in FE modeling [36, 6, 16, 21] and in boundary element modeling (see, e.g., [10]). In [2, 5, 18], coarser tetrahedra mesh resolutions were considered so that larger numerical errors resulted with CCs below 0.98 for radial dipoles with eccentricities above 90%. In [2, 5], local mesh refinement was used to achieve acceptable results for all realistic eccentricities. Nevertheless, with regard to the inverse problem, the setup of source-location dependent locally refined meshes is difficult to implement and time-consuming to compute and thus might not be practical for an inverse source analysis. We propose to use a single mesh that is sufficiently fine and that resolves the geometry. For the efficient solution of the inverse problem the lead-field bases concept can then be used [32]. As shown in [31], the amount of work for the computation of the lead-field bases can be reduced by means of an AMG-CG solver.

In subsequent studies, we will perform profound comparisons of the subtraction approach with the diverse direct methods [36, 6, 30, 27, 21] for the computation of the EEG and MEG inverse problems both in anisotropic sphere models as well as in realistic anisotropic head volume conductors in order to gain deeper insight into the advantages and disadvantages of our new approach. A first comparison of the subtraction method with a direct potential approach using partial integration [30, 21] and with a direct potential approach using the principle of Saint Venant [6] can be found in [35]. As shown in the theory section of this paper, the subtraction approach enables the inclusion of local anisotropy in the source area. It is well known that the human cortex is about 1:2 anisotropic and that both EEG and MEG forward problems are especially sensitive toward local conductivity changes [16, 33]. As a final note, instead of trying to reduce numerical errors for the probably "over-singular" mathematical point dipole, it is important to reconsider other and especially smoother source models, taking into account the fact that the primary current sources are continuous throughout the cortical tissue [28, 24]. This is where the FE-based subtraction method might provide a further important contribution to EEG and MEG source analyses.

Acknowledgments. The authors would like to thank U. Rüde, C. Pantev, S. Börm, A. Anwander, R. S. MacLeod, and C. R. Johnson for their support and the many important and helpful comments. We are especially grateful to J. C. de Munck for providing his software for the analytical solution and for his quick responses whenever needed and to the referees and the associate editor for improving our manuscript.

REFERENCES

[1] K. A. Awada, D. R. Jackson, J. T. Williams, D. R. Wilton, S. B. Baumann, and A. C. Papanicolaou, *Computational aspects of finite element modeling in EEG source localization*, IEEE Trans. Biomed. Engrg., 44 (1997), pp. 736–751.

[2] O. Bertrand, M. Thévenet, and F. Perrin, *3D finite element method in brain electrical activity studies*, in Biomagnetic Localization and 3D Modeling, J. Nenonen, H. M. Rajala, and T. Katila, eds., Tech. rep., Department of Technical Physics, Helsinki University of Technology, Otaniem, Finland, 1991, pp. 154–171.

[3] BioPSE, *Problem Solving Environment for Modeling, Simulation, and Visualization of Bioelectric Fields*, Scientific Computing and Imaging Institute (SCI), Salt Lake City, UT, 2002, http://software.sci.utah.edu/biopse.html.

[4] D. Braess, *Finite Elements: Theory, Fast Solvers and Applications in Solid Mechanics*, Cambridge University Press, Cambridge, UK, 2001.

[5] S. P. van den Broek, *Volume Conduction Effects in EEG and MEG*, Proefschrift, Universiteit Twente, Enschede, The Netherlands, 1997.

[6] H. Buchner, G. Knoll, M. Fuchs, A. Rienäcker, R. Beckmann, M. Wagner, J. Silny, and J. Pesch, *Inverse localization of electric dipole current sources in finite element models of the human head*, Electroenc. Clin. Neurophysiol., 102 (1997), pp. 267–278.

[7] D. Camacho, R. Hopper, G. Lin, and B. Myers, *An improved method for finite element mesh generation of geometrically complex structures with application to the skullbase*, J. Biomech., 30 (1997), pp. 1067–1070.

[8] J. Härdtlein and C. Pflaum, *Efficient and user-friendly computation of local stiffness matrices*, in Frontiers in Simulation, Simulationstechnique, 18th Symposium, Erlangen, 2005, pp. 748–753.

[9] Compumedics Neuroscan, *Current Reconstruction and Imaging (CURRY), Version* 4.6, Compumedics, El Paso, TX, http://www.neuro.com.

[10] M. Fuchs, R. Drenckhahn, H. A. Wischmann, and M. Wagner, *An improved boundary element method for realistical volume conductor modeling*, IEEE Trans. Biomed. Engrg., 45 (1998), pp. 980–997.

[11] N. G. Gencer and C. E. Acar, *Sensitivity of EEG and MEG measurements to tissue conductivity*, Phys. Med. Biol., 49 (2004), pp. 701–717.

[12] M. Gnewuch and S. A. Sauter, *Boundary Integral Equations for Second Order Elliptic Boundary Value Problems*, preprint 55, MPI for Mathematics in the Sciences, Leipzig, Germany, 1999.

[13] G. Haase, M. Kuhn, and S. Reitzinger, *Parallel algebraic multigrid methods on distributed memory computers*, SIAM J. Sci. Comput., 24 (2002), pp. 410–427.

[14] W. Hackbusch, *Elliptic Differential Equations. Theory and Numerical Treatment*, Springer-Verlag, Berlin, 1992.

[15] H. Hallez, B. Vanrumste, P. Van Hese, Y. D'Asseler, I. Lemahieu, and R. Van de Walle, *A finite difference method with reciprocity used to incorporate anisotropy in electroencephalogram dipole source localization*, Phys. Med. Biol., 50 (2005), pp. 3787–3806.

[16] J. Haueisen, C. Ramon, H. Brauer, and H. Nowak, *The influence of local conductivity changes on MEG and EEG*, Biomedizinische Technik, 45 (1999), pp. 211–214.

[17] J. Haueisen, D. S. Tuch, C. Ramon, P. H. Schimpf, V. J. Wedeen, J. S. George, and J. W. Belliveau, *The influence of brain tissue anisotropy on human EEG and MEG*, NeuroImage, 15 (2002), pp. 159–166.

[18] G. Marin, C. Guerin, S. Baillet, L. Garnero, and G. Meunier, *Influence of skull anisotropy for the forward and inverse problem in EEG: Simulation studies using the FEM on realistic head models*, Human Brain Mapping, 6 (1998), pp. 250–269.

[19] J. W. H. Meijs, O. W. Weier, M. J. Peters, and A. van Oosterom, *On the numerical accuracy of the boundary element method*, IEEE Trans. Biomed. Engrg., 16 (1989), pp. 1038–1049.

[20] M. Mertens and B. Lütkenhöner, *Efficient neuromagnetic determination of landmarks in the somatosensory cortex*, Clinical Neurophysiol., 111 (2000), pp. 1478–1487.

[21] M. Mohr, *Simulation of Bioelectric Fields: The Forward and Inverse Problem of Electroencephalographic Source Analysis*, Ph.D. thesis, Friedrich-Alexander-Universität Erlangen-Nürnberg, Arbeitsberichte des Instituts für Informatik, Band 37 (6), 2004.

[22] J. C. de Munck, B. W. van Dijk, and H. Spekreijse, *Mathematical dipoles are adequate to describe realistic generators of human brain activity*, IEEE Trans. Biomed. Engrg., 35 (1988), pp. 960–966.

[23] J. C. de Munck and M. Peters, *A fast method to compute the potential in the multisphere model*, IEEE Trans. Biomed. Engrg., 40 (1993), pp. 1166–1174.

[24] S. Murakami and Y. C. Okada, *Contributions of principal neocortical neurons to magnetoencephalography and electroencephalography signals*, J. Physiol., 575 (2006), pp. 925–936.

[25] C. Pantev, M. Hoke, B. Lütkenhöner, and K. Lehnertz, *Tonotopic organization of the auditory cortex: Pitch versus frequency representation*, Science, 246 (1989), pp. 486–488.

[26] J. Sarvas, *Basic mathematical and electromagnetic concepts of the biomagnetic inverse problem*, Phys. Med. Biol., 32 (1987), pp. 11–22.

[27] P. H. Schimpf, C. R. Ramon, and J. Haueisen, *Dipole models for the EEG and MEG*, IEEE Trans. Biomed. Engrg., 49 (2002), pp. 409–418.

[28] O. Tanzer, S. Järvenpää, J. Nenonen, and E. Somersalo, *Representation of bioelectric current sources using Whitney elements in finite element method*, Phys. Med. Biol., 50 (2005), pp. 3023–3039.

[29] T. D. Waberski, H. Buchner, K. Lehnertz, A. Hufnagel, M. Fuchs, R. Beckmann, and A. Rienäcker, *The properties of source localization of epileptiform activity using advanced headmodelling and source reconstruction*, Brain Topography, 10 (1998), pp. 283–290.

[30] D. Weinstein, L. Zhukov, and C. Johnson, *Lead-field bases for electroencephalography source imaging*, Annals of Biomed. Engrg., 28 (2000), pp. 1059–1066.

[31] C. H. Wolters, M. Kuhn, A. Anwander, and S. Reitzinger, *A parallel algebraic multigrid solver for finite element method based source localization in the human brain*, Comput. Vis. Sci., 5 (2002), pp. 165–177.

[32] C. H. Wolters, L. Grasedyck, and W. Hackbusch, *Efficient computation of lead field bases and influence matrix for the FEM-based EEG and MEG inverse problem*, Inverse Problems, 20 (2004), pp. 1099–1116.

[33] C. H. Wolters, A. Anwander, X. Tricoche, S. Lew, and C. R. Johnson, *Influence of local and remote white matter conductivity anisotropy for a thalamic source on EEG/MEG field and return current computation*, Int. J. Bioelectromag., 1 (2005), pp. 203–206.

[34] C. H. Wolters, A. Anwander, D. Weinstein, M. Koch, X. Tricoche, and R. MacLeod, *Influence of tissue conductivity anisotropy on EEG/MEG field and return current computation in a realistic head model: A simulation and visualization study using high-resolution finite element modeling*, NeuroImage, 30 (2006), pp. 813–826.

[35] C. H. Wolters, H. Köstler, C. Möller, J. Härdtlein, and A. Anwander, *Numerical approaches for dipole modeling in finite element method based source analysis*, in International Congress Series 1300, Elsevier Science, Amsterdam, The Netherlands, 2007, pp. 189–192.

[36] Y. Yan, P. L. Nunez, and R. T. Hart, *Finite-element model of the human head: Scalp potentials due to dipole sources*, Med. Biol. Engrg. Comput., 29 (1991), pp. 475–481.

2.2 EEG and MEG transfer matrix approach: Theory

Efficient Computation of Lead Field Bases and Influence Matrix for the FEM-based EEG and MEG Inverse Problem
Wolters, C.H., Grasedyck, L. and Hackbusch, W., *Inverse Problems*, Vol.20, No.4, pp. 1116–1099, 2004.

Corresponding author: C.H. Wolters

Institute of Physics Publishing | Inverse Problems

Inverse Problems **20** (2004) 1099–1116 PII: S0266-5611(04)71929-2

Efficient computation of lead field bases and influence matrix for the FEM-based EEG and MEG inverse problem

C H Wolters[1,2,3], L Grasedyck[2] and W Hackbusch[2]

[1] Scientific Computing and Imaging Institute, University of Utah, 50 S Central Campus Dr., Salt Lake City, UT 84112, USA
[2] Max Planck Institute for Mathematics in the Sciences, Inselstr. 22-26, 04103 Leipzig, Germany
[3] Max Planck Institute for Human Cognitive and Brain Sciences, Stephanstr. 1a, 04103 Leipzig, Germany

E-mail: wolters@sci.utah.edu, lgr@mis.mpg.de and wh@mis.mpg.de

Received 11 November 2003
Published 21 May 2004
Online at stacks.iop.org/IP/20/1099
DOI: 10.1088/0266-5611/20/4/007

Abstract

The inverse problem in electro- and magneto-encephalography (EEG/MEG) aims at reconstructing the underlying current distribution in the human brain using potential differences and/or magnetic fluxes that are measured non-invasively directly, or at a close distance, from the head surface. The simulation of EEG and MEG fields for a given dipolar source in the brain using a volume-conduction model of the head is called the forward problem. The finite element (FE) method, used for the forward problem, is able to realistically model tissue conductivity inhomogeneities and anisotropies, which is crucial for an accurate reconstruction of the current distribution. So far, the computational complexity is quite large when using the necessary high resolution FE models. In this paper we will extend the concept of the EEG lead field basis to the MEG and present algorithms for their efficient computation. Exploiting the fact that the number of sensors is generally much smaller than the number of reasonable dipolar sources, our lead field approach will speed up the state-of-the-art forward approach by a factor of more than 100 for a realistic choice of the number of sensors and sources. Our approaches can be applied to inverse reconstruction algorithms in both continuous and discrete source parameter space for EEG and MEG. In combination with algebraic multigrid solvers, the presented approach leads to a highly efficient solution of FE-based source reconstruction problems.

1. Introduction

It is common practice in cognitive research and in clinical routine and research to reconstruct current sources in the human brain by means of non-invasive field measurements outside the head domain. The activity that is measured in EEG and MEG is the result of movements of ions, the so-called *primary currents*, within activated regions in the cortex sheet of the human brain. The primary current can be modelled mathematically by means of a *current dipole* [1–5]. The current dipole causes Ohmic *return currents* to flow through the surrounding medium. The EEG measures the potential differences from the return currents at the scalp surface, whereas the MEG measures the magnetic flux of both primary and return currents. The reconstruction of the dipole sources is called the *inverse problem* of EEG/MEG. Its solution requires the repeated simulation of the field distribution in the head for a given dipole in the brain, the so-called *forward problem*. One of the major advantages of EEG and MEG source reconstruction over other brain imaging techniques such as positron emission tomography (PET) or functional magnetic resonance imaging (fMRI) is its high temporal resolution.

For the forward problem, the volume conductor head has to be modelled. It is known that the head tissue compartments scalp, skull, cerebro-spinal fluid, brain grey matter and white matter have different conductivities and that the layers skull and white matter are anisotropic conductors [6–9]. Different numerical approaches for the forward problem have been used such as multi-layer sphere [10], boundary element (BE) [11–13] and finite element (FE) [4, 14–18] head modelling, where only the FE method is able to treat both realistic geometries and inhomogeneous and anisotropic material parameters. In most cases, magnetic resonance images (MRI) are exploited for the construction of BE and FE head models.

Figure 1 [18] shows an axial cut through a five tissue tetrahedra FE head model with 147 287 nodes and 892 115 elements. The tetrahedra of the layers scalp (light brown), skull (green), cerebro-spinal fluid (light blue), brain grey matter (dark blue) and white matter (yellow) are indicated with different colours. The model was generated by means of a bimodal T1/PD-weighted MRI registration and segmentation approach [18, section 1] followed by a surface-based Delaunay tetrahedrization [18, section 4.7.3]. It is generally assumed that the weak volume currents outside the skull and far away from the EEG and MEG sensors have a negligible influence on the measurements. Therefore, the parts of the head mask lying outside a dilated outer skull surface mask have been cut away when generating the presented volume conductor model. In figure 2 [18], the white matter conductivity anisotropy is shown on the underlying T1-MRI by means of tensor ellipsoids (red) in the barycentres of the white matter finite elements (not shown in the figure).

The influence of skull and white matter conductivity anisotropy on the EEG/MEG forward problem was studied in realistic FE models in [17–20, 21]. In [15, 18, 21, 22], the sensitivity of the EEG inverse problem towards skull conductivity anisotropy was examined. The sensitivity of source reconstruction methods on realistic white matter anisotropy for both EEG and MEG was studied in [18, 22]. In those studies it has been shown that an exact modelling of tissue conductivity inhomogeneity and anisotropy is crucial for an accurate reconstruction of the sources.

An important question is how to handle the computational complexity of FE-modelling with regard to the EEG/MEG inverse problem. It is the state-of-the-art approach for the EEG/MEG inverse methods to solve a forward problem for each possible dipolar source [4, 10–13, 17, 23]. For the FE method, in general, iterative solvers such as the successive over-relaxation (SOR) or the preconditioned conjugate gradient (CG) method with preconditioners such as Jacobi (Jacobi-CG) or incomplete Cholesky (IC-CG) have been used (see, e.g., [4]). In the last few years, algebraic multigrid (AMG) solvers have been developed (see, e.g., [24, 25]).

For the considered application, it was shown in [26] that the AMG, used as a preconditioner for the CG method, is more efficient than IC with or without threshold-techniques. In [27], the AMG solver was found to be superior to an SOR method and to a symmetric SOR preconditioned CG method in finite difference discretizations of the volume conductor. A parallel AMG–CG approach for the forward problem in source localization has been used in [18, 20, 23]. When comparing the parallel AMG–CG on the anisotropic head model shown in figures 1 and 2 with a standard Jacobi-CG on a single processor, speed-up factors of about 80 have been achieved, 10 through multigrid preconditioning and 8 through parallelization on 8 processors [18, 20, 23]. Still, the repeated solution of such a system with a constant geometry matrix for thousands of right-hand sides (the sources) is the major time consuming part within the inverse localization process and limits the resolution of the models.

A further very efficient concept for the reduction of the computational complexity has been described, the concept of reciprocity ([16, 28–30] and [18 section 6.3]). The theory of reciprocity was already introduced in 1853 by [28] and was intensively studied for both the electric and the magnetic cases in [29 sections 11, 12]. The reciprocity theorem for the electric case states that the field of the so-called *lead vectors* is the same as the current field raised by feeding a reciprocal current to the lead [29, section 11.6.3]. The concept allows us to switch the role of the sensors with the dipole locations. For the FE-based EEG source reconstruction, it was shown in [16] how to use this principle for the efficient computation of a so-called *node-oriented lead field basis*, a matrix with 'number sensors' rows and 'number FE nodes' columns. This matrix can then be exploited within the EEG inverse problem. In [30], reciprocity was used for the efficient solution of the EEG inverse problem when using the finite difference method for the forward problem. The application of reciprocity to MEG is nontrivial and has been studied in [31], where the *magnetic lead field theorem* was proved. Nevertheless, as far as we know, it is not yet clear how to efficiently compute the lead field basis for the MEG in combination with the FE method for the forward problem.

In this paper, we will simply apply the mathematical law of associativity with respect to the matrix multiplication. Then, for each head model, we only have to solve 'number of EEG/MEG sensors' times a large sparse FE system of equations in order to compute the lead field basis for both EEG and MEG. This set-up can be computed efficiently using the parallel AMG–CG solver. Each forward solution is then reduced to the multiplication of the lead field basis to a FE right-hand side vector.

The paper is organized as follows: in the next section we describe the electric and the magnetic forward problems. In section 3, FE discretization aspects are discussed. Section 4 contains a brief description of inverse methods on discrete [12, 32–37] and on continuous [11, 18, 38] source parameter space. In section 5, we estimate the complexity of the state-of-the-art approach to the EEG/MEG inverse problem. Section 6 contains our new approach resulting in two algorithms that solve the EEG and MEG inverse problem. In section 7, we will discuss the applicability of the mathematical dipole model in combination with the subtraction method in the context of our new approach. Finally, we conclude and give some perspectives in section 8.

2. Forward problem formulation

2.1. The Maxwell equations

Let us begin with the introduction of some notation: let $\mathbf{E}$ and $\mathbf{D}$ be the electric field and electric displacement, respectively, ρ the electric free charge density, ϵ the electric permeability and $\mathbf{j}$

the electric current density. By μ we denote the magnetic permeability and by $\mathbf{H}$ and $\mathbf{B}$ the magnetic field and induction, respectively.

In the considered low frequency band (frequencies below 2000 Hz), the capacitive component of tissue impedance, the inductive effect and the electromagnetic propagation effect and thus the temporal derivatives can be neglected in the Maxwell equations of electrodynamics [39]. It can be assumed that μ is constant over the whole volume and is equal to the permeability of vacuum [39]. Therefore, the electric and magnetic fields can be described by the quasi-static Maxwell equations

$$\operatorname{div} \mathbf{D} = \rho$$

$$\operatorname{curl} \mathbf{E} = 0$$

$$\operatorname{curl} \mathbf{B} = \mu \mathbf{j} \tag{1}$$

$$\operatorname{div} \mathbf{B} = 0 \tag{2}$$

with the material equations

$$\mathbf{D} = \epsilon \mathbf{E}$$

$$\mathbf{B} = \mu \mathbf{H},$$

since biological tissue mainly behaves as an electrolyte [39]. The electric field can be expressed as a negative gradient of a scalar potential,

$$\mathbf{E} = -\operatorname{grad} \mathrm{u}. \tag{3}$$

The current density is generally divided into two parts [39], the so-called *primary* or impressed current, $\mathbf{j}^p$, and the *secondary* or return currents, $\underline{\underline{\sigma}}\mathbf{E}$,

$$\mathbf{j} = \mathbf{j}^p + \underline{\underline{\sigma}}\mathbf{E}, \tag{4}$$

where $\underline{\underline{\sigma}}$ denotes the 3×3 conductivity tensor. The sources to be localized during the inverse problem and to be modelled in the forward problem, the primary currents $\mathbf{j}^p$, are movements of ions within the dendrites of the large pyramidal cells of activated regions in the cortex sheet of the human brain. Stimulus-induced activation of a large number of excitatory synapses of a whole pattern of neurons leads to negative current monopoles under the brain surface and to positive monopoles quite closely underneath. Various modelling possibilities for the primary currents are discussed in the literature [1–5]. While the so-called *mathematical dipole model* [2, 18] will be considered later in section 7, we will restrict ourselves in the following to the *blurred dipole model* [4, 18].

2.2. The electric forward problem

We now assume that the conductivity distribution $\underline{\underline{\sigma}}$ in the head domain is given. Taking the divergence of equation (1) (divergence of a curl of a vector is zero) and using equations (3) and (4) gives the equation

$$-\operatorname{div}(\underline{\underline{\sigma}} \operatorname{grad} \mathrm{u}) = -\operatorname{div} \mathbf{j}^p \qquad \text{in } \Omega, \tag{5}$$

which describes the potential distribution in the head domain Ω due to a primary current $\mathbf{j}^p$ in the brain. For the forward problem, the primary current and the conductivity distribution in the volume conductor are known, and the equation has to be solved for the unknown potential distribution. The boundary condition

$$(\underline{\underline{\sigma}}_1 \operatorname{grad} \mathrm{u}_1, \mathbf{n})|_{\text{at surface}} = (\underline{\underline{\sigma}}_2 \operatorname{grad} \mathrm{u}_2, \mathbf{n})|_{\text{at surface}}$$

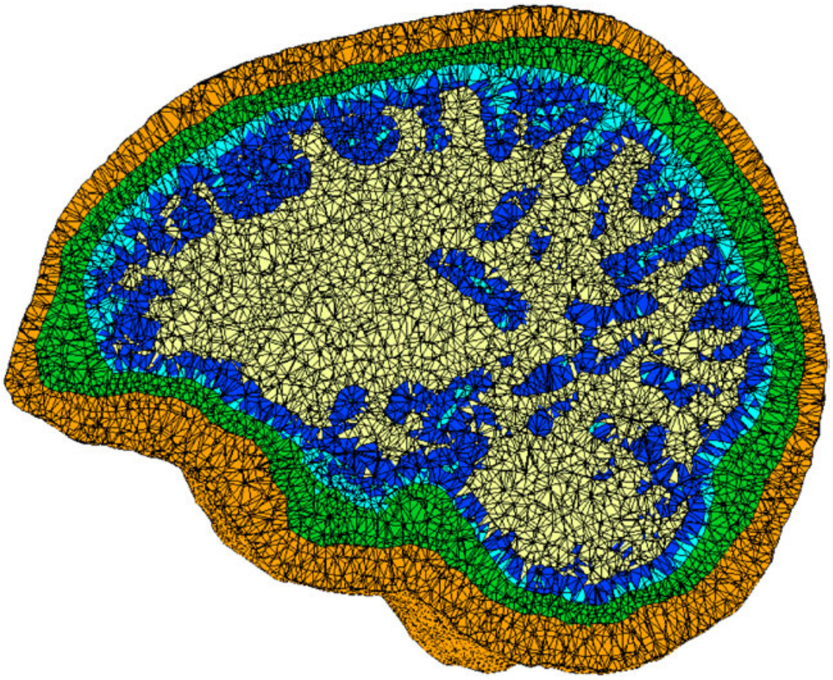

Figure 1. Five tissue FE head model with 147 287 nodes and 892 115 elements. The tetrahedra of the layers scalp, skull, cerebro-spinal fluid, brain grey matter and white matter are indicated with different colors.

with $\mathbf{n}$ the unit surface normal expresses the continuity of the current density across any surface between regions of different conductivity. We find homogeneous Neumann conditions on the head surface $\Gamma = \partial\Omega$,

$$(\underline{\underline{\sigma}}\,\mathrm{grad}\,\mathrm{u}, \mathbf{n})|_{\Gamma} = 0, \tag{6}$$

and, additionally, a reference electrode with given potential, i.e.,

$$\mathrm{u}_{\mathrm{ref}} = 0. \tag{7}$$

2.3. The magnetic forward problem

Since the divergence of $\mathbf{B}$ is zero (see Maxwell equation (2)), a magnetic potential $\mathbf{A}$ with $\mathbf{B} = \mathrm{curl}\,\mathbf{A}$ can be introduced and, using Coulomb's gauge $\mathrm{div}\,\mathbf{A} = 0$, Maxwell's equation (1) transforms to

$$\mu(\mathbf{j}^p - \underline{\underline{\sigma}}\,\mathrm{grad}\,\mathrm{u}) = \mathrm{curl}\,(\mathrm{curl}\,\mathbf{A}) = \mathrm{grad}\,(\mathrm{div}\,\mathbf{A}) - \Delta\mathbf{A} = -\Delta\mathbf{A}.$$

The source term is vanishing outside the volume conductor, so that the solution of this Poisson equation is given by [40]

$$\mathbf{A}(\mathbf{x}) = \frac{\mu}{4\pi}\int_{\Omega}\frac{\mathbf{j}^p(\mathbf{y}) - \underline{\underline{\sigma}}(\mathbf{y})\mathrm{grad}\,\mathrm{u}(\mathbf{y})}{|\mathbf{x}-\mathbf{y}|}\,\mathrm{d}\mathbf{y}. \tag{8}$$

Let F be the surface enclosed by the MEG magnetometer flux transformer $\Upsilon = \partial F$. A typical MEG magnetometer conduction loop Υ is shown in figure 3(b). The magnetic flux Ψ through Υ is determined as a surface integral over the magnetic induction for the coil area F, or, using

Figure 2. White matter anisotropy modelled with conductivity tensor ellipsoids in the barycentres of the white matter finite elements presented on an underlying magnetic resonance image.

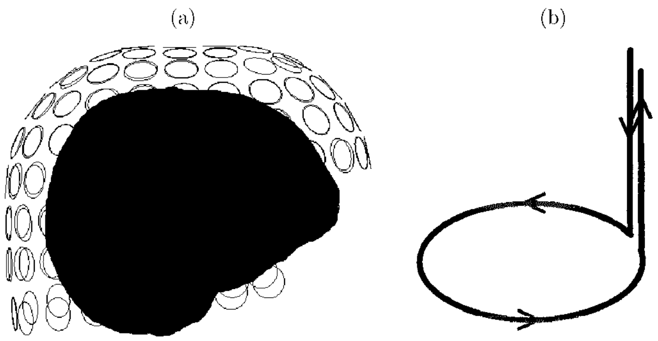

Figure 3. (a) Sensors of whole head BTI-148-channel MEG system together with the outer surface of the head model of figure 1 [18]. (b) A typical magnetometer flux transformer.

the Stokes theorem [40], as

$$\Psi = \int_F \mathbf{B} \cdot \mathrm{d}\mathbf{f} = \oint_\Upsilon \mathbf{A}(\mathbf{x}) \cdot \mathrm{d}\mathbf{x} \overset{(8)}{=} \oint_\Upsilon \frac{\mu}{4\pi} \int_\Omega \frac{\mathbf{j}^p(\mathbf{y})}{|\mathbf{x}-\mathbf{y}|} \,\mathrm{d}\mathbf{y} \cdot \mathrm{d}\mathbf{x} + \oint_\Upsilon \frac{\mu}{4\pi} \int_\Omega \frac{-\underline{\underline{\sigma}}(\mathbf{y}) \operatorname{grad} \mathrm{u}(\mathbf{y})}{|\mathbf{x}-\mathbf{y}|} \,\mathrm{d}\mathbf{y} \cdot \mathrm{d}\mathbf{x}.$$

The first part of this magnetic flux is called the *primary magnetic flux* and in the following denoted with Ψ_p, and the second is the so-called *secondary magnetic flux* Ψ_{sec}.

Ψ_p is only dependent on the source model and can in general be computed by simply evaluating an analytical formula [11, 18, 41, 42].

If we define

$$\mathbf{C}(\mathbf{y}) = \oint_{\Upsilon} \frac{1}{|\mathbf{x}-\mathbf{y}|}\,\mathrm{d}\mathbf{x}, \tag{9}$$

and if the potential distribution u is given, the final equation for Ψ_{sec} emerges from the secondary (return) currents and can be given by

$$\Psi_{\mathrm{sec}} = -\frac{\mu}{4\pi}\int\limits_{\Omega} (\underline{\underline{\sigma}}(\mathbf{y})\operatorname{grad}\mathrm{u}(\mathbf{y}), \mathbf{C}(\mathbf{y}))\,\mathrm{d}\mathbf{y}. \tag{10}$$

3. Discretization aspects for the forward problem

3.1. Discretizing the electric forward problem

For the numerical solution, we choose a finite-dimensional subspace with dimension N and a standard nodal finite element basis $\psi_1, \ldots, \psi_N$. The numerical solution process depends on the chosen model for the primary source. Here, we will refer to the literature for a deeper discussion and restrict ourselves to the following remarks.

The mathematical dipole model together with the subtraction approach [14, 18, 43] will be discussed later in section 7.

The blurred dipole model [4, 18] follows the law of St Venant and is made up from monopolar loads on all neighbouring FE nodes so that the dipolar moment is fulfilled and the source load is as regular as possible. The dipole moment is then only a means for visualization. In this case, variational and FE techniques can be directly applied to equation (5) with boundary conditions (6) and reference potential (7). This yields a system of linear equations

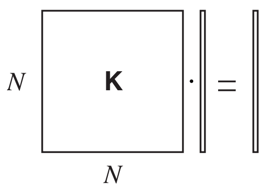

$$\mathsf{K}\underline{\mathrm{u}} = \underline{\mathrm{j}}^{\mathrm{blur}} \tag{11}$$

where the stiffness or geometry matrix has entries

$$\mathsf{K}_{ij} = \int_{\Omega} (\operatorname{grad}\psi_j(\mathbf{y}), \underline{\underline{\sigma}}(\mathbf{y})\operatorname{grad}\psi_i(\mathbf{y}))\,\mathrm{d}\mathbf{y} \qquad \forall 1 \leqslant i, j \leqslant N \tag{12}$$

and is symmetric positive definite. The positive definiteness follows from the ellipticity of the underlying bilinear form [18]. The right-hand-side $\underline{\mathrm{j}}^{\mathrm{blur}}$ has only c_{nz} non-zero entries, if c_{nz} is the number of neighbouring FE nodes to that FE node which is closest to the location of the dipole. The vector $\underline{\mathrm{u}} \in \mathbb{R}^N$ denotes the solution vector for the total potential.

Let us further assume that the $(s_{\mathrm{eeg}}-1)$ non-reference EEG electrodes directly correspond to FE nodes at the surface of the head model. It is then easy to determine a restriction matrix $\mathsf{R} \in \mathbb{R}^{(s_{\mathrm{eeg}}-1)\times N}$, which has only one non-zero entry with the value 1 in each row and which maps the potential vector onto the non-reference EEG electrodes

$$s_{eeg}-1\ \underset{N}{\boxed{\quad\mathsf{R}\quad}} \cdot \Big\| = \Big\| \qquad \mathsf{R}\underline{\mathrm{u}} =: \underline{\mathrm{u}}_{\mathrm{eeg}}. \tag{13}$$

3.2. Discretizing the magnetic forward problem

For the magnetic forward problem, the flux transformers of the MEG device have to be modelled (see equation (9)). As an example, the sensors of the whole head BTI-148-channel MEG system together with the outer surface of the head model of figure 1 are shown in figure 3(a). A typical magnetometer coil Υ is shown in figure 3(b). Following [42], we model such a coil by means of a thin, closed conductor loop, using isoparametric quadratic row elements. When approximating the potential u by means of its Galerkin projection, equation (10) can be written in matrix form

$$s_{meg}\ \underset{N}{\boxed{\quad\mathsf{S}\quad}} \cdot \Big\| = \Big\| \qquad \mathsf{S}\underline{\mathrm{u}} =: \underline{\Psi}_{\mathrm{sec}} \tag{14}$$

with $\mathsf{S} \in \mathbb{R}^{s_{\mathrm{meg}}\times N}$ the so-called *secondary flux matrix*. S maps the potential onto the secondary flux vector $\underline{\Psi}_{\mathrm{sec}} \in \mathbb{R}^{s_{\mathrm{meg}}}$. The secondary flux matrix has the entries

$$\mathsf{S}_{ij} = -\frac{\mu}{4\pi}\int_{\Omega}(\underline{\underline{\sigma}}(\mathbf{y})\operatorname{grad}\psi_j(\mathbf{y}), \mathbf{C}_i(\mathbf{y}))\,\mathrm{d}\mathbf{y} \qquad \forall 1 \leqslant j \leqslant N$$

where $\mathbf{C}_i(\mathbf{y})$ denotes the function (9) for the *i*th MEG magnetometer Υ_i $(1 \leqslant i \leqslant s_{\mathrm{meg}})$. For the computation of the matrix entries of S, a FE ansatz for the integrand and Gauss integration is used [42].

4. The inverse problem

The non-uniqueness of the inverse problem in EEG and MEG implies that assumptions on the source model, as well as anatomical and physiological *a priori* knowledge about the source region, should be taken into account to obtain a unique solution.

In the following, we will distinguish two classes of inverse methods, those in *discrete source parameter space* and those in *continuous source parameter space*. The dipole model for the primary current is regarded as the ‘atomic’ structure for both classes.

4.1. Inverse methods for a discrete source parameter space

One piece of physiological *a priori* information about the source region (*influence space*) is the assumption that the generators must be located on the folded surface of the brain inside the cortex, ignoring white matter and deeper structures such as basal ganglia, brain stem and cerebellum. If convolutions of the cortical surface are appropriately modelled by the segmentation procedure, another addition is the anatomical information that the generators are perpendicular to this surface [3, 44]. This limitation to normally oriented dipoles is called the *normal-constraint*. Because the dipole models an active source region with a certain extent and the resolution of the inverse current reconstruction by means of noisy EEG or MEG data is limited, most inverse methods (see, e.g., [12, 32–37]) and especially all so-called *current density methods* [12, 32, 36, 37] are based on a discretized influence space. The discretization can be represented, for example, by the vertices of a cortical triangulation when using the physiological constraint. Other approaches use regular 3D discretizations of the whole brain volume. The so-called *influence nodes* are the n_{inf} vertices of the discretized influence space. Since the differential equation is linear, it is possible to set up a so-called *influence matrix* $\mathrm{L} \in \mathbb{R}^{\mathrm{s}\times\mathrm{r}}$ (often also called *lead field matrix*). A forward solution for a dipole on one of the n_{inf} influences nodes with unit strength in one Cartesian direction at the

$$\mathrm{s} = s_{\mathrm{eeg}} + s_{\mathrm{meg}}$$

EEG/MEG measurement sensors is stored as a column of L. If the physiological *a priori* information and the normal-constraint are applied, there is only one possible dipole direction for each influence node and thus every dipole location $i \in \{1, \ldots, n_{\mathrm{inf}}\}$ is represented by only one column in the influence matrix, i.e. $\mathrm{r} = n_{\mathrm{inf}}$. For the unconstrained case, three columns in L represent the three orthogonal unit dipoles at a specific location, i.e. $\mathrm{r} = 3n_{\mathrm{inf}}$.

If once, the discretization of the influence space has been fixed, the block of the r right-hand sides $\underline{\mathrm{j}}^{\mathrm{blur}} \in \mathbb{R}^N$ (see section 7 for the mathematical dipole model) can be set up. The goal is then a fast computation of the influence matrix L, which can subsequently be used for the whole variety of inverse reconstruction methods for discrete source parameter space.

4.2. Inverse methods for a continuous source parameter space

The second class of inverse methods exploits a continuous source parameter space [11, 18, 38]. One could imagine, for example, the restriction of the inverse reconstruction to a limited number of dipoles (with respect to the application: one up to three). Their nonlinear location parameters are optimized continuously in the brain volume, while the remaining parameters are determined with a linear fit to the measured EEG/MEG data within each optimization step. This is done, e.g., within the so-called *dipole fit methods* [11, 18, 38]. The number r of necessary forward simulations in such methods is dependent on the convergence speed of the optimization method. This class of inverse algorithms cannot exploit the influence matrix concept (apart from interpolation techniques [13]), since the new dipole parameters and thus the new right-hand sides are only determined within the previous optimization step. Still, we can apply our new approach successfully.

5. State-of-the-art approach in EEG/MEG source reconstruction

For the considered inhomogeneous and anisotropic volume conductor models, the AMG–CG iterative solver [18, 20, 23, 26] turned out to be an asymptotically optimal solver method for the numerical solution of (11), where the operation count and memory demand are of the order $\mathcal{O}(N)$. Our approach can also be applied in combination with other solver methods, but in the following we will only consider the AMG–CG.

We will now describe the state-of-the-art approach for the EEG/MEG inverse problem which covers both classes of inverse methods. A new FE right-hand side vector is determined by the inverse algorithm, and the AMG–CG solver is used for the numerical solution of the potential distribution. For the computation of the secondary flux at the MEG-sensors, the potential distribution is then multiplied by the secondary flux matrix following equation (14). The restriction (13) terminates the forward computation.

The numerical tests are performed on a Sun Ultrasparc III with 900 MHz CPU clock rate. We only use a single processor for the following computations.

5.1. Complexity estimation for AMG–CG solver

We first estimate the complexity for an AMG–CG solution [23], following the MultiGrid operation count of [45, section 10.4.4]. With $c_{nz} * N$ being the sparsity of the geometry/stiffness matrix, we assume $C_S * c_{nz} * N$ operations for the smoother, $C_D * c_{nz} * N$ for the computation of defect and restriction and $C_P * N$ for the prolongation of the error. Here, C_S denotes the cost factor for the smoother which is an iteration-specific constant. We use Gauss–Seidel smoothing for which it is $C_S = 2 - 2/c_{nz}$ [45, section 4.6.1]. C_P and C_D depend on the chosen prolongation operator. As described in [23], our prolongation matrix interpolates the value of a fine grid node (which is not at the same time a coarse grid node) only from strong neighbour coarse grid nodes, i.e. $C_P \ll c_{nz}$. In our application, the restriction matrix is the transpose of the prolongation matrix. We use a V-cycle with only one pre- and one post-smoothing step within each preconditioning operation. We then obtain as an approximation of the necessary work for the MG preconditioner [45, theorem 10.4.2]:

$$\tfrac{8}{7} * (2 * C_S + C_D + C_P/c_{nz}) * c_{nz} * N.$$

We furthermore have to count one matrix-vector multiplication ($2 * c_{nz} * N$ operations), two scalar products ($2 * 2 * N$ operations) and three vector additions ($3 * N$ operations) for the CG step. If we assume that i iterations have to be carried out, we will need for one AMG–CG solution approximately $i * k * N$ operations with

$$k := \tfrac{8}{7} * (2 * C_S + C_D + 2 + (C_P + 7)/c_{nz}) * c_{nz}.$$

We will study the head model of figures 1 and 2 with $N = 147\,287$ FE nodes as an example: in order to reach a sufficient accuracy, we have to reduce the relative error by a factor of 10^8 which can be accomplished by $i = 20$ iterations of AMG–CG [18, 20, 23, 26]. On our machine, each iteration takes 1.269 s, i.e. 25.38 s to solve for each right-hand side.

5.2. Complexity estimation for the state-of-the-art approach

Let us now have a look at the complexity of the state-of-the-art approach for the inverse problem.

For the matrix-vector multiplication in equation (14), $2 * s_{\mathrm{meg}} * N$ operations are needed. Let us neglect the work for the restriction $\underline{u}_{\mathrm{eeg}} = \mathsf{R}\underline{u}$ and for the computation of the FE right-hand side vector. Then, for each inverse algorithm with r different right-hand sides, the state-of-the-art approach needs

$$\mathrm{r} * ((i * k + 2 * s_{\mathrm{meg}}) * N)$$

operations.

In EEG/MEG source reconstruction, r is generally quite large, especially because the results of various different inverse algorithms based on different hypotheses on the underlying current distribution are compared to each other. Already an anatomically correct discretization of the cortical surface, respecting all curvatures of the cortical sulci and gyri, results in at least 10^4 influence nodes [18, figure 2.5]. This number would be even exceeded in the case of a 3D discretization of the whole brain volume. In contrast to that, the number of sensors s is rather small. The most modern vector-MEG devices have at most 500 sensors and for the EEG, not more than 150 sensors can be fixed on the head surface. In most applications, the number of sensors is below 150 (see figure 3(a)) as an example).

In our model problem, we have $s_{\mathrm{meg}} = 150$ sensors and $\mathrm{r} = 30\,357$ right-hand sides (possible dipoles). The solution of the FE system for 30 357 right-hand sides and subsequent matrix-vector multiplication with S from equation (14) takes

$$774\,331\ \mathrm{s} = 215\ \mathrm{h},$$

which is too expensive for realistic applications. In the next section, we explain how one can severely reduce this complexity, down to 1 h.

6. Computation of the lead field basis and influence matrix

The inverse of the geometry/stiffness matrix, K^{-1}, exists, but its computation is a difficult task, since the sparseness of K will be lost while inverting. But with regard to the EEG inverse problem, we are only interested in computing

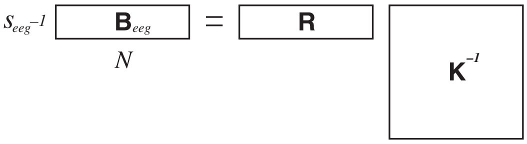

$$\mathsf{B}_{\text{eeg}} := \mathsf{RK}^{-1} \in \mathbb{R}^{(s_{\text{eeg}}-1)\times N}, \tag{15}$$

which describes the direct mapping of a FE right-hand side vector to the non-reference electrodes:

$$\mathsf{B}_{\text{eeg}}\underline{\mathsf{j}}^{\text{blur}} \overset{(15)}{=} \mathsf{RK}^{-1}\underline{\mathsf{j}}^{\text{blur}} \overset{(11)}{=} \mathsf{R}\underline{u} \overset{(13)}{=} \underline{u}_{\text{eeg}}.$$

Weinstein *et al* [16] introduced the notation *EEG lead field basis* for B_{eeg}. We will now see that we face a comparable situation with regard to the MEG inverse problem. In fact, let us define the *MEG lead field basis*:

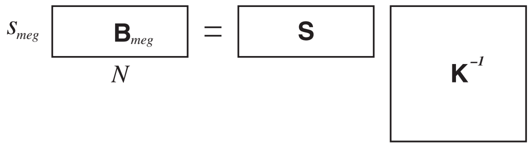

$$\mathsf{B}_{\text{meg}} := \mathsf{SK}^{-1} \in \mathbb{R}^{s_{\text{meg}}\times N}. \tag{16}$$

One should note that the rows of B_{eeg} do indeed form a basis in the mathematical sense, while this is not necessarily true for B_{meg}. B_{meg} describes the direct mapping of the FE right-hand side vector to the secondary magnetic flux vector:

$$\mathsf{B}_{\text{meg}}\underline{\mathsf{j}}^{\text{blur}} \overset{(16)}{=} \mathsf{SK}^{-1}\underline{\mathsf{j}}^{\text{blur}} \overset{(11)}{=} \mathsf{S}\underline{u} \overset{(14)}{=} \underline{\Psi}_{\text{sec}}.$$

The lead field basis can be computed as follows: if we multiply the matrix equation

$$\begin{bmatrix} \mathsf{B}_{\text{eeg}} \\ \mathsf{B}_{\text{meg}} \end{bmatrix} = \begin{bmatrix} \mathsf{R} \\ \mathsf{S} \end{bmatrix} \mathsf{K}^{-1}$$

with K from the right-hand side and transpose both sides, we obtain

$$\mathsf{K}\left[\mathsf{B}_{\text{eeg}}^{\text{tr}} \quad \mathsf{B}_{\text{meg}}^{\text{tr}}\right] = [\mathsf{R}^{\text{tr}} \quad \mathsf{S}^{\text{tr}}].$$

The last step uses the symmetry of the geometry matrix (see equation (12)).

Algorithm 1 INVERSE PROBLEM WITH MODERATE SIZE OF THE LEAD FIELD BASIS

Precompute B_{eeg} and B_{meg} and store both matrices
repeat
  INVERSE ALGORITHM COMPUTES NEW $\underline{\mathsf{j}}^{\text{blur}}$
  MULTIPLY $\underline{\mathsf{j}}^{\text{blur}}$ BY B_{eeg} AND B_{meg}: USE SPECIAL STRUCTURE OF $\underline{\mathsf{j}}^{\text{blur}}$
until TERMINATION OF INVERSE ALGORITHM

Algorithm 2 INVERSE PROBLEM WITH LARGE SIZE OF THE LEAD FIELD BASIS

PRECOMPUTE $\mathrm{J}^{\mathrm{blur}} \in \mathbb{R}^{N\times \mathrm{r}}$ IN CSC-FORMAT
for $\mathrm{i} = 1, \ldots, \mathrm{s}$ **do**
  DETERMINE THE iTH ROW OF THE LEAD FIELD BASIS
  MULTIPLY THIS ROW BY $\mathrm{J}^{\mathrm{blur}}$, I.E., COMPUTE iTH ROW OF L
  STORE iTH ROW IN $\mathrm{L} \in \mathbb{R}^{\mathrm{s}\times \mathrm{r}}$
end for
USE L FOR INVERSE METHODS ON DISCRETE PARAMETER SPACE

6.1. Algorithms

Let us first assume that we are equipped with a computer memory which is large enough to store $\mathrm{s} * N$ doubles for the lead field bases $\mathsf{B}_{\mathrm{eeg}}$ and $\mathsf{B}_{\mathrm{meg}}$. In this case, algorithm 1 can be used. In a set-up phase, $\mathsf{B}_{\mathrm{eeg}}$ and $\mathsf{B}_{\mathrm{meg}}$ are computed once per head-model by means of solving s large sparse FE-systems of equations using, e.g., the iterative AMG-CG solver. The lead field bases can then be exploited for any new FE right-hand side within the inverse algorithm for both classes of inverse methods, discrete and continuous. Remember that for the blurred dipole model, $\underline{\mathrm{j}}^{\mathrm{blur}}$ has only c_{nz} non-zero entries, which can efficiently be used within the matrix-vector multiplication.

The mathematical dipole would lead to dense right-hand side vectors (no non-zero entries). In this case, we suggest special techniques described in section 7.

If the computer memory is too small to store $\mathrm{s} * N$ doubles for $\mathsf{B}_{\mathrm{eeg}}$ and $\mathsf{B}_{\mathrm{meg}}$ and if only inverse methods for discrete source parameter space in combination with the blurred dipole model are of interest, algorithm 2 is the appropriate one. In a set-up phase, the block with r right-hand sides $\underline{\mathrm{j}}^{\mathrm{blur}}$ for all blurred dipoles of the influence space is precomputed and stored using a compressed sparse column (CSC) format [46]. Let us denote this matrix with $\mathrm{J}^{\mathrm{blur}} \in \mathbb{R}^{N\times \mathrm{r}}$. Each row of the lead field basis can then be computed using AMG-CG and directly multiplied to $\mathrm{J}^{\mathrm{blur}}$. The result is a row of the influence matrix $\mathrm{L} \in \mathbb{R}^{\mathrm{s}\times \mathrm{r}}$ from chapter 4.1. L can then be exploited by means of all inverse methods working on that specific discrete influence space.

6.2. Complexity of algorithms 1 and 2

Let us now have a look at the complexity of algorithm 1 that computes the lead field bases $\mathsf{B}_{\mathrm{eeg}}$ and $\mathsf{B}_{\mathrm{meg}}$.

As in section 5.2 we consider the tetrahedra model problem (figures 1 and 2) with $\mathrm{r} = 30\,357$ right-hand sides and $\mathrm{s} = s_{\mathrm{meg}} = 150$ sensors. In brackets we give the concrete time for the computations on our machine (cf section 6).

After a set-up with

$$\mathrm{s} * i * k * N \text{ operations} \qquad (3807\text{ s}),$$

which is a unique calculation for each individual head geometry, we only have to multiply the new FE right-hand side vector by the lead field bases. For r full right-hand side vectors, this amounts to

$$\mathrm{r} * (2 * \mathrm{s} * N) \text{ operations} \qquad (3871\text{ s}).$$

If, furthermore, the blurred dipole is used, this operation count is reduced to only

$$\mathrm{r} * (2 * \mathrm{s} * c_{nz}) \text{ operations} \qquad (4.7\text{ s})$$

for each inverse method. Note that this number is independent of the mesh-resolution. The overall complexity in this case is

$$\mathrm{s} * i * k * N + 2 * \mathrm{r} * \mathrm{s} * c_{nz} \qquad (3812\ \mathrm{s}),$$

i.e. it is mainly determined by the set-up phase. The complexity of algorithm 2 is the same (if the blurred dipole is used). The overall complexity of our approach is thus by a factor r/s (in our model problem: 200) smaller than the complexity for the state-of-the-art approach. If various inverse methods are compared to each other, this factor will grow with the number r of FE right-hand sides.

7. Mathematical dipole and subtraction approach

For the mathematical dipole [14, 18, 43], a subtraction approach is used for the solution of the electric forward problem. The total potential u is split into two parts, the singularity potential u^∞ corresponding to the location of the dipole, $y \in \mathbb{R}^3$, with the dipole moment $M(y) \in \mathbb{R}^3$ [41],

$$\mathrm{u}^\infty(x) := \frac{1}{4\pi}\frac{\langle M(y), x-y\rangle}{\|x-y\|^3}, \qquad \operatorname{div}\operatorname{grad}\mathrm{u}^\infty = J^p := \operatorname{div} M(y)\delta(x-y) \tag{17}$$

and the unknown *correction potential* $\mathrm{u}^{\mathrm{corr}}$:

$$\mathrm{u} = \mathrm{u}^\infty + \mathrm{u}^{\mathrm{corr}}.$$

A FE ansatz for the correction potential leads to a linear system of equations

$$\mathsf{K}\underline{u}^{\mathrm{corr}} = \underline{\mathsf{j}}^{\mathrm{corr}} \tag{18}$$

with the same geometry matrix K as in (12). The right-hand side $\underline{\mathsf{j}}^{\mathrm{corr}} \in \mathbb{R}^N$ is a full vector and $\underline{u}^{\mathrm{corr}} \in \mathbb{R}^N$ denotes the solution vector for the correction potential. A precise definition of the right-hand side is

$$\underline{\mathsf{j}}^{\mathrm{corr}} = (\mathsf{K}_\Delta - \mathsf{K} + \mathsf{K}_\mathrm{n})\underline{u}^\infty. \tag{19}$$

K_Δ is the discrete Laplacian and K_n the discretization of the inhomogeneous Neumann boundary conditions at the surface of the volume conductor induced by u^∞ (see, e.g., [18, sections 4.4.1, 4.7.4]). The sparsity pattern of both matrices, K_Δ and K_n, is contained in the sparsity pattern of K. Therefore, $c_{nz} * N$ is also the sparsity of $\mathsf{K}_\Delta + \mathsf{K}_\mathrm{n}$.

The restriction matrix R from (13) maps the potential vector onto the potential of the non-reference EEG electrodes

$$\underline{u}_{\mathrm{eeg}} := \mathsf{R}(\underline{u}^{\mathrm{corr}} + \underline{u}^\infty) \overset{(18)}{=} \mathsf{R}\mathsf{K}^{-1}\underline{\mathsf{j}}^{\mathrm{corr}} + \mathsf{R}\underline{u}^\infty \overset{(19)}{=} \mathsf{R}\mathsf{K}^{-1}(\mathsf{K}_\Delta + \mathsf{K}_\mathrm{n})\underline{u}^\infty. \tag{20}$$

Equation (14) then gets

$$\underline{\Psi}_{\mathrm{sec}} := \mathsf{S}(\underline{u}^{\mathrm{corr}} + \underline{u}^\infty) \overset{(18)}{=} \mathsf{S}\mathsf{K}^{-1}\underline{\mathsf{j}}^{\mathrm{corr}} + \mathsf{S}\underline{u}^\infty \overset{(19)}{=} \mathsf{S}\mathsf{K}^{-1}(\mathsf{K}_\Delta + \mathsf{K}_\mathrm{n})\underline{u}^\infty. \tag{21}$$

Algorithm 3 INVERSE PROBLEM WITH CONTINUOUS SOURCE PARAMETER SPACE

Precompute $\mathsf{B}^\infty_{\mathrm{eeg}}$ and $\mathsf{B}^\infty_{\mathrm{meg}}$ and store both matrices
repeat
  INVERSE ALGORITHM COMPUTES NEW $\underline{u}^\infty$
  MULTIPLY $\underline{u}^\infty$ BY $\mathsf{B}^\infty_{\mathrm{eeg}}$ AND $\mathsf{B}^\infty_{\mathrm{meg}}$
until TERMINATION OF INVERSE ALGORITHM

The matrices

$$\mathsf{B}^{\infty}_{\mathrm{eeg}} := \mathsf{R}\mathsf{K}^{-1}(\mathsf{K}_{\Delta} + \mathsf{K}_{\mathrm{n}}) \in \mathbb{R}^{(s_{\mathrm{eeg}}-1)\times N}$$

and

$$\mathsf{B}^{\infty}_{\mathrm{meg}} := \mathsf{S}\mathsf{K}^{-1}(\mathsf{K}_{\Delta} + \mathsf{K}_{\mathrm{n}}) \in \mathbb{R}^{s_{\mathrm{meg}}\times N}$$

can be precomputed and used for any right-hand side $\underline{\mathrm{u}}^{\infty}$ coming either from a discrete or a continuous source parameter space.

7.1. Algorithms and complexity for the mathematical dipole

In the following we give in brackets the concrete times for the computations on our machine (cf section 5.2) for the tetrahedra model problem (figures 1 and 2).

For a continuous source parameter space algorithm 3 is applicable. Here, one has to precompute $\mathsf{B}^{\infty}_{\mathrm{eeg}}$ and $\mathsf{B}^{\infty}_{\mathrm{meg}}$ with a complexity of

$$\mathrm{s} * i * k * N + \mathrm{s} * c_{nz} * N \qquad (3876\ \mathrm{s})$$

and can then use these matrices to compute $\underline{\mathrm{u}}_{\mathrm{eeg}}$ and $\underline{\Psi}_{\mathrm{sec}}$ with a complexity of $\mathrm{s} * N$ (0.1 s) for each dipole (i.e. for each $\underline{\mathrm{u}}^{\infty}$). For a total of $\mathrm{r} = 30\,357$ dipoles this complexity is

$$\mathrm{r} * (2 * \mathrm{s} * N) \qquad (3871\ \mathrm{s}).$$

The total complexity for both set-up and solution phase is

$$(i * k + c_{nz} + 2 * \mathrm{r}) * \mathrm{s} * N \text{ operations} \qquad (7747\ \mathrm{s}),$$

which is 100 times less than the complexity for the state-of-the-art approach.

For a discrete source parameter space the r possible dipole locations are known. In this case we can use the same strategy as for the blurred dipole, namely to store the whole matrix U^{∞} whose columns are the vectors $\underline{\mathrm{u}}^{\infty}$ for the respective dipole locations. However, the matrix U^{∞} is not sparse. A new technique to store matrices of this type in a data-sparse form are so-called hierarchical matrices, or short $\mathcal{H}$-matrices [47–50]. This format exploits the fact that the function $\mathrm{u}^{\infty}(x)$ can be interpolated efficiently. The dependence of $\mathrm{u}^{\infty}(x)$ on the dipole location y is complicated, but we can split the function u^{∞} into

$$\mathrm{u}^{\infty}(x) = \sum_{i=1}^{3} \frac{M(y)_i}{4\pi} \cdot \frac{(x_i - y_i)}{\|x - y\|^3},$$

such that only the term $(x_i - y_i)/\|x - y\|^3$ has to be interpolated, i.e. we have to fulfil the standard *admissibility condition*

$$\min\{\mathrm{diam}(X), \mathrm{diam}(Y)\} \leqslant \mathrm{dist}(X, Y)$$

Algorithm 4 INVERSE PROBLEM WITH CONTINUOUS SOURCE PARAMETER SPACE

PRECOMPUTE $\mathsf{U}^{\infty} \in \mathbb{R}^{N\times \mathrm{r}}$ IN $\mathcal{H}$-MATRIX FORMAT
for $\mathrm{i} = 1, \ldots, \mathrm{s}$ **do**
  DETERMINE THE iTH ROW OF THE LEAD FIELD BASIS $\mathsf{B}^{\infty}_{\mathrm{eeg}}, \mathsf{B}^{\infty}_{\mathrm{meg}}$
  MULTIPLY THIS ROW BY U^{∞}, I.E., COMPUTE iTH ROW OF L
  STORE iTH ROW IN $\mathrm{L} \in \mathbb{R}^{\mathrm{s}\times \mathrm{r}}$
end for
USE L FOR INVERSE METHODS ON DISCRETE PARAMETER SPACE

Figure 4. The transpose of the matrix U^∞ in $\mathcal{H}$-matrix format where each green block is stored in a data-sparse low-rank format.

for regions $X \times Y \ni (x, y)$ where we want to replace the function u^∞ by its interpolant (cf [50]).

Standard geometrically balanced clustering [49] yields a partition of the matrix U^∞ as shown in figure 4. Each green block in figure 4 allows for a data-sparse low rank approximation while the red (but small) ones are stored in standard dense matrix format. The whole matrix U^∞ can be assembled and stored with $c_{as} * \log(N) * N$ operations (81.4 s)—much less than the $c * \mathrm{r} * N$ operations (1026.8 s) needed without the data-sparse $\mathcal{H}$-matrix format. Once the matrix has been assembled and stored in this (packed) format, it allows for a fast matrix-vector multiplication with $c_{mv} * \log(N) * N$ operations (8.34 s) [49]. Algorithm 4 uses the $\mathcal{H}$-matrix format and exploits the fast matrix-vector multiplication. The total set-up complexity is

$$(i * k + c_{nz} + c_{mv} * \log(N)) * \mathrm{s} * N \qquad (5208.4\ \mathrm{s})$$

for the influence matrix L. This is 149 times less than the complexity for the state-of-the-art approach. The influence matrix L can, of course, be used for any inverse method working on that specific discrete influence space.

8. Conclusions and perspective

In this paper we presented a new approach to strongly reduce the algorithmic complexity of EEG/MEG inverse source reconstruction algorithms which are based on the finite element (FE) volume conductor modelling of the human head. The FE computational complexity of the state-of-the-art approach can be seen as the main disadvantage of FE compared to multi-layer sphere [10] or boundary element (BE) [11–13] head modelling. Our approach turns out to be very effective if the number of EEG/MEG sensors is much smaller than the number of sources for which a forward computation has to be carried out. This is the case in most applications, since the number of sensors is about 10^2, while the number of necessary forward computations is often beyond 10^4.

Our approach opens new possibilities concerning the resolution of FE head modelling. The number of large sparse linear systems that have to be solved per head geometry is now limited to the number of EEG/MEG sensors in order to compute the EEG/MEG lead field basis, a matrix with 'number of EEG/MEG sensors' rows and 'number of FE nodes' columns. The parallel algebraic multigrid preconditioned conjugate gradient method is an efficient solver for this set-up phase, as shown in [18, 20, 23, 26]. Each FE forward computation within inverse methods on both continuous and discrete source parameter space is then reduced to the multiplication of the FE right-hand side with the lead field basis. In combination with the blurred dipole model, a FE forward solution is then limited to $2 * \mathrm{s} * c_{nz}$ operations with s the number of EEG/MEG sensors and c_{nz} the number of neighbours to a FE node.

Furthermore, for the blurred dipole model [4, 18], we presented an algorithm for the row-wise computation of the influence matrix which only uses one row of the lead field basis at a time so that the full lead field basis does not have to be stored at all. This method is suitable for all inverse methods on discrete source parameter space with high resolutions of the FE approach and a large number of EEG/MEG sensors.

The treatment of the mathematical dipole in the subtraction method [14, 18, 43] with our new approach is enhanced by using the data-sparse $\mathcal{H}$-matrix format.

The potential resolution for FE head modelling is now less limited by the complexity of the FE forward computations, but rather by the memory necessary to save the structures for the AMG-CG approach and the lead field basis. For very high resolutions, a parallel FE solver approach [18, 23] and the parallelization of the lead field basis multiplication seems to be necessary in order to distribute the memory on the computational nodes.

The new approach encourages the use and further development of the SimBio[4] mesh generation tool VGRID [51]. The current version of VGRID generates high-resolution FE meshes which are especially refined at tissue boundaries. In the future, a follow-up mesher could be developed in order to refine the FE mesh in areas of diffuse anisotropy.

The methods presented in this paper even motivate the use of the current resolution of the MR machines as the FE mesh resolution, i.e. FE meshing is no longer necessary at all.

Acknowledgment

The authors would like to thank Dr Alfred Anwander from the Max-Planck-Institute of Cognitive Neuroscience Leipzig for the discussions about reciprocity.

References

[1] Okada Y 1981 Neurogenesis of evoked magnetic fields *Biomagnetism* ed S N Erné, H D Hahlbohm and H Lübbig (Berlin: de Gruyter) pp 399–408

[2] de Munck J C, van Dijk B W and Spekreijse H 1988 Mathematical dipoles are adequate to describe realistic generators of human brain activity *IEEE Trans. Biomed. Eng.* **35** 960–6

[3] Nunez P L 1990 Localization of brain activity with electroencephalography *Advances in Neurology, Magnetoencephalography* vol 54 ed S Sato (New York: Raven Press) pp 39–65

[4] Buchner H, Knoll G, Fuchs M, Rienäcker A, Beckmann R, Wagner M, Silny J and Pesch J 1997 Inverse localization of electric dipole current sources in finite element models of the human head *Electroencephalogr. Clin. Neurophysiol.* **102** 267–78

[5] Andrä W and Nowak H 1998 *Magnetism in Medicine—A Handbook* (Berlin: Wiley–VCH)

[6] Geddes L A and Baker L E 1967 The specific resistance of biological material. A compendium of data for the biomedical engineer and physiologist *Med. Biol. Eng.* **5** 271–93

[7] Nicholson P W 1965 Specific impedance of cerebral white matter *Exp. Neurol.* **13** 386–401

[8] Rush S and Driscoll D A 1968 Current distribution in the brain from surface electrodes *Anesth. Analg.* **47** 717–23

[9] Akhtari M, Bryant H C, Marmelak A N, Heller L, Shih J J, Mandelkern M, Matlachov A, Ranken D M, Best E D and Sutherling W W 2000 Conductivities of three-layer human skull *Brain Topgr.* **13** 29–42

[10] de Munck J C 1988 The potential distribution in a layered anisotropic spheroidal volume conductor *J. Appl. Phys.* **64** 465–9

[11] Knösche T R 1997 Solutions of the neuroelectromagnetic inverse problem *PhD Thesis* University of Twente

[12] Fuchs M, Wagner M, Köhler T and Wischmann H A 1999 Linear and nonlinear current density reconstructions *J. Clin. Neurophysiol.* **16** 267–95

[13] Yvert B, Crouzeix-Cheylus A and Pernier J 2001 Fast realistic modeling in bioelectromagnetism using lead-field interpolation *Hum. Brain Mapp.* **14** 48–63

[14] Awada K A, Jackson D R, Williams J T, Wilton D R, Baumann S B and Papanicolaou A C 1997 Computational aspects of finite element modeling in EEG source localization *IEEE Trans. Biomed. Eng.* **44** 736–51

[4] SimBio: A generic environment for bio-numerical simulation. IST-programme of the European Commission, project no 10378, http://www.simbio.de, 2000–2003.

[15] Ollikainen J, Vauhkonen M, Karjalainen P A and Kaipio J P 1999 Effects of local skull inhomogeneities on EEG source estimation *Med. Eng. Phys.* **21** 143–54

[16] Weinstein D, Zhukov L and Johnson C 2000 Lead-field bases for electroencephalography source imaging *Ann. Biomed. Eng.* **28** 1059–66

[17] Haueisen J, Tuch D S, Ramon C, Schimpf P H, Wedeen V J, George J S and Belliveau J W 2002 The influence of brain tissue anisotropy on human EEG and MEG *NeuroImage* **15** 159–66

[18] Wolters C 2003 *Influence of Tissue Conductivity Inhomogeneity and Anisotropy on EEG/MEG-Based Source Localization in the Human Brain* (*MP Series in Cognitive Neuroscience* no 39) (Leipzig: MPI of Cognitive Neuroscience)

see also Wolters C 2003 *Dissertation* University of Leipzig, http://dol.uni-leipzig.de/pub/2003-33

[19] van den Broek S P, Reinders F, Donderwinkel M and Peters M J 1998 Volume conduction effects in EEG and MEG *Electroencephalogr. Clin. Neurophysiol.* **106** 522–34

[20] Wolters C H, Anwander A, Koch M, Reitzinger S, Kuhn M and Svensén M 2001 Influence of head tissue conductivity anisotropy on human EEG and MEG using fast high resolution finite element modeling, based on a parallel algebraic multigrid solver *Forschung und wissenschaftliches Rechnen* (*Contributions to the Heinz-Billing Award* no 58) (Göttingen Gesellschaft für wissenschaftliche Datenverarbeitung mbH) ed T Plesser, V Macho pp 111–157 See http://www. billingpreis.mpg.de

[21] Marin G, Guerin C, Baillet S, Garnero L and Meunier G 1998 Influence of skull anisotropy for the forward and inverse problem in EEG: simulation studies using the FEM on realistic head models *Hum. Brain Mapp.* **6** 250–69

[22] Anwander A, Wolters C H, Dümpelmann M and Knösche T R 2002 Influence of realistic skull and white matter anisotropy on the inverse problem in EEG/MEG-source localization *Proc. 13th Int. Conf. on Biomagnetism* ed H Nowak, J Hauiesen, F Giessler and R Huonker (Berlin: VDE) pp 679–81 http://biomag2002.uni_jena.de

[23] Wolters C H, Kuhn M, Anwander A and Reitzinger S 2002 A parallel algebraic multigrid solver for finite element method based source localization in the human brain *Comput. Vis. Sci.* **5** 165–77

[24] Reitzinger S 2001 Algebraic multigrid methods for large scale finite element equations *PhD Thesis* Schriften der Johannes-Kepler-Universität Linz, Reihe C-Technik und Naturwissenschaften no 36

[25] Haase G, Kuhn M and Reitzinger S 2002 Parallel AMG on distributed memory computers *SIAM J. Sci. Comput.* **24** 410–27

[26] Wolters C, Reitzinger S, Basermann A, Burkhardt S, Hartmann U, Kruggel F and Anwander A 2000 Improved tissue modeling and fast solver methods for high resolution FE -modeling in EEG/MEG-source localization. *Proc. 12th Int. Conf. on Biomagnetism (Helsinki 13–17 Aug)* ed J Nenonen, R J Ilmoniemi and T Katila pp 655–8 See http://biomag2000.hut.fi/papers_all.html

[27] Mohr M and Vamrunste B 2003 Comparing iterative solvers for linear systems associated with the finite difference discretisation of the forward problem in electro-encephalographic source analysis *Med. Biol. Eng. Comput.* **41** 75–84

[28] Helmholtz H L F 1853 Über einige Gesetze der Vertheilung elektrischer Ströme in körperlichen Leitern mit Anwendung auf die thierisch-elektrischen Versuche *Ann. Phys. Chem.* **89** 211–33, 354–77

[29] Malmivuo J and Plonsey R 1995 *Bioelectromagnetism: Principles and Applications of Bioelectric and Biomagnetic Fields* (New York: Oxford University Press)

[30] Vamrunste B, Van Hoey G, Van de Walle R, D'Havé M R P, Lemahieu I A and Boon P A J M 2001 The validation of the finite difference method and reciprocity for solving the inverse problem in EEG dipole source analysis *Brain Topogr.* **14** 83–92

[31] Nolte G 2003 The magnetic lead field theorem in the quasi-static approximation and its use for magnetoencephalography forward calculation in realistic volume conductors *Phys. Med. Biol.* **48** 3637–52

[32] Hämäläinen M S and Ilmoniemi R J 1984 Interpreting measured magnetic fields of the brain: estimates of current distributions *Technical Report* TKK-F-A559 Helsinki University of Technology

[33] Louis A and Maaß P 1990 A mollifier method for linear operator equations of the first kind *Inverse Problems* **6** 427–40

[34] Mosher J C, Lewis P S and Leahy R M 1992 Multiple dipole modeling and localization from spatio-temporal MEG data *IEEE Trans. Biomed. Eng.* **39** 541–57

[35] Wolters C H, Beckmann R F, Rienäcker A and Buchner H 1999 Comparing regularized and non-regularized nonlinear dipole fit methods: a study in a simulated sulcus structure *Brain Topogr.* **12** 3–18

[36] Schmitt U and Louis A K 2002 Efficient algorithms for the regularization of dynamic inverse problems: I. Theory *Inverse Problems* **18** 645–58

[37] Schmitt U, Louis A K, Wolters C H and Vauhkonen M 2002 Efficient algorithms for the regularization of dynamic inverse problems: II. Applications *Inverse Problems* **18** 659–76

[38] Scherg M and von Cramon D 1985 Two bilateral sources of the late AEP as identified by a spatio-temporal dipole model *Electroencephalogr. Clin. Neurophysiol* **62** 32–44
[39] Plonsey R and Heppner D 1967 Considerations on quasi-stationarity in electro-physiological systems *Bull. Math. Biophys.* **29** 657–64
[40] Nolting W 1992 *Grundkurs: Theoretische Physik, Elektrodynamik* (Ulmen: Zimmermann-Neufang)
[41] Sarvas J 1987 Basic mathematical and electromagnetic concepts of the biomagnetic inverse problem *Phys. Med. Biol.* **32** 11–22
[42] Pohlmeier R 1996 Lokalisation elektrischer Gehirnaktivität durch inverse Analyse des Magnetoenzephalogramms (MEG) mit Finite-Elemente-Modellen des Kopfes *Diplomarbeit in Elektrotechnik* RWTH Aachen
[43] von Rango J, Schlitt H A, Halling H and Müller-Gärtner H-W 1997 Finite integration techniques for the MEG forward problem *Quantitative and Topological EEG and MEG Analysis* ed H Witte, U Zwiener, B Schack and A Doering (Jena: Druckhaus Mayer) pp 336–8
[44] Lorente de No R 1938 Cerebral cortex: architecture, intracortical connections, motor projections *Physiology of the Nervous System* ed J F Fulton (Oxford: Oxford University Press) chapter 15
[45] Hackbusch W 1994 *Iterative Solution of Large Sparse Systems* (New York: Springer)
[46] Saad Y 1996 *Iterative Methods for Sparse Linear Systems* (New York: PWS Publishing)
[47] Börm S, Grasedyck L and Hackbusch W 2003 Introduction to hierarchical matrices with applications *Eng. Anal. Bound. Elem.* **27** 405–22
[48] Hackbusch W 1999 A sparse matrix arithmetic based on $\mathcal{H}$-matrices: I. Introduction to $\mathcal{H}$-matrices *Computing* **62** 89–108
[49] Grasedyck L and Hackbusch W 2003 Construction and arithmetics of $\mathcal{H}$-matrices *Computing* **70** 295–334
[50] Börm S and Grasedyck L 2002 Low-rank approximation of integral operators by interpolation *Technical Report* 72 Max Planck Institute for Mathematics in the Sciences (*Computing* at press)
[51] Basermann A, Berti G, Fingberg J and Hartmann U 2002 Head-mechanical simulations with SimBio *NEC Res. Devel.* **43**

2.3 Algebraic Multigrid with Multiple Right-Hand Side Treatment.

Algebraic Multigrid with Multiple Right-Hand Side Treatment for an Efficient Computation of EEG and MEG Lead Field Bases.
Wolters, C.H., Anwander, A., Reitzinger, S. and Haase, G., In *Halgren, E., Ahlfors, S., Hämäläinen, M. and Cohen, D. (eds.): BIOMAG 2004, Proc. of the 14th Int. Conf. on Biomagnetism, Boston, USA*, pp. 465–466 (2004).

Corresponding author: C.H. Wolters

Algebraic MultiGrid with Multiple Right-Hand Side Treatment for an Efficient Computation of EEG and MEG Lead Field Bases

C.H.Wolters[1,2,3], A. Anwander[3], S. Reitzinger[4] and G. Haase[5]

(1) Scientific Computing and Imaging Institute, University of Utah, Salt Lake City, USA
(2) Max Planck Institute for Mathematics in the Sciences, Leipzig, Germany
(3) Max Planck Institute for Human Cognitive and Brain Sciences, Leipzig, Germany
(4) CST GmbH, Darmstadt, Germany
(5) Inst. for Mathematics and Computational Sciences, University of Graz, Austria.

ABSTRACT

Iterative solver techniques are used for the computation of EEG and MEG lead field bases for finite element method based volume conductor mode ling. Within this paper, we will discuss a new efficient strategy, the algebraic multigrid preconditioned conjugate gradient method with simultaneous treatment of multiple right-hand sides. We will show that this solver leads to a much higher cache hit rate, which speeds the computation by more than a factor of 2. Together with the concept of the EEG and MEG lead field bases, the complexity of realistic high resolution anisotropic finite element forward modeling within the EEG/MEG inverse problem is significantly reduced and can now be performed in approximately the same time as boundary element head modeling.

KEY WORDS

EEG/MEG Source Reconstruction, Finite Element Method, Lead Field Bases, Algebraic MultiGrid, Preconditioned Conjugate Gradient Methods, Treatment of Multiple Right-Hand Sides, Cache Algorithms

INTRODUCTION

When choosing the Finite Element (FE) method for volume conductor modeling within the EEG/MEG inverse problem, the construction of the lead field bases requires "number of EEG/MEG sensors" many solutions of large sparse systems of linear equations [Wolters, 2004]. Therefore, preconditioning techniques for the iterative solution process are important to speed the computation. It was previously shown that the Algebraic MultiGrid preconditioned Conjugate Gradient (AMG-CG) method is a very efficient solver for inhomogeneous anisotropic high resolution FE forward modeling [Wolters 2001, Wolters, 2002, Mohr, 2003]. Within this paper, we will discuss a new strategy for a further speedup, the simultaneous treatment of multiple right-hand sides.

METHODS

In a first step, compared to the AMG-CG presented, e.g., in [Wolters, 2001], general algorithmical improvements were implemented for the new Multiple Right-Hand Side AMG-CG (MultiRHS-AMG-CG) [Haase, 2003].

The old memory management for the stiffness and interpolation matrices was replaced by the classical Compact Row Storage (CRS) format in order to decrease the number of cache misses. Within the AMG algorithm, defect calculation follows forward Gauss-Seidel (GS) smoothing and both operations require matrix-vector operations. For symmetric stiffness matrices, parts of the matrix-vector operation from the last GS smoothing can be efficiently stored and reused by the defect calculation, a merging which leads to a reduction of the operation count. The AMG-procedure on the next coarser level is called with a zero- initial correction vector. This can be used, too, so that the first forward GS smoothing sweep on the coarser levels is reduced to half of the arithmetic and memory operations. If a V-cycle is chosen, i.e., only one pre-smoothing sweep is performed, the special structure of this smoother on the coarser levels furthermore leads to a reduction of the subsequent defect computation.

Since the RHSs in the lead field bases approach are computed beforehand and the stiffness matrix remains the same, we can simultaneously solve for a whole block of RHSs. The most computationally expensive operations in the AMG-CG method are the matrix-vector operations within the CG and within the AMG components smoothing, defect calculation, interpolation and prolongation. If the vector for one RHS is exchanged against a whole block of vectors for multiple RHSs and if this block is not stored as a matrix, but as a long vector (first the first entries of the RHSs, then the second entries etc., resulting in a long vector), then each matrix entry only has to be accessed once and can be multiplied to all corresponding values in the block-vector. This procedure results in much higher cache hit rates, which speeds the computations. For the simultaneous treatment of 3 RHS, the inner loops were manually unrolled, leading to a further reduction of the solver time.

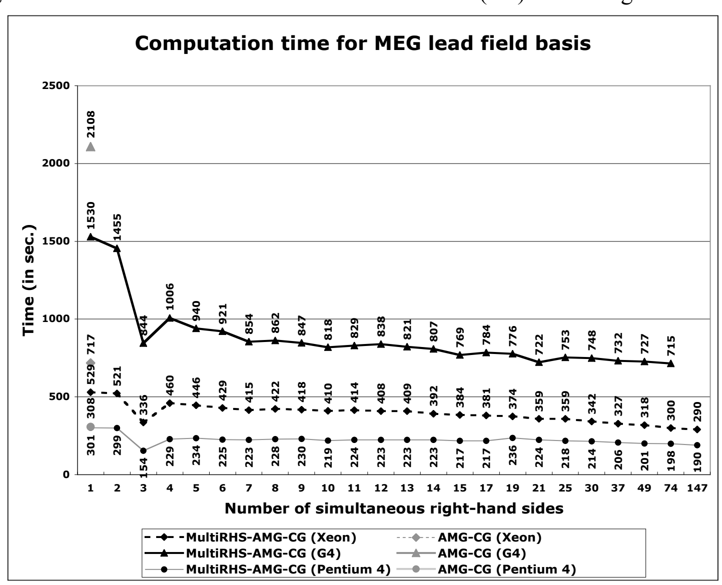

Figure 1 Time for the computation of the MEG lead field basis on a Mac-OSX PowerBook G4 and on Red-Hat Linux PC's with either Xeon or Pentium 4 architecture using the conventional AMG-CG and the new AMG-CG with simultaneous treatment of multiple right-hand sides.

RESULTS

As a basis for our computations, we chose a realistic anisotropic tetrahedral FE model with 147287 nodes and 892115 elements, a 71 electrode EEG and a 147 channel MEG configuration. We compared the computation time for the construction of the EEG and MEG lead field bases for the Jakobi-preconditioned CG (J-CG), the symmetric Incomplete Cholesky preconditioned CG without fill-in (symIC(0)-CG) and the AMG-CG (see [Wolters, 2001] for these approaches) with the new MultiRHS-AMG-CG while varying the number of simultaneously treated RHSs. Speedup tests were performed on three different platforms, a Mac-OSX with PowerBook G4 proc (1Ghz, 512 KB cache), a Red-Hat Linux PC with Xeon proc (2.4Ghz, 512 KB cache) and a Red-Hat Linux PC with Pentium 4 proc (3.2 Ghz, 1024 KB cache). The computation time for the EEG/MEG lead field bases with J-CG (symIC(0)-CG) on those three platforms were 4978/13361 sec. (2620/7261 sec.), 1543/4061 sec. (729/2089 sec.) and 929/2512 sec. (498/1322 sec.). The results for AMG-CG and MultiRHS-AMG-CG for MEG and EEG are shown in Figs. 1 and 2. The computation time for a specific number of simultaneous RHSs is indicated above the curves.

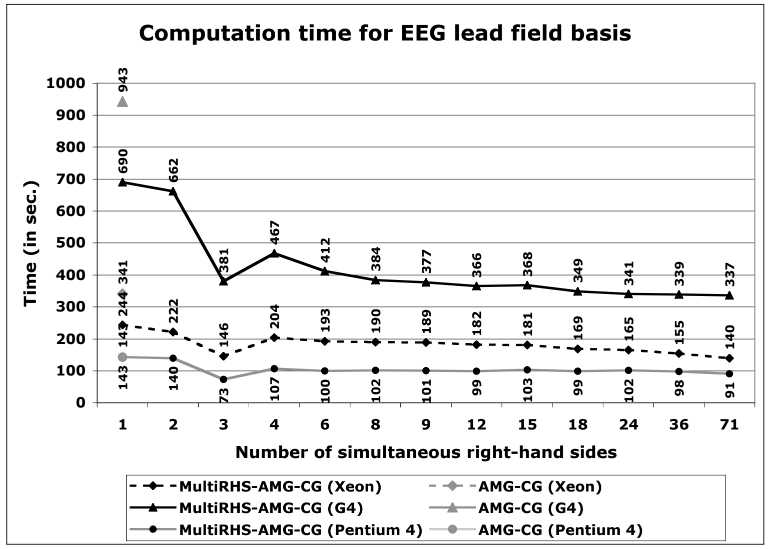

Figure 2 Time for the computation of the EEG lead field basis on a Mac-OSX PowerBook G4 and on Red-Hat Linux PC's with either Xeon or Pentium 4 architecture using the conventional AMG-CG and the new AMG-CG with simultaneous treatment of multiple right-hand sides.

DISCUSSION

On all platforms, the treatment of multiple RHSs within the new MultiRHS-AMG-CG reduced the computation time for the EEG and MEG lead field bases by at least a factor of 2. With the manual unrollment of inner loops for the simultaneous treatment of 3 RHS, this approach belongs to the fastest on all platforms so that we would recommend that choice for the RHS parameter. On platforms with a smaller cache and a slower access to the main memory, the improvement of the data-structures by means of the CSR storage for stiffness and interpolation matrices led to a further speedup factor of up to 1.38.

The combination of the lead field bases concept [Wolters, 2004] with the presented MultiRHS-AMG-CG solver for the setup phase reduces significantly the complexity of anisotropic high resolution finite element head modeling. The computation for the presented head model with nearly a million tetrahedral elements can be performed on a single processor platform in roughly the same time as boundary element head modeling. If the resolution still has to be increased (e.g., to the resolution of the MRI), the use of the parallel version of our software NeuroFEM-Pebbles [Anwander, 2002] [Wolters, 2002] gets necessary in order to distribute the memory.

ACKNOWLEDGEMENTS

This work has been supported by the MPI for Mathematics in the Sciences Leipzig, by the IST-program of the European Commission, project No.10378, http://www.simbio.de, by the NIH NCRR center for Bioelectric Field Modeling, Simulation and Visualization and by the Austrian Science Fund-'Fonds zur Förderung der wissenschaftlichen Forschung'-within the SFB F013 "Numerical and Symbolic Scientific Computing".

REFERENCES

Anwander, A., Wolters, C.H., Dümpelmann, M. Knösche, T. Influence of realistic skull and white matter anisotropy on the inverse problem in EEG/MEG-source reconstructtion. in Biomag2002, Proc. 13th Int. Conf. on Biomagnetism, H.Nowak, J.Haueisen, F.Giessler, and R.Huonker, eds. (VDE Verlag GmbH, Berlin, Offenbach, 2002, http://biomag2002.uni-jena.de, p.679-81.

Haase, G., Reitzinger, S. Cache Issues of Algebraic Multigrid Methods for Linear Systems with Multiple Right-Hand Sides SFB-Report 02-05, University Linz, SFB F013, June 2002.

Mohr, M. and Vamrunste, B. Comparing Iterative Solvers for Linear Systems associated with the Finite Difference Discretisation of the Forward Problem in Electro-Encephalographic Source Analysis. Med. Biol. Eng. Comp., 2003. p. 75-84.

Wolters, C.H., Reitzinger, S., Basermann, A., Burkhardt, S., Hartmann, U., Kruggel, F. , Anwander, A. Improved Tissue Modeling and Fast Solver Methods for High Resolution FE-Modeling in EEG/MEG-Source Localization. in Biomag2000, Proc. 12th Int. Conf. on Biomagnetism, J. Nenonen, R.J. Ilmoniemi, and T. Katila, eds. (Helsinki Univ. of Tech., Espoo, Finland, 2001, http://biomag2000.hut.fi), p.655-58.

Wolters, C.H., Kuhn, M., Anwander, A., Reitzinger, S. A Parallel Algebraic Multigrid Solver for Finite Element Method Based Source Localization in the Human Brain. Comp.Vis.Sci. 5(3), 2002, p.165-77.

Wolters, C.H., Grasedyck, L., Anwander, A. and Hackbusch, H. Efficient Computation of Lead Field Bases and Influence Matrix for the FEM-based EEG and MEG Inverse Problem. in Biomag2004, Proc. 14th Int. Conf. on Biomagnetism, Boston, USA, August 2004.

2.4 EEG and MEG transfer matrix approach: Evaluation

Efficient Computation of Lead Field Bases and Influence Matrix for the FEM-based EEG and MEG Inverse Problem.
Wolters, C.H., Grasedyck, L., Anwander, A. and Hackbusch, W., In *Halgren, E., Ahlfors, S., Hämäläinen, M. and Cohen, D. (eds.): BIOMAG 2004, Proc. of the 14th Int. Conf. on Biomagnetism, Boston, USA*, http://www.biomag2004.org, pp. 104–107 (2004).

Corresponding author: C.H. Wolters

Efficient Computation of Lead Field Bases and Influence Matrix for the FEM-based EEG and MEG Inverse Problem

C.H.Wolters[1,2,3], L.Grasedyck[2] , A.Anwander[3] and W.Hackbusch[2]

(1) Scientific Computing and Imaging Institute, University of Utah, Salt Lake City, USA
(2) Max Planck Institute for Mathematics in the Sciences, Leipzig, Germany
(3) Max Planck Institute for Human Cognitive and Brain Sciences, Leipzig, Germany

ABSTRACT

The inverse problem in EEG and MEG aims at reconstructing the underlying current distribution in the human brain. The finite element method, used for the forward problem, is able to realistically model tissue conductivity inhomogeneities and anisotropies. So far, the computational complexity is quite large when using the necessary high resolution finite element models. It is already known that the so-called reciprocity can strongly reduce this complexity with regard to the EEG modality. We will derive algorithms for the efficient computation of EEG and MEG lead field bases which exploit the fact that the number of sensors is generally much smaller than the number of reasonable dipolar sources. Each finite element forward solution is then reduced to a simple matrix-vector multiplication instead of an expensive iterative finite element solution process. Our approaches can be applied to inverse reconstruction algorithms in both continuous and discrete source parameter space for EEG and MEG. In combination with modern solver methods, the presented approach leads to a highly efficient solution of FE-based source reconstruction problems.

KEY WORDS

EEG/MEG Source Reconstruction, Conductivity Anisotropy and Inhomogeneity, Finite Element Method, Inverse Algorithms, Reciprocity, Lead Field Bases, Algebraic Multigrid Solver, Preconditioned Conjugate Gradient Methods

INTRODUCTION

For the forward problem in EEG/MEG source reconstruction, the volume conductor head has to be modeled. It is known that the head tissue compartments scalp, skull, cerebro-spinal fluid, brain gray matter and white matter have different conductivities and that the layers skull and white matter are anisotropic conductors [Wolters, 2003]. Different numerical approaches for the forward problem have been used such as Multi-Layer Sphere, Boundary Element (BE) and Finite Element (FE) head modeling, where only the FE method is able to treat both realistic geometries as well as inhomogeneous and anisotropic material parameters. The influence of skull and white matter conductivity anisotropy on the EEG/MEG forward and inverse problem was studied in realistic FE models in [Marin, 1998], [Haueisen, 2002], [Wolters, 2003]. In those studies it has been shown that an exact modeling of tissue conductivity inhomogeneity and anisotropy is crucial for an accurate reconstruction of the sources.

An important question is how to handle the computational complexity of FE-modeling with regard to the inverse problem. It is the state-of-the-art approach for FE-based forward modeling in EEG/MEG inverse methods to solve an FE equation system for each possible dipolar source [Buchner, 1997]. For the FE method, we recently developed fast solver approaches based on multigrid ideas, speeding the computations by factors of up to 100 compared to standard approaches [Wolters, 2002]. In that study we used parallelization to speed the computations and to distribute the memory between the computational nodes. Still, the repeated solution of such a system with a constant geometry matrix for thousands of right-hand sides (the sources) is the major time consuming part within the inverse localization process and limits the resolution of the models.

A further very efficient concept for the reduction of the computational complexity has been described for the EEG, the concept of reciprocity [Weinstein, 2000], [Vanrumste, 2001]. The reciprocity theorem for the electric case states that the field of the so-called lead vectors is the same as the current field raised by feeding a reciprocal current to the lead. The concept allows to switch the role of the sensors with the dipole locations. For FE based EEG source reconstruction, it was shown in [Weinstein, 2000] how to use this principle for the efficient computation of a so-called *node-oriented lead field basis*, a matrix with ``number sensors'' rows and ``number FE nodes'' columns. This matrix can then be exploited within the EEG inverse problem. In [Vanrumste, 2001], reciprocity was used for the efficient solution of the EEG inverse problem when using the Finite Difference method for the forward problem. The application of reciprocity to MEG is non-trivial and has been studied in [Nolte, 2003], where the *magnetic lead field theorem* was proven. Nevertheless, as far as we know, it is not yet clear how to efficiently compute the lead field basis for the MEG in combination with the FE method for the forward problem.

In this paper, we will simply apply the mathematical law of associativity with respect to the matrix multiplication. Then, for each head model, we only have to solve ``number of EEG/MEG sensors'' times a large sparse FE system of equations in order to compute the lead field basis for both EEG and MEG. This setup can be computed efficiently using the MultiRHS-AMG-CG solver [Wolters, 2004/2]. Each forward solution is then reduced to the multiplication of the lead field basis to an FE right-hand side vector. Simulation studies with a high resolution anisotropic FE head model and a blurred dipole model will then show that an influence matrix with a resolution of 2mm can be computed in only a few seconds on a simple single processor PC.

METHODS

The electric forward problem:

From the quasistatic Maxwell equations, we can derive the equation

$$-\nabla \cdot (\sigma \nabla \Phi) = -\nabla \vec{j}^{\,p}, \tag{1}$$

which describes the potential distribution Φ in the head domain due to a primary source $\vec{j}^{\,p}$ in the brain. We assume that the 3x3 conductivity tensors σ are given for the head domain. For the forward problem, the primary current and the conductivity distribution in the volume conductor are known and the equation has to be solved for the unknown potential distribution. The boundary condition $(\sigma_1 \nabla \Phi_1, \vec{n})\big|_{\text{surface}} = (\sigma_2 \nabla \Phi_2, \vec{n})\big|_{\text{surface}}$ with $\vec{n}$ the unit surface normal expresses the continuity of the current density across any surface between regions of different conductivity. We find homogeneous Neumann conditions on the head surface Γ, $(\sigma \nabla \Phi, \vec{n})\big|_{\Gamma} = 0$, and, additionally, a reference electrode with given potential, i.e., $\Phi_{\text{ref}} = 0$.

The magnetic forward problem:

Since the divergence of the magnetic induction $\vec{B}$ is zero, a magnetic vector potential $\vec{A}$ with $\vec{B} = \nabla \times \vec{A}$ can be introduced. From the Maxwell equations, using Coulomb's gauge $\nabla \cdot \vec{A} = 0$, we can therefore derive a Laplace equation for $\vec{A}$ and, since the magnetic permeability μ is constant over the whole space, solve it as shown in (2) and described in more detail in [Wolters, 2004/1]. Let Ω be the head domain and let F be the surface enclosed by the MEG magnetometer flux transformer $\Upsilon = \partial F$. The magnetic flux Ψ through Υ is determined as a surface integral over the magnetic induction for the coil area F, or, using Stokes theorem, as

$$\Psi = \int_F \vec{B} \cdot d\vec{f} = \oint_\Upsilon \vec{A}(\vec{x}) \cdot d\vec{x} = \oint_\Upsilon \frac{\mu}{4\pi} \int_\Omega \frac{\vec{j}^{\,p}(\vec{y})}{|\vec{x} - \vec{y}|} d\vec{y} \cdot d\vec{x} - \oint_\Upsilon \frac{\mu}{4\pi} \int_\Omega \frac{\sigma(\vec{y}) \nabla \Phi(\vec{y})}{|\vec{x} - \vec{y}|} d\vec{y} \cdot d\vec{x}. \tag{2}$$

The first part of this magnetic flux is called the *primary magnetic flux* and in the following denoted with Ψ_p and the second is the so-called *secondary magnetic flux* Ψ_{sec}. Ψ_p is only dependent on the source model and can in general be computed by simply evaluating an analytical formula [Pohlmeier,1996]. If we define

$$\vec{C}(\vec{y}) = \oint_\Upsilon \frac{1}{|\vec{x} - \vec{y}|} d\vec{x} \tag{3}$$

and if the potential distribution Φ is given, the final equation for Ψ_{sec} emerges from the secondary (return) currents and can be given by

$$\Psi_{\text{sec}} = -\frac{\mu}{4\pi} \int_\Omega (\sigma(\vec{y}) \nabla \Phi(\vec{y}), \vec{C}(\vec{y})) d\vec{y} \tag{4}$$

Finite element discretization aspects for the EEG forward problem:

For the numerical solution, we choose a finite dimensional subspace with dimension N and a standard nodal finite element basis $\psi_1, \ldots, \psi_N$.
The numerical solution process depends on the chosen model for the primary source. Here, we will refer to the literature for a deeper discussion and restrict ourselves to the following remarks. The mathematical dipole model together with the subtraction approach leads to a right-hand side vector $\underline{j}^{\text{math}} \in R^N$ with N non-zero entries [Wolters, 2003]. The blurred dipole model [Buchner,1997] [Wolters, 2003] follows the law of St.Venant and is made up from monopolar loads on all neighboring FE nodes so that the dipolar moment is fulfilled and the source load is as regular as possible. The dipole moment is then only a means for visualization. In this case, the right-hand side vector $\underline{j}^{\text{blur}} \in R^N$ has only c_{nz} nonzero entries with c_{nz} the number of neighboring FE nodes. In the following derivation of the theory, we will only consider the case $\underline{j} = \underline{j}^{\text{blur}}$. Nevertheless, as shown in [Wolters, 2004/1], for $\underline{j} = \underline{j}^{\text{math}}$, the theory is very similar. The application of variational and FE techniques yields a system of linear equations

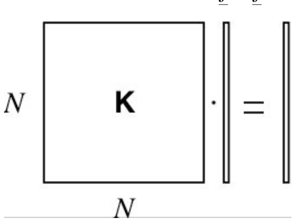

$$\mathbf{K}\underline{\Phi} = \underline{j}, \tag{5}$$

where the stiffness or geometry matrix has the entries

$$\mathbf{K}_{ij} = \int_\Omega (\nabla \psi_j(\vec{y}), \sigma(\vec{y}) \nabla \psi_i(\vec{y})) d\vec{y}, \forall 1 \le i, j \le N$$

and is symmetric positive definite. Let us further assume that the $(s_{\text{EEG}} - 1)$ non-reference EEG electrodes directly correspond to FE nodes at the surface of the head model. It is then easy to determine a restriction matrix $\mathbf{R} \in R^{(s_{EEG}-1) \times N}$, which has only one non-zero entry with the value 1 in each row and which maps the potential vector onto the non-reference EEG electrodes:

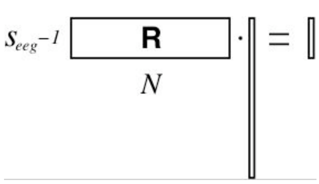

$$\mathbf{R}\underline{\Phi} =: \underline{\Phi}_{\text{EEG}} \tag{6}$$

Finite element discretization aspects for the MEG forward problem:

For the magnetic forward problem, the flux transformers of the MEG device have to be modeled. Following [Pohlmeier, 1996], we model such a coil by means of a thin, closed conductor loop, using isoparametric quadratic row elements. When approximating the potential Φ by means of its Galerkin projection, Equation (4) can be written in matrix form

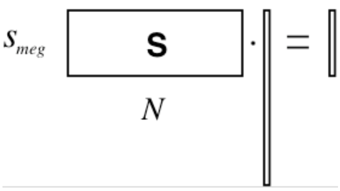

$$\mathbf{S}\underline{\Phi} =: \underline{\Psi}_{\text{sec}} \tag{7}$$

with $\mathbf{S} \in R^{s_{\text{MEG}} \times N}$ the so-called *secondary flux matrix*. $\mathbf{S}$ maps the potential onto the secondary flux vector $\underline{\Psi}_{\text{sec}} \in R^{s_{\text{MEG}}}$. The secondary flux matrix has the entries

$$\mathbf{S}_{ij} = -\frac{\mu}{4\pi}\int_{\Omega}(\sigma(\vec{y})\nabla\psi_j(\vec{y}), \vec{C}_i(\vec{y}))d\vec{y}, \forall 1 \le j \le N$$

where $\vec{C}_i(\vec{y})$ denotes the function (3) for the i$^{\text{th}}$ MEG magnetometer $\Upsilon_i, \forall 1 \le i \le s_{\text{MEG}}$. For the computation of the matrix entries of $\mathbf{S}$, a FE ansatz for the integrand and Gauss integration is used [Pohlmeier, 1996].

Computation of the lead field bases:

The inverse of the geometry/stiffness matrix, $\mathbf{K}^{-1}$, exists, but its computation is a difficult task, since the sparseness of $\mathbf{K}$ will be lost while inverting. But with regard to the EEG inverse problem, we are only interested in computing

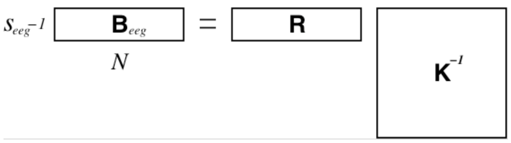

$$\mathbf{B}_{\text{EEG}} := \mathbf{R}\mathbf{K}^{-1} \in R^{(s_{\text{EEG}}-1)\times N} \tag{8}$$

which describes the direct mapping of a FE right-hand side vector to the non-reference electrodes:

$$\mathbf{B}_{\text{EEG}}\underline{j} = \mathbf{R}\mathbf{K}^{-1}\underline{j} = \mathbf{R}\underline{\Phi} = \Phi_{\text{EEG}} \tag{9}$$

[Weinstein, 2000] introduced the notation *EEG lead field basis* for $\mathbf{B}_{\text{EEG}}$. We will now see that we face a comparable situation with regard to the MEG inverse problem. In fact, let us define the *MEG lead field basis*:

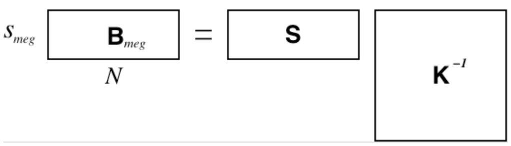

$$\mathbf{B}_{\text{MEG}} := \mathbf{S}\mathbf{K}^{-1} \in R^{s_{\text{MEG}}\times N} \tag{10}$$

One should note that the rows of $\mathbf{B}_{\text{EEG}}$ do indeed form a basis in the mathematical sense, while this is not necessarily true for $\mathbf{B}_{\text{MEG}}$. $\mathbf{B}_{\text{MEG}}$ describes the direct mapping of the FE right-hand side vector to the secondary magnetic flux vector:

$$\mathbf{B}_{\text{MEG}}\underline{j} = \mathbf{S}\mathbf{K}^{-1}\underline{j} = \mathbf{S}\underline{\Phi} = \Psi_{\text{sek}} \tag{11}$$

The lead field basis can be computed as follows: If we multiply the matrix equation

$$\begin{bmatrix}\mathbf{B}_{\text{EEG}} \\ \mathbf{B}_{\text{MEG}}\end{bmatrix} = \begin{bmatrix}\mathbf{R} \\ \mathbf{S}\end{bmatrix}\mathbf{K}^{-1} \tag{12}$$

with $\mathbf{K}$ from the right side, transpose both sides and use symmetry of $\mathbf{K}$, we obtain

$$\mathbf{K}\begin{bmatrix}\mathbf{B}_{\text{EEG}}^{\text{tr}} & \mathbf{B}_{\text{MEG}}^{\text{tr}}\end{bmatrix} = \begin{bmatrix}\mathbf{R}^{tr} & \mathbf{S}^{tr}\end{bmatrix} \tag{13}$$

From the last equation, we can compute the lead field bases by solving $s := (s_{\text{EEG}} - 1) + s_{\text{MEG}}$ large sparse FE equation systems using iterative solver methods as described in [Wolters, 2004/2]. For $\underline{j} = \underline{j}^{\text{math}}$, the theory is very similar [Wolters, 2004/1]. With regard to the forward computation complexity, the main difference between both source models is that a vector with only nonzero entries has to be multiplied to the lead field bases in contrast to only c_{nz} nonzeros for $\underline{j} = \underline{j}^{\text{blur}}$.

RESULTS

The new approach was tested by means of an influence matrix computation, which is the basis for all current density reconstruction methods. Nevertheless, the presented approach can be used for all inverse algorithms in discrete and also continuous parameter space such as MUSIC, dipole fitting etc.. For the following computational complexity considerations, we chose an anisotropic tetrahedral FE head model with 892,119 elements and 147,287 nodes. The brain surface was represented by a triangular mesh with 2mm mesh resolution, resulting in an influence space with 19106 triangles and 9555 nodes. We chose a 71 electrode EEG configuration and a 147 channel whole head BTI MEG. The influence matrices were computed without normal constraint but with a tangential constraint for the MEG, so that 9555*3=28665 forward computations were necessary for the EEG influence matrix and 9555*2=19110 for the MEG. We performed the simulations on two platforms, a 3.2GHz Pentium 4 PC with 2GB main and 1024 KB cache memory running Red-Hat Linux and a 1GHz G4 Apple Macintosh PowerBook with 1GB main and 512 KB cache memory running OSX. We compared the new lead field bases approach, i.e., solving (13) in a setup phase and then, for each forward solution, Equation (9) or (11), with the standard approach in FEM source reconstruction [Buchner, 1997], i.e., for each dipole in the influence space first solving Equation (5) and then Equation (6) or (7). The iterative FE solver method is indicated in column 3 of Table 1, we refer to [Wolters, 2004/2] for more informations. The setup time, column 4 in Table 1, only occurs once per head model. For both methods we measure the setup time for the preconditioner. For the lead field bases approach, we furthermore have to add the time for solving (13). Simulations concerning the computational complexity for the influence matrix were performed for both, the blurred [Buchner, 1997][Wolters, 2003] and the mathematical dipole [Wolters, 2003]. This is indicated in column 5 of Table 1 by means of the number of non-zeros of the FE Right-Hand Side (RHS) being c_{nz} for the blurred and N for the mathematical dipole. We also indicate the maximal memory necessary for the current implementation in our FE based source reconstruction software NeuroFEM (http://www.simbio.de).

Table 1 Comparing the computational complexity between the lead field bases- and the standard- approach in an influence matrix computation

Platform	Method	Solver method	Setup time		RHS:#nonzeros	Influence matrix		Max.memory (in MB)	
			MEG	EEG		MEG	EEG	MEG	EEG
Pentium 4 PC	New Lead field bases approach	3RHS-AMG-CG	2.6min	1.3min	$c_{nz} \approx 20$	18 sec	21 sec	654	405
			5min	3.1min	$N = 147287$	3 h	2.2 h	654	405
	Standard	symIC(0)-CG	0.2sec	0.2sec	$c_{nz} \approx 20$	52 h	59 h	432	219
Mac G4	New Lead field bases approach	3RHS-AMG-CG	14min	6.5min	$c_{nz} \approx 20$	63 sec	56 sec	654	405
			23min	11.3min	$N = 147287$	8.4 h	6 h	654	405
	Standard	symIC(0)-CG	0.5sec	0.5sec	$c_{nz} \approx 20$	230 h	302 h	432	219

DISCUSSION

In this paper we presented a new approach to strongly reduce the algorithmic complexity of EEG/MEG inverse source reconstruction algorithms, which are based on FE volume conductor modeling of the human head. The FE computational complexity of the standard approach can be seen as the main disadvantage of FE compared to Multi-Layer Sphere or BE head modeling. Our approach turns out to be very effective if the number of EEG/MEG sensors is much smaller than the number of sources for which a forward computation has to be carried out. This is the case in most applications, since the number of sensors is about 10^2, while the number of necessary forward computations is often beyond 10^4. Our approach opens new possibilities concerning the resolution of FE head modeling. The number of large sparse linear systems that have to be solved per head geometry is now limited to the number of EEG/MEG sensors in order to compute the lead field basis, a matrix with ``number of sensors" rows and ``number of FE nodes" columns. The algebraic multigrid preconditioned conjugate gradient method with simultaneous treatment of multiple right-hand sides is an efficient solver for this setup phase, as shown in [Wolters, 2004/2]. Each FE forward computation within inverse methods on both continuous and discrete source parameter space is then reduced to the multiplication of the FE right-hand side with the lead field basis. In combination with the blurred dipole model, a FE forward solution is then limited to $2 * s * c_{\mathrm{nz}}$ operations with s the number of sensors and c_{nz} the number of neighbours to a FE node. For the mathematical dipole model we show in [Wolters, 2004/1] how to further speedup the influence matrix computations by using the data-sparse H-matrix format. In combination with [Wolters, 2002], the parallelization of our new lead field approach is straight forward, important especially for higher resolutions where the memory has to be distributed.

ACKNOWLEDGEMENTS

This work has been supported by the MPI for Mathematics in the Sciences Leipzig, by the IST-program of the European Commission, project No.10378, http://www.simbio.de and by the NIH NCRR center for Bioelectric Field Modeling, Simulation and Visualization.

REFERENCES

Buchner, H., Knoll, G., Fuchs, M., Rienaecker, A., Beckmann, R., Wagner, M., Silny, J. and Pesch, J. Inverse localization of electric dipole current sources in finite element models of the human head. Electroenc.Clin.Neurophysiol., 102, 1997, p.267-78.

Marin, G., Guerin, C., Baillet, S., Garnero, L., Meunier G. Influence of skull anisotropy for the forward and inverse problem in EEG: simulation studies using the FEM on realistic head models. Human Brain Mapping, 6, 1998, p.250-69.

Haueisen, J., Tuch, D.S., Ramon, C., Schimpf, P.H., Wedeen, V.J., George, J.S., Belliveau, J.W.. The Influence of Brain Tissue Anisotropy on Human EEG and MEG. Neuroimage, 15, 2002, p.159-66.

Nolte, G.. The magnetic lead field theorem in the quasi-static approximation and its use for magnetoencephalography forward calculation in realistic volume conductors. Phys. Med. Biol., 48 (22), 2003, p.3637-52.

Pohlmeier, R. Lokalisation elektrischer Gehirnaktivitaet durch inverse Analyse des Magnetoenzephalogramms (MEG) mit Finite-Elemente-Modellen des Kopfes. Diplomarbeit in Elektrotechnik, RWTH Aachen, 1996.

Vamrunste, B., Van Hoey, G., Van de Walle, R., D'Have, M.R.P., Lemahieu, I.A., Boon, P.A.J.M. The Validation of the Finite Difference Method and Reciprocity for Solving the Inverse Problem in EEG Dipole Source Analysis. Brain Topography, 14 (2), 2001, p. 83--92.

Weinstein, D., Zhukov, L., Johnson, C. Lead-field bases for EEG source imaging. Annals of Biomed.Eng., 28 (9), 2002, p. 1059--66.

Wolters, C.H., Kuhn, M., Anwander, A., Reitzinger, S. A Parallel Algebraic Multigrid Solver for Finite Element Method based Source Localization in the Human. Comp.Vis.Sci., 5, 2002, p.165-77.

Wolters, C.H. Influence of Tissue Conductivity Inhomogeneity and Anisotropy on EEG/MEG based Source Localization in the Human Brain. MPI Series in Cognitive Neuroscience, No. 39, Leipzig: MPI of Cognitive Neuroscience, also: Dissertation, University of Leipzig, http://dol.uni-leipzig.de/pub/2003-33, 2003.

Wolters, C.H., Grasedyck, L., Hackbusch, W. Efficient Computation of Lead Field Bases and Influence Matrix for the FEM-based EEG and MEG Inverse Problem. Inverse Problems, 20 (4), 2004, p.1099-116.

Wolters, C.H., Anwander, A., Reitzinger, S., Haase G. Algebraic MultiGrid with Multiple Right-Hand Side Treatment for an Efficient Computation of EEG and MEG Lead Field Bases. in Biomag2004, Proc. 14th Int. Conf. on Biomagnetism, Boston, USA, August 2004.

2.5 Validation of the projected subtraction and Venant FE approaches for the EEG and MEG forward problem

Validating Finite Element Method Based EEG and MEG Forward Computations. Lanfer, B., Wolters, C.H., Demokritov, S.O. and Pantev, C., In: Proc. Biomedizinische Technik, Aachen, Germany, BMT, ISSN: 0939-4990, September 26-29, 2 pages (2007).

Corresponding author: B. Lanfer (Physics diploma thesis student of C.H. Wolters and S. Demokritov, Institute for Applied Physics, University of Münster).

Validating Finite Element Method Based EEG and MEG Forward Computations

Lanfer, Benjamin, Institut für Biomagnetismus und Biosignalanalyse (IBB), Münster, Germany
Wolters, Carsten H., Institut für Biomagnetismus und Biosignalanalyse (IBB), Münster, Germany
Demokritov, Sergej O., Institut für Angewandte Physik, Münster, Germany
Pantev, Christo, Institut für Biomagnetismus und Biosignalanalyse (IBB), Münster, Germany

Abstract

For the accurate reconstruction of current sources in the brain from measured EEG and MEG data accurate forward computations of the electric potentials resp. the magnetic fields are necessary. In complex head volume conductors the simulation of the electric potentials and magnetic fields can be done using the Finite Element Method (FEM).
The task of this work is to study how accurate the forward problem can be solved using FEM. This is done by comparing the numerical solution to an analytical reference solution, which exists for multilayer sphere models. The numerical solution is calculated using two different models for the mathematical dipole: Venant's principle and the subtraction approach.
The results showed, that EEG and MEG can be simulated very accurately for sources at realistic excentricities and for both dipole models using FEM. For realistic volume conductors similar accuracies of the numerical method can be expected.

1 Introduction

For the accurate reconstruction of current sources in the brain from measured EEG and MEG data, accurate forward computations of the electric potentials resp. the magnetic fields are necessary. For complex head volume conductors this simulation of the electric potentials and magnetic fields needs numerical methods. Very interesting is the Finite Element Method (FEM) as it is able to handle arbitrary geometries and inhomogeneous and anisotropic conductivities. At the IBB the software toolbox *IP-NeuroFEM* is developed in which this method is implemented [1]. The task of this work is to study how accurately the forward problem can be solved with FEM. This is done by comparing the numerical solution to an analytical reference solution, which exists for multilayer-sphere models.

2 Materials and Methods

2.1 The Sphere Model

The EEG and MEG forward computations were performed for a 3-layer sphere model. The spheres have radii of 92 mm, 86 mm and 80 mm. The conductivities of the compartments are 0.33 S/m, 0.0042 S/m and 0.33 S/m resp..
The EEG was simulated at 134 electrodes, distributed on the surface of the model in a very regular way. The MEG was simulated for 2 sets of 258 magnetometers each. The positions of the centres were distributed in a very regular way on a concentric sphere. The magnetometers are radially oriented for the first set and tangentially for the second set of sensors.
The potentials and fields were computed for dipoles at 79 positions from the centre of the spheres in steps of 1mm along the z-axis. By definition the highest dipole has an excentricity of 1.0. For the EEG the potentials were computed for radial and tangential, for the MEG only for tangential dipoles.
With the software CURRY [2] tetrahedra meshes and with VGRID [1] regular cube meshes, both with an average element width of 2 mm and approx. 400 000 nodes, were built.

2.2 The Error Measures

For the validation of our numerical solution the FEM results were compared to the analytical solution for a multilayer sphere [3,4]. Therefore two different error measures were employed.
The first measure is the *relative difference measure, RDM* [5]. It describes the difference in the topography between the analytical and numerical solution. The best value of the RDM is 0.
The second measure is the *magnification error, MAG* [5]. It indicates differences in the total strength of the potentials resp. fields. The best value of the MAG is 1.

2.3 The Dipole Models

In our study we used two methods for modelling the mathematical dipole: *Venant's principle* [6] and the *subtraction approach* [7].

3 Results

3.1 EEG

For reasonable excentricities, for both dipole directions and for both dipole models the RDM is below 0.05. For highest excentricities the RDM for the subtraction approach gets worse than the error for Venant's approach. This is suspected to be due to a not yet optimal implementation of the method. Better integration already showed to substantially improve results. Similar findings with regard to the EEG have been achieved in [8].

3.2 MEG

Radial magnetometers

The error of the primary flux can always be neglected as it is computed analytically and therefore very accurate. Nearly no difference between Venant's principle and the subtraction approach can be observed for the total flux (**Figure 1**).

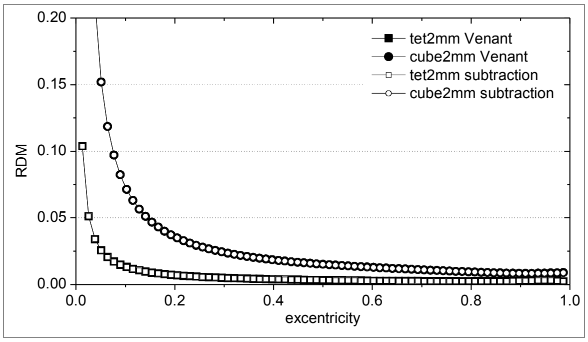

Figure 1 RDM for the total magnetic flux and radial magnetometers.

To lower excentricities the RDM rises, because the error for the secondary magnetic flux gets more important for low excentricities where the strength of the total magnetic flux strongly decays. The MAG for realistic excentricities resides between 0.95 and 1.05.

Tangential magnetometers

Here volume currents in a sphere have a significant contribution to the total magnetic flux. The RDM for the secondary magnetic flux is always below 0.03.

In the error curves of the Venant approach large oscillations are noticeable, because the accuracy of Venant's approach depends on the position of the current dipole relative to the next node of the mesh.

It can be observed that the subtraction approach is more accurate than the Venant approach.

For the total magnetic flux (**Figure 2**) the subtraction approach gives excellent results. Again, for lower excentricities, the errors of the secondary magnetic flux get more important. The MAG for realistic excentricities resides between 0.90 and 1.05.

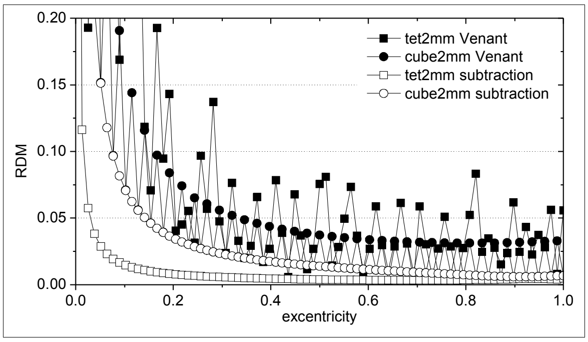

Figure 2 RDM for the total magnetic flux and tangential magnetometers.

4. Discussion

In this study it was shown that the forward problem for the EEG and the MEG can be accurately solved using the Finite Element Method. Furthermore the presented results indicate that very high accuracies for both radial and tangential magnetometers are achieved by using the subtraction approach.

It was proven in [7] that similar accuracies can be expected for realistic models of the human head. In future studies we will focus our interest on using FEM for modeling realistic volume conductors with regard to the inverse EEG and MEG problem.

5. References

[1] DFG-project FEMINVERS (Wo1425/1-1), 2006-2009;
SimBio, IST-Program of the European Commission, Project No.10378, *http://www.simbio.de,* 2000-2003

[2] CURRY, CURrent Reconstruction and Imaging, http://*www.neuroscan.com*

[3] de Munck, J.C. and Peters, M.: A fast method to compute the potential in multi sphere models. IEEE Trans. Biomed. Eng. 40 (1993)

[4] Sarvas, J.: Basic Mathematical and Electromagnetic Concepts of the Biomagnetic Inverse Problem. Phys.Med.Biol. Vol. 32, No. 1, 1987

[5] Meijs, J.W.H. et al.: On the Numerical Accuracy of the Boundary Element Method. IEEE Trans.Biomed.Eng. 36 (1989)

[6] Buchner, H. et al.: Inverse Localisation of Electric Dipole Current Sources in Finite Element Models of the Human Head. Electroenc. Clin. Neurophysiol. 102 *(*1997)

[7] Wolters, C.H. et al.: Numerical Mathematics of the Subtraction Method for the Modeling of a Current Dipole in EEG Source Reconstruction Using Finite Element Head Models. SIAM J. of Scientific Computing, 2007, in press

[8] Wolters, C. H. et al.: Numerical approaches for dipole modeling in finite element method based source analysis. International Congress Series, ICS-07008, 2007, in press

2.6 Validation of the projected subtraction, Venant and partial integration FE approaches for the EEG forward problem

Numerical approaches for dipole modeling in finite element based source analysis.
Wolters, C.H., Köstler, H., Möller, C., Härdtlein, J. and Anwander, A.. *International Congress Series, ICS-07008*, Vol.1300, pp.189-192 (June 2007).

Corresponding author: C.H. Wolters

International Congress Series 1300 (2007) 189 – 192
www.ics-elsevier.com

Numerical approaches for dipole modeling in finite element method based source analysis

C.H. Wolters [a,b,*], H. Köstler [b,c], C. Möller [c], J. Härdtlein [c], A. Anwander [d]

[a] *Institute for Biomagnetism and Biosignalanalysis, Münster University Hospital, Münster, Germany*
[b] *Scientific Computing and Imaging Institute, University of Utah, Salt Lake City, USA*
[c] *Department of Computer Science 10, University Erlangen-Nuremberg, Erlangen, Germany*
[d] *Max Planck Institute for Human Cognitive and Brain Sciences, Leipzig, Germany*

Abstract. In EEG/MEG source analysis, a mathematical dipole is widely used as the "atomic" structure of the primary current distribution. When using realistic finite element models for the forward problem, the current dipole introduces a singularity on the right-hand side of the governing differential equation that has to be treated specifically. We evaluated and compared three different numerical approaches, a subtraction method, a direct approach using partial integration and a direct approach using the principle of Saint Venant. Evaluation and comparison were carried out in a four-layer sphere model using quasi-analytical formulas. © 2007 Elsevier B.V. All rights reserved.

Keywords: EEG; MEG; Source analysis; Dipole; Finite Element method; Singularity treatment; Subtraction method; Direct potential approach

1. Introduction

An important aspect in Finite Element (FE) method based volume conductor modelling in EEG/MEG source analysis is the way of modelling the current dipole. We developed and implemented three different numerical approaches,

a) a *subtraction* potential method [1,5,7,11]
b) a direct potential approach using *Partial Integration* [6,8] and
c) a direct potential approach using Saint *Venant*'s principle [2,9,10].

* Corresponding author. Malmedyweg 15, 48149 Münster, Germany. Tel.: +49 251 83 56904; fax: +49 251 83 56874.

E-mail address: carsten.wolters@uni-muenster.de (C.H. Wolters).

doi:10.1016/j.ics.2007.02.014

In this paper, we evaluate and compare the different techniques with regard to their accuracy in a four-layer sphere model [3].

2. Theory

a) The *subtraction* potential approach divides the total potential into a singularity potential (dipole in infinite region of homogeneous conductivity) and a correction potential. When subtracting the differential equation for the singularity potential from the starting potential equation, a singularity free Poisson-problem with inhomogeneous Neumann boundary conditions for the correction potential results. Our 3D FE approach for anisotropic head models is closely related to the 2D implementation in [1]. We additionally performed a numerical analysis with a correction potential existence and uniqueness proof and FE convergence properties [11].

b) *Partial Integration* can be used on the right-hand-side (RHS) of the starting Poisson-like potential equation in the variational FE formulation. The RHS is then identical to an evaluation of the scalar product of the dipole moment with the gradient of the basis-function evaluated at the source position. For linear Ansatz-functions, the gradient is constant and non-zero only over the source element, so that the resulting FE linear equation system has only 8 non-zero RHS entries (identical to monopolar loads) when using hexahedra elements. This approach was used, e.g., in [6,8].

c) Saint *Venant*'s principle states that the specific (fine) details of load application do not influence the results observed in some distance away from the locus of load application. Following [2], a dipole can be modeled by placing monopolar sources on all neighboring FE nodes to that FE node which is closest to the source. By means of solving a local Tikhonov–Phillips regularization problem, the monopolar loads are computed so that, multiplied with their "lever arms" (distance of the node to the source), the dipole moment is optimally matched.

3. Method

The quasi-analytical series expansion formulas [3] were used as a basis for our accuracy studies. A four-layer sphere model (radii 92, 86, 80, 78 mm with conductivities of 0.33, 0.0042, 1.0, 0.33 S/m, respectively) was discretized with a 2 mm regular hexahedra mesh (426 K nodes, 406 K elements) using the software VGRID (http://www.simbio.de). For all forward EEG simulations, the software NeuroFEM-COLSAMM (http://www.simbio.de, see [4] for COLSAMM) was used with linear FE Ansatz-functions and an Algebraic MultiGrid preconditioned Conjugate Gradient (AMG-CG) method for solving the resulting FE linear equation systems up to a relative accuracy of 10^{-8} [9]. 134 electrodes were distributed in a most regular way over the outer sphere surface. The topography error Relative Difference Measure (RDM) and the MAGnification error (MAG) [5,7,11] between quasi-analytic and numeric results at those measurement sensors were evaluated for dipoles with fixed x and z and varying (in 1 mm steps) y-coordinate (depths) and either tangential or radial orientation. The eccentricity was limited to a percentage of the inner layer depending on the number of compartments, because it can be expected that the dipole is at least 2 mm below the surface in the middle of the gray matter compartment. Dipole strengths of 1 nAm were used.

4. Results

As Fig. 1 shows, one important advantage of the subtraction approach over the direct methods was that the error curves (and thus the cost functions during inverse optimization) were smooth, while the accuracy of both Venant's and Part.Int. direct potential methods were oscillating. While Venant performed best for sources on FE nodes (i.e. x, y and z are even numbers in Fig. 1), Part.Int. performed best if the source is positioned in the center of an element (x, y and z odd numbers). On the other hand, the subtraction approach with linear basis-functions was computationally more expensive and more sensitive to conductivity jumps in source vicinity if the source was pointing towards the jump (Fig. 1, radial sources). For the subtraction approach, highest relative AMG-CG solver accuracies were needed for the most eccentric sources with 10^{-4} being sufficient for the whole eccentricity range [11].

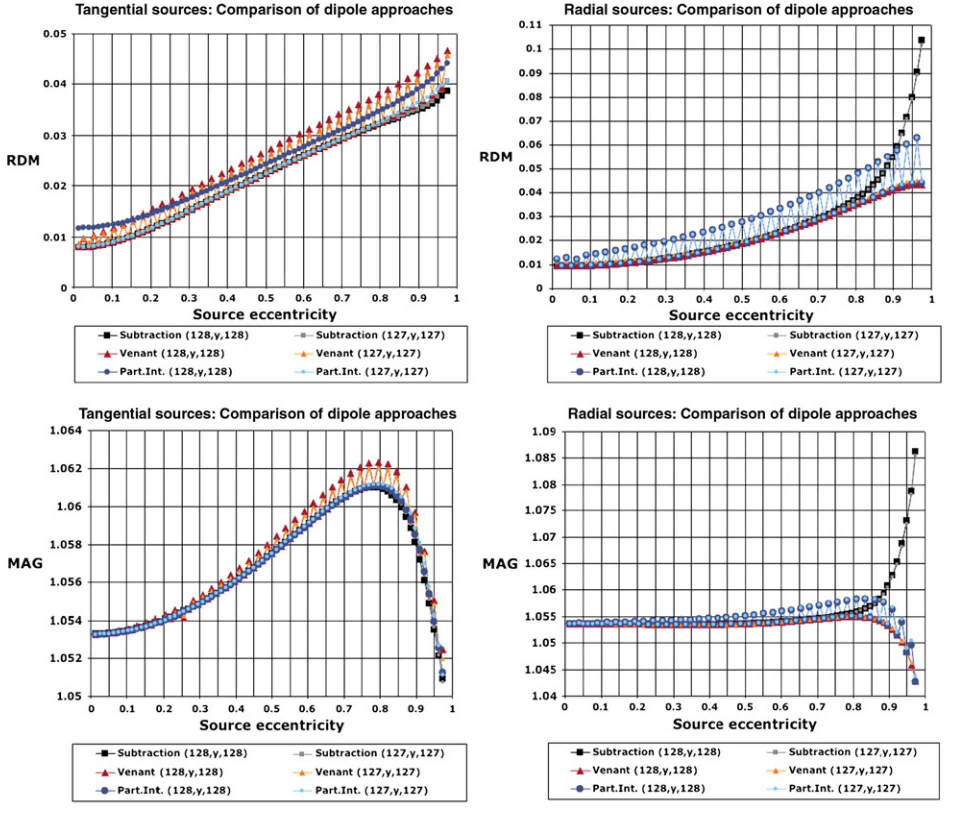

Fig. 1. Accuracy in 2 mm regular hexahedra FE model of the four compartment sphere: RDM (top row) and MAG (bottom row) for tangentially (left) and radially (right) oriented sources for the three FE forward modeling techniques subtraction (cubes: black, gray), Venant (triangles: red, orange) and Partial Integration (spheres: dark and light blue). Dipoles with fixed x and z and varying y-coordinate at realistic source eccentricities of 0 to 97% of the inner compartment at either (128, y, 128) (along nodes and faces) or (127, y, 127) (through element barycenters) were examined. (For interpretation of the references to colour in this figure legend, the reader is referred to the web version of this article.)

5. Conclusions

Inverse source analysis: All presented numeric approaches could exploit the computationally efficient EEG/MEG lead field bases concept which reduced the "number of FE equation systems to solve" to the "number of sensors" [8,9]. Each FE based forward solution was then especially cheap for the direct potential methods [9]. With our current implementation, we recommend the choice of the Venant direct potential approach at least for those inverse methods exploiting influence matrices (beamformer, current density approaches, scanning methods). The direct potential approaches are less appropriate for inverse optimization methods in continuous parameter space (e.g., dipole fits using simplex optimization), because of the presented error curve oscillations, there might be a higher risk to get stuck in local minima.

Anisotropy: All three FE approaches can treat *remote tissue anisotropy* (skull, white matter) [10], but a clear theory for *local anisotropy* (gray matter) only exists for the subtraction approach [11].

Perspective: The subtraction method is theoretically best understood and bears the highest future potential. An improved numerical quadrature should solve the accuracy problems when the source approaches a conductivity jump.

Acknowledgement

This research was supported by the German Research Foundation (DFG, WO 1425/1-1).

References

[1] K.A. Awada, et al., Computational aspects of finite element modeling in EEG source localization, IEEE Trans. Biomed. Eng. 44 (8) (1997) 736–751.

[2] H. Buchner, et al., Inverse localization of electric dipole current sources in finite element models of the human head, Electroencephalogr. Clin. Neurophysiol. 102 (4) (1997) 267–278.

[3] J.C. de Munck, M.J. Peters, A fast method to compute the potential in the multisphere model, IEEE Trans. Biomed. Eng. 40 (11) (1993) 1166–1174.

[4] J. Härdtlein, C. Pflaum, Efficient and User-friendly Computation of Local Stiffness Matrices, Frontiers in Simulation, Simulations technique, 18th Symposium in Erlangen, ISBN: 3-936150-41-9, Sep. 2005, pp. 748–753.

[5] G. Marin, et al., Influence of skull anisotropy for the forward and inverse problem in EEG: simulation studies using the FEM on realistic head models, Hum. Brain Mapp. 6 (1998) 250–269.

[6] Mohr, M. Simulation of Bioelectric Fields: The Forward and Inverse Problem of Electro-encephalographic Source Analysis. PhD thesis, Universität Erlangen-Nürnberg, Arbeitsberichte des Instituts für Informatik, 37 (6), ISSN 1611–4205, 2004.

[7] P.H. Schimpf, C.R. Ramon, J. Haueisen, Dipole models for the EEG and MEG, IEEE Trans. Biomed. Eng. 49 (5) (2002) 409–418.

[8] D. Weinstein, L. Zhukov, C. Johnson, Lead-field bases for electroencephalography source imaging, Ann. Biomed. Eng. 28 (9) (2000) 1059–1066.

[9] C.H. Wolters, L. Grasedyck, W. Hackbusch, Efficient computation of lead field bases and influence matrix for the FEM-based EEG and MEG inverse problem, Inverse Problems 20 (2004) 1099–1116.

[10] C.H. Wolters, et al., Influence of tissue conductivity anisotropy on EEG/MEG field and return current computation in a realistic head model: a simulation and visualization study using high-resolution finite element modeling, NeuroImage 30 (3) (2006) 813–826.

[11] Wolters, C.H.,Köstler, H. , Möller, C., Härdtlein, J., Grasedyck, L., and Hackbusch, W., Numerical mathematics for the modeling of a current dipole in EEG source analysis using finite element head models, SIAM J. Sci. Comp., in review, pp. 1–19, 2006.

2.7 Geometry-adapted hexahedra improve accuracy of FEM based EEG source analysis.

Geometry-adapted hexahedral meshes improve accuracy of finite element method based EEG source analysis.
Wolters, C.H., Anwander, A., Berti, G. and Hartmann, U. *IEEE Trans. Biomed. Eng.*, Vol.54, No.8, pp.1446-1453, 2007.

Corresponding author: C.H. Wolters

Geometry-Adapted Hexahedral Meshes Improve Accuracy of Finite-Element-Method-Based EEG Source Analysis

Carsten H. Wolters*, Alfred Anwander, Guntram Berti, and Ulrich Hartmann

***Abstract*—Mesh generation in finite-element- (FE) method-based electroencephalography (EEG) source analysis generally influences greatly the accuracy of the results. It is thus important to determine a meshing strategy well adopted to achieve both acceptable accuracy for potential distributions and reasonable computation times and memory usage. In this paper, we propose to achieve this goal by smoothing regular hexahedral finite elements at material interfaces using a node-shift approach. We first present the underlying theory for two different techniques for modeling a current dipole in FE volume conductors, a subtraction and a direct potential method. We then evaluate regular and smoothed elements in a four-layer sphere model for both potential approaches and compare their accuracy. We finally compute and visualize potential distributions for a tangentially and a radially oriented source in the somatosensory cortex in regular and geometry-adapted three-compartment hexahedra FE volume conductor models of the human head using both the subtraction and the direct potential method. On the average, node-shifting reduces both topography and magnitude errors by more than a factor of 2 for tangential and 1.5 for radial sources for both potential approaches. Nevertheless, node-shifting has to be carried out with caution for sources located within or close to irregular hexahedra, because especially for the subtraction method extreme deformations might lead to larger overall errors. With regard to realistic volume conductor modeling, node-shifted hexahedra should thus be used for the skin and skull compartments while we would not recommend deforming elements at the grey and white matter surfaces.**

***Index Terms*—Dipole, direct potential approach, EEG, finite-element method, geometry-adapted hexahedra, realistic head modeling, regular hexahedra, source reconstruction, subtraction potential approach.**

I. Introduction

THE localization of current sources in the human brain from surface electroencephalography (EEG) measurements (the *inverse problem*) requires a model for the *forward problem*, i.e., the determination of surface potentials from current sources in the volume. Because of its ability to treat volume conductors of arbitrary complexity and model inhomogeneous and anisotropic tissue conductivity, the finite-element method (FEM) has become popular to solve the forward problem [1], [2], [4], [5], [14], [19], [25]–[27]. An essential prerequisite for FE modeling is the generation of a mesh which represents the geometric and electric properties of the volume conductor. So far, *surface-based tetrahedral tesselations* were mainly used [1], [2], [4], [5], [14], [25], [27]. Only few studies examined regular hexahedral elements exploiting the spatial discretization inherent in medical tomographic data [19], [23], whose excellent performance has been shown in a recent accuracy study [19], and found to perform better than the surface-based tetrahedra [23]. Adaptive methods [2], [4] disallow use of lead field bases [7], [8], [21], [24] (discussed later) and loose efficiency when solving the inverse problem. The problematic stair-like approximation of curved boundaries with regular hexahedra has been addressed by [6] in a biomechanical context, where it was shown that a node-shifting approach can significantly reduce errors in von Mises stress at the surface, in spite of detrimental effects of deformed elements.

In this paper, we first present the underlying theory for two different techniques for modeling a current dipole in FE volume conductors, a subtraction and a direct potential method. We then test the hypothesis that node-shift hexahedra surface smoothing reduces EEG forward modeling errors. We evaluate the new mesh-generation approach in a four-layer sphere model for both the subtraction and the direct potential method, using statistical metrics for a comparison of the numerical results with an analytical solution at surface measurement points. We then present electric potential visualization results for a tangentially and a radially oriented source in the somatosensory cortex in regular and geometry-adapted three-compartment hexahedra FE volume conductor models of the human head using both the subtraction and the direct potential method. We finally discuss our results and conclude in the last chapter.

Manuscript received June 23, 2006; revised November 5, 2006. This work was supported by the IST-program of the European Community, project SIMBIO (http://www.simbio.de), by the Deutsche Forschungsgemeinschaft (WO1425/1-1) and the NIH NCRR Center for Integrative Biomedical Computing (http://www.sci.utah.edu/cibc). *Asterisk indicates corresponding author.*

*C. H. Wolters is with the Institute for Biomagnetism and Biosignalanalysis, Westfälische Wilhelms-Universität Münster, Malmedyweg 15, 48149 Münster, Germany, and also with the Scientific Computing and Imaging Institute, University of Utah, Salt Lake City, UT 84112 USA (e-mail: carsten.wolters@uni-muenster.de).

A. Anwander is with the Max Planck Institute for Human Cognitive and Brain Sciences, 04103 Leipzig, Germany (e-mail: anwander@cbs.mpg.de).

G. Berti is with the C&C Research Laboratories, NEC Europe Ltd., 53757 St. Augustin, Germany (e-mail: berti@ccrl-nece.de).

U. Hartmann is with the University of Applied Sciences Koblenz, Department of Mathematics, RheinAhrCampus Remagen, 53424 Remagen, Germany (e-mail: Hartmann@RheinAhrCampus.de).

Color versions of one or more of the figures in this paper are available online at http://ieeexplore.ieee.org.

Digital Object Identifier 10.1109/TBME.2007.890736

II. Methods

A. The FEM-Based EEG Forward Problem

In the quasistatic approximation of Maxwell's equations, the distribution of electric potentials Φ in the head domain Ω of conductivity σ, resulting from a primary current $\mathbf{j}^p$ is governed by the Poisson equation with homogeneous Neumann boundary conditions on the head surface $\Gamma = \partial\Omega$[18]

$$\nabla \cdot (\sigma \nabla \Phi) = \nabla \cdot \mathbf{j}^p = J^p \text{ in } \Omega, \quad \langle \sigma \nabla \Phi, \mathbf{n} \rangle = 0 \text{ on } \Gamma \quad (1)$$

with $\mathbf{n}$ the unit surface normal, and a reference electrode with given potential, i.e., $\Phi(\mathbf{x}_{\text{ref}}) = 0$.

The primary currents are generally modeled by a mathematical dipole at position $\mathbf{x}_0 \in \mathbb{R}^3$ with the moment $\mathbf{M}_0 \in \mathbb{R}^3$[18],

$$\mathbf{j}^p(\mathbf{x}) = \mathbf{M}_0 \delta(\mathbf{x} - \mathbf{x}_0). \tag{2}$$

1) The Subtraction Approach: For the subtraction method [1], [2], [4], [14], [19], [23], the total potential Φ is split into two parts

$$\Phi = \Phi^\infty + \Phi^{\text{corr}}, \tag{3}$$

where the singularity potential Φ^∞ is defined as the solution for a dipole in an unbounded homogeneous conductor with constant conductivity σ^∞ (the conductivity at the source position). The solution of Poisson's equation for the singularity potential

$$\Delta\Phi^\infty = \frac{\nabla \cdot \mathbf{j}^p}{\sigma^\infty} \tag{4}$$

can be formed analytically by use of (2)[18]

$$\Phi^\infty(\mathbf{x}) = \frac{1}{4\pi\sigma^\infty} \frac{\langle \mathbf{M}_0, (\mathbf{x} - \mathbf{x}_0)\rangle}{|\mathbf{x} - \mathbf{x}_0|^3}.$$

Subtracting (4) from (1) yields a Poisson equation for the correction potential

$$-\nabla \cdot (\sigma \nabla \Phi^{\text{corr}}) = \nabla \cdot ((\sigma - \sigma^\infty)\nabla\Phi^\infty) \text{ in } \Omega \tag{5}$$

with inhomogeneous Neumann boundary conditions at the surface

$$\langle \sigma \nabla \Phi^{\text{corr}}, \mathbf{n}\rangle = -\langle \sigma \nabla \Phi^\infty, \mathbf{n}\rangle \text{ on } \Gamma. \tag{6}$$

The advantage of (5) is that the right-hand side is free of any source singularity, because in a subdomain around the dipole, the conductivity $\sigma - \sigma^\infty$ is zero. For the numerical approximation of the correction potential, we use the FE method with isoparametric transformations of the deformed cube elements to the reference cube element and piecewise trilinear basis functions φ_i at nodes $\boldsymbol{\xi}_i$, i.e., $\varphi_i(\boldsymbol{\xi})_i = 1$ and $\varphi_j(\boldsymbol{\xi}_i) = 0$ for all $j \neq i$. When projecting both the singularity and the correction potential into the FE space, i.e., $\Phi^\infty(\mathbf{x}) \approx \Phi_h^\infty(\mathbf{x}) = \sum_{i=1}^N \varphi_i(\mathbf{x}) u_i^\infty$ with $u_i^\infty = \Phi^\infty(\boldsymbol{\xi}_i)$ and $\Phi^{\text{corr}}(\mathbf{x}) \approx \Phi_h^{\text{corr}}(\mathbf{x}) = \sum_{j=1}^N \varphi_j(\mathbf{x}) u_j^{\text{corr}}$, and applying variational and FE techniques to (5),(6), we finally arrive at a linear system

$$K \underline{u}^{\text{corr}} = \underline{J}^{\text{corr}} \tag{7}$$

with the stiffness matrix

$$K^{[i,j]} = \int_\Omega \langle \sigma \nabla \varphi_i, \nabla \varphi_j \rangle \tag{8}$$

the right-hand side vector

$$\underline{J}^{\text{corr}} = -K^{\text{corr}} \underline{u}^\infty - S \underline{u}^\infty \tag{9}$$

with matrices

$$(K^{\text{corr}})^{[i,j]} = \int_\Omega \langle (\sigma - \sigma^\infty) \nabla \varphi_i, \nabla \varphi_j \rangle,$$
$$S^{[i,j]} = \int_\Gamma \langle \sigma^\infty \nabla \varphi_j, \mathbf{n} \rangle \varphi_i$$

and with $\underline{u}^\infty = (u_1^\infty, \ldots, u_N^\infty)$ being the coefficient vector for Φ_h^∞. We then seek for the coefficient vector $\underline{u}^{\text{corr}} = (u_1^{\text{corr}}, \ldots, u_N^{\text{corr}})$ and, using (3), the total potential can be computed. In a small subdomain around the dipole position, the linear approximation of the singularity potential Φ^∞ through Φ_h^∞ is quite rough, but $\sigma - \sigma^\infty$ is zero so that, under the condition that the source is not too close to a next conductivity jump, (5) and (6) are appropriately modeled with the presented linear FE approach.

2) Direct Potential Approach: Even if the mathematical dipole (2), consisting of an infinitesimal separation between the two poles, an infinite current sink and source and a finite dipole moment, is widely used in source analysis, a smoother model based on finite monopolar source and sink distributions and separations might be even more realistic [5], [19], [21], [26], [27]. However, from a more practical point of view, dipole vectors contain more information (strength and orientation) and ease the interpretation of inversely calculated source configurations. Therefore, it has been proposed to approximate the mathematical dipole with a smoother *blurred dipole* using a collection of monopolar sources and sinks on all neighboring FE mesh nodes in order to optimally match a given dipole moment vector [5]. In the following, we present the theory for the direct potential approach using the blurred dipole model. We will closely follow the ideas of [5], where the blurred dipole model was used in tetrahedra volume conductors, but our matrix-based reformulation easifies understanding and implementation and allows a direct comparison with the subtraction approach especially with regard to the computational effort in both tetrahedra and regular and node-shifted hexahedra FE volume conductors. Starting from the basic relation for a dipole moment $\mathbf{T}_l \in \mathbb{R}^3$ at position $\mathbf{x}_l \in \mathbb{R}^3$ ($\mathbf{x}_l$ being an arbitrary position in the grey matter compartment, i.e., not necessarily an FE node), $\mathbf{T}_l = \int_\Omega (\mathbf{x} - \mathbf{x}_l) J^p(\mathbf{x}) d\mathbf{x}$ (see, e.g., [16, formula (2.92)]), and assuming discrete sources on only C neighboring FE mesh nodes, it is $\mathbf{T}_l = \sum_{c=1}^C \Delta\mathbf{x}_{cl} \underline{j}_l^{[c]}$ with $\Delta\mathbf{x}_{cl}$ denoting the vector from FE node c to source position $\mathbf{x}_l$. When using higher moments $\underline{\bar{T}}_l^r \in \mathbb{R}^{n_0+1}$ with $n_0 = 1, 2$ and the Cartesian direction $r (r = x, y, z)$, it is

$$\left(\underline{\bar{T}}_l^r\right)^{[n]} = \left(\underline{\bar{T}}_l^r\right)^{[n]} \left(\underline{j}_l\right) = \sum_{c=1}^C \left(\Delta\bar{x}_{cl}^r\right)^n \underline{j}_l^{[c]} \quad \forall\, n \in 0, \ldots, n_0 \tag{10}$$

(for a motivation of higher moments see [5]). The bar indicates a scaling with a reference length a_{ref}, so that

$$\Delta\bar{x}_{cl}^r = \frac{\Delta x_{cl}^r}{a_{\text{ref}}} \overset{!}{<} 1 \tag{11}$$

is dimensionless and the physical dimension of the resultant scaled n^{th} order moment, $\left(\underline{\bar{T}}_l^r\right)^{[n]}$, is that of a current (i.e., A, Ampère). $a_{\rm ref}$ has to be chosen so that $\Delta \bar{x}_{cl}^r$ is smaller 1. This is expressed by the exclamation mark in (11). The equation is well known from mechanical engineering, where small forces in combination with long lever arms have the same effect on the system as large forces in combination with short lever arms. If we now define the matrix $\bar{X}_l^r \in \mathbb{R}^{(n_0+1)\times C}$, the moment vector $\underline{\bar{M}}_l^r \in \mathbb{R}^{n_0+1}$, computed from the given dipole moment vector $\mathbf{M}_l$, and the diagonal source weighting matrix $\bar{W}_l^r \in \mathbb{R}^{C\times C}$ by

$$\begin{aligned}\left(\bar{X}_l^r\right)^{[n,c]} &= \left(\Delta \bar{x}_{cl}^r\right)^n \\ \left(\underline{\bar{M}}_l^r\right)^{[n]} &= M_l^r \left(\frac{1}{2a_{\rm ref}}\right)^n \left(1-(-1)^n\right) \\ \bar{W}_l^r &= \mathrm{DIAG}\left(\left(\Delta \bar{x}_{1l}^r\right)^s, \ldots, \left(\Delta \bar{x}_{Cl}^r\right)^s\right) \end{aligned} \tag{12}$$

with $s=0$ or $s=1$, then we compute the monopole load vector $\underline{j}_l$ of the blurred dipole on the C neighboring FE nodes from the given dipole moment vector $\mathbf{M}_l$ at position $\mathbf{x}_l$ by means of minimizing the following functional:

$$\begin{aligned}F_\lambda(\underline{j}_l) &= \|\underline{\bar{M}}_l^r - \underline{\bar{T}}_l^r(\underline{j}_l)\|_2^2 + \lambda\|\bar{W}_l^r \underline{j}_l\|_2^2 \\ &= \|\underline{\bar{M}}_l^r - \bar{X}_l^r \underline{j}_l\|_2^2 + \lambda\|\bar{W}_l^r \underline{j}_l\|_2^2 \\ &\stackrel{!}{=} \min. \end{aligned}$$

The first part of the functional F_λ ensures a minimal difference between the moments of the blurred dipole $\underline{\bar{T}}_l^r$ and the target ones $\underline{\bar{M}}_l^r$, while the second part, a Tikhonov-Phillips regularizer with λ the *dipole regularization parameter*, smoothes the monopole distribution in a weighted sense and enables a unique minimum for F_λ. The solution of the minimization problem is given by

$$\left(\left(\bar{X}_l^r\right)^{tr} \bar{X}_l^r + \lambda \left(\bar{W}_l^r\right)^{tr} \bar{W}_l^r\right) \underline{j}_l = \left(\bar{X}_l^r\right)^{tr} \underline{\bar{M}}_l^r$$

(see, e.g., [13, Theorem 4.2.1]) so that the final solution for the monopole source vector $\underline{j}_l$ of the blurred dipole is given by

$$\underline{j}_l = \left(\sum_{r=1}^{3}\left\{\left(\bar{X}_l^r\right)^{tr} \bar{X}_l^r + \lambda \left(\bar{W}_l^r\right)^{tr} \bar{W}_l^r\right\}\right)^{-1} \times \sum_{r=1}^{3}\left\{\left(\bar{X}_l^r\right)^{tr} \underline{\bar{M}}_l^r\right\}. \tag{13}$$

The highest order is generally chosen as $n_0 = 1$ or $n_0 = 2$, where the latter effects a spatial concentration of loads in the dipole axis. Furthermore, $s = 1$ stresses the spatial concentration of loads around the dipole.

In the direct potential approach in combination with the blurred dipole, the total potential $\Phi(x) \approx \Phi_h(x) = \sum_{j=1}^N \varphi_j(x)u_j$ is projected into the FE space and, using variational and FE techniques for (1), a linear system

$$K\underline{u} = \underline{J}^{\rm blur} \tag{14}$$

is derived with the same stiffness matrix as in (8). The right-hand side vector $\underline{J}^{\rm blur} \in \mathbb{R}^N$ has only C nonzero entries at the neighboring FE nodes to the considered dipole location. It is determined by

$$\left(\underline{J}^{\rm blur}\right)^{[i]} = \begin{cases} j_l^{[c]}, & if \exists c \in \{1,\ldots,C\} : i = \mathrm{GLOB}(c) \\ 0, & \text{otherwise} \end{cases} \tag{15}$$

for a source at location $\mathbf{x}_l$, where the function GLOB determines the global index i to each of the local indices c.

3) Efficient Solution Methods: We employ an algebraic multigrid preconditioned conjugate gradient (AMG-CG) method for solving the linear systems (7) and (14). We solve up to a relative error of 10^{-8} in the controllable $KN^{-1}K$-energy norm (with N^{-1} being one V-cycle of the AMG) [22].

As shown above, the linear systems (7) and (14) have the same stiffness matrix (8), but the right-hand side vector is dense for the subtraction approach (9) and sparse with C entries (the number of neighboring FE nodes) for the blurred dipole approach (15). This has implications for the computational effort when using the *lead field basis* approach [24] (additionally, see [7], [8], [21]), which limits the total number of FE linear equation systems to be solved for any inverse method to the number of sensors $\mathrm{nb\_sens}$. After computing the $\mathrm{nb\_sens}$ vectors of the lead field basis, each forward problem can be solved by a single multiplication of the right-hand side $\underline{J}$ with the basis [24], resulting in a computational effort of $2 * \mathrm{nb\_sens} * P$ operations, where $P = N$ for the subtraction approach and $P = C$ for the blurred dipole direct potential approach. Note that the lead field basis can not be used when the mesh is adapted according to varying source positions within the inverse problem. We therefore attempt to avoid local mesh refinement techniques as used in [2] and [4].

B. FE Volume Conductor Models

In source reconstruction, head modeling is generally based on segmented magnetic resonance (MR) data, where curved tissue boundaries have a stair-step representation. We segmented a three tissue realistically-shaped head model with compartments skin, skull and brain and an isotropic voxel size of 1 mm^3 from a T1- and proton-density-weighted MR dataset of a healthy 32-year-old male subject. The bi-modal MR approach allowed an improved modeling of the skull-shape as described in detail in [23]. We chose conductivities of 0.33, 0.0042, and 0.33 S/m for the three compartments [5].

For node-shift hexahedra evaluation purposes, we furthermore discretized a four-compartment sphere model in a 3-D data volume with 1 mm^3 voxel resolution. The layers represent the compartments skin, skull, cerebrospinal fluid and brain with outer surfaces of radii 92, 86, 80, and 78 mm, respectively. We chose conductivities of 0.33 S/m, 0.0042, 1.0, and 0.33 S/m for the four compartments [2], [19].

C. Generation of Hexahedral FE Meshes

Voxels from a segmented MR volume can be used directly as hexahedral elements, possibly reducing resolution by prior subsampling of the volume as we do below for our volume conductor models. In order to increase conformance to the real geometry and to mitigate the stair-case effects of a voxel mesh, a technique was proposed in [6] to shift nodes on material interfaces in order to obtain smoother and more accurate boundaries. Nodes on a two-material interface are moved into the direction of the centroid of the set of incident voxels with *minority material*, i.e., the material occuring three times or less in the 8 surrounding voxels. If the centroid of these minority voxels relative to a node is (x, y, z), it is shifted by

$$(\Delta x, \Delta y, \Delta z) = (ns * x, ns * y, ns * z) \tag{16}$$

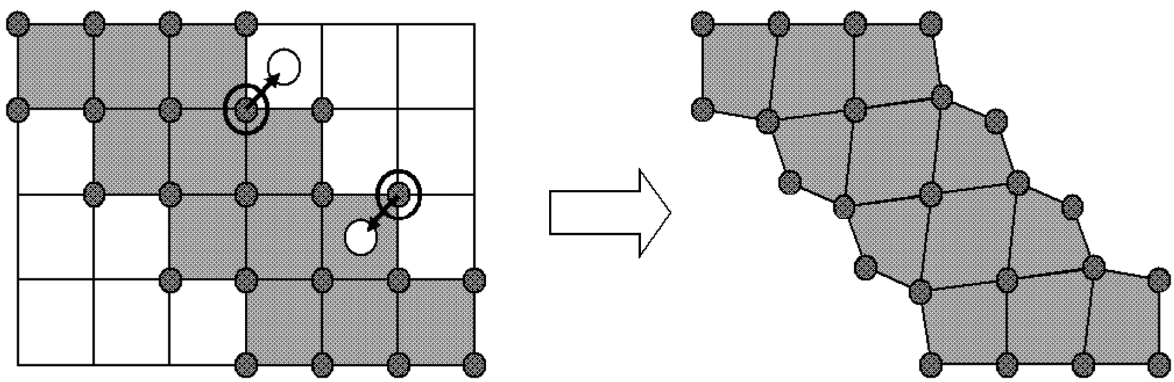

Fig. 1. Concept of the hexahedral node-shift approach for the smoothing of interface boundaries in a 2D scenario: On the left side of the figure, the procedure is illustrated for only two boundary nodes from which one is moved outside and the other one is moved inside towards the centroids of their minority elements. The final result of the node-shift, a smoothed boundary representation using deformed hexahedra, is shown on the right side.

with the user-defined node-shift factor $ns \in [0, 0.5)$ (cf. Fig. 1). The choice $ns \in [0, 0.5)$ ensures that interior angles at element vertices remain convex and the Jacobian determinant remains positive [6].

D. Error Measures in Sphere Models

In [15], series expansion formulas were derived for a mathematical dipole in a multilayer sphere model, denoted now as the *analytical solution*. We compare analytic and numeric solutions using two error criteria that are commonly evaluated in source analysis [2], [14], [19], the *relative difference measure* (RDM)

$$\mathrm{RDM} = \sqrt{\sum_{i=1}^{s}\left(\frac{\underline{\phi}_{\mathrm{ana}}^{[i]}}{\|\underline{\phi}_{\mathrm{ana}}\|_2} - \frac{\underline{\phi}_{\mathrm{num}}^{[i]}}{\|\underline{\phi}_{\mathrm{num}}\|_2}\right)^2}$$

and the *magnification factor* (MAG)

$$\frac{\mathrm{MAG} = \|\underline{\phi}_{\mathrm{num}}\|_2}{\|\underline{\phi}_{\mathrm{ana}}\|_2,}$$

where $\|\cdot\|_2$ denotes the Euclidian norm and $\underline{\phi}_{\mathrm{ana}}, \underline{\phi}_{\mathrm{num}} \in \mathbb{R}^{\mathrm{nb\_sens}}$ the analytic or numeric solution vectors at measurement electrodes. The RDM is a measure for the topography error and the MAG indicates changes in the potential amplitude.

We furthermore define the *node-shift improvement factor* for the RDM (MAG) as the ratio of the RDM (MAG-1) in the regular $(ns = 0)$ versus the RDM (MAG-1) in a node-shifted $(ns > 0)$ hexahedra model.

E. Parameter Choice for the Blurred Dipole in the Direct Potential Approach

We choose the parameters of the blurred dipole as follows: The maximal dipole order n_0(10) and the scaling reference length a_{ref}(11) are set to $n_0 = 2$ and $a_{\mathrm{ref}} = 20.0$ mm, respectively. Since the chosen mesh size (discussed later) is a large factor smaller than the reference length, the second order term $(\Delta\bar{x}_{cl}^{r})^2$ is small and the model focuses on fulfilling the dipole moments of the zeros and first order. The exponent of the source weighting matrix in (12) is fixed to $s = 1$ and the regularization parameter in (13) is chosen as $\lambda = 10^{-6}$. The settings effect a spatial concentration of the monopole loads in the dipole axis around the dipole location and gave best results in former evaluations of the presented blurred dipole model in tetrahedra [5], [23] and also regular hexahedra volume conductors [23].

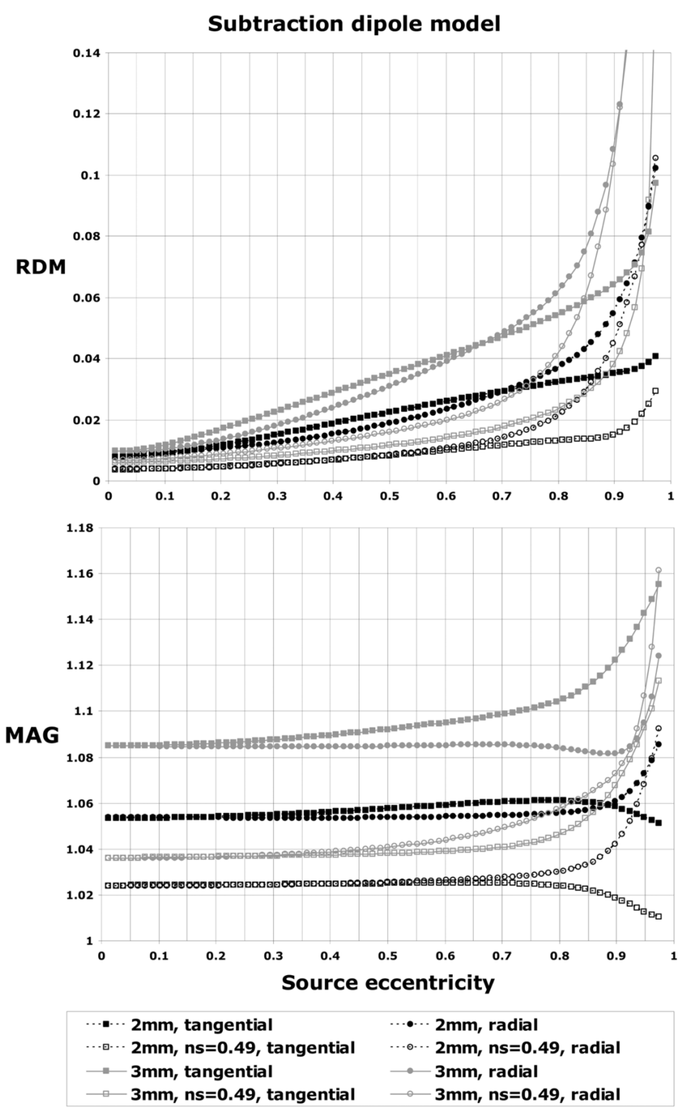

Fig. 2. Subtraction potential approach: Comparison of the numerical accuracy for regular $(ns = 0)$ and node-shifted $(ns = 0.49)$ 2- and 3-mm hexahedra models for radially and tangentially oriented sources.

TABLE I
SUBTRACTION APPROACH: RDM AND MAG NODE-SHIFT IMPROVEMENT FACTORS FOR 2-mm HEXAHEDRA MODELS

	tangential			radial		
	Min	Max	Average	Min	Max	Average
ns	RDM improvement factors					
0.20	1.26	1.52	1.49	1.03	1.51	1.41
0.40	1.38	2.29	2.12	1.00	2.19	1.90
0.49	1.38	2.74	2.48	0.97	2.44	2.05
ns	MAG improvement factors					
0.20	1.40	1.62	1.43	1.00	1.41	1.35
0.40	1.96	3.17	2.10	0.96	1.98	1.80
0.49	2.21	4.91	2.49	0.93	2.24	2.00

III. RESULTS

As a programming platform for the presented subtraction and direct potential approach, we used our software environment IP-NeuroFEM [20].

A. Evaluation of the Hexahedra Node-Shift in Sphere Models

Hexahedral models of the 4-layer sphere were subsampled to 2- (426 K nodes) and 3-mm (130 K nodes) voxels and node-shift factors ns(16) of 0 (regular), 0.2, 0.4, and 0.49 were used for our evaluation. To achieve independence of the specific choice of the sensor configuration, we distribute $\mathrm{nb\_sens} = 134$ electrodes in a most-regular way over the outer sphere surface. Comparisons between the numeric and the analytic solutions at the electrode positions are carried out for dipoles located on one axis at depths (*eccentricities*) of 0%–97% (in 1-mm steps) of the inner layer (78-mm radius) using both radial and tangential orientations. We limit the eccentricity to 97%, because it can be expected that the dipole location is at least 2 mm below the surface of the innermost sphere in the middle of the grey matter compartment. We use dipole strengths of 1 nAm.

1) Subtraction Potential Approach: Fig. 2 plots RDM and MAG for the regular $(ns = 0)$ and the node-shifted $(ns = 0.49)$ 2- and 3-mm hexahedra models for all realistic source eccentricities. In the 2-mm model, we observe a maximal RDM of 0.105 and a maximal MAG of 9.2% over all depths and for both source orientations. For the 3-mm model, RDM accuracies below 0.14 are only achieved for eccentricities up to 91% and therefore for the vast majority of realistic source positions, but the results for higher eccentricities are above this threshold and the MAG is equipped with an error of up to 16.1%. In Table I, minimal, maximal and average RDM and MAG node-shift improvement factors are shown for the 2-mm model. For the 3-mm model, the results are very similar (only shown for $ns = 0.49$ in Fig. 2). The average improvement factors for both mesh resolutions increase continuously with increasing node-shift values and, for the maximal examined deformation, they are higher than 2.28 for tangential and 1.6 for radial sources. However, as it can be observed in both Fig. 2 and Table I, the node-shift might cause a deterioration of the overall error for sources located within a deformed element or in its direct neighbor element.

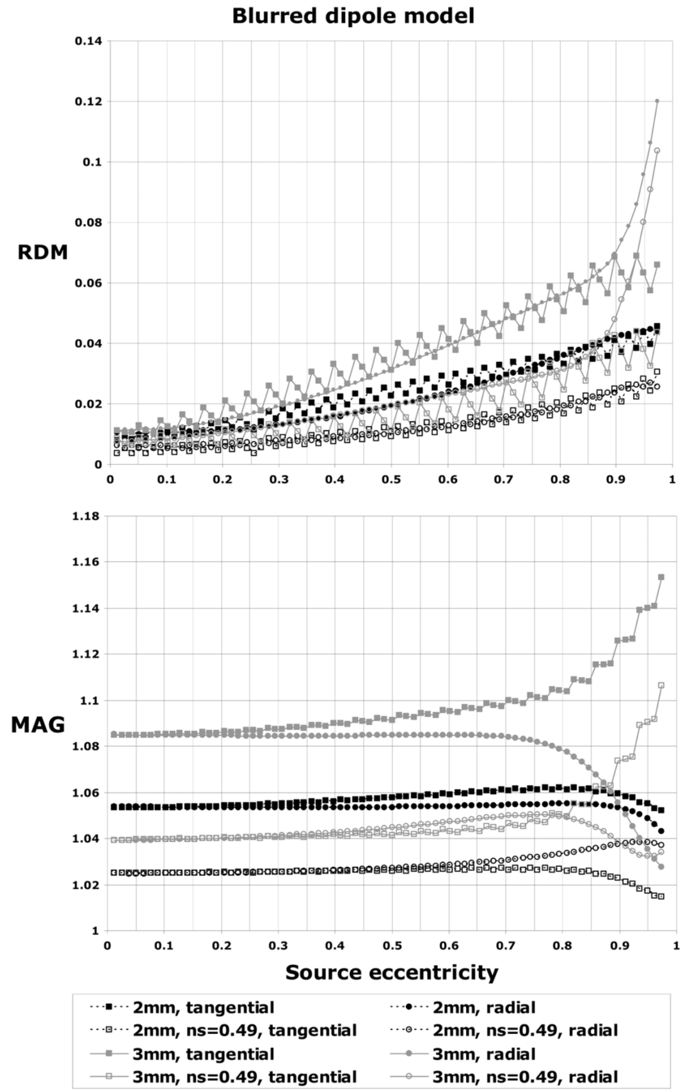

Fig. 3. Direct potential approach: Comparison of the numerical accuracy for regular $(ns = 0)$ and node-shifted $(ns = 0.49)$ 2- and 3-mm hexahedra models for radially and tangentially oriented sources.

2) Direct Potential Approach: In Fig. 3, RDM and MAG are plotted for regular $(ns = 0)$ and node-shifted $(ns = 0.49)$ 2- and 3-mm hexahedra models for all realistic source eccentricities. Again, the error curves are rising with increasing source eccentricity. When compared to the numerical performance of the subtraction approach, the direct approach is less sensitive with smaller errors for sources close to conductivity discontinuities. However, due to variations of the dipole approximation of the blurred dipole model depending on the location within an element, error curve oscillations can be observed. The node-shift improvement factors for the 2-mm model are shown in Table II. All factors are above 1.0, so that a general improvement through node-shifting can be concluded. We achieve very similar results for the 3-mm model, the only significant difference to the 2-mm results is that the MAG improvement factors for the two most eccentric radial sources is slightly below one (see Fig. 3). The average improvement factors for both mesh resolutions increase

TABLE II
DIRECT APPROACH: RDM AND MAG NODE-SHIFT IMPROVEMENT FACTORS FOR 2-mm HEXAHEDRA MODELS

	tangential			radial		
	Min	Max	Average	Min	Max	Average
ns	RDM improvement factors					
0.20	1.24	1.65	1.41	1.31	1.41	1.37
0.40	1.43	2.57	1.88	1.62	1.83	1.73
0.49	1.49	3.04	2.10	1.67	1.95	1.83
ns	MAG improvement factors					
0.20	1.39	1.56	1.41	1.14	1.40	1.34
0.40	1.91	2.68	2.00	1.18	1.93	1.74
0.49	2.14	3.55	2.30	1.17	2.17	1.90

continuously with increasing node-shift values and, for the maximal deformation, they are higher than 2.05 for tangential and 1.56 for radial sources.

B. Application of Node-Shift Hexahedra Meshing to Realistic Volume Conductor Modeling

The three-compartment realistic volume conductor model was meshed using 2-mm regular and node-shift ($ns = 0.49$) hexahedra. This resulted in hexahedra FE models with 386 K nodes and 366 K elements. The dipole strengths are 100 nAm.

The potential distribution in the regular and node-shifted hexahedra models were then computed and visualized using both the subtraction (Fig. 4) and the direct potential approach using the blurred dipole (Fig. 5) for a radially and a tangentially oriented source in somatosensory cortex. As it can be observed in the figures, with regard to the mesh properties, the three surfaces skin, outer and inner skull are represented in a much smoother way in the node-shifted mesh compared to the stair-step approximation in the regular hexahedra model. While the surfaces of outer and inner skull are directly visible in the node-shift hexahedra model, they otherwise can only be estimated indirectly from the bends in the isopotential lines at both skull surfaces. The consequence with regard to the field patterns is, that the smoothness property of the mesh is taken over to the isopotential-lines, which at both skull surfaces appear smoother in the node-shifted meshes.

IV. DISCUSSION AND CONCLUSION

The focus of our study is the validation of a node-shift hexahedral meshing approach for a subtraction and a direct potential approach in FE-based EEG source analysis, a method which was shown to perform well in a biomechanical FE application [6]. The node-shifted hexahedra better describe the smooth tissue boundaries, but, following convergence proofs in FE numerical analysis, they might also cause larger numerical errors.

We chose a four compartment sphere model with the classic conductivity values of 0.33, 0.0042, 1.0,and 0.33 S/m (see, e.g., [2] and [19]), i.e., a ratio of 1:80 between the skull and the brain compartment. Recent works suggest that the skull conductivity should be only 15 [17] to 25 [10] times lower than the brain conductivity. However, in [11], we presented a low resolution conductivity estimation algorithm that we recently applied to the estimation of the brain:skull conductivity, where we found the classic ratio of 1:80 [12]. In any case, when applying the nodeshift hexahedral meshing approach to a four layer sphere model with a skull to brain ratio of 1:15, the results are very similar to the results shown in this paper, the overall numerical errors of both presented numerical approaches are only lower.

From the evaluation in this paper we can conclude that, with average node-shift improvement factors around 2 for a 2-mm hexahedra resolution, both topography and magnitude errors at surface measurement locations are strongly reduced by the node-shift approach, if the source is not located within a deformed element or its direct neighbor. For a 2-mm mesh resolution, the node-shift always improved the results for the direct potential method, while for sources within the deformed element or its direct neighbor, results of the subtraction approach were slightly spoiled for radial sources. With regard to realistic head modeling, we conclude that the boundaries of the skin, outer and inner skull should be smoothed using the hexahedra node-shift, while we would not recommend deforming elements at the grey and white matter surfaces.

For the used zero-mean EEG data, the RDM can be related to the correlation coefficient (CC) through $\mathrm{RDM} = \sqrt{2(1 - \mathrm{CC})}$ [19] and a CC above 0.99 (i.e., RDM below 0.14) was associated with a localization error of no more than 1 mm [9], [19]. We can therefore conclude that, for the presented sphere model and for both the direct and the subtraction approach, regular and especially node-shifted 2-mm hexahedra models achieve satisfying numerical accuracy. No mesh adaptation is needed in contrast to tetrahedral local mesh-refinement strategies [2], [4], where elements are refined depending on the varying source position within the inverse problem. We can therefore exploit lead field bases [24], the computationally very efficient solution strategies for the EEG and magnetoencephalography (MEG) inverse problem as described in Section II-A. With increasing eccentricity, the errors begin to rise, a behavior, which has also been observed in [1], [2], [4], [5], [14], and [19]. The decrease in numerical accuracy with increasing eccentricity is stronger for the presented subtraction approach compared to the presented direct method. For the direct potential approach, due to the mesh-dependent implementation of the blurred dipole, we observe oscillations in the error curves. This can be explained by the choice of the C neighboring nodes to the source position $\mathbf{x}_l$ in formula (10). In our implementation, the C FE nodes are chosen like follows: First, the closest FE node $\mathbf{x}_p$ to $\mathbf{x}_l$ is determined. For the modeling of the blurred dipole, we then compute monopole sources on those C FE nodes, which have a common edge with $\mathbf{x}_p$. As Fig. 3 shows, the best approximation to the mathematical dipole can thus be achieved if the distance $|\mathbf{x}_l - \mathbf{x}_p|$ is zero (the source is positioned at a FE-node), while the approximation is worst if $\mathbf{x}_l$ approaches the center of an element. With regard to continuous dipole fits during an inverse EEG analysis, this might be a disadvantage of the presented direct approach compared to the presented subtraction method, where error curves and thus inverse cost functions are smooth.

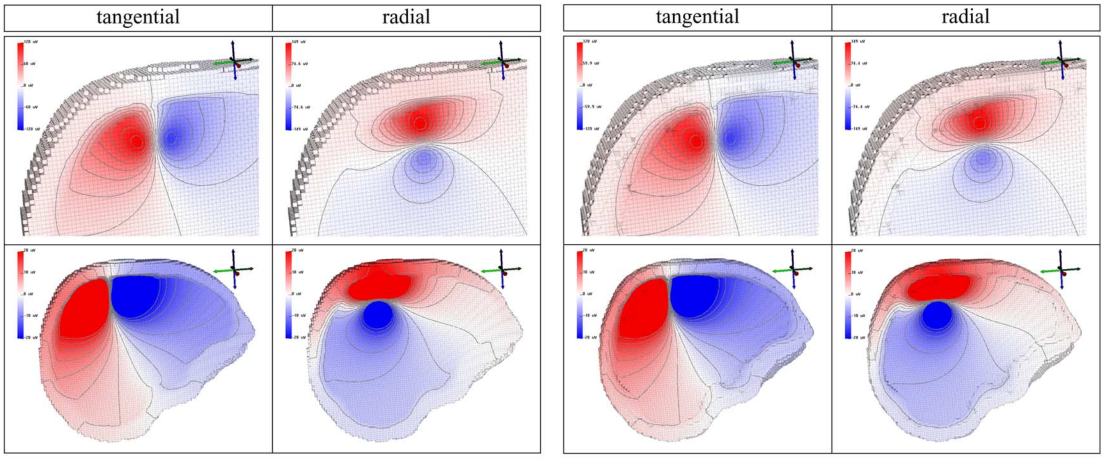

(a) (b)

Fig. 4. Subtraction potential approach in 3-compartment realistic volume conductor of the human head: Visualization of the total potential for a tangentially and a radially oriented dipole in the somatosensory cortex in a regular (a) and a node-shifted $(ns = 0.49)$ hexahedra FE model (b). The sagittal cutplane was chosen in a distance of 9mm from the source position. 15 isopotential lines are shown from the minimal to the maximal potential value in the given plane (upper row) and for an interval of $-20\ \mu\mathrm{V}$ to 20 $\mu\mathrm{V}$ (lower row). Visualization was carried out using BioPSE [3]. (For interpretation of the references to colour in this figure legend, the reader is referred to the web version of this paper).

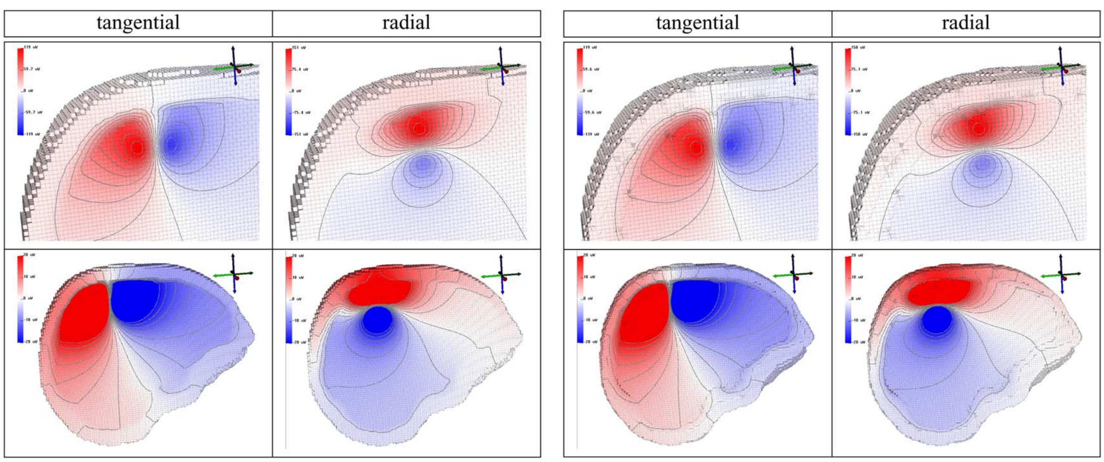

(a) (b)

Fig. 5. Direct potential approach using the blurred dipole in a 3-compartment realistic volume conductor of the human head: Visualization of the potential distribution for a tangentially and a radially oriented dipole in the somatosensory cortex in a regular (a) and a node-shifted $(ns = 0.49)$ 2mm hexahedra FE model (b). The sagittal cutplane was chosen in a distance of 9mm from the source position. 15 isopotential lines are shown from the minimal to the maximal potential value in the given plane (upper row) and for an interval of − 20 to 20 $\mu\mathrm{V}$ (lower row). Visualization was carried out using BioPSE [3]. (For interpretation of the references to colour in this figure legend, the reader is referred to the web version of this paper).

ACKNOWLEDGMENT

The authors would like to thank J. de Munck for providing his software for the analytical solution and for his quick responses whenever needed.

REFERENCES

[1] K. A. Awada, D. R. Jackson, J. T. Williams, D. R. Wilton, S. B. Baumann, and A. C. Papanicolaou, "Computational aspects of finite element modeling in EEG source localization," *IEEE Trans. Biomed. Eng.*, vol. 44, no. 8, pp. 736–751, Aug. 1997.

[2] O. Bertrand, M. Thévenet, and F. Perrin, J. Nenonen, H.M. Rajala, and T. Katila, Eds., "3D finite element method in brain electrical activity studies," in *Biomagn. Localization 3D Modelling*, 1991, pp. 154–171.

[3] Problem Solving Environment for Modeling, Simulation, and Visualization of Bioelectric Fields BioPSE, Scientific Computing and Imaging Institute (SCI), 2002 [Online]. Available: http://software.sci.utah.edu/biopse.html

[4] S. P. van den Broek, *Volume Conduction Effects in EEG and MEG*. Enschede, The Netherlands: Proefschrift Univ. Twente, 1997.

[5] H. Buchner, G. Knoll, M. Fuchs, A. Rienäcker, R. Beckmann, M. Wagner, J. Silny, and J. Pesch, "Inverse localization of electric dipole current sources in finite element models of the human head," *Electroencephalogr. Clin. Neurophysiol.*, vol. 102, pp. 267–278, 1997.

[6] D. Camacho, R. Hopper, G. Lin, and B. Myers, "An improved method for finite element mesh generation of geometrically complex structures with application to the skullbase," *J. Biomech.*, vol. 30, no. 10, pp. 1067–1070, 1997.

[7] N. G. Gencer and C. E. Acar, "Sensitivity of EEG and MEG measurements to tissue conductivity," *Phys. Med. Biol.*, vol. 49, pp. 701–717, 2004.

[8] H. Hallez, B. Vanrumste, P. Van Hese, Y. D'Asseler, I. Lemahieu, and R. Van de Walle, "A finite difference method with reciprocity used to incorporate anisotropy in electroencephalogram dipole source localization," *Phys. Med. Biol.*, vol. 50, pp. 3787–3806, 2005.

[9] J. Haueisen, A. Böttner, H. Nowak, H. Brauer, and C. Weiller, "The influence of conductivity changes in boundary element compartments on the forward and inverse problem in EEG and MEG," *Biomedizinische Technik*, vol. 44, no. 6, pp. 150–157, 1999.

[10] Y. Lai, W. van Drongelen, L. Ding, K. E. Hecox, V. L. Towle, D. M. Frim, and B. He, "Estimation of in vivo human brain-to-skull conductivity ratio from simultaneous extra- and intra-cranial electrical potential recordings," *Clin. Neurophysiol.*, vol. 116, pp. 456–465, 2005.

[11] S. Lew, C. Wolters, A. Anwander, S. Makeig, and R. S. MacLeod, D. Cheyne, B. Ross, G. Stroink, and H. Weinberg, Eds., "Low resolution conductivity estimation to improve source localization," in *Proc. 15th Int. Conf. Biomagnetism* International Conference Series, 2007, vol. 1300c, pp. 149–152.

[12] S. Lew, C. Wolters, A. Anwander, S. Makeig, and R. S. MacLeod, "Low resolution conductivity estimation to improve source localization," NeuroImage, in review, 2007.

[13] A. K. Louis, *Inverse und schlecht gestellte Probleme*. Leipzig, Germany: Teubner-Verlag, 1989.

[14] G. Marin, C. Guerin, S. Baillet, L. Garnero, and G. Meunier, "Influence of skull anisotropy for the forward and inverse problem in EEG: Simulation studies using the FEM on realistic head models," *Hum. Brain Mapp.*, vol. 6, pp. 250–269, 1998.

[15] J. C. de Munck and M. Peters, "A fast method to compute the potential in the multisphere model," *IEEE Trans. Biomed. Eng.*, vol. 40, no. 11, pp. 1166–1174, Nov. 1993.

[16] W. Nolting, *Grundkurs: Theoretische Physik, Elektrodynamik*. Ulmen, Germany: Zimmermann-Neufang, 1992.

[17] T. F. Oostendorp, J. Delbeke, and D. F. Stegeman, "The conductivity of the human skull: Results of *in vivo* and *in vitro* measurements," *IEEE Trans. Biomed. Eng.*, vol. 47, no. 11, pp. 1487–1492, Nov. 2000.

[18] J. Sarvas, "Basic mathematical and electromagnetic concepts of the biomagnetic inverse problem," *Phys. Med. Biol.*, vol. 32, no. 1, pp. 11–22, 1987.

[19] P. H. Schimpf, C. R. Ramon, and J. Haueisen, "Dipole models for the EEG and MEG," *IEEE Trans. Biomed. Eng.*, vol. 49, no. 5, pp. 409–418, May 2002.

[20] SimBio: A Generic Environment for Bio-Numerical Simulation, IST-Program of the European Commission Project No. 10378, 2000–2003 [Online]. Available: http://www.simbio.de

[21] D. Weinstein, L. Zhukov, and C. Johnson, "Lead-field bases for electroencephalography source imaging," *Ann. Biomed. Eng.*, vol. 28, no. 9, pp. 1059–1066, 2000.

[22] C. H. Wolters, M. Kuhn, A. Anwander, and S. Reitzinger, "A parallel algebraic multigrid solver for finite element method based source localization in the human brain," *Comp. Vis. Sci.*, vol. 5, no. 3, pp. 165–177, 2002.

[23] C. H. Wolters, "Influence of tissue conductivity inhomogeneity and anisotropy on EEG/MEG based source localization in the human brain" Ph.D. dissertation, Leipzig, Univ., Leipzig, Germany, 2003 [Online]. Available: http://dol.uni-leipzig.de

[24] C. H. Wolters, L. Grasedyck, and W. Hackbusch, "Efficient computation of lead field bases and influence matrix for the FEM-based EEG and MEG inverse problem," *Inverse Prob.*, vol. 20, no. 4, pp. 1099–1116, 2004.

[25] C. H. Wolters, A. Anwander, D. Weinstein, M. Koch, X. Tricoche, and R. MacLeod, "Influence of tissue conductivity anisotropy on EEG/MEG field and return current computation in a realistic head model: A simulation and visualization study using high-resolution finite element modeling," *NeuroImage*, vol. 30, no. 3, pp. 813–826, 2006.

[26] Y. Yan, P. L. Nunez, and R. T. Hart, "Finite-element model of the human head: Scalp potentials due to dipole sources," *Med. Biol. Eng. Comput.*, vol. 29, pp. 475–481, 1991.

[27] Y. Zhang, L. Ding, W. van Drongelen, K. Hecox, D. Frim, and B. He, "A cortical potential imaging study from simultaneous extra- and intracranial electrical recordings by means of the finite element method," *NeuroImage*, vol. 31, pp. 1513–1524, 2006.

Carsten H. Wolters received the M.Sc. degree (with highest honors) in mathematics with a minor in medicine from the RWTH Aachen, Aachen, Germany, and the Ph.D. (*magna cum laude*) degree in mathematics from the University of Leipzig, Leipzig, Germany, in 1997 and 2003, respectively.

From 1997 to 2004, he was with the Max Planck Institutes for Human Cognitive and Brain Sciences and Mathematics in the Sciences, Leipzig, and contributed to the EU-project SimBio. In 2004, he joined the Scientific Computing and Imaging Institute at the University of Utah, Salt Lake City. Since 2005, he is a Research Associate with the Institute for Biomagnetism and Biosignalanalysis at the University of Münster, Münster, Germany. His research interests are in the field of neuroscience with a focus on EEG/MEG source analysis.

Alfred Anwander received the M.Sc. degree in electrical engineering from the University of Karlsruhe, Karlsruhe, Germany, in 1996, and the M.Sc. (DEA) and Ph.D. degrees from INSA Lyon Scientific and Technical University of Lyon, Lyon, France, in 1996 and 2001, respectively.

Since 2000, he is a Scientist the Max Planck Institute for Human Cognitive and Brain Sciences, Leipzig, Germany. His research interests are in EEG/MEG source localization and quantitative connectivity from diffusion MRI.

Guntram Berti received the M.Sc. degree (Diplom) in mathematics from the University of Dortmund, Dortmund, Germany, in 1994 and the Ph.D. degree in mathematics from the University of Cottbus, Cottbus, Germany, in 2000.

In 2001, he joined the C&C Research Laboratories of NEC Europe Ltd., St. Augustin, Germany, where he leads the Medical and Life Science Applications Team. He contributed to the EU projects SimBio, GEMSS and @neurIST. His research interests include mesh generation and geometry processing for medical applications.

Ulrich Hartmann studied physics in Heidelberg and Göttingen, Germany. The main focus of his studies was in medical physics in the area of SPECT imaging. After having received the diploma degree from the physics department of the University of Göttingen in 1995 he began working towards the Ph.D. degree at the Max Planck Institute for Human Cognitive and Brain Sciences, Leipzig, Germany, in the field of finite-element modelling.

In 1998, he took the position as a Research Staff Member at the NEC Research Laboratories, St. Augustin, Germany. He continued his work on finite-element models in medicine and started working on the European project SimBio. In 2001, he became Professor of Medical Engineering and Informatics at the University of Applied Sciences, Koblenz, Germany, where he is responsible for the biomechanics laboratory.

2.8 A full subtraction approach for dipole modeling in EEG source analysis using the FE method

A highly accurate full subtraction approach for dipole modeling in EEG source analysis using the finite element method
Drechsler, F., Wolters, C. H., Dierkes, T., Si, H. and Grasedyck, L.. submitted to *Applied Numerical Mathematics*, (2007).

Corresponding author: C.H. Wolters

A highly accurate full subtraction approach for dipole modelling in EEG source analysis using the finite element method

F. Drechsler[1], C. H. Wolters[2,*], T. Dierkes[2], H. Si[3], L. Grasedyck[1]

(1) Max-Planck-Institut für Mathematik in den Naturwissenschaften, Leipzig, Germany

(2) Institut für Biomagnetismus und Biosignalanalyse, Westfälische Wilhelms-Universität Münster, Münster, Germany

(3) Weierstraß-Institut für Angewandte Analysis und Stochastik, Berlin, Germany.

Abstract

A mathematical dipole is widely used as a model for the primary current source in electroencephalography (EEG) source analysis. In the governing Poisson-type differential equation, the dipole leads to a singularity on the right-hand side, which has to be treated specifically. In this paper, we will present a full subtraction approach where the total potential is divided into a singularity and a correction potential. The singularity potential is due to a dipole in an infinite region of homogeneous conductivity. The correction potential is computed using the finite element (FE) method. Special care is taken to appropriately evaluate the right-hand side integral with the objective of achieving highest possible convergence order for linear basis functions. Our new approach allows the construction of transfer matrices for fast computation of the inverse problem for volume conductors with arbitrary local and remote conductivity anisotropy. A constrained Delaunay tetrahedralisation (CDT) approach is used for the generation of high-quality FE meshes. We validate the new approach in a four-layer sphere model with anisotropic skull compartment. For radial and tangential sources with eccentricities up to 1mm below the cerebrospinal fluid compartment, we achieve a maximal relative error of 0.71% in a tetrahedra model with 360K nodes which is not locally refined around the source singularity. The combination of the full subtraction approach with the high quality CDT meshes leads to accuracies that, to the best of the authors knowledge, have not yet been presented before.

Key words: source reconstruction, electroencephalography, finite element method, dipole, full subtraction approach, constrained Delaunay tetrahedralisation, validation in four-layer sphere models, projected subtraction approach, transfer matrices

Preprint submitted to Elsevier *15 October 2007*

1 Introduction

Inverse methods are used to reconstruct current sources in the human brain by means of electroencephalography (EEG) or magnetoencephalography (MEG) measurements of, e.g., event related fields or epileptic seizures [15,18,30]. A critical component of the inverse neural source reconstruction is the solution of the forward problem [32], i.e., the simulation of the fields at the head surface for a known primary current source in the brain. Because of the availability of quasi-analytical forward problem solution formulas, the head volume conductor is still often represented by a multi-layer sphere model [6]. However, this model is just a rough approximation to the reality, so that numerical approximation methods are more and more frequently used such as the boundary element method (BEM) [8], the finite volume method (FVM) [16], the finite difference method (FDM) [11] or the finite element method (FEM) [3,1,29,13,23,33]. We will focus on the FEM because of its enormous ability and accuracy in modelling the forward problem in geometrically complicated inhomogeneous and anisotropic volume conductors, as will be presented in this paper.

It is shown in [22,7,17] that the mathematical dipole is an adequate model to represent the primary current which is caused by a synchronous activity of tens of thousands of densely packed apical dendrites of large pyramidal cells oriented in parallel in the human cortex. The dipole model is thus considered to be the "atomic" structure of the primary current density distribution that has to be reconstructed within the inverse problem. Hence, one of the key questions for all 3D forward modelling techniques is the appropriate modelling of the potential singularity introduced into the differential equation by means of the mathematical dipole.

Direct potential approaches [38,5] approximate the dipole moment through optimally distributed monopolar sources and sinks on neighbouring FE nodes of the source location. This approach leads to finite distances between the poles that seem reasonable as it performs well in validation studies [5,35]. However, direct approaches are strongly mesh-dependent and bear the risk that monopoles are introduced into compartments with different conductivities. Another disadvantage of direct approaches is the absence of a well-understood mathematical theory, especially the interplay with tissue anisotropy is not yet sufficiently examined. In recent comparison studies of different direct meth-

* Corresponding author. Institut für Biomagnetismus und Biosignalanalyse, Westfälische Wilhelms-Universität Münster, Malmedyweg 15, 48149 Münster, Germany, Tel.: +49/(0)251-83-56904, Fax: +49/(0)251-83-56874, http://biomag.uni-muenster.de

Email address: fdr@mis.mpg.de,carsten.wolters@uni-muenster.de, thomas.dierkes@uni-muenster.de,si@wias-berlin.de,lgr@mis.mpg.de (F. Drechsler[1], C. H. Wolters[2,*], T. Dierkes[2], H. Si[3], L. Grasedyck[1]).

ods with the subtraction approach [1,23], it is concluded that the overall best performance is achieved using the latter method.

A subtraction approach for the modelling of a mathematical dipole in FE-based source analysis is widely suggested [3,1,29,13,23,33]. All proposed approaches have in common that the total potential is divided into an analytically known singularity potential and a singularity-free correction potential which can then be approximated numerically using an FE approach. In [33], we give a theoretical insight into the subtraction approach. A proof is given for existence and uniqueness of the weak solution in the function space of zero-mean potential functions and convergence properties of the FE-approach to the correction potential are stated. In this article, a *projected subtraction method* is proposed where the singularity potential is projected in the FE space. This approach is shown to perform well in a three-compartment (skin, skull, brain) sphere model with anisotropic skull compartment provided that the so-called *source eccentricity* is limited to 95%. The eccentricity is generally defined as the percent ratio of the distance between the source location and the model midpoint divided by the radius of the inner sphere. When considering a three-shell model, 95% eccentricity seems reasonable because the dipoles that are located in the cortex will have an eccentricity even lower than 92% as reported in [13].

However, the three-compartment model of the head ignores the cerebrospinal fluid (CSF) compartment between the cortex and the skull. The CSF has a much higher conductivity than the brain compartment [2]. Additionally. it is shown to have a significant influence on the forward problem [21,31]. In four-compartment models, this layer is taken into account, but source eccentricity then has to be determined with regard to the inner CSF surface, i.e., the most eccentric sources are only 1 or 2mm apart from the next conductivity discontinuity. Therefore, eccentricities of more than 98% have to be examined. It is well-known (and in [33], a theoretical reasoning is given for this fact), that with increasing eccentricity, the numerical accuracy in sphere model validations decreases [3,29,13,33]. This is not only the case for the subtraction approach, but also for the direct approach in FE modelling [38,5] and in BE modelling (see, e.g., [8]). In [3,29,13], coarse tetrahedral meshes are considered yielding unacceptably large numerical errors already at eccentricities above 90%. In [3,29], local mesh refinement around the source is used to achieve better results. However, with regard to the inverse problem, the setup of source-location dependent locally refined meshes is difficult to implement and time-consuming to compute and thus might not be practicable for an inverse source analysis.

In this paper, we propose a so-called *full subtraction approach* which appropriately evaluates the right-hand side integral for the correction potential with the objective of achieving highest possible convergence order for linear basis functions. Our new approach does not need local mesh refinement around the source. As we will show, it therefore allows the construction of transfer matrices for fast computation of the inverse problem for volume conductors with arbitrary local (at the source position, i.e., grey matter) and remote (with a minimal distance to the source position, i.e., white matter) conductivity anisotropy. The transfer matrices are introduced for the projected subtraction method in [37,33], but those developments are still limited to the modelling of only remote anisotropy. A constrained Delaunay tetrahedralisation (CDT) approach is used for the generation of high-quality FE meshes, while former studies are limited to ordinary Delaunay tetrahedralisation [33]. We validate the new approach in a four-layer sphere model with anisotropic skull compartment and sources up to 1mm below the CSF compartment. We compare the accuracy of our new method with the projected subtraction approach from [33] and the literature. It will be shown that the combination of the full subtraction approach with the CDT-FE meshes leads to very high accuracies.

2 The Continuous Forward Problem

The mathematical model for the numerical simulation of electric and magnetic fields in the human head is based on the quasistatic approximation of Maxwell's equations. A linearisation of these equations leads to the following forward problem in source analysis [20,22]:

Assumption 1 *Let $\sigma : \mathbb{R}^3 \to \mathbb{R}^{3\times 3}$ be a mapping such that $\sigma(x)$ is a symmetric positive definite 3×3 matrix (the electric conductivity depending on x), and let $\Omega \subset \mathbb{R}^3$ be a bounded polygonal domain (the head). For each $y \in \Omega$ a vector $M(y) \in \mathbb{R}^3$ (the current dipolar moment) is given.*

Notation 2 *(1) We denote the divergence of a function $f : \Omega \to \mathbb{R}^3$ by*

$$\mathrm{div} f(x) := \sum_{j=1}^{3} \partial_j f(x).$$

(2) The gradient of a function $f : \Omega \to \mathbb{R}$ is the vector

$$\nabla f(x) := (\partial_1 f(x), \partial_2 f(x), \partial_3 f(x)).$$

(3) By $n(x)$ we denote the outer unit normal of Ω at the point $x \in \partial\Omega$.

Definition 3 (The continuous forward problem) *The forward problem in source analysis is to find for each primary current density function*

$$f = f^y, \quad f^y(x) = \mathrm{div} M(y)\delta(x - y), \qquad y \in Y \subset \Omega, \;\; M(y) \in \mathbb{R}^3, \tag{1}$$

a solution for the electric potential u (in an appropriate space) such that

$$\begin{aligned} \operatorname{div} \sigma(x)\ \nabla u(x) &= f(x) \quad \textit{for a.e. } x \in \Omega, \\ \langle \sigma(x)\nabla u(x), n(x)\rangle &= 0 \quad \textit{for a.e. } x \in \partial\Omega, \\ \int_\Omega u(x)dx &= 0. \end{aligned} \tag{2}$$

Here δ denotes the Dirac delta distribution and $\langle \cdot, \cdot \rangle$ the inner product.

In order to understand the difficulties of a discretisation of the forward problem we consider a simple example where the solution is known analytically.

Example 4 *Let $y \in \Omega$. For the case $\Omega = \mathbb{R}^3$ (unbounded!) and $\sigma(x) \equiv \sigma(y)$ for all $x \in \Omega$, the solution $u^{\infty,y}$ for the right-hand side f^y of (2) is*

$$u^{\infty,y}(x) := \frac{1}{4\pi\sqrt{\det \sigma(y)}} \frac{\langle M(y), \sigma(y)^{-1}(x-y)\rangle}{\langle \sigma(y)^{-1}(x-y), x-y\rangle^{3/2}}. \tag{3}$$

At infinity ($x \to \infty$) it fulfills the Neumann boundary conditions. The singularity of $u^{\infty,y}$ at $x = y$ is of order 2, so that $u^{\infty,y}$ does not belong to $H^1(\Omega)$ (refer, e.g., to [4] for a definition of the function spaces), not even $L^2(\Omega)$. In order to resolve the singularity in the discretisation, one would have to include special singular basis functions or use a locally refined grid.

In the following, we will derive a continuous formulation where the singularity in the right-hand side is removed so that standard discretisation techniques are applicable.

3 Full Subtraction Approach and Finite Element Discretisation

In order to apply a finite element discretisation, we have to reformulate the problem, because neither the right-hand side f nor the solution u allow for a good approximation by standard finite elements. Moreover, the variational formulation would require an integration by parts (Gauß integral theorem, resp. Green's identity), which might not be applicable for general functions like u that are not in $H^1(\Omega)$.

Definition 5 (Continuous subtraction forward problem) *Let $u^{\infty,y}$ denote the solution defined in (3). The subtraction forward problem is to find for each*

$$f = f^y, \quad f^y(x) = \operatorname{div} M(y)\delta(x-y),$$

a solution $u^{\mathrm{corr,y}}$ (in an appropriate space) such that

$$\begin{aligned} \text{div } \sigma(x)\ \nabla(u^{\text{corr,y}}(x) + u^{\infty,y}(x)) &= f(x) \quad \textit{for a.e. } x \in \Omega, \\ \langle \sigma(x) \nabla(u^{\text{corr,y}}(x) + u^{\infty,y}(x)), n(x) \rangle &= 0 \quad \textit{for a.e. } x \in \partial\Omega, \\ \int_\Omega (u^{\text{corr,y}}(x) + u^{\infty,y}(x)) dx &= 0. \end{aligned} \tag{4}$$

Equation (4) can be written in the form

$$\begin{aligned} \text{div } \sigma(x)\ \nabla u^{\text{corr,y}}(x) &= \text{div } (\sigma(y) - \sigma(x))\ \nabla u^{\infty,y}(x) \quad \text{for a.e. } x \in \Omega, \\ \langle \sigma(x) \nabla u^{\text{corr,y}}(x), n(x) \rangle &= -\langle \sigma(x) \nabla u^{\infty,y}(x), n(x) \rangle \quad \text{for a.e. } x \in \partial\Omega, \\ \int_\Omega u^{\text{corr,y}}(x) dx &= -\int_\Omega u^{\infty,y}(x) dx. \end{aligned} \tag{5}$$

In order to remove the singularities in the right-hand side of (5), we need the assumption that the difference $\sigma(y) - \sigma(x)$ vanishes in a ball around y.

Assumption 6 *Let $\epsilon > 0$ s.t. for every $y \in Y$, the tensor $\sigma(x)$ is constant in a small ball*

$$\Omega_\epsilon^y := \{x \in \Omega \mid \|x - y\|_2 < \epsilon\} \subset \Omega$$

around y.

Lemma 7 *Using the Assumption 6, the right-hand side*

$$\text{div}(\sigma(y) - \sigma(x))\ \nabla u^{\infty,y}(x)$$

in (5) belongs to $L^2(\Omega)$.

Proof: Let $\overline{u}^{\infty,y}$ denote a smooth extension of $u^{\infty,y}$ for all $x \in \Omega \setminus \Omega_\epsilon^y$. Then,

$$(\sigma(y) - \sigma(x)) \nabla \overline{u}^{\infty,y}(x) = (\sigma(y) - \sigma(x)) \nabla u^{\infty,y}(x) \quad \forall x \in \Omega \setminus \Omega_\epsilon^y$$

holds. The function $\overline{u}^{\infty,y}$ is smooth in $\Omega \setminus \Omega_\epsilon^y$ so that $div(\sigma(y) - \sigma(x)) \nabla \overline{u}^{\infty,y}$ is smooth in $\Omega \setminus \Omega_\epsilon^y$. Hence $u^{\infty,y}$ is smooth in $\Omega \setminus \Omega_\epsilon^y$. With the assumption 6, it is

$$(\sigma(y) - \sigma(x)) \nabla u^{\infty}(x) = 0 \quad \forall x \in \Omega_\epsilon^y.$$

Therefore $u^{\infty,y}$ is in $L^2(\Omega)$. ■

Assumption 8 *Let $V \subset H^1(\Omega)$ be an infinite space and let $V_N \subset V$ be an N-dimensional subspace of V.*

The role of V_N is that of a finite element space, e.g. piecewise polynomials up to a certain degree. The space V might, due to higher regularity assumptions, be $H^{1+\varepsilon}(\Omega)$ with $\varepsilon \in]0,1[$.

Now we can apply the Gauß integral theorem

$$\begin{aligned}\int_\Omega v(x)\mathrm{div}\sigma(x)\nabla u(x)dx = &-\int_\Omega \langle\nabla v(x), \sigma(x)\nabla u(x)\rangle dx \\ &+\int_{\partial\Omega} v(x)\langle n(x), \sigma(x)\nabla u(x)\rangle dx\end{aligned}$$

and arrive at the variational formulation that is suitable for a finite element discretisation.

Definition 9 (Analytical forward problem) *For an arbitrary mapping $\alpha : \Omega \to \mathbb{R}^{3\times 3}$ we define the bilinear form*

$$a_\alpha : V \times V \to \mathbb{R}, \quad a_\alpha(u,v) := \int_\Omega \langle\alpha(x)\nabla u(x), \nabla v(x)\rangle dx.$$

The analytical forward problem is to find $u^{corr,y} \in V$ s.t.

$$\begin{aligned}\forall v \in V: \quad a_\sigma(u^{corr,y}, v) &= a_{\sigma(y)-\sigma}(u^{\infty,y}, v) - \int_{\partial\Omega} v(x)\langle n(x), \sigma(y)\nabla u^{\infty,y}(x)\rangle dx, \\ \int_\Omega u^{corr,y}(x)dx &= -\int_\Omega u^{\infty,y}(x)dx.\end{aligned}$$

In [33, section 3.5], it is shown that a unique solution of the analytical forward problem exists and the solution $u^{corr,y}$ belongs to $H^1(\Omega)$.

Definition 10 (Finite element forward problem) *The finite element forward problem is to find $u_N \in V_N$ s.t.*

$$\begin{aligned}&\forall v \in V_N : \\ &a_\sigma(u_N, v) = a_{\sigma(y)-\sigma}(u^{\infty,y}, v) - \int_{\partial\Omega} v(x)\langle n(x), \sigma(y)\nabla u^{\infty,y}(x)\rangle dx, \\ &\int_\Omega u_N(x)dx = -\int_\Omega u^{\infty,y}(x)dx.\end{aligned}$$

Let $\tau = \{\tau_1, \ldots, \tau_T\}$ be a triangulation of the polygonal domain Ω into tetrahedra τ_i. For the finite element space V_N we use standard conforming linear elements, i.e. $V_N = \{v \in V \mid v|_{\tau_i} \text{ affine } \forall i = 1, \ldots, T\}$. Let $\operatorname{span}\{\varphi_i \mid i \in \mathcal{I}\}$ denote the standard Lagrange basis of V_N using local basis functions φ_i, $i \in \mathcal{I}, \#\mathcal{I} = N$. By ξ_i we denote the Lagrange point of the FE basis function φ_i.

The linear system to be solved is

$$Ku = b, \tag{6}$$

where the entries of the stiffness matrix K and right-hand side b are

$$K_{i,j} := a_\sigma(\varphi_j, \varphi_i),$$

$$b_i := \int_\Omega \langle (\sigma(y) - \sigma(x)) \nabla u^{\infty,y}(x), \nabla \varphi_i(x) \rangle dx \tag{7}$$

$$- \int_{\partial\Omega} \varphi_i(x) \langle n(x), \sigma(y) \nabla u^{\infty,y}(x) \rangle dx. \tag{8}$$

The discrete solution is

$$u_N(x) = \sum_{i \in \mathcal{I}} u_i \varphi_i(x).$$

The gradient of $u^{\infty,y}$ is

$$\nabla u^{\infty,y}(x) = \frac{1}{4\pi\sqrt{\det \sigma(y)}} \cdot \frac{\sigma(y)^{-1} M(y)}{\langle \sigma(y)^{-1}(x-y), x-y \rangle^{3/2}}$$
$$- \frac{1}{4\pi\sqrt{\det \sigma(y)}} \cdot \frac{3\langle M(y), \sigma(y)^{-1}(x-y) \rangle \sigma(y)^{-1}(x-y)}{\langle \sigma(y)^{-1}(x-y), x-y \rangle^{5/2}}.$$

Remark 11 *(1) The term $\nabla \varphi_i$ is constant for linear elements. Thus, entries of K can be computed easily.*

(2) The entries of the right-hand side need to be accurate enough in order to preserve the finite element convergence. Since we project the correction potential into the space V_N of piecewise linear elements, it is sufficient to have a perturbation of size $\mathcal{O}(h^2)$ which is achieved by a second order accurate quadrature formula. In the numerics section we will verify that this order is necessary and sufficient to produce a negligible quadrature error.

(3) We assemble the first term of b_i element-wise where each element contributes to $\mathcal{O}(1)$ entries. For $x \to y$ the integral even vanishes, cf. Assumption 6. The second term involves the normal vector and the basis function itself. Thus, we need a quadrature formula that resolves $\nabla u^{\infty,y}$ at the boundary (where it is very smooth) and that is accurate for linear functions. Again, a second order quadrature formula for the surface triangles is necessary and sufficient.

In [33], a projected subtraction approach is presented where the function $u^{\infty,y}$ is projected in the finite element space V_N by

$$u^\infty(x) \approx u_N^\infty(x) = \sum_{i=1}^{N} \varphi_i(x) u_i^\infty, \quad u_i^\infty = u^\infty(\xi_i). \tag{9}$$

Introducing the coefficient vector $u_\infty := (u_1^\infty, \dots, u_N^\infty)$, the equation system

$$Ku = -K^{corr} u_\infty - S u_\infty,$$

is obtained where the matrices are defined by

$$K_{i,j}^{corr} := -\int_\Omega \langle (\sigma(y) - \sigma(x)) \nabla \varphi_i(x), \nabla \varphi_j(x) \rangle dx \tag{10}$$

and

$$S_{i,j} := \int_{\partial\Omega} \langle \sigma(y) \nabla \varphi_j(x), n(x) \rangle \varphi_i(x) dx. \tag{11}$$

The drawback of the projected subtraction approach to compute the correction potential is the additional approximation error by (9). We will see in the numerical validation section that the presented full subtraction approach in which u^∞ is not approximated in the space V_N, has a much higher degree of accuracy.

4 Transfer matrix

The forward problem in EEG and MEG source analysis has to be solved for many right-hand sides $f = f^y$, $y \in Y$ (most often several thousands). In this case, the following assumption is necessary for an efficient computation of all solutions.

Assumption 12 *We demand that the FE mesh is the same for all right-hand* *sides $f = f^y$, i.e., we want to avoid local mesh refinement with regard to a specific source location.*

However, the full solution vector is not required for all right-hand sides. Instead, only a linear transform of the function u,

$$Au \in \mathbb{R}^m, \qquad m \ll N, \quad A : V \to \mathbb{R}^m,$$

is of interest with m being the number of measurement sensors. In this case, one can precompute the so-called *transfer matrix*

$$B := \hat{A}K^{-1} \in \mathbb{R}^{m \times N}$$

where $\hat{A}$ is the matrix representation of the linear mapping A restricted to the finite dimensional space V_N in the basis $\{\varphi_i \mid i \in \mathcal{I}\}$ [37] [1]. In case of the EEG, $\hat{A}$ is either a restriction or a surface interpolation of the potential vector to those FE nodes which represent the EEG electrodes. In case of the MEG, $\hat{A}$ is the secondary flux integration matrix [37].

The full subtraction method EEG forward solution is thus obtained by

$$Au \approx A(u_N + u^{\infty,y}) = \hat{A}K^{-1}b + \hat{A}u^{\infty,y} = Bb + \hat{A}u^{\infty,y},$$

a matrix-vector multiplication with the $m \times N$ transfer matrix B. The MEG forward solution can exploit the precomputed MEG transfer matrix in a very similar fashion for the secondary magnetic flux parts [37]. The setup of the transfer matrix B requires m times the solution of the $N \times N$ system K. Using an optimal method, e.g., multigrid, this can be done in $\mathcal{O}(m \cdot N)$ [10, Theorem 10.4.2]. The term $\hat{A}u^{\infty,y}$ can be computed easily because the solution $u^{\infty,y}$ is given analytically and it is smooth at the boundary where the support of $\hat{A}$ typically lies.

The projected subtraction approach [33] leads to the transfer matrix

$$\hat{A}K^{-1}(-K^{corr} - S).$$

This approach is only useful, if all right-hand sides f^y have the same conductivity at all possible cortical source positions. This means that for the projected subtraction approach,

$$\sigma(y) = \sigma_c, \sigma_c \in \mathbb{R}^{3\times3}, \sigma_c \text{ is isotropic},$$

[1] The transfer matrix is called *lead field basis* in [37]

has to be assumed to allow for the use of the fast transfer matrix approach because the entries of the matrices K^{corr} and S in equations (10), (11) depend on the conductivity at the dipole position. In contrast, the conductivity for different source positions might vary for the presented full subtraction approach. This is a further advantage of the full subtraction approach, since the cortex is sometimes referred to be a slightly anisotropic conductor (see the discussion section).

5 Influence Matrix

Most inverse EEG and MEG source analysis algorithms are based on precomputed forward solutions for a set of anatomically and physiologically meaningful sources, i.e., right-hand sides $(f^y)_{y\in Y}$. It is then advantageous to precompute the so-called *influence matrix*

$$L \in \mathbb{R}^{m \times \#Y},$$

whose entry $L_{i,y}$ is the forward computed field for source y at sensor i. The influence matrix can be computed by

(1) multiplying each right-hand side b^y with the transfer matrix B in $\mathcal{O}(mN\#Y)$ and each analytic solution $u^{\infty,y}$ by $\hat{A}$, or
(2) multiplying each row of the transfer matrix B (from the left) by the matrix

$$R \in \mathbb{R}^{N\times\#Y}, \qquad R_{i,y} := b^y_i$$

of right-hand sides (and adding the term $\hat{A}u^{\infty,y}$). The complexity for the naive approach would again be $\mathcal{O}(mN\#Y)$. However, the matrix R can be cast into the $\mathcal{H}$-matrix format [37] so that each matrix-vector multiplication is of complexity $\mathcal{O}(N \log N)$. The multiplication $\hat{A}u^{\infty,y}$ can as well be performed after casting the right-hand sides $u^{\infty,y}$ into the $\mathcal{H}$-matrix format. Hence, the total complexity reduces in this case to

$$\mathcal{O}(mN \log N).$$

6 Validation and numerical experiments

6.1 Analytical solution in an anisotropic multilayer sphere model

De Munck and Peters [6] derive series expansion formulas for a mathematical dipole in a multilayer sphere model, denoted here as the "analytical solution". A rough overview of the formulas will be given in this section. The model consists of S shells with radii $r_S < r_{S-1} < \ldots < r_1$ and constant radial, $\sigma^{\text{rad}}(r) = \sigma_j^{\text{rad}} \in \mathbb{R}^+$, and constant tangential conductivity, $\sigma^{\text{tang}}(r) = \sigma_j^{\text{tang}} \in \mathbb{R}^+$, within each layer $r_{j+1} < r < r_j$. It is assumed that the source at position x_0 with radial coordinate $r_0 \in \mathbb{R}$ is in a more interior layer than the measurement electrode at position $x_e \in \mathbb{R}^3$ with radial coordinate $r_e = r_1 \in \mathbb{R}$. The spherical harmonics expansion for the mathematical dipole (1) is expressed in terms of the gradient of the monopole potential to the source point. Using an asymptotic approximation and an addition-subtraction method to speed up the series convergence yields

$$\mathrm{u}_{\mathsf{ana}}(x_0, x_e) = \frac{1}{4\pi}\langle \mathbf{M}, S_0 \frac{x_e}{r_e} + (S_1 - \cos\omega_{0e} S_0)\frac{x_0}{r_0}\rangle$$

with ω_{0e} being the angular distance between source and electrode, and with

$$\begin{aligned} S_0 = & \frac{F_0}{r_0} \frac{\Lambda}{(1 - 2\Lambda\cos\omega_{0e} + \Lambda^2)^{3/2}} \\ & + \frac{1}{r_0} \sum_{n=1}^{\infty} \left\{(2n+1) R_n(r_0, r_e) - F_0 \Lambda^n\right\} P_n'(\cos\omega_{0e}) \end{aligned} \tag{12}$$

and

$$\begin{aligned} S_1 = & F_1 \frac{\Lambda\cos\omega_{0e} - \Lambda^2}{(1 - 2\Lambda\cos\omega_{0e} + \Lambda^2)^{3/2}} \\ & + \sum_{n=1}^{\infty} \left\{(2n+1) R_n'(r_0, r_e) - F_1 n \Lambda^n\right\} P_n(\cos\omega_{0e}). \end{aligned} \tag{13}$$

The coefficients R_n and their derivatives, R_n', are computed analytically and the derivative of the Legendre polynomials, P_n, are determined by means of a recursion formula. We refer to [6] for the derivation of the above series of differences [2] and for the definition of F_0, F_1 and Λ. Here, it is only important

[2] The following is a result of a discussion with J.C. de Munck: While constants in formulas (71) and (72) in the original paper [6] have to be flipped, our versions of S_0 and S_1 in Equations (12) and (13) are correct.

that the latter terms are independent of n and that they can be computed from the given radii and conductivities of layers between source and electrode and of the radial coordinate of the source. The computations of the series (12) and (13) are stopped after the k-th term, if the following criterion is fulfilled

$$\frac{t_k}{t_0} \leq \upsilon, \qquad t_k := (2k+1)R'_k - F_1 k \Lambda^k. \tag{14}$$

In the following simulations, a value of 10^{-6} is chosen for υ in (14). Using the asymptotic expansion, no more than 30 terms are needed for the series computation at each electrode.

6.2 Numerical quadrature and FE solver

Table 1
Quadrature formulas of Stroud [28] for the volume integral from Equation (7) and the surface integral from Equation (8) .

Formula	degree	number integration points	Reference
Volume integral from Equation (7)			
$T_n : 1-1$	1	1	[28, Chapter 8.8, p.307]
$T_n : 2-1$	2	$n+1$	[28, Chapter 8.8, p.307]
$T_3 : 7-1$	7	64	[28, Chapter 8.8, p.315]
Surface integral from Equation (8)			
$T_n : 1-1$	1	1	[28, Chapter 8.8, p.307]
$T_n : 2-1$	2	$n+1$	[28, Chapter 8.8, p.307]
$T_2 : 7-1$	7	16	[28, Chapter 8.8, p.314]

For the numerical integration of the right-hand side (7), (8), we use quadrature formulas of Stroud [28]. As shown in Table 1, the overall numerical accuracy of the full subtraction approach will be evaluated for quadrature orders of 1, 2 and 7. Our notation in Table 1 closely follows the one of the tables in [28]. T_n indicates an n-dimensional simplex [28, Chapter 7.8] (in our case: $n = 3$).

We employ an algebraic multigrid preconditioned conjugate gradient (AMG-CG) method for solving the linear system (6). We solve up to a relative error of 10^{-8} in the controllable $KN^{-1}K$-energy norm (with N^{-1} being one V-cycle of the AMG) [34,9].

6.3 Error criteria

We compare numerical solutions with analytical solutions using three error criteria that are commonly evaluated in source analysis [14,3,29,13,23,33]. The *relative (Euclidean) error* (RE) is defined as

$$\mathrm{RE} = ||\underline{\mathrm{u}}^{\mathrm{num}} - \underline{\mathrm{u}}^{\mathrm{ana}}||_2 / ||\underline{\mathrm{u}}^{\mathrm{ana}}||_2,$$

where $\underline{\mathrm{u}}^{\mathrm{ana}}, \underline{\mathrm{u}}^{\mathrm{num}} \in \mathbb{R}^{\mathrm{m}}$ denote the analytical and the numerical solution vector, resp., at m measurement electrodes. In order to better distinguish between the topography (driven primarily by changes in dipole location and orientation) and the magnitude error (indicating changes in source strength), Meijs et al. [14] introduced the *relative difference measure* (RDM)

$$\mathrm{RDM} = \sqrt{\sum_{i=1}^{\mathrm{m}} \left(\underline{\mathrm{u}}_i^{\mathrm{ana}} / ||\underline{\mathrm{u}}^{\mathrm{ana}}||_2 - \underline{\mathrm{u}}_i^{\mathrm{num}} / ||\underline{\mathrm{u}}^{\mathrm{num}}||_2\right)^2}$$

(for zero-mean data holds $0 \leq \mathrm{RDM} \leq 2$ [23]) and the *magnification factor* (MAG)

$$\mathrm{MAG} = ||\underline{\mathrm{u}}^{\mathrm{num}}||_2 / ||\underline{\mathrm{u}}^{\mathrm{ana}}||_2$$

(minimal error: MAG = 1), respectively.

6.4 Validation platform

Table 2
Parameterisation of the anisotropic four layer sphere model.

Medium	Scalp	Skull	CSF	Brain
Outer shell radius	92mm	86mm	80mm	78mm
Tangential conductivity	0.33S/m	0.042S/m	1.79S/m	0.33S/m
Radial conductivity	0.33S/m	0.0042S/m	1.79S/m	0.33S/m

The validation of the presented full subtraction approach is carried out in a four compartment sphere model with anisotropic skull compartment, whose parameterisation is shown in Table 2. For the choice of these parameters, we closely followed [11,13].

The numerical forward solution is validated by means of the corresponding analytic solution for dipoles located on the y axis at depths of 0% to 98.7%

(in 1mm steps) of the brain compartment (78mm radius) using both radial and tangential dipole orientations. *Eccentricity* is defined here as the percent ratio of the distance between the source location and the model midpoint divided by the radius of the inner sphere (78mm radius). The most eccentric source considered is thus only 1mm below the CSF compartment. Tangential sources are oriented in the +z axis and radial dipoles in the +y axis. The dipole amplitudes are chosen to be 1nAm.

To achieve error measures which are independent of the specific choice of the sensor configuration, we distribute electrodes in a most-regular way over a given sphere surface. In this way we generate a 748 electrode configuration on the surface of the outer sphere.

6.5 Tetrahedral mesh generation.

The FE meshes of the four layer sphere model are generated by the software TetGen [25] which uses a *Constrained Delaunay Tetrahedralisation* (CDT) approach [27]. The meshing procedure starts with the preparation of a suitable boundary discretisation of the model. To begin with, for each of the four layers and for a given triangle edge length, nodes are distributed in a most-regular way and connected through triangles. This yields a valid triangular surface mesh for each of the four layers. Meshes of different layers are not intersecting each other. The CDT approach is then used to construct a tetrahedralisation conforming to the surface meshes. It first builds a Delaunay tetrahedralisation of the vertices of the surface meshes. It then uses a local degeneracy removal algorithm combining vertex perturbation and vertex insertion to construct a new set of vertices which includes the input set of vertices. In the last step, a fast facet recovery algorithm is used to construct the CDT [27].

This approach is combined with two further constraints to the size and shape of the tetrahedra. The first constraint can be used to restrict the volume of the generated tetrahedra in a certain compartment, the so-called *volume constraint*. The second constraint is important for the generation of quality tetrahedra. If R denotes the radius of the unique circumsphere of a tetrahedron and L its shortest edge length, the so-called *radius-edge ratio* of the tetrahedron can be defined as

$$Q = \frac{R}{L}.$$

The radius-edge ratio can distinguish almost all badly-shaped tetrahedra except one type of tetrahedra, so-called *slivers*. A sliver is a very flat tetrahedron which has no small edges, but can have arbitrarily large dihedral angles (close

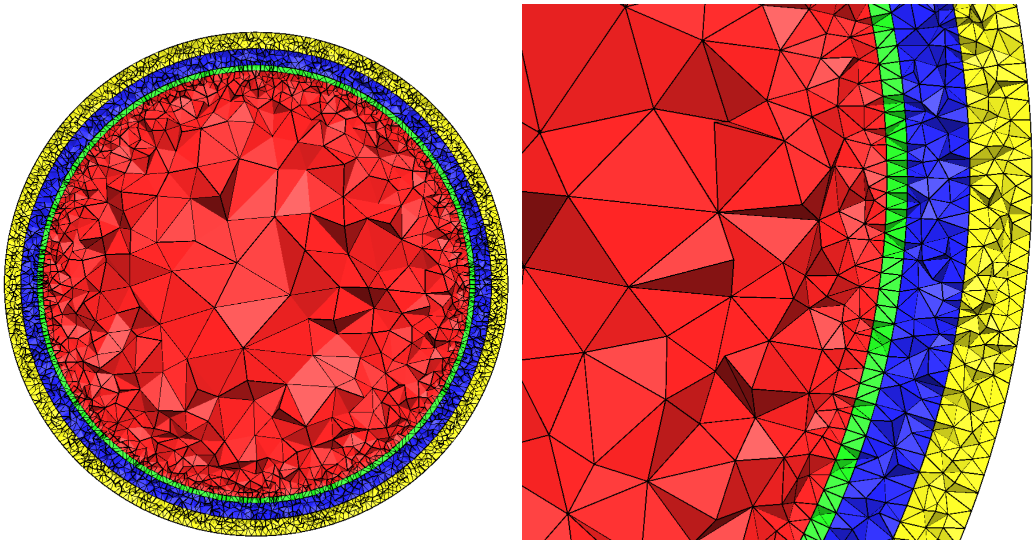

Fig. 1. Cross-section of the tetrahedral mesh `tet360K` of the four compartment sphere model. Visualisation is done using Tetview [26].

to π). For this reason, an additional mesh smoothing and optimization step is used to remove the slivers and improve the overall mesh quality.

Table 3
The number of nodes and elements of the three tetrahedra models used for numerical accuracy tests.

Model	Nodes	Elements
tet360K	$360,056$	$2,165,281$
tet287K	$287,217$	$1,712,360$
tet39K	$38,928$	$229,311$

In Table 3, the number of nodes and elements of the three tetrahedral meshes are shown which will be used for numerical accuracy tests. The tetrahedral mesh `tet360K` of the four compartment sphere model is shown in Figure 1. For this model, we distribute 31,680 nodes on each of the four surfaces for the CDT procedure. We allow for a maximal radius-edge ratio of $Q = 1.2$. The volumes of the tetrahedra in the compartments skin, skull and CSF are furthermore restricted correspondingly to the chosen surface triangle edge length. As it can be observed in Figure 1, no volume constraint is used for the brain layer since for this compartment, the entries of the volume integral (7) are zero ($(\sigma(y) - \sigma(x)) = 0$ for all x in the brain compartment) so that a coarse resolution will not spoil the overall numerical accuracy, but reduce the computational amount of work.

6.6 Validation results in anisotropic four layer sphere model

6.6.1 Evaluation with regard to right-hand side quadrature order

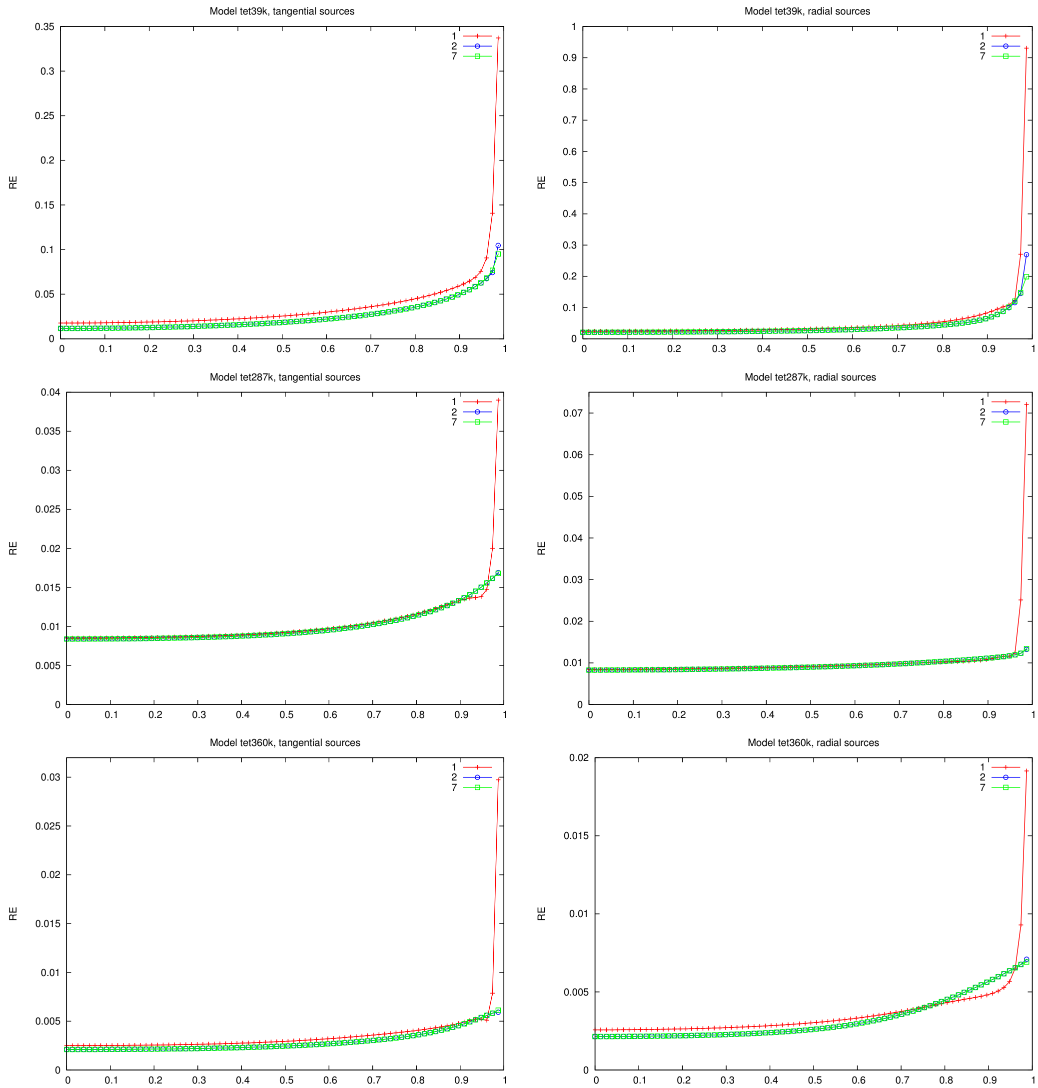

Fig. 2. Relative error for tangentially (left) and radially (right) oriented dipoles with quadrature orders of 1,2 and 7: Model `tet39K` (top row), `tet287K` (middle row) and `tet360K` (bottom row). Note the different scaling for the RE.

In the first study, we compare the numerical accuracy of the presented full subtraction approach for quadrature formulas with different integration order for the right-hand side (7), (8). The goal of this study is to verify that second order integration formulas are necessary and sufficient as stated in Remark 11. Figure 2 shows the relative errors between the numerical and the quasi-analytical solutions for tangential (left column) and radial sources (right column) for the models `tet39K` (top row), `tet287K` (middle row) and `tet360K` (bottom row) from Table 3. The different quadrature orders of 1, 2 and 7 are represented with different labels in the figure. Especially for eccentric sources, the integration order 1 performs worse than order 2. This shows the necessity of second order integration. Second order integration is also sufficient since the difference between order 2 and 7 in Figure 2 is not visible (models `tet287K` and `tet360K`) or very small (model `tet39K`) and, in any case, not worth the much larger computational amount of work for the higher quadrature order.

6.6.2 Evaluation with regard to mesh resolution

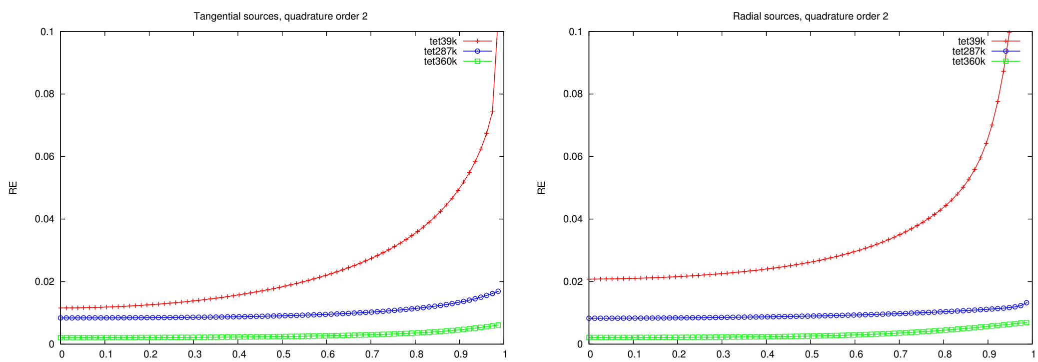

Fig. 3. Relative error for the FE meshes of Table 3 and quadrature order 2 for tangentially (left) and radially oriented dipoles (right).

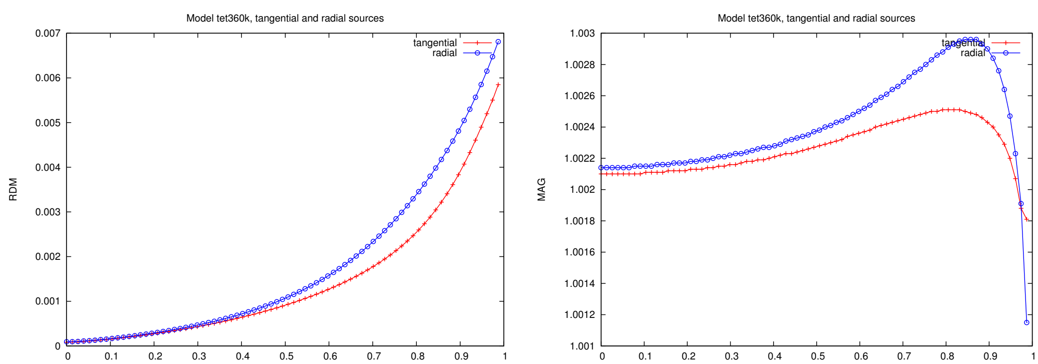

Fig. 4. RDM (left) and MAG errors (right) for model `tet360K` for tangentially and radially oriented dipoles.

In the second study, we evaluate the numerical errors with regard to the resolution of the FE discretisation. Following the results of Section 6.6.1, a quadrature order of 2 is used for the integration of the right-hand side. Figure 3 shows the RE for the three models of Table 3 for tangentially (left) and radially oriented dipoles (right). A clear convergence can be observed, i.e., the RE decreases over all eccentricities with increasing mesh resolution. The accuracy increase is especially distinct for eccentric sources. With the finest model `tet360K`, we are able to decrease the maximal RE over all eccentricities and source orientations to a value of 0.71% for the most eccentric radial source 1mm below the CSF compartment. Figure 4 shows the corresponding RDM and MAG errors for the finest model `tet360K`. The largest topography error is an RDM of 0.34% and the largest magnitude error a MAG of 0.3%.

6.6.3 Comparison of projected and full subtraction approach

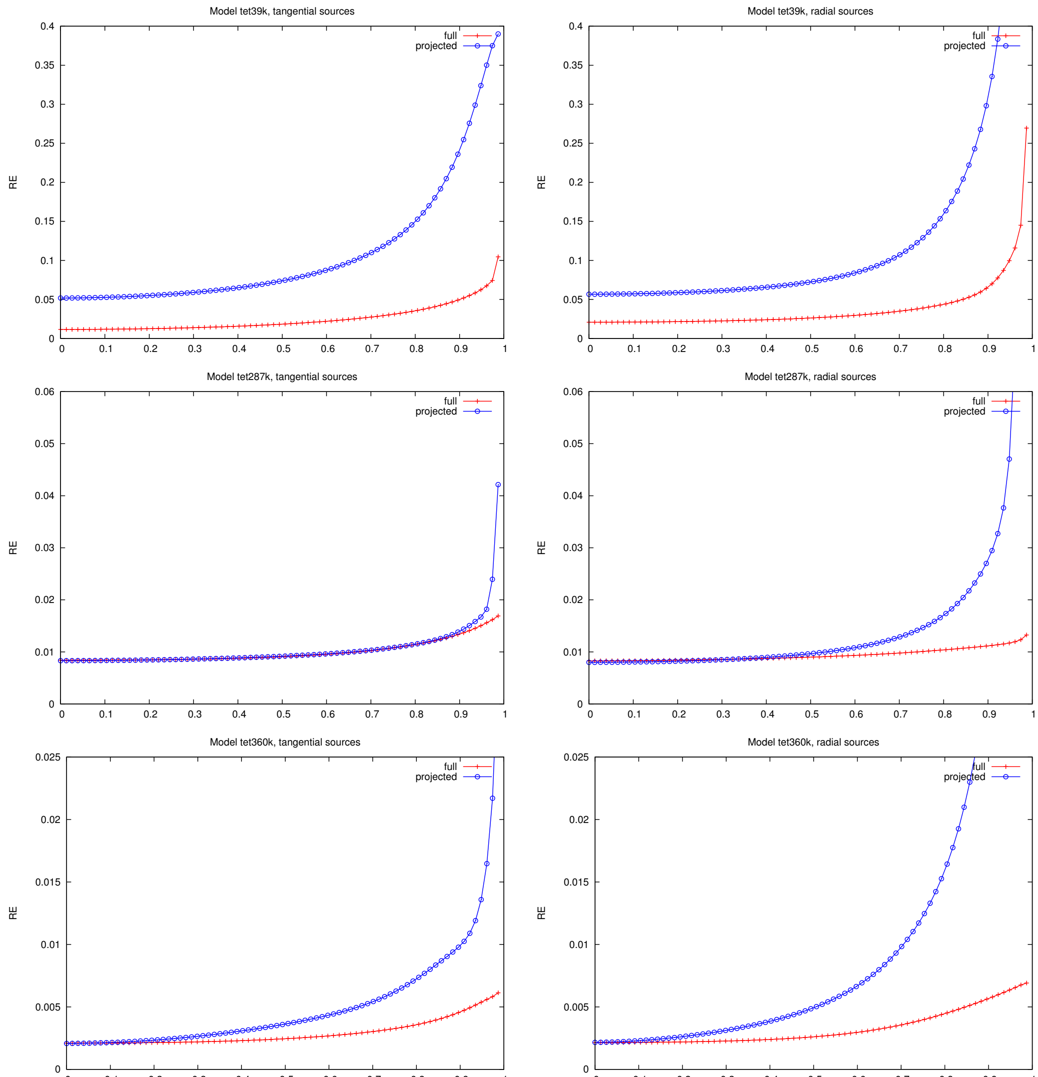

Fig. 5. Comparison between the presented full subtraction approach and the projected subtraction approach from [33] with regard to the relative error for tangential (left) and radial sources (right): Model `tet39K` (top row), `tet287K` (middle row) and `tet360K` (bottom row).

In a last study, we compare the presented full subtraction approach with the projected subtraction method from [33]. Figure 5 shows the RE for tangential (left column) and radial sources (right column) for the models `tet39K` (top row), `tet287K` (middle row) and `tet360K` (bottom row) from Table 3. It can be summarized that the presented full subtraction approach is a major step forward with regard to accuracy for all examined mesh resolutions, which is especially prominent for eccentric sources. For the finest model `tet360K` (bottom row), the largest RE of 5% for the projected subtraction approach is reduced by more than a factor of 7 to a maximal RE of 0.71% for the presented full subtraction approach.

7 Discussion and conclusion

We present theory and numerical experiments of a full subtraction approach to model a mathematical dipole in finite element (FE) method based electroencephalography (EEG) source reconstruction. Since the magnetoencephalography (MEG) forward problem is also based on the computed electric potential (see, e.g., [37]), our method is directly applicable to MEG source analysis. We embed the approach for the computation of the correction potential in the general FE convergence theory and find that under the assumption of higher regularity than H^1, i.e., $H^{1+\varepsilon}(\Omega)$ with $\varepsilon \in]0,1[$, it might be important to integrate the right-hand side of the differential equation for the correction potential with a quadrature order of 2 for achieving highest possible accuracy.

We validate our implementation of the method in a four-compartment sphere model with anisotropic skull layer. In the numerical experiments, we find that second order integration is necessary and sufficient, as the theory predicts. The evaluation of the convergence order is a difficult task because the convergence constant is strongly depending on the distance of the source to the next conductivity discontinuity (a theoretical reasoning for this fact is given in [33]). Furthermore, our quasi-analytical formulas are currently limited to measurement points with larger radial location components than the source. Consequently, error-norms of the entire numerical potential solution could not yet be computed. However, with regard to the EEG inverse problem, an evaluation of the numerical accuracy at the surface electrodes seems to be sufficient. Our new approach is shown to converge, i.e., with increasing mesh size, numerical errors decrease. We consider it to be very progressive that the full subtraction method yields a maximal relative error (RE) of 0.71% over all source eccentricities for sources up to 1mm below the CSF compartment for the finest of the examined high-quality constrained Delaunay tetrahedralisation (CDT) FE meshes with 360K nodes which is not locally refined around the source singularity: maximal examined eccentricity of 98.7%, maximal relative difference measure (maxRDM): 0.34%, maximal magnification factor (maxMAG): 0.3%. Schimpf et al. [23] investigate an FE subtraction approach in a four layer sphere model with isotropic skull and sources up to 1mm below the CSF compartment. In their article, a regular 1mm cube model is used (thus a much higher FE resolution) and a maxRDM of 7% and a maxMAG of 25% is achieved. In a locally refined (around the source singularity) tetrahedral mesh with 12,500 nodes of a four layer sphere model with anisotropic skull and first order FE basis functions, Bertrand et al. [3] report numerical accuracies up to a maximal eccentricity of 97.6%. A maximal RDM of above 20% and a maximal MAG up to 70% are documented for the most eccentric source. Van den Broek [29] also uses a locally refined (around the source singularity) tetrahedral mesh with 3,073 nodes of a three layer sphere model with anisotropic skull. For the maximal examined eccentricity of 94.2%, an RDM of up to 50% is given. It is mentioned in the conclusion that in some cases the accuracy can not further be improved by adding points globally as the numerical stability of the matrix equation that is to be solved is reduced. Marin et al. [13] use second order FE basis functions, but their finest tetrahedral mesh of 87,907 nodes is restricted to eccentricities of 81% in order to reach a sufficient accuracy for radial dipole forward solutions in a three compartment sphere model with anisotropic skull. Awada et al. [1] implement a 2D subtraction approach and compare its numerical accuracy with a direct potential method in a 2D sphere model. A direct comparison with our results is therefore difficult, but the authors conclude that the subtraction method is generally more accurate than the direct approach. In a direct comparison with the projected subtraction approach from [33], we find that the new method is by an order of magnitude more accurate for dipole sources close to the next conductivity discontinuity. The fact that, in a realistic head model, most sources of interest have eccentricities between 50% and 98% shows the importance of our results.

Besides its higher accuracy, the possibility of also modelling cortical anisotropy in combination with the efficient transfer matrix approach might be a further advantage of the full subtraction approach when compared to the projected subtraction approach from [33], since the cortex is sometimes referred to be a slightly anisotropic conductor [39,19]. There is a strong debate about cortical anisotropy since DTI measurements rather show that the grey matter is an isotropic compartment [24]. However, at least the infant grey matter might be slightly anisotropic because of yet less developed synaptic connections to the cortical pyramidal cells. Furthermore, it is shown that even slight degrees of cortical anisotropy might already have a large influence on the forward EEG and MEG modelling accuracy [12,36]. In subsequent studies, we will perform profound comparisons of the full subtraction approach with direct potential methods in locally and remotely anisotropic volume conductors.

8 Acknowledgement

This work was supported by the Deutsche Forschungsgemeinschaft (WO1425/1-1, GR3179/1-1). The authors would like to thank J.C. de Munck for providing the software for the quasi-analytical solution in multilayer sphere models and for his quick responses whenever needed.

References

[1] K. Awada, D. Jackson, J. Williams, D. Wilton, S. Baumann, A. Papanicolaou, Computational aspects of finite element modeling in EEG source localization, IEEE Trans Biomed. Eng. 44 (8) (1997) 736–751.

[2] S. Baumann, D. Wozny, S. Kelly, F. Meno, The electrical conductivity of human cerebrospinal fluid at body temperature, IEEE Trans Biomed. Eng. 44 (3) (1997) 220–223.

[3] O. Bertrand, M. Thévenet, F. Perrin, 3D finite element method in brain electrical activity studies, in: J. Nenonen, H. Rajala, T. Katila (eds.), Biomagnetic Localization and 3D Modelling, Report of the Dep. of Tech.Physics, Helsinki University of Technology, 1991.

[4] D. Braess, Finite Elements: Theory, Fast Solvers and Applications in Solid Mechanics., Cambridge University Press, 2007.

[5] H. Buchner, G. Knoll, M. Fuchs, A. Rienäcker, R. Beckmann, M. Wagner, J. Silny, J. Pesch, Inverse localization of electric dipole current sources in finite element models of the human head, Electroenc. Clin. Neurophysiol. 102 (1997) 267–278.

[6] J. de Munck, M. Peters, A fast method to compute the potential in the multi sphere model, IEEE Trans Biomed. Eng. 40 (11) (1993) 1166–1174.

[7] J. de Munck, B. van Dijk, H. Spekreijse, Mathematical dipoles are adequate to describe realistic generators of human brain activity, IEEE Trans Biomed. Eng. 35 (11) (1988) 960–966.

[8] M. Fuchs, R. Drenckhahn, H. Wischmann, M. Wagner, An improved boundary element method for realistical volume conductor modeling, IEEE Trans Biomed. Eng. 45 (8) (1998) 980–997.

[9] G. Haase, M. Kuhn, S. Reitzinger, Parallel AMG on distributed memory computers, SIAM J. Sci.Comp. 24 (2) (2002) 410–427.

[10] W. Hackbusch, Iterative solution of large sparse systems of equations, Springer Verlag, Applied Mathematical Sciences 95, 1994.

[11] H. Hallez, B. Vanrumste, P. V. Hese, Y. D'Asseler, I. Lemahieu, R. V. de Walle, A finite difference method with reciprocity used to incorporate anisotropy in electroencephalogram dipole source localization., Phys.Med.Biol. 50 (2005) 3787–3806.

[12] J. Haueisen, C. Ramon, H. Brauer, H. Nowak, The influence of local conductivity changes on MEG and EEG, Biomedizinische Technik 45 (7-8) (2000) 211–214.

[13] G. Marin, C. Guerin, S. Baillet, L. Garnero, G. Meunier, Influence of skull anisotropy for the forward and inverse problem in EEG: simulation studies using the FEM on realistic head models, Human Brain Mapping 6 (1998) 250–269.

[14] J. Meijs, O. Weier, M. Peters, A. van Oosterom, On the numerical accuracy of the boundary element method, IEEE Trans Biomed. Eng. 36 (1989) 1038–1049.

[15] C. Michel, M. Murray, G.Lantz, S.Gonzalez, L.Spinelli, R. de Peralta, EEG source imaging, Clin.Neurophysiol. 115 (2004) 2195–2222, invited review.

[16] M. Mohr, Simulation of Bioelectric Fields: The Forward and Inverse Problem of Electroencephalographic Source Analysis, vol. 37 of Arbeitsberichte des Instituts für Informatik, Friedrich-Alexander-Universität Erlangen-Nürnberg, 2004, ISSN 1611-4205.

[17] S. Murakami, Y. Okada, Contributions of principal neocortical neurons to magnetoencephalography and electroencephalography signals, J.Physiol. 575 (3) (2006) 925–936.

[18] C. Pantev, M. Hoke, B. Lütkenhöner, K. Lehnertz, Tonotopic organization of the auditory cortex: Pitch versus frequency representation, Science 246 (1989) 486–488.

[19] M. Peters, J. de Munck, The influence of model parameters on the inverse solution based on MEGs and EEGs, Acta Otolaryngol [Suppl] (Stockh) 491 (1991) 61–69.

[20] R. Plonsey, D. Heppner, Considerations on quasi-stationarity in electrophysiological systems, Bull.math.Biophys. 29 (1967) 657–664.

[21] C. Ramon, P. Schimpf, J. Haueisen, M. Holmes, A. Ishimaru, Role of soft bone, CSF and gray matter in EEG simulations, Brain Topography 16 (4) (2004) 245–248.

[22] J. Sarvas, Basic mathematical and electromagnetic concepts of the biomagnetic inverse problem, Phys.Med.Biol. 32 (1) (1987) 11–22.

[23] P. Schimpf, C. Ramon, J. Haueisen, Dipole models for the EEG and MEG, IEEE Trans Biomed. Eng. 49 (5) (2002) 409–418.

[24] J. S. Shimony, R. McKinstry, E.Akbudak, J.A.Aronovitz, A.Z.Snyder, N.F.Lori, T.S.Cull, T.E.Conturo, Quantitative diffusion-tensor anisotropy brain MR imaging: Normative human data and anatomic analysis, Radiology 212 (1999) 770–784.

[25] H. Si, TetGen, a quality tetrahedral mesh generator and three-dimensional delaunay triangulator, v1.3, user's manual, Tech. Rep. 9, Weierstrass Institute for Applied Analysis and Stochastics (2004).

[26] H. Si, TetView, http://tetgen.berlios.de/tetview.html (2007).

[27] H. Si, K. Gärtner, Meshing piecewise linear complexes by constrained Delaunay tetrahedralizations, in: Proc. 14th International Meshing Roundtable, Sandia National Laboratories, 2005.

[28] A. H. Stroud, Approximate calculation of multiple integrals, Prentice-Hall, Inc., 1971.

[29] S. van den Broek, Volume conduction effects in EEG and MEG, Ph.D. thesis, Proefschrift Universiteit Twente Enschede, The Netherlands (1997).

[30] T. Waberski, H. Buchner, K. Lehnertz, A. Hufnagel, M. Fuchs, R. Beckmann, A. Rienäcker, The properties of source localization of epileptiform activity using advanced headmodelling and source reconstruction, Brain Top. 10 (4) (1998) 283–290.

[31] C. Wolters, A. Anwander, D.Weinstein, M.Koch, X.Tricoche, R.S.MacLeod, Influence of tissue conductivity anisotropy on EEG/MEG field and return current computation in a realistic head model: A simulation and visualization study using high-resolution finite element modeling., NeuroImage 30 (3) (2006) 813–826, http://dx.doi.org/10.1016/j.neuroimage.2005.10.014.

[32] C. Wolters, J. de Munck, Volume conduction, Encyclopedia of Computational Neuroscience, Scholarpedia. http://www.scholarpedia.org, (2007) invited review.

[33] C. Wolters, H. Köstler, C. Möller, J. Härtlein, L. Grasedyck, W. Hackbusch, Numerical mathematics of the subtraction method for the modeling of a current dipole in EEG source reconstruction using finite element head models., SIAM J. on Scientific Computing, in press.

[34] C. Wolters, M. Kuhn, A. Anwander, S. Reitzinger, A parallel algebraic multigrid solver for finite element method based source localization in the human brain, Comp.Vis.Sci. 5 (3) (2002) 165–177.

[35] C. H. Wolters, A. Anwander, G. Berti, U. Hartmann, Geometry-adapted hexahedral meshes improve accuracy of finite element method based EEG source analysis., IEEE Trans.Biomed.Eng. 54 (8) (2007) 1446–1453.

[36] C. H. Wolters, A. Anwander, X. Tricoche, S. Lew, C. Johnson, Influence of local and remote white matter conductivity anisotropy for a thalamic source on EEG/MEG field and return current computation, Int.Journal of Bioelectromagnetism 7 (1) (2005) 203–206.

[37] C. H. Wolters, L. Grasedyck, W. Hackbusch, Efficient computation of lead field bases and influence matrix for the FEM-based EEG and MEG inverse problem, Inverse Problems 20 (4) (2004) 1099–1116.

[38] Y. Yan, P. Nunez, R. Hart, Finite-element model of the human head: Scalp potentials due to dipole sources, Med.Biol.Eng.Comput. 29 (1991) 475–481.

[39] M. Yedlin, H. Kwan, J. Murphy, H. Nguyen-Huu, J. Wong, Electrical conductivity in cat cerebellar cortex, Exp.Neurol. 43 (1974) 555–569.

2.9 Comparison of solver times and dipole modeling accuracy for the FEM based EEG forward and inverse problem

2.9.1 Accuracy and time comparison for different potential approaches and iterative solvers for the FEM based EEG forward problem

Accuracy and time comparison for different potential approaches and iterative solvers in finite element method based EEG source analysis
Lew, S., Wolters C.H., Dierkes, T., Röer, C., MacLeod, R.S.. submitted to *Applied Numerical Mathematics*, (2008).

Corresponding author: C.H. Wolters (S. Lew is PhD student of C.H.Wolters and R.S. MacLeod)

Accuracy and run-time comparison for different potential approaches and iterative solvers in finite element method based EEG source analysis

S. Lew [a,b] C.H. Wolters [c,*] T. Dierkes [c] C. Röer [c] R.S. MacLeod [a,b]

[a] *Scientific Computing and Imaging Institute, University of Utah, Salt Lake City, USA*

[b] *Department of Bioengineering, University of Utah, Salt Lake City, USA*

[c] *Institut für Biomagnetismus und Biosignalanalyse, Westfälische Wilhelms-Universität Münster, Münster, Germany*

Abstract

Accuracy and run-time play an important role in medical diagnostics and research as well as in the field of neuroscience. In Electroencephalography (EEG) source reconstruction, a current distribution in the human brain is reconstructed noninvasively from measured potentials at the head surface (the EEG inverse problem). Numerical modeling techniques are used to simulate head surface potentials for dipolar current sources in the human cortex, the so-called EEG forward problem.

In this paper, the efficiency of algebraic multigrid (AMG), incomplete Cholesky (IC) and Jacobi preconditioners for the conjugate gradient (CG) method are compared for iteratively solving the finite element (FE) method based EEG forward problem. The interplay of the three solvers with a full subtraction approach and two direct potential approaches, the Venant and the partial integration method for the treatment of the dipole singularity is examined. The examination is performed in a four-compartment sphere model with anisotropic skull layer, where quasi-analytical solutions allow for an exact quantification of computational speed versus numerical error. Specifically-tuned constrained Delaunay tetrahedralization (CDT) FE meshes lead to high accuracies for both the full subtraction and the direct potential approaches. Best accuracies are achieved by the full subtraction approach if the homogeneity condition is fulfilled. It is shown that the AMG-CG achieves an order of magnitude higher computational speed than the CG with the standard preconditioners with an increasing gain factor when decreasing mesh size. Our results should broaden the application of accurate and fast high-resolution FE volume conductor modeling in source analysis routine.

Key words: electroencephalography, source reconstruction, finite element method, dipole singularity, full subtraction potential approach, Venant potential approach, partial integration potential approach, preconditioned conjugate gradient method, algebraic multigrid, incomplete Cholesky, Jacobi, constrained Delaunay tetrahedralization, anisotropic four-layer sphere model.

1. Introduction

Electroencephalography (EEG) based source reconstruction of cerebral activity (the EEG inverse problem) is an important tool both in clinical practice and research [34], and in cognitive neuroscience [2]. Methods for solving the inverse problem are based on solutions to the corresponding forward problem, i.e., the simulation of EEG potentials for a given primary source in the brain using a volume-conduction model of the human head. While the theory of this forward problem is well established and many numerical implementations exist, there remain unresolved questions regarding the accuracy and efficiency of contemporary approaches. In this study, we compared a range of numerical techniques and source representation approaches and have shown that careful choice of both are critical in order to solve realistic electroencephalographic forward (and inverse) problems.

The general approach for solving bioelectric field problems under realistic conditions is well established. All quantitative solutions for the EEG forward problem are based on the quasi-static Maxwell equations [25]. The primary sources are electrolytic currents within the dendrites of the large pyramidal cells of activated neurons in the human cortex. Even if there are also smoother models [32], most often the primary sources are formulated as a mathematical point current dipole [25,6,18]. The finite element (FE) method is often used for the solution of the forward problem, because it allows for a realistic representation of the complicated head volume conductor with its tissue conductivity inhomogeneities and anisotropies [40,3,1,33,4,15,20,36,26,38,7].

To implement the point current dipole as a current source in the brain, the FE method requires careful consideration of the singularity of the potential at the source position. One way to address the singularity is to use a “subtraction approach”, which divides the total potential into an analytically known singularity potential and a singularity-free correction potential, which can then be approximated numerically using an FE approach [3,1,33,15,26,38,7]. For the correction potential, the existence and uniqueness for a weak solution in a zero-mean function space have been proven and FE convergence properties are known [38]. It has also been established that a full subtraction approach [7] leads to an order of magnitude more accurate solution than a common alternative, the projected subtraction approach [38], especially when considering sources that are close to a conductivity inhomogeneity. Another family of source representation methods, known as direct FE approaches to the total potential [40,1,4,36,26], are computationally less expensive, but also mathematically less sound under the assumption that a point dipole is the more realistic source model.

* Corresponding author. Institut für Biomagnetismus und Biosignalanalyse, Westfälische Wilhelms-Universität Münster, Malmedyweg 15, 48149 Münster, Germany, Tel.: +49/(0)251-83-56904, Fax: +49/(0)251-83-56874, http://biomag.uni-muenster.de

Email addresses: slew@sci.utah.edu (S. Lew), carsten.wolters@uni-muenster.de (C.H. Wolters), thomas.dierkes@uni-muenster.de (T. Dierkes), c.roeer@uni-muenster.de (C. Röer), macleod@sci.utah.edu (R.S. MacLeod).

Another general prerequisite for FE modeling of bioelectric fields is the generation of a mesh that represents the geometry and electric properties of the volume conductor. An effective meshing strategy will balance acceptable forward problem accuracy against reasonable computation times and memory usage. Very high accuracies can be achieved by making use of a Constrained Delaunay Tetrahedralization (CDT) in combination with a full subtraction approach [7]. Adaptive methods, using local refinement around the source singularity [3,33], are another potential utility but they preclude the use of fast transfer matrices [36,8,39,11] and lose efficiency in solving the inverse problem (see discussion section).

Solving the forward problem is rarely the ultimate goal in calculating bioelectric fields but rather a step towards solving the associated inverse problem. Thus the quest for numerical accuracy and efficiency of the forward solution requires some anticipation of the ultimate use in inverse solutions. The longtime state-of-the-art approach has been to solve an FE equation system for each anatomically and physiologically meaningful dipolar source (each source results in one FE right-hand side (RHS) vector) [3,1,33,4,15]. The use of standard direct (banded LU factorization for a 2D source analysis scenario [1]) or iterative (Conjugate Gradient (CG) without preconditioning [3] or Successive OverRelaxation (SOR) [26]) FE solver techniques limit the overall resolution of the geometric model because of their computational cost. The preconditioned CG method was used with standard preconditioners like Jacobi (Jacobi-CG) [36] or incomplete Cholesky without fill-in, IC(0)-CG [4].

One recent approach to achieve efficient computation of the FE-based forward problem is to pre-compute transfer matrices that encapsulate the relationship between source locations and sensor sites based only on the geometric and conductivity characteristics of the volume conductor, i.e., they are independent of the source. Techniques exist to construct transfer matrices for problem formulations based on EEG [36,11] or combined EEG and MEG [8,39]. Using this principle, for each head model, one only has to solve one large sparse FE system of equations for each of the possible sensor locations in order to compute the full transfer matrix. Each forward solution is then reduced to multiplication of the transfer matrix by an FE RHS vector containing the source load. Exploiting the fact that the number of sensors (currently up to about 600) is much smaller than the number of reasonable dipolar sources (tens of thousands), the transfer matrix approach is substantially faster than the state-of-the-art forward approach (i.e., solving an FE equation system for each source) and can be applied to inverse reconstruction algorithms in both continuous and discrete source parameter space for EEG and MEG. Still, the solution of hundreds of large linear FE equation systems for the construction of the transfer matrices is a major time consuming part within FE-based source analysis.

The first goal of this study was therefore to compare the numerical accuracy of the full subtraction approach [7] with the two direct approaches using partial integration [40,1,36] and Venant [4] in specifically-tuned CDT meshes of an anisotropic four-compartment sphere model for which quasi-analytical solutions exist [5]. We then examine the interplay of the source model approaches with three FE solver methods: a Jacobi-CG, an incomplete Cholesky CG (e.g., [27]), and an algebraic multigrid preconditioned CG (AMG-CG), which has already shown to be especially suited for problems with discontinuous and anisotropic coefficients [23,31,22,9,37].

2. Theory

In the quasi-static approximation of the Maxwell equations, the distribution of electric potentials Φ in the head domain Ω of conductivity σ, resulting from a primary current $\mathbf{j}^p$ is governed by the Poisson equation with homogeneous Neumann boundary conditions on the head surface $\Gamma = \partial\Omega$ [21,25], which we can express as

$$\nabla \cdot (\sigma \nabla \Phi) = \nabla \cdot \mathbf{j}^p \; = \mathrm{J}^p \text{ in } \Omega, \quad \langle \sigma \nabla \Phi, \mathbf{n} \rangle = 0 \;\text{ on } \Gamma, \tag{1}$$

with $\mathbf{n}$ the unit surface normal, and assuming a reference electrode with given potential, i.e., $\Phi(\mathbf{x}_{\text{ref}}) = 0$. The primary currents are modeled by a mathematical dipole at position $\mathbf{x}_0 \in \mathbb{R}^3$ with moment $\mathbf{M}_0 \in \mathbb{R}^3$ [25,6,18],

$$\mathrm{J}^p = \nabla \cdot \mathbf{j}^p(\mathbf{x}) = \nabla \cdot (\mathbf{M}_0 \delta(\mathbf{x} - \mathbf{x}_0)) \,. \tag{2}$$

2.1. *Finite element modeling techniques for the potential singularity*

One of the key questions for all three-dimensional EEG forward modeling techniques is the appropriate treatment of the potential singularity introduced into the differential equation by the formulation of the mathematical dipole (2). This study examined the interplay of FE solver methods (see Section 2.2) with the solution accuracy in four-layer sphere models applying three singularity treatment techniques: a full subtraction approach, a partial integration direct method and a Venant direct method.

2.1.1. *Full subtraction approach*

The subtraction approach [3,1,38,7] splits the total potential Φ into two parts,

$$\Phi = \Phi_0 + \Phi_{\text{corr}}, \tag{3}$$

where the singularity potential, Φ_0, is defined as the solution for a dipole in an unbounded homogeneous conductor with constant conductivity σ_0. $\sigma_0 \in \mathbb{R}^{3\times 3}$ is the conductivity at the source position, which is assumed to be constant in a non-empty subdomain Ω_0 around $\mathbf{x}_0$, in the following called the *homogeneity condition.* The solution of Poisson's equation under these conditions for the singularity potential

$$\nabla \cdot (\sigma_0 \nabla \Phi_0) = \nabla \cdot \mathbf{j}^p \tag{4}$$

can be formed analytically for the mathematical dipole (2) [7] as

$$\Phi_0(\mathbf{x}) = \frac{1}{4\pi\sqrt{\det \sigma_0}} \frac{\langle \mathbf{M}_0, (\sigma_0)^{-1}(\mathbf{x} - \mathbf{x}_0)\rangle}{\langle (\sigma_0)^{-1}(\mathbf{x} - \mathbf{x}_0), (\mathbf{x} - \mathbf{x}_0)\rangle^{3/2}}. \tag{5}$$

Subtracting (4) from (1) yields a Poisson equation for the correction potential

$$-\nabla \cdot (\sigma \nabla \Phi_{\text{corr}}) = -\nabla \cdot ((\sigma_0 - \sigma)\nabla \Phi_0) \quad \text{in } \Omega, \tag{6}$$

with inhomogeneous Neumann boundary conditions at the surface:

$$\langle \sigma \nabla \Phi_{\text{corr}}, \mathbf{n} \rangle = -\langle \sigma \nabla \Phi_0, \mathbf{n} \rangle \quad \text{on } \Gamma. \tag{7}$$

The advantage of (6) is that the right-hand side is free of any source singularity, because of the homogeneity condition — the conductivity $\sigma_0 - \sigma$ is zero in Ω_0. Existence and uniqueness of the solution and FE convergence properties are shown for the correction potential in [38]. For the numerical approximation of the correction potential, we use the FE method with piecewise linear basis functions φ_i. When projecting the correction potential into the FE space, i.e., $\Phi_{\text{corr}}(\mathbf{x}) \approx \Phi_{\text{corr},h}(\mathbf{x}) = \sum_{j=1}^{N_h} \varphi_j(\mathbf{x})\underline{u}_{\text{corr},h}^{[j]}$, and applying variational and FE techniques to (6) and (7), we finally arrive at a linear system [7]

$$K_h \underline{u}_{\text{corr},h} = \underline{j}_{\text{corr},h}, \tag{8}$$

with the stiffness matrix

$$K_h^{[i,j]} = \int_\Omega \langle \sigma \nabla \varphi_j, \nabla \varphi_i \rangle dx, \tag{9}$$

for $K_h \in \mathbb{R}^{N_h \times N_h}$, and the right-hand side vector $\underline{j}_{\text{corr},h} \in \mathbb{R}^{N_h}$ with entries

$$\underline{j}_{\text{corr},h}^{[i]} = \int_\Omega \langle (\sigma_0 - \sigma) \nabla \Phi_0, \nabla \varphi_i(x) \rangle dx - \int_{\partial\Omega} \varphi_i(x) \langle n(x), \sigma_0 \nabla \Phi_0(x) \rangle dx. \tag{10}$$

We then seek for the coefficient vector $\underline{u}_{\text{corr},h} = (\underline{u}_{\text{corr},h}^{[1]}, \ldots, \underline{u}_{\text{corr},h}^{[N_h]}) \in \mathbb{R}^{N_h}$ and, using (3), compute the total potential. In [7], the theoretical reasoning and a validation in a four-compartment sphere model with anisotropic skull is given for the fact that second order integration is necessary and sufficient for the right-hand side integration in Equation (10). Direct comparisons with the projected subtraction approach from [38] have shown that the full subtraction approach is an order of magnitude more accurate for dipole sources close to a conductivity discontinuity [7].

2.1.2. *The partial integration direct approach*

Multiplying both sides of Equation (1) by a linear FE basis function φ_i and integrating over the head domain leads to a partial integration direct approach for the total potential [1,35,17] expressed as

$$\int_\Omega \nabla \cdot (\sigma \nabla \Phi) \, \varphi_i dx = \int_\Omega \nabla \cdot \mathbf{j}^p \varphi_i dx.$$

Integration by parts, applied to both sides of the above equation, yields

$$-\int_\Omega \langle \sigma \nabla \Phi, \nabla \varphi_i \rangle dx + \int_\Gamma \langle \sigma \nabla \Phi, \mathbf{n} \rangle \varphi_i d\Gamma = -\int_\Omega \langle \mathbf{j}^p, \nabla \varphi_i \rangle dx + \int_\Gamma \langle \mathbf{j}^p, \mathbf{n} \rangle \varphi_i d\Gamma.$$

Using the homogeneous Neumann boundary condition from Equation (1) and the fact that the current density vanishes on the head surface, we arrive at

$$\int_\Omega \langle \sigma \nabla \Phi, \nabla \varphi_i \rangle dx = \int_\Omega \langle \mathbf{j}^p, \nabla \varphi_i \rangle dx \overset{(2)}{=} \langle \mathbf{M}_0, \nabla \varphi_i \left(\mathbf{x}_0\right) \rangle.$$

Setting $\Phi(\mathbf{x}) \approx \Phi_h(\mathbf{x}) = \sum_{j=1}^{N_h} \varphi_j(\mathbf{x}) \underline{u}_h^{[j]}$, leads to the linear system

$$K_h \underline{u}_h = \underline{j}_{\text{PI},h}, \tag{11}$$

with the same stiffness matrix as in (9) and the right-hand side vector $\underline{j}_{\text{PI},h} \in \mathbb{R}^{N_h}$ with entries

$$\underline{j}_{\text{PI},h}^{[i]} = \begin{cases} \langle \mathbf{M}_0, \nabla \varphi_i \left(\mathbf{x}_0\right) \rangle & \text{if } i \in \textsc{NodesOfEle}(\mathbf{x}_0), \\ 0 & \text{otherwise.} \end{cases} \tag{12}$$

The function $\textsc{NodesOfEle}(\mathbf{x}_0)$ determines the set of nodes of the element which contains the dipole at position $\mathbf{x}_0$. Note that while the right-hand side vector (10) is fully populated, $\underline{j}_{\mathrm{PI},h}$ has only $|\textsc{NodesOfEle}|$ non-zero entries. Here, $|\cdot|$ denotes the number of elements in the set NodesOfEle. For the linear basis functions φ_i considered here, the right-hand side (12) and thus the computed solution for the total potential in (11) will be constant for all $\mathbf{x}_0$ within a finite element.

2.1.3. *The Venant direct approach*

To derive the Venant direct potential approach, we follow the ideas of [4] and start from the basic relation for a dipole moment $\mathbf{T}_0 \in \mathbb{R}^3$ at position $\mathbf{x}_0 \in \mathbb{R}^3$, $\mathbf{T}_0 = \int_\Omega (\mathbf{x}-\mathbf{x}_0)\mathrm{J}^p(\mathbf{x})d\mathbf{x}$ (see, e.g., [19, formula (2.92)]). Assuming discrete sources and sinks on only the C neighboring FE mesh nodes to the FE node which is closest to $\mathbf{x}_0$, $\mathbf{T}_0 = \sum_{c=1}^{C} \Delta\mathbf{x}_{c0}\underline{j}_0^{[c]}$ with $\Delta\mathbf{x}_{c0}$ denoting the vector from FE node c to source position $\mathbf{x}_0$. When using higher moments $\underline{\bar{T}}_0^r \in \mathbb{R}^{n_0+1}$ with $n_0 = 1, 2$ and the Cartesian direction r ($r = x, y, z$), this expression becomes

$$\left(\underline{\bar{T}}_0^r\right)^{[n]} = \left(\underline{\bar{T}}_0^r\right)^{[n]}(\underline{j}_0) = \sum_{c=1}^{C} \left(\Delta\bar{x}_{c0}^r\right)^n \underline{j}_0^{[c]} \qquad \forall n \in 0,\ldots,n_0 \tag{13}$$

(for a motivation of higher moments see [4]). The bar indicates a scaling with a reference length a_{ref}, so that

$$\Delta\bar{x}_{c0}^r = \Delta x_{c0}^r / a_{\mathrm{ref}} \overset{!}{<} 1 \tag{14}$$

is dimensionless and the physical dimension of the resultant scaled n^{th} order moment, $\left(\underline{\bar{T}}_0^r\right)^{[n]}$, is that of a current (i.e., Amps). The reference length a_{ref} has to be chosen so that $\Delta\bar{x}_{c0}^r$ is less than 1. The equation is well known from the Saint Venant law in mechanical engineering — small forces in combination with long lever arms have the same effect on the system as large forces in combination with short lever arms.

If we now define the matrix $\bar{X}_0^r \in \mathbb{R}^{(n_0+1)\times C}$, the moment vector $\underline{\bar{M}}_0^r \in \mathbb{R}^{n_0+1}$, computed from a given dipole moment vector $\mathbf{M}_0$, and the diagonal source weighting matrix $\bar{W}_0^r \in \mathbb{R}^{C\times C}$ by

$$\begin{aligned}
\left(\bar{X}_0^r\right)^{[n,c]} &= \left(\Delta\bar{x}_{c0}^r\right)^n \\
\left(\underline{\bar{M}}_0^r\right)^{[n]} &= M_0^r \left(\frac{1}{2a_{\mathrm{ref}}}\right)^n \left(1-(-1)^n\right) \\
\bar{W}_0^r &= \mathrm{DIAG}\left(\left(\Delta\bar{x}_{10}^r\right)^s, \ldots, \left(\Delta\bar{x}_{C0}^r\right)^s\right)
\end{aligned} \tag{15}$$

with $s = 0$ or $s = 1$, then we can compute the monopole load vector $\underline{j}_0 \in \mathbb{R}^C$ for the Venant direct approach on the C neighboring FE nodes from a given dipole moment vector $\mathbf{M}_0$ at position $\mathbf{x}_0$ by means of minimizing the following functional

$$F_\lambda(\underline{j}_0) = \|\underline{\bar{M}}_0^r - \underline{\bar{T}}_0^r(\underline{j}_0)\|_2^2 + \lambda\|\bar{W}_0^r\underline{j}_0\|_2^2 = ||\underline{\bar{M}}_0^r - \bar{X}_0^r\underline{j}_0||_2^2 + \lambda\|\bar{W}_0^r\underline{j}_0\|_2^2 \overset{!}{=} \min.$$

The first part of the functional F_λ ensures a minimal difference between the moments of the Venant approach $\underline{\bar{T}}_0^r$ and the target moments $\underline{\bar{M}}_0^r$, while the second part smoothes the monopole distribution in a weighted sense and enables a unique minimum for F_λ. The solution of the minimization problem is given by

$$\left((\bar{X}_0^r)^{tr}\bar{X}_0^r + \lambda(\bar{W}_0^r)^{tr}\bar{W}_0^r\right)\underline{j}_0 = (\bar{X}_0^r)^{tr}\underline{\bar{M}}_0^r$$

(see, e.g., [14, Theorem 4.2.1]), so that the final solution for the monopole source vector $\underline{j}_0$ of the Venant approach is given by

$$\underline{j}_0 = \left(\sum_{r=1}^{3} \left\{ (\bar{X}_0^r)^{tr} \bar{X}_0^r + \lambda (\bar{W}_0^r)^{tr} \bar{W}_0^r \right\} \right)^{-1} \sum_{r=1}^{3} \left\{ (\bar{X}_0^r)^{tr} \underline{\bar{M}}_0^r \right\}. \tag{16}$$

The order n_0 is generally chosen as $n_0 = 1$ or $n_0 = 2$, where the latter imposes a spatial concentration of loads in the dipole axis. Furthermore, $s = 1$ stresses the spatial concentration of loads around the dipole. With $\Phi(\mathbf{x}) \approx \Phi_h(\mathbf{x}) = \sum_{j=1}^{N_h} \varphi_j(\mathbf{x}) \underline{u}_h^{[j]}$, we can derive the linear system

$$K_h \underline{u}_h = \underline{j}_{\mathrm{Venant},h} \tag{17}$$

with the same stiffness matrix as in (9). The right-hand side vector $\underline{j}_{\mathrm{Venant},h} \in \mathbb{R}_h^N$ has only C non-zero entries and is determined by

$$\underline{j}_{\mathrm{Venant},h}^{[i]} = \begin{cases} \underline{j}_0^{[c]} & \text{if } \exists c \in \{1, \ldots, C\} : i = \textsc{glob}(c), \\ 0 & \text{otherwise} \end{cases} \tag{18}$$

for a source at location $\mathbf{x}_0$. The function GLOB determines the global index i to each of the local indices c.

2.2. *FE solver methods*

The solution of hundreds of large scale systems of equations (8), (11) or (17) with the same symmetric positive definite (SPD) stiffness matrix (9) is the major time consuming task of the inverse source localization process. The spectral condition of the SPD matrix K_h is equal to

$$\kappa_2(K_h) = \frac{\lambda_{\max}}{\lambda_{\min}}$$

with $\lambda_{\max}$ the largest and $\lambda_{\min}$ the smallest eigenvalues, respectively, of K_h [10, §2.10]. The condition number behaves asymptotically as $\mathcal{O}(h^{-2})$ and condition numbers of more than 10^7 have been computed for FE problems in EEG source analysis [37]. Large condition numbers are the reason for slow convergence of common iterative solvers [10,24] and any effective solution approach has to minimize the effects of this poor conditioning.

The Preconditioned Conjugate Gradient (PCG) iterative solver shown in Algorithm 1 (see, e.g.,[27,10,24]) can provide efficient procedures for such problems. Note that, in theory, the convergence speed of the PCG is independent of the right-hand side $\underline{j}_h$ of the linear equation system [10, §3.4]. The goal of a preconditioner, $C_h \in \mathbb{R}^{N_h \times N_h}$, is the reduction of $\kappa_2(C_h^{-1} K_h)$ for the preconditioned equation system $C_h^{-1} K_h \underline{u}_h = C_h^{-1} \underline{j}_h$. Further requirements are that it is cheap with regard to arithmetic and memory costs to solve linear systems $C_h \underline{w}_h = \underline{r}_h$ with $\underline{w}_h$ the residual for the preconditioned system.

Theorem 2.1 (Error estimate for PCG method) *Let K_h and C_h be positive definite. If $\underline{u}_h^*$ denotes the exact solution of the equation system, then the k's iterate of the PCG method $\underline{u}_h^k$ fulfills the following energy norm estimate*

$$\|\underline{u}_h^k - \underline{u}_h^*\|_{K_h} \le c^k \frac{2}{1 + c^{2k}} \|\underline{u}_h^0 - \underline{u}_h^*\|_{K_h}, \qquad c := \frac{\sqrt{\kappa_2(C_h^{-1} K_h)} - 1}{\sqrt{\kappa_2(C_h^{-1} K_h)} + 1}.$$

Algorithm 1 PCG : $(K_h, \underline{u}_h, \underline{j}_h, C_h, \text{ACCURACY}) \rightarrow (\underline{u}_h)$

$\underline{r}_h = \underline{r}_h^0 = \underline{j}_h - K_h\underline{u}_h$

SOLVE $C_h\underline{w}_h = \underline{r}_h$

$\underline{s}_h = \underline{w}_h$

$\gamma^0 = \gamma = \gamma_{\text{OLD}} =< \underline{w}_h, \underline{r}_h >$

while $\left(\gamma/\gamma^0 = \left(\frac{||\underline{r}_h||_{C_h^{-1}}}{||\underline{r}_h^0||_{C_h^{-1}}}\right)^2 = \left(\frac{||K_h\underline{e}_h||_{C_h^{-1}}}{||K_h\underline{e}_h^0||_{C_h^{-1}}}\right)^2 = \left(\frac{||\underline{e}_h^i||_{K_hC_h^{-1}K_h}}{||\underline{e}_h^0||_{K_hC_h^{-1}K_h}}\right)^2 > \text{ACCURACY}^2 \right)$ **do**

$\underline{v}_h = K_h\underline{s}_h$

$\alpha = \gamma / < \underline{s}_h, \underline{v}_h >$

$\underline{u}_h = \underline{u}_h + \alpha\underline{s}_h$

$\underline{r}_h = \underline{r}_h - \alpha\underline{v}_h$

SOLVE $C_h\underline{w}_h = \underline{r}_h$

$\gamma =< \underline{w}_h, \underline{r}_h >$

$\beta = \gamma/\gamma_{\text{OLD}}$, $\gamma_{\text{OLD}} = \gamma$

$\underline{s}_h = \underline{w}_h + \beta\underline{s}_h$

end while

Proof: Hackbusch [10, Theorem 9.4.14]. ■

As indicated in Algorithm 1, the PCG method is stopped after the k^{th} iteration if the relative error, i.e., $\underline{e}_h^k = \underline{u}_h^k - \underline{u}_h^*$ in the controllable $K_hC_h^{-1}K_h$-energy norm is below a given ACCURACY. In the following, the three different preconditioners for the CG method are presented and their relative performances evaluated in Section 4.

2.2.1. *Jacobi preconditioning or scaling*

It can be shown, that the smallest (largest) eigenvalue of a symmetric matrix is at most (at least) as large as the smallest (largest) diagonal element, so that the condition number is at least as large as the quotient of maximal and minimal diagonal element [27, p.258]. Diagonal entries in K_h of FE nodes from inside the skull are much smaller than from outside (because of a jump in conductivity at each internal and external boundary). The simplest preconditioner is thus the scaling or Jacobi-preconditioning ([24, pp.265f], [27, pp.257f]), where

$$C_h := D_h^2, \qquad D_h := \text{DIAG}(\sqrt{K_h^{[11]}}, \ldots, \sqrt{K_h^{[N_hN_h]}}).$$

When splitting the Jacobi-preconditioner between left and right (row and column scaling), one has to solve $\tilde{K}_h\underline{v}_h = D_h^{-1}\underline{j}_h$ with $\tilde{K}_h = D_h^{-1}K_hD_h^{-tr}$ and $\underline{u}_h = D_h^{-tr}\underline{v}_h$. Row and column scaling preserves symmetry, so that the scaled matrix $\tilde{K}_h$ is again SPD with unit diagonal entries. The scaling may therefore lead to a first substantial condition improvement.

Theorem 2.2 *Let K_h be SPD and $C_h := D_h^2$ the Jacobi-preconditioner. Assume that each row of K_h does not contain more than* d *nonzero entries. Then, for all diagonal matrices $\tilde{D}_h^{-1}$, it is*

$$\kappa_2(C_h^{-1}K_h) \le \mathrm{d}\ \kappa_2(\tilde{D}_h^{-1}K_h),$$

i.e., the chosen diagonal preconditioner is close to the optimal one.
Proof: Hackbusch [10, Theorem 8.3.3]. ■

2.2.2. *Incomplete Cholesky preconditioning*

The SPD stiffness matrix K_h can be decomposed into a left triangular matrix L_h and its transpose using the Cholesky-decomposition, $K_h = L_h L_h^{tr}$ [27, pp.209f]. Nevertheless, because of a large fill-in, $C_h := L_h L_h^{tr}$ would not be appropriate as a preconditioner. The Incomplete Cholesky (IC) preconditioner without fill-in, IC0, is defined as $C_h := L_0 L_0^{tr}$ where L_0 is the Cholesky-decomposition of the scaled stiffness matrix $\tilde{K}_h$ which is restricted to the same non-zero-pattern as the lower triangular part of $\tilde{K}_h$. For incomplete factorizations, the preconditioning operation $C_h \underline{w}_h = \underline{r}_h$ in Algorithm 1 is solved by a forward-back sweep. The existence of IC0 is not necessarily guaranteed for general SPD matrices. Therefore, a reduction of non-diagonal stiffness matrix entries has to be carried out in certain applications before IC0 computation is possible [27, p.266]. If the scaled stiffness matrix is decomposed by means of $\tilde{K}_h = E_h + \mathrm{Id}_h + E_h^{tr}$, with $E_h \in \mathbb{R}^{N_h \times N_h}$ its strict lower triangular part, the reduction can be formulated as

$$\breve{K}_h = \mathrm{Id}_h + \frac{1}{1+\varsigma}(E_h + E_h^{tr}). \tag{19}$$

For sufficiently large $\varsigma \in \mathbb{R}_0^+$, the existence of IC0 is guaranteed, but with increasing ς, the preconditioning effect decreases. Note that for certain special cases, a condition improvement to $\mathcal{O}(h^{-1})$ can be proven as, e.g., when using a modified ILU_ω-preconditioning with $\omega = -1$ (in the symmetric case, the ILU_0 is equal to the IC0) for diagonally dominant symmetric matrices arising from a 5-point discretization of a two-dimensional Poisson equation (Hackbusch [10, Theorem 8.5.15 and Remarks 8.5.16,17]).

2.2.3. *Algebraic multigrid preconditioning*

The above preconditioning methods have the disadvantage that the convergence rate, i.e., the factor by which the error is reduced in each iteration, is still dependent on the mesh size h. With decreasing mesh size and thus increasing order of the equation system, the convergence rate tends to 1 from below, so that the number of iterations needed to achieve a given accuracy increases. For the Geometric Multi-Grid (GMG), an h-independent convergence rate $\rho < 1$ and an h-independent condition number has been proven in [10, Lemma 10.7.1,Theorem 10.7.15] as

$$\kappa_2(C_h^{-1}K_h) \le \frac{1}{1-\rho^m}, \tag{20}$$

with C_h the preconditioner resulting from m steps of the GMG method. As shown in [12,10,31], a robust method which provides a small convergence rate for a wide class of real-life problems is given by exploiting the MG-method as a preconditioner for the CG method. With MG(m)-CG, we denote the MG-preconditioned CG method with m the number of MG iterations for the CG preconditioning step. The GMG(m)-CG can improve the convergence rate to $\rho/4$, if ρ is assumed to be small, as shown in [10, §10.8.3].

In contrast to GMG, in which a grid hierarchy is required explicitly, Algebraic MG (AMG) is able to construct a matrix hierarchy and corresponding transfer operators based only on the entries in K_h (see, e.g., [23,31,22,9]). It is well known that the classical AMG method is robust for M-matrices and, with regard to our application, that small positive off-diagonal entries are admissible [23,31,22]. The method is especially well suited for our problem with discontinuous and anisotropic coefficients, in which an optimal tuning of the GMG is difficult ([23, §4.1,4.6.4],[31, §4.1]). Stand-alone AMG is hardly ever optimal as there may be some very specific error components which are reduced with significantly less efficiency, causing a few eigenvalues of the AMG iteration matrix to be much closer to 1 than the remaining ones [31, §3.3]. In such a case, acceleration by means of using AMG as a basis for the CG method eliminates these particular frequencies very efficiently.

As in GMG, the basic idea in AMG is to reduce high and low frequency components of the error by the efficient interplay of smoothing and coarse grid correction, respectively. In analogy to GMG, the denotation *coarse grids* will be used, although these are purely virtual and do not have to be constructed explicitly as FE meshes. The diagonal entry of the i^{th} row of K_h is considered as being related to a grid point in ω_h (the index set of nodes), and an off-diagonal entry is related to an edge in an FE grid. A description of AMG is now given for a symmetric two grid method, where h is related to the fine grid and H to the coarse grid. Each AMG algorithm consists of the following components:

(a) Coarsening: define the splitting $\omega_h = \omega_C \cup \omega_F$ of ω_h into sets of coarse and fine grid nodes ω_C and ω_F, respectively.

(b) Transfer operators: prolongation $P_{h,H} : \mathbb{R}^{N_H} \mapsto \mathbb{R}^{N_h}$ and its adjoint as the restriction

$$R_{H,h} := P_{h,H}^{tr}. \tag{21}$$

(c) Definition of the coarse matrix by Galerkin's method, i.e.,

$$K_H := R_{H,h} K_h P_{h,H}. \tag{22}$$

Because of (b), $K_H \in \mathbb{R}^{N_H \times N_H}$ is again SPD.

(d) Appropriate smoother for the considered problem class: In order to achieve a symmetric method, e.g., a forward Gauss-Seidel method for pre-smoothing and the adjoint, a backward Gauss-Seidel method for post-smoothing ([10, §4.8.3,§10.7.1,2],[23, §4.4]).

[(a)—] Coarsening: The coarsening process has the task of reducing the number of nodes such that $N_H = |\omega_C| < N_h = |\omega_h|$. The grid points ω_h can be split into two disjoint subsets ω_C (coarse grid nodes) and ω_F (fine grid nodes), i.e., $\omega_h = \omega_C \cup \omega_F$ and $\omega_C \cap \omega_F = \emptyset$ such that there are (almost) no direct connections between any two coarse grid nodes and such that the resulting number of coarse grid nodes is as large as possible [31, p.12]. Instead of considering all connections between nodes as being of the same rank, the following sets are introduced

$$\begin{aligned} N_h^i &= \left\{ j \mid |K_h^{[ij]}| \geq \zeta |K_h^{[i,i]}|,\, i \neq j \right\}, && (23) \\ S_h^i &= \left\{ j \in N_h^i \mid |K_h^{[ij]}| > \text{coarse}(i,j,K_h) \right\}, \\ S_h^{i,T} &= \left\{ j \in N_h^i \mid i \in S_h^j) \right\}, && (24) \end{aligned}$$

where N_h^i is the index set of neighbors (a pre-selection is carried out by the threshold-parameter $\zeta \in \mathbb{R}_0^+$), S_h^i denotes the index set of nodes with a *strong connection* from node i and $S_h^{i,T}$ is related to the index set of nodes with a strong connection to node i. In addition, coarse(i, j, K_h) is an appropriate cut-off (coarsening) function, e.g.,

$$\text{coarse}(i, j, K_h) := \alpha \cdot \max_{j, j \neq i} \{|K_h^{[ij]}|\}, \tag{25}$$

with $\alpha \in [0, 1]$ (see, e.g., [23, §4.6.1]).

Algorithm 2 COARSE : $(\{S_h^{i,T}\}, \omega_h) \to (\omega_C, \omega_F)$

$\omega_C \leftarrow \emptyset, \quad \omega_F \leftarrow \emptyset$
while $\omega_C \cup \omega_F \neq \omega_h$ **do**
  $i \leftarrow \textsc{Pick}(\omega_h \setminus (\omega_C \cup \omega_F))$
  if $|S_h^{i,T}| + |S_h^{i,T} \cap \omega_F| = 0$ **then**
    $\omega_F \leftarrow \omega_h \setminus \omega_C$
  else
    $\omega_C \leftarrow \omega_C \cup \{i\}$
    $\omega_F \leftarrow \omega_F \cup (S_h^{i,T} \setminus \omega_C)$
  end if
end while

With those definitions a splitting into coarse and fine grid nodes can be achieved. For our application, a modified splitting algorithm is used [23, §4.6] as shown in Algorithm 2. Therein, the function

$$i \leftarrow \textsc{Pick}(\omega_h \setminus (\omega_C \cup \omega_F))$$

returns a node i for which the number $|S_h^{i,T}| + |S_h^{i,T} \cap \omega_F|$ is maximal. Note that tissue conductivity inhomogeneity and anisotropy are taken into account within the coarsening algorithm.

(b) Prolongation: To achieve prolongation, the operator $P_{h,H} : V_H \mapsto V_h$ has to be defined correctly. The form that turned out to be the most efficient for the presented application was proposed in [13] and is given by

$$P_{h,H}^{[ij]} = \begin{cases} 1 & i = j \in \omega_C\,, \\ 1/|S_h^{i,T} \cap \omega_C| & i \in \omega_F,\ j \in S_h^{i,T} \cap \omega_C\,, \\ 0 & \text{else}\,. \end{cases} \tag{26}$$

After the proper definition of the prolongation and coarse grid operators, it is possible to create in a recursive way a matrix hierarchy and an associated multigrid cycle, shown in Algorithm 3. Therein, the variable $\textsc{CoarseGrid}$ denotes the level at which a direct solver is applied. For an m-$V(\nu_F, \nu_B)$-cycle AMG preconditioned CG method, the operation $\textsc{Solve}\ C_h \underline{w}_h = \underline{r}_h$ in Algorithm 1 is realized by m calls of $\text{MG}(K_h, \underline{w}_h, \underline{r}_h, \nu_F, \nu_B)$.

3. Methods

3.1. *Validation platform*

The numerical examinations of the theory presented above were carried out in a four-layer sphere model with anisotropic skull compartment whose parameterization is shown

Algorithm 3 V-cycle MG : $(K_h, \underline{u}_h, \underline{j}_h, \nu_F, \nu_B) \rightarrow (\underline{u}_h)$

if CoarseGrid **then**

  $\underline{u}_h \leftarrow \text{DirectSolve}(K_h \underline{u}_h = \underline{j}_h)$

else

  $\underline{u}_h \leftarrow \nu_F$ TIMES SMOOTH FORWARD$(K_h, \underline{u}_h, \underline{j}_h)$

  $\underline{d}_h = K_h \underline{u}_h - \underline{j}_h$

  $\underline{d}_H = P_{h,H}^{tr} \underline{d}_h$

  $\underline{w}_H = 0$

  $\underline{w}_H = \text{MG}(K_H, \underline{w}_H, \underline{d}_H)$

  $\underline{w}_h = P_{h,H} \underline{w}_H$

  $\underline{u}_h = \underline{u}_h - \underline{w}_h$

  $\underline{u}_h \leftarrow \nu_B$ TIMES SMOOTH BACKWARD$(K_h, \underline{u}_h, \underline{j}_h)$

end if

Table 1
Parameterization of the anisotropic four-layer sphere model.

Medium	Scalp	Skull	CSF	Brain
Outer shell radius	92mm	86mm	80mm	78mm
Tangential conductivity	0.33S/m	0.042S/m	1.79S/m	0.33S/m
Radial conductivity	0.33S/m	0.0042S/m	1.79S/m	0.33S/m

in Table 1. For the choice of these parameters, we closely followed [11,15]. Forward solutions were computed for dipoles of 1 nAm amplitude located on the y axis at depths of 0% to 98.7% (in 1 mm steps) of the brain compartment (78 mm radius) using both radial (directed away from the center of the model) and tangential (directed parallel to the scalp surface) dipole orientations. *Eccentricity* is defined here as the percent ratio of the distance between the source location and the model midpoint divided by the radius of the inner sphere (78 mm). The most eccentric source position considered was thus only 1 mm below the CSF compartment. To achieve error measures which were independent of the specific choice of the sensor configuration, we distributed 748 electrodes in a regular fashion over the outer sphere surface. All simulations ran on a Linux-PC with an Intel Pentium 4 processor (3.2GHz) using the SimBio software environment [30].

3.2. *Analytical solution in an anisotropic multilayer sphere model*

De Munck and Peters [5] derived series expansion formulas for a mathematical dipole in a multi-layer sphere model, denoted here as the *analytical solution*. The model consists of S shells with radii $r_S < r_{S-1} < \ldots < r_1$ and constant radial, $\sigma^{\text{rad}}(r) = \sigma_j^{\text{rad}} \in \mathbb{R}^+$, and constant tangential conductivity, $\sigma^{\text{tang}}(r) = \sigma_j^{\text{tang}} \in \mathbb{R}^+$, within each layer $r_{j+1} < r < r_j$. It is assumed that the source at position x_0 with radial coordinate $r_0 \in \mathbb{R}$ is in a more interior layer than the measurement electrode at position $x_e \in \mathbb{R}^3$ with radial coordinate $r_e = r_1 \in \mathbb{R}$. The spherical harmonics expansion for the mathematical dipole (2) is expressed in terms of the gradient of the monopole potential to the source point. Using an asymptotic approximation and an addition-subtraction method to speed up the series convergence yields

$$\phi_{\mathtt{ana}}(x_0, x_e) = \frac{1}{4\pi}\langle \mathbf{M}, S_0\frac{x_e}{r_e} + (S_1 - \cos\omega_{0e}S_0)\frac{x_0}{r_0}\rangle$$

with ω_{0e} the angular distance between source and electrode, and with

$$S_0 = \frac{F_0}{r_0}\frac{\Lambda}{(1 - 2\Lambda\cos\omega_{0e} + \Lambda^2)^{3/2}} + \frac{1}{r_0}\sum_{n=1}^{\infty}\{(2n+1)R_n(r_0, r_e) - F_0\Lambda^n\}\, P_n'(\cos\omega_{0e}) \tag{27}$$

and

$$S_1 = F_1\frac{\Lambda\cos\omega_{0e} - \Lambda^2}{(1 - 2\Lambda\cos\omega_{0e} + \Lambda^2)^{3/2}} + \sum_{n=1}^{\infty}\{(2n+1)R_n'(r_0, r_e) - F_1 n\Lambda^n\}\, P_n(\cos\omega_{0e}). \tag{28}$$

The coefficients R_n and their derivatives, R_n', are computed analytically and the derivative of the Legendre polynomials, P_n, are determined by means of a recursion formula. We refer to [5] for the derivation of the above series of differences and for the definition of F_0, F_1 and Λ. Here, it is only important that the latter terms are independent of n and that they can be computed from the given radii and conductivities of layers between source and electrode and of the radial coordinate of the source. The computations of the series (27) and (28) are stopped after the k-th term if the following criterion is fulfilled

$$t_k/t_0 \leq \upsilon, \qquad t_k := (2k+1)R_k' - F_1 k\Lambda^k. \tag{29}$$

In the following simulations, a value of 10^{-6} was chosen for υ in (29). Using the asymptotic expansion, no more than 30 terms were needed for the series computation at each electrode.

3.3. *Tetrahedral mesh generation.*

The FE meshes of the four-layer sphere model were generated by the software TetGen [28] which used a *Constrained Delaunay Tetrahedralization* (CDT) approach [29]. This meshing procedure starts with the preparation of a suitable boundary discretization of the model in which for each of the layers and for a given triangle `edge` length, nodes are distributed in a regular fashion and connected through triangles. This yields a valid triangular surface mesh for each of the layers. Meshes of different layers are not intersecting each other. The CDT approach is then used to construct a tetrahedralization conforming to the surface meshes. It first builds a Delaunay tetrahedralization starting with the vertices of the surface meshes. The CDT then uses a local degeneracy removal algorithm combining vertex perturbation and vertex insertion to construct a new set of vertices which includes the input set of surface vertices. In a last step, a fast facet recovery algorithm is used to construct the CDT [29].

This approach is combined with two further constraints to the size and shape of the tetrahedra. The first constraint is important for the generation of quality tetrahedra. If R denotes the radius of the unique circumsphere of a tetrahedron and L its shortest edge length, the so-called *radius-edge ratio* of the tetrahedron can be defined as

$$\mathtt{radius} - \mathtt{edge} - \mathtt{ratio} = R/L. \tag{30}$$

Table 2
The six tetrahedra models used for the solver time comparison and accuracy tests. The table shows the number of `nodes` and `elements` of each mesh and `factor` indicates the ratio of the number of nodes of the most highly resolved to both other models within each group. Additionally, the chosen `radius-edge-ratio` (see Equation (30)), the average `edge` length of the four triangular surface meshes, the corresponding `volume` constraint (see Equation (31)) and the compartments where the volume constraint was not applied are indicated.

	Group 1			Group 2		
Model	`tet503K`	`tet125K`	`tet33K`	`tet508K`	`tet128K`	`tet32K`
`nodes`	503,180	124,624	32,509	508,435	127,847	31,627
`elements`	3,068,958	733,022	187,307	3,175,737	781,361	190,060
`factor`	1	4.04	15.48	1	3.98	16.08
`radius-edge-ratio`	1.0	1.0	1.1	1.0	1.0	1.1
`edge` (in mm)	1.75	2.7	5.2	2.42	3.9	6.87
`volume` (in mm^3)	0.63	2.32	16.57	1.67	6.99	38.21
no volume constraint in	brain	brain	brain	/	/	/

The radius-edge ratio can distinguish almost all badly-shaped tetrahedra except one type of tetrahedra, so-called *slivers*. A sliver is a very flat tetrahedron which has no small edges, but can have arbitrarily large dihedral angles (close to π). For this reason, an additional mesh smoothing and optimization step is required to remove the slivers and improve the overall mesh quality.

A second constraint can be used to restrict the volume of the generated tetrahedra in a certain compartment. We follow the formula for regular tetrahedra:

$$\texttt{volume} = \sqrt{2}/12 \cdot \texttt{edge}^3 \tag{31}$$

Table 2 shows the number of `nodes` and `elements` of the six tetrahedra models used for the solver run-time comparison and accuracy tests. `factor` indicates the ratio of the number of nodes of the most highly resolved to both other models within each group. Additionally, the table contains the chosen `radius-edge-ratio` (see Equation (30)), the average `edge` length of the four triangular surface meshes, the corresponding `volume` constraints (see Equation (31)) for the tetrahedra and the compartments where the volume constraint is not applied. The most highly resolved meshes `tet503K` and `tet508K` of both groups had approximately the same resolution, while the others were chosen to have a `factor` of 4 coarser resolution with regard to the number of nodes. The meshes of group 1 concentrated the nodes in the outer three compartments because no volume constraint was applied for the inner brain compartment, while the nodes in the meshes of group 2 were distributed in a regular way throughout all four compartments. The meshes of group 1 were thus preferentially beneficial to the full subtraction approach, since the entries of the volume integral in Equation (10) are zero ($(\sigma(x) - \sigma_0) = 0$ for all x in the brain compartment) so that a coarse resolution can be expected to have no impact on the overall numerical accuracy, but will reduce the computational cost. In contrast, the meshes of group 2 were beneficial to both direct potential approaches. Figure 1 shows samples from the six tetrahedra models that were generated using the parametrizations from Table 2.

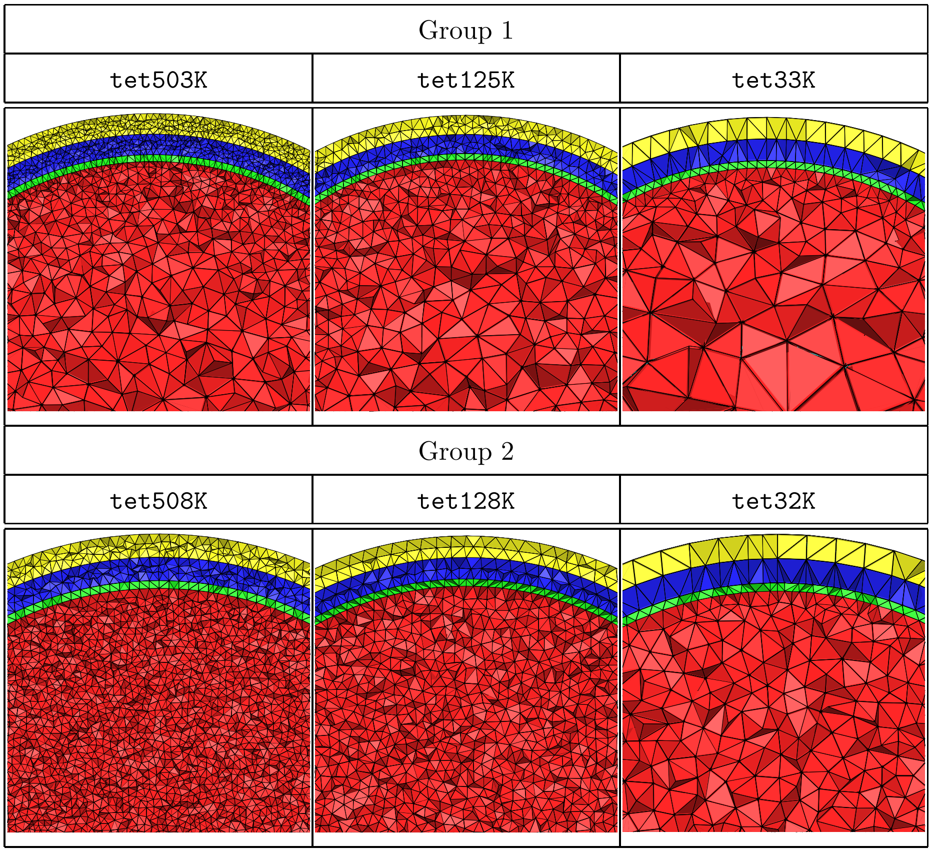

Fig. 1. Cross-sections of the six tetrahedral meshes of the four compartment sphere model. The corresponding parametrizations of the models are shown in Table 2. Visualization was done using the software TetView [28].

3.4. *Error criteria*

We compared numerical solutions with analytical solutions using three common error criteria [16,3,33,15,26]. The *relative (Euclidean) error* (RE) is defined as

$$\mathrm{RE} := \frac{||\underline{\phi}_{\mathtt{num}} - \underline{\phi}_{\mathtt{ana}}||_2}{||\underline{\phi}_{\mathtt{ana}}||_2},$$

where $\underline{\phi}_{\mathtt{ana}}, \underline{\phi}_{\mathtt{num}} \in \mathbb{R}^{\mathrm{m}}$ denote the analytical and the numerical solution vectors, respectively, at the $\mathrm{m} = 748$ measurement electrodes. We furthermore defined

$$\mathrm{RE}(\%) := 100 \cdot \mathrm{RE}, \quad \mathrm{maxRE}(\%) := \max_j \left(\mathrm{RE}(\%)_j\right) \tag{32}$$

where j is the source eccentricity. In order to better distinguish between the topography (driven primarily by changes in dipole location and orientation) and the magnitude error (indicating changes in source strength), Meijs et al. [16] introduced the *relative difference measure* (RDM) and the *magnification factor* (MAG), respectively. For the RDM, we can show that

$$\mathrm{RDM} := \left\|\frac{1}{\|\underline{\phi}_{\mathtt{ana}}\|_2}\underline{\phi}_{\mathtt{ana}} - \frac{1}{\|\underline{\phi}_{\mathtt{num}}\|_2}\underline{\phi}_{\mathtt{num}}\right\|_2 = \sqrt{2\left(1-\cos\angle(\underline{\phi}_{\mathtt{ana}},\underline{\phi}_{\mathtt{num}})\right)}. \qquad (33)$$

It therefore holds that $0 \leq \mathrm{RDM} \leq 2$, so that we can furthermore define

$$\mathrm{RDM}(\%) := 100 \cdot \mathrm{RDM}/2, \quad \mathrm{maxRDM}(\%) := \max_j \left(\mathrm{RDM}(\%)_j\right). \qquad (34)$$

The MAG is defined as

$$\mathrm{MAG} := \|\underline{\phi}_{\mathtt{num}}\|_2 / \|\underline{\phi}_{\mathtt{ana}}\|_2$$

so that error minimum is at MAG = 1 and we therefore defined

$$\mathrm{MAG}(\%) = |1-\mathrm{MAG}| \cdot 100, \quad \mathrm{maxMAG}(\%) := \max_j \left(\mathrm{MAG}(\%)_j\right). \qquad (35)$$

With $\mathrm{maxRE}(\%)^k$ we denote the maximal relative error in percent over all source eccentricities for an accuracy level of ACCURACY $= 10^{-k}$. The so-called *plateau-entry* for an iterative solver is then defined as the first k at which the condition

$$\left|\mathrm{maxRE}(\%)^k - \mathrm{maxRE}(\%)^{k+1}\right| / \mathrm{maxRE}(\%)^{k+1} < 0.05 \qquad (36)$$

is true.

3.5. *FEM and solver parameter settings*

The parameters of the Venant approach were chosen as proposed in [4]: The maximal dipole order n_0 (13) and the scaling reference length a_{ref} (14) were set to $n_0 = 2$ and $a_{\mathrm{ref}} = 20.0$ mm, respectively. Since the chosen mesh size was a large factor smaller than the reference length, the second order term $(\Delta\bar{x}^r_{cl})^2$ was small and the model focused on fulfilling the dipole moments of the zeros and first order. The exponent of the source weighting matrix in (15) was fixed to $s = 1$ and the regularization parameter in (16) was chosen as $\lambda = 10^{-6}$. These settings effect a spatial concentration of the monopole loads in the dipole axis around the dipole location.

The initial solution guess for all solvers was a zero potential vector. For the IC0, $\varsigma = 0$ was chosen for (19). For the AMG-CG, the 1-$V(1,1)$-cycle AMG-preconditioner was used with $\alpha = 0.01$ for (25). The factorization in Algorithm 3 was carried out whenever the size of the coarsest grid (COARSEGRID) in the preconditioner-setup was below 1000 and the coarse system was solved using a Cholesky-factorization. The setup times for the preconditioners were neglected in all calculations of computational cost because this step must be performed only once per head model. The evaluation with regard to relative solver accuracy in Algorithm 1 was limited to the discrete set of *accuracy levels* ACCURACY $= 10^{-k}$ with $k \in \{0, \ldots, 9\}$.

4. Results

4.1. *Numerical error versus potential approach*

In a first study, we compared the numerical accuracy of the full subtraction approach (Section 2.1.1) with the two direct methods: Venant (Section 2.1.3) and partial integration (Section 2.1.2). Figure 2 shows the $RE(\%)$ for the different source eccentricities for the

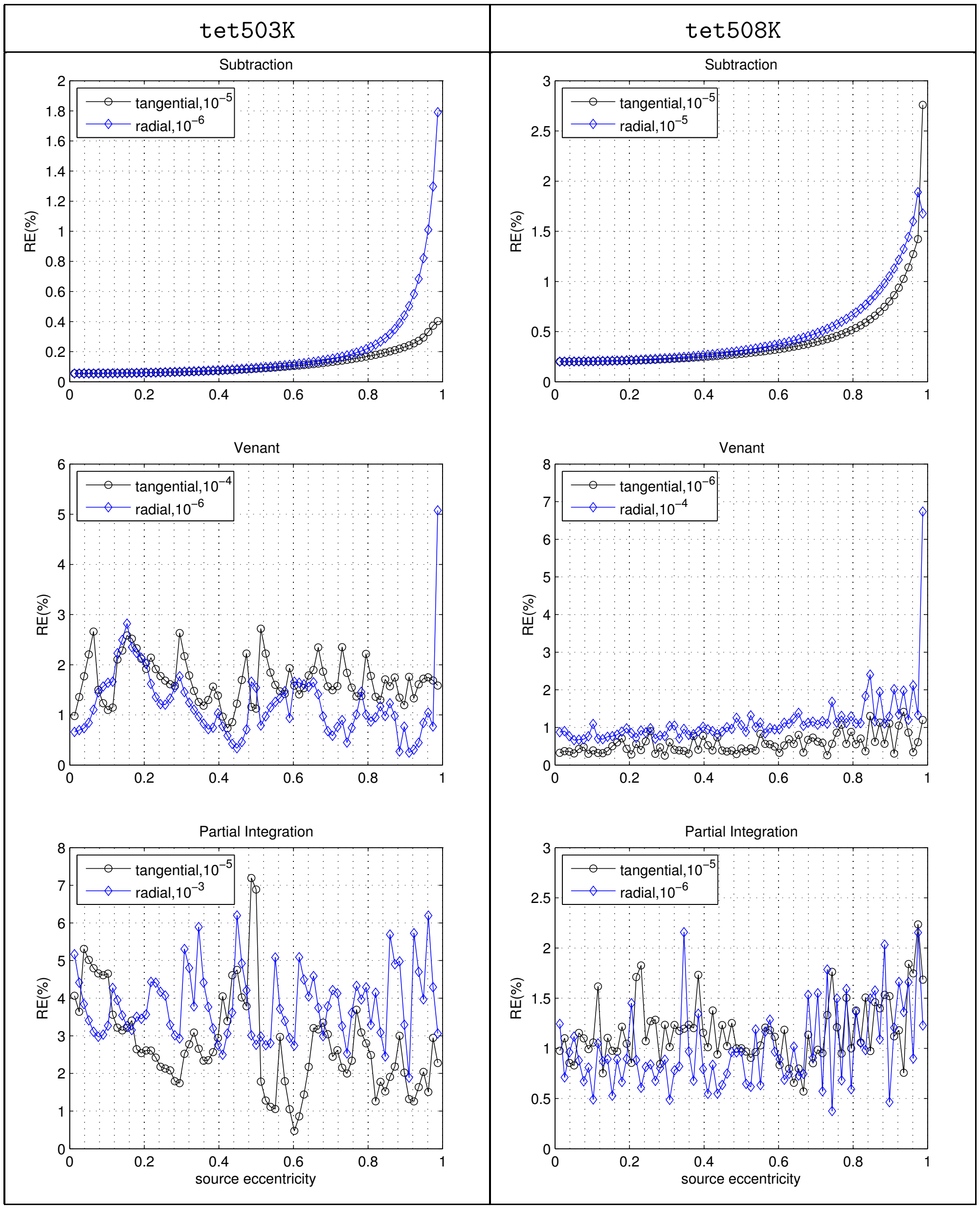

Fig. 2. $RE(\%)$ versus source eccentricity for the two most highly resolved models `tet503K` of group 1 (left) and `tet508K` of group 2 (right) using the full subtraction (top row), the Venant (middle row) and the partial integration (bottom row) potential approaches. The necessary ACCURACY in Algorithm 1 for the plateau-entry (36) of the AMG-CG is indicated for both source orientation scenarios.

two finest models `tet503K` of group 1 (left) and `tet508K` of group 2 (right) (see Figure 1 and Table 2) with regard to the full subtraction (top row), the Venant (middle row) and the partial integration approach (bottom row). The results were computed with

Table 3
Values of maxRE(%), maxRDM(%) and maxMAG(%) accuracies for the full subtraction (Sub), the Venant (Ven) and the partial integration (PI) approach for all six tetrahedra models (see Figure 1 and Table 2) and both source orientation scenarios at the AMG-CG plateau-entry (36).

Group 1									
tangential source									
model	`tet503K`			`tet125K`			`tet33K`		
potential approach	Sub	Ven	PI	Sub	Ven	PI	Sub	Ven	PI
maxRE(%)	0.403	2.719	7.195	4.192	2.722	6.603	12.543	10.246	10.367
maxRDM(%)	0.202	1.311	3.450	1.322	1.296	3.304	6.020	4.920	4.674
maxMAG(%)	0.149	1.840	1.810	3.217	1.395	2.142	2.863	3.307	4.066
radial source									
model	`tet503K`			`tet125K`			`tet33K`		
potential approach	Sub	Ven	PI	Sub	Ven	PI	Sub	Ven	PI
maxRE(%)	1.791	5.077	6.200	2.522	16.867	5.517	33.860	22.810	19.898
maxRDM(%)	0.820	1.408	2.846	1.066	1.662	2.727	17.184	6.730	9.958
maxMAG(%)	0.708	5.035	3.426	1.372	16.804	1.827	6.338	19.344	7.729
Group 2									
tangential source									
model	`tet508K`			`tet128K`			`tet32K`		
potential approach	Sub	Ven	PI	Sub	Ven	PI	Sub	Ven	PI
maxRE(%)	2.760	1.414	2.235	6.206	3.457	3.654	17.000	17.977	11.113
maxRDM(%)	0.874	0.599	0.965	2.202	1.665	1.814	6.721	8.715	5.031
maxMAG(%)	2.121	0.753	1.110	4.277	1.011	1.243	9.542	4.474	4.296
radial source									
model	`tet508K`			`tet128K`			`tet32K`		
potential approach	Sub	Ven	PI	Sub	Ven	PI	Sub	Ven	PI
maxRE(%)	1.890	6.738	2.157	7.660	19.413	5.054	21.111	20.232	21.000
maxRDM(%)	0.804	1.131	1.051	1.212	1.893	2.141	10.616	9.120	9.188
maxMAG(%)	1.183	6.608	1.101	7.404	19.329	2.836	8.831	10.577	8.617

the AMG-CG and the necessary ACCURACY in Algorithm 1 for the plateau-entry (36) is indicated for both source orientation scenarios. In Table 3, the maximal errors over all source eccentricities at the AMG-CG plateau-entry (36) are shown for all tetrahedra models, both source orientation scenarios and the three dipole modeling approaches.

Figure 2 clearly presents the advantages of the full subtraction approach whose error curves are smooth, while Venant and partial integration show an oscillating behavior. With RDM and MAG errors below 1% over all source eccentricities and for both orientation scenarios (see Table 3), the full subtraction approach performs best for all source eccentricities for model `tet503K` (its mesh resolution was sufficiently high and the FE nodes were concentrated in the compartments CSF, skull and skin), where both direct approaches showed oscillations with a relatively high magnitude. As the results for model `tet508K` show, the oscillation magnitudes for the direct approaches could be strongly reduced by means of distributing the FE nodes in a regular way over all four compartments, hence decreasing the mesh size in the brain compartment. Nevertheless, even for model `tet508K`, the full subtraction approach was the most accurate method for nearly all source eccentricities. It was only outperformed by partial integration for the source which was only 1 mm below the CSF compartment. As both Figure 2 and Table 3 show, the partial integration approach performed well if the mesh was sufficiently fine in the brain compartment. The oscillation magnitudes of the Venant approach were generally even slightly smaller than for the partial integration approach, with only one exception (the result for the radial source 1 mm below the CSF compartment, shown in the middle row of Figure 2). The main reason for the outlier was that for the source 1 mm below the CSF, monopoles were positioned in the CSF compartment, which had a strong effect on the MAG for the radially oriented source.

4.2. *Numerical error versus PCG accuracy*

Figure 3 shows the numerical error maxRE(%) versus the PCG solver ACCURACY from Algorithm 1 for the discrete set of accuracy levels from 10^0 to 10^{-9}. Results for the high-resolution model `tet503K` of group 1 are shown in the left and from the high-resolution model `tet508K` of group 2 in the right column for the AMG-CG (top row), the IC(0)-CG (middle row) and the Jacobi-CG (bottom row).

Table 4
Maximally needed $k \in \{0, \dots, 9\}$ for a PCG ACCURACY $= 10^{-k}$ for the plateau-entry (36) over all three potential approaches.

Group 1						
	tangential source			radial source		
solver	AMG-CG	IC(0)-CG	Jacobi-CG	AMG-CG	IC(0)-CG	Jacobi-CG
tet503K	5	6	7	6	5	6
tet125K	5	5	6	5	5	6
tete33K	4	5	6	3	3	5

Group 2						
	tangential source			radial source		
solver	AMG-CG	IC(0)-CG	Jacobi-CG	AMG-CG	IC(0)-CG	Jacobi-CG
tet508K	6	6	7	6	7	8
tet128K	4	5	6	4	4	6
tete32K	3	5	6	3	4	5

The PCG accuracy measures the error in the solution vector of the FE linear equation system (8) (correction potential), (11) and (17) (total potential). For the full subtraction approach, maxRE(%) was thus not equal to 100 for ACCURACY $= 10^0$ because $\underline{\phi}_{\mathtt{num}}$ is equal to the analytically computed singularity potential $\underline{\Phi}_0$ from Equation (5). Because

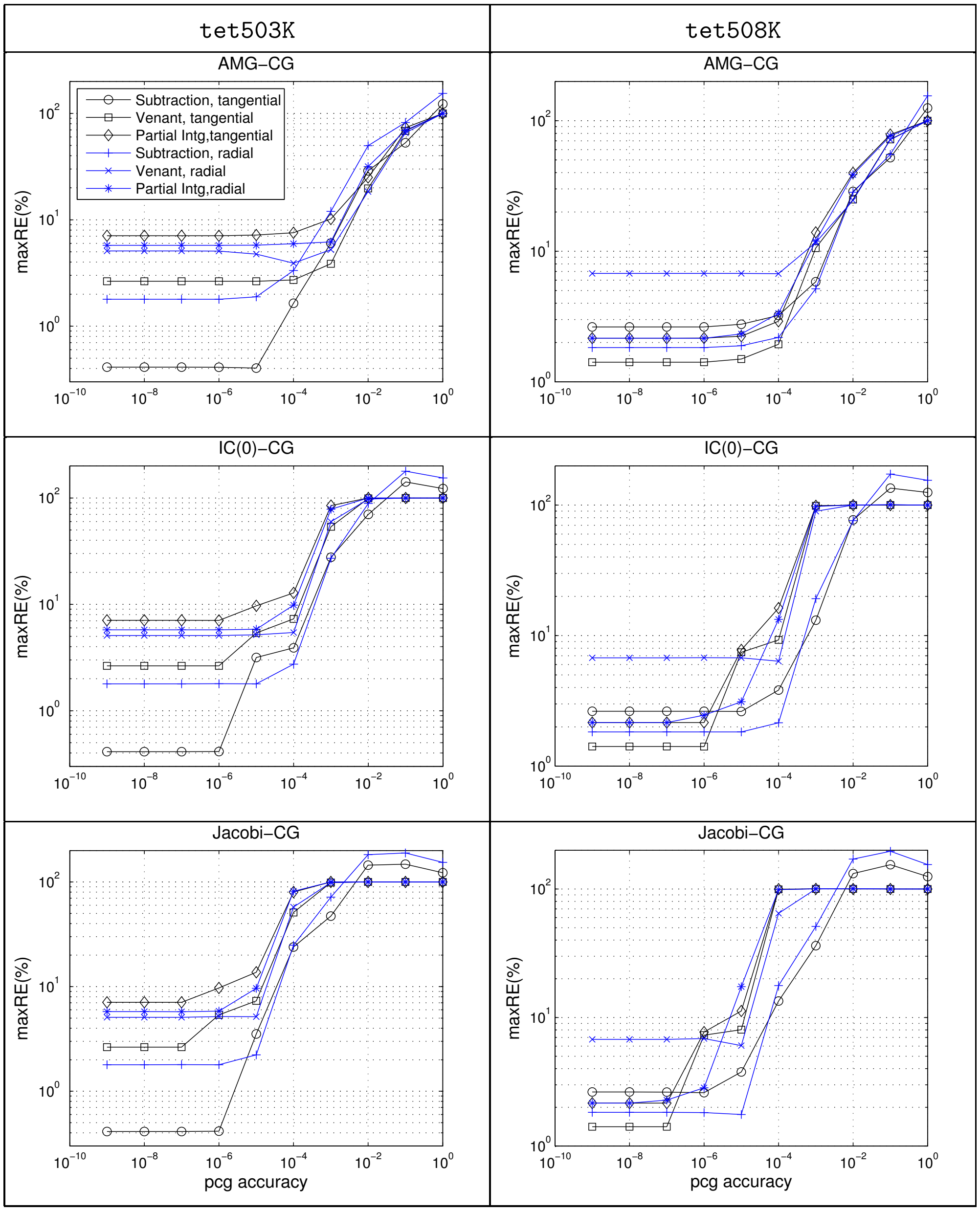

Fig. 3. maxRE(%) versus PCG solver ACCURACY (see Algorithm 1 and Section 3.5) for models `tet503K` of group 1 (left column) and `tet508K` of group 2 (right column) for the AMG-CG (top row), the IC(0)-CG (middle row) and the Jacobi-CG (bottom row). Source orientations and potential approaches can be distinguished by their specific labels. The plot is in log-log scale.

the PCG accuracy is measured in the $K_h C_h^{-1} K_h$-energy norm, the plateau-entry (36) differs for different preconditioners C_h. As shown in Figure 3 for the high-resolution models and as collected in Table 4 for all six tetrahedra models, the maximally needed k

(for a PCG accuracy of ACCURACY $= 10^{-k}$) decreased when the preconditioning quality increased (except for the radial source orientation in model `tet503K`, see Fig. 3). Furthermore, as Table 4 shows, a higher PCG accuracy was needed for the plateau-entry when the mesh resolution increased.

4.3. *Numerical error versus solver time*

In a last study, we compared solver wall-clock time versus numerical accuracy for the three different CG preconditioners AMG, IC(0) and Jacobi. The time for the setup of the preconditioner was not included, because this step was carried out only once per head model.

In Figure 4, the solver time is shown versus the maxRE(%) for different levels of PCG accuracy for models `tet503K` and `tet33K` of group 1. The largest examined PCG ACCURACY level 10^{-k} is indicated in the figure. Please note that this level does not necessarily correspond to the plateau-entry level. In most cases results are presented up to one level higher.

Table 5
Average solver time (sec.) and iteration count (iter) over all source eccentricities, source orientations and potential approaches for plateau-entry (36). For all tetrahedra models of groups 1 and 2, results are presented for the three different CG preconditioners AMG, IC(0) and Jacobi. The gain factor indicates the performance gain of the AMG-CG relative to the Jakobi-CG.

	group 1						group 2					
	`tet503K`		`tet125K`		`tet33K`		`tet508K`		`tet128K`		`tet32K`	
solver	time	iter	time	iter	time	iter	time	iter	time	iter	time	iter
AMG-CG	12.25	11.20	1.87	9.04	0.18	5.89	9.18	10.40	1.36	7.27	0.15	5.81
IC(0)-CG	112.03	233.43	8.40	128.39	0.45	72.63	72.41	215.05	5.20	98.96	0.31	52.84
Jacobi-CG	167.82	679.43	16.98	414.00	0.76	229.52	99.60	578.04	9.62	331.15	0.47	161.68
gain factor	13.70	60.66	9.08	45.8	4.22	38.97	10.85	55.58	7.07	45.55	3.13	27.83

For all tetrahedra models of groups 1 and 2, average solver times and iteration counts over all source eccentricities, source orientations and potential approaches for a plateau-entry (36) are collected in Table 5. Both Figure 4 and Table 5 clearly show the superiority of the AMG preconditioner. In all cases, even for the low-resolution grids `tet33K` and `tet32K`, the AMG-CG was the fastest solver, followed by the IC(0)-CG and the Jacobi-CG. The main result of Table 5 is the so-called *gain factor*, which is defined here as the result (solver time or iteration count) for the Jacobi-CG divided by the result for the AMG-CG. The gain factors clearly showed that the higher the mesh-resolution, i.e., the higher the condition number of the corresponding FE stiffness matrix, the larger the difference in performance between AMG-CG, IC(0)-CG, and Jacobi-CG. An increasing mesh-resolution led to a strong increase in the number of iterations of IC(0)-CG (factor of 3.2 between `tet503K` and `tet33K` and 4.1 between `tet508K` and `tet32K`) and Jacobi-CG (factor of 3.0 between `tet503K` and `tet33K` and 3.6 between `tet508K` and `tet32K`), while the number of AMG-CG iterations was only slightly increasing (factor of 1.9 between `tet503K` and `tet33K` and 1.8 between `tet508K` and `tet32K`). This clearly shows the stronger h-dependence of the IC(0) and Jacobi preconditioners.

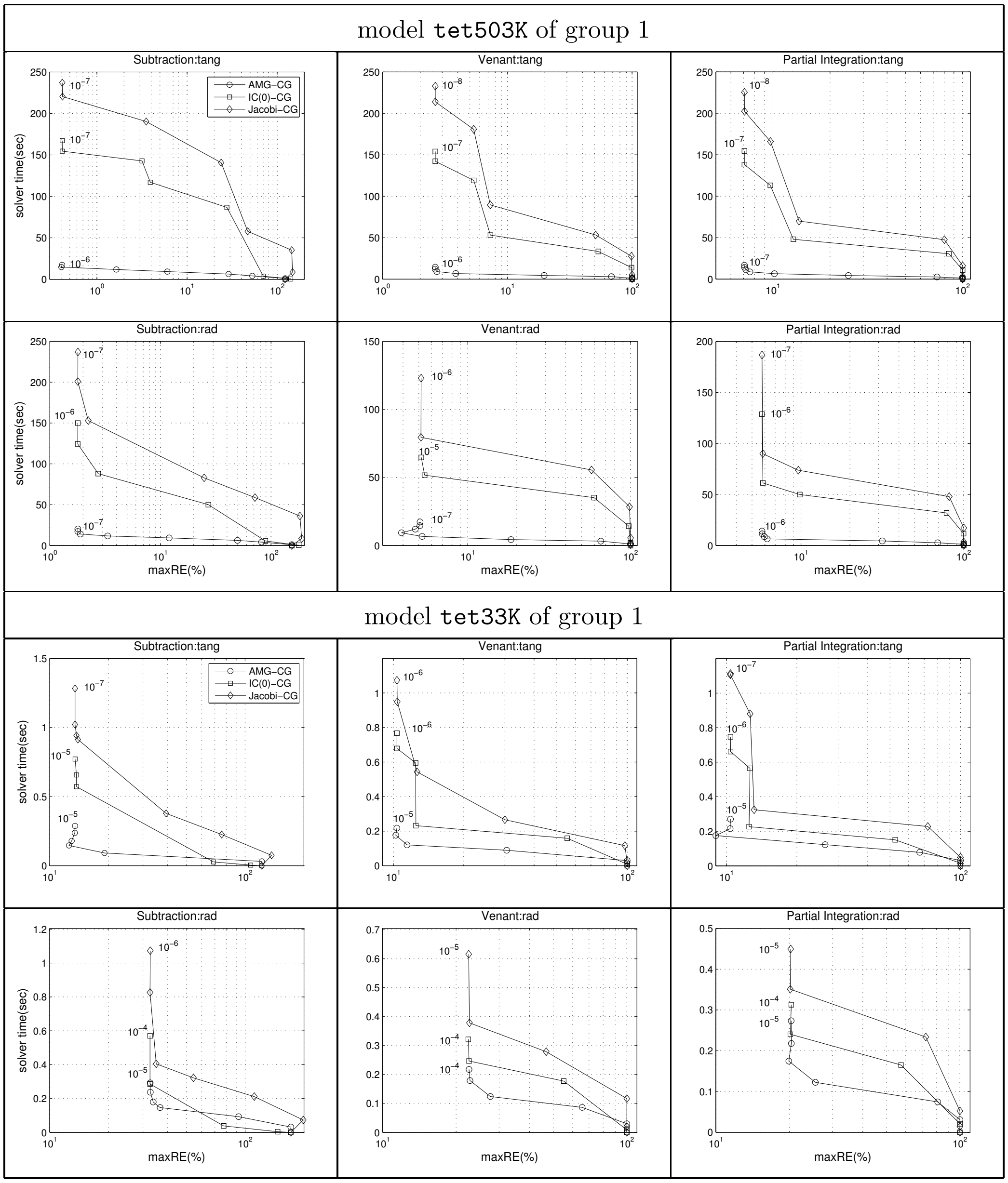

Fig. 4. Solver time versus maxRE(%) for models `tet503K` and `tet33K` of group 1 for tangentially and radially oriented sources for the potential approaches full subtraction (left), Venant (middle), and partial integration (right). Results are presented for the three different CG preconditioners AMG, IC(0) and Jacobi. Each marker represents a PCG ACCURACY $= 10^{-k}$ level and the largest examined level is indicated. The x-axis is in log scale.

5. Discussion

The goals of this technical study of finite element (FE) based solution techniques for the electroencephalographic forward problem were twofold. The first aim was to compare three efficient iterative FE solver techniques under realistic conditions that still allowed quasi-analytical solutions. The second aim was to evaluate three different numerical formulations of the current dipole, which is the bioelectric source most commonly used to represent neural electrical activity. A major motivation of such studies is the special need to achieve high accuracy and efficiency with FE based approaches for this problem. The many advantages of this approach are often hindered by the unacceptable computation costs of implementing it so that improved efficiency will provide substantial progress to the field.

When using the $K_h C_h^{-1} K_h$-energy norm stopping criterion for the PCG algorithm applied on meshes with up to 500K nodes, a relative solver accuracy of 10^{-6} for AMG-CG, 10^{-7} for IC(0)-CG and 10^{-8} for Jacobi-CG was necessary and sufficient to fall below the discretization error. The AMG-CG achieved an order of magnitude higher computational speed than the CG with the standard preconditioners with an increasing gain factor with decreasing mesh size. However, the AMG-CG was not optimal in our application with a slight h-dependence shown by a slightly increasing iteration count with increasing mesh resolution. Such a result had to be expected because the source analysis stiffness matrix was not an M-matrix and the prolongation operator of the presented AMG-CG was tuned for speed and not for an optimal behavior with regard to the iteration count. A discrete harmonic extension as proposed in [23] improved the interpolation properties, but the application of this prolongation operator is more expensive, which decreased the overall run-time performance in our application.

We generated two groups of Constrained Delaunay tetrahedralization (CDT) FE meshes, tuned for the specific needs of the different potential approaches. In group 1, for the full subtraction approach [7], FE nodes were concentrated in the CSF, skull and skin, while the brain compartment was meshed as coarsely as possible. Group 2 was tuned for the needs of both direct potential approaches [40,4,1,36], which profit more from a regular distribution of FE nodes over all four compartments and especially a higher resolution at the source positions.

With regard to the numerical error, in the tuned FE meshes with about 500K nodes we achieved high accuracies—in the range of a few percent maximal relative error (maxRE)—over all source eccentricities for both the full subtraction and the two direct potential approaches. With a maximal relative difference measure (maxRDM) and a maximal magnification factor (maxMAG) of less than 1% over all source eccentricities for sources up to 1 mm below the CSF compartment (model `tet503K`, maximal examined eccentricity of 98.7%), the full subtraction approach performed consistently better than both direct approaches. Our results clearly illustrate the advantages of the full subtraction approach as long as the homogeneity condition is fulfilled, i.e., as long as the distance of the source to the next conductivity inhomogeneity is large enough or the resolution of the FE mesh at the nearest conductivity inhomogeneity to the source is fine enough. A theoretical reasoning for this finding is given in [38]. While error curves oscillated for both direct approaches, they were smooth for the full subtraction approach.

Schimpf et al. [26] investigated different FE potential approaches in a four-layer sphere model with isotropic skull and sources up to 1 mm below the CSF compartment. In their report, a regular 1 mm cube model was used (thus a much higher FE resolution) and a maxRDM of 7% and a maxMAG of 25% was achieved with a subtraction approach, which performed best in their comparison. Awada et al. [1] implemented a two-dimensional subtraction approach and compared its numerical accuracy with a partial integration method in a two-dimensional multi-layer sphere model. A direct comparison with our results is therefore difficult, but the authors concluded that the subtraction method was more accurate than the direct approach. In a locally refined (around the source singularity) tetrahedral mesh with 12,500 nodes of a four-layer sphere model with anisotropic skull and first order FE basis functions in a subtraction approach, Bertrand et al. [3] reported a maxRDM of above 20% and a maxMAG up to 70% for a maximal eccentricity of 97.6%. Van den Broek [33] used a subtraction approach in a locally refined (around the source singularity) tetrahedral mesh with 3,073 nodes of a three-layer sphere model with anisotropic skull. For the maximal examined eccentricity of 94.2%, they reported a maxRDM of up to 50%.

However, the right-hand side (RHS) vector is expensive to compute and is densely populated (i.e., N_h non-zeros) for the full subtraction approach (10) and sparse with just some few ($|\textsc{NodesOfEle}|$ for partial integration (12), and C for Venant (18)) non-zero vector entries for the direct approaches, which has implications for the computational effort when using the fast FE transfer matrix approach for EEG and MEG [39] (additionally, see [36,8,11]), which limits the total number of FE linear equation systems to be solved for any inverse method to the number of sensors m. After solving m FE linear equation systems to compute the transfer matrix, each forward problem can be solved by a single multiplication of the RHS vector with the transfer matrix [39], resulting in a computational effort of $2 * \mathrm{m} * P$ operations with $P = N_h$ for the full subtraction, $P = |\textsc{NodesOfEle}|$ for partial integration and $P = C$ for the Venant approach. Note that the transfer matrix approach can not be used if the mesh is adapted according to varying source positions within the inverse problem. We therefore attempted to avoid local mesh refinement techniques as used in [3,33].

6. Conclusion

The AMG-CG turned out to achieve an order of magnitude higher computational speed than Jacobi-CG or incomplete Cholesky-CG for the FEM based EEG forward and inverse problem. Our results corroborate the theoretical results that the higher the FE resolution, the greater the advantage of using MG preconditioning. The AMG-CG together with the fast transfer matrix approach now enable resolutions which seemed to be impracticable before. In the comparison of dipole modeling approaches, highest accuracies were achieved with the full subtraction approach in CDT meshes where nodes were concentrated in the compartments CSF, skull and skin.

Acknowledgment

This research was supported by the German Research Foundation (DFG), project Wo1445/1-1 and by the Center for Integrative Biomedical Computing, NIH NCRR Project 2-P41-RR12553-07.

References

[1] K. Awada, D. Jackson, J. Williams, D. Wilton, S. Baumann, A. Papanicolaou, Computational aspects of finite element modeling in EEG source localization, IEEE Trans Biomed. Eng. 44 (8)

(1997) 736–751.

[2] S. Baillet, J. Mosher, R. Leahy, Electromagnetic brain mapping, IEEE Signal Processing Magazine 18 (6) (November 2001) 14–30.

[3] O. Bertrand, M. Thévenet, F. Perrin, 3D finite element method in brain electrical activity studies, in: J. Nenonen, H. Rajala, T. Katila (eds.), Biomagnetic Localization and 3D Modelling, Report of the Dep. of Tech.Physics, Helsinki University of Technology, 1991.

[4] H. Buchner, G. Knoll, M. Fuchs, A. Rienäcker, R. Beckmann, M. Wagner, J. Silny, J. Pesch, Inverse localization of electric dipole current sources in finite element models of the human head, Electroenc. Clin. Neurophysiol. 102 (1997) 267–278.

[5] J. de Munck, M. Peters, A fast method to compute the potential in the multi sphere model, IEEE Trans Biomed. Eng. 40 (11) (1993) 1166–1174.

[6] J. de Munck, B. van Dijk, H. Spekreijse, Mathematical dipoles are adequate to describe realistic generators of human brain activity, IEEE Trans Biomed. Eng. 35 (11) (1988) 960–966.

[7] F. Drechsler, C. Wolters, T. Dierkes, H. Si, L. Grasedyck, A highly accurate full subtraction approach for dipole modelling in EEG source analysis using the finite element method., J. Applied Numerical MathematicsIn review.

[8] N. Gencer, C. Acar, Sensitivity of EEG and MEG measurements to tissue conductivity., Phys.Med.Biol. 49 (2004) 701–717.

[9] G. Haase, M. Kuhn, S. Reitzinger, Parallel AMG on distributed memory computers, SIAM J. Sci.Comp. 24 (2) (2002) 410–427.

[10] W. Hackbusch, Iterative solution of large sparse systems of equations, Springer Verlag, Applied Mathematical Sciences 95, 1994.

[11] H. Hallez, B. Vanrumste, P. V. Hese, Y. D'Asseler, I. Lemahieu, R. V. de Walle, A finite difference method with reciprocity used to incorporate anisotropy in electroencephalogram dipole source localization., Phys.Med.Biol. 50 (2005) 3787–3806.

[12] M. Jung, U. Langer, Applications of multilevel methods to practical problems, Surv.Math.Ind. 1 (1991) 217–257.

[13] F. Kickinger, Algebraic multigrid for discrete elliptic second-order problems, in: W. Hackbusch (ed.), Multigrid Methods V. Proceedings of the 5th European Multigrid conference, Berlin: Springer Lecture Notes Comput. Sci. Eng. 3, 1998.

[14] A. Louis, Inverse und schlecht gestellte Probleme, Teubner-Verlag, 1989.

[15] G. Marin, C. Guerin, S. Baillet, L. Garnero, G. Meunier, Influence of skull anisotropy for the forward and inverse problem in EEG: simulation studies using the FEM on realistic head models, Human Brain Mapping 6 (1998) 250–269.

[16] J. Meijs, O. Weier, M. Peters, A. van Oosterom, On the numerical accuracy of the boundary element method, IEEE Trans Biomed. Eng. 36 (1989) 1038–1049.

[17] M. Mohr, Simulation of Bioelectric Fields: The Forward and Inverse Problem of Electroencephalographic Source Analysis, vol. Band 37 of Arbeitsberichte des Instituts für Informatik, Friedrich-Alexander-Universität Erlangen-Nürnberg, 2004, iSSN 1611-4205.

[18] S. Murakami, Y. Okada, Contributions of principal neocortical neurons to magnetoencephalography and electroencephalography signals, J.Physiol. 575 (3) (2006) 925–936.

[19] W. Nolting, Grundkurs: Theoretische Physik, Elektrodynamik, Zimmermann-Neufang, Ulmen, 1992.

[20] J. Ollikainen, M. Vauhkonen, P. Karjalainen, J. Kaipio, Effects of local skull inhomogeneities on EEG source estimation, Med.Eng.Phys. 21 (1999) 143–154.

[21] R. Plonsey, D. Heppner, Considerations on quasi-stationarity in electro-physiological systems, Bull.Math.Biophys. 29 (1967) 657–664.

[22] S. Reitzinger, Algebraic multigrid methods for large scale finite element equations, Ph.D. thesis, Schriften der Johannes-Kepler-Universität Linz, Reihe C - Technik und Naturwissenschaften, No.36 (2001).

[23] J. Ruge, K. Stüben, Algebraic multigrid (AMG), in: S. McCormick (ed.), Multigrid Methods, vol. 5 of Frontiers in Applied Mathematics, SIAM, Philadelphia, 1986, pp. 73–130.

[24] Y. Saad, Iterative methods for sparse linear systems, PWS Publishing Company, 1996.

[25] J. Sarvas, Basic mathematical and electromagnetic concepts of the biomagnetic inverse problem, Phys.Med.Biol. 32 (1) (1987) 11–22.

[26] P. Schimpf, C. Ramon, J. Haueisen, Dipole models for the EEG and MEG, IEEE Trans Biomed. Eng. 49 (5) (2002) 409–418.

[27] H. Schwarz, Methode der finiten Elemente, B.G.Teubner Stuttgart, 1991.

[28] H. Si, TetGen, a quality tetrahedral mesh generator and three-dimensional delaunay triangulator, v1.3, user's manual, Tech. Rep. 9, Weierstrass Institute for Applied Analysis and Stochastics (2004).

[29] H. Si, K. Gärtner, Meshing piecewise linear complexes by constrained Delaunay tetrahedralizations, in: Proc. 14th International Meshing Roundtable, Sandia National Laboratories, 2005.

[30] SimBio: A Generic Environment for Bio-Numerical Simulation, IST-Program of the European Commission, Project No.10378, http://www.simbio.de. (2000-2003).

[31] K. Stüben, A review of algebraic multigrid, Techn. Report 69, GMD, http://www.gmd.de (Nov. 1999).

[32] O. Tanzer, S. Järvenpää, J. Nenonen, E.Somersalo, Representation of bioelectric current sources using whitney elements in finite element method, Phys.Med.Biol. 50 (2005) 3023–3039.

[33] S. van den Broek, Volume conduction effects in EEG and MEG, Ph.D. thesis, Proefschrift Universiteit Twente Enschede, The Netherlands (1997).

[34] T. Waberski, H. Buchner, K. Lehnertz, A. Hufnagel, M. Fuchs, R. Beckmann, A. Rienäcker, The properties of source localization of epileptiform activity using advanced headmodelling and source reconstruction, Brain Top. 10 (4) (1998) 283–290.

[35] D. Weinstein, L. Zhukov, C. Johnson, Lead-field bases for EEG source imaging, Annals of Biomed. Eng. 28 (9) (2000) 1059–66.

[36] D. Weinstein, L. Zhukov, C. Johnson, Lead-field bases for electroencephalography source imaging, Annals of Biomed.Eng. 28 (9) (2000) 1059–1066.

[37] C. Wolters, Influence of Tissue Conductivity Inhomogeneity and Anisotropy on EEG/MEG based Source Localization in the Human Brain, No. 39 in MPI Series in Cognitive Neuroscience, MPI of Cognitive Neuroscience Leipzig, 2003, iSBN 3-936816-11-5 (also: Leipzig, Univ., Diss., http://lips.informatik.uni-leipzig.de/pub/2003-33/en).

[38] C. Wolters, H. Köstler, C. Möller, J. Härtlein, L. Grasedyck, W. Hackbusch, Numerical mathematics of the subtraction method for the modeling of a current dipole in EEG source reconstruction using finite element head models., SIAM J. on Scientific Computing 30 (1) (2007) 24–45.

[39] C. H. Wolters, L. Grasedyck, W. Hackbusch, Efficient computation of lead field bases and influence matrix for the FEM-based EEG and MEG inverse problem, Inverse Problems 20 (4) (2004) 1099–1116.

[40] Y. Yan, P. Nunez, R. Hart, Finite-element model of the human head: Scalp potentials due to dipole sources, Med.Biol.Eng.Comput. 29 (1991) 475–481.

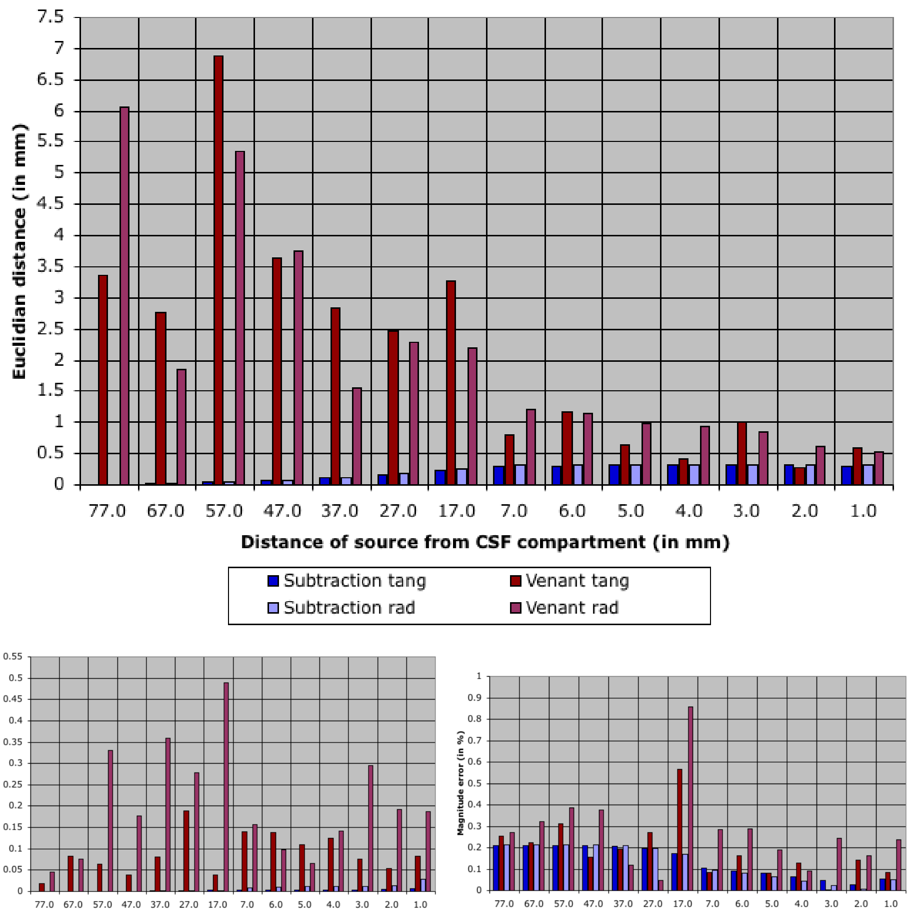

Figure 2.1: Dipole fit errors of the FE full subtraction and Venant approaches in model tet360K from Fig.1 in Chapter 2.8 when using the quasi-analytical solutions in the four-layer sphere model with anisotropic skull as reference EEG data at 748 regularly distributed electrodes.

2.9.2 EEG single dipole fit reconstruction error of the full subtraction and the Venant potential approaches

Goal of this study

The results of this section were not yet published elsewhere. The section is dedicated to the examination of the EEG inverse single dipole fit reconstruction errors resulting from the presented forward modeling errors (RE, RDM and MAG) for the full subtraction and the Venant FE approach in specifically-tuned CDT FE meshes. The single dipole fit error is an additional measure, which might be more concrete and descriptive with regard to the medically interesting accuracy of the inverse problem.

EEG single dipole fit reconstruction errors

In Chapter 2.8, the forward modeling errors RE, RDM and MAG were studied for the full subtraction approach in the CDT FE model `tet360K`. This model was specifically tuned for the needs of the full subtraction approach, i.e., the nodes were concentrated in skin, skull and CSF compartment while the brain layer was meshed as coarse as possible under the constraint of retaining mesh quality.

The single dipole fit reconstruction errors for this model are presented in Figure 2.1. For each dipole with a specific distance from the inner sphere surface as indicated on the x-axes, a quasi-analytical solution (Section 6.1, Chapter 2.8) was computed at the 748 EEG electrode locations (Section 6.4, Chapter 2.8) in the anisotropic four-layer sphere model (Table 2, Chapter 2.8). This reference potential distribution was used as the input data to an inverse single dipole fit approach based on the FE model using a Nelder-Mead simplex optimization. For all dipole eccentricities, the seed-point was positioned to the midpoint of the sphere model. The simplex was parameterized so that the error of the optimization process was minimized at the expense of a more computationally intensive run-time.

With a maximal inverse source localization error of 0.3mm, orientation errors below 0.03 degree and magnitude errors below 0.21% for a source positioned just 1mm below the CSF compartment, the full subtraction approach performed much better than the Venant approach (max. errors: 7mm, 0.5 degree, 1%). The Venant approach suffered from the coarse elements in the depth of the volume conductor, where the largest errors occurred.

Figure 2.2 shows the same examination in a CDT FE model with 161K regularly distributed nodes and 988K elements. With a maximal inverse source reconstruction error of 1.7mm (localization), 0.32 degree (orientation) and 0.5% (magnitude [1]), the Venant approach slightly outperforms the full subtraction approach (max. errors: 2.4mm, 0.25 degree, 0.6%), if localization is considered to be more important than orientation and strength.

It can be summarized that in properly chosen meshes and with high mesh resolution, the numerical errors of both full subtraction and Venant FE approach can be expected to be less important than errors resulting from, e.g., data noise or inaccurate conductivity values. The Venant method needs an especially high mesh resolution in the source area to avoid that monopoles are placed in other tissue compartments, while other compartments can be meshes with a lower resolution.

[1] except the large error of about 7% where Venant monopole sources are placed in the CSF compartment for the most eccentric source, which especially affects the error for the radially oriented dipole

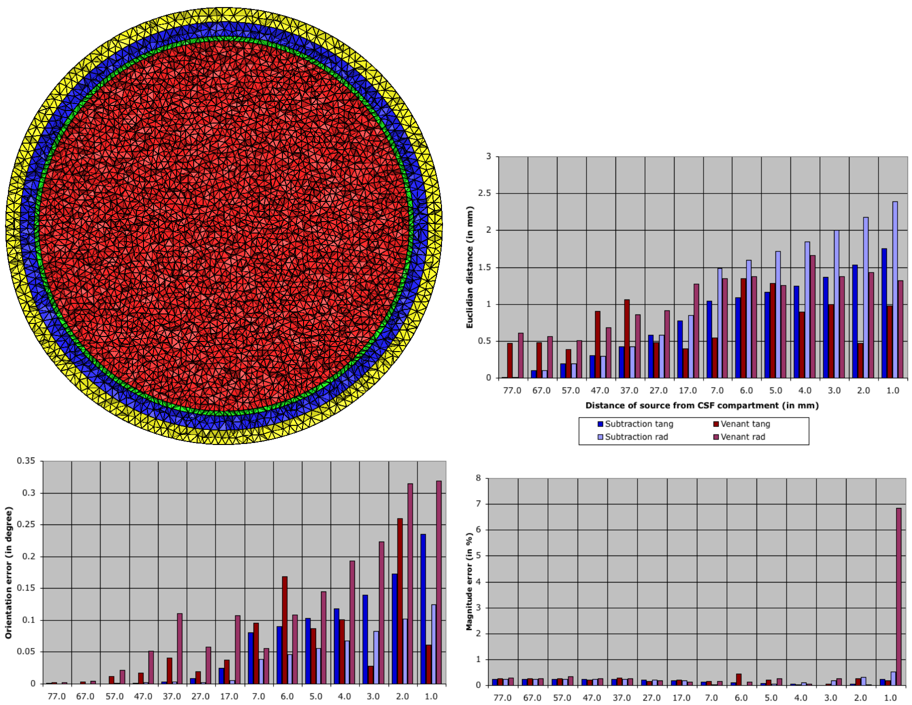

Figure 2.2: CDT FE mesh of the anisotropic four-layer sphere model when using a regular distribution of 161K nodes over all four compartments (top,left). Dipole fit localization (top, right), orientation (bottom, left) and magnitude (bottom, right) errors of the FE full subtraction and Venant approaches when using the quasi-analytical solutions as EEG data at 748 regularly distributed electrodes.

For the subtraction approach, it was found that all layers except the source compartment have to be meshed with a sufficiently high mesh resolution to obtain acceptable numerical errors.

2.9.3 Treatment of error curve oscillations of the direct FE approaches

The forward modeling error curves of the direct FE approaches were shown to oscillate on a low error level. This does not have to be a disadvantage because, as shown in Figure 2.3 for tetrahedral meshes, the minimum error is achieved for sources on FE nodes, so that a lead field interpolation technique (Yvert et al. [2001]) can be used to avoid oscillations and further decrease the numerical error. First promising results for a second-order Bézier interpolation (Bernstein polynomials) of precomputed Venant FE lead field have already been achieved.

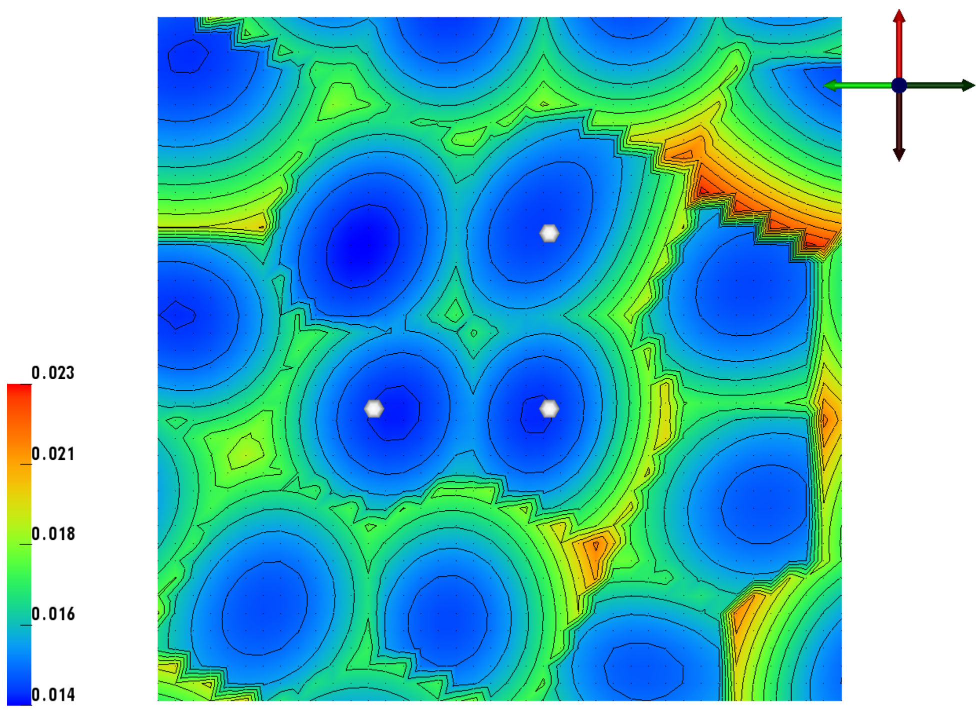

Figure 2.3: Result from the diploma thesis of Lanfer [2007]: RDM between the FEM EEG solutions and the analytical solution for dipoles on a plane grid. The gray spheres indicate the positions of the nodes of one tetrahedron of the FE mesh. For dipoles at the nodes, the RDM is at a minimum. Visualization was carried out using BioPSE [2002].

2.10 Comparison of FE and BE modeling in EEG source analysis with regard to accuracy and computational speed

Comparison of finite element and boundary element modeling in EEG source analysis with regard to accuracy and computational speed
Lanfer, B., Wolters, C.H., Anwander, A., Dümpelmann, M., and Knösche, T.R.. submitted to *Phys.Med.Biol.*, (2007).

Corresponding author: B. Lanfer (Physics diploma thesis student of C.H. Wolters and S. Demokritov, Institute for Applied Physics, University of Münster).

Comparison of finite element and boundary element modeling in EEG source analysis with regard to accuracy and computational speed

B. Lanfer[1], C.H. Wolters[1], A. Anwander[2], M. Dümpelmann[3], F. Zanow[3] and T.R. Knösche[2]

[1]Institut für Biomagnetismus und Biosignalanalyse
Westfälische Wilhelms-Universität Münster
Malmedyweg 15
48149 Münster
Germany.
http://biomag.uni-muenster.de
[2]Max Planck Institute for Human Cognitive and Brain Science
Stephanstr.1a
04103 Leipzig
Germany
http://www.cbs.mpg.de
[3]ANT B.V. (Advanced Neuro Technology)
Colosseum 22
7521 PT Enschede
The Netherlands
http://www.ant-neuro.com

E-mail: `benjamin.lanfer@uni-muenster.de`, `carsten.wolters@uni-muenster.de`, `anwander@cbs.mpg.de`, `mduempelmann@yahoo.com`, `fzanow@ant-neuro.com`, `knoesche@cbs.mpg.de`

Submitted to Physics in Medicine and Biology on December 28, 2007

Abstract. The inverse problem in electroencephalography (EEG) aims at reconstructing the underlying current distribution in the human brain from potential differences that are measured non-invasively at the head surface. The simulation of the EEG for a given dipolar source in the brain using a volume-conduction model of the head is called the forward problem. Recent studies have shown that, for the forward problem, realistic volume conductor modeling using the boundary element method (BEM) or the finite element method (FEM) is essential for an accurate EEG source analysis. While the BEM is restricted to isotropic tissue conductivities, the FEM is able to realistically model tissue conductivity inhomogeneities and anisotropies. So far, the computational complexity of the FEM was considered to be too great for practical application when using the necessary high resolution FE models.

This paper shows that, when combined with the concept of EEG transfer matrices, a Venant FE direct potential approach can outperform a collocation BE forward approach using the isolated skull approach and analytically integrated linear basis elements with regard to both accuracy and computational speed. We compare both forward approaches in an isotropic three-layer sphere model using relative difference measure (RDM) and magnification factor (MAG) for a comparison of the numerical results with quasi-analytical series expansion formulas. For a 2 mm geometry-adapted hexahedra FE model, the maximal RDM (MAG) of the FEM approach of 1% (5%) is about two (four) times lower than the maximal RDM (MAG) of the BEM approach and, with 0.7ms, the FE forward computation is more than four times faster than the BE forward computation. It is then shown that, in a high-resolution constrained Delaunay tetrahedralization FE model of an anisotropic four layer sphere volume conductor, with only 2.4ms computation time per FE forward computation, a maximal RDM of about 1% and a maximal MAG below 5% is achieved for source eccentricities up to 97.4%.

Keywords

EEG source analysis, realistic head model, finite element method, boundary element method, dipole model, transfer matrix, validation in multi-layer sphere model, conductivity anisotropy, computational speed.

1. Introduction

Electroencephalography (EEG) source reconstruction seeks to determine the active brain areas from the measured electric potentials at the head surface. These potentials are generated by movements of ions mainly within the apical dendrites of pyramidal cells in the cortex sheet of the human brain [27], the primary currents. The primary currents are commonly modeled by a mathematical point current dipole [30].

EEG source analysis is strongly affected by the accuracy in modeling the volume conductor properties of the human head with regard to both geometry and conductivity of the various head tissues [3, 13, 29, 38]. While tissue geometry can most often be segmented from magnetic resonance (MRI) or computed tomography (CT) images, the determination of the conductivity properties of the head tissues is more difficult. First attempts to measure the conductivities of biological tissues were made in vitro, often using samples taken from animals [29]. The conductivity of human cerebrospinal fluid was measured in [5] and that of the human skull in [1]. The skull consists of a soft bone layer (spongiosa) enclosed by two hard bone layers (compacta). Since the spongiosa has a much higher measured conductivity than the compacta [1], the skull is quite often described by an anisotropic conductivity [6, 8, 38]. Recently, methods were proposed to determine in vivo conductivities of head tissues by using an electrical impedance tomography based approach [14] or by estimating them from measured EEG [22] or EEG together with simultaneous intracranial data [20]. With regard to the intracranial tissues such as brain grey and white matter, an indirect determination of the anisotropic conductivity through diffusion tensor MRI (DT-MRI) was examined in [34].

Different approaches have been proposed for the EEG forward problem. A quasi-analytical solution in a volume conductor model consisting of an arbitrary number of concentric anisotropic layers of different conductivities was presented in [26]. Besides the fact that such models are still frequently used in source analysis routine, they also serve as validation tools for more realistic numeric modeling. In order to better take into account the realistic shape of the scalp and skull surfaces, boundary element (BE) head models have been developed, being adequate for piecewise homogeneous isotropic compartments [4]. Numerical accuracy of the BE approach could be improved, e.g., through the isolated skull approach (ISA) [23, 18, 44] and the use of linear basis functions with analytically integrated elements (vertex approach) [25, 44], in the following called the *ISA vertex collocation BE approach*. 3D discretization methods such as the finite difference (FD) method [17] and the finite element (FE) method [6, 9, 8, 31, 13, 29, 38] are able to treat inhomogeneous and anisotropic material parameters. While the FD method is restricted to regular grids, the FE method is generally considered to be more flexible with regard to an accurate modeling of the geometry as will be shown in this article using geometry-adapted hexahedra [40] and constrained Delaunay tetrahedralization (CDT) [11] FE meshes. A key component in FE-based source analysis is the modeling of the potential singularity introduced into the equation by the point current dipole. Different FE approaches for modeling the potential singularity are known from the literature: a subtraction approach [6, 8, 2, 39, 11], a Partial Integration direct method [2], and a Venant direct method [9]. Both the Partial Integration and the Venant direct FE methods approximate the dipole through monopolar sources and sinks on neighboring FE nodes with the constraint to optimally match the given dipole moment vector. In this study we used the Venant approach based on comparison of the accuracy of the above approaches in multilayer sphere models, which suggested that for sufficiently regular meshes, the direct methods yield suitable accuracy over all realistic source locations [41]. The direct approaches have the additional advantage of high computational efficiency when used in combination with the FE transfer matrix approach, which limits the total number of FE linear equation systems to be solved for any inverse method to the number of sensors [37].

Sensitivity studies have been carried out in realistic FE models examining the influence of skull anisotropy [8, 38] and realistic white matter anisotropy [38, 15] on EEG source analysis, supporting the hypothesis that modeling skull and white matter anisotropy is crucial for accurate EEG source reconstruction. It is furthermore widely accepted that local conductivity changes in the vicinity of the primary source as caused by brain lesions [8], or skull-holes from trepanation [8] have a non-negligible effect on EEG source analysis.

In the past, the heavy computational load of the FE method was seen as a drawback, especially when many evaluations of the forward problem are needed, e.g., in source localization schemes [28]. It was speculated that BEM models are less computationally intensive compared to FEM models, while providing improved computational accuracy relative to simple analytical models [28]. Additionally, the difficult construction of the volume discretization was seen to be a major disadvantage of the FEM compared to the BEM which only requires the use of surface triangulation meshes [19]. Due to the excessive computational burden created by previous FEM techniques, evaluation studies often only used sub-optimal numbers of nodes [6, 9, 8, 43]. For example, in [43], a tetrahedra Venant FE model with only 10,731 nodes was used and it was mentioned in the discussion that, for a general clinical use of FE source analysis, a finer FE discretization and parallel computing is needed. In [9], the setup of a lead field matrix with 8,742 unknown dipole components in a tetrahedra Venant FE approach with 18,322 nodes took roughly a week of computation time.

In this paper, a direct comparison between the ISA vertex collocation BE approach and the Venant FE approach will be carried out in an isotropic three layer sphere volume conductor model. The computational costs of FE mesh generation will be examined for geometry-adapted hexahedra and constrained Delaunay tetrahedralization (CDT) FE meshes. A fast transfer matrix approach will be derived and its efficiency will be shown for both BE and FE forward modeling. Finally, the accuracy and computational complexity of the Venant FE approach will be examined in an anisotropic four compartment sphere model taking the conductivity of the cerebrospinal fluid (CSF) and the skull conductivity anisotropy into account. Our study will show that the Venant FE approach is highly accurate and very flexible with regard to the modeling of realistic tissue conductivity properties and that it outperforms the ISA vertex collocation BE approach in the isotropic three layer sphere model with regard to both accuracy and computational complexity.

2. Theory

2.1. The basic differential and boundary integral equations

The mathematical dipole is commonly used to model the primary current density distribution (impressed current) [30, 27],

$$\mathbf{j}_p(\mathbf{x}) = \mathbf{M}_p \delta(\mathbf{x} - \mathbf{x}_p), \tag{1}$$

with $\mathbf{x}_p \in \mathbb{R}^3$ and $\mathbf{M}_p \in \mathbb{R}^3$ denoting the position and the moment of the point dipole, respectively.

When expressing the electric field as the negative gradient of the scalar potential the condition of the continuity of charge can be written as

$$\nabla \cdot (\sigma \nabla \Phi) = \nabla \cdot \mathbf{j}_p = J_p \text{ in } \Omega, \quad \langle \sigma \nabla \Phi, \mathbf{n} \rangle = 0 \text{ on } \Gamma_1 \tag{2}$$

with $\Gamma_1 = \partial\Omega$ being the surface of the head domain Ω. This is the quasi-static approximation of Maxwell's equations describing the generation of the electric potential Φ in the volume conductor with conductivity distribution σ due to the current source density distribution J_p. Between regions of different conductivity, the potential Φ and the current density $\langle \sigma \nabla \Phi, \mathbf{n} \rangle$ are continuous over the boundaries. To unambiguously determine the electric potential, finally, the potential at a reference electrode has to be fixed: $\Phi(\mathbf{x}_{\text{ref}}) = 0$.

With regard to the boundary element approach, it is assumed that Ω consists of three nested regions: skin with Γ_1 the outer and Γ_2 the inner surface, skull with Γ_2 the outer and Γ_3 the inner surface and brain with the surface Γ_3. It is furthermore assumed that the surfaces are non-intersecting and that the conductivities are constant and isotropic within each compartment ($\sigma_i^+, \sigma_i^- \in \mathbb{R}$ denote the conductivities outside and inside the surface Γ_i, respectively). The sources $\mathbf{j}_p$ are furthermore restricted to be within the brain compartment. If we define the *singularity function*

$$s(\mathbf{x}, \mathbf{y}) = \frac{1}{4\pi} \frac{1}{|\mathbf{x} - \mathbf{y}|}$$

and the so-called *double layer dipole kernel* [16]

$$d(\mathbf{x}, \mathbf{y}) := 2 \frac{\partial}{\partial \mathbf{n}(\mathbf{y})} s(\mathbf{x}, \mathbf{y}) = \frac{1}{2\pi} \frac{< \mathbf{n}(\mathbf{y}), \mathbf{x} - \mathbf{y} >}{|\mathbf{x} - \mathbf{y}|^3},$$

the following Fredholm integral equation of the second kind can be derived using a double layer potential approach [30, 16, 19]: $\forall \mathbf{x} \in \Gamma_i, \forall \mathbf{y} \in \Gamma_j, i, j = 1, 2, 3$:

$$\Phi(\mathbf{x}) = \frac{2\sigma_3^-}{\sigma_i^+ + \sigma_i^-} \Phi_p(\mathbf{x}) - \sum_{j=1}^{3} \frac{\sigma_j^+ - \sigma_j^-}{\sigma_i^+ + \sigma_i^-} \int_{\Gamma_j} d(\mathbf{x}, \mathbf{y}) \Phi(\mathbf{y}) d\Gamma_j \tag{3}$$

with

$$\Phi_p(\mathbf{x}) = \frac{1}{4\pi\sigma_3^-} \frac{< \mathbf{M}_p, \mathbf{x} - \mathbf{x}_p >}{|\mathbf{x} - \mathbf{x}_p|^3} \tag{4}$$

2.2. Solution techniques for the EEG forward problem

2.2.1. Quasi-analytical solution in multilayer sphere models In [26], series expansion formulas were derived for a mathematical dipole in a multilayer sphere model, denoted now as "the quasi-analytical solution". A rough overview of the formulas is given in this section. The model consists of shells 1 up to S with radii $r_S < r_{S-1} < \ldots < r_1$ and constant radial, $\sigma^{\mathrm{rad}}(r) = \sigma_j^{\mathrm{rad}} \in \mathbb{R}^+$, and constant tangential conductivity, $\sigma^{\mathrm{tang}}(r) = \sigma_j^{\mathrm{tang}} \in \mathbb{R}^+$, within each layer $r_{j+1} < r < r_j$. It is assumed, that the source at position $\mathbf{x}_p$ with radial coordinate $r_p \in \mathbb{R}$ is in a more interior layer than the measurement electrode at position $\mathbf{x}_e \in \mathbb{R}^3$ with radial coordinate $r_e \in \mathbb{R}$. The spherical harmonics expansion for the mathematical dipole (1) is expressed in terms of the gradient of the monopole potential with respect to the source point, using an asymptotic approximation and an addition-subtraction method to speed up the series convergence [26]. This results in

$$\Phi(\mathbf{x}_p, \mathbf{x}_e) = \frac{1}{4\pi} \langle \mathbf{M}_p, \mathbf{x}_e \frac{S_0}{r_e} + \mathbf{x}_p \left(\frac{S_1}{r_p} - \cos\omega_{pe} \frac{S_0}{r_p}\right) \rangle \tag{5}$$

with ω_{pe} being the angular distance between source and electrode and with

$$S_0 = \frac{F_0}{r_p} \frac{\Lambda}{(1 - 2\Lambda\cos\omega_{pe} + \Lambda^2)^{3/2}} + \frac{1}{r_p} \sum_{n=1}^{\infty} \{(2n+1) R_n(r_p, r_e) - F_0 \Lambda^n\} P_n'(\cos\omega_{pe}) \tag{6}$$

and

$$S_1 = F_1 \frac{\Lambda\cos\omega_{pe} - \Lambda^2}{(1 - 2\Lambda\cos\omega_{pe} + \Lambda^2)^{3/2}} + \sum_{n=1}^{\infty} \{(2n+1) R_n'(r_p, r_e) - F_1 n \Lambda^n\} P_n(\cos\omega_{pe}). \tag{7}$$

The coefficients R_n and their derivatives R_n' can be computed analytically and the derivative of the Legendre polynomial can be determined by means of a recursion formula. Refer to [26] for the derivation of the above series of differences and for the definition of F_0, F_1 and Λ ‡. Here, it is only important that these terms can be computed from the given radii and conductivities of layers between source and electrode and of the radial coordinate of the source and that they are independent of n.

For the quasi-analytical potential vector $\left(\underline{\Phi}_{\mathrm{eeg}}^{\mathrm{ana}}\right)_p \in \mathbb{R}^{s_{\mathrm{eeg}}}$ with s_{eeg} the number of electrodes with locations $\mathbf{x}_e^i$,

$$\left(\underline{\Phi}_{\mathrm{eeg}}^{\mathrm{ana}}\right)_p^{[i]} \stackrel{(5)}{:=} \Phi(\mathbf{x}_p, \mathbf{x}_e^i), \quad \forall\, i = 1, \ldots, s_{\mathrm{eeg}}, \tag{8}$$

the computation of the series (6) and (7) are stopped after the k's term, if the following criterion is fulfilled

$$\frac{t_k}{t_0} \leq \upsilon, \qquad t_k := (2k+1) R_k' - F_1 k \Lambda^k. \tag{9}$$

‡ The following is a result of a discussion with J.C. de Munck: While constants in formulas (71) and (72) in the original paper [26] have to be flipped, our versions of S_0 and S_1 in Equations (6) and (7) are correct.

2.2.2. The FEM direct potential approach The theory for the Venant direct potential approach is presented now, closely following the ideas of [9]. Starting from the basic relation for a dipole moment $\mathbf{T}_p \in \mathbb{R}^3$ at position $\mathbf{x}_p \in \mathbb{R}^3$, $\mathbf{T}_p = \int_\Omega (\mathbf{x} - \mathbf{x}_p) \mathrm{J}_p(\mathbf{x}) d\mathbf{x}$, and assuming discrete sources and sinks on only the C neighboring FE mesh nodes to the FE node which is closest to $\mathbf{x}_p$, it is $\mathbf{T}_p = \sum_{c=1}^{C} \Delta \mathbf{x}_{cp} \underline{j}_p^{[c]}$ with $\Delta \mathbf{x}_{cp}$ denoting the vector from FE node c to source position $\mathbf{x}_p$. When using higher moments $\underline{\bar{T}}_p^r \in \mathbb{R}^{n_0+1}$ with $n_0 = 1, 2$ and the Cartesian direction r ($r = x, y, z$), it is

$$\left(\underline{\bar{T}}_p^r\right)^{[n]} = \left(\underline{\bar{T}}_p^r\right)^{[n]} (\underline{j}_p) = \sum_{c=1}^{C} \left(\Delta \bar{x}_{cp}^r\right)^n \underline{j}_p^{[c]} \qquad \forall n \in 0, \ldots, n_0 \tag{10}$$

(for a motivation of higher moments see [9]). The bar indicates a scaling with a reference length a_{ref}, so that

$$\Delta \bar{x}_{cp}^r = \Delta x_{cp}^r / a_{\mathrm{ref}} \overset{!}{<} 1 \tag{11}$$

is dimensionless and the physical dimension of the resultant scaled n^{th} order moment, $\left(\underline{\bar{T}}_p^r\right)^{[n]}$, is that of a current (i.e., A, Ampère). a_{ref} has to be chosen so that $\Delta \bar{x}_{cp}^r$ is smaller 1. The equation is well known from the Saint Venant law in mechanical engineering, where small forces in combination with long lever arms have the same effect on the system as large forces in combination with short lever arms. If we now define the matrix $\bar{X}_p^r \in \mathbb{R}^{(n_0+1) \times C}$, the moment vector $\underline{\bar{M}}_p^r \in \mathbb{R}^{n_0+1}$, computed from the given dipole moment vector $\mathbf{M}_p$, and the diagonal source weighting matrix $\bar{W}_p^r \in \mathbb{R}^{C \times C}$ by

$$\begin{aligned}
\left(\bar{X}_p^r\right)^{[n,c]} &= \left(\Delta \bar{x}_{cp}^r\right)^n \\
\left(\underline{\bar{M}}_p^r\right)^{[n]} &= M_p^r \left(\frac{1}{2a_{\mathrm{ref}}}\right)^n (1 - (-1)^n) \\
\bar{W}_p^r &= DIAG\left(\left(\Delta \bar{x}_{1p}^r\right)^s, \ldots, \left(\Delta \bar{x}_{Cp}^r\right)^s\right)
\end{aligned} \tag{12}$$

with $s = 0$ or $s = 1$, then we compute the monopole load vector $\underline{j}_p \in \mathbb{R}^C$ for the Venant direct approach on the C neighboring FE nodes from the given dipole moment vector $\mathbf{M}_p$ at position $\mathbf{x}_p$ by means of minimizing the following functional

$$F_\lambda(\underline{j}_p) = \|\underline{\bar{M}}_p^r - \underline{\bar{T}}_p^r(\underline{j}_p)\|_2^2 + \lambda \|\bar{W}_p^r \underline{j}_p\|_2^2 = ||\underline{\bar{M}}_p^r - \bar{X}_p^r \underline{j}_p||_2^2 + \lambda \|\bar{W}_p^r \underline{j}_p\|_2^2 \overset{!}{=} \min.$$

The first part of the functional F_λ ensures a minimal difference between the moments of the Venant approach $\underline{\bar{T}}_p^r$ and the target ones $\underline{\bar{M}}_p^r$, while the second part smoothes the monopole distribution in a weighted sense and enables a unique minimum for F_λ. The solution of the minimization problem is given by

$$\left((\bar{X}_p^r)^{tr} \bar{X}_p^r + \lambda (\bar{W}_p^r)^{tr} \bar{W}_p^r\right) \underline{j}_p = (\bar{X}_p^r)^{tr} \underline{\bar{M}}_p^r,$$

so that finally the solution for the monopole source vector $\underline{j}_p$ of the Venant approach is given by

$$\underline{j}_p = \left(\sum_{r=1}^{3} \left\{ (\bar{X}_p^r)^{tr} \bar{X}_p^r + \lambda (\bar{W}_p^r)^{tr} \bar{W}_p^r \right\} \right)^{-1} \sum_{r=1}^{3} \left\{ (\bar{X}_p^r)^{tr} \underline{\bar{M}}_p^r \right\}. \tag{13}$$

The highest order is generally chosen as $n_0 = 1$ or $n_0 = 2$, where the latter effects a spatial concentration of loads in the dipole axis. Furthermore, $s = 1$ stresses the spatial concentration of loads around the dipole.

In the Venant direct potential approach, we use the FE method with piecewise linear basis functions φ_i at nodes ξ_i, i.e., $\varphi_i(\xi_i) = 1$ and $\varphi_i(\xi_j) = 0\ \forall j \neq i$. The total potential $\Phi(\mathbf{x}) \approx \Phi_h(\mathbf{x}) = \sum_{j=1}^{N^{\mathrm{FE}}} \varphi_j(\mathbf{x}) \left(\underline{\Phi}^{\mathrm{FE}}\right)^{[j]}$ with N^{FE} the number of FE nodes is then projected into the FE space and, using variational and FE techniques for equation (2), a linear system

$$K\underline{\Phi}^{\mathrm{FE}} = \underline{J}^{\mathrm{FE}} \tag{14}$$

is derived with the sparse symmetric positive definite stiffness matrix $K \in \mathbb{R}^{N^{\mathrm{FE}} \times N^{\mathrm{FE}}}$

$$K^{[i,j]} = \int_\Omega \langle \sigma \nabla \varphi_i, \nabla \varphi_j \rangle. \tag{15}$$

We then seek for the coefficient vector $\underline{\Phi}^{\mathrm{FE}} \in \mathbb{R}^{N^{\mathrm{FE}}}$. The right-hand side vector $\underline{J}^{\mathrm{FE}} \in \mathbb{R}^{N^{\mathrm{FE}}}$ has only C non-zero entries at the neighboring FE nodes to the considered dipole location. It is determined by

$$\left(\underline{J}^{\mathrm{FE}}\right)^{[i]} = \begin{cases} \underline{j}_p^{[c]} & \textit{if } \exists c \in \{1, \ldots, C\} : i = \textsc{glob}(c) \\ 0 & \text{otherwise,} \end{cases} \tag{16}$$

for a source at location $\mathbf{x}_p$, where the function GLOB determines the global index i to each of the local indices c.

2.2.3. The BEM direct potential approach For numerically solving the integral equation (3), we use a collocation approach [18, 23, 25, 44, 12]. The three boundaries ($1 \leq i \leq 3$) are discretized into triangles with $N(i)$ nodes $\mathbf{x}_m^i$ ($1 \leq m \leq N(i)$). Piecewise linear Lagrange-functions h_n^j ($h_n^j(\mathbf{x}_m^i) = \delta_{ij}\delta_{mn}$) are chosen as the basis for the approximation of the potential [25]. When compared to the constant potential approach with the triangle centers of mass as collocation points [18, 23], the linear approach was shown to overall yield better numerical results [36] . Substitution into (3) yields a linear equation system

$$\underline{\Phi}_i^{\mathrm{BE}} = \underline{J}_i^{\mathrm{BE}} + \sum_{j=1}^{3} A_{ij} \underline{\Phi}_j^{\mathrm{BE}} \tag{17}$$

with matrices $A_{ij} \in \mathbb{R}^{N(i) \times N(j)}$ and vectors $\underline{\Phi}_i^{\mathrm{BE}}, \underline{J}_i^{\mathrm{BE}} \in \mathbb{R}^{N(i)}$ defined as

$$A_{ij}^{[m,n]} := \frac{\sigma_j^+ - \sigma_j^-}{\sigma_i^+ + \sigma_i^-} D_{ij}^{[m,n]} \quad \text{with} \quad D_{ij}^{[m,n]} := \int_{\Gamma_j} d(\mathbf{x}_m^i, \mathbf{y}) h_n^j(\mathbf{y}) d\Gamma_j \tag{18}$$

$$\left(\underline{J}_i^{\mathrm{BE}}\right)^{[m]} := \frac{2\sigma_3^-}{\sigma_i^+ + \sigma_i^-} \Phi_p(\mathbf{x}_m^i) \tag{19}$$

where the entries $D_{ij}^{[m,n]}$ are computed analytically [25, 36]. Note that the denotation $\underline{J}_i^{\mathrm{BE}}$ was chosen with regard to Section 2.2.4, even if its unit is the one of a potential and not the one of a current source density. In [18, 23], the so-called *isolated skull approach* (ISA) was introduced to account for the numerical difficulties in the computation of the potentials on the outer surfaces Γ_1 and Γ_2 caused by the presence of the poorly conducting skull. Later studies [44, 24] pinpoint the importance of the ISA in reducing the numerical error. The ISA decomposes the potential

$$\underline{\Phi}_i^{\mathrm{BE}} = \underline{w}_i + \underline{w}_i^p \tag{20}$$

with $\underline{w}_i^p \in \mathbb{R}^{N(i)}$, $\underline{w}_1^p = \underline{w}_2^p = \underline{0}$ and $\underline{w}_3^p$ being the solution vector for the integral equation for the isolated brain compartment, i.e., the solution for (3) with $\sigma_3^+ = \sigma_2^\pm = \sigma_1^\pm = 0$:

$$\underline{w}_3^p = \frac{1}{\sigma_3^-} H^{-1} \underline{\Phi}_3^p \quad \text{with} \quad H := I - D_{33} \in \mathbb{R}^{N(3)\times N(3)} \tag{21}$$

The numerical solution for the corresponding multi-layer integral equation for the unknown w [18, Equations (20, 21)] can then numerically more accurately be solved [18, 44]. In this way, the following formula was derived for a numerically stable computation of the potential vector for the linear collocation approach on all three surfaces [44]:

$$\underline{\Phi}^{\mathrm{BE}} = G \underline{J}^{\mathrm{BE}} \tag{22}$$

with the fully populated matrix $G \in \mathbb{R}^{N^{\mathrm{BE}} \times N^{\mathrm{BE}}}$ $(N^{\mathrm{BE}} := \sum_{i=1}^{3} N(i))$ defined as

$$G := \frac{\sigma_3^+}{\sigma_3^-}(I - A)^{-1} \begin{pmatrix} I & 0 & 0 \\ 0 & I & 0 \\ 0 & 0 & (I - 2H^{-1}) \end{pmatrix} + \frac{\sigma_3^+ + \sigma_3^-}{\sigma_3^-} \begin{pmatrix} 0 & 0 & 0 \\ 0 & 0 & 0 \\ 0 & 0 & H^{-1} \end{pmatrix}$$

As shown in [25, 36], the matrices H and $I - A$ have an eigenvalue 0 to the eigenvector $\underline{1}$, because the potential is only defined up to an additive constant. The inversion by means of direct solution techniques can thus only be performed after a proper deflation (e.g., instead of H, we consider $H + \frac{1}{N}\underline{1} \cdot \underline{1}^{tr}$) [18, 25, 36].

2.2.4. Fast transfer matrix approach Let us assume that the EEG electrodes directly correspond to FE or BE nodes at the surface of the head model (otherwise, interpolation is needed). It is then easy to determine a restriction matrix $R \in \mathbb{R}^{(s_{\mathrm{eeg}}-1)\times N}$, which has only one non-zero entry with the value 1 in each row and which maps the potential vector onto the $(s_{\mathrm{eeg}} - 1)$ non-reference EEG electrodes:

$$R\, \underline{\Phi} =: \underline{\Phi}_{\mathrm{eeg}}. \tag{23}$$

We then define the following *BE transfer matrix* for the EEG:

$$T^{\mathrm{BE}} := R^{\mathrm{BE}}\, G \quad \in \mathbb{R}^{(s_{\mathrm{eeg}}-1)\times N^{\mathrm{BE}}}. \tag{24}$$

Matrix T^{BE} only has to be computed once per head model and directly maps the BE right-hand-side vector onto the unknown electrode potentials:

$$T^{\mathrm{BE}} \underline{J}^{\mathrm{BE}} \stackrel{(24)}{=} R^{\mathrm{BE}}\, G \underline{J}^{\mathrm{BE}} \stackrel{(22)}{=} R^{\mathrm{BE}} \underline{\Phi}^{\mathrm{BE}} \stackrel{(23)}{=} \underline{\Phi}_{\mathrm{eeg}}^{\mathrm{BE}}. \tag{25}$$

For the FE approach, the situation is similar. With the following definition of the *FE transfer matrix* for the EEG,

$$T^{\mathrm{FE}} := R^{\mathrm{FE}}\, K^{-1} \quad \in \mathbb{R}^{(s_{\mathrm{eeg}}-1)\times N^{\mathrm{FE}}}, \tag{26}$$

a direct mapping of an FE right-hand side vector onto the unknown electrode potentials is given:

$$T^{\rm FE}\,\underline{J}^{\rm FE} \stackrel{(26)}{=} R^{\rm FE}\,K^{-1}\underline{J}^{\rm FE} \stackrel{(14)}{=} R^{\rm FE}\underline{\Phi}^{\rm FE} \stackrel{(23)}{=} \underline{\Phi}^{\rm FE}_{\rm eeg}. \tag{27}$$

Note that while $\underline{J}^{\rm BE}$ is fully populated so that the operation $T^{\rm BE}\underline{J}^{\rm BE}$ amounts in $2\cdot(s_{\rm eeg}-1)\cdot N^{\rm BE}$ operations, $\underline{J}^{\rm FE}$ has only C non-zero entries so that $T^{\rm FE}\underline{J}^{\rm FE}$ only amounts in $2\cdot(s_{\rm eeg}-1)\cdot C$ operations. The fast transfer matrix approach can not be used when the mesh is adapted according to varying source positions within the inverse problem. We therefore attempt to avoid local mesh refinement techniques as used in [6, 8].

The inverse FE stiffness matrix K^{-1} from (15) exists, but its computation is a difficult task, since the sparseness of K will be lost while inverting. By means of multiplying equation (26) with the symmetric matrix K from the right side and transposing both sides, we obtain

$$K\left(T^{\rm FE}\right)^{tr} = \left(R^{\rm FE}\right)^{tr}. \tag{28}$$

The FE transfer matrix can thus be computed by means of iteratively solving $(s_{\rm eeg}-1)$ large sparse FE linear equation systems. Note that a fast FE transfer matrix for the Magnetoencephalography (MEG) forward problem can be derived on a similar way [37, 13]. For the computation of (26) by means of (28), we employ an algebraic multigrid preconditioned conjugate gradient (AMG-CG) method. We solve up to a relative error of 10^{-6} in the controllable $KC^{-1}K$-energy norm (with C^{-1} being one V-cycle of the AMG) [37].

3. Methods

3.1. Validation platform

Medium	Scalp	Skull	Brain
Outer shell radius	92mm	86mm	80mm
Conductivity	0.33S/m	0.0042S/m	0.33S/m

Table 1. Parameterization of the isotropic three layer sphere model for BEM and FEM accuracy and speed comparison.

The comparison of the BE- and FE-based EEG forward computations with regard to speed and accuracy are carried out in an isotropic three compartment sphere model, whose parameterization is shown in Table 1.

We furthermore study accuracy and speed of the proposed FE approach in a four compartment sphere model which additionally includes a CSF compartment [29, 38] and accounts for conductivity anisotropy of the skull [6, 8, 38]. The parameterization of this volume conductor model is shown in Table 2. BE and FE forward solutions are computed for dipoles located on the z axis in 1 mm steps up to a radius of 76 mm,

Medium	Scalp	Skull	CSF	Brain
Outer shell radius	92mm	86mm	80mm	78mm
Tangential conductivity	0.33S/m	0.042S/m	1.79S/m	0.33S/m
Radial conductivity	0.33S/m	0.0042S/m	1.79S/m	0.33S/m

Table 2. Parameterization of the anisotropic four layer sphere model for a further evaluation of the FEM accuracy and speed.

which corresponds to an eccentricity of 97.4% using both radial and tangential dipole orientations and amplitudes of 1 nAm. *Eccentricity* is defined here as the percent ratio of the distance between the source location and the model midpoint divided by the radius of the inner sphere in the four layer model(78 mm radius). The most eccentric source considered is thus only 2 mm below the CSF compartment in the four layer sphere model and 4 mm below the skull compartment in the three layer sphere model. To achieve error measures which are independent of the specific choice of the sensor configuration, we distribute 134 electrodes in a most-regular way over the outer sphere surface. The evaluations with regard to wall clock time, memory and accuracy are run on a 64bit Linux-PC with an Intel Xeon 5130 processor (2GHz) with 8GB of main memory using the SimBio software environment [32], which contains both the presented BE [44] and a variety of FE forward approaches [37, 40].

3.2. Forward problem parameter settings

A value of 10^{-6} is chosen for v in the stopping criterion (9) for the quasi-analytical series expansion formulas.

The parameters of the Venant FE approach are chosen as follows: The maximal dipole order n_0 in (10) and the scaling reference length a_{ref} in (11) are set to $n_0 = 2$ and $a_{\mathrm{ref}} = 20.0$ mm, respectively. Since the chosen mesh size is much smaller than the reference length, the second order term $\left(\Delta \bar{x}^r_{cp}\right)^2$ is small and the model focuses on fulfilling the dipole moments of the zeros and first order. The exponent of the source weighting matrix in (12) is fixed to $s = 1$ and the regularization parameter in (13) is chosen as $\lambda = 10^{-6}$. The settings effect a spatial concentration of the monopole loads in the dipole axis around the dipole location [9].

3.3. Mesh generation

In source reconstruction, head modeling is generally based on segmented magnetic resonance (MR) data, where curved tissue boundaries have a stair-step representation. Both BE and FE meshes are therefore created starting from synthetic MR images of the spherical volume conductors with 1 mm^3 voxel resolution. Tetrahedra and regular and geometry-adapted hexahedra FE meshing is examined. Two resolutions (one coarse and one fine) are considered for each meshing strategy.

3.3.1. BE mesh generation The BEM requires a surface mesh for each of the compartment boundaries. We use triangle meshes which are constructed as follows. Refer to [35] for a detailed description. In a first step, a boundary is segmented from the synthetic MR image of the sphere and vertices are regularly distributed on it. For a given triangle edge `width` of the resultant surface mesh, the distance between two neighboring vertices is modified. In a second step, using again parameter `width`, auxiliary surfaces are generated by means of erosions of the initial boundary, followed by a vertex thinning of all auxiliary surfaces. As a result, vertices are spread across the whole volume inside the initial boundary. A Delaunay tetrahedralization is then constructed from all vertices. The surface triangles from the tetrahedralization finally form the triangle mesh of the compartment boundary. In this way the two BE meshes with varying element `width`

model	**width**			**# nodes**	**# elements**
	scalp	**outer skull**	**inner skull**		
fine3700_3layer_iso	10.0 mm	9.5 mm	8.0 mm	3727	7462
coarse2000_3layer_iso	14.5 mm	13.5 mm	10.5 mm	2015	4018

Table 3. Fine and coarse BE meshes used for the studies in the isotropic three layer sphere model.

were constructed, which are shown in Table 3. For BE mesh generation, the software CURRY is used [10].

3.3.2. FE mesh generation

Regular hexahedra The generation of regular hexahedra meshes takes advantage of the cubic voxel structure which is inherent to MR images. Regular hexahedra meshes with edge length `width` are constructed by combining $\texttt{width}^3$ voxels of the MRI to form one element. Each hexahedron is labeled according to the majority of its inner voxel labels. Tables 4 and 7 present the regular hexahedra models generated for the isotropic three

model	**width**	**# nodes**	**# elements**
cube426k_3layer_iso	2.0 mm	425631	418816
cube56k_3layer_iso	4.0 mm	56043	50918

Table 4. Fine and coarse regular hexahedra FE meshes used for the studies in the isotropic three layer sphere model.

layer sphere model and for the anisotropic four layer sphere model, respectively. For regular hexahedra FE mesh generation, the software VGRID from the SimBio-project is used [32].

Geometry-adapted hexahedra In order to increase conformance to the real geometry and to mitigate the stair-case effects of a regular hexahedra mesh, a technique can be applied to shift nodes on material interfaces in order to obtain smoother and more accurate boundaries. Nodes on a two-material interface are moved into the direction of the centroid of the set of incident hexahedra with minority material, i.e., the material occurring three times or less in the 8 surrounding hexahedra. If the centroid of these minority voxels relative to a node is (x, y, z), it is shifted by

$$(\Delta x, \Delta y, \Delta z) = (0.49 \cdot x, 0.49 \cdot y, 0.49 \cdot z).$$

For the Venant FE approach in EEG source analysis, the `nodeshift` was shown to reduce both topography and magnitude errors by more than a factor of 2 for tangential and 1.5 for radial sources [40]. Tables 5 and 7 show the parameterization of the geometry-adapted hexahedra meshes. In addition, a cross-section of the nodeshift hexahedra mesh of the four compartment sphere model is presented in Figure 1(a). Geometry-adapted hexahedra FE meshes are generated using the software VGRID from the SimBio-project [32].

model	**width**	**# nodes**	**# elements**	**nodeshift**
cubens426k_3layer_iso	2.0 mm	425631	418816	yes
cubens56k_3layer_iso	4.0 mm	56043	50918	yes

Table 5. Fine and coarse geometry-adapted hexahedra FE meshes used for the studies in the isotropic three layer sphere model.

Tetrahedra mesh generation Tetrahedra FE meshes of the three and four layer sphere models are generated by means of the software TetGen [33] which uses a *Constrained Delaunay Tetrahedralization* (CDT) approach [33]. The starting point are triangle surface meshes of the compartment boundaries, which are obtained as described in Section (3.3.1). The CDT approach is then used to construct a tetrahedralization conforming to the surface meshes. It first builds a Delaunay tetrahedralization of the vertices of the surface meshes. It then uses a local degeneracy removal algorithm combining vertex perturbation and vertex insertion to construct a new set of vertices which includes the input set of vertices. In the last step, a fast facet recovery algorithm is used to construct the CDT [33]. This approach is combined with two further constraints to the size and shape of the tetrahedra. The first constraint is important for the generation of quality tetrahedra. If `rad` denotes the radius of the unique circumsphere of a tetrahedron and `minwidth` its shortest edge length, the quality of the tetrahedron can be defined as

$$\texttt{quality} = \texttt{rad}/\texttt{minwidth}. \tag{29}$$

The quality can distinguish almost all badly-shaped tetrahedra except one type of tetrahedra, so-called slivers. A sliver is a very flat tetrahedron which has no small

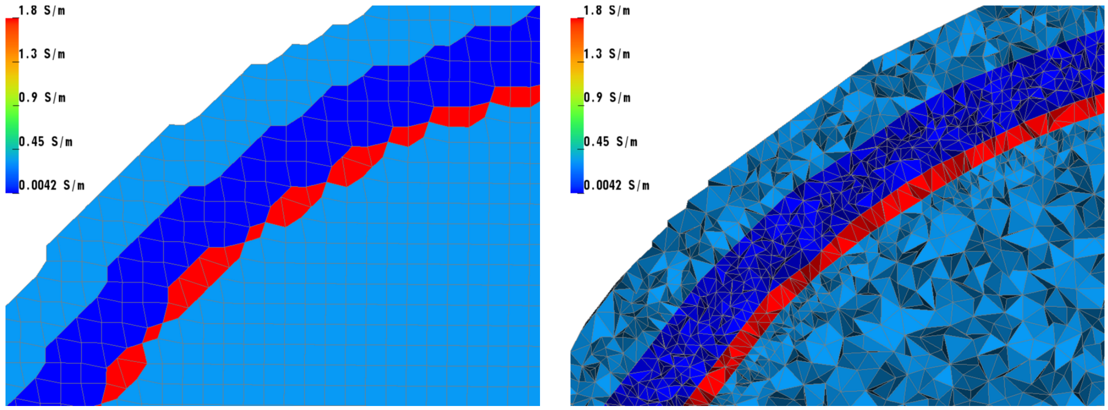

(a) cubens426k_4layer_aniso (b) tet716k_4layer_aniso

Figure 1. Detail of the cross-section of (a) the geometry-adapted hexahedra model and (b) the high-resolution CDT tetrahedra FE mesh of the four compartment sphere model. Visualization was carried out using BioPSE [7].

edges, but can have arbitrarily large dihedral angles (close to π). For this reason, an additional mesh smoothing and optimization step is used to remove the slivers and improve the overall mesh quality. The second constraint can be used to restrict the volume of the generated tetrahedra in a certain compartment. We follow the formula for regular tetrahedra:

$$\texttt{volume} = \sqrt{2}/12 \cdot \texttt{width}^3 \tag{30}$$

model	width	# nodes	# elements	quality	volume
tet660k_3layer_iso	2.2 mm	660321	4158422	1.4	1.3
tet103k_3layer_iso	4.0 mm	103182	636951	1.4	7.5

Table 6. Fine and coarse CDT tetrahedra meshes used for the studies in the isotropic three layer sphere model. The used quality (29) and volume (30) constraints are also indicated.

Table 6 presents the parameterization of the generated CDT tetrahedra meshes for the isotropic three compartment sphere studies.

model	element type	# nodes	# elements
cube426k_4layer_aniso	hexahedra	425631	418816
cubens426k_4layer_aniso	geometry-adapted hexahedra	425631	418816
tet716k_4layer_aniso	tetrahedra	715721	4504002

Table 7. The high-resolution FE meshes used for the studies in the anisotropic four layer sphere model.

Finally, a CDT mesh is created for the anisotropic four layer sphere model. A cross-section of this model is presented in Figure 1(b) and Table 7 shows its main parameterization. The mesh is generated with a quality constraint of 1.4. A volume constraint of 0.5 is used for the skull compartment since the modeling of its anisotropy requires specifically small elements. Additionally, we define a cortex compartment of 4mm thickness (radius between 74mm and 78mm) and use a volume constraint of 0.3 in order to enforce small elements close to the first conductivity inhomogeneity at the inner CSF border. Volume constraints of 1.0, 3.0 and 3.0 were used for the compartments skin, CSF and white matter (radius <74mm), respectively.

3.4. Error criteria

For the comparison of the numerical BE (25) and FE (27) solution vectors at the electrodes, $\underline{\Phi}^{\mathrm{num}}_{\mathrm{eeg}}$, to the quasi-analytical (8) one, $\underline{\Phi}^{\mathrm{ana}}_{\mathrm{eeg}}$, we used two error criteria that are commonly used in source analysis [23, 6, 8, 31], the relative difference measure (RDM) and the magnification factor (MAG). The RDM is defined as

$$\mathrm{RDM} = \left\| \frac{1}{\left\|\underline{\Phi}^{\mathrm{ana}}_{\mathrm{eeg}}\right\|_2} \underline{\Phi}^{\mathrm{ana}}_{\mathrm{eeg}} - \frac{1}{\left\|\underline{\Phi}^{\mathrm{num}}_{\mathrm{eeg}}\right\|_2} \underline{\Phi}^{\mathrm{num}}_{\mathrm{eeg}} \right\|_2 \tag{31}$$

with $\|\cdot\|_2$ denoting the L_2 norm. The RDM indicates errors in the topography of the numerically computed potentials. It is $0 \leq \mathrm{RDM} \leq 2$, so that we can furthermore define

$$\mathrm{RDM}(\%) := 100 \cdot \mathrm{RDM}/2. \tag{32}$$

The second similarity measure, the MAG, is defined as

$$\mathrm{MAG} = \left\|\underline{\Phi}^{\mathrm{num}}_{\mathrm{eeg}}\right\|_2 / \left\|\underline{\Phi}^{\mathrm{ana}}_{\mathrm{eeg}}\right\|_2 . \tag{33}$$

It indicates changes in the source amplitude. The minimum is at MAG = 1 and we therefore define

$$\mathrm{MAG}(\%) = 100 \cdot |1 - \mathrm{MAG}|. \tag{34}$$

4. Results

4.1. Validity of the BE and FE comparison

The first study shall show that the comparison of BE models with mesh resolutions of some thousand nodes with FE models with mesh resolutions of some hundred thousand nodes is valid. Therefore, the wall clock time is measured for the BE and FE models with highest mesh resolution. With regard to the inverse problem in EEG source analysis, it should be distinguished between the setup-computation (the transfer matrices T^{BE} from (24) and T^{FE} from (26)) that only has to be carried out once per head model and computations that have to be carried out thousands of times within the inverse problem (right-hand side computations in (16) and (19) and multiplications to the transfer matrices in (25) and (27)). Furthermore, the total time needed for simulating the electric potential for 30,000 dipole sources, which approximately corresponds to the time for computing a lead field with 10,000 influence nodes and no constraint on the dipole orientations, is measured.

model	setup	rhs	mult	lead field
fine3700_3layer_iso	70 min 59.6 s	0.4 ms	2.7 ms	72 min 33 s
cubens426k_3layer_iso	29 min 14.3 s	0.6 ms	0.1 ms	29 min 35 s
tet716k_4layer_aniso	56 min 31.6 s	2.2 ms	0.2 ms	57 min 43 s

Table 8. Wall clock time for the most accurate BE and FE meshes: *Setup* measures the time for computing the transfer matrices T^{BE} from (24) and T^{FE} from (26), *rhs* for the right-hand side computation (16) and (19) and *mult* for the multiplication of the transfer matrix to the rhs in (25) and (27). *lead field* indicates the cumulated time for the computation of a lead field matrix with 30,000 embedded forward computations.

Table 8 summarizes our time measurements. It is shown that for both BE and FE modeling, the setup, which only has to be carried out once per headmodel, is the most time-consuming operation. The transfer matrix approach then allows very fast forward computations on a millisecond scale for both BE and FE volume conductor modeling. The main result is thus that FE modeling is not excessively more expensive than BE modeling, in contrast, in our current implementation, it is even faster. When comparing the time required for the computation of the exemplary lead field matrix in the three compartment sphere model using the BEM model `fine3700_3layer_iso` and the FEM model `cubens426k_3layer_iso`, the BEM- takes more than twice the time of the FEM-computation. The FEM forward computations (operations *rhs* and *mult* in Table 8) are faster than the BEM forward computations, because most entries in the FEM-rhs in (16) are zero, while the BEM-rhs (19) is fully-populated.

Depending on whether tetrahedra or hexahedra elements are chosen, the mesh generation process might be more complex for the FEM, because a 3D discretization of the volume conductor is needed. Because of its simplicity, with 6.2 s, the generation of the geometry-adapted hexahedra model `cubens426k_3layer_iso` is extremely fast, while, with a wall clock time of 7 min 9 s, the generation of the CDT tetrahedra FE-model `tet716k_4layer_aniso` is more time-consuming. With regard to memory consumption, the FEM computation is more expensive than the BEM computation. In our current implementation, about 3.5 GB of main memory is needed for model `tet716k_4layer_aniso`, if, among others, the large FE transfer matrix T^{FE} of 732 MB, all FE grid hierarchies for the AMG-CG solver and the tensor-valued conductivities are kept in the main memory in parallel. However, the memory amount is strongly reduced when computing T^{FE} row-wise (i.e., sensor-wise), as shown in [37].

4.2. Accuracy comparison in the isotropic three layer sphere model

In a second examination, the accuracy of BEM and FEM is studied in the three compartment sphere model from Table 1.

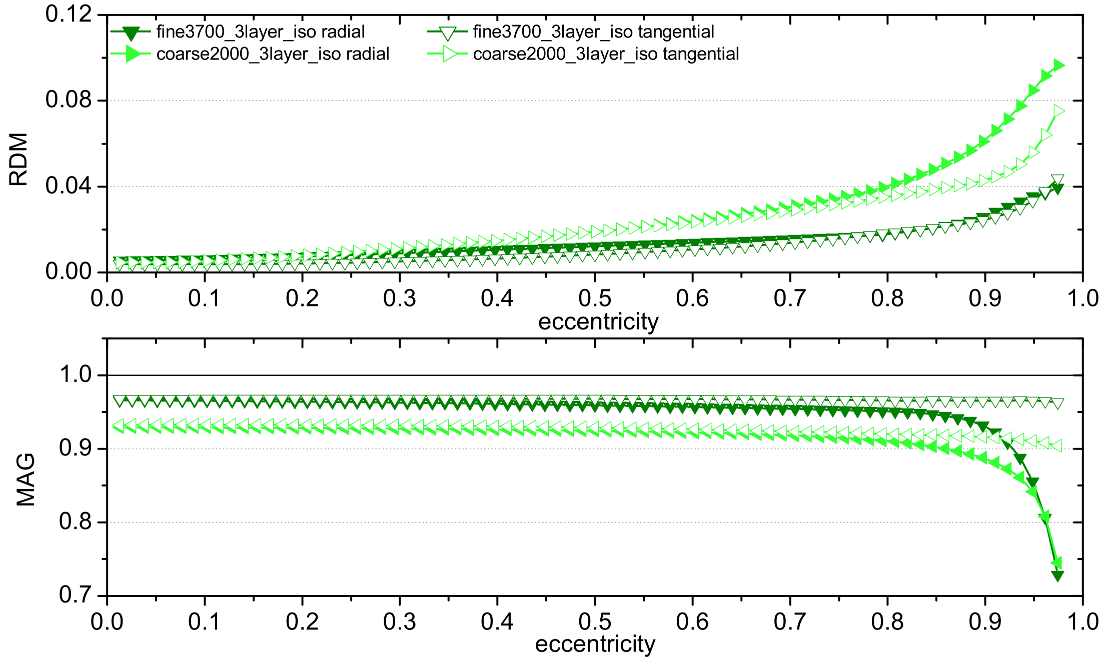

Figure 2. Isotropic three layer sphere model: Topography (RDM) and magnitude (MAG) errors for the BE approach using the coarse and the fine triangle mesh from Table 3.

The parameterization for the coarse and the fine triangle meshes used for the BEM simulations can be seen in Table 3, while Figure 2 shows their RDM and MAG errors.

Figures 3, 4 and 5 show the topography and magnitude errors for the direct Venant FE forward approach using the coarse and the fine regular and geometry-adapted hexahedra and CDT tetrahedra meshes listed in Tables 4, 5 and 6, respectively.

The first observation is that both BE and FE (for all element types) forward approaches are converging, i.e., with decreasing mesh size, the numerical errors are decreasing. Furthermore, for both BE and FE approaches, numerical errors are increasing with increasing eccentricity, especially for radial dipole orientations. While smooth error curves can be observed for the BE approach, the Venant FE approach shows slight error curve oscillations, i.e., a slight mesh-dependence of the dipole model.

In order to allow a direct comparison, the BEM and FEM errors for the high mesh resolutions are presented in Figure 6. It can be observed, that the BEM is slightly more accurate than the best Venant FE solution for low eccentricities up to 0.7. For dipoles at eccentricities larger 0.7, the FEM solutions in geometry-adapted hexahedra and CDT tetrahedra meshes are more accurate than the BEM solution. Highest errors for the most eccentric sources are for the BE approach in the range of 2% RDM (32) and up to 28% MAG (34), while they are only 1% RDM and 5% MAG for the geometry-adapted hexahedra FE model. With regard to the dependence of the FE solution accuracy on the element type, the geometry-adapted hexahedra perform best in this study while regular hexahedra are worst.

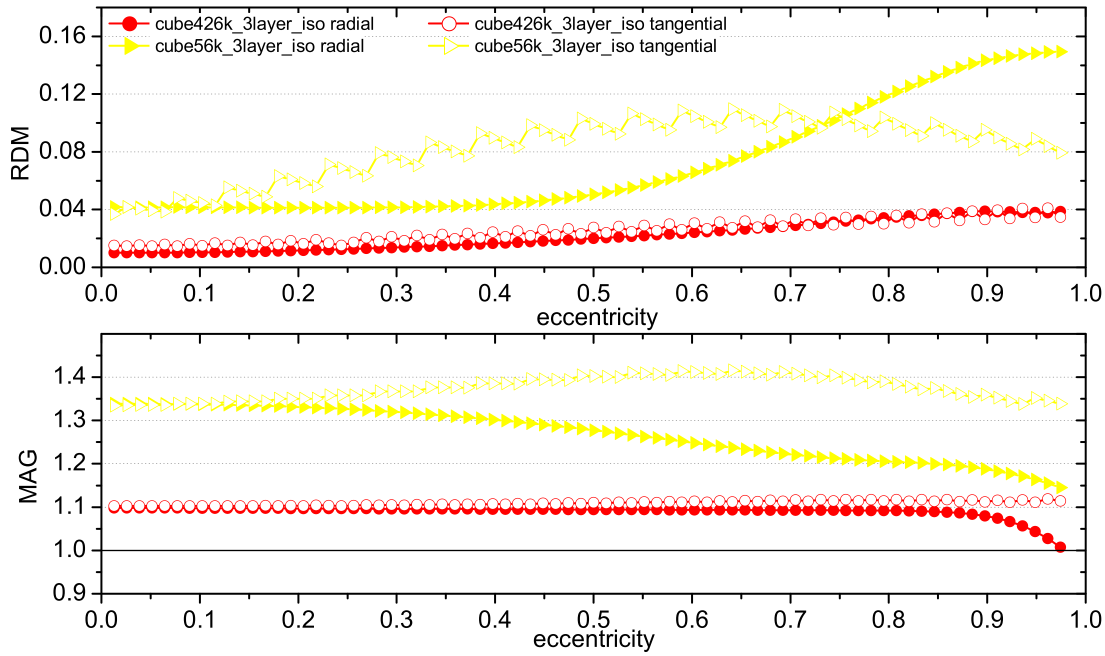

Figure 3. Isotropic three layer sphere model: Topography (RDM) and magnitude (MAG) errors for the FEM solution using the coarse and the fine regular hexahedra meshes from Table 4.

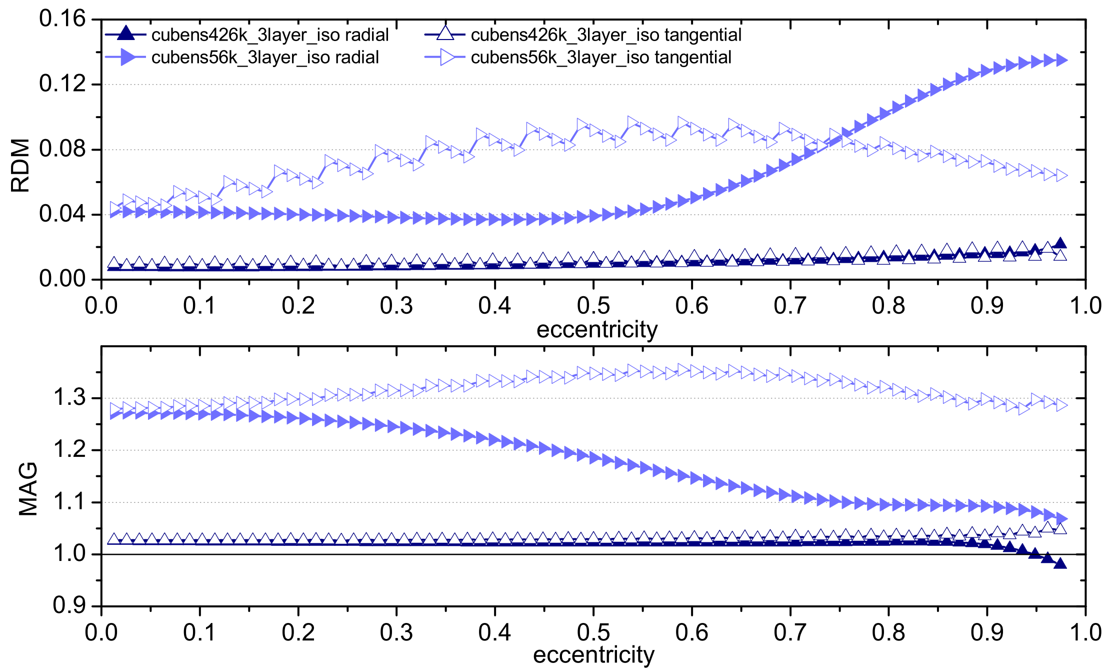

Figure 4. Isotropic three layer sphere model: Topography (RDM) and magnitude (MAG) errors for the FEM solution using the coarse and the fine geometry-adapted hexahedra meshes from Table 5.

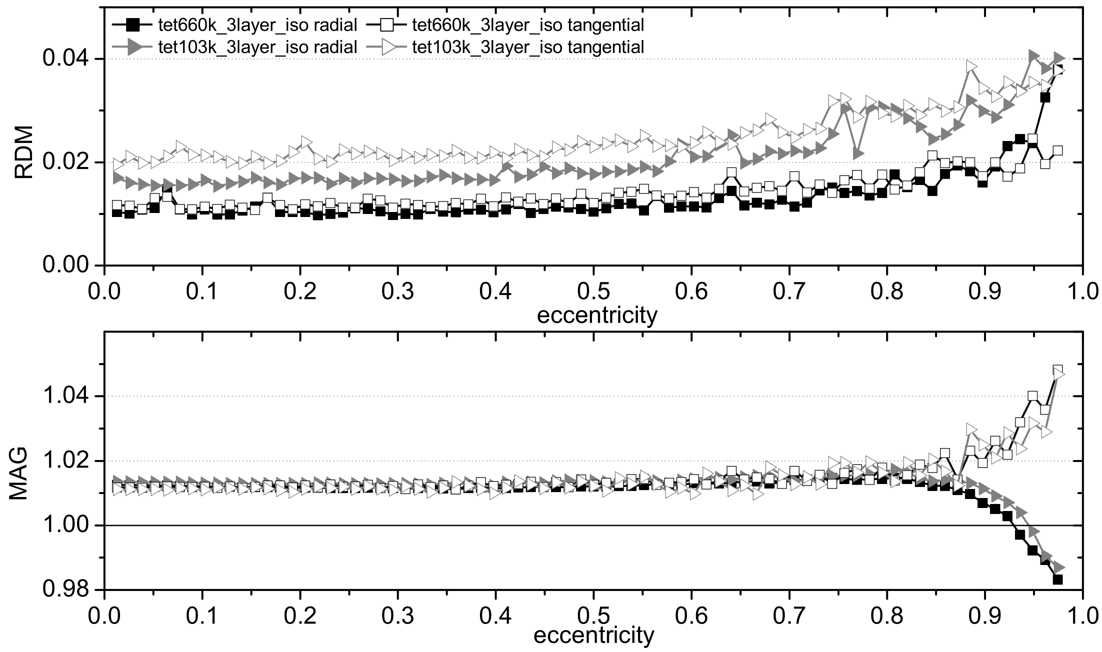

Figure 5. Isotropic three layer sphere model: Topography (RDM) and magnitude (MAG) errors for the FEM solution using the coarse and the fine CDT tetrahedra meshes from Table 6.

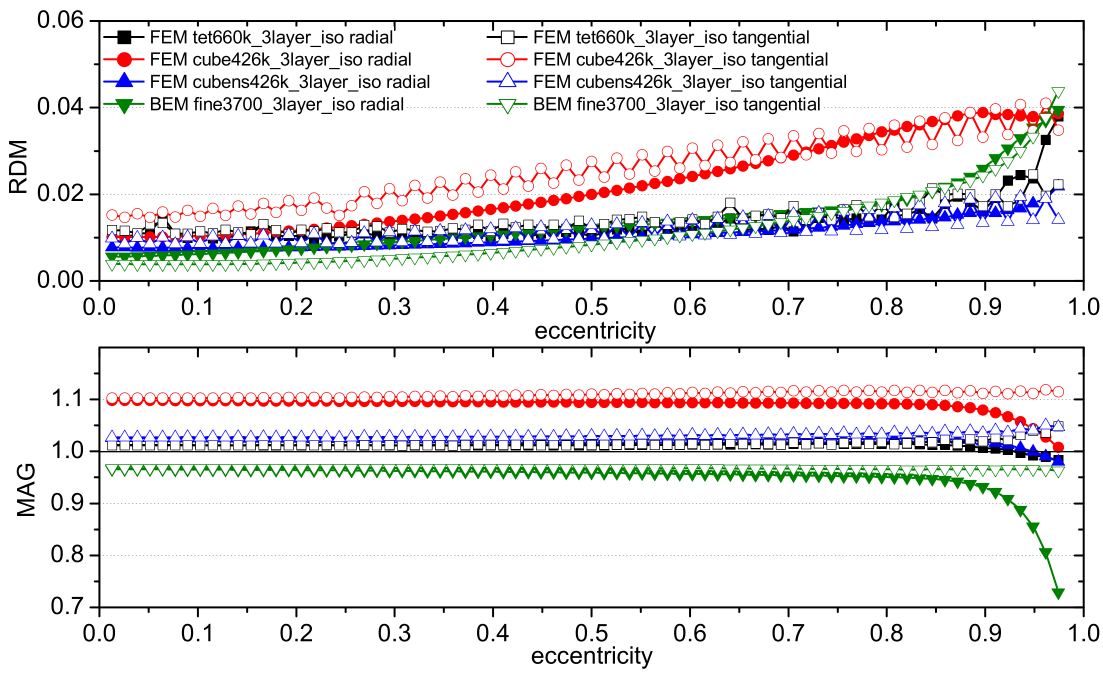

Figure 6. Isotropic three layer sphere model: Topography (RDM) and magnitude (MAG) errors for the high resolution BE and FE forward computations.

4.3. FEM accuracy in the anisotropic four layer sphere model

The goal of the last study is to show the flexibility of the Venant FE approach, i.e., that very high accuracies with short computation times (see the computation times for model `tet716k_4layer_aniso` in Table 8) are also achieved in volume conductors with more complex and even anisotropic conductivity profiles. Therefore, the numerical accuracy of the Venant FE approach is examined in the four layer spherical volume conductor with anisotropic skull from Table 2. Note again that the distance of the most eccentric dipole to the closest conductivity inhomogeneity (i.e., to the CSF) is now only 2 mm unlike in Section 4.2, where it was 4 mm (to the skull).

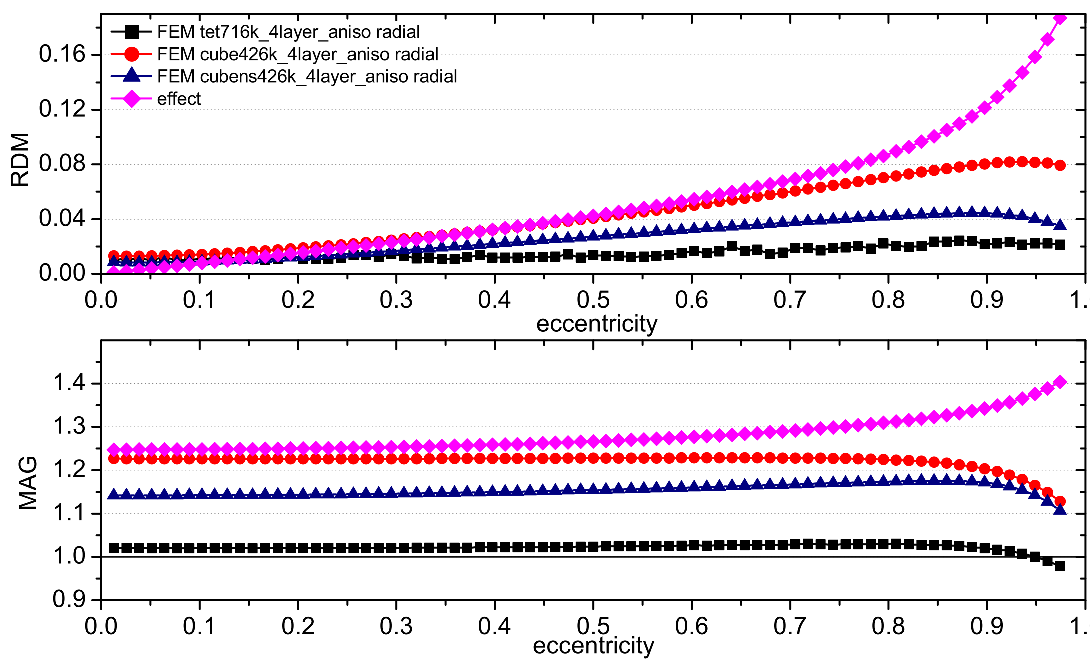

Figure 7. Anisotropic four layer sphere model, radial dipole orientations: RDM and MAG errors for the Venant FE approach using the meshes from Table 7. *effect* shows the RDM and MAG error of the isotropic three layer sphere model, i.e., when neglecting the skull anisotropy and the high conductivity of the CSF compartment.

The RDM and MAG errors for the FE meshes from Table 7 for radial and tangential dipoles are shown in Figures 7 and 8, respectively. In addition, the error between the quasi-analytical solution in the isotropic three layer sphere model from Table 1 and the quasi-analytical solution for the anisotropic four layer sphere model from Table 2 is presented. This curve demonstrates the *effect* of neglecting the CSF layer and the anisotropic conductivity of the skull in the solution of the forward problem.

Figures 7 and 8 clearly show that the numerical error of especially model `tet716k_4layer_aniso` is significantly smaller than the errors caused by assuming a simplified isotropic three compartment volume conductor. Furthermore, with a maximal RDM of 1% and a maximal MAG below 5% for sources with maximal eccentricities of

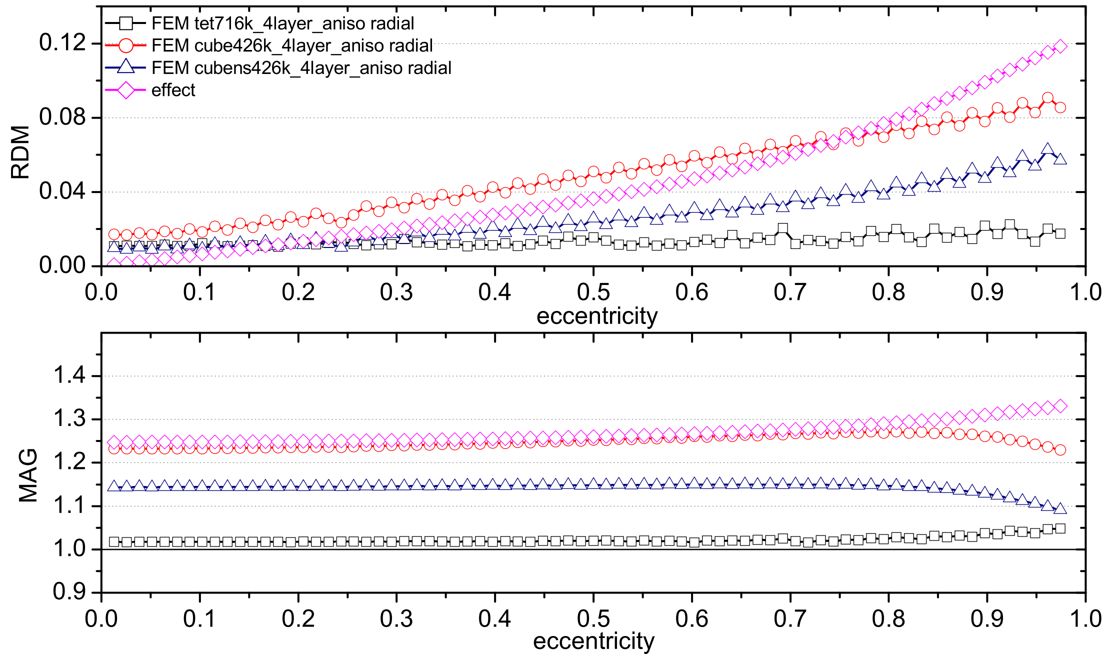

Figure 8. Anisotropic four layer sphere model, tangential dipole orientations: RDM and MAG errors for the Venant FE approach using the meshes from Table 7. *effect* shows the RDM and MAG error of the isotropic three layer sphere model, i.e., when neglecting the skull anisotropy and the high conductivity of the CSF compartment.

up to 97.4%, comparable errors to those in the more simple isotropic three layer sphere model study in Section 4.2 are achieved with the highly-tuned CDT tetrahedra model. The errors of the geometry-adapted hexahedra (maximal RDM of about 3% and a maximal MAG of about 18%) and especially the regular hexahedra model (maximal RDM of about 4.5% and a maximal MAG of about 27%) are higher than in Section 4.2. This shows that high mesh resolutions are especially needed in the anisotropic skull compartment.

5. Discussion and conclusion

In EEG source analysis literature, the difficulty of FE mesh generation [19] and the computational complexity of FE forward modeling [9, 43, 28] was generally considered to be a drawback for routine practical application, even if the flexibility with regard to the modeling of tissue conductivity inhomogeneity and anisotropy was widely honored [6, 9, 8, 43, 31, 13, 29, 38, 28]. In [9], the computation of a lead field matrix with 8,742 unknown dipole components in a tetrahedra Venant FE approach with 18,322 nodes took roughly a week of computation time. In [43], a tetrahedra Venant FE model with only 10,731 nodes was used and it was discussed that, for a general clinical use of FE source analysis in presurgical epilepsy diagnosis, a finer FE discretization and parallel computing is needed. In [28] it was speculated that BEM models are less computationally intensive and more accurate in three layer sphere studies than FEM models.

In light of these considerations and speculations, the main results of our study are that Venant FE volume conductor modeling with resolutions of even hundreds of thousands FE nodes in combination with the transfer matrix approach in an anisotropic four layer sphere model is very accurate (maximal RDM of 1% and a maximal MAG below 5% for sources with maximal eccentricities of up to 97.4%, i.e., up to 2 mm under the CSF compartment) and at the same time very fast (2.4 milliseconds for a forward computation in an FE model with 716K nodes on a single processor of a standard 64bit Linux machine). Furthermore, with FE mesh generation wall clock times of 6.2 seconds for a geometry-adapted hexahedra model with 425K nodes and about 7 minutes for the generation of a highly-tuned constrained Delaunay tetrahedralization FE-model with 716K nodes, even the 3D FE meshing does no longer pose a large problem with modern tools such as TetGen [33], used for our study.

In the isotropic three layer sphere model, we compared the Venant FE approach [9] with the ISA vertex collocation BE approach, i.e., a collocation BE approach [4] using the isolated skull approach [23, 18, 44] and linear basis functions with analytically integrated elements [25, 44]. Both numerical approaches were combined with transfer matrices [37] for a fast BE and FE forward modeling. For a 2mm geometry-adapted hexahedra FE model, the maximal RDM (MAG) of the FEM approach of 1% (5%) was about two (four) times lower than the maximal RDM (MAG) of the BEM approach. At the same time, with 0.7 ms, the FE forward computation is more than four times faster than the BE forward computation. The error curves of the Venant FE approach were shown to slightly oscillate. This does not have to be a disadvantage because, as shown for tetrahedra meshes in [21], the minimum error is achieved for sources on FE nodes, so that a lead field interpolation technique [42] can be used to avoid oscillations and further decrease the numerical error.

As recent investigations show, the BE method can still be improved through the use of a Galerkin approach [24], a symmetric BE approach [19], or virtual mesh refinement [12]. However, as shown in [11] using a full subtraction approach (maximal RDM of 0.34% and a maximal MAG of 0.3% for sources with maximal eccentricities of up to 98.7%, i.e., up to 1mm under the CSF compartment), this is also true for the FE method.

Acknowledgment

The authors would like to thank J.C. de Munck for providing his software for the analytical solution and for his quick responses whenever needed. This work was supported by the Deutsche Forschungsgemeinschaft (JU445/5-1, KN588/2-1) and by the IST-program of the European Community, project SimBio (http://www.simbio.de).

6. References

[1] M. Akhtari, H.C. Bryant, A.N. Marmelak, E.R. Flynn, L. Heller, J.J. Shih, M. Mandelkern, A. Matlachov, D.M. Ranken, E.D. Best, M.A.DiMauro, R.R. Lee and W.W. Sutherling, *Conductivities of Three-Layer Live Human Skull*, Brain Topography, 14 (3), 2002, pp. 151–167.

[2] K.A. Awada, D.R. Jackson, J.T. Williams, D.R.Wilton, S.B. Baumann and A.C. Papanicolaou, *Computational Aspects of Finite Element Modeling in EEG Source Localization*, IEEE Trans Biomed Eng, 44 (8), 1997, pp. 736–751.

[3] S.Baillet, J.C. Mosher and R.M. Leahy, *Electromagnetic brain mapping*, IEEE Signal Processing Magazine, 18 (6), 2001, pp. 14-30.

[4] A.C.L. Barnard, J.M. Duck, M.S. Lynn and W.P. Timlake, *The application of electromagnetic theory to electrocardiology II*, Biophys.J., 7, 1967, pp 463-491.

[5] S.B. Baumann, D.R. Wozny, S.K. Kelly and F.M. Meno, *The Electrical Conductivity of Human Cerebrospinal Fluid at Body Temperature*, IEEE Trans Biomed Eng, 44 (3), 1997, pp. 220–223.

[6] O. Bertrand, M. Thévenet and F. Perrin, *3D Finite Element Method in Brain Electrical Activity Studies*, in Biomagnetic Localization and 3D Modelling, Report of the Dep. of Tech.Physics, Helsinki University of Technology, J.Nenonen, H.M. Rajala and T. Katila, eds., 1991, pp. 154–171.

[7] BioPSE, 2002. Problem Solving Environment for modeling, simulation, and visualization of bioelectric fields. Scientific Computing and Imaging Institute (SCI), http://software.sci.utah.edu/biopse.html.

[8] S.P. van den Broek, *Volume Conduction Effects in EEG and MEG*, Proefschrift Universiteit Twente Enschede, The Netherlands, ISBN 90-365-0919-x, 1997.

[9] H. Buchner, G. Knoll, M. Fuchs, A. Rienäcker, R. Beckmann, M. Wagner, J. Silny and J. Pesch, *Inverse Localization of Electric Dipole Current Sources in Finite Element Models of the Human Head*, Electroenc. Clin. Neurophysiol., 102, 1997, pp. 267–278.

[10] CURRY, *CURrent Reconstruction and Imaging.*, http://www.neuro.com, 2000.

[11] F. Drechsler, C.H. Wolters, T. Dierkes, H. Si and L. Grasedyck, *A highly accurate full subtraction approach for dipole modelling in EEG source analysis using the finite element method.*, J. Applied Numerical Mathematics, in review, 2007.

[12] M. Fuchs and R. Drenckhahn and H.A. Wischmann and M. Wagner, *An improved boundary element method for realistical volume conductor modeling.*, IEEE Trans. Biomed. Eng., 45 (8), 1998, pp. 980–997.

[13] N.G.Gencer and C.E.Acar, *Sensitivity of EEG and MEG measurements to tissue conductivity.*, Phys.Med.Biol., 49, 2004, pp. 701–717.

[14] S.I. Goncalves, J.C. de Munck, J.P.A. Verbunt, F. Bijma, R.M. Heethaar and F.H. Lopes da Silva, *In Vivo Measurement of the Brain and Skull Resistivities Using an EIT-Based Method and Realistic Models for the Head.*, IEEE Trans.Biomed.Eng., 50 (6), 2003, pp. 754-767.

[15] D. Güllmar, J. Haueisen, M. Eiselt, F. Giessler, L. Flemming, A. Anwander, T.R. Knösche, C.H. Wolters, M. Dümpelmann, D.S. Tuch and J. R. Reichenbach, *Influence of Anisotropic Copnductivity on EEG Source Reconstruction: Investigations in a Rabbit Model*, IEEE Trans.Biomed.Eng., 53 (9), 2006, pp. 1841–1850.

[16] W. Hackbusch, *Integralgleichungen, Theorie und Numerik.*, Teubner Studienbücher, 1989.

[17] H. Hallez, B. Vanrumste, P. Van Hese, Y. D'Asseler, I. Lemahieu and R. Van de Walle, *A finite difference method with reciprocity used to incorporate anisotropy in electroencephalogram dipole source localization.*, Phys.Med.Biol., 50, 2005, pp. 3787–3806.

[18] M.S. Hämäläinen and J. Sarvas, *Realistic conductivity geometry model of the human head for interpretation of neuromagnetic data*, IEEE Trans Biomed Eng, 1989, 36, pp. 165–171.

[19] J. Kybic, M. Clerc, T. Abboud, O. Faugeras, R. Keriven and T. Papadopoulo, *A*

common formalism for the integral formulations of the forward EEG problem, IEEE Trans. Med. Imag., 24 (1), 2005, pp. 12–18.

[20] Y. Lai, W. van Drongelen, L. Ding, K.E. Hecox, V.L. Towle, D.M. Frim and B. He, *Estimation of in vivo human brain-to-skull conductivity ratio from simultaneous extra- and intra-cranial electrical potential recordings*, Clin. Neurophysiol., 116, 2005, pp. 456–465.

[21] B.Lanfer, *Validation and comparison of realistic head modeling techniques and application to tactile somatosensory evoked EEG and MEG data*, Master thesis in Physics, Institut für Biomagnetismus und Biosignalanalyse, Westfälische Wilhelms-Universität Münster, 2007.

[22] S. Lew, C. Wolters, A. Anwander, S. Makeig and R.S. MacLeod, *Low resolution conductivity estimation to improve source localization*, International Congress Series, vol.1300, pp.149-152 (June 2007), http://dx.doi.org/10.1016/j.ics.2006.12.058.

[23] J.W.H Meijs, O.W. Weier, M.J. Peters and A. van Oosterom, *On the Numerical Accuracy of the Boundary Element Method*, IEEE Trans Biomed Eng., 1989, 36, pp. 1038–1049.

[24] J.C. Mosher and R.M. Leahy and P.S. Lewis, *EEG and MEG: Forward solutions for inverse methods.*, IEEE Trans Biomed Eng, 46 (3), 1999, pp. 245–259.

[25] J.C. de Munck, *A linear discretization of the volume conductor boundary integral equation using analytically integrated elements*, IEEE Trans Biomed Eng, 39 (9), 1992, pp. 986–990.

[26] J.C. de Munck and M. Peters, *A fast method to compute the potential in the multi sphere model*, IEEE Trans Biomed Eng, 40 (11), 1993, pp. 1166–1174.

[27] S. Murakami and Y.C. Okada, *Contributions of principal neocortical neurons to magnetoencephalography and electroencephalography signals*, J.Physiol., 575, 3, 2006, pp.925–936.

[28] S.M. Plis, J.S. George, S.C. Jun, D.M. Ranken, P.L. Volegov and D. M. Schmidt, *Probabilistic forward model for electroencephalography*, Phys.Med.Biol., 52 (2007), pp. 5309–5327.

[29] C. Ramon and P. Schimpf and J. Haueisen and M. Holmes and A. Ishimaru, *Role of soft bone, CSF and gray matter in EEG simulations*, Brain Topography, 16 (4), 2004, pp. 245–248.

[30] J. Sarvas, *Basic Mathematical and Electromagnetic Concepts of the Biomagnetic Inverse Problem*, Phys.Med.Biol., 32 (1), 1987, pp. 11–22.

[31] P.H. Schimpf, C.R. Ramon and J. Haueisen, *Dipole Models for the EEG and MEG*, IEEE Trans Biomed Eng, 49 (5), 2002, pp. 409–418.

[32] SimBio, 2000-2003 *SimBio: A Generic Environment for Bio-Numerical Simulation*, IST-Program of the European Commission, Project No.10378, http://www.simbio.de.

[33] H. Si *TetGen, A Quality Tetrahedral Mesh Generator and Three-Dimensional Delaunay Triangulator, V1.3, User's Manual*, Weierstrass Institute for Applied Analysis and Stochastics, 2004.

[34] D.S. Tuch, V.J. Wedeen, A.M. Dale, J.S. George and J.W. Belliveau *Conductivity tensor mapping of the human brain using diffusion tensor MRI*, PNAS, 98 (20), 2001, pp. 11697–11701.

[35] M. Wagner, *Rekonstruktion neuronaler Ströme aus bioelektrischen und biomagnetischen Messungen auf der aus MR-Bildern segmentierten Hirnrinde*, PhD thesis, Shaker-Verlag Aachen, ISBN 3-8265-4293-2, 1998.

[36] C.H. Wolters, *Direkte Methoden zur Berechnung dipolinduzierter elektrischer und magnetischer Felder und inverse Strategien zur Quellokalisation im Gehirn*, Diploma thesis in Mathematics, Institut für Geometrie und Praktische Mathematik, RWTH Aachen, 1997.

[37] C.H. Wolters, L. Grasedyck and W. Hackbusch, *Efficient Computation of Lead Field Bases and Influence Matrix for the FEM-based EEG and MEG Inverse Problem*, Inverse Problems, 20 (4), 2004, pp. 1099–1116.

[38] C.H. Wolters, A. Anwander, D.Weinstein, M.Koch, X.Tricoche and R.MacLeod, *Influence of Tissue Conductivity Anisotropy on EEG/MEG Field and Return Current Computation in a Realistic Head Model: A Simulation and Visualization Study using High-*

Resolution Finite Element Modeling., NeuroImage, 30 (3), 2006, pp. 813–826.

[39] C.H. Wolters, H. Köstler, C. Möller, J. Härtlein, L. Grasedyck and W. Hackbusch, *Numerical mathematics of the subtraction method for the modeling of a current dipole in EEG source reconstruction using finite element head models.*, SIAM J. on Sci. Comp., vol. 30, no.1, pp.24-45, 2007.

[40] C. H. Wolters, A. Anwander, G. Berti and U. Hartmann, *Geometry-adapted hexahedral meshes improve accuracy of finite element method based EEG source analysis.*, IEEE Trans.Biomed.Eng., 54 (8), 2007, pp. 1446–1453.

[41] C.H. Wolters, H. Köstler, C. Möller, J. Härdtlein and A. Anwander, *Numerical approaches for dipole modeling in finite element method based source analysis.*, International Congress Series, 1300, 2007, pp. 189–192, http://dx.doi.org/10.1016/j.ics.2007.02.014.

[42] B. Yvert, A. Crouzeix-Cheylus and J. Pernier *Fast Realistic Modeling in Bioelectromagnetism using lead-field interpolation*, Human Brain Mapping, 14, 2001, pp. 48–63.

[43] T.D. Waberski, H. Buchner, K. Lehnertz, A. Hufnagel, M. Fuchs, R. Beckmann and A. Rienäcker *The properties of source localization of epileptiform activity using advanced headmodelling and source reconstruction.*, Brain Topography,10 (4), 1998, 283–290.

[44] F. Zanow *Realistically shaped models of the head and their application to EEG and MEG.*, PhD thesis, University of Twente, The Netherlands, 1997.

2.11 Improved EEG source analysis using low resolution conductivity estimation in a realistic head model

Improved EEG source analysis using low resolution conductivity estimation in a realistic head model
Lew, S., Wolters C.H., Anwander, A., Makeig, S. and MacLeod, R.S. submitted to *NeuroImage* (2007).

Corresponding author: C.H. Wolters (S. Lew is PhD student of C.H.Wolters and R.S. MacLeod)

Improved EEG source analysis using low resolution conductivity estimation in a realistic head model

S. Lew+ [a,b] C.H. Wolters+ [c,*] A. Anwander [d] S. Makeig [e] R. MacLeod [a,b]

[a] *Scientific Computing and Imaging Institute, University of Utah, Salt Lake City, USA*

[b] *Department of Bioengineering, University of Utah, Salt Lake City, USA*

[c] *Institut für Biomagnetismus und Biosignalanalyse, Universität Münster, Münster, Germany*

[d] *Max-Planck-Institut für Kognitions- und Neurowissenschaften, Leipzig, Germany*

[e] *Swartz Center for Computational Neuroscience, University of California, San Diego, USA*

+ both authors contributed equally to this work.

Abstract

Bioelectric source localization in the human brain from scalp Electroencephalography signals is sensitive to geometry and conductivity properties of the different head tissues. We propose a Low Resolution Conductivity Estimation (LRCE) method using simulated annealing optimization on high-resolution finite element models that individually optimizes a realistically-shaped volume conductor with regard to the tissue conductivities. As input data, the method needs T1- and PD-weighted magnetic resonance images and scalp potential data. Our simulation studies showed that for realistic signal-to-noise somatosensory evoked potentials, the LRCE method was able to simultaneously reconstruct both the brain and the skull conductivity together with the underlying dipole source in somatosensory cortex and provided an improved source analysis result. Furthermore, using scalp potentials with a high signal-to-noise ratio, the LRCE method was even able to simultaneously reconstruct the brain and the skull conductivity together with the underlying bi-hemispheric dipole sources. The new method was then applied to measured tactile somatosensory evoked potentials. The LRCE estimated the brain conductivity to be 0.48S/m, which is higher than the commonly used value of 0.33S/m. The skull conductivity was fitted to the value of 0.004S/m, which is in the range of the commonly used value. With these results, we have shown the viability of an approach that computes its own conductivity values and thus reduces the dependence on assiging values from the literature and likely produces a more robust estimate of

Preprint submitted to NeuroImage *15 October 2007*

source location. Using the LRCE method, the individually optimized (with regard to both geometry and conductivity) volume conductor model can in a second step be used for the analysis of clinical or cognitive data acquired from the same subject.

Key words:
EEG, source localization, realistic head modeling, in vivo conductivity estimation, brain and skull conductivity, simulated annealing, finite element method, somatosensory evoked potentials, T1- and PD-weighted MRI.

---

1 Introduction

The electroencephalographic inverse problem aims at reconstructing the underlying current distribution in the human brain using potential differences measured non-invasively from the head surface. A critical component of source reconstruction is the head volume conductor model used to reach an accurate solution of the associated forward problem, i.e., the simulation of the electroencephalogram (EEG) for a known current source in the brain. The volume conductor model contains both the geometry and the electrical conduction properties of the head tissues and the accuracy of both parameters has direct (but not fully predictable) impact on the accuracy of the source localization (Buchner et al., 1997; Gençer and Acar, 2004; Ramon et al., 2004). The practical challenges of creating patient specific models currently prohibit this degree of customization for each routine case of clinical source localization, thus it is essential to identify the parameters that have the largest impact on solution accuracy and to attempt to customize them to the particular case.

Magnetic Resonance (MR) or Computer Tomography (CT) imaging provides the geometry information for the brain, the cerebrospinal fluid (CSF), the skull, and the scalp (Pham and Prince, 1999; Huiskamp et al., 1999; Wolters, 2003; Ramon et al., 2004). MRI has the advantage of being a completely safe and noninvasive method for imaging the head, while CT provides better definition of hard tissues such as bone. However, CT is not justified for routine

* Corresponding author. Institut für Biomagnetismus und Biosignalanalyse, Westfälische Wilhelms-Universität Münster, Malmedyweg 15, 48149 Münster, Germany, Tel.: +49/(0)251-83-56904, Fax: +49/(0)251-83-56874, http://biomag.uni-muenster.de

Email addresses: slew@sci.utah.edu (S. Lew+), carsten.wolters@uni-muenster.de (C.H. Wolters+), anwander@cbs.mpg.de (A. Anwander), smakeig@ucsd.edu (S. Makeig), macleod@cvrti.utah.edu (R. MacLeod).

physiological studies in healthy human subjects. In this study we used a combination of T1-weighted MRI, which is well suited for the identification of soft tissues (scalp, brain) and proton-density (PD) weighted MRI, enabling the segmentation of the inner skull surface. This approach leads to an improved modeling of the skull thickness over standard (T1) weighted MRI, an important parameter for a successful application of the proposed low resolution conductivity estimation (LRCE) method. The volume conductor model used in this study consisted of four individually and accurately shaped compartments, the scalp, skull, CSF, and brain.

Determining the second component of the head model, the conductivities of the tissues, does not have the support of a technology as capable as MRI or CT. The electric conductivities of the head tissues vary across individuals and within the same individual due to variations in age, disease state and environmental factors. First attempts to measure the conductivities of biological tissues were *in vitro*, often using samples taken from animals (Geddes and Baker, 1967). The conductivity of human CSF has been measured by Baumann et al. (Baumann et al., 1997) and Latikka et al. (Latikka et al., 2001) investigated the conductivity of living intracranial tissues from nine patients under surgery. As the skull has considerably higher resistivity than the other head tissues—and thus could be expected to play a bigger role in the electric currents in the head—much attention focused on determining its conductivity. Rush and Driscoll measured impedances for a half-skull immersed in fluid(Rush and Driscoll, 1968, 1969) and since then the brain:skull conductivity ratio of 80 has been commonly used in bioelectric source analysis (Homma et al., 1995). A similar ratio of 72 averaged over six subjects was reported recently using two different *in vivo* approaches(Gonçalves et al., 2003b), one method using the principles of electrical impedance tomography (EIT) and the other method based on an estimation through a combined analysis of the evoked somatosensory potentials/fields (SEP/SEF). However, those results remain controversial because other studies have reported the following ratios: 15 (based on *in vitro* and *in vivo* measurements)(Oostendorp et al., 2000), 23 (averaged value over nine subjects estimated from combined SEP/SEF data) (Baysal and Haueisen, 2004), 25 (estimated from intra- and extra-cranial potential measurements) (Lai et al., 2005), and 42 (averaged over six subjects using EIT measurements) (Gonçalves et al., 2003a). At this point, there is little hope of a resolution of these large discrepancies, some of which may originate in interpatient differences or natural variations over time, so that we propose an approach that seeks to resolve variation for each individual case by making conductivity an additional parameter to be solved.

The growing body of evidence suggesting that the quality and fidelity of the volume conductor model of the head plays a key role in solution accuracy(Cuffin, 1996; Huiskamp et al., 1999; Ramon et al., 2004) also drives the choice of numerical methods. There is a wide range of approaches including multi-layer sphere models(de Munck and Peters, 1993), the boundary element method (BEM) (Sarvas, 1987; Fuchs et al., 1998; Huiskamp et al., 1999), the finite difference method (Hallez et al., 2005) and the finite element method (FEM) (Bertrand et al., 1991; Yan et al., 1991; Marin et al., 1998; Weinstein et al., 2000; Ramon et al., 2004; Wolters, 2003). The FEM offers the most flexibiliy in assigning both accurate geometry and detailed conductivity attributes to the model at the cost of both creating and computing on the resulting geometric model. The use of recently developed transfer matrix (or lead field bases) approaches (Weinstein et al., 2000; Gençer and Acar, 2004; Wolters et al., 2004) and advances in efficient FEM solver techniques for source analysis (Wolters et al., 2002) drastically reduce the complexity of the computations so that the main disadvantage of FEM modeling no longer exists.

In this paper, we propose a Low Resolution Conductivity Estimation (LRCE) method using simulated annealing optimization in a realistically-shaped four compartment (scalp, skull, CSF and brain) finite element volume conductor model that individually optimizes the brain and the skull conductivity parameters. Like other source localization approaches, the LRCE method uses a geometric model, in this case based on T1-/PD-MRI, and scalp potentials as input. The method then determines the best combination of sources within the somatosensory cortex together with the two individually optimized brain and skull conductivity values over a discrete parameter space, i.e., for each source and for each tissue conductivity the user has to define a reasonable set of *a priori* values. We evaluate the accuracy of the LRCE method in simulation studies before applying it to tactile somatosensory evoked potentials with the focus on establishing the best values for the individual brain and skull conductivity. Besides using our new method for an improved source analysis of somatosensory evoked potentials, the major future perspective for the LRCE is to provide an individually optimized volume conductor model that can then be used in a second step for the analysis of clinical or cognitive EEG data.

2 Theory

2.1 Finite element method based forward problem

In the considered low frequency band (frequencies below 1000 Hz), the capacitive component of tissue impedance, the inductive effect and the electromagnetic propagation effect can be neglected so that the relationship between bioelectric fields and the underlying current sources in the brain can be represented by the quasi-static Maxwell equation

$$\nabla \cdot (\sigma \nabla \phi) = \nabla \cdot j_p \text{ in } \Omega \tag{1}$$

with homogeneous Neumann boundary conditions at the head surface

$$\sigma \frac{\partial \phi}{\partial n} \;=\; 0 \text{ on } \Gamma = \partial\Omega \tag{2}$$

and a reference electrode with given potential, i.e., $\phi(x_{ref}) = 0$, where σ is the conductivity distribution, ϕ is the scalar electric potential, j_p is the primary (impressed) current, Ω the head domain, Γ its surface and n the surface normal at Γ (Plonsey and Heppner, 1967; Sarvas, 1987). The primary current is generally modeled by a mathematical dipole at position x_0 with the moment M_0, $j_p = M_0\delta(x - x_0)$. For a given primary current and conductivity distribution, the potential can be uniquely determined for what is known as the *bioelectric forward problem.*

For the numerical approximation of equations (1) and (2) in combination with the reference electrode, we use the finite element (FE) method. Three different FE approaches for modeling the source singularity are known from the literature: a subtraction approach(Bertrand et al., 1991; Wolters et al., 2007b), a Partial Integration direct method (Weinstein et al., 2000), and a Venant direct method (Buchner et al., 1997). In this study we used the Venant approach based on comparison of the performance of all three in multilayer sphere models, which suggested that for sufficiently regular meshes, it yields suitable accuracy over all realistic source locations (Wolters et al., 2007a,b). This approach has the additional advantage of high computational efficiency when used in combination with the lead field basis approach (Wolters et al., 2004). We used standard piecewise linear basis functions $\varphi_i(x) = 1$ for $x = \xi_i$, where ξ_i is the i-th FE node, and $\varphi_j(x) = 0$ for all $j \neq i$. The potential is projected into the FE space, i.e., $\phi(x) \approx \phi_h(x) = \sum_{j=1}^{N} \varphi_j(x)u_j$, where N is the number of FE nodes. Standard variational and FE techniques for equations (1) and (2) yield the linear system

$$\begin{aligned} K \cdot u &= J^{Ven} \\ K_{ij} &= \int\limits_{\Omega} < \nabla\varphi_i, \sigma\nabla\varphi_j > \mathrm{d}\Omega,\; 1 \leq i,\; j \leq N, \end{aligned} \tag{3}$$

where K is the stiffness matrix (N * N), u the coefficient vector for ϕ_h (N * 1), J^{Ven} the Venant approach right-hand-side vector (N * 1) (Buchner et al., 1997; Wolters et al., 2007a), and $< \cdot, \cdot >$ the scalar product.

A key feature of this study was to pursue solutions that achieve high computational efficiency. With S the number of scalp electrodes, R the number of possible source locations, and C the number of neighbors of the closest FE node to the dipole source, J^{Ven} is particularly sparse because it has only C non-zero entries. Thus the resulting combination of the lead field basis approach with the Venant method leads to implementations that are especially efficient, an essential feature for our study as will become clear in Section 2.3. We distinguish clearly here between the *lead field basis* (a matrix of dimension $S \times N$) and the *influence matrix* (a matrix of dimension $S \times R \cdot 3$) (Wolters et al., 2004). To solve numercially the resulting linear FE equations, we employed an algebraic multigrid preconditioned conjugate gradient (AMG-CG) method (Wolters et al., 2002), solved to a relative error of 10^{-9} in the controllable $KN^{-1}K$-energy norm (with N^{-1} one V-cycle of the AMG).

2.2 The inverse problem: Dipole fit in a discrete influence space

The non-uniqueness of the EEG inverse problem requires a combination of a viable forward problem, anatomical information, and *a priori* constraints on some aspect(s) of the solution. Here, we followed a dipole fit procedure that restricted the number of active sources to an application dependent number, k, of some few dipoles (Scherg and von Cramon, 1985; Mertens and Lütkenhöner, 2000). In addition, we defined a set of R discrete permissable source locations, or an influence space that was constrained to nodes of the geometric model that lay within the cortical gray matter. Given this influence space, the S scalp electrode locations, and a fixed volume conductor, we used the fast FE forward computation methods from Section 2.1 to compute an influence matrix, L, which mapped sources directly to electrode potentials:

$$L \cdot J = \Phi_{sim}, \tag{4}$$

where J is a current source vector of dimension $3R \times 1$ defined at the discrete source space and Φ_{sim} is the simulated potential vector of dimensiona $S \times 1$. L has dimension $S \times 3R$ because we do not use the normal constraint, i.e., sources on the discrete influence space can have orientations in any direction.

Since the potential depends linearly on the source moment (dipole direction and strength) and nonlinearly on the source location, we use a two phase approach for source localization (Buchner et al., 1997; Wolters et al., 1999). We start with k initial source locations and apply a linear least squares fit to the EEG data that determines uniquely the source orientation and strength, J_s $(3k*1)$. The numerical solver employed a TSVD (Truncated Singular Value Decomposition) with a threshold of 10^{-6} for the minimization (Wolters et al., 1999), based on a cost function, g_f, that is the L_2 norm of the difference between the simulated potential, Φ_{sim}, and the measured EEG potential, Φ_{EEG} $(S*1)$:

$$g_f = min \, \|\Phi_{EEG} - \Phi_{sim}\|_2 = \min_{J_s} \|\Phi_{EEG} - L_s \cdot J_s\|_2 \tag{5}$$

In this equation, L_s $(S * 3k)$ indicates the reduced influence matrix for the current choice of source locations $s = (s_1, \cdots, s_k)$ with s_i the i-th source location $(1 \leq i \leq k)$.

2.2.1 Globally minimizing the cost function

Since the volume conduction properties are incorporated in the influence matrix L_s, the free nonlinear optimization parameters in this case are only the source locations. Optimization methods such as the Nelder-Mead simplex approach (Nelder and Mead, 1965), the Levenberg-Marquardt algorithm (Marquardt, 1963), and Simulated Annealing (SA) from combinatorial optimization (Kirkpatrick et al., 1983) are all able to update the source locations based on the previous source location and misfit value. The optimization procedure continues until the cost function meets a predefined tolerance criterion or a maximum allowable number of iterations. The challenge of local optimizers such as the Nelder-Mead simplex and the Levenberg-Marquardt algorithm lies in determining the initial estimation of multiple parameters in the presence of multiple local minima; a global optimizer such as SA is generally more effective in localizing multiple parameters because it eliminates the need for high quality initial estimates (Haneishi et al., 1994; Gerson et al., 1994; Uutela et al., 1998; Wolters et al., 1999). We used an SA method that follows the Metropolis algorithm for the stochastic optimization process (Metropolis et al., 1953). The energy (the cost function in our case) for the assigned parameters in each iteration was compared with a previous energy and when the energy state was smaller than the previous $\Delta E < 0$, the parameters were always accepted. When the energy was larger than the previous $\Delta E > 0$, the acceptance of the parameters depended on the probability based on the Metropolis criterion (6) (Kirkpatrick et al., 1983). This stochastic acceptance test prevents the search from getting trapped in local minima.

The following equation describes the process:

$$\begin{aligned} P(\Delta E, T) &= \exp^{-(\Delta E/T)} \\ T &= f_T \cdot T_{previous}, \end{aligned} \tag{6}$$

where T is a so-called temperature factor that regulates the acceptance probability. Throughout the optimization process, T decreases according to a cooling rate f_T. When the cooling is slow enough, SA has been shown to converge to the global minimum of a given cost function in a large search space (Geman and Geman, 1984). Initially the temperature is set to a high value, resulting in the acceptance of most new parameters and as the temperature decreases, it is less likely for new parameters to be accepted. This enables the search to focus on the vicinity of the minima at the later stages of the optimization process.

2.3 Low resolution conductivity estimation

The proposed LRCE method adds electrical tissue conductivities as additional optimization parameters to the cost function to the already parameterized source locations. Here the set of optimization parameters including the conductivities was

$$X = \{s, \sigma\} = \{s_1, s_2, \cdots, s_k, \sigma_1, \sigma_2, \cdots, \sigma_l\}, \tag{7}$$

where σ_i is the conductivity parameter for the i-th tissue compartment ($1 \leq i \leq l$, l is the number of tissue compartments). Each source location s_i was allowed to vary within the defined discrete influence space as described in Section 2.2. The conductivity σ_i of tissue compartment i was allowed to have its value from a predefined discrete set of possible conductivity values

$$\sigma_i \in \{\sigma_{1j_i}, 1 \leq j_i \leq h_i\}. \tag{8}$$

Here, h_i is the number of possible conductivity values for tissue compartment i. Theoretically we could choose h_i to be a large number (high resolution) for each tissue, but this would strongly increase computational costs and might be rather unrealistic given the limited SNR in measured EEG data. Therefore, we confined each tissue to a rather small set of conductivity values.

Given the influence source space and the electrode locations, we precomputed a set of influence matrices and collected them in a global influence matrix, Λ, which corresponded to all possible combinations (with repetition taking into account the ordering) of conductivity values for all tissue compartments of interest. This resulted in the number $\prod_{i=1}^{l} h_i$ of influence matrices in Λ.

$$\Lambda = \{L\left(\sigma_{1j_1}, \ldots, \sigma_{1j_l}\right) : 1 \leq j_i \leq h_i, 1 \leq i \leq l\}, \tag{9}$$

with $L\left(\sigma_{1j_1}, \cdots, \sigma_{lj_l}\right)$ being the $(S*3R)$ influence matrix for the specific choice of conductivities. Here, we describe an extension to the EEG lead field basis approach, described in Section 2.1, aimed at enhancing the computation of Λ. During each iteration of the SA method, the set of optimization parameters includes not just a new estimate of the bioelectric source, but a new configuration of both sources and conductivities in which we allow changing the value of only one parameter chosen randomly per iteration. By limiting the choice of conductivities to a discrete set of values, we maintain computational efficiency by applying the associated precomputed influence matrix Λ. The total number of possible configurations for sources and conductivities is

$$\prod_{i=1}^{k}(R-i+1)\cdot\prod_{i=1}^{l}h_i. \tag{10}$$

The SA optimizer searches for an optimal configuration of dipole source locations s and tissue conductivities σ that ensure the best fit to the measured data:

$$g_f = \min_{s,\sigma} \|\Phi_{EEG} - \Phi_{sim}(s,\sigma)\|_2 = \min_{s,\sigma} \|\Phi_{EEG} - L_s(\sigma)\cdot J_s\|_2 \tag{11}$$

The following summarizes the general procedure of the low resolution conductivity estimation.

- Define the discrete influence space with R nodes.
- Fix the number k of sources to be fitted.
- Define a discrete set of conductivity values for each tissue, i.e., fix all σ_{ij_i}, $1 \le i \le l$
- Precompute the global influence matrix Λ corresponding to each of the possible conductivity combinations.
- **Repeat:**
  - Allow SA optimizer to choose a configuration of source locations $s = (s_1, \cdots, s_k)$ and conductivities $\sigma = (\sigma_1, \cdots, \sigma_l)$
  - Get lead field matrix $L_s(\sigma)$ for the chosen source and conductivity configuration.
  - Compute a cost function, $g_f = min\|\Phi_{EEG} - L_s(\sigma)J_s\|_2$ with respect to source moments J_s.
- **Until** cost function meets a tolerance criterium or the number of iterations exceeds a limit.
- Accept the configuration of source locations and conductivities as an optimal configuration.

3 Methods and materials

Mesh generation

To carry out the LRCE analysis requires the construction of detailed realistic head models, in this case from MRI image data. Here we outline the steps for costructing such a model. Our approach emphasizes accurate modeling of the skull thickness, as the influence of this parameter is closely related to the influence of skull conductivity and therefore important for a successful application of the presented LRCE algorithm.

MRI data acquisition

To achieve the required accuracy of the head models, we made use of a combination of two different MRI modalities applied to a single subject. T1-weighted MRI is well suited for the segmentation of tissue boundaries like gray matter, outer skull and skin. In contrast, the identification of the inner skull surface is more successful from a Proton density MRI (PD-MRI) sequence because the difference in the quantity of water protons between intracranial and bone tissues is large. MR imaging of a healthy 32 year-old, male subject was performed on a 3 Tesla whole-body scanner (Medspec 30/100, Bruker, Ettlingen/Germany). For the T1-MRI, an inversion recovery MDEFT sequence (Lee et al., 1995) was employed (flip angle of 25°, TR=11.7 ms, TE=6 ms, TMD=1.3 s). For the 3D PD-MRI, acquired one week later, we used a 3D FLASH protocol (Haase et al., 1986) with TE=6 ms, a flip angle of 25°, and TR=11.7 ms. The scan resolution was 1 x 1 x 1.5 mm^3 in both acquisitions, which were linearly interpolated to an isotropic 1 mm^3 voxel size.

Registration and Segmentation

To construct a realistic volume conductor model requires segmentation of the different tissues within the head with special attention to the poorly conducting human skull and the highly conductive CSF (Cuffin, 1996; Huiskamp et al., 1999; Ramon et al., 2004). In order to correct for different subject positions and geometrical distortions, we first aligned T1- and PD-MRI images with a voxel-similarity based affine registration without pre-segmentation using a cost-function based on mutual information (Wolters, 2003). The T1 images provided the information on soft tissues while the registered PD image enabled the segmentation of the inner skull surface and thus a correct modeling of skull and CSF compartmental thickness. Our nearly automatic segmentation process consisted of a 3D implementation of an Adaptive Fuzzy C-Means classification method that compensates for image intensity inhomogeneities (based on the original work in two dimensions of Pham and Prince (Pham and Prince, 1999)), followed by a deformable model algorithm to smooth the inner and outer skull surfaces (Wolters, 2003). We segmented four head compartments out of the bimodal dataset; skin, skull, CSF, and brain. In source reconstruction, it is generally accepted that the weak volume currents outside the skull and far away from the EEG sensors have a negligible influence on the measured fields (Buchner et al., 1997; Fuchs et al., 1998). We therefore did not make any effort to segment the face and used instead a cutting procedure typical in realistic source analysis (Buchner et al., 1997; Fuchs et al., 1998). Figure 1 shows the results of this approach for the segmentation of the inner skull surface compared with results from an estimation procedure that used exclusively the T1-MRI. The estimation procedure started from a segmented brain surface and estimateed the inner skull by means of closing and inflating the brain surface. Figure 2 shows a magnification of an area in which the

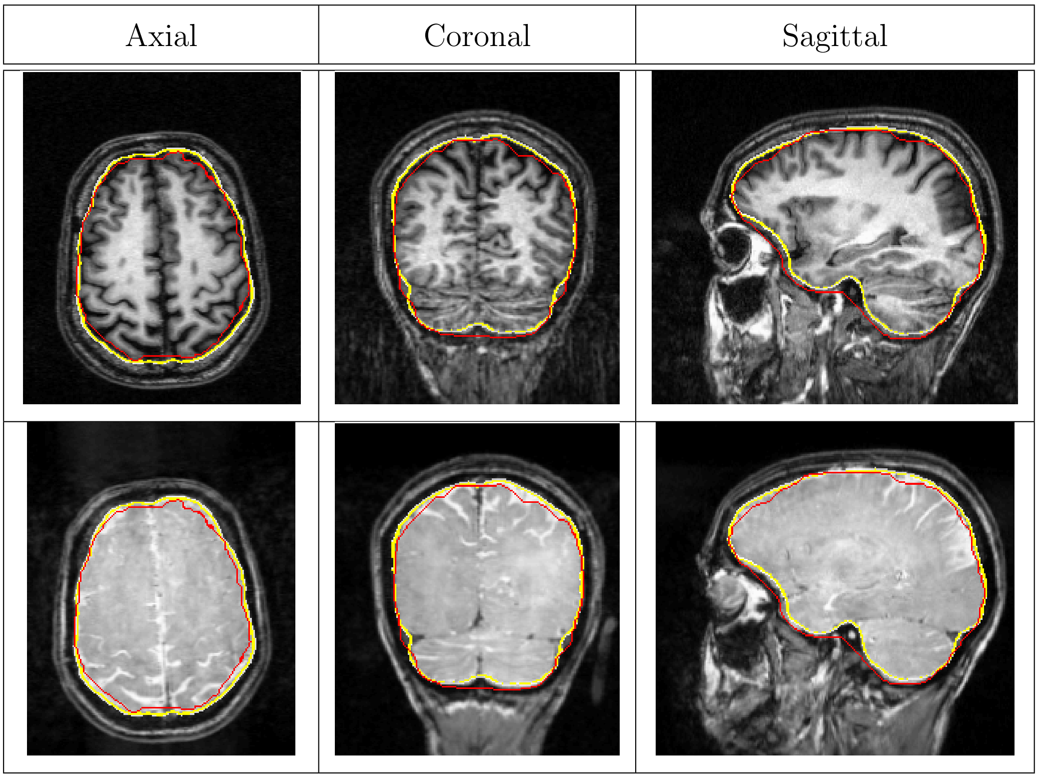

Fig. 1. Segmentation of the inner skull surface: Comparison of the results using the bimodal T1- and PD-MRI data set (in yellow) with the inner skull estimation approach using exclusively the T1-MRI (in red) on underlying T1-MRI (top row) and PD-MRI (bottom row).

bimodal MRI approach significantly improved the modeling of skull and CSF compartmental thickness.

Volume conductor FE mesh generation

A prerequisite for FE modeling is the generation of a mesh that represents the geometric and electric properties of the head volume conductor. To generate the mesh, we used the CURRY software (CURRY, 2000) to create a surface-based tetrahedral tessellation of the four segmented compartments (skin, skull, CSF, brain). The procedure exploited the Delaunay-criterion, enabling the generation of compact and regular tetrahedra (Buchner et al., 1997; Wolters, 2003) and resulted in a finite element model with 245,257 nodes and 1,503,357 tetrahedra elements. The FE mesh is shown in Figure 3.

Influence space mesh generation

An influence source space that represented the brain gray matter in which dipolar source activities occur was extracted from a surface 2 mm beneath the outer cortical boundary. The influence space was tessellated with a 2 mm mesh resulting in 21,383 influence nodes and 42,916 triangular elements (shown in Figure 3 together with the FE model). Since any influence mesh is only a rough

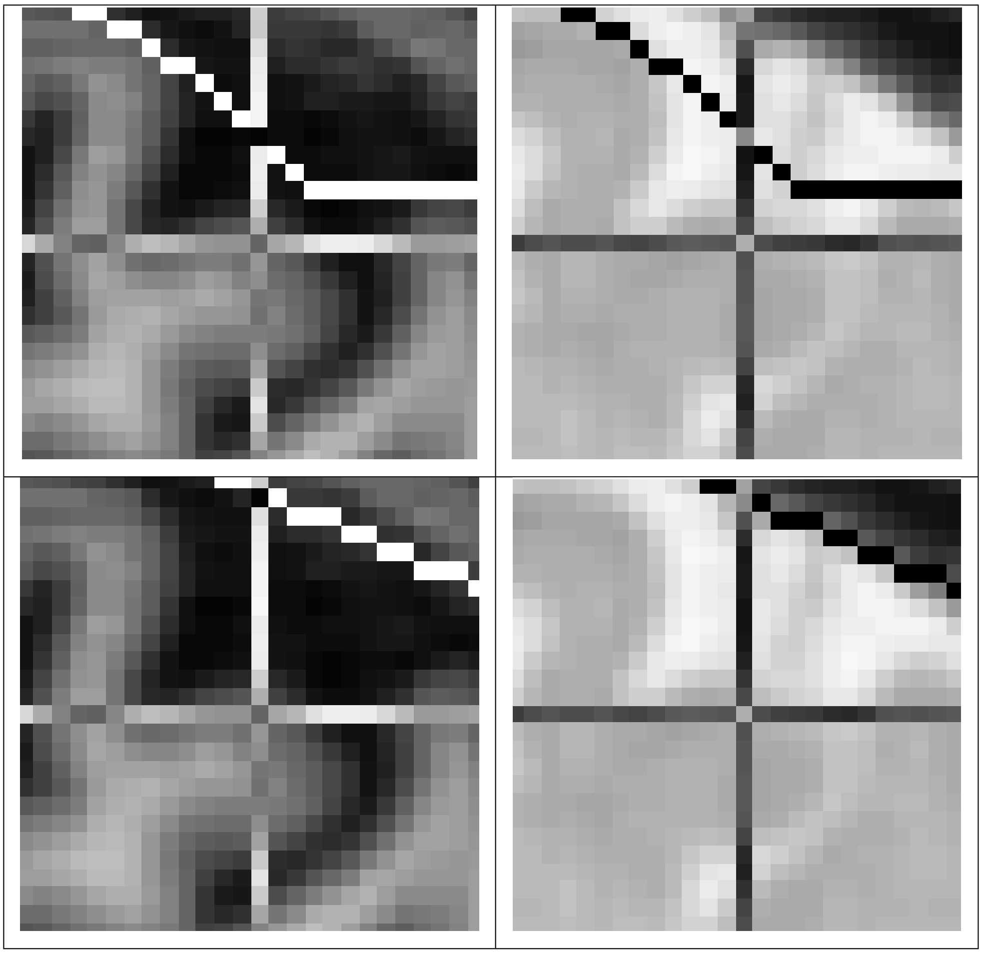

Fig. 2. Segmentation of the inner skull surface: Result of the estimation procedure (upper row) on T1-MRI (left) and PD-MRI (right) and result of the bimodal T1- and PD-MRI approach (lower row). The parietal area of the neurocranial roof was magnified where the CSF layer is thicker than being estimated by means of the T1-MRI based estimation procedure.

approximation of the real folded surface and does not appropriately model the cortical convolutions and deep sulci, no normal-constraint was used, i.e., the dipole sources were not restricted to be oriented perpendicular to the source space. Instead, dipole sources in the three Cartesian directions were allowed.

Setup of the LRCE simulation studies

Simulation studies were carried out to validate the new LRCE approach. For the reference volume conductor, isotropic conductivity values of 0.33 (see (Haueisen, 1996) and references therein), 0.0132 (Lai et al., 2005), 1.79 (Baumann et al., 1997), and 0.33 S/m (see (Haueisen, 1996) and references therein) were assigned to the scalp, skull, CSF, and brain compartment, respectively. This led to a brain:skull ratio of 25 for the reference volume conductor. For the modeling of the EEG, 71 electrodes were placed on the reference volume conductor surface according to the international 10/20 EEG system.

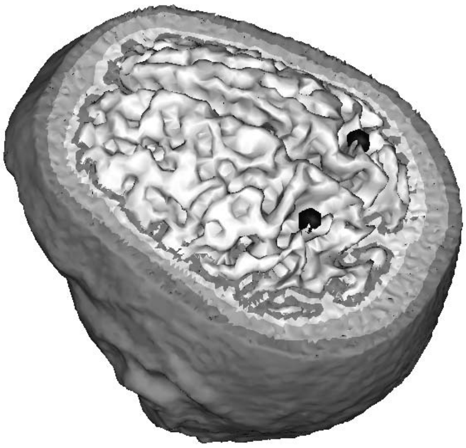

Fig. 3. Four compartment (scalp, skull, CSF and brain) realistic finite element head model together with the cortical influence source space, visualized by SCIRun. The somatosensory dipole source positions are indicated by black dots.

Two reference dipole sources were positioned on influence nodes in area 3b of the primary somatosensory cortex (SI) in both hemispheres, as shown in Figure 3. Two source orientation scenarios were considered, in which both sources were either oriented quasi-tangentially or quasi-radially with regard to the inner skull surface. In both scenarios, the two sources were simultaneously activated using current densities of 100 nAm. Another experiment consisted of just a single source in the left SI with quasi-tangential or quasi-radial direction and a source strength of 100 nAm. Forward potential computations were carried out for the different scenarios using the direct FE approach as described in Section 2.1. Noncorrelated Gaussian noise was then added such that the signal-to-noise-ratio (SNR) were 40, 25, 20, and 15 dB, where SNR in dB is calculated as $20 * \log_{10}(\frac{\sum_{i=1}^{S}|R_i|}{\sum_{i=1}^{S}|R_i - N_i|} \cdot \frac{1}{S})$, with N_i being the noisy signal, R_i the noise-free reference signal at electrode i, and S the number of electrodes.

Figure 4 shows the potential maps for the two-sources experiment for both orientation scenarios, the quasi-tangential (top row) and the quasi-radial orientations (bottom row) for different SNR values.

SEP measurement

We measured somatosensory evoked potential (SEP) data in order to apply our LRCE approach to real empirical EEG data. Tactile somatosensory stimuli were presented to the right index finger of the right-handed subject from Section 3 using a balloon diaphragm driven by bursts of compressed air. We compensated for the delay between the electrical trigger and the arrival of the pressure pulse at the balloon diaphragm as well as the delay caused by the inertia of the pneumatic stimulation device (half-way displacement of the membrane), together 52 ms in our measurements. Following standard practice (Mertens and Lütkenhöner, 2000), the stimuli were presented at 1 Hz (±10%

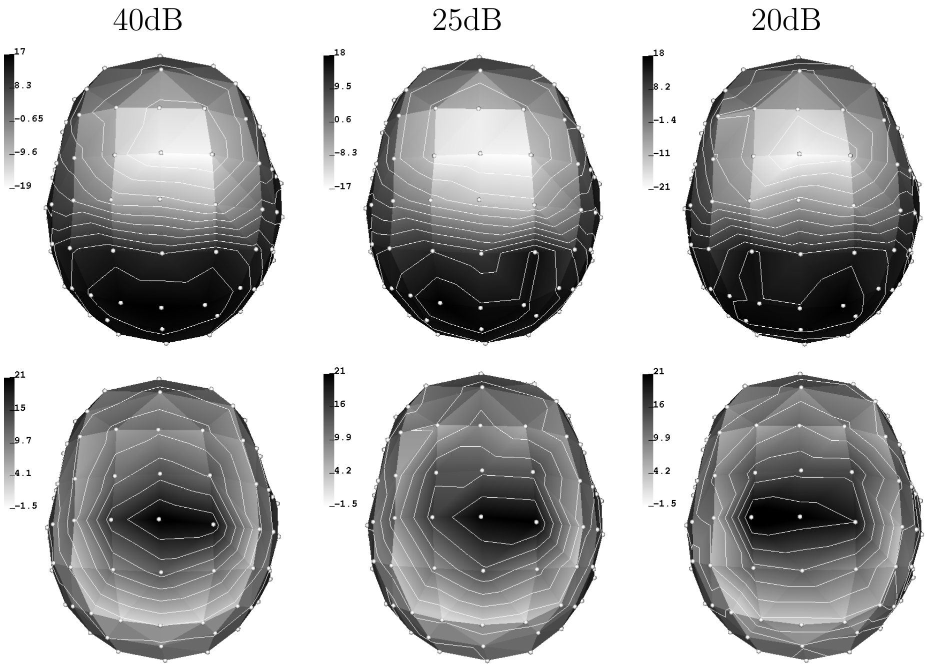

Fig. 4. Simulated noisy (40, 25, and 20dB from left to right) reference data for the two-sources and two orientation scenarios in the reference volume conductor model (σ_{brain}:σ_{skull} = 25). The top row shows the maps of the simultaneously active quasi-tangentially oriented somatosensory sources and the bottom row the quasi-radially oriented source. The potential maps are linearly interpolated over the electrodes (white spheres). White lines indicate isopotentials (in μV).

variation to avoid habituation effects). A 63 channel (10% system) CTF EEG system (VSM Medtech Ltd.) recorded the raw time signals for the SEP study. Two EOG (Electro-oculo-graphy) electrodes were furthermore used for horizontal and vertical eye movement control. The collection protocol consisted of three runs of 10 minutes each EEG data with a sampling rate of 1200 samples/sec using a real time low pass filter of 0-300 Hz. The BESA software (BESA, 2007) was then used for a rejection of noise-contaminated epochs (e.g., epochs containing eye movements detected by means of the EOG channels) and for averaging the non-contaminated epochs within each run. In order to optimize the SNR, the SEP data were furthermore averaged over the three averaged runs. The baseline-corrected (from -35 ms to 0 ms pre-stimulus) averaged EEG dataset was filtered using a 4th order butterfly digital filter with a bandwidth of 0.1 to 45 Hz. When using the prestimulus interval between -20 ms and 0 ms for the determination of the noise level and the peak of the first tactile component at 35.3ms as the signal, we achieved a SNR of 24dB. Finally, by means of a channel-selection procedure (43 out of the 63 EEG electrodes), we were able to even increase the SNR to 26.4 dB. A butterfly- and a position-plot of the SEP data is shown in Fig. 5.

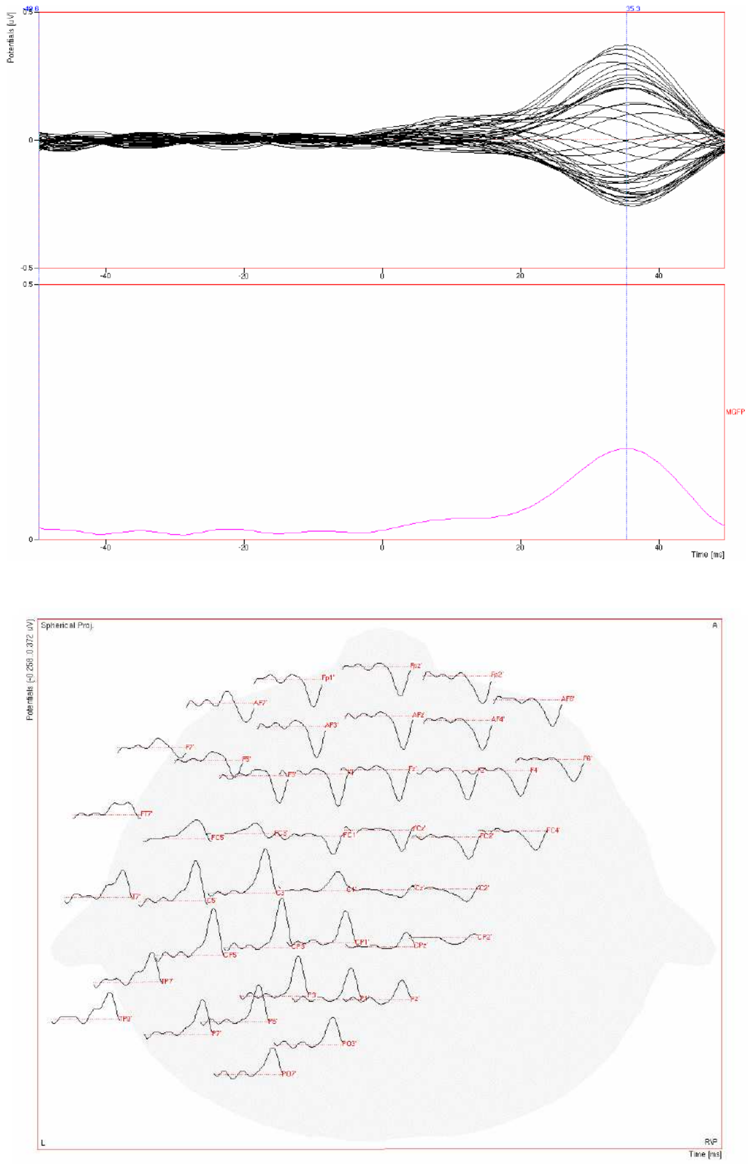

Fig. 5. First tactile SEP component at the 43 selected electrodes. Selection was performed in order to optimize the SNR. (a) Butterfly and (b) position plot.

4 Results

4.1 LRCE simulation studies

4.1.1 Simultaneous reconstruction of brain and skull conductivity and a pair of somatosensory sources

We performed the LRCE procedure as desribed in Section 3 with an inverse two-dipole fit on the discrete influence space, while additionally allowing skull

Table 1
Results of the LRCE algorithm when applied to the simultaneous reconstruction of the brain and the skull conductivity together with a pair of active sources in the somatosensory cortex.

Reference SEP	Localization error(mm)		Estimated conductvity		Residual
(tangential)	right dipole	left dipole	$\sigma_{brain}(S/m)$	$\sigma_{brain} : \sigma_{skull}$	expl. var.(%)
Noise free	0	0	0.33	25	100
40dB	2.246	2.246	0.33	25	99.76
25dB	3.175	10.721	0.12	10	99.06
20dB	13.436	10.388	0.48	15	97.44
Reference SEP	Localization error(mm)		Estimated conductvity		Residual
(radial)	right dipole	left dipole	$\sigma_{brain}(S/m)$	$\sigma_{brain}/\sigma_{skull}$	expl. var.(%)
Noise free	0	0	0.33	25	100
40dB	3.013	3.013	0.33	25	99.44
25dB	6.430	7.379	0.48	25	96.57
20dB	5.218	12.462	0.48	25	92.76

and brain conductivity to vary as free discrete optimization parameters. The permitted brain conductivities (σ_{brain}) were 0.12, 0.33 (Haueisen, 1996), and 0.48 S/m with scalp and brain conductivities set to be equal. For each brain conductivity, the skull conductivity (σ_{skull}) was allowed to vary so as to achieve brain:skull ratios of 80, 40, 25, 15, 10, 8, and 5. The CSF conductivity remained fixed at 1.79 S/m. This resulted in a total of 21 conductivity configurations.

$$
\begin{aligned}
X &= \{s_{left_{somato}},\ s_{right_{somato}},\ \sigma_{skull},\ \sigma_{brain}\} \\
\sigma_{brain} &\in \{0.12,\ 0.33,\ 0.48\ S/m\} \\
\sigma_{skull} &\in \{\sigma_{brain}/r,\ where\ r = 80, 40, 25, 15, 10, 8, 5\} \\
\sigma_{scalp} &= \ \sigma_{brain},\quad \sigma_{CSF} = \ 1.79\ S/m
\end{aligned}
$$

Following Equation (10), the total number of possible source and conductivity configurations in this simulation was thus approximately 9.3 billion. For the SA optimization, we used a very slow cooling schedule with the cooling rate (f_T) of 0.99 in order to make sure that the search reached the global minimum of the cost function. The current acceptance probability was determined by setting a current temperature T_k at 99% of the previous temperature T_k, i.e., $T_{k+1} = 0.99 * T_k$. The maximum number of SA iterations was set to 50 million.

Table 1 contains the LRCE results for the simulated reference SEP data. In this table, the localization error is defined as the Euclidian distance between the somatosensory reference source locations and the inversely fitted ones resulting from the LRCE. The residual variance v was calculated as the percentile misfit between the noisy reference potential and the fitted potential that was computed from the fitted source parameters and conductivities. The explained variance shown in the table is $100\% - v$. As Table 1 shows, besides appropriately localizing both sources, the LRCE was able to accurately select the reference conductivity values of the brain and the skull compartment in the cases of noise free and low-noise (40 dB SNR) SEP data. However, for the noisy data with a SNR of 25 or lower, neither the somatosensory sources nor the brain and the skull conductivity values could be selected correctly.

4.1.2 Simultaneous reconstruction of brain and skull conductivity and a single source in the left somatosensory cortex

In the second simulation, we first generated noise-free and noisy reference data for a single dipole source in the left somatosensory cortex and then performed a single dipole fit with skull and brain conductivity as two additional free optimization parameters in the LRCE. We used the same scalp, skull, CSF, and brain conductivity values as in the previous simulation:

$$\begin{aligned} X &= \{s_{left_{somato}},\ \sigma_{skull},\ \sigma_{brain}\} \\ \sigma_{brain} &\in \{0.12,\ 0.33,\ 0.48\ S/m\} \\ \sigma_{skull} &\in \{\sigma_{brain}/r,\ where\ r = 80, 40, 25, 15, 10, 8, 5\} \\ \sigma_{scalp} &= \ \sigma_{brain},\quad \sigma_{CSF} = \ 1.79\ S/m \end{aligned}$$

The number of possible source and conductivity configurations was 449K, which was also used as the maximum number of SA iterations and the cooling rate (f_T) was set to 0.99.

As shown in Table 2, the conductivity was accurately estimated for reference data with 40dB and 25dB SNR and the localization errors were acceptable. For 20dB, the localization was still acceptable, but the brain conductivity was no longer correctly reconstructed, while the skull to brain conductivity ratio was still correct. Still higher noise levels led to inacceptable results.

4.1.3 Simultaneous reconstruction of the brain:skull conductivity ratio and a pair of somatosensory sources

Using the reference volume conductor model and the reference SEP data from Section 3, we carried out a third simulation, in which only skull conductivity was allowed to vary with a fixed conductivity values for brain (0.33 S/m),

Table 2
Results of the LRCE algorithm when applied to the simultaneous reconstruction of the brain and the skull conductivity together with single source in the left somatosensory cortex.

Reference SEP	Localization error	Estimated conductvity		Residual
(tangential)	(mm)	$\sigma_{brain}(S/m)$	$\sigma_{brain} : \sigma_{skull}$	expl. var.(%)
Noise free	0	0.33	25	100
40dB	0	0.33	25	99.85
25dB	2.245	0.33	25	96.73
20dB	4.141	0.48	25	95.76
15dB	9.420	0.12	25	83.39
Reference SEP	Localization error	Estimated conductvity		Residual
(radial)	(mm)	$\sigma_{brain}(S/m)$	$\sigma_{brain}/\sigma_{skull}$	expl. var.(%)
Noise free	0	0.33	25	100
40dB	0	0.33	25	99.94
25dB	2.246	0.33	25	98.40
20dB	4.140	0.12	25	90.04
15dB	10.769	0.48	10	78.95

scalp (0.33 S/m), and CSF (1.79 S/m). The brain:skull conductivity ratio was chosen as follows.

$$
\begin{aligned}
X &= \{s_{left_{somato}},\ s_{right_{somato}},\ \sigma_{skull}\} \\
\sigma_{brain} &= \sigma_{scalp} = 0.33\ S/m,\ \sigma_{CSF} = 1.79\ S/m \\
\sigma_{skull} &\in \{\sigma_{brain}/r,\ where\ r = 80, 40, 25, 15, 10, 8, 5\}
\end{aligned}
$$

The total number of possible source and conductivity configurations for this scenario was 3.1 billions and again we used a cooling rate of $(f_T) = 0.99$ and a maximum number of SA iterations of 10 million.

As shown in Table 3, for both source orientation scenarios, the LRCE estimated the skull conductivity correctly up to a 20 dB level, while acceptable source localization errors were only achieved up to 25 dB. The LRCE reconstruction failed to give acceptable results for both the source positions and the brain:skull conductivity ratio only at noise ratios at or above 15 dB.

Table 3
Results of the LRCE algorithm when applied to the simultaneous reconstruction of the brain:skull conductivity ratio and of a pair of active sources in the somatosensory cortex.

Reference SEP	Localization error(mm)		Estimated	Residual
(tangential)	right dipole	left dipole	$\sigma_{brain}/\sigma_{skull}$	expl. var.(%)
Noise free	0	0	25	100
40dB	2.246	2.246	25	99.76
25dB	2.008	3.329	25	99.04
20dB	6.025	5.941	25	97.43
15dB	17.596	41.099	15	64.31
Reference SEP	Localization error(mm)		Estimated	Residual
(radial)	right dipole	left dipole	$\sigma_{brain}/\sigma_{skull}$	expl. var.(%)
Noise free	0	0	25	100
40dB	3.013	3.013	25	99.44
25dB	7.379	7.511	25	96.55
20dB	5.218	10.676	25	92.72
15dB	24.639	13.209	5	89.14

4.1.4 Simulation with a fixed condcutivty and a pair of somatosensory sources

In a last simulation, volume conductors with fixed skull conductivity values from the set of σ_{skull} were used. For these fixed volume conductors, only the two somatosensory sources were reconstructed on the discrete influence space using the simulated annealing optimizer with reference EEG data at a SNR of 25dB.

The results in Table 4 show the effects of an erroneous choice of the brain:skull conductivity ratio (80, 40, 15, 10, 8, 5) on the localization accuracy in comparison to the localization errors caused just by the the addition of noise when using the correct brain:skull ratio of 1:25. Incorrect skull conductivity within the source localization caused large localization errors. As expected, the correct skull conductivity ($\sigma_{brain}/\sigma_{skull} = 25$) gave the smallest localization errors and the highest explained variance for both source orientation scenarios.

Table 4
Localization error(mm) for a fixed brain:skull conductivity ratio using the simulated reference SEP data with a SNR ratio of 25dB. Residual variance in %.

σ_{brain}	Tangential source			Radial source		
to σ_{skull}	right	left	expl. var.	right	left	expl. var.
80	12.702	10.816	98.562	13.131	15.230	95.924
40	3.757	11.228	98.960	7.514	8.281	96.445
25	2.008	3.329	99.042	7.379	7.511	96.548
15	3.175	10.725	99.038	6.736	10.041	96.452
10	2.246	10.722	98.993	7.101	10.862	96.297
8	7.101	10.722	98.692	10.093	10.769	96.093
5	3.330	20.531	98.892	9.992	18.131	96.281

4.2 Application of LRCE to the SEP data

In a last examination, the new LRCE algorithm was applied to the post stimulus P35 component of the averaged SEP data at the peak latency of 35.3ms as indicated in Figures 5. The detailed four compartment (scalp, skull, CSF, and brain) finite element model with improved segmentation of the skull geometry described in Section 3 was used as the volume conductor. Because of the limiting SNR of 26.4 dB for the SEP data and based on our simulation results from Section 4.1, we focused on the simultaneous reconstruction of the contralateral somatosensory P35 source in combination with the estimation of both the brain and the skull conductivities. Accordingly, we assigned fixed isotropic conductivities to scalp (0.33 S/m) and fixed CSF conductivity (1.79 S/m). Again, the source space from Section 3 was used as the influence space for simulated annealing optimization together with brain:skull conductivity ratios of 140, 120, 100, 80, 72, 60, 42, 25, 23, 15, 10, 8 and 5 ((Hoekema et al., 2003), who claimed ratios of 10 up to only 4).

$$
\begin{aligned}
X &= \{s_{somato},\ \sigma_{brain},\ \sigma_{skull}\} \\
\sigma_{scalp} &= \ 0.33\ S/m,\ \ \sigma_{CSF} = \ 1.79\ S/m \\
\sigma_{brain} &\in \{0.12,\ 0.33,\ 0.48,\ 0.57\ S/m\} \\
\sigma_{skull} &= \{\sigma_{brain}/r,\ \ where\ r = 140, 120, 100, 80, 72, 60, 42, 25, 23, 15, 10, 8, 5\}
\end{aligned}
$$

The total number of possible source and conductivity configurations, as well as the maximum of SA iterations was 1,026K and we again chose an SA cooling rate of $(f_T) = 0.99$.

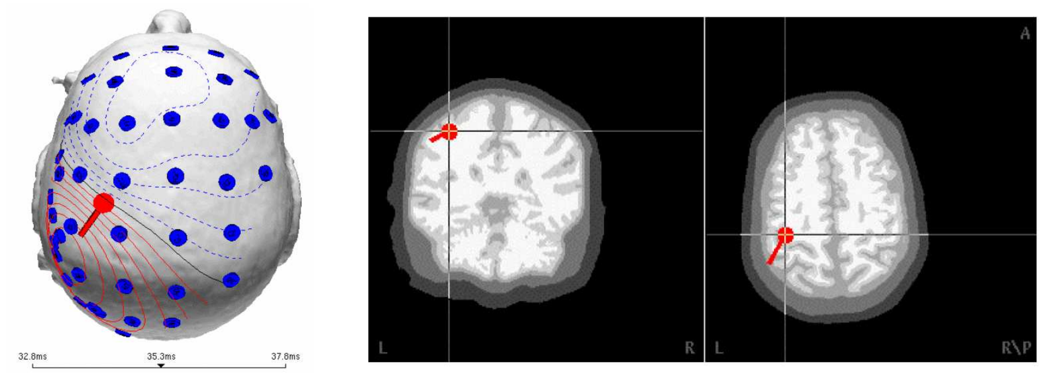

Fig. 6. Source reconstruction result for the first tactile SEP component at the peak latency of 35.3ms.

Applying the LRCE approach resulted in the contralateral somatosensory source shown in Fig. 6, in the brain conductivity of 0.48S/m, and in a brain:skull conductivity ratio of 120, i.e., a skull conductivity of 0.004 S/m, with an explained variance of 98.98%. While the value of skull conductivity is close to what is generally used in source analysis (0.0042 S/m, see (Buchner et al., 1997; Fuchs et al., 1998; de Munck and Peters, 1993)), the estimated brain conductivity and thus also the brain:skull ratio is higher than the traditional values proposed (Haueisen, 1996; Homma et al., 1995).

5 Discussion and conclusion

We developed a Low Resolution Conductivity Estimation(LRCE) procedure to individually optimize a volume conductor model from a human head with regard to both geometry and tissue conductivities. We exploited a combined T1-/PD-MRI dataset for the construction of a four-tissue volume conductor FE model with a special focus on an improved modeling of the skull shape and thickness. Obtaining accurate skull geometry is important because changes in skull conductivity are known to be closely related to changes in its compartmental thickness. The correction for geometry errors in modeling the skull compartment were furthermore shown to be essential for the measurement of skull conductivity (Gonçalves et al., 2003a). While other authors have used parameter estimation in continuous parameter space with local optimization algorithms (Gutiérrez et al., 2004; Fuchs et al., 1998), we propose the combination of a discrete low resolution parameter estimation with a global optimization method applied to realistic geometry to better take into account the limited SNR of real EEG measurement data. Because the cost function is shallow (Gonçalves et al., 2003b), the proposed computationally expensive procedure using realistic FE volume conductor modeling and global Simulated Annealing (SA) optimization is important.

In a first study, we evaluated the LRCE algorithm in EEG simulations for its ability to determine both the brain and the skull tissue conductivities together with the reconstruction of one and two somatosensory reference sources. At relatively low noise levels (up to 25 dB SNR in the single source scenario and up to 40 dB SNR in the two source scenario), the LRCE resulted in acceptable localization errors for the reference sources and correctly estimated reference tissue conductivities, while results became unstable when further increasing the noise. We also set up a simulation for the reconstruction of the skull to brain conductivity ratio in which results were satisfying (correct skull:brain conductivity ratio, source localization errors smaller than 3.4 mm) up to noise levels of 25 dB for the mainly tangentially oriented somatosensory reference sources. We found in our simulations that the most accurate source reconstructions were always associated with the correctly estimated conductivities (or conductivity ratio) and, moreover, that assuming an incorrect conductivity ratio had a profoundly negative effect on the source reconstruction accuracy.

In a last examination, we applied the LRCE to measured tactile Somatosensory Evoked Potentials (SEP) with the focus on estimating both the brain and the skull conductivity. With an SNR of 26.4 dB, the data were in the noise range of the second simulation study, which was based on a single equivalent current dipole model. As shown in numerous studies (Mertens and Lütkenhöner, 2000; Hari and Forss, 1999), this source model is adequate because the early SEP component arises from area 3b of the primary somatosensory cortex (SI) contralateral to the side of stimulation. Our explained variance to the measured data of about 99% for this source model further supports our choice. The results from the LRCE analysis were a brain conductivity of 0.48 S/m and a skull conductivity of 0.004 S/m. While this skull conductivity corresponds to the traditional value in the literature (de Munck and Peters, 1993; Buchner et al., 1997; Fuchs et al., 1998), we found the brain to have a lower resistance than generally assumed (Haueisen, 1996). Many recent papers have focused on the brain:skull conductivity ratio and a large variability of results have been reported for this value including 80 (Homma et al., 1995), 72 (Gonçalves et al., 2003b), 42 (Gonçalves et al., 2003a), 25 (Lai et al., 2005), 23 (Baysal and Haueisen, 2004), 15 (Oostendorp et al., 2000) and 8 (Hoekema et al., 2003). Because of the higher conductivity of the brain, with an estimated ratio of 120, our LRCE result is larger than the largest previously reported value of 80(Homma et al., 1995).

The current results clearly illustrate the feasibility of building an optimized volume conductor model with regard to both geometry and conductivity. As we have formulated it, such a study requires accurate head geometry, in this case from both T1- and PD-weighted MRI. The highly conducting CSF (Baumann et al., 1997) should not be neglected in the headmodel as shown in (Ramon et al., 2004; Wolters et al., 2006) and our procedure takes this compartment into account. By obtaining somatosensory evoked potential data, which allows independent localization of the underlying bioelectric source, it is then possible to estimate the optimal conductivities for the individual subject using the proposed LRCE approach in highly realistic finite element models, provided that the data has a sufficient signal-to-noise ratio. A related finding from this study is, there is a trade off between the number of independent parameters that can be determined and the complexity of the assumed source model. The specific trade off point is also strongly influenced by the quality of the measured electric potentials. Thus the number of parameters that can be dependably estimated is a function of both the signal quality and the number and quality of *a priori* knowledge about, for example, the source location or orientation through a combination with fMRI or anatomical and/or functional arguments (e.g., a strong restriction of the source location to anatomically and physiologically reasonable areas close to the somatosensory SI area). In this context, others have suggested that by including MEG data in the scheme (Huang et al., 2007), it will be possible to improve stability considerably. Plis et al. have also recently shown the necessity for stabilization when using only EEG data (Plis et al., 2007). We note that our approach differs from both these others with regard to both head modeling and conductivity optimization.

The success of the conductivity optimization approach and the more general advantages of customized geometric models suggest a procedure for clinical applications. First of all, one could use SEP data with high SNR together with T1- and PD-MR images from the patient to construct a model that would be optimized for both geometric accuracy and individual conductivity values. With this volume conductor model in place, recorded potentials from more complex and clinically interesting sources could drive the inverse solution and source localization.

A better approximation to the real volume conductor using the proposed LRCE method is an important step towards simultaneous EEG/MEG source analysis (Fuchs et al., 1998). Combining EEG and MEG modalities compensates each others disadvantages, i.e., poor sensitivity of MEG to radial sources and the much stronger conductivity dependency of EEG. Using combined somatosensory evoked potentials and fields (SEP/SEF) in combination with T1- and PD-MRI should further stabilize the application of the presented LRCE method for the estimation of tissue conductivities. For the quasi-tangentially oriented P35 somatosensory source, MEG-SEF data can be exploited to strongly restrict the source location and especially its depth as shown, e.g., in (Fuchs et al., 1998; Huang et al., 2007), so that the resolution of the proposed LRCE method with regard to the conductivities of the different compartments could be increased. With such data in hand, the presented LRCE method using FE volume conductor modeling might also contribute to the estimation of anisotropy ratios in the skull and brain compartments (Marin et al., 1998; Haueisen et al., 2002; Wolters et al., 2006).

6 Acknowledgment

This research was supported by the Center for Integrative Biomedical Computing, NIH NCRR Project 2-P41-RR12553-07 and by the German Research Foundation (DFG), project JU 445/5-1.

References

Baumann, S., Wozny, D., Kelly, S., Meno, F., 1997. The electrical conductivity of human cerebrospinal fluid at body temperature. IEEE Trans. Biomed. Eng. 44 (3), 220–3.

Baysal, U., Haueisen, J., 2004. Use of a priori information in estimating tissue resistivities-application to human data in vivo. Physiol. Meas. 25, 737–48.

Bertrand, O., Thévenet, M., Perrin, F., 1991. 3D finite element method in brain electrical activity studies. In: Nenonen, J., Rajala, H., Katila, T. (Eds.), Biomagnetic Localization and 3D Modelling. Report of the Dep. of Tech.Physics, Helsinki University of Technology, pp. 154–171.

BESA, 2007. Brain Electric Source Analysis, http://www.besa.de.

Buchner, H., Knoll, G., Fuchs, M., Rienäcker, A., Beckmann, R., Wagner, M., Silny, J., Pesch, J., 1997. Inverse localization of electric dipole current sources in finite element models of the human head. Electroenc. Clin. Neurophysiol. 102, 267–278.

Cuffin, B. N., 1996. EEG localization accuracy improvements using realistically shaped head model. IEEE Trans. Biomed. Eng. 43, 299–303.

CURRY, 2000. CURrent Reconstruction and Imaging, http://www.neuro.com.

de Munck, J., Peters, M., 1993. A fast method to compute the potential in the multi sphere model. IEEE Trans Biomed Eng 40 (11), 1166–1174.

Fuchs, M., Wagner, M., Wischmann, H., Köhler, T., Theißen, A., Drenckhahn, R., Buchner, H., 1998. Improving source reconstructions by combining bioelectric and biomagnetic data. Electroenc. Clin. Neurophysiol. 107, 93–111.

Geddes, L., Baker, L., 1967. The specific resistance of biological materials. A compendium of data for the biomedical engineer and physiologist. Med. Biol. Eng. 5, 271–93.

Geman, S., Geman, D., 1984. Stochastic relaxation, Gibbs distribution and the Bayesian restoration of images. IEEE Trans. Pattern Anal. Mach. Intell. PAMI-6 (6), 721–41.

Gençer, N. G., Acar, C. E., 2004. Sensitivity of EEG and MEG measurements to tissue conductivity. Phys. Med. Biol. 49, 701–17.

Gerson, J., Vardenas, V. A., Fein, G., 1994. Equivalent dipole parameter estimation using simulated annealing. Electroenceph. Clin. Neurophysiol. 92, 161–8.

Gonçalves, S., de Munck, J. C., Jeroen, P. A., B, V. F., Heethaar, R. M., da Silva, F. L. L., 2003a. In vivo measurement of the brain and skull resistivities using an EIT-based method and realistic models for the head. IEEE Trans. Biomed. Eng. 50 (6), 754–67.

Gonçalves, S., de Munck, J. C., Verbunt, J. P. A., Heethaar, R. M., da Silva, F. H. L., 2003b. In vivo measurement of the brain and skull resistivities using an EIT-based method and the combined analysis of SEF/SEP data. IEEE Trans. Biomed. Eng. 50 (9), 1124–1128.

Gutiérrez, D., Nehorai, A., Muravchik, C. H., 2004. Estimating brain conductivities and dipole source signals with EEG arrays. IEEE Trans. Biomed. Eng. 51, 2113–2122.

Haase, A., Frahm, J., Matthaei, D., Hänicke, W., Merboldt, K. D., 1986. FLASH imaging: rapid NMR imaging using low flip-angle pulses. J. Magn. Reson. 67, 258–66.

Hallez, H., Vanrumste, B., Hese, P. V., D'Asseler, Y., Lemahieu, I., de Walle, R. V., 2005. A finite difference method with reciprocity used to incorporate anisotropy in electroencephalogram dipole source localization. Phys.Med.Biol. 50, 3787–3806.

Haneishi, H., Ohyama, N., Sekihara, K., Honda, T., 1994. Multiple current dipole estimation using simulated annealing. IEEE Trans. Biomed. Eng. 41 (11), 1004–9.

Hari, R., Forss, N., 1999. Magnetoencephalography in the study of human somatosensory cortical processing. Phil. Trans. R. Soc. Lond. 354 (Ser. B), 1145–1154.

Haueisen, J., 1996. Methods of numerical field calculation for neuromagnetic source localization. Ph.D. thesis, Shaker-Verlag Aachen, ISBN 3-8265-1691-5.

Haueisen, J., Tuch, D., Ramon, C., Schimpf, P., Wedeen, V., George, J., Belliveau, J., 2002. The influence of brain tissue anisotropy on human EEG and MEG. NeuroImage 15, 159–166.

Hoekema, R., Wieneke, G. H., Leijten, F. S. S., van Veelen, C. W. M., van Rijen, P. C., Huiskamp, G. J. M., Ansems, J., van Huffelen, A. C., 2003. Measurement of the conductivity of skull, temporarily removed during epilepsy surgery. Brain Topogr. 16 (1), 29–38.

Homma, S., Musha, T., Nakajima, Y., Okamoto, Y., Blom, S., Flink, R., Hagbarth, K. E., 1995. Conductivity ratios of scalp-skull-brain model in estimating equivalent dipole sources in human brain. Neurosci. Res. 22, 51–5.

Huang, M., Song, T., Hagler, D., Podgorny, I., Jousmaki, V., L.Cui, K.Gaa, D.L.Harrington, Dale, A., R.R.Lee, J.Elman, E.Hargren, 2007. A novel integrated MEG and EEG analysis method for dipolar sources. NeuroImage 37, 731–748.

Huiskamp, G., Vroeijenstijn, M., van Dijk, R., Wieneke, G., van Huffelen, A., 1999. The need for correct realistic geometry in the inverse EEG problem. IEEE Trans. Biomed. Eng. 46 (11), 1281–1287.

Kirkpatrick, S., Gelatt Jr, C. D., Vecchi, M. P., 1983. Optimization by simulated annealing. Science 220, 671–80.

Lai, Y., van Drongelen, W., Ding, L., Hecox, K. E., Towle, V. L., Frim, D. M., He, B., 2005. Estimation of in vivo human brain-to-skull conductivity ratio from simultaneous extra- and intra-cranial electrical potential recordings. Clin.Neurophysiol. 116, 456–65.

Latikka, J., Kuume, T., Eskola, H., 2001. Conductivity of living intracranial tissues. Phys. Med. Biol. 46, 1611–1616.

Lee, J. H., Garwood, M., Meno, R., Adriany, G., Anderson, P., Truwit, C. L., Ugurbil, K., 1995. High contrast and fast 3D magnetic resonance imaging at high fields. Magn. Reson. Med. 34, 308–312.

Marin, G., Guerin, C., Baillet, S., Garnero, L., Meunier, G., 1998. Influence of skull anisotropy for the forward and inverse problem in EEG: simulation studies using the FEM on realistic head models. Hum. Brain Mapp. 6, 250–69.

Marquardt, D. W., 1963. An algorithm for least-squares estimation of nonlinear parameters. J. Soc. Indust. Appl. Math. 11, 431–41.

Mertens, M., Lütkenhöner, B., 2000. Efficient neuromagnetic determination of landmarks in the somatosensory cortex. Clin. Neurophysiol. 111, 1478–87.

Metropolis, N., Rosenbluth, A., Rosenbluth, M., Teller, A., Teller, E., 1953. Equation of state calculations by fast computing machines. J. of Chem. Phys. 21, 1087–92.

Nelder, J. A., Mead, R., 1965. A simplex method for function minimization. Comput. J. 7 (4), 308–13.

Oostendorp, T. F., Delbeke, J., Stegeman, D. F., 2000. The conductivity of the human skull: Results of *in vivo* and *in vitro* measurements. IEEE Trans. Biomed. Eng. 47, 1487–92.

Pham, D. L., Prince, J. L., 1999. Adaptive fuzzy segmentation of magnetic resonance images. IEEE Trans. Med. Imag. 18 (9), 737–52.

Plis, S. M., George, J. S., Jun, S. C., Ranken, D. M., Volegov, P. L., Schmidt, D. M., 2007. Probabilistic forward model for electroencephalography source analysis. Phys. Med. Biol. 52, 5309–5327.

Plonsey, R., Heppner, D., 1967. Considerations on quasi-stationarity in electrophysiological systems. Bull. Math. Biophys. 29, 657–64.

Ramon, C., Schimpf, P., Haueisen, J., Holmes, M., Ishimaru, A., 2004. Role of soft bone, CSF and gray matter in EEG simulations. Brain Topogr. 16 (4), 245–8.

Rush, S., Driscoll, D., 1968. Current distribution in the brain from surface electodes. Anesth. Analg. 47 (6), 717–23.

Rush, S., Driscoll, D., 1969. EEG electrode sensitivity: An application of reciprocity. IEEE Trans. Biomed. Eng. 16, 15–22.

Sarvas, J., 1987. Basic mathematical and electromagnetic concepts of the biomagnetic inverse problem. Phys. Med. Biol. 32 (1), 11–22.

Scherg, M., von Cramon, D., 1985. Two bilateral sources of the late AEP as identified by a spatio-temporal dipole model. Electroencephalogr Clin Neurophysiol 62 (1), 32–44.

Uutela, K., Hämäläinen, M., Salmelin, R., 1998. Global optimization in the localization of neuromagnetic sources. IEEE Trans. Biomed. Eng. 45 (6), 716–23.

Weinstein, D., Zhukov, L., Johnson, C., 2000. Lead-field bases for EEG source imaging. Annals of Biomed. Eng. 28 (9), 1059–66.

Wolters, C., Anwander, A., Berti, G., Hartmann, U., 2007a. Geometry-adapted hexahedral meshes improve accuracy of finite element method based EEG source analysis. IEEE Trans.Biomed.Eng. 54 (8), 1446–1453.

Wolters, C., Anwander, A., D.Weinstein, M.Koch, X.Tricoche, R.S.MacLeod, 2006. Influence of tissue conductivity anisotropy on EEG/MEG field and return current computation in a realistic head model: A simulation and visualization study using high-resolution finite element modeling. NeuroImage 30 (3), 813–826, http://dx.doi.org/10.1016/j.neuroimage.2005.10.014.

Wolters, C., Beckmann, R., Rienäcker, A., Buchner, H., 1999. Comparing regularized and non-regularized nonlinear dipole fit methods: a study in a simulated sulcus structure. Brain Topogr. 12 (1), 3–18.

Wolters, C., Grasedyck, H. L., Hackbusch, W., 2004. Efficient computation of lead field bases and influence matrix for the FEM-based EEG and MEG inverse problem,. Inverse Problems 40, 1099–116.

Wolters, C., Köstler, H., Möller, C., Härtlein, J., Grasedyck, L., Hackbusch, W., 2007b. Numerical mathematics of the subtraction method for the modeling of a current dipole in EEG source reconstruction using finite element head models. SIAM J. on Scientific Computing 30 (1), 24–45.

Wolters, C. H., 2003. Influence of tissue conductivity inhomogeneity and anisotropy on EEG/MEG based source localization in the human brain. In:MPI Series in Cognitive Neuroscience, Leipzig, also: Leipzig, Univ., Diss, http://lips.informatik.uni-leipzig.de/pub/2003-33/en.

Wolters, C. H., Kuhn, M., Anwander, A., Reitzinger, S., 2002. A parallel algebraic multigrid solver for finite element method based source localization in the human brain. Comp. Vis. Sci. 5, 165–77.

Yan, Y., Nunez, P. L., Hart, R. T., 1991. A finite-element model of the human head: scalp potentials due to dipole sources. Med. Biol. Eng. Comput. 29, 475–81.

2.12 STR: A new spatio-temporal approach for accurate and efficient current density reconstruction

STR: A new Spatio-Temporal Approach for Accurate and Efficient Current Density Reconstruction
Schmitt, U., Wolters, C.H., Anwander, A. and Knösche, T., In *Halgren, E., Ahlfors, S., Hämäläinen, M. and Cohen, D. (eds.): BIOMAG 2004, Proc. of the 14th Int. Conf. on Biomagnetism, Boston, USA*, http://www.biomag2004.org, pp. 591–592, 2004.

Schmitt, U., Wolters, C.H., Anwander, A. and Knösche, T., Poster presentation, *BIOMAG 2004, Proc. of the 14th Int. Conf. on Biomagnetism, Boston, USA*, 2004.

STR: A new Spatio-Temporal Approach for Accurate and Efficient Current Density Reconstruction

U. Schmitt[1], C. H. Wolters[2,3,4], A. Anwander[4], T. Knösche[4]

(1) University Saarbrücken, Institute for Applied Mathematics, Germany
(2) Scientific Computing and Imaging Institute, University of Utah, Salt Lake City, USA
(3) Max Planck Institute for Mathematics in the Sciences, Leipzig, Germany
(4) Max Planck Institute for Human Cognitive and Brain Sciences, Leipzig, Germany.

ABSTRACT

We will present a new and fast regularization procedure for reconstructing current densities based on EEG and / or MEG measurements. It is our goal to achieve an additional stabilization of the solution which is superior to known procedures: our approach does not only consider spatial smoothness but also temporal smoothness of activation curves as a-priori information.

KEY WORDS

Current density reconstructions; linear regularization; Spatio temporal regularization; model adapted filtering; dynamic inverse problems.

INTRODUCTION

Current source density reconstruction algorithms are based on the linear relationship between a time series of *measurement vectors* m_t and a time series of *solution vectors* j_t regarding T time steps, representing the strengths of a collection of predefined current dipoles, usually sampling the entire possible solution space. This relationship is mediated by a *lead field matrix* L. It is well known that the inverse problem of EEG and MEG suffers from general non-uniqueness, i.e. there is always an entire class of possible solutions. This is due to the fact that the vectors j_t have a higher dimension than the measurement vectors m_t. If the solution space is not restricted beforehand by e.g. assuming a single focal generator, additional assumptions have to be used to get an unique solution of the problem, in most cases one defines a generalized inverse L^+ which avoids this shortcoming. However, the resulting linear estimators suffer from a bad condition, i.e. small perturbation in the measurement, e.g. by noise, lead to unusable solutions. This leads to the necessity of regularization. For example, the well-known Tikhonov-Philips based regularization procedure solves

$$\sum_t \left\| L\, j_t - m_t \right\|^2 + \lambda \sum_t \left\| R\, j_t \right\|^2 \to \min$$

Here R is a *regularization matrix*, e.g. $R = I$ or $R = \Delta$. The parameter λ is called *regularization parameter*. The second sum models a-priori information as spatial smoothness and stabilizes the solution in the presence of noise. In this formulation no temporal couplings occur.

As activation curves of neural activity are smooth, we introduce *temporal smoothness* as further a-priori information about the current densities we are searching for. We thus extend the method above as follows:

$$\sum_t \left\| L\, j_t - m_t \right\|^2 + \lambda \sum_t \left\| R\, j_t \right\|^2 + \mu \sum_t \left\| j_{t+1} - j_t \right\|^2 \to \min$$

The last term measures temporal smoothness, minimizing the last sum favors current densities with smooth activation curves. This extension can be applied to other problems as dynamic computerized tomography and dynamic impedance tomography, see [Schmitt, 2002].

METHODS

Trying to solve the second minimization task with the same methods used for solving known Tikhonov-Philips based minimization problems one encounters efficiency problems which lead to unacceptable solution times ranging from some days to weeks. But using the difference matrix $D = (-\delta_{i,j} + \delta_{i+1,j})_{i,j}$ of size $(T-1) \times T$, that is D has the value -1 where $j = i$ and $+1$ in the case $j = i+1$, our problem is equivalent to solving the so-called Sylvester equation [Schmitt, 2002]

$$(L^T L + \lambda\, R^T R)\; X + \mu\, X\, D^T D = M$$

which can be solved much faster. Solution times range from seconds to a few minutes on a standard desktop computer, depending on the size of the problem. Here the temporal measurements form the matrix M by column wise arranging. In the same way the solutions form the columns of X. For some special regularization operators, e.g. $R = I$, we can achieve further speedup solving a Sylvester equation involving LL^T [Schmitt, 2002], which is in general much smaller than $L^T L$: if L is $n \times 3N$, where n is the number of measurement channels and N is the number of influence nodes, then LL^T is $n \times n$ and $L^T L$ is $(3N) \times (3N)$.

RESULTS

For studying the general behavior of STR, we used a simple setup, see Fig. 1: The influence space is a 10x10 grid in two dimensions. Nine sensors are placed in a planar array above the grid with center (5.5, 5.5, 2). The center of the influence space is (5.5, 5.5, 0). We assume constant conductivity in the whole space, so the leadfield matrix can be computed analytically. Two equally oriented dipoles with moment (0,0,1) at x=3, 8 both at y=5 are placed on the 10x10 grid.. Gaussian dipole-strength time series are assigned to each dipole, they are drawn in Fig. 2. We generated synthetic data and added 30% uniform noise. All methods use $R = I$ as regularization matrix. We calculated temporal uncoupled Tikhonov-Phillips solutions and STR solutions. The first used temporal smoothed data (Savitzky-Golay filter of order three and length five). Based on these results, Figure 1 shows current density reconstructions, in Figure 2 reconstructed activation curves are drawn. The improved stability in presence of noise is apparent.

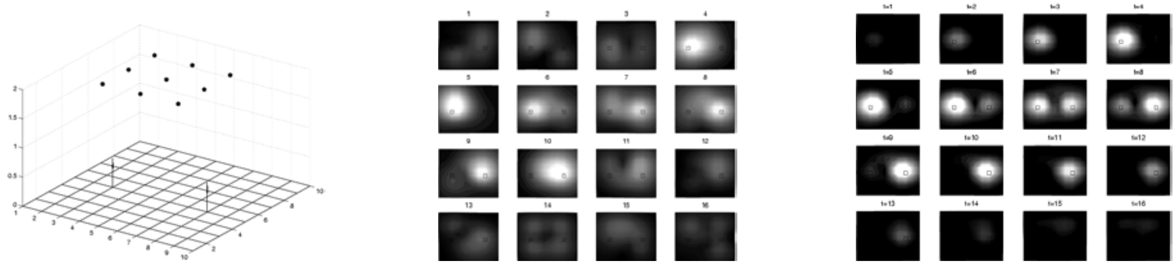

Figure 1: Left: setup of the simulation . **Middle**: current densities calculated from temporal uncoupled Tikhonov-Phillips solution. **Right**: current densities calculated from STR reconstruction.

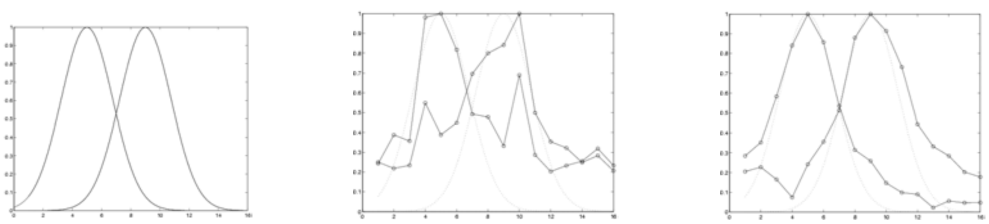

Figure 2: **Left**: activation curves of the two dipoles used for generating synthetic data. **Middle**: activation curves based on temporal uncoupled Tikhonov-Phillips solutions. **Right**: activation curves calculated from STR reconstruction.

DISCUSSION

One important question is if we can achieve the same results by smoothing the data before using uncoupled linear methods. Regarding regularization procedures $T_\lambda : Y \to N(A)^\perp \subseteq X$ of an ill posed operator $A : X \to Y$, one can define the filter $F_\gamma := AT_\gamma$ which acts on data. We can reconstruct the regularization T_γ from F_γ by applying the Moore-Penrose inverse A^+ to the filter: $A^+ F_\gamma = A^+ A T_\gamma = P_{N(A)^\perp} T_\gamma = T_\gamma$. That is, one can switch from filters to regularizations and vice versa. These filters are not arbitrary, they are adopted to the underlying problem. For a deeper discussion see [Louis, 1999].

We computed the filter F_{STR} which belongs to the STR procedure, explored the structure of this matrix and observed that a decomposition $F_{STR} = (I_T \otimes F_{spatial})(F_{temporal} \otimes I_N)$ is not possible in general, except for unrealistic cases as T=1 and N=1. Here $\otimes$ denotes the Kronecker product. As a result, STR reconstructions cannot be obtained by applying known spatial regularizers to temporally smoothed data. STR interweaves spatial and temporal a-priori information to a new regularization method.

REFERENCES

A K Louis. A Unified Approach to Regularization Methods for Linear Ill-Posed Problems. Inverse Problems 15 (1999), pp. 489 – 498

U Schmitt, A K Louis. Efficient algorithms for the regularization of dynamic inverse problems: I. Theory. Inverse Problems 18 (2002), pp. 645-658.

U Schmitt, A K Louis, C Wolters, M Vauhkonen. Efficient algorithms for the regularization of dynamic inverse problems: II. Applications . Inverse Problems 18 (2002), pp. 659-676.

STR: A new Spatio-Temporal Approach for Accurate and Efficient Current Density Reconstruction

U. Schmitt[1], C. H. Wolters[2,3,4], A. Anwander[4], T. Knösche[4]

(1) Institute for Applied Mathematics, Saarland University Saarbrücken, Germany, (2) Scientific Computing and Imaging Institute, University of Utah, Salt Lake City, USA
(3) Max Planck Institute for Mathematics in the Sciences, Leipzig, Germany (4) Max Planck Institute for Human Cognitive and Brain Sciences, Leipzig, Germany.

Present situation

Current density reconstructions try to reconstruct distributed sources based on EEG/MEG measurements.

Mathematical formulation: Leadfieldmatrix L maps currents j_t to measurements m_t for each timestep t.

The problem $L j_t = m_t$ is **ill-posed**, that is: it has no unique solution and noise in the measurements leads to unusable results if this linear system is inverted.

Remedy: Regularization procedures, e.g. **Tikhonov-Phillips** (**TP**) method:

$$\sum_t \|L j_t - m_t\|^2 + \lambda \sum_t \|R j_t\|^2 \to \min$$

Leads to unique, stable and spatial smooth currents, but solution is in general **not smooth in time**, which contradicts neurological assumptions.

Improvement by STR

Incorporate temporal smoothness of currents in existing linear regularization methods by favoring temporally smooth solutions. Tikhonov-Phillips method is extended to

$$\sum_t \|L j_t - m_t\|_2^2 + \lambda \sum_t \|R j_t\|_2^2 + \mu \sum_t \|j_{t+1} - j_t\|_2^2 \to \min$$

The last term is a measure for temporal smoothness. Naive solution by so called **normal equation** leads to **unacceptable solution time**. **STR** transforms the normal equation to so-called **Sylvester equations** and considers the special structure of involved matrices.

➡ **speedup up to 10^6 compared to solving normal equations**, slower than TP by a factor ~9 for large problems. Further speed-up for certain regularization operators.

Analysis of STR Algorithm

A filter can be constructed for each regularization procedure in such a way that the regularization is equivalent to applying this filter followed by un-regularized inversion.

Question: Can one decompose the filter induced by STR to linear temporal filtering followed by spatial filtering ?

Answer: NO.

Conclusion: STR can not be replaced by linear filtering of the data, followed by pure spatial regularization.

Statistical evaluation

For evaluation and studying STR we used a **simple model** consisting of an 11x11 grid of influence nodes, 4 x 4 grid of EEG sensors. We assumed constant conductivity in an unbounded volume conductor, so that the forward model can be computed analytically. We placed **one dipole** perpendicular to the influence space and attached a **gaussian activation curve**. See figures below.

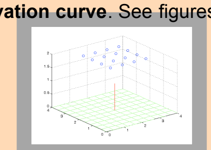

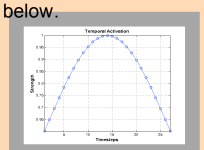

We compared TP applied to temporally smoothed data versus STR applied to unsmoothed data. See figures to the right.

We made 500 runs at each noise level. Measurement of **spatial localization error** (upper row) and **temporal deviation** (lower row). We calculated mean errors and their variance.

TP STR

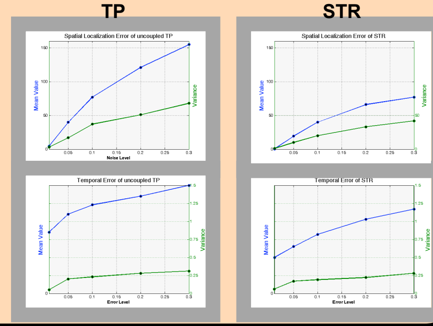

Example Reconstructions

We used an **anisotropic high resolution** tetrahedral **Finite Element model** with 147287 nodes and 892115 elements, and a 67 channel EEG configuration. As influence space we chose a smoothed brain surface: triangular mesh, 2 mm resolution. FEM calculations were done with the software package **IP-NeuroFEM-Pebbles** (www.neurofem.com), which yields outstanding computing times using the method described in [1].

We simulated **EEG data** for 2 **radial dipoles** in temporal areas of both hemispheres having overlapping **Gaussian activation curves**. We added averaged **realistic noise** (0.1 – 30 Hz) from an auditory experiment, assuming 500 epochs and a max. signal amplitude of 15 µV.

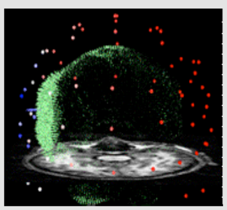

Timestep 14

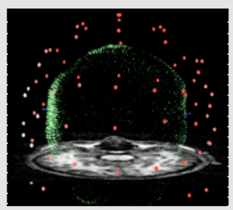

Timestep 20

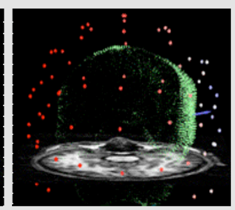

Timestep 26

[1] Wolters C H, Grasedyck L, Hackbusch W: Efficient Computiation of Lead Field Bases and Influence Matrix for the FEM-based EEG and MEG Inverse Problem, Inverse Problems 20 (2004), p 1099-1116

Discussion

As we could show, **STR is a new algorithm,** which can be **implemented efficiently** and scales well with the temporally uncoupled TP method.

Statistical tests in a simple volume conductor show **superior reconstruction results** compared to temporally uncoupled TP.

The same technique is used to handle temporal inverse problems like dynamical CT and dynamical impedance tomography.

References:

U Schmitt and A K Louis: Efficient Algorithms for the regularization of dynamic inverse problems: I Theory, Inverse Problems 18 (2002) p 645-658.

U Schmitt, A K Louis, C Wolters, M Vauhkonen: Efficient Algorithms for the regularization of dynamic inverse problems: II Applications, Inverse Problems 18 (2002) p 659-676.

2.13 Influence of remote tissue conductivity anisotropy on EEG/MEG field and return current computations

Influence of Tissue Conductivity Anisotropy on EEG/MEG Field and Return Current Computation in a realistic Head Model: A Simulation and Visualization Study using High-Resolution Finite Element Modeling
Wolters, C.H., Anwander, A., Tricoche, X., Weinstein, D., Koch, M.A., and MacLeod, R.S. *NeuroImage*, Vol.30, No.3, pp.813-826 (2006).
DOI: http://dx.doi.org/10.1016/j.neuroimage.2005.10.014,

Corresponding author: C.H. Wolters

Paper award: Evaluated for Faculty of 1000 Biology:
http://www.f1000biology.com/article/id/1030531/evaluation

NeuroImage

www.elsevier.com/locate/ynimg
NeuroImage 30 (2006) 813 – 826

Influence of tissue conductivity anisotropy on EEG/MEG field and return current computation in a realistic head model: A simulation and visualization study using high-resolution finite element modeling

C.H. Wolters,[a,b,*] A. Anwander,[c] X. Tricoche,[b] D. Weinstein,[b] M.A. Koch,[d] and R.S. MacLeod[b,e]

[a]*Westfälische Wilhelms-Universität Münster, Institut für Biomagnetismus und Biosignalanalyse, Malmedyweg 15, 48149 Münster, Germany*
[b]*University of Utah, Scientific Computing and Imaging Institute, 50 S. Central Campus Dr., Room 3493, Salt Lake City, UT 84112, USA*
[c]*Max Planck Institute for Human Cognitive and Brain Sciences, Stephanstr.1a, 04103 Leipzig, Germany*
[d]*University Medical Center Hamburg-Eppendorf, Department of Systems Neuroscience, Martinistr. 52, 20246 Hamburg, Germany*
[e]*University of Utah, The Nora Eccles Harrison Cardiovascular Research and Training Institute (CVRTI), Bioengineering Department, Salt Lake City, UT, USA*

Received 15 July 2005; revised 15 September 2005; accepted 5 October 2005
Available online 20 December 2005

To achieve a deeper understanding of the brain, scientists, and clinicians use electroencephalography (EEG) and magnetoencephalography (MEG) inverse methods to reconstruct sources in the cortical sheet of the human brain. The influence of structural and electrical anisotropy in both the skull and the white matter on the EEG and MEG source reconstruction is not well understood.

In this paper, we report on a study of the sensitivity to tissue anisotropy of the EEG/MEG forward problem for deep and superficial neocortical sources with differing orientation components in an anatomically accurate model of the human head.

The goal of the study was to gain insight into the effect of anisotropy of skull and white matter conductivity through the visualization of field distributions, isopotential surfaces, and return current flow and through statistical error measures. One implicit premise of the study is that factors that affect the accuracy of the forward solution will have at least as strong an influence over solutions to the associated inverse problem.

Major findings of the study include (1) anisotropic white matter conductivity causes return currents to flow in directions parallel to the white matter fiber tracts; (2) skull anisotropy has a smearing effect on the forward potential computation; and (3) the deeper a source lies and the more it is surrounded by anisotropic tissue, the larger the influence of this anisotropy on the resulting electric and magnetic fields. Therefore, for the EEG, the presence of tissue anisotropy both for the skull and white matter compartment substantially compromises the forward potential computation and as a consequence, the inverse source reconstruction. In contrast, for the MEG, only the anisotropy of the white matter compartment has a significant effect. Finally, return currents with high amplitudes were found in the highly conducting cerebrospinal fluid compartment, underscoring the need for accurate modeling of this space.

Keywords: EEG; MEG; Source reconstruction; Tissue conductivity anisotropy; CSF; Forward problem; Finite element method; Return current; Visualization

Introduction

The inverse problem in EEG and MEG aims at reconstructing the underlying current distribution in the human brain using potential differences and/or magnetic fluxes measured non-invasively directly from the head surface or from a close distance. The goal of this study was to examine the sensitivity of the associated EEG/MEG forward problem especially to conductive anisotropy within the brain. We computed forward solutions for both isotropic and anisotropic versions of realistic head models using the finite element approach and evaluated the results throughout the head using sophisticated visualization techniques as well as statistical metrics.

A major premise of this study is that there are regions of the head that do not conduct electrical current isotropically, i.e., equally in all directions, but rather they conduct preferentially in directions related to the underlying tissue structure (Geddes and Baker, 1967; Haueisen, 1996). The human skull consists of a soft bone layer (spongiosa) enclosed by two hard bone layers (compacta). Since the spongiosa has a much higher conductivity than the compacta (Akhtari et al., 2002), the skull can be described by an effective anisotropic conductivity with a ratio of up to 1:10 radially to tangentially to the skull surface (Rush and

* Corresponding author. Westfälische Wilhelms-Universität Münster, Institut für Biomagnetismus und Biosignalanalyse, Malmedyweg 15, 48149 Münster, Germany. Fax: +49 251 83 56874.

E-mail address: carsten.wolters@uni-muenster.de (C.H. Wolters).

Available online on ScienceDirect (www.sciencedirect.com).

1053-8119/$ - see front matter © 2005 Elsevier Inc. All rights reserved.
doi:10.1016/j.neuroimage.2005.10.014

Driscoll, 1968). It is also known that brain white matter has an anisotropic conductivity with a ratio of about 1:10 (normal: parallel to fibers) (Nicholson, 1965), but no direct techniques exist for its robust and non-invasive measurement. Recently, however, formalisms have been described for relating the effective electrical conductivity tensor of brain tissue to the effective water diffusion tensor as measured by diffusion tensor magnetic resonance imaging (DT-MRI) (Basser et al., 1994b; Tuch et al., 2001). The underlying assumption is that the same structural features that result in anisotropic mobility of water molecules (detected by DT-MRI) also result in anisotropic conductivity. The quantitative expression for this assumption is that the eigenvectors of the conductivity tensor are the same as those from the water diffusion tensor (Basser et al., 1994b). Even more specifically, Tuch et al. have applied a differential effective medium approach to porous brain tissue and derived a linear relationship between the eigenvalues of the DT and the conductivity tensors (Tuch et al., 2001).

A critical component of source reconstruction is the numerical approximation method used to reach an accurate solution of the associated forward problem, i.e., the simulation of fields for known dipolar sources in the brain. Although there are several different approaches in common use for this type of problem the finite element (FE) method is able to treat both realistic geometries and inhomogeneous and anisotropic material parameters (Haueisen, 1996; Buchner et al., 1997; van den Broek et al., 1998; Marin et al., 1998; Schimpf et al., 2002) and so is the approach we employed. Previous work has not sufficiently investigated the impact of tissue anisotropy on EEG and MEG. One impediment to using the FE method – and to this type of modeling in general – has been the high computational cost of carrying out the simulations. The use of recently developed advances in the FE method in EEG/MEG inverse problems (Weinstein et al., 2000; Wolters et al., 2002; Gencer and Acar, 2004; Wolters et al., 2004b) dramatically reduces the complexity of the computations, so that the main disadvantage of FE modeling no longer exists. In realistic FE models, sensitivity studies have been carried out for the influence of skull anisotropy on EEG and MEG (van den Broek et al., 1998; Marin et al., 1998; Wolters, 2003), while, to our knowledge, only a few studies have investigated the influence of realistic white matter anisotropy (Haueisen et al., 2002; Wolters, 2003). Those studies support the hypothesis that modeling anisotropy is crucial for accurate source reconstruction. The major limit of these studies that we have addressed is that their result evaluation was restricted to scalp potentials/fields. In this study, we have computed, compared and visualized potentials and especially the return current flow throughout the volume of the head. Those additional information allows a much more detailed examination of the effects of anisotropy than is possible from the evaluation of scalp values alone.

Using our realistic, anisotropic head model and a variety of sources, we were able to compare throughout the head volume the effects of anisotropic conductivity on bioelectric fields. Our results support those from previous studies suggesting that inclusion of anisotropy can be essential to accurate modeling of electric and magnetic fields and, by extension, to accurate source localization. In addition, our results show the nature of the current flow in regions of anisotropy and provide fundamental indications of the interplay between tissue characteristics and bioelectric fields.

Methods

To carry out the analysis of sensitivity of brain source simulation requires the construction of detailed realistic head models, in this case, from MRI image data. Here, we outline the steps we used to construct such a model and then apply advanced numerical techniques to the solution of forward problems.

MRI data acquisition

T1-weighted MRI is well suited for the segmentation of tissue boundaries like white and gray matter, outer skull, and skin. In contrast, the identification of the inner skull surface is more successful from proton density (PD) weighted MRI sequence because the difference in the quantity of water protons between intracranial and bone tissues is large. We regarded the skull and white matter layers as anisotropic compartments, the description of which we obtained from T1-/PD-MRI and whole-head DT-MRI with the associated segmentation process.

Measurement of T1- and PD-MRI

MR imaging of a healthy 32-year-old male subject was performed on a 3-T whole-body scanner (Medspec 30/100, Bruker, Ettlingen/Germany). For the T1-MRI, an inversion recovery MDEFT sequence (Lee et al., 1995) was employed (flip angle of 25°, TR = 11.7 ms, TE = 6 ms, T_{MD} = 1.3 s). For the 3 D PD-MRI, acquired 1 week later, we used a 3 D FLASH protocol (Haase et al., 1986) with TE = 6 ms, a flip angle of 25°, and TR = 11.7 ms. The scan resolution was $1 \times 1 \times 1.5$ mm^3 in both acquisitions, which were linearly interpolated to an isotropic 1 mm^3 voxel size.

Whole-head DT-MRI measurements

Whole-head DT-MRI was performed using a 4-slice displaced Ultra-Fast Low Angle RARE (U-FLARE) protocol with centric phase encoding (Norris and Börnert, 1993). Diffusion weighting was implemented as a Stejskal–Tanner type spin-echo preparation (Koch, 2000). Although Echo Planar Imaging (EPI) is widely applied for DT-MRI purposes, U-FLARE avoids spatial deformation of the DT-MRI and the resulting misregistration between it and the anatomic 3 D data. The effective echo time was TE = 120 ms and TR = 11 s. The diffusion weighting gradient pulses had a duration of δ = 22 ms, and their onset was separated by Δ = 40 ms. Four different **b** matrices with evenly spaced trace **b** between 50 and 800 s/mm^2 were applied through variation of the gradient strength (Koch, 2000). The slices were axially oriented and 5 mm thick with in-plane resolution of 2×2 mm^2. In order to increase the signal-to-noise ratio, 5 to 16 images (depending on **b**) with identical diffusion weighting were averaged. Due to the long measurement time (50 min for 4 slices) data acquisition was split into 8 sessions. Diffusion tensor calculation (Basser et al., 1994a) was based on a multivariate regression algorithm in IDL (Interactive Data Language, Research Scientific, Bolder, Colorado/USA). T1-weighted images were acquired in the same session as anatomical reference for the offline registration process.

Registration and segmentation

To construct a realistic volume conductor model requires segmentation of the different tissues within the head with special attention to the poorly conducting human skull and the highly conductive CSF (Hämäläinen and Sarvas, 1987; Cuffin, 1996; Roth et al., 1993; Huiskamp et al., 1999; Ramon et al., 2004).

T1-/PD-MRI

In order to correct for different subject positions and geometrical distortions, we first aligned T1- and PD-MRI with a voxel similarity based affine registration without presegmentation using a cost function based on mutual information (Wolters, 2003). The T1 images provided the information on soft tissues while the registered PD image enabled the segmentation of the inner skull surface.

Our nearly automatic segmentation process consisted of a 3D implementation of an Adaptive Fuzzy C-Means classification method that compensates for image intensity inhomogeneities (based on the original work in two dimensions of Pham and Prince (1999)), followed by a deformable model algorithm to smooth the inner and outer skull surfaces (Wolters, 2003). We segmented five head compartments out of the bimodal dataset: skin, skull, CSF, gray, and white matter. In source reconstruction, it is generally accepted that the weak volume currents either outside the skull or far away from EEG and MEG sensors have a negligible influence on the measured fields (Bruno et al., 2004). We therefore did not make any effort to segment the face and used instead a cutting procedure like that reported in standard boundary element head modeling (e.g., Wagner, 1998).

Fig. 1 shows an axial, a coronal, and a sagittal cut through a five tissue segmentation result, in which one can observe the segmentation produced by our method.

DT-MRI

The coregistered T1 images of the same slices allowed the registration of the DT-MRI data onto the 3D T1 data set. The registered DT data were then resampled to 1 mm^3. In order to handle the orientation information in the registered DT images appropriately, the matrix of each diffusion tensor, $\mathbf{D}^{\mathrm{eff}}$, was rotated with the rotation matrix $\mathbf{R}$ of the respective registration process via the similarity transform $\mathbf{D} = \mathbf{R}\mathbf{D}^{\mathrm{eff}}\mathbf{R}^{T}$. Since water diffusion coefficients in CSF are much larger than in the brain, a large contrast was achieved at the brain surface, which provided a quality check of the registration.

Fig. 2 shows a map of the *Fractional Anisotropy* (FA, for the definition see Basser and Pierpaoli, 1996) of the registered DT data, masked with the white matter mask from the segmentation procedure. The first row shows the FA values overlaid on the T1-MRI. With FA = 0.74, the highest value was found in the splenium of the corpus callosum. In the second row, the color coded directions (Pajevic and Pierpaoli, 1999) of the first tensor eigenvector weighted with the FA are presented and overlaid on the T1-MRI. Note the strong anisotropy of the corpus callosum and the pyramidal tracts. Furthermore, as Fig. 2 shows, the registered DT-MRI slices were not exactly parallel because the images were acquired in multiple sessions. Any missing values were filled with isotropic tensors with a trace value characteristic of white matter.

Volume conductor FE mesh generation

A prerequisite for FE modeling is the generation of a mesh that represents the geometric and electric properties of the head volume conductor. To generate the mesh, we used the software CURRY (2000) to create a surface-based tetrahedral tessellation of the five segmented compartments. The procedure exploits the Delaunay criterion, enabling the generation of compact and regular tetrahedra, and is described in detail elsewhere (Wagner, 1998; Wolters, 2003). The process resulted in a finite element model with 147,287 nodes and 892,115 tetrahedra elements as shown in Fig. 3.

Finite element conductivity

The finite elements were then labeled according to their compartment membership and assigned the following conductivities for the isotropic reference model (Geddes and Baker, 1967; Rush and Driscoll, 1968; Haueisen, 1996; Baumann et al., 1997): skin = 0.33 S/m, skull = 0.0042 S/m (skull to skin conductivity ratio of approximately 1:80), CSF = 1.79 S/m, gray matter = 0.33 S/m, and white matter = 0.14 S/m.

Modeling the skull conductivity anisotropy

The human skull shows a conductivity with high resistance in the radial direction (as a first approximation, a series connection of a high, a low, and a high resistor for inner compacta, spongiosa, and outer compacta) and much lower resistance in the tangential directions (parallel connection of the same three resistors) (Rush and Driscoll, 1968).

Determination of the tensor eigenvectors. Marin et al. have pointed out the importance of well-defined skull conductivity tensor eigenvectors by reporting errors in the simulated EEG for the case of an erroneous modeling (Marin et al., 1998). We determined the radial direction from a strongly smoothed triangular mesh, which was shrunken from the outer skull onto the outer spongiosa surface using a discrete deformable surface model (Wolters, 2003).

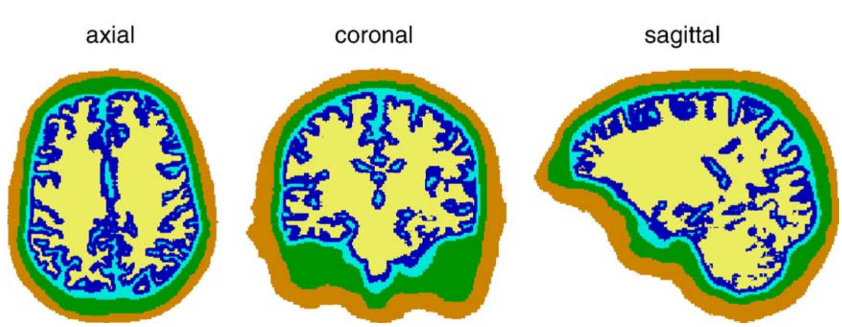

Fig. 1. Five tissue head model: the result of the segmentation in axial (left), coronal (middle), and sagittal (right) view. The color labels correspond to yellow—white matter, dark blue—gray matter, light blue—CSF, green—skull, brown—skin.

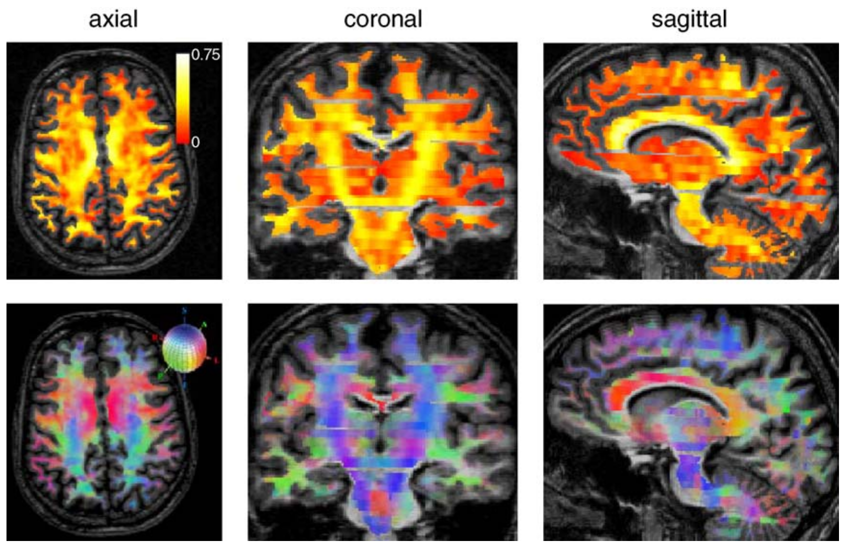

Fig. 2. Visualization of the fractional anisotropy (FA) of the DT-MRI measurements in the white matter compartment. The first row shows the FA values in red–yellow–white color scale overlaid on the T1-MRI. The second row shows the orientation of the principal tensor eigenvector in color coding according to the red–green–blue sphere (shown in the left figure) with red indicating mediolateral, green anteroposterior and blue superoinferior direction. The brightness of the color is scaled to the FA (max. 0.75). The white matter fiber orientation map is overlaid on the T1-MRI.

Fig. 4 shows the result on the underlying T1 image. For each skull finite element, we then defined the radial orientation component from the outward normal direction of the computed surface.

Determination of the tensor eigenvalues. Realistic modeling of the conductivity tensor eigenvalues in the skull is a difficult task, not only because the absolute and relative thicknesses of spongiosa and compacta layers vary and their boundaries are difficult to segment, but especially because of inhomogeneous skull resistivity and an inter- and intrasubject variability which can be related to age, diseases, environmental factors, and personal constitution (Rush and Driscoll, 1968; Law, 1993; Haueisen, 1996; Pohlmeier et al., 1997; Ollikainen et al., 1999; Akhtari et al., 2002). We therefore started from the commonly used isotropic conductivity value of $\sigma_{\mathrm{skull}} = 0.0042$ S/m (Huiskamp et al., 1999; Cuffin, 1996; Buchner et al., 1997; Wagner, 1998) and simulated the anisotropic case in the following way: for a given anisotropy ratio, $\sigma^{\mathrm{rad}}{:}\sigma^{\mathrm{tang}}$, we calculated radial and tangential eigenvalues by obeying one of the following two constraints:

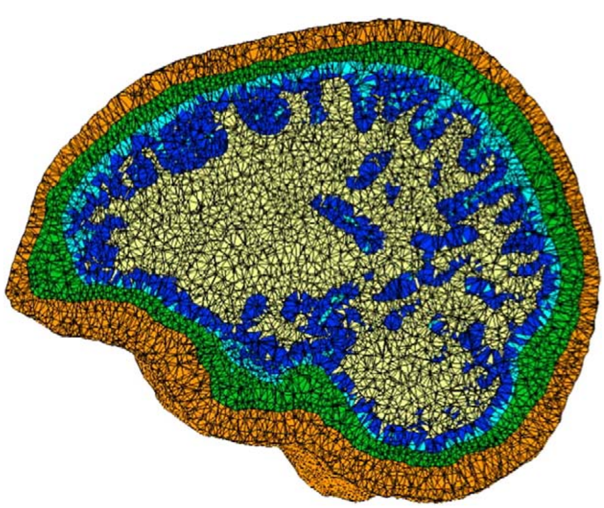

Fig. 3. Sagittal cut through the five tissue tetrahedra model (color labeling like in Fig. 1). For visualization, the software tool SimBio (2000–2003)-VM (VM: visualization module) was used.

(1) Wang et al. (2001) constraint, which states that the product of radial and tangential conductivity has to stay constant and has to be equal to the square of the isotropic conductivity:

$$\sigma^{\mathrm{rad}}\sigma^{\mathrm{tang}} \overset{!}{=} \sigma^2_{\mathrm{skull}}, \tag{1}$$

(2) and a *volume constraint* (Wolters, 2003), which retains the geometric mean of the eigenvalues and thus the volume of the conductivity tensor, i.e.,

$$\frac{4}{3}\pi\sigma^{\mathrm{rad}}(\sigma^{\mathrm{tang}})^2 \overset{!}{=} \frac{4}{3}\pi\sigma^3_{\mathrm{skull}} \tag{2}$$

According to Rush and Driscoll (1968); de Munck (1988); Peters and de Munck (1991); van den Broek et al. (1998); and Marin et al. (1998), the skull has an anisotropy ratio of 1:10. Given the paucity of measurements of skull anisotropy, we decided to include a wide range of values, spanning the only measured value of 1:10 (Rush and Driscoll, 1968) by an order of magnitude in both directions. Our primary goal was then to evaluate the overall effect of anisotropy on the electric and magnetic fields. Table 1 shows the 5 chosen anisotropy ratios and the calculated eigenvalues under the respective constraint.

Fig. 5 shows the modeled conductivity tensors of the skull.

Modeling the white matter conductivity anisotropy

Determination of the tensor eigenvectors. Following the proposition of Basser et al. (1994b), we assumed that the conductivity

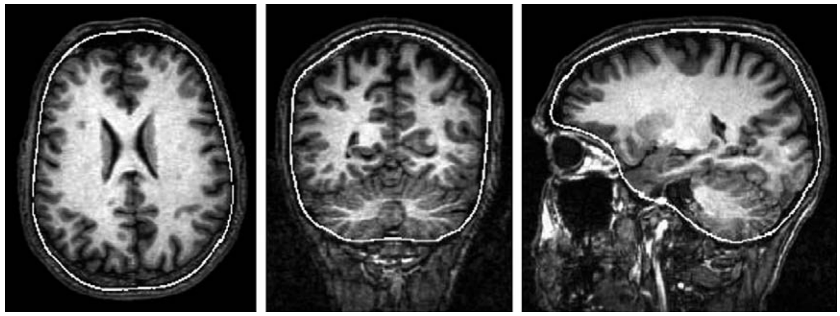

Fig. 4. Visualization of the computed surface for the determination of radial skull anisotropy directions onto the underlying T1-MRI.

tensors share the eigenvectors with the measured diffusion tensors. Shimony et al. measured diffusion anisotropy in 12 regions of interest in human white and gray matter and showed that in commissural, projection, and also association white matter, the shape of the diffusion ellipsoids is strongly prolate ("cigar-shaped"), while gray matter was measured to be close to isotropic (Shimony et al., 1999). Therefore, we assumed prolate rotationally symmetric tensor ellipsoids for the white matter compartment and modeled the conductivity tensor σ for a white matter finite element as

$$\sigma = \mathbf{S}\ \mathrm{diag}\ \left(\sigma^{\mathrm{long}},\sigma^{\mathrm{trans}},\sigma^{\mathrm{trans}}\right)\mathbf{S}^{T}, \tag{3}$$

where $\mathbf{S}$ is the orthogonal matrix of unit length eigenvectors of the measured diffusion tensor at the barycenter of the white matter finite element and σ^{long} and σ^{trans} are the eigenvalues parallel (longitudinal) and perpendicular (trans-verse) to the fiber directions, respectively, with $\sigma^{\mathrm{long}} \geq \sigma^{\mathrm{trans}}$.

Determination of the tensor eigenvalues. As for the skull compartment, we started from the commonly used isotropic conductivity value of σ_{wm} = 0.14 S/m for the white matter compartment (Geddes and Baker, 1967; Haueisen, 1996) and used Wang's constraint (see Eq. (1)) and the volume constraint (see Eq. (2)) to setup the eigenvalues for the anisotropic case. According to Nicholson (1965); Tuch et al. (2001); Shimony et al. (1999), the white matter has an anisotropy ratio of 1:10. Given the paucity of direct measurements of white matter conductivity anisotropy (Nicholson, 1965), as for the skull, we decided to include the same wide range of anisotropy ratios also for the white matter compartment (Table 1). Fig. 5 presents the normalized and colored (by trace) tensor ellipsoids for 1:2 (volume constraint) skull and white matter anisotropy in the barycenters of the finite elements. Note the left–right and top–bottom anisotropy of the corpus callosum and the pyramidal tract, respectively.

Finite element forward modeling

To represent the relationship between brain sources and bioelectric fields, we made use of the standard approaches to simulation based on the quasistatic Maxwell equations. These lead to an expression of Poisson's equation (Sarvas, 1987)

$$\nabla\cdot(\sigma\nabla\Phi) = -\nabla\cdot\mathbf{j}^{\mathrm{p}}\ in\ \Omega, \tag{4}$$

in which $\mathbf{j}^{p}$ is the primary or impressed current, Φ is the scalar potential and is the head domain. Homogeneous Neumann conditions apply on the head surface $\Gamma = \partial\Omega$,

$$(\sigma\nabla\Phi\cdot\mathbf{n})|_{\Gamma} = 0, \tag{5}$$

where $\mathbf{n}$ is the unit surface normal. Additionally, a reference electrode (FPz) is used with given zero potential. For the forward problem, the primary current and the conductivity of the volume conductor are known, and the equation is solved for the potential distribution by means of an FE Ansatz. We used a standard variational procedure in order to transform the differential Eq. (4) into an algebraic system of linear equations (Buchner et al., 1997; Wolters, 2003). For the modeling of the primary current, we used a "blurred dipole", which has been previously described and intensively validated (Buchner et al., 1997; Wolters, 2003). We solved the resulting high-resolution linear equation system, which has a large but sparse symmetric system matrix by means of an iterative Algebraic MultiGrid (AMG) preconditioned conjugate gradient method, which was parallelized for distributed memory computers (Wolters et al., 2002, 2004a). The outstanding performance of the AMG preconditioner in comparison with other methods has been demonstrated previously (Wolters et al., 2000, 2002; Mohr and Vamrunste, 2003). The AMG approach is especially suitable for anisotropic problems, and in Wolters et al. (2002), we showed its stability within this context.

Table 1
Simulated values for the skull conductivity tensor eigenvalues: the ratio was given and the eigenvalues were computed under the respective constraint

Ratio	Skull tensor eigenvalues				White matter tensor eigenvalues			
	Volume constraint		Wang's constraint		Volume constraint		Wang's constraint	
	σ^{rad}	σ^{tang}	σ^{rad}	σ^{tang}	σ^{trans}	σ^{long}	σ^{trans}	σ^{long}
1:1 (iso)	0.0042	0.0042	0.0042	0.0042	0.14	0.14	0.14	0.14
1:2	0.0026	0.0053	0.003	0.0058	0.111	0.222	0.099	0.19798
1:5	0.00143	0.0072	0.00188	0.00938	0.0818	0.41	0.0626	0.31309
1:10	0.000905	0.00905	0.00133	0.01326	0.065	0.65	0.04427	0.4427
1:100	0.000195	0.0195	0.00042	0.042	0.03016	3.016	0.014	1.4

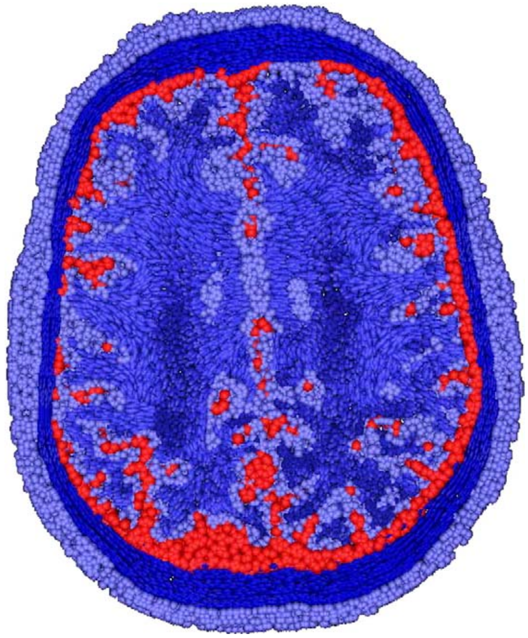

Fig. 5. Conductivity tensor ellipsoids in the barycenters of the tetrahedra elements: Normalized and colored (by trace) for 1:2 (vol.const.) skull and white matter anisotropy. The highest trace values can be found in the CSF compartment (red) and the lowest in the skull compartment (dark blue). Note the mainly top–bottom fiber directions of the pyramidal tracts and the mainly left–right orientation over the corpus callosum. Tensor validation and visualization was carried out using the software BioPSE (2002).

To describe the associated magnetic field from brain sources, one can define

$$C(y) = \oint_{\Upsilon} \frac{1}{|x-y|} dx, \tag{6}$$

where Υ is the outer contour of a MEG coil. One can then compute the magnetic flux Ψ at a MEG sensor as (Wolters et al., 2004b):

$\Psi = \Psi_{\mathrm{p}} + \Psi_{\mathrm{s}}$, with

$$\Psi_{\mathrm{p}} = \frac{\mu}{4\pi} \int_{\Omega} \mathbf{j}^{\mathrm{p}}(\mathbf{y}) C(\mathbf{y}) d\mathbf{y}, \text{ and} \tag{7}$$

$$\Psi_{\mathrm{s}} = -\frac{\mu}{4\pi} \int_{\Omega} \sigma(\mathbf{y}) \nabla \Phi(\mathbf{y}) \cdot C(\mathbf{y}) d\mathbf{y} \tag{8}$$

In these equations, Ψ_{p} is the so-called *primary magnetic flux* and Ψ_{s} the *secondary magnetic flux*, emerging from the primary or the secondary (return) currents, respectively.

To perform these computations, we used the software package NeuroFEM (NeuroFEM, 2000–2005) for EEG and MEG forward modeling. We transformed both the potential distribution within the volume conductor and, independently, the computed distributions at the EEG and MEG sensors to common average reference before error analysis and visualization.

Simulated sources

We carried out forward simulation studies for two classes of dipoles, superficial and deep sources. For the class of superficial neocortical sources, we chose two dipoles in the right somatosensory cortex, one of them approximately tangentially oriented (in the posterior–anterior direction) and the other approximately radially oriented (in the inferior–superior direction). Because it is known that both EEG and MEG are especially sensitive to conductivity changes in the vicinity of the dipole (Haueisen et al., 2000; Gencer and Acar, 2004), we checked the environment of the superficial somatosensory sources and found that only 15% of the surrounding finite elements were labeled as white matter and 0% as skull. The representative of the second class, deep sources, was chosen in the left thalamus, where the source orientation is approximately radial. The thalamus belongs to human gray matter (Shimony et al., 1999), so that the vicinity of the dipole was isotropic. The source strength of each dipole was 100 nAm.

Simulation setup to assess the influence of anisotropy

In order to model the EEG, 71 electrodes were placed on the head surface according to the international 10/20 EEG system. For the MEG, we used a BTI[1] 148 channel whole-head system. Each magnetometer flux transformer was modeled by means of a thin, closed conductor loop with a diameter of 11.5 mm, using 8 isoparametric quadratic finite row elements.

We based our evaluation of the effect of anisotropy on forward field modeling on well-known statistical difference metrics and especially on sophisticated, three-dimensional visualization techniques.

Statistical difference metrics

Meijs et al. (1989) introduced the two difference metrics that we used to compare forward solutions under different conductivity assumptions. The first is the Relative Difference Measure (RDM), defined as

$$\mathrm{RDM} = \sqrt{\sum_{i=1}^{m} \left(\frac{\underline{u}_{\mathrm{iso}}^{[i]}}{\sqrt{\sum_{i=1}^{m} \left(\underline{u}_{\mathrm{iso}}^{[i]}\right)^2}} - \frac{\underline{u}_{\mathrm{ani}}^{[i]}}{\sqrt{\sum_{i=1}^{m} \left(\underline{u}_{\mathrm{ani}}^{[i]}\right)^2}} \right)}, \tag{9}$$

where m denotes the number of sensors and $\underline{u}_{\mathrm{iso}}^{[i]}$ and $\underline{u}_{\mathrm{ani}}^{[i]}$ the ith component of the simulated field vector ($\underline{u}$ is either the potential ϕ or the magnetic flux Ψ) in the isotropic and the anisotropic case, respectively. The RDM is a measure for the topography error (minimal error: RDM = 0). The second error measure, the MAGnification factor (MAG), is defined as

$$\mathrm{MAG} = \frac{\sqrt{\sum_{i=1}^{m} \left(\underline{u}_{\mathrm{ani}}^{[i]}\right)^2}}{\sqrt{\sum_{i=1}^{m} \left(\underline{u}_{\mathrm{iso}}^{[i]}\right)^2}} \tag{10}$$

and gives an indication of errors in the magnitude (minimal error: MAG = 1).

Visualization of return currents

In our experience, the visualization of return currents $\sigma\mathbf{E}$ is both intuitive and highly informative when trying to understand the effect of anisotropy. Using a Line Integral Convolution (LIC) technique (Cabral and Leedom, 1993), we computed the return

[1] 4-D NeuroImaging, San Diego, USA.

current directly over the surface of the head and on coronal slices through the head. This technique permits a continuous depiction of the directional information of the current flow and is combined with a color mapping of the current magnitude that gives insight into the qualitative and quantitative aspects of the current flow.

We also used a technique called stream surfaces (Garth et al., 2004) to assess the influence of tissue conductivity anisotropy.

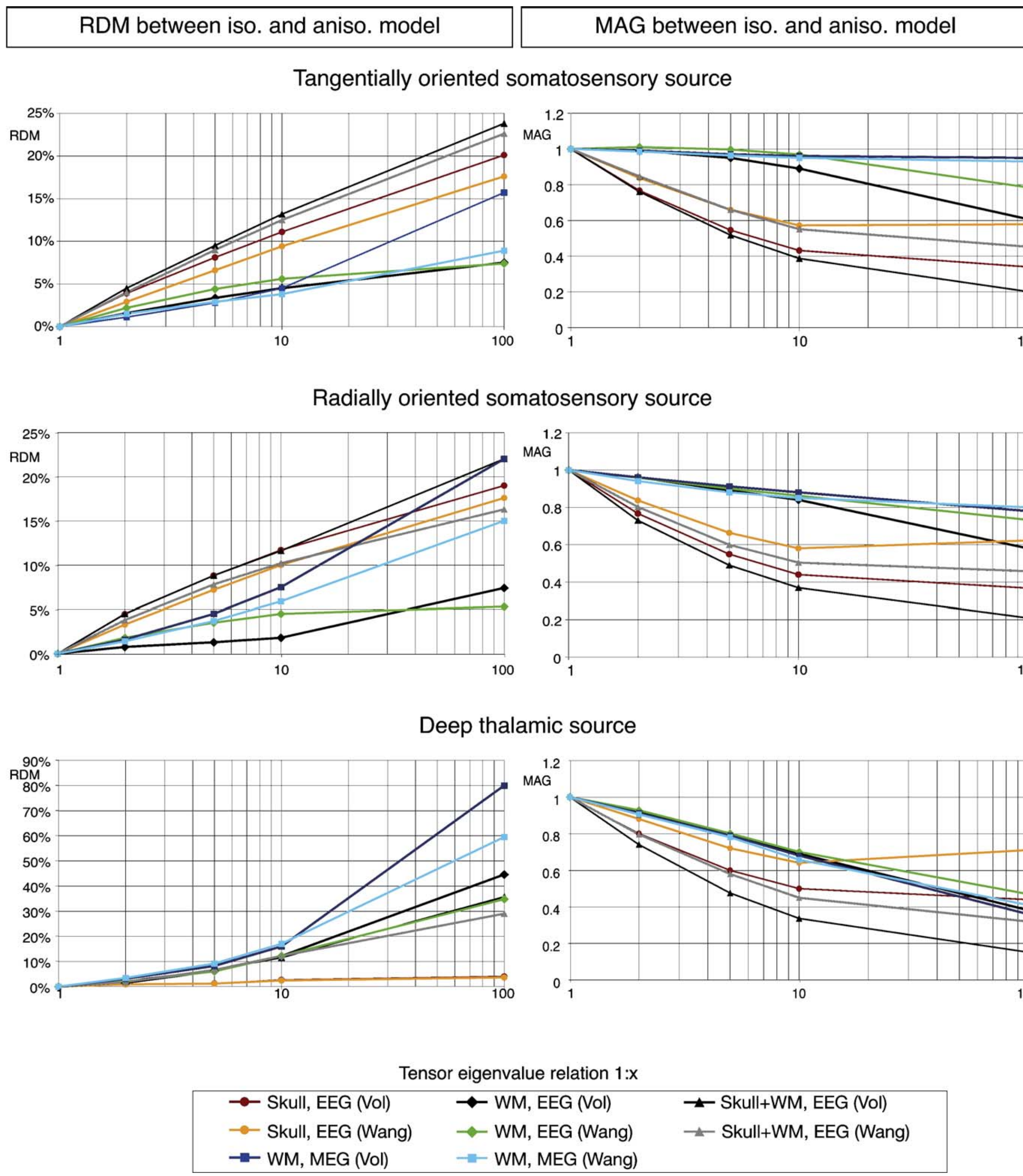

Fig. 6. Tangentially (top row) and radially (middle row) oriented somatosensory source and deep thalamic source (bottom row): EEG and MEG topography error (left) and magnitude error (right) for different anisotropy ratios: for the EEG, errors due to anisotropy effects of skull, white matter and both skull and white matter are presented for the tensor volume retaining (Vol) and Wang's constraint (Wang). For MEG, only white matter anisotropy effects for both constraints are presented because skull anisotropy was found to have no influence.

Stream surfaces are defined as surfaces generated by an arbitrary starting curve that is then advected along the vector field. They often constitute a significant improvement over individual streamlines because they provide a better understanding of depth and spatial relationships in the exploration of three-dimensional flows.

Results

The goal of this study was to evaluate the influence of anisotropic conductivity on the simulation of electric and magnetic fields from dipolar sources in the brain. We present here results from the 3 dipole source types described above and, for each case, compare the results with isotropic and anisotropic assumptions for each of the white matter and the skull. We used a source magnitude of 100 nAm and, except for the statistical metrics in Fig. 6, we compared the isotropic case with the 1:10 (volume constraint) anisotropic case, which is considered closest to realistic white matter (Nicholson, 1965) and skull anisotropy (Rush and Driscoll, 1968).

Tangentially oriented superficial source

Fig. 6 (top row) shows the resulting topography (left) and magnification (right) errors for various anisotropy ratios, when either obeying the volume or Wang's constraint. In Fig. 7, the EEG and MEG field distribution, linearly interpolated between the sensors (top row), and isopotential surfaces within the volume conductor (bottom row) are shown for the isotropic case (left), for anisotropy of skull (middle) and white matter compartment (right). In Fig. 8, we used the stream surface technique to visualize the effect of skull anisotropy with regard to the return current flow.

Figs. 7 and especially 8 clearly show that skull anisotropy smears out and weakens the EEG, resulting in a pattern that looks more like one of a deeper and weaker dipole. In contrast to the isotropic model, the isopotential surfaces for -5 μV and 5 μV were no longer able to break through the skull compartment (Fig. 7). Fig. 8 furthermore shows the effect of the Neumann boundary conditions (Eq. (5)) on the return currents, namely that the normal component of the current is zero at the head surface which is expressed by the wide opening of the stream surfaces at the head boundary. Skull anisotropy led to a topography error (RDM) of about 10% and a magnification factor of about 0.5 (Fig. 6, top row, circles). The volume constraint (in black) produced larger errors in comparison to the Wang constraint (in red). Skull anisotropy was found to have no influence (RDM < 1%, MAG ≈ 1) on the MEG topography and magnitude for both constraints (not shown in Fig. 6).

Including white matter anisotropy (isotropic skull layer) resulted in low RDM (5%) and magnitude (MAG of about 0.95) errors.

Including anisotropy of both skull and the white matter layer led to a topography error of about 13% for EEG for both constraints (Fig. 6, top row, triangles) which was only marginally higher than the values for skull anisotropy alone.

Radially oriented superficial source

For the case of a radially oriented dipole, Fig. 6 (middle row) shows the RDM(left) and MAG (right) errors and Fig. 9 the EEG and MEG fields (top row) and isopotential surfaces (bottom row) for the isotropic model (left) and the models with an anisotropic skull compartment (middle) and an anisotropic white matter layer (right).

Including anisotropy of the skull (Fig. 6, middle row, circles), we found an RDM for the EEG of about 11% and a MAG of close to 0.5. Again, the volume constraint (in black) produced slightly bigger errors than Wang's constraint (in red). As Fig. 9 shows, skull anisotropy again smeared out and weakened the EEG, the pattern looking like one of a deeper and weaker dipole. In contrast to the isotropic model, the isopotential surfaces for -1 μV and 7 μV were no longer able to break through the skull compartment. As with the tangential superficial source, we found no influence of skull anisotropy on the MEG field distribution.

Including white matter anisotropy had a slightly weaker influence on the topography of the EEG (less than 5% for both constraints) compared to the tangential dipole case but a larger effect (MAG = 0.85) on the magnitude error (Fig. 6, middle row, squares). For the MEG, we note that both RDM and MAG errors are nearly twice as large when compared with the tangential case (Fig. 6, middle row, in blue).

If both compartments were simultaneously anisotropic (Fig. 6, middle row, triangles), the errors for the EEG were very similar to

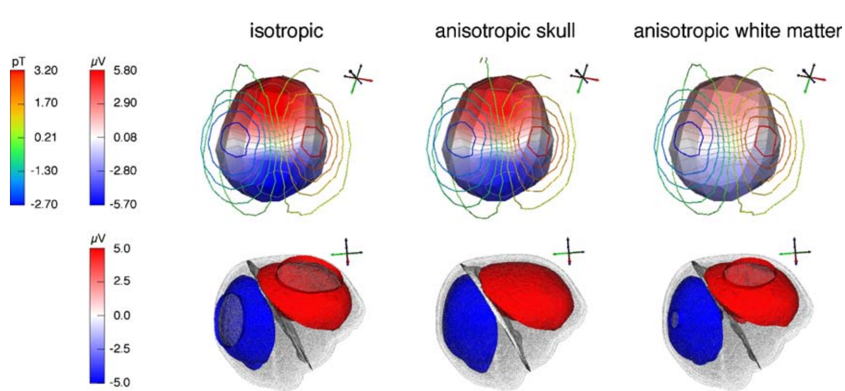

Fig. 7. Linearly interpolated EEG isopotential lines (in a blue–white–red scale) and MEG isofield lines (in a rainbow scale) (top row) and isopotential surfaces for -5 μV (blue), 0 μV (white), and 5 μV (red) (bottom row) for a mainly tangentially oriented source in somatosensory cortex: isotropic model (Left), 1:10 anisotropic skull using the volume constraint (middle) and 1:10 anisotropic white matter using the volume constraint (right).

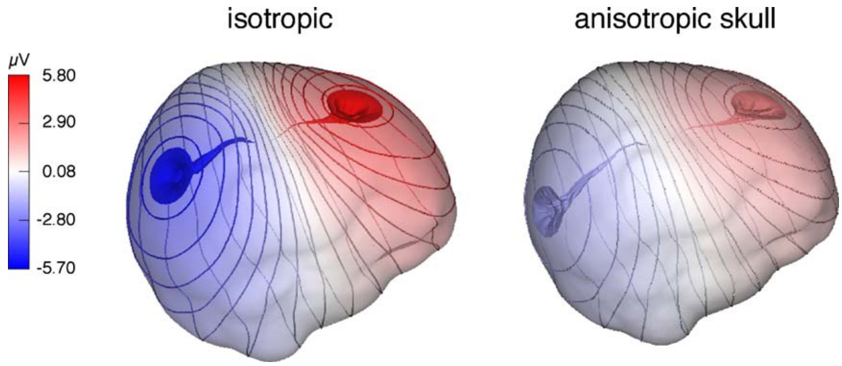

Fig. 8. Visualization of return current surfaces for the mainly tangentially oriented source in somatosensory cortex for the isotropic model (left) and the model with 1:10 anisotropic skull compartment (right): in order to define a starting line for the flow integration, we divided the interval from highest to lowest surface potential for both isotropic and anisotropic model into 19 intervals (18 isopotential lines). The flow computation then started at the maximal and minimal isopotential lines for both models and integrated along the return current flow into the volume until close to the singularity of the primary current. We used the color of the surface isopotential value for the color coding of the corresponding flow surface.

the errors of pure skull anisotropy, while the errors for the MEG were approximately identical to the errors of white matter anisotropy (not shown).

Influence on a deep thalamic source

Fig. 6 (bottom row) shows the resulting RDM and MAG errors and Fig. 10 the EEG and MEG fields (top row) and isopotential surfaces (bottom row) for the isotropic model (left) and the models with an anisotropic skull compartment (middle) and an anisotropic white matter layer (right) for the deep thalamic source.

Results in both figures show that for the deep source, with an RDM of more than 10% for the EEG and more than 15% for the MEG, white matter anisotropy (Fig. 6, bottom row, squares) was the leading cause of topography error. Furthermore, this error was strongly increasing for the 1:100 anisotropy ratio. With a MAG error of about 0.7, white matter anisotropy strongly weakened the EEG and MEG.

While the topography error was negligible, skull anisotropy (Fig. 6, bottom row, circles) strongly weakened the magnitude of the simulated fields, so that the isopotential surfaces for -3 μV and 3 μV in Fig. 10 (middle) no longer reached the model surface.

Fig. 11 shows results from the line integral convolution technique to visualize the return current flow on the surface of the FE model. We found two return current areas of minimal amplitude (in blue), one on the top and one on the bottom of the model (not shown). The amplitude of the return currents was well correlated to the thickness of the skull (compare the color scaling of the return currents with the segmented model in Fig. 1). While high return currents were flowing in the thin lateral areas, they were significantly attenuated in the thicker occipital areas and in the areas of the frontal sinuses. The white matter anisotropy mainly weakened the surface return currents.

In Fig. 12, we visualized the projection of the return current vector field onto a coronal slice (in black) for the deep thalamic source for the isotropic case and the case of the anisotropic white matter compartment. The amplitude of the return current was color coded on two linear scales, one from 0.3 to 0.003 A/m^2 in the neighborhood of the source and the second from 0.003 to 0 A/m^2 for remote locations. In the isotropic case, the return currents flowed on nearly circular loops in the classic dipolar pattern. In the anisotropic case, we observe that the main direction component (main eigenvector) of the conductivity tensors, i.e., the main fiber direction, and the computed return current in the white matter compartment are highly parallel.

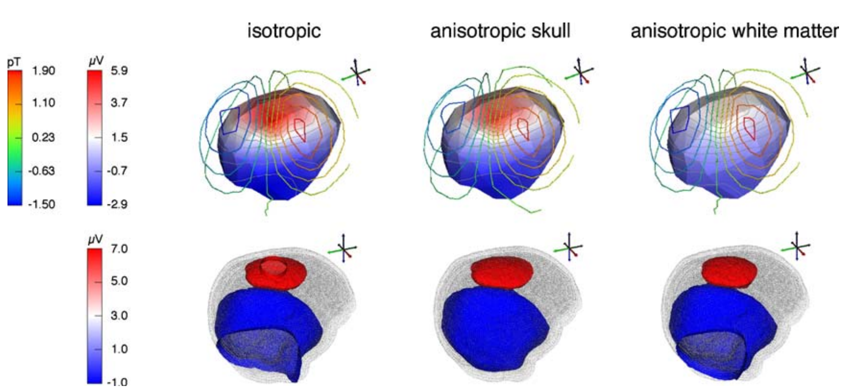

Fig. 9. Linearly interpolated EEG isopotential lines (in a blue–white–red scale) and MEG isofield lines (in a rainbow scale) (top row) and isopotential surfaces for -1 μV and 7 μV (bottom row) for a mainly radially oriented source in somatosensory cortex: isotropic model (Left), 1:10 anisotropic skull using the volume constraint (middle) and 1:10 anisotropic white matter using the volume constraint (right).

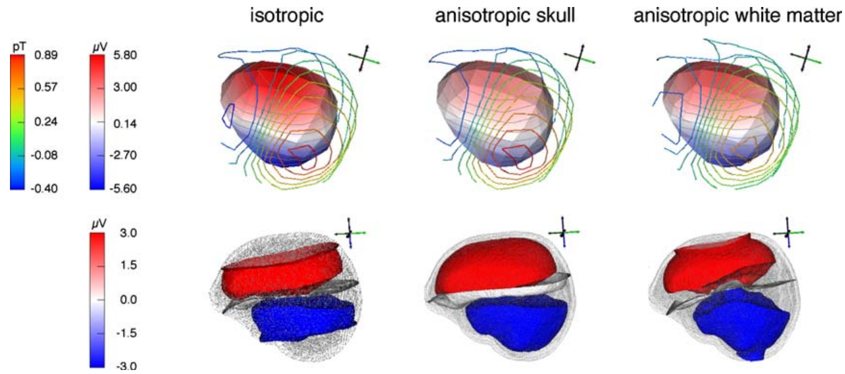

Fig. 10. Linearly interpolated EEG isopotential lines (in a blue–white–red scale) and MEG isofield lines (in a rainbow scale) (top row) and isopotential surfaces for -3 µV, 0 µV, and 3 µV (bottom row) for a deep thalamic source: isotropic model (Left), 1:10 anisotropic skull using the volume constraint (middle) and 1:10 anisotropic white matter using the volume constraint (right).

The results in Fig. 13 support this observation by showing the cosine (color coded from 0 to 1) of the angle between the main eigenvector of the white matter conductivity tensor in the anisotropic model (its projection onto the coronal plane is shown in black) and the return current vector (not shown here) for a slice in the isotropic model and the model with anisotropic white matter compartment. While in the isotropic case, values close to 1 appeared just by chance, in the anisotropic case, there was close concordance between current direction and local fiber orientation, as the areas of red and yellow coloring in Fig. 13 show. The white matter anisotropy thus strongly influenced the flow of the return currents and therefore the EEG and MEG.

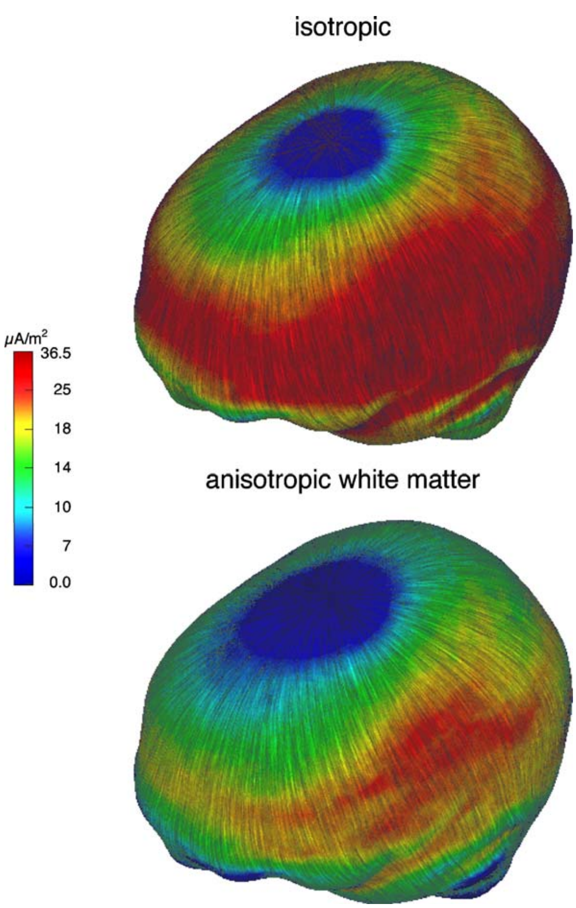

Fig. 11. Surface return current for the left thalamic source in the isotropic model and in the model with 1:10 anisotropic white matter compartment (volume constraint) visualized with the LIC technique. The magnitude of the return current is color coded. The direction is indicated by the texture.

In Fig. 14, we applied the LIC visualization technique to the return currents on a coronal slice of the model color coded with the return current amplitude for the isotropic (top row) and anisotropic (bottom row) white matter compartments to further quantify the effect of volume conduction for the deep source. Our first observation was that the currents close to the source and, because of its high conductivity, in the CSF compartment, have relatively high amplitudes. With regard to the white matter compartment, the figure further underscores our hypotheses of increased return current flow along the fiber bundles in the anisotropic model (bottom row) when compared to the isotropic case (top row). This figure also shows the effect of the poorly conducting skull compartment; current flowed along the inner skull boundary, entered the skull, and penetrated it in a clearly radial direction while its amplitude was strongly weakened; it entered the skin compartment and fulfilled the Neumann condition at the head surface, i.e., the condition that the normal component of the current is zero, by either flowing tangentially to the surface or having a zero amplitude on top and on the bottom of the model (compare to the areas with zero amplitude in Fig. 11).

Discussion and conclusion

In this paper, we built a realistic finite element head volume conductor model taking into account skull and white matter anisotropy. We exploited a combined T1-/PD-MRI dataset for the construction of a five-tissue model with an anisotropic skull compartment and a whole-head DT-MRI dataset to determine white matter anisotropy. Our goal was to study the influence of anisotropic tissue conductivity on forward EEG and MEG computations. We used sophisticated high-resolution visualization techniques and statistical error quantifications to provide insights into the effect of anisotropy.

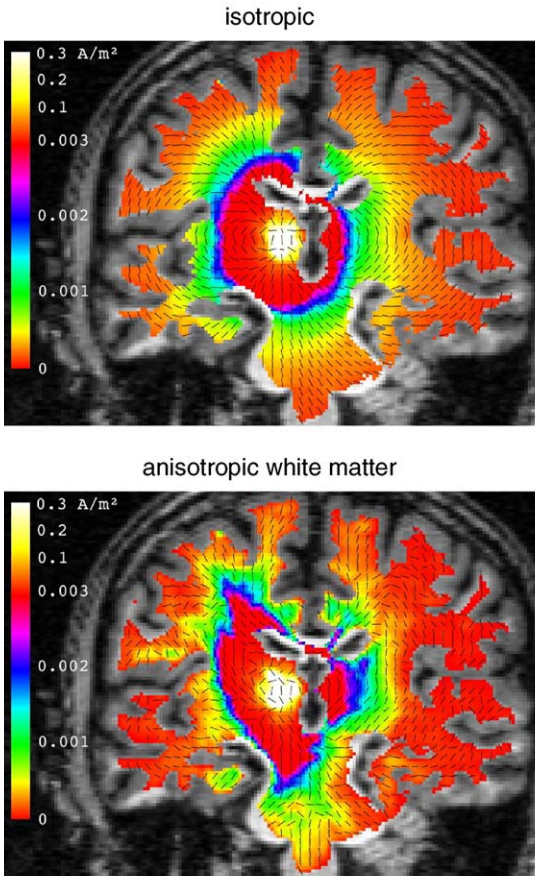

Fig. 12. Visualization of the return currents (thalamic source) within the white matter mask on a coronal slice passing through the thalamus overlaid on the T1-MRI for the isotropic model and the corresponding model with anisotropic white matter compartment (volume constraint): the projections of the current directions on the image plane are shown as black lines and the magnitude is color coded (two linear scales, one from 0.3 to 0.003 A/m^2 in the neighborhood of the source and the second from 0.003 to 0 A/m^2 for remote locations.

For a superficial tangentially oriented source in the somatosensory cortex, our results concerning the influence of skull anisotropy on the EEG potential distribution are in agreement with the observations of others (Marin et al., 1998; van den Broek et al., 1998). We visualized the effect of skull anisotropy on the return currents and showed that skull anisotropy smears out and weakens the EEG, resulting in a pattern that looks more like that of a deeper and weaker dipole.

The MEG results, in contrast, suggest that skull anisotropy has no influence (RDM < 1%, MAG ≈ 1) on MEG topography and magnitude. This is in agreement with the results of van den Broek et al. (1998) in a realistic FE head model and with the generally accepted idea that volume currents in the skull layer provide negligible contributions to the magnetic field (Hämäläinen and Sarvas, 1987). The effect of white matter anisotropy was, by contrast, negligible with an RDM of only about 5% and a MAG close to 1.0 for a realistic anisotropy ratio of 1:10, observations which agree well with those of Haueisen et al. (2002). Note here, that only 15% of the finite elements in the vicinity of the somatosensory source were labeled as white matter and, following the results of Haueisen et al. (2000) and Gencer and Acar (2004), we would expect a much larger influence for sources (even for eccentric ones) which are closer to or which are even embedded in an anisotropic medium.

For a superficial and radially oriented source, the EEG results for skull anisotropy agree well with the observations of others (Marin et al., 1998; van den Broek et al., 1998). With an RDM of about 11% and a MAG of about 0.5, the influence on the potential topography was similar to that for the tangential dipole. The influence of skull anisotropy on the MEG was again minimal, in agreement with the reports of other groups (Hämäläinen and Sarvas, 1987; van den Broek et al., 1998). In our study, realistic white matter anisotropy only had a weak effect on the topography of the EEG (RDM < 5%), most likely because only few finite elements in the neighborhood of the source were assigned to the white matter compartment (Haueisen et al., 2000; Gencer and Acar, 2004). For the MEG, when compared to the error for the tangentially oriented source, RDM and MAG errors were twice as large, a result which again agrees with other reports (Haueisen et al., 2002) (our MEG results have to be compared to the flux density component B_y in Table 2 of Haueisen et al., 2002). The large MEG topography error can be explained by the fact that white matter anisotropy influences the secondary (return) currents.

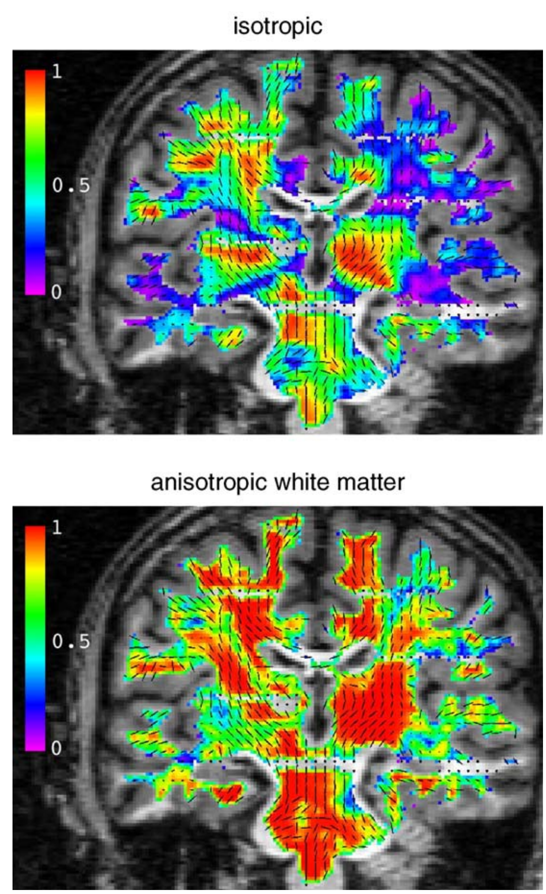

Fig. 13. As a measure of the parallelity/similarity, the cosine of the angle between the main eigenvector of the conductivity tensor in anisotropic white matter (its projection onto the coronal plane is shown in black) and the return current vector (not shown here) is color coded within the white matter mask and overlaid on the T1-MRI for the isotropic model (top) and the corresponding model with anisotropic white matter compartment (volume constraint, bottom row).

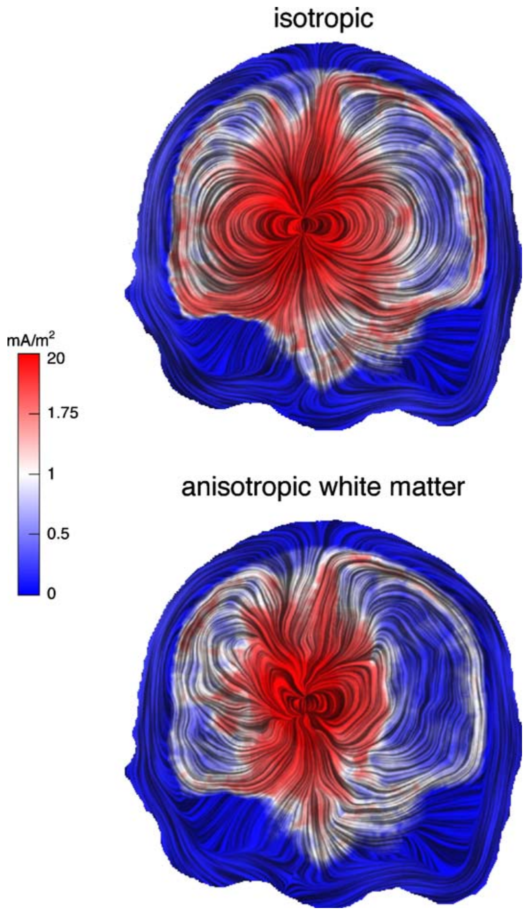

Fig. 14. Return currents for the left thalamic source on a coronal cut through the isotropic model (top row) and the model with 1:10 anisotropic white matter compartment (volume constraint, bottom row): the return current directions are indicated by the texture and the magnitude is color coded (the upper scale was limited to 0.02 A/m^2, see Fig. 12 for the correct magnitude in the source area).

The ratio of the secondary to the primary magnetic flux increases with increasing ratio of the radial to the tangential dipole orientation components (Haueisen, 1996).

The last simulated source was a deeper and therefore mainly radially oriented source in the left thalamus. In contrast to the superficial sources, there was a strong remote tissue anisotropy in the region between the source and the measurement sensors. From the line integral convolution visualization of the return currents, we found multiple areas where the main fiber direction and the return current vector in the model with anisotropic white matter compartment are highly parallel with highest degrees of parallelity within the bigger white matter fiber bundles, e.g., the left and right pyramidal tracts. In the isotropic case, the return currents are smoothly dipolar in shape, but in the anisotropic case, the fiber geometry influences the flow to be largely parallel to the white matter fiber tracts. Thus, for deeper sources, the leading cause for topography error was no longer the anisotropy of the skull but that of the white matter compartment. With an RDM of more than 15% for the MEG and more than 10% for the EEG and a MAG of about 0.7, the effect of white matter anisotropy should not be neglected.

We have presented here the effect of remote anisotropy, i.e., in which the thalamus was modeled as an isotropic structure. Our reasoning was that the thalami are part of the human gray matter compartment (Shimony et al., 1999). Nevertheless, most histological methods identify 14 functionally specific anisotropic thalamic clusters referred to as nuclei (Buren and Borke, 1972). Recently, it was shown that DT-MRI can non-invasively resolve the fiber orientation of those nuclei, using an automatic segmentation method (Wiegell et al., 2003). Therefore, in an even more realistic volume conductor model, the thalamus by itself would have to be considered as anisotropic gray matter tissue. Furthermore, the whole cortex is known to have an anisotropy ratio of about 1:2 (Nicholson and Freeman, 1975). If we then take into account that local conductivity changes in the vicinity of the sources have a large effect on EEG and MEG (Haueisen et al., 2000; Gencer and Acar, 2004), then the errors might be substantially larger than those presented in this study.

Our visualization results also showed the importance of the CSF compartment in determining bioelectric fields. Because of its high conductivity, the return current in this layer was much more distinct than in the rest of the head model so that it can be seen as a compartment with a strong "current distribution" effect. Because the conductivity of the human CSF is known quite accurately (Baumann et al., 1997), this result further underscores the importance of realistic high-resolution finite element head modeling when compared to boundary or spherical head modeling.

We conclude that with the new visualization techniques for return current flow in high-resolution FE models, presented in our paper, insight is gained into the effect of tissue anisotropy, which is now more easily accessible. One implicit premise of our study was that if anisotropy affects the accuracy of the forward solution, it will have at least as strong an influence over solutions to the associated inverse problem, which will be examined in a consequent paper (Anwander et al., 2002, in preparation). We summarize that the modeling of skull anisotropy is important for EEG and can be neglected for MEG studies. Our results suggest that the exact representation of the CSF compartment and the modeling of gray and white matter anisotropy is important for both EEG and MEG based reconstruction of the neural sources. Concerning white matter anisotropy, this is especially true with regard to the reconstruction of the orientation and strength components of the sources in the associated EEG and MEG inverse problem. The more the source is surrounded by anisotropy, the larger the influence. Recent developments for the finite element method in EEG/MEG source reconstruction (Weinstein et al., 2000; Wolters et al., 2002, 2004b; Gencer and Acar, 2004) dramatically reduce the complexity of the computations, so that the main disadvantage of FE modeling no longer exists and such modeling even with very high resolutions is now practical.

Acknowledgments

The authors would like to thank A. Friederici from the MPI for Human Cognitive and Brain Sciences Leipzig, E. Zeidler and W. Hackbusch from the MPI for Mathematics in the Sciences and Seok Lew and Chris Johnson from the SCI Institute in Salt Lake City for their support and the many important and helpful comments. This work was supported by the MPI for Mathematics in the Sciences, Leipzig, by the IST-program of the European Community, project SIM-BIO (http://www.simbio.de) and the NIH NCRR center for Bioelectric Field Modeling, Simulation and Visualization (http://www.sci.utah.edu/ncrr).

References

Akhtari, M., Bryant, H., Marmelak, A., Flynn, E., Heller, L., Shih, J., Mandelkern, M., Matlachov, A., Ranken, D., Best, E., DiMauro, M., Lee, R., Sutherling, W., 2002. Conductivities of three-layer live human skull. Brain Topogr. 14 (3), 151–167.

Anwander, A., Wolters, C., Dümpelmann, M., Knösche, T., 2002. Influence of realistic skull and white matter anisotropy on the inverse problem in EEG/MEG-source localization. Proceedings of The 13th International Conference on Biomagnetism, pp. 679–681.

Anwander, A., Wolters, C., Dümpelmann, M., Knösche, T., in preparation. Influence of realistic skull and white matter anisotropy on the inverse problem in EEG/MEG-source localization.

Basser, P., Pierpaoli, C., 1996. Microstructural and physiological features of tissues elucidated by quantitative-diffusion-tensor MRI. J. Magn. Reson., B 111, 209–219.

Basser, P., Bihan, D.L., Mattiello, J., 1994a. Estimation of the effective self-diffusion-tensor from the NMR spin echo. J. Magn. Res., B 103, 247–254.

Basser, P., Mattiello, J., LeBihan, D., 1994b. MR diffusion tensor spectroscopy and imaging. Biophys. J. 66, 259–267.

Baumann, S., Wozny, D., Kelly, S., Meno, F., 1997. The electrical conductivity of human cerebrospinal fluid at body temperature. IEEE Trans. Biomed. Eng. 44 (3), 220–223.

BioPSE, 2002. Problem Solving Environment for modeling, simulation, and visualization of bioelectric fields. Scientific Computing and Imaging Institute (SCI), http://software.sci.utah.edu/biopse.html.

Bruno, P., Vatta, F., Minimel, S., Inchingolo, P., 2004. Referenced EEG and head volume conductor model: Geometry and parametrical setting. Proc. of the 26th Annual Int. Conf. IEEE Engineering in Medicine and Biology Society. San Francisco, USA, Sep. 1–5, http://www.ucsfresno.edu/embs2004.

Buchner, H., Knoll, G., Fuchs, M., Rienäcker, A., Beckmann, R., Wagner, M., Silny, J., Pesch, J., 1997. Inverse localization of electric dipole current sources in finite element models of the human head. Electroencephalogr. Clin. Neurophysiol. 102, 267–278.

Buren, J.V., Borke, R., 1972. Variations and Connections of the Human Thalamus vol. 2. Springer-Verlag, New York.

Cabral, B., Leedom, L.C., 1993. Imaging vector fields using line integral convolution. Proceeding of SIGGRAPH 1993 Conference, pp. 263–272.

Cuffin, B., 1996. EEG localization accuracy improvements using realistically shaped head models. IEEE Trans. Biomed. Eng. 43, 299–303.

CURRY, 2000. CURrent Reconstruction and Imaging, http://www.neuro.com.

de Munck, J., 1988. The potential distribution in a layered anisotropic spheroidal volume conductor. J. Appl. Phys. 64, 465–469.

Garth, C., Tricoche, X., Salzbrunn, T., Bobach, T., Scheuermann, G., May 2004. Surface techniques for vortex visualization. In: Proceedings of Joint Eurographics-IEEE TCVG Symposium on Visualization. (to appear). URL http://www.sci.utah.edu/publications/garth04/vissym04.pdf.

Geddes, L., Baker, L., 1967. The specific resistance of biological material. A compendium of data for the biomedical engineer and physiologist. Med. Biol. Eng. 5, 271–293.

Gencer, N., Acar, C., 2004. Sensitivity of EEG and MEG measurements to tissue conductivity. Phys. Med. Biol. 49, 701–717.

Haase, A., Frahm, J., Matthaei, D., Hänicke, W., Merboldt, K.-D., 1986. FLASH imag.: rapid NMR imag. using low flip-angle pulses. J. Magn. Reson. 67, 258–266.

Hämäläinen, M., Sarvas, J., 1987. Feasibility of the homogeneous head model in the interpretation of neuromagnetic fields. Phys. Med. Biol. 32, 91–97.

Haueisen, J., 1996. Methods of numerical field calculation for neuromagnetic source localization. PhD thesis, Shaker-Verlag Aachen, ISBN 3-8265-1691-5.

Haueisen, J., Ramon, C., Brauer, H., Nowak, H., 2000. The influence of local conductivity changes on MEG and EEG. Biomed. Tech. 45 (7–8), 211–214.

Haueisen, J., Tuch, D., Ramon, C., Schimpf, P., Wedeen, V., George, J., Belliveau, J., 2002. The influence of brain tissue anisotropy on human EEG and MEG. NeuroImage 15, 159–166.

Huiskamp, G., Vroeijenstijn, M., van Dijk, R., Wieneke, G., van Huffelen, A., 1999. The need for correct realistic geometry in the inverse EEG problem. IEEE Trans. Biomed. Eng. 46 (11), 1281–1287.

Koch, M., 2000. Measurement of the self-diffusion tensor of water in the human brain. PhD thesis, Univ. of Leipzig, Germany.

Law, S., 1993. Thickness and resistivity variations over the upper surface of the human skull. Brain Topogr. 2, 99–109.

Lee, J., Garwood, M., Menon, R., Adriany, G., Anderson, P., Truwit, C., Ugurbil, K., 1995. High contrast and fast 3 D magnetic resonance imaging at high fields. Magn. Reson. Med. 34, 308–312.

Marin, G., Guerin, C., Baillet, S., Garnero, L., Meunier, G., 1998. Influence of skull anisotropy for the forward and inverse problem in EEG: simulation studies using the FEM on realistic head models. Hum. Brain Mapp. 6, 250–269.

Meijs, J., Weier, O., Peters, M., van Oosterom, A., 1989. On the numerical accuracy of the boundary element method. IEEE Trans. Biomed. Eng. 36, 1038–1049.

Mohr, M., Vamrunste, B., 2003. Comparing iterative solvers for linear systems associated with the finite difference discretisation of the forward problem in electro-encephalographic source analysis. Med. Biol. Eng. Comput. 41, 75–84.

NeuroFEM, 2000–2005. A parallel MPI-based C^{++} class structured code for fast high-resolution EEG and MEG forward modeling. A. Anwander and C.H. Wolters SimBio (2000–2003).

Nicholson, P., 1965. Specific impedance of cerebral white matter. Exp. Neurol. 13, 386–401.

Nicholson, C., Freeman, J., 1975. Experimental optimization of current source-density technique for anuran cerebellum. J. Neurophysiol. 38 (2), 369–382.

Norris, D., Börnert, P., 1993. Coherence and interference in ultra-fast RARE experiments. J. Magn. Reson., A 105, 123–127.

Ollikainen, J., Vauhkonen, M., Karjalainen, P., Kaipio, J., 1999. Effects of local skull inhomogeneities on EEG source estimation. Med. Eng. Phys. 21, 143–154.

Pajevic, S., Pierpaoli, C., 1999. Color schemes to represent the orientation of anisotropic tissues from diffusion tensor data: application to white matter fiber tract mapping in the human brain. Magn. Reson. Med. 42, 526–540.

Peters, M., de Munck, J., 1991. The influence of model parameters on the inverse solution based on MEGs and EEGs. Acta Oto-Laryngol, Suppl. (Stockh) 491, 61–69.

Pham, D., Prince, J., 1999. An adaptive fuzzy C-means algorithm for image segmentation in the presence of intensity inhomogeneities. Pat. Rec. Let. 20, 57–68.

Pohlmeier, R., Buchner, H., Knoll, G., Rienäcker, A., Beckmann, R., Pesch, J., 1997. The influence of skull-conductivity misspecification on inverse source localization in realistically shaped finite element head models. Brain Topogr. 9 (3), 157–162.

Ramon, C., Schimpf, P., Haueisen, J., Holmes, M., Ishimaru, A., 2004. Role of soft bone, CSF and gray matter in EEG simulations. Brain Topogr. 16 (4), 245–248.

Roth, B., Balish, M., Gorbach, A., Sato, S., 1993. How well does a three-sphere model predict positions of dipoles in a realistically shaped head. Electroencephalogr. Clin. Neurophysiol. 87, 175–184.

Rush, S., Driscoll, D., 1968. Current distribution in the brain from surface electrodes. Anesth. Analg. 47 (6), 717–723.

Sarvas, J., 1987. Basic mathematical and electromagnetic concepts of the biomagnetic inverse problem. Phys. Med. Biol. 32 (1), 11–22.

Schimpf, P., Ramon, C., Haueisen, J., 2002. Dipole models for the EEG and MEG. IEEE Trans. Biomed. Eng. 49 (5), 409–418.

Shimony, J.S., McKinstry, R., Akbudak, E., Aronovitz, J.A., Snyder, A.Z., Lori, N.F., Cull, T.S., Conturo, T.E., 1999. Quantitative diffusion-tensor anisotropy brain MR imaging: normative human data and anatomic analysis. Radiology 212, 770–784.

SimBio, 2000–2003. SimBio: A Generic Environment for Bio-Numerical Simulation, IST-Program of the European Commission, Project No.10378, http://www.simbio.de.

Tuch, D., Wedeen, V., Dale, A., George, J., Belliveau, J., 2001. Conductivity tensor mapping of the human brain using diffusion tensor MRI. Proc. Natl. Acad. Sci. U. S. A. 98 (20), 11697–11701.

van den Broek, S., Reinders, F., Donderwinkel, M., Peters, M., 1998. Volume conduction effects in EEG and MEG. Electroencephalogr. Clin. Neurophysiol. 106, 522–534.

Wagner, M., 1998. Rekonstruktion neuronaler Ströme aus bioelektrischen und biomagnetischen Messungen auf der aus MR-Bildern segmentierten Hirnrinde. PhD thesis, Shaker-Verlag Aachen, ISBN 3-8265-4293-2.

Wang, Y., Haynor, D., Kim, Y., 2001. An investigation of the importance of myocardial anisotropy in finite-element modeling of the heart: methodology and application to the estimation of defibrillation efficacy. IEEE Trans. Biomed. Eng. 48 (12).

Weinstein, D., Zhukov, L., Johnson, C., 2000. Lead-field bases for electroencephalography source imaging. Ann. Biomed. Eng. 28 (9), 1059–1066.

Wiegell, M., Tuch, D., Larsson, H., Wedeen, V., 2003. Automatic segmentation of thalamic nuclei from diffusion tensor magnetic resonance imaging. NeuroImage 19, 391–401.

Wolters, C., 2003. Influence of Tissue Conductivity Inhomogeneity and Anisotropy on EEG/MEG based Source Localization in the Human Brain. No. 39 in MPI Series in Cognitive Neuroscience. MPI of Cognitive Neuroscience Leipzig, iSBN 3-936816-11-5 (also: Leipzig, Univ., Diss., http://dol.uni-leipzig.de).

Wolters, C., Reitzinger, S., Basermann, A., Burkhardt, S., Hartmann, U., Kruggel, F., Anwander, A., 2000. Improved tissue modeling and fast solver methods for high resolution FE-modeling in EEG/MEG-source localization. In: Nenonen, J., Ilmoniemi, R., Katila, T. (Eds.), BIOMAG2000, Proc. of the 12th Int. Conf. on Biomagnetism. Helsinki Univ. of Tech., Finland, Aug. 13–17. pp. 655–658. http://biomag2000.hut.fi.

Wolters, C., Kuhn, M., Anwander, A., Reitzinger, S., 2002. A parallel algebraic multigrid solver for finite element method based source localization in the human brain. Comput. Vis. Sci. 5 (3), 165–177.

Wolters, C.H., Anwander, A., Reitzinger, S., Haase, G., 2004. Algebraic multigrid with multiple right-hand-side treatment for an efficient computation of EEG and MEG lead field bases. In: Halgren, E., Ahlfors, S., Hämäläinen, M., Cohen, D. (Eds.), BIOMAG2004, Proc. of the 14th Int. Conf. on Biomagnetism. Boston, USA, Aug. 8–12. pp. 465–466. http://www.biomag2004.org.

Wolters, C.H., Grasedyck, L., Hackbusch, W., 2004b. Efficient computation of lead field bases and influence matrix for the FEM-based EEG and MEG inverse problem. Inverse Problems 20 (4), 1099–1116.

2.14 Influence of local tissue conductivity anisotropy on EEG/MEG field and return current computations

Influence of Local and Remote White Matter Conductivity Anisotropy for a Thalamic Source on EEG/MEG Field and Return Current Computation
Wolters, C.H., Anwander, A., Tricoche, X., Lew, S. and Johnson, C.R., *Int. Journal of Bioelectromagnetism*, Vol. 7, No.1, pp.203-206, (2005).

Corresponding author: C.H. Wolters

Influence of Local and Remote White Matter Conductivity Anisotropy for a Thalamic Source on EEG/MEG Field and Return Current Computation

C. H. Wolters[1+2], A. Anwander[3], X. Tricoche[1], S. Lew[1] and C. R. Johnson[1]
[1]Scientific Computing and Imaging Institute, University of Utah, Salt Lake City, USA
[2]Institute for Biomagnetism and Biosignalanalysis, Westfalian Wilhelms-University of Münster, Münster, Germany
[3]Max-Planck-Institute for Human Cognitive and Brain Sciences, Leipzig, Germany

Abstract—**Inverse methods are used to reconstruct current sources in the human brain by means of Electroencephalography (EEG) and Magnetoencephalography (MEG) measurements of event related fields or epileptic seizures. There exists a persistent uncertainty regarding the influence of anisotropy of the white matter compartment on neural source reconstruction. In this paper, we study the sensitivity to anisotropy of the EEG/MEG forward problem for a thalamic source in a high resolution finite element volume conductor. The influence of anisotropy on computed fields will be presented by both high resolution visualization of fields and return current flow and topography and magnitude error measures. We pay particular attention to the influence of local conductivity changes in the neighborhood of the source. The combination of simulation and visualization provides deep insight into the effect of white matter conductivity anisotropy.**

We found that for both EEG and MEG formulations, the local presence of electrical anisotropy in the tissue surrounding the source substantially compromised the forward field computation, and correspondingly, the inverse source reconstruction. The degree of error resulting from the uncompensated presence of tissue anisotropy depended strongly on the proximity of the anisotropy to the source; remote anisotropy had a much weaker influence than anisotropic tissue that included the source.

Keywords— **anisotropy, EEG/MEG source reconstruction, finite element method, local conductivity changes, return currents, thalamus, visualization**

I. Introduction

A critical component of the inverse neural source reconstruction is the numerical approximation method used to reach an accurate solution of the associated forward problem, i.e., the simulation of fields for known dipolar sources in the brain. The forward problem requires a geometric model of the volume conductor (the head and brain), often in the form of spherical shell, Boundary Element (BE) [1] or Finite Element (FE) models. Only the FE method is able to treat both realistic geometries and inhomogeneous and anisotropic material parameters [2,3,4,5].

Past studies have shown that the inclusion of anisotropy is important for an accurate reconstruction of neural sources [2,5,6,7]. Furthermore, recent developments for the FE method in EEG/MEG inverse problems [8,9] dramatically reduce the complexity of the computations, so that the main disadvantage of FE modeling no longer exists. In spherical models of the head, the influence of compartmental conductivity anisotropy (radial versus tangential) on forward and inverse problems in EEG and MEG were studied by [6,7]. However, the white matter compartment is poorly represented by such a model. There have been relatively few studies of the influence of white matter anisotropy on forward EEG and MEG simulation [2,5]. In [10], a strong influence of local conductivity changes around the source to EEG and MEG was reported.

In this paper, we study the effect of white matter anisotropy for the forward EEG and MEG computation for a thalamic source. We especially examine the effects of anisotropy near the source. For deep sources that are surrounded by large anisotropic white matter fiber bundles, such as the pyramidal tract and the corpus callosum, we provide insight into the sensitivity towards anisotropy by means of visualization and interpretation of computed fields and return current flow and the examination of the Relative Difference Measure (RDM) and MAGnification factor (MAG) error measures [1].

II. Methods

The first step in constructing a realistic volume conductor model is to segment the different tissues within the head. Modeling of the low conducting human skull is of special importance for EEG/MEG source reconstruction. As such, we used a pair of T1-weighted and PD-weighted Magnetic Resonance Images (MRI). We aligned both image datasets with a voxel-similarity based affine

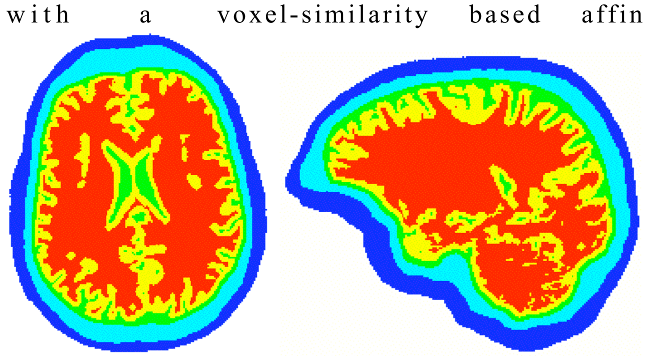

Fig. 1. Segmented five tissue head model: skin (blue), skull (light blue), CSF (green), gray matter (yellow) and white matter (red).

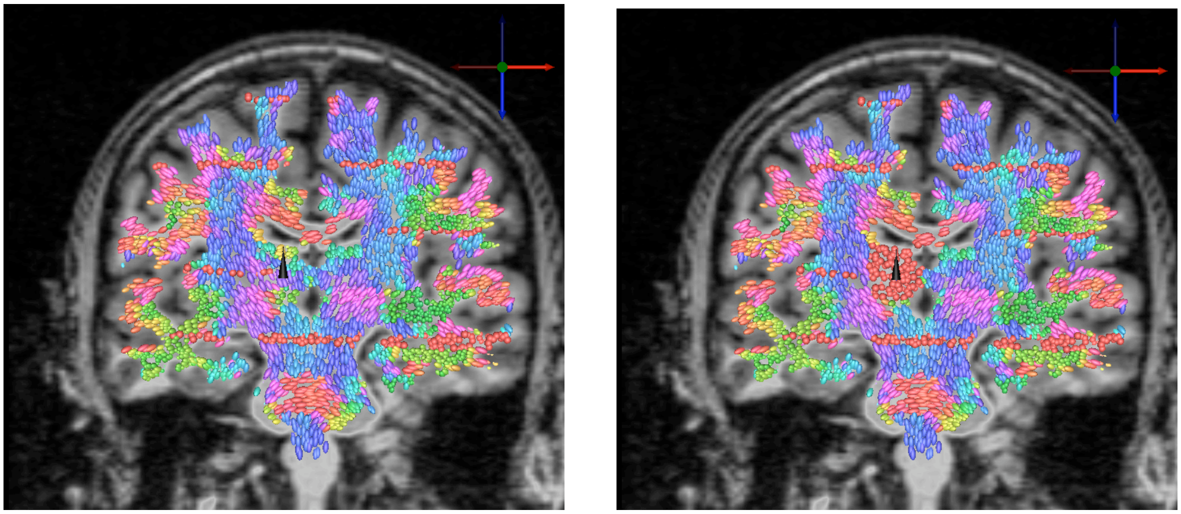

Fig. 2. Coronal slice of the models *aniso_thalaniso* (left) and *aniso_thaliso* (right) with left thalamic dipole source. The conductivity tensors of finite elements in the white matter are displayed on the underlying T1-MRI using 1:2 anisotropy.

registration without pre-segmentation using a cost-function based on mutual information [5]. Our nearly automatic segmentation process consisted of a 3D implementation of an Adaptive Fuzzy C-Means classification method which compensates for image intensity inhomogeneities, followed by a deformable model algorithm to smooth the inner and outer skull surfaces [5]. We segmented five head compartments; skin, skull, cerebrospinal fluid (CSF), gray and white matter. Because the fractional anisotropy within the thalamus is a factor three times higher than the fractional anisotropy of neocortical gray matter, we assigned both thalami to the white matter compartment for the following simulation study. The segmented five tissue headmodel is shown in Fig.1.

In the second step, we generated a FE model using a surface-based tetrahedral tessellation of the segmented compartments, resulting in 147,287 nodes and 892,115 elements. The following isotropic conductivities were assigned to skin (0.33 S/m), skull (0.0042 S/m), CSF (1.79 S/m), brain gray (0.33 S/m) and white matter (0.14 S/m). Anisotropic conductivity ratios of approximately 1:9 (normal to parallel to fibers) have been measured for brain white matter [11]. Following the proposition of [12], we assumed that the conductivity tensors share the eigenvectors with the water diffusion tensors, measured by means of Diffusion Tensor MRI (DT-MRI). Using multiple sessions, we measured whole-head DT-MRI. The MRI slices were axially oriented and 5mm thick with an inplane resolution of 2mm x 2mm. We computed the eigenvalues for the white mater conductivity tensors using two constraints, a volume constraint that retains the geometric mean, i.e., the volume, of the eigenvalues [5], and Wang's constraint [13], where the product of the longitudinal and one transversal eigenvalue is kept constant and equal to the square of the isotropic value. The resulting tensor-valued conductivity slices were not exactly parallel and we filled the gaps with the isotropic white matter conductivity.

For the EEG forward computation, we placed 71 electrodes interactively on the head surface according to the international 10/20 system. For the MEG, we modeled each magnetometer flux transformer of the BTI (4-D NeuroImaging, San Diego, USA) 148 channel whole-head system with eight isoparametric quadratic finite row elements.

Using the dipole model of [14], we performed EEG and MEG forward computations for a left thalamic source in the isotropic five-compartment FE model and in the corresponding models with white matter anisotropy (Fig.2). In order to study the influence of local conductivity changes, we considered two different anisotropic models. For the first model *aniso_thalaniso*, we treated the finite elements in the neighborhood of the thalamic source as anisotropic elements (Fig.2, left), while in the second model *aniso_thaliso*, we extracted 1113 neighboring finite elements and modeled them as isotropic (Fig.2, right).

To quantify the error between isotropic and anisotropic field values at the sensors, we used the RDM and MAG error measures [1]. The RDM is a measure for the topography error (Minimal error: RDM=0), while the MAG indicates magnitude differences (Minimal error: MAG=1).

In order to better assess the influence of anisotropy, the return current on the model surface is visualized by means of a Line Integral Convolution (LIC) technique[15] computed directly over the head geometry. This method

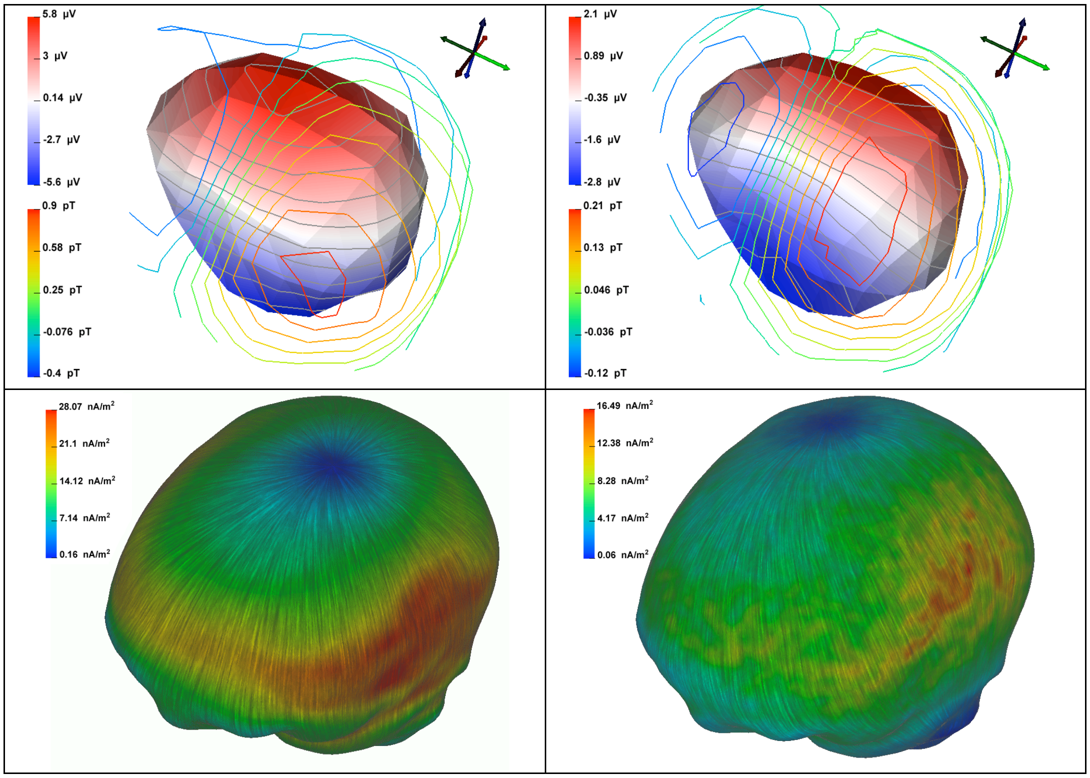

Fig.3: Isofield EEG and MEG distribution (top row) and surface return current (bottom row) for the left thalamic source in the isotropic model (left) and in model *aniso_thalaniso* with 1:10 white matter anisotropy (right).

permits a continuous depiction of the directional information and is combined with a color mapping of the current magnitude that gives insight into the quantitative aspects of the electrical flow.

III. RESULTS

The Figs.3 and 4 clearly show the importance of local conductivity changes around the source for both EEG and MEG. In model *aniso_thalaniso* (Fig.3, right column, and Fig.4, in red), with topography differences to the corresponding isotropic model of about 80% for EEG and about 50% for MEG, the 1:10 white matter anisotropy substantially compromises the forward field computation. Furthermore, in addition to this topography error, the anisotropy significantly weakens the fields, which is expressed by a MAG of less than 0.5 for the EEG and even less than 0.3 for the MEG and the strongly reduced amplitude of the surface return currents. We find two return current areas of minimal amplitude (in blue), one on the top and one on the bottom of the model (not shown). As it can be observed, the 1:10 white matter anisotropy in model *aniso_thalaniso* strongly shifts the minimal amplitude return current points in comparison to the isotropic case. In both cases, the amplitude of the return currents is well correlated to the thickness of the skull (compare the color scaling of the return currents with the segmented model in Fig.1). While high return currents are flowing in the thin lateral areas, they are significantly attenuated in the thicker occipital areas and in the areas of the frontal sinuses. The white matter anisotropy diffuses the surface return currents.

In contrast to those results, the effect of the white matter anisotropy in combination with the local isotropy in model *aniso_thaliso* is much weaker, for a ratio of 1:10 the RDM is below 10% and the MAG close to the optimum.

IV. DISCUSSION

It was found that conductivity (anisotropy) changes around the source have a strong influence on the EEG and MEG forward problem, while anisotropy in a certain distance from the source has only a smaller effect. This is in agreement with a study of local (isotropic) conductivity changes in [10]. The sources are embedded in brain gray matter structure, which has a measured anisotropy ratio of about 1:2 (tangentially:perpendicular to the cortical surface) [10] or higher for gray matter structures such as the thalami, as the fractional anisotropy ratio of the DTI data shows. Furthermore, most sources are very close to the white matter compartment. It can therefore be expected that the modeling of the gray and white matter anisotropy is important for an accurate reconstruction of the sources, as also reported by [2,5]. As a final note, the

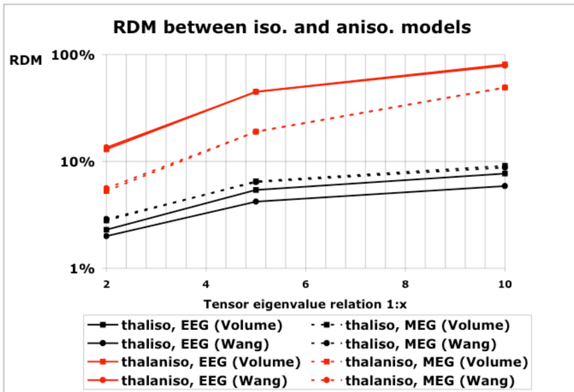

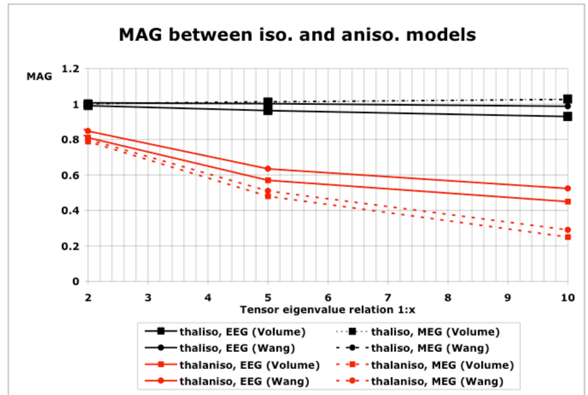

Fig.4: EEG and MEG topography (left, log. Y-axes) and magnitude error (right) for the volume and Wang's constraint for various white matter anisotropy ratios and both models *aniso_thalaniso* (red) and *aniso_thaliso* (black).

source model via an accurate implementation method for the dipole will be of significant importance [5,16].

V. Conclusion

The modeling of gray and white matter anisotropy is important for an accurate EEG/MEG based reconstruction of the neural sources, especially with regard to the orientation and strength components. The more the source is surrounded by anisotropy, the larger is the influence.

Acknowledgment

We are grateful to Rob MacLeod and Dave Weinstein from the SCI Institute. This work was financially supported by the MPI for Mathematics in the Sciences, Leipzig, by the IST-program of the European Community, project SIMBIO (http://www. simbio.de) and the NIH NCRR center for Bioelectric Field Modeling, Simulation and Visualization (http://www.sci.utah.edu/ncrr).

References

[1] J.W.H Meijs, O.W. Weier, M.J. Peters and A. van Oosterom, “On the Numerical Accuracy of the Boundary Element Method”, *IEEE Trans. Biomed.. Eng.*, vol. 36, pp. 1038--1049, 1989.

[2] J. Haueisen et al., “The Influence of Brain Tissue Anisotropy on Human EEG and MEG,” *NeuroImage*, vol. 15, pp. 159-166, 2002.

[3] R. van Uitert and C.R. Johnson, "Can a Spherical Model Substitute for a Realistic Head Model in Forward and Inverse MEG Simulations?", In:*Proc. of the 13th Int. Conf. on Biomagnetism*, H. Nowak, J. Haueisen, F. Giessler, and R. Huonker, VDE Verlag GmbH, Berlin, Offenbach, http://biomag2002.uni-jena.de., 2002.

[4] R. van Uitert, D.Weinstein and C.R. Johnson, "Volume Currents in Forward and Inverse Magnetoencephalographic Simulations Using Realistic Head Models.” *Annals of Biomed. Eng.*, vol. 31, pp. 21-31, 2003.

[5] C.H. Wolters, “Influence of Tissue Conductivity Inhomogeneity and Anisotropy on EEG/MEG based Source Localization in the Human Brain”, In:*MPI Series in Cognitive Neuroscience,* MPI of Cognitive Neuroscience Leipzig, ISBN 3-936816-11-5 (also: Leipzig, Univ., Diss, http://dol.uni-leipzig.de/pub/2003-33, 2003.

[6] M.J. Peters and J.C. de Munck, "The influence of model parameters on the inverse solution based on MEGs and EEGs.”, *Acta Otolaryngol [Suppl] (Stockh)*, vol. 491, pp.61-69, 1991.

[7] H. Zhou and A. van Oosterom, "Computation of the Potential Distribution in a Four-Layer Anisotropic Concentric Spherical Volume Conductor", *IEEE Trans. Biomed.. Eng.*, vol. 39, no.2, pp. 154-158, 1992.

[8] C.H. Wolters, L. Grasedyck and W. Hackbusch, “Efficient Computation of Lead Field Bases and Influence Matrix for the FEM-based EEG and MEG Inverse Problem”, *Inverse Problems,* vol. 40, no. 4, pp. 1099-1116, 2004.

[9] C.H. Wolters, M. Kuhn, A. Anwander and S. Reitzinger, “A parallel algebraic multigrid solver for finite element method based source localization in the human brain,” *Comp. Vis. Sci.*, vol. 5, no.3, pp. 165-177, 2002.

[10] J. Haueisen, C. Ramon, H. Brauer and H. Nowak, "The Influence of Local Conductivity Changes on MEG and EEG", *Biomedizinische Technik*, vol.45, no.7-8, pp.211-214, 2000.

[11] P.W. Nicholson, "Specific impedance of cerebral white matter", *Exp.Neurol.*, vol. 13, pp. 386-401, 1965.

[12] P.J. Basser, J. Mattiello, and D. LeBihan, “MR Diffusion Tensor Spectroscopy and Imaging”, *Biophys.*, vol. 66, pp. 259-267, 1994.

[13] Y. Wang, D.R. Haynor and Y. Kim, "An Investigation of the Importance of Myocardial Anisotropy in Finite-Element Modeling of the Heart: Methodology and Application to the Estimation of Defibrillation Efficacy", *IEEE Trans. Biomed.. Eng.*, vol. 48, no.12, 2001.

[14] H. Buchner, G. Knoll, M. Fuchs, A. Rienäcker, R. Beckmann, M. Wagner et al., "Inverse Localization of Electric Dipole Current Sources in Finite Element Models of the Human Head", *Elec. Clin. Neurophysiol.*, vol. 102, pp.267-278, 1997.

[15] B. Cabral and L. C. Leedom, "Imaging Vector Fields using Line Integral Convolution", *Proc. of SIGGRAPH 1993 Conf.*, pp. 263--272, 1993.

[16] Wolters, C.H. and Koestler, H. et al., "Theory and practice of dipole models for bioelectric field computations.", Technical Report, Institute for Informatics, Friedrich-Alexander University Erlangen-Nürnberg, in preparation, 2005.

2.15 The Influence of Volume Conduction Effects on the EEG/MEG reconstruction of the Sources of the Early Left Anterior Negativity

The Influence of Volume Conduction Effects on the EEG/MEG Reconstruction of the Sources of the Early Left Anterior Negativity
Wolters, C.H., Anwander, A., Maess, B., MacLeod, R.S. and Friederici, A.D., In *Proc. of the 26th Annual Int. Conf. IEEE Engineering in Medicine and Biology Society, San Francisco, USA*, http://www.ucsfresno.edu/embs2004, September 1-5, pp.3569-3572 (2004).

Corresponding author: C.H. Wolters

Proceedings of the 26th Annual International Conference of the IEEE EMBS
San Francisco, CA, USA • September 1-5, 2004

The influence of volume conduction effects on the EEG/MEG reconstruction of the sources of the Early Left Anterior Negativity

C.H.Wolters[1+2+3], A.Anwander[2], B.Maess[2], R.S.MacLeod[1] and A.D.Friederici[2]
[1]Scientific Computing and Imaging Institute, University of Utah, Salt Lake City, USA
[2]Max Planck Institute for Human Cognitive and Brain Sciences, Leipzig, Germany
[3]Max Planck Institute for Mathematics in the Sciences, Leipzig, Germany

Abstract—**To achieve a deeper understanding of language processing in the human brain, scientists and clinicians use Electroencephalography (EEG) and Magnetoencephalography (MEG) inverse methods to reconstruct sources of Event Related Potentials. There exists a persistent uncertainty regarding the influence of volume conduction effects such as the anisotropy of tissue conductivity of the skull and the white matter layers on the inverse results. In this paper, we will study the sensitivity to anisotropy of the source reconstruction of the Early Left Anterior Negativity (ELAN) component in language processing. For EEG, the presence of tissue anisotropy substantially compromises the restoration ability of an L1-norm current density approach. The centers of activity are strongly shifted along the Sylvian fissure in the anterior direction. In contrast, MEG in combination with the L1 norm approach is able to reconstruct the main features of the ELAN source distribution even in the presence of anisotropic conductivity.**

Keywords—**EEG/MEG source reconstruction, influence of skull and white matter anisotropy, finite element method, L1 norm current density reconstruction, ELAN**

I. Introduction

Reconstructing sources of brain activity and their dynamic interplay is an important part of the study of how language processing occurs. Previous findings suggest the existence of three Event Related Potential (ERP) components that correlate with language comprehension processes [1]. The first ERP, the so-called Early Left Anterior Negativity (ELAN) was observed and interpreted to reflect a processing phase during the input is parsed into an initial syntactic structure. The reconstruction of the ELAN sources is of substantial interest and Friederici et al. have suggested a dipole fit approach with seedpoints from functional Magnetic Resonance Imaging (MRI) [1]. The study provided a clear indication that both temporal and fronto-lateral cortical regions in both hemispheres support early syntactic processing with a dominance in the left hemisphere.

A critical component of source reconstruction, an inverse problem, is the numerical approximation method used to reach an accurate solution of the associated forward problem, i.e., the simulation of fields for known dipolar sources in the brain. The forward problem requires a geometric model of the volume conductor (the head and brain), often in the form of spherical shell- or Boundary Element (BE) models [1,2]. The BE method is adequate for piecewise homogeneous isotropic compartments skin, skull and brain, but it does not allow a realistic representation of the anisotropy of conductivity of the skull and white matter. In contrast, the Finite Element (FE) method is able to treat both realistic geometries and inhomogeneous and anisotropic material parameters. First studies show that the inclusion of anisotropy is crucial for an accurate reconstruction of the sources [3,4,5,6,7,8]. Furthermore, newest developments for the FE method in EEG/MEG inverse problems [9,10] dramatically reduce the complexity of the computations, so that the main disadvantage of FE modeling no longer exists.

In this study, we focused on the influence of anisotropy on the reconstruction of the ELAN sources. We constructed a high resolution model of the head, simulated electrical and magnetic fields from given sources, and compared the influence of anisotropy on the accuracy of source reconstruction using an L1-norm current density approach. Our results suggest that including anisotropic conduction is essential for EEG-based source localization but that MEG-based reconstructions suffer less from the omission of anisotropy.

II. Methodology

The first step in the construction of a realistic anisotropic volume conductor model is the segmentation of head tissues with different conductivity properties. For this study, we used T1- and PD-weighted MRI as the input to the segmentation process (Fig.1). The first step was to align the two image sets, for which we used a voxel-similarity based affine registration without pre-segmentation using a cost function based on mutual information. The main components in our nearly automatic segmentation program are a 3D implementation of an Adaptive Fuzzy C-Means classification algorithm which compensates for image intensity inhomogeneities, followed by an algorithm that uses a deformable model to smooth the inner and outer skull surfaces [8]. The result is a 5-tissue segmentation, an

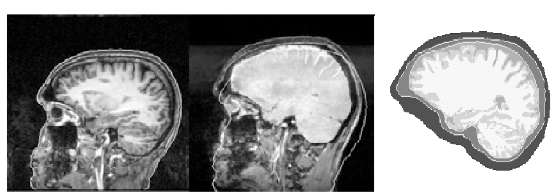

Fig. 1. The segmented head model (right) was generated from a pair of T1- (left) and PD- (middle) MRI with a special focus on an improved segmentation of the skull layer.

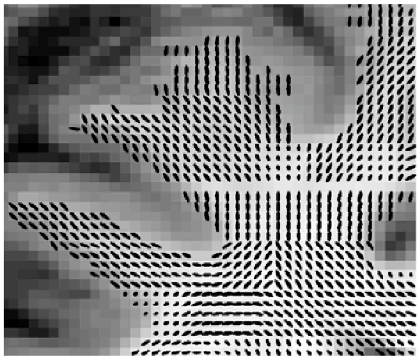

Fig. 2. Detail of the projection of the conductivity tensor ellipsoids onto a coronal cut of the T1-MRI through the Commissura anterior.

example of which is presented in Fig.1 (right).

From the segmented images, we then generated FE models, the first of which included a surface-based tetrahedral tessellation of the relevant 5 compartments, resulting in 147,287 nodes and 892,115 elements. A node-shifted cube approach [8] led to a second, hexahedral FE mesh with 385,901 nodes and 366,043 elements. The following isotropic conductivity values were assigned to skin (0.33 S/m), skull (0.0042 S/m), cerebrospinal fluid (1.79 S/m), brain gray (0.33 S/m) and white matter (0.14 S/m) and ventricular system (1.79 S/m).

Diffusion Tensor MRI (DT-MRI) measurements formed the basis for a realistic modeling of white matter anisotropy [5,6,8]. Following the proposition of [11], we assumed that the conductivity tensors share the eigenvectors with the diffusion tensors. For the determination of skull conductivity tensor eigenvectors, we used a deformable model to generate a smooth surface model of the spongiosa, i.e., a strongly smoothed triangular mesh, which was shrunken from the outer skull mask onto the outer spongiosa surface. The tensor eigenvectors could then be determined from the normal vectors of the triangular mesh [5].

We computed the eigenvalues for both skull and white matter conductivity tensors using a volume constraint that retains the geometric mean of the eigenvalues [5], i.e., the volume of each tensor remains constant. For the anisotropic case, we used a relation of 1:10 for the eigenvalues of skull (radially:tangentially) [3,4,5] and white matter

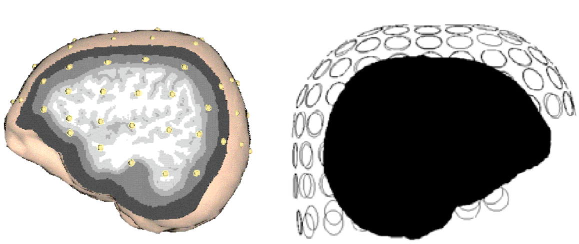

Fig. 3. The 71 EEG sensors and the 148 MEG magnetometer coils.

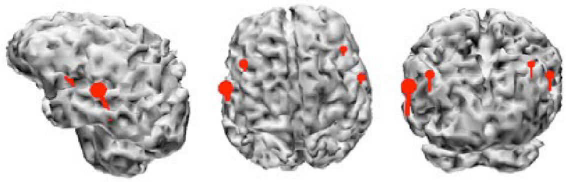

Fig. 4. The four reference ELAN sources.

(longitudinally:transversally) [5,8]. Fig.2 contains a sample projection of the conductivity tensor ellipsoids.

The sensors of the EEG and MEG systems are shown in Fig.3. For the EEG, 71 electrodes were placed on the head surface according to the international 10/20 system [8]. For the MEG, we modeled each magnetometer flux transformer of the BTI (4-D Neuroimaging, San Diego, USA) 148 channel whole-head system with 8 isoparametric quadratic finite row elements.

A cortical influence space surface was generated by means of a dilation of the white matter mask by 1 mm, while taking care that the dilated mask was topologically equivalent to a sphere. In a subsequent step, the surface of the resulting mask was triangulated with 5 mm resolution into 6742 regularly shaped triangles and 3373 vertices. This mesh is a rough representation of the neocortical surface, neglecting deeper gray matter structures such as the basal ganglia. Because such a representation neglects detailed neocortical curvatures, we did not apply a normal-constraint, i.e., sources in all Cartesian directions were allowed for each mesh vertex during source reconstruction. An EEG/MEG lead field matrix **L** was computed for the isotropic tetrahedra model, using the fast FE solver methods described in [8,9,10]. Each of the 3*3373 columns of this matrix stores the simulated 71 EEG potentials and the 148 MEG flux values.

Fig.4 shows the four ELAN reference dipoles we simulated on vertices of the influence space mesh, a source with 33 nAm strength in the vicinity of the left auditory cortex, a left fronto-lateral source with 20 nAm strength and their right hemisphere homologue dipoles with 18 nAm and 16 nAm, respectively.

For the inverse reconstruction, we define the data term

$$Data(\mathbf{j}) := \left\| \mathbf{D}^{-1}(\mathbf{L}\mathbf{j} - \mathbf{u}^m) \right\|_2^2 \qquad (1)$$

with **D** a diagonal channel weighting matrix, **j** the current density vector on the influence space mesh, and $\mathbf{u}^m$ the EEG/MEG data and an L1 norm model term as

$$Model(\mathbf{j}) := \left\| \mathbf{W}\mathbf{j} \right\|_1 \qquad (2)$$

with a diagonal source location weighting matrix **W**. The goal of the L1 norm current density reconstruction is the minimization of the functional

$$F_{\lambda}(\mathbf{j}) := Data(\mathbf{j}) + \lambda \cdot Model(\mathbf{j}) \tag{3}$$

with respect to **j**. λ is the so-called regularization parameter. We chose an L1 norm model term, because this method is well-known to be favorable for the reconstruction of focal sources when compared to L2 norm model term definitions [2,12]. We minimized F by means of a nonlinear Polak-Ribiere CG method [8] and for the choice of the regularization parameter λ, we used the L-curve method [2,12] and the X^2-criterion [12]. The diagonal entries of **D** were set to the absolute value of the difference between isotropic and anisotropic data $\mathbf{u}^m$. Knowing that we are confronted with superficial reference sources, **W** was chosen as the identity operator, i.e., the reconstructed current distribution gives preference to superficial sources.

III. Results

A. Influence of anisotropy on forward isopotential distribution

In a first study, we carried out forward computations for the left temporal ELAN source in the nodeshifted hexahedra model. Fig.5 shows the resulting isopotential distributions on a coronal slice through the location of the source for the isotropic case (left) and for the corresponding cases with anisotropy of skull (middle) and WM (right) compartment. Skull anisotropy leads to a slight shift of the ELAN ERP component from lateral to medial directions on the head surface. This can be seen by following the isopotential line marked in black in Fig.5. While for the isotropic case (left panel), this isocontour represented the strongest negative isopotential that reached the surface, in the anisotropic case, the same isopotential line was not able to break through the skull layer. Instead, the a less negative contour was the first to reach the surface and at a more medial location (middle panel). The iso-line marked in brown in Fig.5 shows the effect of white matter anisotropy. It appears that in the anisotropic white matter case (right panel), this isopotential line is forced to follow more strongly a direction perpendicular to the fiber bundles of the corticospinal tract because of an increased volume current flow along the fibers, so that it enters the skull compartment at a different location and, in contrast to the isotropic case, is then able to break through the skull.

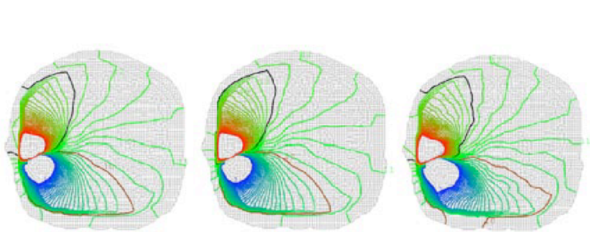

Fig. 5. Isopotential distribution for the left temporal ELAN source: isotropic (left), anisotropic skull (middle), anisotropic white matter (right).

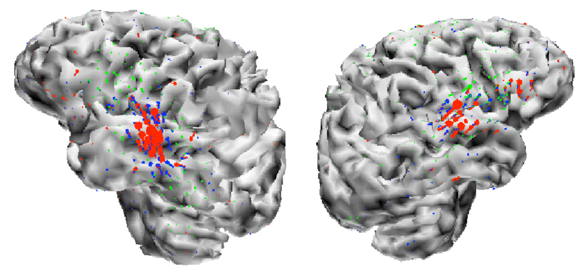

Fig. 6. MEG: L1 norm current density reconstruction results for isotropic (red), and anisotropic (blue, green) reference MEG data using the L-curve method (blue) and the X^2-method (green).

B. Influence of anisotropy on the L1 norm current density reconstruction

We carried out L1 norm current density reconstructions using the simulated isotropic or anisotropic (skull and white matter) data $\mathbf{u}^m$. Fig.6 shows the results for isotropic MEG data (red) and anisotropic MEG data using the L-curve-criterion (blue) and the X^2-criterion (green). The solution of the L1 norm for isotropic MEG data shows three centers of activity. This is the error introduced through the choice of the source model (focal reference sources reconstructed by means of a current density method). Surprisingly, the left (which is stronger than the right) fronto-lateral ELAN source could not be reconstructed in contrast to both the temporal and the right fronto-lateral centers. The result of the L1 norm reconstruction (L-curve-criterion) by means of the anisotropic MEG data is only a little more smeared out, but the three activity centers are still distinguishable. This is no longer the case when using the X^2-criterion, where the activity between the fronto-lateral and the temporal reference centers is strongly smeared out on both hemispheres. Fig.7 shows the result for the EEG. In the isotropic case (left), even the focusing L1 norm is not able to distinguish between the temporal and the fronto-lateral centers of activity. Instead of two centers, the activity is smeared out over the whole cortical area between both ELAN sources. The MEG solutions in Fig.6 were much better focused around the reference sources. The reconstructed activity on the left hemisphere dominates over the right hemisphere (not shown). The error is much more

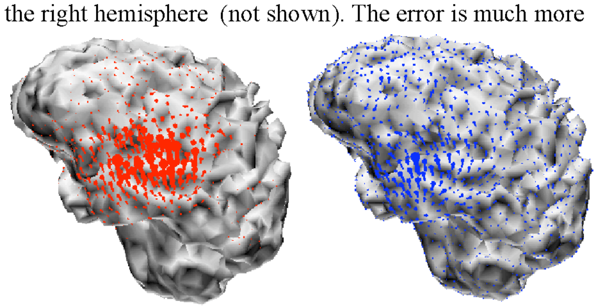

Fig. 7. EEG: L1 norm current density reconstruction results for isotropic (red) and anisotropic (blue) reference EEG data using the L-curve method.

distinct for the anisotropic data (right), where, additionally, the center of activity was strongly shifted in the anterior direction along the Sylvian fissure so that the sources would no longer be expected in the vicinity of the auditory cortex. The results for L2 norm current density reconstruction have comparable properties only that the current density distribution is even more spread out [8] (not shown here).

IV. Discussion

Our results for the influence of anisotropy were mainly in agreement with the literature at least to the extend that such solutions exist. Skull anisotropy had a non-negligible influence on the EEG and nearly no influence on the MEG, as also reported in [3,4,5,8]. We found that the more the source was surrounded by white matter structure, the more important white matter anisotropy modeling became for both EEG and MEG [5,6,7,8]. For MEG, this influence was especially strong for sources with mainly a radial orientation component.

With regard to the reconstruction of the four superficial and tangentially oriented ELAN sources [1], white matter and skull anisotropy were found to have a negligible influence on the MEG reconstruction. In contrast, reconstruction based on the EEG was severely compromised without proper incorporation of anisotropy both for the instantaneous L1 current density reconstruction as well as for regularized multi-dipole fit procedures [8]. The sensitivity of two instantaneous current density reconstruction methods towards skull anisotropy was also studied for EEG in [4]. Marin et al. also studied the sensitivity of current density reconstruction to skull anisotropy. They used the linear L2 norm and a non-linear S-MAP regularization, where the latter, like our L1 norm approach, produces more focalized results than the linear method. In agreement with our results, they reported that skull anisotropy totally compromised the localization ability of the L2 approach and that the restoration of very close active regions was profoundly disabled for both the linear and the non-linear regularization method.

V. Conclusion

With the newest developments in FE modeling for the EEG/MEG inverse problem, the complexity of the computations is now dramatically reduced [9,10], so that the former main disadvantage of FE modeling no longer exists. In localizing EEG ELAN activity, source reconstruction is sensitive to tissue anisotropy and for such cases, FE forward modeling should improve inverse reconstructions. If the sources to be reconstructed are either radially oriented or relatively deep and surrounded by white matter fibers, the MEG based reconstruction will also be sensitive to white matter anisotropy.

Acknowledgment

This work was supported by the MPI for Mathematics in the Sciences, by the IST-program of the European Community, project SIMBIO (www.simbio.de) and the NIH NCRR center for Bioelectric Field Modeling, Simulation and Visualization.

References

[1] A.D. Friederici, Y. Wang, C.S. Herrmann, B. Maess, and U. Oertel, "Localization of Early Syntactic Processes in Frontal and Temporal Cortical Areas: An MEG Study," *Human Brain Map.*, vol. 11, pp. 1-11, 2000.

[2] M. Fuchs, M. Wagner, T.Koehler, and H.A. Wischmann, "Linear and Nonlinear Current Density Reconstructions", *Jour. Clin.Neurophysiol.*, vol. 16, no.3, pp. 267-295, 1999.

[3] S.P. van den Broek, "Volume Conduction Effects in EEG and MEG," Proefschrift Universiteit Twente Enschede, The Netherlands, ISBN: 90-365-0919-x, 1997.

[4] G.Marin, C. Guerin, S. Baillet, L. Garnero, and G. Meunier, "Influence of skull anisotropy for the forward and inverse problem in EEG: simulation studies using the FEM on realistic head models," *Human Brain Map.*, vol. 6, pp. 250-269, 1998.

[5] C.H. Wolters et al., "Influence of head tissue conductivity anisotropy on human EEG and MEG using fast high resolution finite element modeling", In:*Forschung und wissenschaftliches Rechnen, Contributions to the Heinz-Billing Award, Gesellschaft fuer wissenschaftliche Datenverarbeitung mbH Goettingen*, T. Plesser, and V. Macho, V., ISSN: 0176-2516, http://www.billingpreis.mpg.de, no. 58, pp. 111–157, 2001.

[6] J. Haueisen et al., "The Influence of Brain Tissue Anisotropy on Human EEG and MEG," *NeuroImage*, vol. 15, pp. 159-166, 2002.

[7] A. Anwander, C.H. Wolters, M. Duempelmann and T.R. Knoesche, "Influence of realistic skull and white matter anisotropy on the inverse problem in EEG/MEG-source localization," In:*Proc. of the 13th Int. Conf. on Biomagnetism*, H. Nowak, J. Haueisen, F. Giessler, and R. Huonker, VDE Verlag GmbH, Berlin, Offenbach, http://biomag2002.uni-jena.de, pp. 679-681, 2002.

[8] C.H. Wolters, "Influence of Tissue Conductivity Inhomogeneity and Anisotropy on EEG/MEG based Source Localization in the Human Brain", In:*MPI Series in Cognitive Neuroscience,* MPI of Cognitive Neuroscience Leipzig, ISBN 3-936816-11-5 (also: Leipzig, Univ., Diss, http://dol.uni-leipzig.de/pub/2003-33, 2003.

[9] C.H. Wolters, L. Grasedyck and W. Hackbusch, "Efficient Computation of Lead Field Bases and Influence Matrix for the FEM-based EEG and MEG Inverse Problem", *Inverse Problems,* in press.

[10] C.H. Wolters, M. Kuhn, A. Anwander and S. Reitzinger, "A parallel algebraic multigrid solver for finite element method based source localization in the human brain," *Comp. Vis. Sci.*, vol. 5, no.3, pp. 165-177, 2002.

[11] P.J. Basser, J. Mattiello, and D. LeBihan, "MR Diffusion Tensor Spectroscopy and Imaging", *Biophys.*, vol. 66, pp. 259-267, 1994.

[12] A. Rienaecker, A., H. Buchner, H. and G. Knoll, "Comparison of Regularized Inverse EEG Analyses in Finite Element Models of the Individual Anatomy", In:*Quant. and Top. EEG/MEG Anal., H.Witte, U.Zwiener, B.Schack and A.Doering* , Druckhaus Mayer Verlag GmbH Jena-Erlangen, pp.459-463, 1997.

2.16 Analysis of tactile somatosensory evoked EEG and MEG data

Unpublished results from
B. Lanfer, Validation and Comparison of Realistic Head Modeling Techniques and Application to Tactile Somatosensory Evoked EEG and MEG Data. Diploma thesis in Physics, Institute for Biomagnetism and Biosignalanalysis (IBB), University of Münster, 09/2007.

Supervisors:
C.H. Wolters, C.Pantev, IBB, University of Münster and
S. Demokritov, Institute for Applied Physics, University of Münster.

2.16.1 Goal of the study

Since it is necessary to model the MEG noise cancellation schemes for a proper MEG forward modeling, this chapter will first present the MEG machine at the Institute for Biomagnetism and Biosignalanalysis of the University of Münster. In the second part, simultaneously measured tactile somatosensory evoked potentials (SEP) and fields (SEF) will be analyzed. It will be shown that, with a proper realistic head model and a larger number of trials for the EEG than for the MEG, both EEG and MEG correctly localize in the primary somatosensory cortex.

2.16.2 FE forward modeling for the *Omega 2005* MEG

FE modeling of the MEG sensors

The IBB at the University of Münster is equipped with the Magnetoencephalography (MEG) machine *Omega 2005* from the manufacturer *VSM Medtech Ltd.*, which is located in a magnetically shielded chamber. The 275 measurement sensors of this machine are axial gradiometers with a baseline of 50 mm. The coils of the gradiometers have a radius of 9 mm. For the noise rejection technique described in the next section, the magnetic flux is furthermore measured at 29 reference sensors which are situated in the dewar above the measurement sensors. The reference sensors are magnetometers and axial and planar gradiometers. The radii of the coils differ between 7.76 and 17.27 mm. The baseline of the reference gradiometers is always 78.74 mm.

Figure 2.4 shows the Finite Element (FE) nodes which are used to model the measurement and reference sensors of this machine. As described in Chapter 2.2 (Section 3.2), for the computation of primary and secondary magnetic flux, the sensor coils are then modeled by means of isoparametric quadratic row elements.

MEG noise rejection using synthetic gradiometers

Environmental magnetic noise, such as the noise of the electrical power system, is generally much larger than the small magnetic fields of the brain. Therefore, a first (passive) noise reduction consists of a magnetically shielded room in which the MEG machine is put up. However, there are still magnetic fields penetrating the shielding and, in addition, there are magnetic fields generated by the human body. The strength of the magnetic field of the human heart, e.g., is more than hundred times larger than the typical magnetic field caused by brain activity. Therefore, a further (active) noise reduction consists of measuring the spatial gradient of the flux using gradiometers instead of magnetometers. As shown in Figure 2.4, the 275 measurement sensors of the Omega 2005 are hardware gradiometers of first order. This concept of noise rejection can be extended within

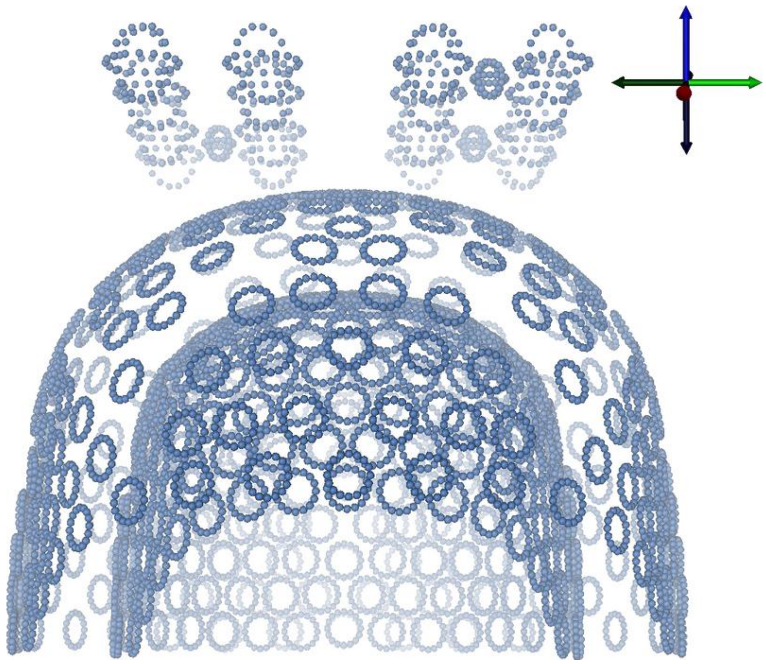

Figure 2.4: Finite element nodes to model the CTF MEG sensor configuration, including measurement and reference sensors. Visualization was carried out using BioPSE [2002].

the Omega 2005 system to synthetic gradiometers of higher order (Vrba [2000]; Vrba and Robinson [2001]). To reduce the noise with higher order, synthetic gradiometers, the field is not only measured at the hardware gradiometers, but also at a number of reference sensors (see Fig. 2.4). Synthetic gradiometers can then be composed of one hardware gradiometer and a number of reference sensors, by subtracting a linear combination of the signals measured by the reference sensors from the signal measured by the hardware gradiometer.

$$\Psi_i^{*,\,\mathrm{meas}} = \Psi_i^{\mathrm{meas}} - \sum_j C_{ij} \cdot \Psi_j^{\mathrm{ref}} \tag{2.1}$$

Here $\Psi^{*,\,\mathrm{meas}}$ and Ψ^{meas} are the signals of the hardware gradiometers with and without applied noise rejection, respectively, and Ψ^{ref} are the signals measured at the reference sensors. C is the coefficient matrix. With the definitions

$$\mathrm{E} = (\mathrm{I}\,|\mathrm{C}) \quad \text{and} \quad \Psi^{\mathrm{meas,\,ref}} = \begin{pmatrix} \Psi^{\mathrm{meas}} \\ \Psi^{\mathrm{ref}} \end{pmatrix} \tag{2.2}$$

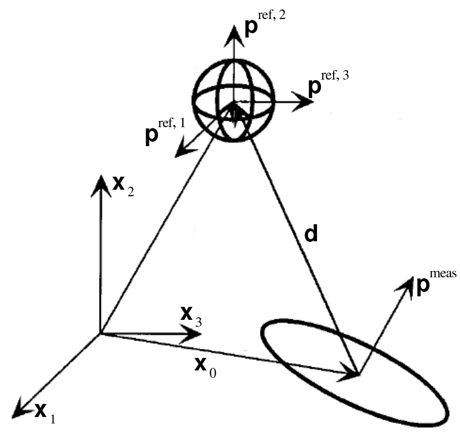

Figure 2.5: Measurement and vector reference magnetometer. Figure from Vrba and Robinson [2001].

equation (2.1) can be rewritten as in equation (2.3).

$$\Psi^{*,\,\mathrm{meas}} = \mathrm{E} \cdot \Psi^{\mathrm{meas,\,ref}} \tag{2.3}$$

The coefficients C for the linear combination of the reference signals are determined in such a way, that the synthetic gradiometer mimics a hardware gradiometer of the same order. How this is done shall be shown for a first order synthetic gradiometer following (Vrba [2000]; Vrba and Robinson [2001]). The signal for a first order synthetic gradiometer can be composed of the signal of one primary measurement magnetometer and one reference vector magnetometer. The vector magnetometer consists of three magnetometers, whose orientations are orthogonal to each other.

When applying a magnetic field B the signal of the measurement magnetometer is

$$\Psi^{\mathrm{meas}} = \alpha_{\mathrm{p}}\,\mathrm{B} \cdot \mathrm{p}^{\mathrm{meas}}\ ,$$

where α_p is the gain of the primary magnetometer and $\mathrm{p}^{\mathrm{meas}}$ is its orientation. The signal of the reference vector magnetometer can be written as a vector Ψ^{ref} with components

$$\Psi_k^{\mathrm{ref}} = \alpha_{\mathrm{ref}} B_k\ .$$

Here α_{ref} is the gain of the vector magnetometers and

$$B_k = \mathrm{p}^{\mathrm{ref,\,k}} \cdot \mathrm{B}$$

is the component of the magnetic flux density parallel to the orientation of the k-th magnetometer of the reference vector magnetometer. Now the magnetic flux density B is approximated by the first terms of a Taylor series around the center of the measurement sensor, x_0.

$$B(x) = B_0 + G_0 (x - x_0) + O\left(x^2\right) \tag{2.4}$$

$G_0 = \nabla B(x)|_{x=x_0}$ denotes the first gradient of the magnetic flux density. With the first two terms of the Taylor expansion and using equation (2.1), the signal of the synthetic first order gradiometer can be written as in equation (2.5).

$$\Psi^{*,\,\mathrm{meas}} = \alpha_{\mathrm{p}}\, p^{\mathrm{meas}} \cdot B_0 + \sum_k C_{1k}\, \alpha_{\mathrm{ref}}\, p^{\mathrm{ref},\,k} \left(B_0 + G_0 \cdot d\right) \tag{2.5}$$

The vector pointing from the center of the measurement magnetometer to the centerer of the reference vector magnetometer is called the baseline d.

The coefficients C_{1k} are chosen in such a way that the synthetic gradiometer mimics a real gradiometer. By definition, an n-th order gradiometer cancels out the contributions from gradients of the magnetic flux densities that are of order $(n-1)$ or below. So in the case of a homogeneous field the signal of the first order synthetic gradiometer has to be zero.

$$\alpha_{\mathrm{p}} p^{\mathrm{meas}} \cdot B_0 = -\sum_k C_{1k} \alpha_{\mathrm{ref}} p^{\mathrm{ref},\,k} \cdot B_0 \tag{2.6}$$

This equation can be solved for the coefficients C_{1k} using the fact, that the orientations of the reference magnetometers are orthogonal to each other. Equation (2.7) shows the solution for the coefficients of a first order synthetic gradiometer.

$$C_{1k} = -\frac{\alpha_{\mathrm{p}}}{\alpha_{\mathrm{ref}}} \left(p^{\mathrm{ref},\,k} \cdot p^{\mathrm{meas}}\right) \tag{2.7}$$

From this equation it can be seen that the coefficients for first order synthetic gradiometers are the orientations of the reference magnetometers projected onto the orientations of the measurement magnetometer and normalized to the latter's gain. The coefficients for higher order synthetic gradiometers can be derived in a similar way.

Although the synthetic gradiometers mainly cancel out lower gradients of the magnetic flux density, which are caused by distant, strong sources, i.e., environmental magnetic noise, it can also influence a signal produced by brain activity. So when an inverse method is to be applied to data, to which the discussed noise rejection was applied, the noise rejection technique also has to be modeled for the forward problem. This means, that one has to simulate the magnetic flux not only at the measurement sensors, but also at the reference sensors and then calculate the signal of the higher order synthetic gradiometers as in Equation (2.1). The noise rejection with synthetic higher order gradiometers for the FEM forward problem therefore had to be implemented into the software SimBio [2000] before being able to analyze the measured MEG data of the SEF experiment in Section 2.16.3.

2.16.3 Source analysis of SEP/SEF data

FE volume conductor model

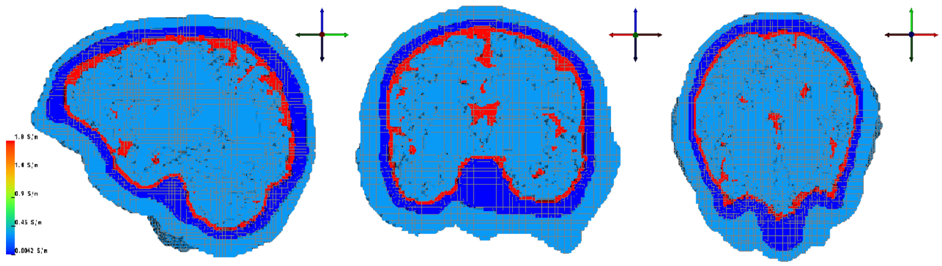

Figure 2.6: Saggital, coronal and axial cross-section of the geometry-adapted hexahedral FE mesh. The conductivity labeling is color-coded. Visualization was carried out using BioPSE [2002].

The basis of the volume conductor modeling, the multimodal T1- and PD-MRI and the registration and segmentation of those datasets is described in detail in Chapter 2.11 (Section 3). A four compartment (skin with conductivity 0.33S/m, skull with 0.0042S/m in radial and 0.042S/m in tangential direction, CSF with 1.79S/m and brain with 0.33S/m) 2mm geometry-adapted hexahedral FE mesh was then generated from the segmented dataset. The FE volume conductor model is shown in Figure 2.6.

The Somatosensory Experiment

For the setup of the tactile somatosensory evoked potentials (SEP) and somatosensory evoked fields (SEF) experiment, it is also referred to the Chapter 2.11 (Section 3). While three runs were averaged in order to get a signal-to-noise (SNR) ratio of 24dB for the EEG, the same SNR could already be achieved for the 275 channel MEG by means of just averaging the epochs of a single run. The averaged and filtered SEP and SEF data are shown in Figure 2.7. The MEG data was in third-order synthetic gradiometer format. The EEG and MEG at 34.5ms, when the signal is at a maximum, can be seen in Figure 2.8.

As shown in (Mertens and Lütkenhöner [2000]; Hari and Forss [1999]), a single equivalent current dipole model was adequate for source analysis because the early tactile SEP and SEF component arises from area 3b of the primary somatosensory cortex (SI) contralateral to the side of stimulation. Therefore single equivalent current dipole fits (Scherg and von Cramon [1985]; Mosher et al. [1992]; Knösche [1997]) were performed separately for EEG and MEG at the signal peak using four different seed-points. The fast transfer matrix approach

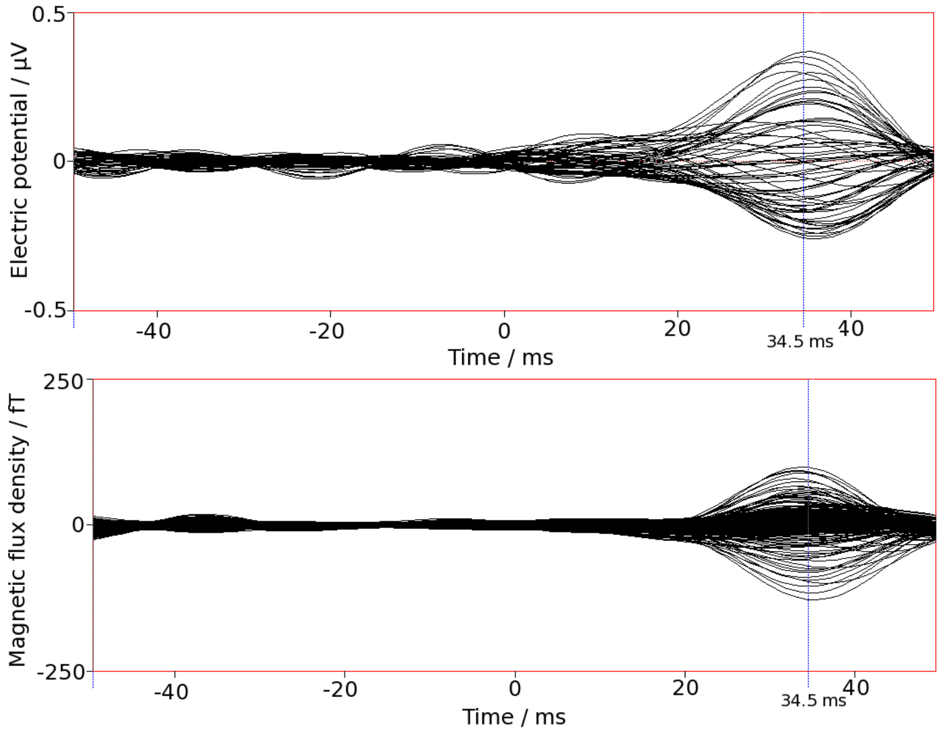

Figure 2.7: The averaged and filtered EEG and MEG signals from the somatosensory experiment.

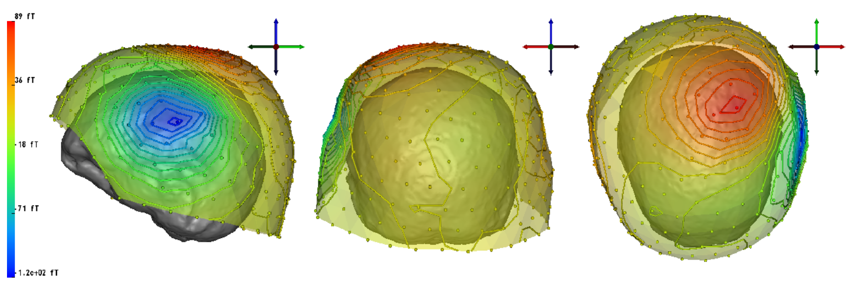

Figure 2.8: MEG sensor configuration displayed together with the magnetic flux at 34.5 ms. Visualization was carried out using BioPSE [2002].

of Chapter 2.2 and the AMG-CG solver of Chapter 2.9 were used for fast EEG and MEG dipole fits. The best fit results are illustrated in Figure 2.9. It can be observed that the resulting dipoles for both EEG and MEG were, as expected, in the left primary somatosensory cortex. With about 98%, the explained variance

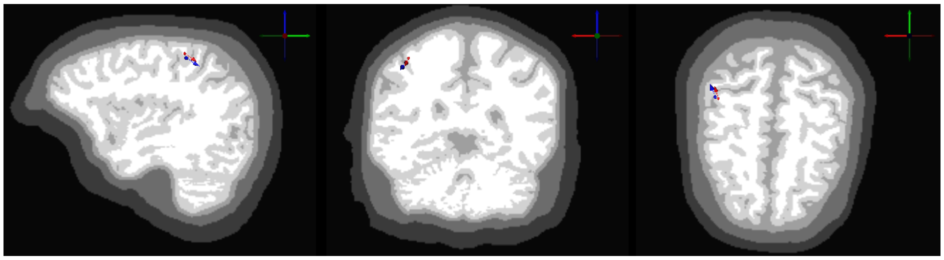

Figure 2.9: Comparison of the EEG (red) and MEG (blue) single dipole fit results in the left primary somatosensory cortex. Visualization was carried out using BioPSE [2002].

to both measured datasets was very high and with a difference in location of only 3.9mm, EEG and MEG reconstructed at nearly the same position. However, the result is not yet completely satisfying. A closer look at Figure 2.9 reveals, that the difference between the localization results mainly is a difference in source depth. This might be due to an overestimation of the skull anisotropy (see Chapter 2.13). A recent study reported that the skull's three-layeredness (outer compacta, spongiosa, inner compacta) should be modeled as a three-layeredness and not indirectly by means of the anisotropy (Sadleir and Argibay [2007]), which also might be a reason for the small difference. A future goal is to use the SEF reconstruction result, which is much less dependent on the individual tissue conductivities such as skull and skin in order to further stabilize the SEP LRCE procedure as proposed in Chapter 2.11. The simultaneously measured SEF might thus help to better estimate the individual tissue conductivities.

2.17 Source analysis of epileptiform activity for presurgical epilepsy diagnosis

2.17.1 EEG source analysis of epileptiform activity with a high resolution FE head model

EEG source analysis of epileptiform activity with a high resolution finite element head model
Rullmann, M., Anwander, A., Warfield, S.K., Duffy, F.H. and Wolters C.H.. submitted to *NeuroImage*, (2008).

Corresponding author: C.H. Wolters

EEG source analysis of epileptiform activity using a high resolution finite element head model.

M. Rullmann[*][†], A. Anwander[‡], M. Dannhaur[§], S.K. Warfield[¶]
F.H. Duffy[||]and C.H. Wolters[**][††]

January 17, 2008

Abstract

Purpose: To evaluate whether non-invasive surface EEG (sEEG) source analysis based on 1mm anisotropic finite element (FE) head modeling can provide additional guidance for presurgical epilepsy diagnosis, different FE-based inverse approaches were applied in a case study to averaged ictal spikes of a medically-intractable epilepsy patient. To the best of the authors knowledge, this level of accuracy in head volume conductor modeling has not yet been applied to source analysis in presurgical epilepsy diagnosis before. The reconstruction results were successfully validated with the outcome of intra-cranial EEG (iEEG) recordings.
Methods A 1mm hexahedra FE volume conductor model of the patient's head with special focus on modeling anisotropic brain conductivity was constructed using non-linearly registered T1-, T2- and Diffusion-Tensor-(DT) Magnetic Resonance Imaging (MRI) data. Different source analysis methods, goal function scan (GFS), Minimum Norm Least Squares (MNLS), spatio-temporal current dipole modeling and standardized low resolution electromagnetic tomography (sLORETA) were applied to the peak of the averaged sEEG spike data. The electrodes of the iEEG measurements were extracted from a registered computed tomography (CT) image.
Results GFS, MNLS and sLORETA clearly showed a single center of activity. Moving and rotating single dipole fits resulted in an explained variance of more than 97%. The dipole fits localized at the border of the lesion and at the border of the iEEG electrodes which mainly received spike activity. Source orientation was towards the epileptogenic tissue. GFS and sLORETA localized at the same position. Their result had an

[*]Forschungs- und Transferzentrum Leipzig e.V., Wächterstr. 13, 04107 Leipzig, Germany
[†]Max Planck Institute for Human Cognitive and Brain Sciences, Stephanstr. 1a, 04103 Leipzig, Germany
[‡]Max Planck Institute for Human Cognitive and Brain Sciences, Stephanstr. 1a, 04103 Leipzig, Germany
[§]Max Planck Institute for Human Cognitive and Brain Sciences, Stephanstr. 1a, 04103 Leipzig, Germany
[¶]Computational Radiology Laboratory, Department of Radiology, Children's Hospital, Harvard Medical School, Boston, USA
[||]Department of Neurology, Children's Hospital, Harvard Medical School, Boston, USA
[**]Corresponding author. Westfälische Wilhelms-Universität Münster, Institut für Biomagnetismus und Biosignalanalyse, Malmedyweg 15, 48149 Münster, Germany
[††]Scientific Computing and Imaging Institute, University of Utah, Salt Lake City, USA.

average distance of only 2.5mm to the dipole fit locations. The average distance of those methods to the MNLS peak was 6.2mm.
Conclusion Non-invasive sEEG source analysis based on 1mm anisotropic FE head modeling might contribute to clinical presurgical evaluation in epilepsy patients.
Keywords Presurgical epilepsy diagnosis, surface- and intra-cranial EEG, source analysis, diffusion-tensor magnetic resonance imaging, tissue conductivity anisotropy, cerebrospinal fluid, finite element method, goal function scan, minimum norm least squares, spatio-temporal dipole modeling, standardized low resolution electromagnetic tomography.

1 Introduction

Surgical resection of epileptogenic cortical tissue in pharmaco-resistant epilepsy patients was shown to safely and effectively control seizures, recover function, improve quality of life and even save lives, but epilepsy surgery is still underused in developed countries and non-existent in most developing countries [46]. The precise localization of the epileptogenic foci, preferably with non-invasive methods, is the major goal of the presurgical evaluation [30]. In addition to evaluation by video and electroencephalography (EEG) long-term monitoring, magnetic resonance imaging (MRI), single photon emission computed tomography and neuropsychological examination, EEG and magnetoencephalography (MEG) source analysis has risen to a promising tool [31, 13, 42, 21, 14, 43, 17, 38, 33]. Source analysis results correlated well with results from intracranial recordings [31, 21, 17] and epileptogenic subcompartments could well be distinguished using source reconstruction techniques [31, 2, 8, 19]. In a large study, source analysis revealed additional localizational information in 35% of the 455 patients and in 10%, it could even considerably contribute to the decision about type, size and eventually necessary prior invasive examinations [38].

The accuracy of source analysis methods depends in part on the volume conductor model used to represent the head. In clinical practice, for EEG, the spherical head model with three homogeneous and isotropically conducting (a single conductivity value) spherical shells representing brain, skull and scalp, and in MEG, the single isotropic compartment sphere model, are still often used. Recent investigations showed that source localization accuracy can be improved through the use of realistically shaped three compartment (brain, skull, scalp, extracted from MRI data) boundary element (BE) head models [31, 13, 14, 43].

However, the cerebrospinal fluid compartment is known to have a much higher conductivity than brain gray and white matter [3] and conductivity anisotropy (different conductivity values in different space directions) with a ratio of about 1 to 9 (normal to parallel to fibers) has been measured for brain white matter [24]. The robust and non-invasive direct in-vivo measurement of brain conductivity anisotropy is not possible. However, in [1], the assumption was introduced that the conductivity tensor shares the eigenvectors with the water diffusion tensor (DT), which can be measured non-invasively by means of DT-MRI. This assumption was recently used in a formalism which describes a linear relationship between the effective electrical conductivity tensor and the effective water diffusion tensor in brain tissues [40, 41]. The mutual restriction of both the ionic and the water mobility by the geometry of the brain medium builds the basis for the described relationship. The assumption is not, of course, that a fundamental relation exists between the free mobility of ionic and water particles. The claim is rather that the restricted mobilities are related through the geometry.

The finite element method (FEM) is able to treat both realistic geometry and inhomogeneous and anisotropic material parameters [5, 4, 12, 28, 49, 53]. Sensitivity studies have been carried out in realistic FE models, supporting the hypothesis that modeling brain conductivity anisotropy has to be taken into account for accurate source reconstruction [12, 49, 10]. It is furthermore known that the high conductivity of the CSF [28, 49] and local conductivity changes in the vicinity of the primary source as caused by brain lesions or cavities from surgery [4] or the difference between gray and white matter conductivity [28] have a non-negligible effect on EEG and MEG source analysis. Even if realistic FE models have already successfully been applied to the field of presurgical epilepsy diagnostic, their real potential was not yet exploited since three compartment (brain, skull, scalp) isotropic FE approaches were used [42]. In the past, the difficult construction of the volume discretization [18] and the heavy computational load of the FE method was seen as a drawback, especially when many evaluations of the forward problem are needed, e.g., in source localization schemes [5, 4, 42, 27]. As shown in this paper, the generation of regular hexahedra FE meshes takes advantage of the cubic voxel structure which is inherent to MR images so that the meshing step just consists of converting the segmented T1-weighted MRI into a hexahedra mesh with the same resolution, which can be performed in seconds. Due to the excessive computational burden created by previous FEM techniques, evaluation studies often only used sub-optimal numbers of nodes [5, 4, 42]. For example, in [42], an FE model with only 10,731 nodes (5mm edge length) was used for the localization of epileptiform activity and it was concluded that, for a general clinical use of FE source analysis, a finer FE discretization and parallel computing is needed. In [5], the setup of a lead field matrix with 8,742 unknown dipole components in a four compartment FE approach with 18,322 nodes took roughly a week of computation time.

In this paper, a 1mm anisotropic hexahedra volume conductor model with about 3.1 Million unknowns will be generated from T1-, T2- and DT-MRI data of a patient who underwent surgery and relapsed. The high-resolution FE model distinguishes the compartments brain white and gray matter, CSF (among others CSF-filled cavity of the first surgery and ventricles), skull and skin. It will be used in goal function scan [22, 16], minimum norm least squares [11, 16], spatio-temporal current dipole [35, 22, 16] and standardized low resolution electromagnetic tomography (sLORETA) [26, 7] EEG inverse source analysis scenarios to localize ictal epileptiform surface EEG (sEEG) activity on a high-resolution 2mm 3D influence source space. As we will show, instead of solving "number of sources many FE equation systems" (in the presented study: 517,098), a fast transfer matrix approach allows us to reduce this huge number to a "number of sensors many FE equation systems" (in the presented study: 24). The computational amount of work is thus reduced by more than a factor of 20,000. Any FE-forward computation can then be performed in only 37ms. The presurgical sEEG source analysis results are successfully validated by means of postsurgical intracranial EEG (iEEG) measurements. "Postsurgical" is defined throughout this paper as the instant in time after craniotomy and placement of iEEG grids.

2 Methods

2.1 Subject

The patient in this case study is an 11-year-old boy suffering from medically intractable localization-related epilepsy. He had his first seizure in the age of three years and underwent a brain tumor (Dysembryoplastic NeuroEpithelial Tumor, DNET) and epileptic focus resection. After recurrence of seizures 8 years later, the same type of tumor was diagnosed just anterior to the motor area at the cavity from the resection of the first surgery. He was then treated again and went under surgery for tumor resection. The data in this study was acquired during the diagnosis phase for the second tumor resection.

2.2 MRI and CT data acquisition

Presurgical MR imaging of the patient's head was performed on a 3T SIEMENS TrioTim at the Massachusetts General Hospital. The T1-weighted MRI had an in-plane resolution of 1×1mm with a slice thickness of 1mm, 256 slices, a field of view of 256mm and an echo time of 3.37ms. The presurgical DTI scan had 30 directions and 5 B0 sets, 220mm field of view with 1.7×1.7mm in-plane resolution and 5mm slice thickness with 20% gap, 23 slices, B-value of 1000, 106ms echo time and 5000ms repetition time. The T2-weighted MRI scan, measured together with the DTI for later DTI to T1-MRI registration purposes, had an in-plane resolution of 0.4×0.4mm with a slice thickness of 5mm, 23 slices and a field of view of 173×230mm.

A postsurgical CT of the patient, showing the implanted intracranial electrodes, was recorded using a GE Medical System LightSpeed Pro 16. The dataset had an in-plane resolution of 0.5×0.5mm with a slice thickness of 0.6mm, 559 slices and a field of view of 250mm.

2.3 FE volume conductor modeling

2.3.1 T1-MRI segmentation

The patient's T1-MRI dataset was aligned to the AC-PC coordinate system. In a first step, a segmentation into three layers (skin, skull and brain) using a surface model approach [36] implemented in FSL (http://www.fmrib.ox.ac.uk/fsl). The result was manually corrected with Anatomist (http://brainvisa.info). In a second step, the segmented brain compartment was specified into CSF, gray and white matter by an interactive thresholding using the Anatomist software and again manually corrected. Finally, the lesion was manually segmented. The result of the segmentation process is shown in Figure 1.

2.3.2 DTI registration and preprocessing

A proper registration of the DTI data onto the structural T1-MRI is an important step in the setup of an anisotropic FE volume conductor model. Distortions in the DTI due to susceptibility artifacts generally have to be corrected in a non-linear fashion [39]. Non-linear registration methods often rely on an initial affine (linear) registration to find a good starting position. We applied

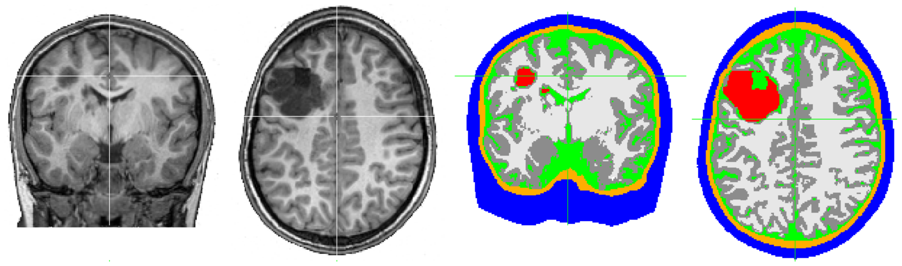

Figure 1: Coronal and axial view of the T1-MRI (left) and the corresponding segmentation (right) with six tissue types: red indicates the lesion, dark gray the gray matter, light gray the white matter, green the CSF, orange the skull and blue indicates the skin.

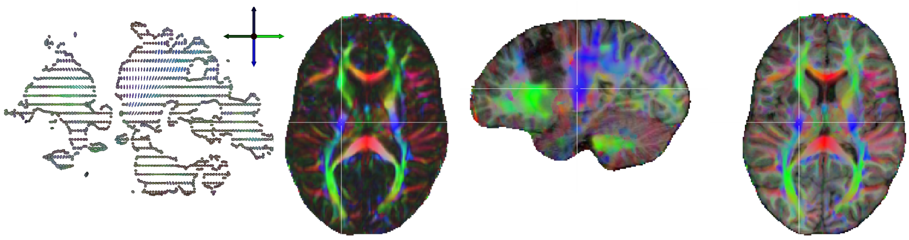

Figure 2: Sagittal slice of the original DTI image (left), axial slice of the color coded fractional anisotropy (FA) image after registration to the T1 anatomy (middle left) and the registered color FA image overlaid on the T1-MRI in sagittal (middle right) and axial (right) view. The color indicates the fiber orientation: red is left-right, green is anterior-posterior and blue is superior-inferior.

a voxel-similarity based affine registration method without presegmentation using a global optimization of the mutual information cost function between the different modalities [15] implemented in FSL.

In a first step, the patient's DTI scans were therefore linearly registered with the high resolution axial T2-weighted slices. Subsequently, an affine registration of the T2-MRI onto the 3D T1-weighted volume was performed. Both transformation matrices were combined and the resulting affine transformation was used to register the DTI to the T1 anatomy. The images were then interpolated to 1 mm voxel resolution. Finally, in order to handle the orientation information in the registered DT images appropriately, the diffusion gradient direction for each scan was rotated with the transformation matrix to account for the new slice orientation of the diffusion scan.

In a second step, the averaged B0 images of the (linearly registered) DTI scan were non-linearly wrapped to the (linearly registered) T2 anatomy following [39]. The computed correction field was applied to the (linearly registered) diffusion weighted scans. The diffusion tensor was then estimated for each voxel with a minimum least square fit. Figure 2 shows a sagittal slice of the original DTI (left), an axial slice of the color coded fractional anisotropy (FA) image after

head compartment *comp*	conductivity σ_{comp}^{iso} (S/m)
les (lesion)	0.33
wm (white matter)	0.142
gm (gray matter)	0.33
csf (cerebrospinal fluid)	1.538
skull	0.0042
skin	0.43

Table 1: Bulk isotropic conductivity σ_{comp}^{iso} for head compartment *comp*.

registration to the T1 anatomy (middle left) and an overlay of the color FA image on the T1 image in a sagittal (middle right) and axial (right) view.

To correct for non-positive definite tensors, the eigenvalues were checked and thresholded for every voxel. If the second eigenvalue was smaller than $1 \cdot 10^{-4}$ or the third eigenvalue was smaller than $1 \cdot 10^{-5}$, the tensor was removed from the dataset. This was the case for some voxels in the inferior frontal lobe due to distortion artifacts. Negative tensor eigenvalues occur due to other measurement errors, e.g. intraventricular CSF pulsation artifacts. The final DTI was masked with the gray and white matter masks for the usage in the head model.

2.3.3 FE mesh generation

The generation of regular hexahedra meshes takes advantage of the cubic voxel structure which is inherent to MR images. A 1 mm hexahedra FE headmodel with 3,098,341 nodes was thus simply generated by means of a conversion step from the segmented T1-MRI with 1 mm voxel resolution from Section 2.3.1.

2.3.4 FE conductivity labeling

Table 1 shows the conductivity values σ_{comp}^{iso} for the head compartments *comp* that are used for a first isotropic labeling of the finite elements [29]. It was not distinguished between hard and soft bone, but the common isotropic value for the conductivity of the compartment skull [14, 6, 5, 42] was used.

For the anisotropic tissue compartments brain white and gray matter, the conductivity tensors were computed from the measured diffusion tensors using the effective medium approach [40, 41], which linearly relates the conductivity tensor σ to the measured diffusion tensor D,

$$\sigma = \mathrm{s}D \quad \text{with} \quad \mathrm{s} := \frac{\sigma_{\mathrm{e}}}{\mathrm{d}_{\mathrm{e}}},$$

where σ_e and d_e are the effective extracellular conductivity and diffusivity, respectively.

We did not use the empirical scaling $\mathrm{s} = 0.736 \frac{S \cdot sec}{mm^3}$ as in [40, 12], but matched s so that the arithmetic mean over all N_{comp} conductivity tensor volumes in the brain tissue compartment *comp* (either *wm* or *gm*) optimally matches the volume of the corresponding tensor with the isotropic conductivity

s ($S \cdot sec/mm^3$)	Mean conductivity (S/m) for	
	gm	wm
0.210	0.211158	0.182963
0.736	0.740057	0.641243

Table 2: The linear scalings s between the diffusion tensor and the conductivity tensor computed for our dataset using Formula (2) (upper row) and from [40, 12] (lower row) with the resulting mean conductivity $\mathrm{s} \cdot d_{comp}$ for gray and white matter.

σ_{comp}^{iso} from Table 1, i.e.,

$$\frac{4\pi}{3}\left(\sigma_{comp}^{iso}\right)^3 \stackrel{!}{=} \frac{\sum_{i=1}^{N_{comp}} \frac{4\pi}{3} \prod_{j=1}^{3} \sigma_i^j}{N_{comp}} = \frac{4\pi}{3} \cdot \frac{\sum_{i=1}^{N_{comp}} \prod_{j=1}^{3} \mathrm{s} d_i^j}{N_{comp}} = \frac{4\pi}{3}\left(\mathrm{s} \cdot d_{comp}\right)^3 \tag{1}$$

with σ_i^j and d_i^j being the j^{th} eigenvalue of the i^{th} conductivity and diffusion tensor of the brain tissue compartment *comp*, respectively, and

$$d_{comp} := \sqrt[3]{\frac{\sum_{i=1}^{N_{comp}} \prod_{j=1}^{3} d_i^j}{N_{comp}}}.$$

For the brain white and gray matter compartments, s can be determined through the least squares fit

$$\mathrm{s} = \frac{d_{wm}\sigma_{wm}^{iso} + d_{gm}\sigma_{gm}^{iso}}{d_{wm}^2 + d_{gm}^2}. \tag{2}$$

For our data, we found the scaling $\mathrm{s} = 0.21 \frac{S \cdot sec}{mm^3}$. Table 2 indicates the mean conductivities, i.e., $\mathrm{s} \cdot d_{comp}$, for white and gray matter resulting from the linear scaling s computed for our dataset using Formula (2) and the one from [40, 12]. The latter would result in much higher mean conductivities for brain gray and white matter than compiled in Table 1. For white and gray matter voxels with no measured diffusion tensor, isotropic conductivities were used.

2.4 sEEG and iEEG measurements

The presurgical scalp EEG (sEEG) dataset, recorded at 24 electrodes with a sampling frequency of 256Hz, contained one seizure, which could be identified by the Long Term Monitoring (LTM) personnel. The single clinical seizure happened while the patient sat in a chair. The first definite clinical sign was head deviation to the right, a right sided jerking followed by a generalized tonic clonic seizure. The EEG data was filtered with a 60Hz notch and a 1 to 10Hz band-stop filter using the BESA software package (MEGIS Software GmbH, Germany). As shown in Figure 3, the F3 delta was followed by more midline FZ-CZ delta. Nine F3 delta bursts were marked by a clinical expert (FHD) and averaged to increase the signal to noise for the further source analysis. For the localization, only a short time window of 7.8ms was used, which included

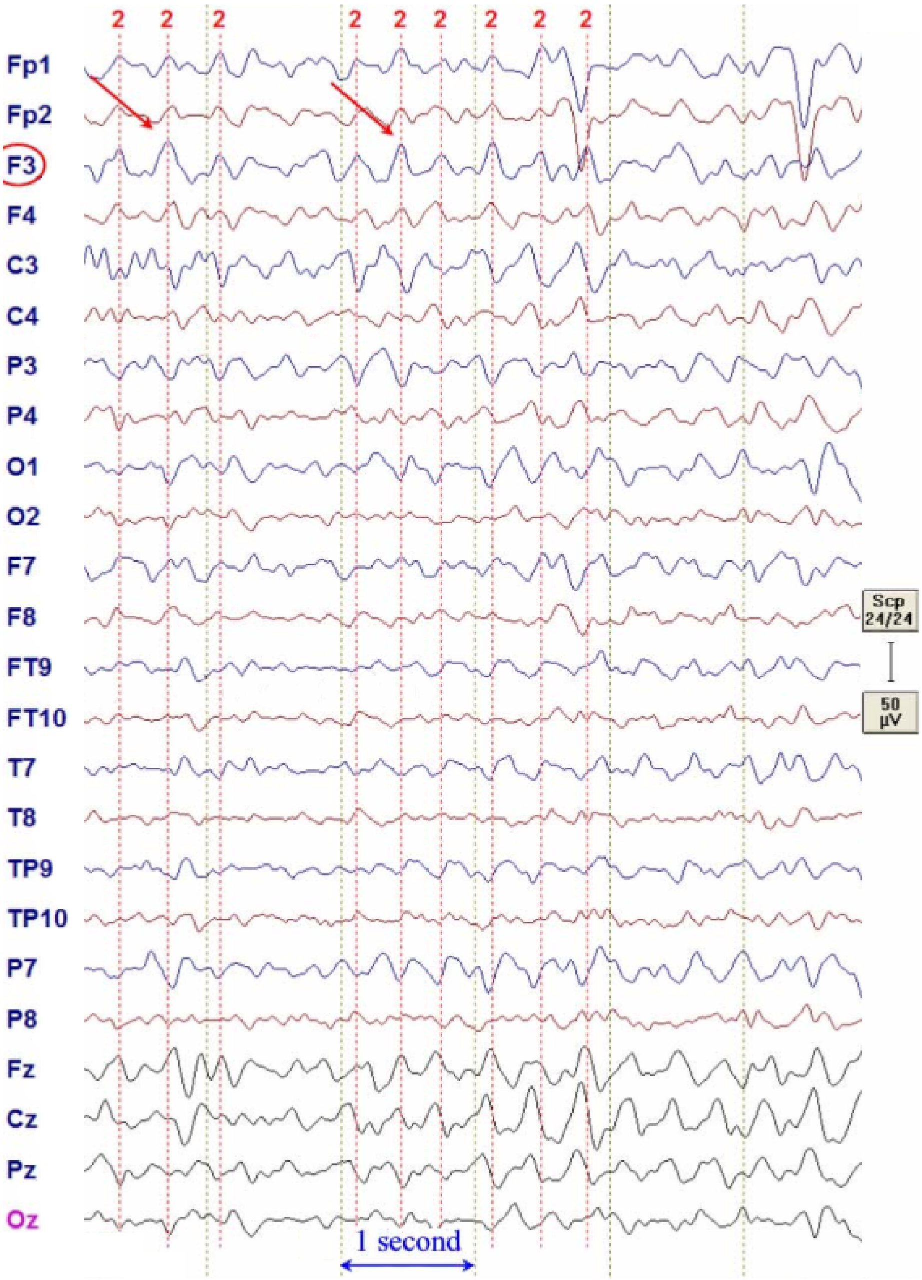

Figure 3: F3 delta spikes in average reference format of the presurgical sEEG.

the two samples at the highest signal peak. No individual sEEG electrode locations were available, so that a standard positioning was applied. SCIRun (http://software.sci.utah.edu/scirun.html) was used to fit the 10-10 standard system electrode positions to the head model. The result is shown in Figure 4 (left). Visualization was carried out using SCIRun. From these positions, the

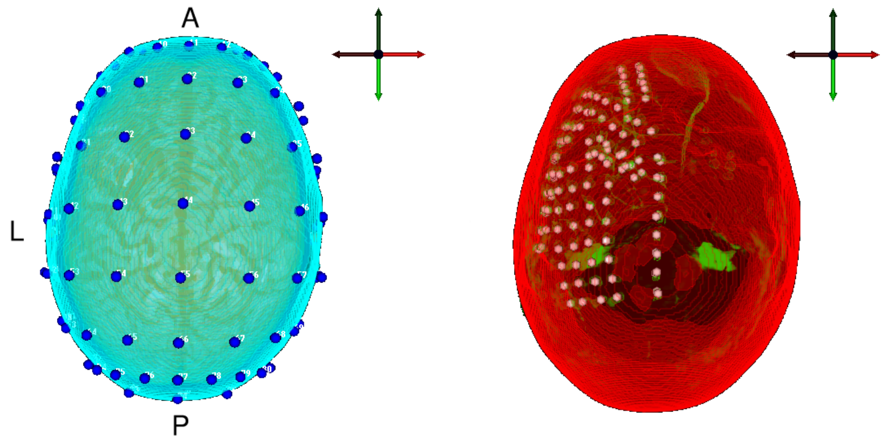

Figure 4: Left: The 10-10 standard system sEEG electrodes (blue spheres) mapped to the head model of the patient. Right: The outermost layer of the head model (red) and a segmented part of the registered CT dataset (green) are shown together with the extracted and mapped iEEG electrode positions.

24 sEEG measurement electrodes were identified according to their labels.

Postsurgically, intracranial long-term video iEEG recordings with 128 electrodes in six grids and a sampling frequency of 256Hz were performed and two datasets were recorded. While the first dataset served for identifying iEEG underlying functional areas, our analysis here uses only the second intracranial dataset for the validation of the presurgical source analysis results. The spikes and seizures of the dataset were identified and the 128 intracranial electrode positions were roughly noted during surgery as shown in Figure 5 and scanned in the CT dataset, which was recorded just after the electrode implantation. A registration of the CT to the head model using SCIRun allowed the identification of the iEEG electrode positions with respect to the headmodel, as shown in Figure 4 (right).

2.5 Bioelectric forward problem

2.5.1 FEM based forward problem

In the considered low frequency band, the relationship between bioelectric surface potentials and the underlying current sources in the brain can be represented by a quasi-static Maxwell equation with homogeneous Neumann boundary conditions at the head surface [34]. The primary current sources are generally modeled by mathematical dipoles [34, 23]. For a given mathematical dipole and head tissue conductivity distribution, the potential can be uniquely determined [50] for what is known as the *bioelectric forward problem*. For the numerical approximation of the bioelectric forward problem, we used the FE method. Three different FE approaches for modeling the mathematical dipole are known from the literature: a subtraction approach [4, 50], a Partial Integration direct method [45], and a Venant direct method [5]. In this study we used the Venant FE approach with piecewise linear basis functions based on

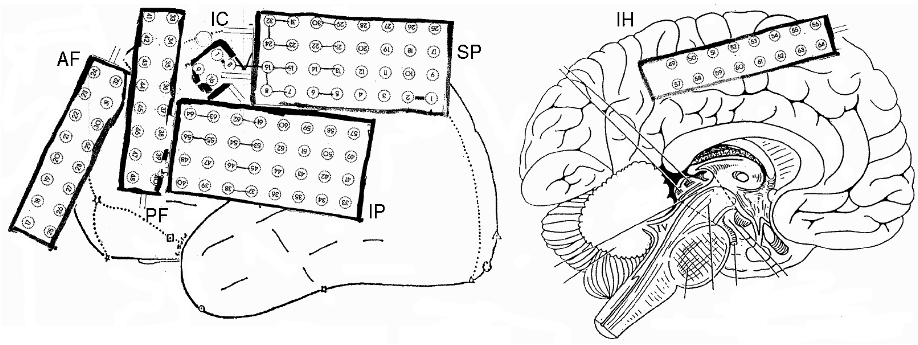

Figure 5: The positions and labels of the iEEG electrodes in the patient's record. Different stripes are shown, where AF means anterior frontal, PF posterior frontal, IC intra cavity, IP inferior parietal, SP superior parietal and IH interhemisphere.

comparison of the performance of all three in multilayer sphere models, which suggested that for sufficiently regular meshes, it yields suitable accuracy over all realistic source locations [51]. Standard variational and FE techniques for the EEG forward problem yield a linear equation system

$$K\underline{\Phi} = \underline{J}^{Ven} \tag{3}$$

where $K \in \mathbb{R}^{N\times N}$ is a sparse symmetric positive definite stiffness matrix, $\underline{\Phi} \in \mathbb{R}^N$ the coefficient vector for the electric potential and $\underline{J}^{Ven} \in \mathbb{R}^N$ the Venant approach right-hand side vector with N the number of FE nodes [5].

2.5.2 Fast transfer matrix approach

Let us assume that the EEG electrodes directly correspond to FE nodes at the surface of the head model (otherwise, interpolation is needed). It is then easy to determine a restriction matrix $R \in \mathbb{R}^{(s_{\text{eeg}}-1)\times N}$, which has only one non-zero entry with the value 1 in each row and which maps the potential vector onto the $(s_{\text{eeg}}-1)$ non-reference EEG electrodes:

$$R\,\underline{\Phi} =: \underline{\Phi}_{\text{eeg}}. \tag{4}$$

When defining the following *FE transfer matrix* for the EEG,

$$T := R\,K^{-1} \quad \in \mathbb{R}^{(s_{\text{eeg}}-1)\times N}, \tag{5}$$

a direct mapping of an FE right-hand side vector onto the unknown electrode potentials is given:

$$T\,\underline{J}^{Ven} \stackrel{(5)}{=} R\,K^{-1}\underline{J}^{Ven} \stackrel{(3)}{=} R\underline{\Phi} \stackrel{(4)}{=} \underline{\Phi}_{\text{eeg}}. \tag{6}$$

Note that $\underline{J}^{Ven}$ has only C non-zero entries at the neighboring FE nodes to the considered dipole location [5], so that $T\underline{J}^{Ven}$ only amounts in $2\cdot(s_{\text{eeg}}-1)\cdot C$ operations.

The inverse FE stiffness matrix K^{-1} in (5) exists, but its computation is a difficult task, since the sparseness of K will be lost while inverting. By means of multiplying equation (5) with the symmetric matrix K from the right side and transposing both sides, we obtain

$$KT^{tr} = R^{tr}. \tag{7}$$

The FE transfer matrix can thus be computed by means of iteratively solving $(s_{\text{eeg}} - 1)$ large sparse FE linear equation systems. Note that a fast FE transfer matrix for the magnetoencephalography (MEG) forward problem can be derived on a similar way [48]. For the computation of (5) by means of (7), we employ an algebraic multigrid preconditioned conjugate gradient (AMG-CG) method. We solve up to a relative error of 10^{-6} in the controllable $KC^{-1}K$-energy norm (with C^{-1} being one V-cycle of the AMG) [48].

2.6 The bioelectric inverse problem

2.6.1 Discrete source space

A 3D influence source space that represents the brain compartment in which dipolar source activities might occur was extracted from the segmented T1-MRI for the discrete parameter space source analysis algorithms (GFS, MNLS and sLORETA, see Section 2.6.2). For the brain compartment, a 3mm eroded mask consisting of the gray and white matter compartments was chosen under the assumption that dipole locations (mainly apical dendrites of layer V pyramidal cells [23]) are well below the cortical surface. The source space mesh had 172,366 nodes and 157,320 regular hexahedra elements with 2 mm resolution. Dipole sources in the three Cartesian directions were allowed on each mesh node. The source space is shown indirectly in the upper two rows of Figure 6 as it underlies the discrete parameter space source reconstruction algorithms. It is clearly visible that both the ventricle and the lesion areas were excluded from the source space because no activity is expected from those areas.

2.6.2 Inverse methods

The non-uniqueness of the inverse problem implies that assumptions on the source model, as well as anatomical and physiological a-priori knowledge about the source region should be taken into account to obtain a unique solution. Therefore, different inverse approaches for continuous and discrete source parameter space have been proposed [11, 35, 22, 9, 16].

The first class of approaches that were used here are the classical spatio-temporal dipole modeling approaches, where the number of possible dipoles is restricted to only some few [35, 22, 16]. The spatio-temporal focal source models differ in the manner in which they describe the time dependence of the data. Generally, they are grouped into three classes, the unconstrained dipole model (moving dipole), a dipole with temporally fixed location (rotating dipole) and a dipole with fixed location and fixed orientation (fixed dipole) [22]. Optimization of the resulting cost function [22] is performed with a Nelder-Mead simplex optimizer which is started from appropriate seed-points and finds the next local minimum of the cost function [16]. The goodness of fit (GOF) of the spatio-temporal dipole model to the data can then be used as an index of the models quality.

The second class of inverse methods are the scanning methods. From this class, the so-called least-squares scanning or goal function scan (GFS) [22, 16] was used here. The GFS scans systematically position by position of the entire discrete source space defined in Section 2.6.1. At each position, a least squares fit is performed to the chosen data samples, i.e., an optimal rotating dipole is computed for the considered location. As a result, the GOF at each position is displayed as a color map on cross-sections of the source space mesh. The GFS is not subject to pitfalls of non-linear search algorithms, such as being trapped in local minima or slow convergence. Additionally, if the underlying sources have distinct EEG topographies and comparable strength, areas of similar GOF can serve as confidence regions [16] and GFS results can be used as seed-points for spatio-temporal dipole models. Since a single dipole at each source space mesh node is fitted to the data, this method will naturally work, if there is a single focal source. However, the GFS might fail, e.g., when there are multiple sources which are close to each other, sources that produce overlapping EEG topographies or EEG's of greatly differing intensities [22].

The last class of inverse approaches that was considered for this study are the current density reconstruction methods. From this class, the minimum norm least squares (MNLS or Tikhonov-regularization) [11, 16] and the standardized low resolution electromagnetic tomography (sLORETA) [26, 7] were used for our study. The MNLS and sLORETA methods act on a distributed source model, where the restriction to a limited number of focal sources is abolished, i.e., sources are allowed to be simultaneously active on all discrete source space mesh nodes. The non-uniqueness of the resulting problem is compensated by the assumption that the energy of the solution should be minimal. The necessary regularization parameter was chosen as the ratio of the variance of the noise and the variance of the current elements, where the latter was approximated as shown in [16, pp.58-59]. It is well-known that a regularization without any depth-weighting gives preference to superficial sources [9]. Therefore, for the MNLS, a source weighting matrix with L2-norms of the corresponding lead field columns as diagonal entries was chosen [9]. As reported in [26], despite of all weighting efforts, linear solutions such as MNLS produced at best images with systematic non-zero localization errors and in a large series of single test source simulations at arbitrary positions and depths in the volume conductor, a standardization of the MNLS as performed in sLORETA was shown to produce zero-localization error.

2.7 Software and computational platform

The SimBio software environment (http://www.simbio.de) was used on a 64bit Linux-PC with an Intel Xeon 5130 processor (2GHz) with 8GB of main memory for all presented FE-based inverse source reconstructions. The SimBio code contains a variety of EEG and MEG inverse source reconstruction algorithms which can be combined with multi-layer sphere, boundary element or finite element forward approaches [16, 52, 48, 50, 51].

Inverse method	Location (in mm)	Location differences (in mm)					GOF
		GFS	MNLS	RotDip	MovDip	sLORETA	
GFS	(45;97;57)	-	6.6	2.6	2.5;2.3	0	97.02
MNLS	(47;103;55) (47;103;55)	6.6	-	5.9	6.2;5.8	6.6	- -
RotDip	(43.6;98.2;55.2)	2.6	5.9	-	0.9;1.9	2.6	97.1
MovDip	(43.1;98.2;55.9) (45.3;97.5;54.8)	2.5 2.3	6.2 5.8	0.9 1.9	- -	2.5 2.2	97.2 97.1
sLORETA	(45;97;57) (45;97;57)	0	6.6	2.6	2.5;2.2	- -	- -

Table 3: Localization results of goal function scan (GFS), minimum norm least squares (MNLS), rotating (RotDip) and moving dipole fit (MovDip) and standardized low resolution electromagnetic tomography (sLORETA) and the localization differences between those approaches are presented. GOF denotes the goodness-of-fit.

3 Results

3.1 Memory and computation time

When measuring the wall-clock time, it should be distinguished between the setup-computation that only has to be carried out once per head model and computations that have to be carried out hundreds or hundreds of thousands of times depending on the inverse procedure. During the setup, the computation of the transfer matrix T in (5) by means of the AMG-CG solver took about 56min, i.e., about 140s per sensor. The resulting transfer matrix has a size of about 0.6GB (i.e., for 128 electrodes about 3.2GB). Each forward computation in (6), i.e., the right-hand side computation, $\underline{J}^{Ven}$, and the multiplication to the transfer matrix, $T\ \underline{J}^{Ven}$ then only took 37ms. The rotating dipole fit, e.g., can then be performed in only 10s of computation time.

3.2 Source analysis results

Five different methods from the presented three classes of inverse approaches in Section 2.6.2 were applied to the two time samples at the peak of the F3 delta spike, namely the GFS, the MNLS, the moving dipole fit followed by the rotating dipole fit and finally sLORETA. The source analysis results are presented in Table 3 and Figure 6. In order to get a first overview of the underlying source structure, the GFS was applied, resulting in a single activity peak with a GOF value of 97.02% in the left hemisphere at the posterior lateral border of the lesion, as shown in the upper row of Figure 6. In a second step, the depth-weighted MNLS was used to corroborate the GFS result. The result is shown in the second row of Figure 6, consisting again of a single activity peak at the posterior lateral border of the lesion. Moving and rotating single dipole fits were then started with the GFS localization result as seedpoint. With a GOF of about 97.1%, the best fit for both moving and rotating dipole model to the data was achieved slightly (about 2.5mm) outside the predefined source

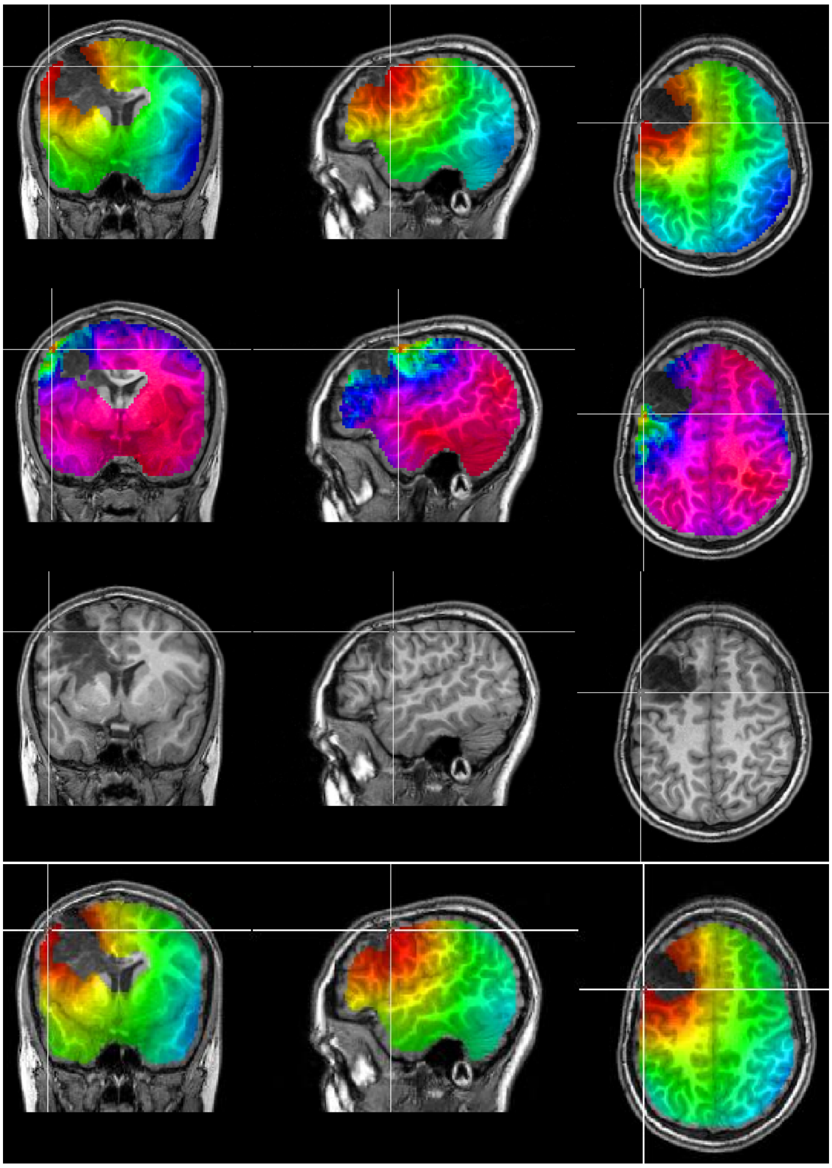

Figure 6: The results of the GFS (top row), MNLS (second row), the rotating dipole fit (third row) and sLORETA (bottom row).

space mesh at the posterior lateral border of the lesion at the gyral crown as shown in the third row of Figure 6. The reconstructed dipoles pointed mainly in posterior direction and had amplitudes of about 200nAm. Finally, the bottom row of Figure 6 shows the sLORETA result. The sLORETA localization result was identical to the one of the GFS.

When summarizing the source analysis results, GFS, MNLS, sLORETA and the spatio-temporal dipole models in the 1mm anisotropic FE model clearly pointed to a focal epileptic area located in the left hemisphere at the posterior lateral border of the lesion. While the MNLS localized about 6mm more posterior, the location differences between GFS, sLORETA and the spatio-temporal dipole models only differed by maximally 2.6mm.

3.3 Validation using the iEEG result

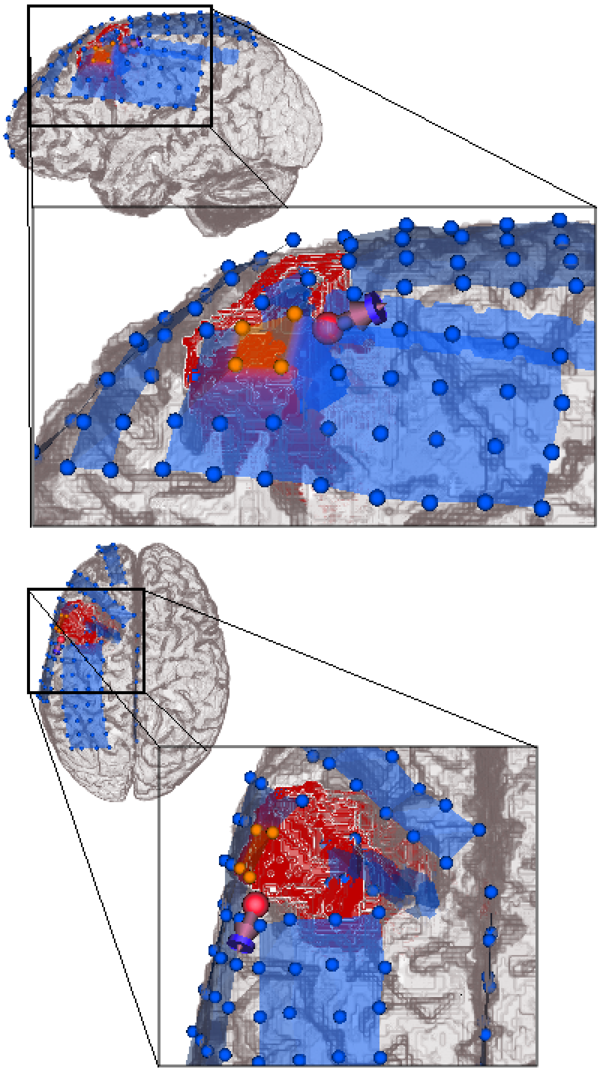

Figure 7: Presurgical sEEG rotating dipole fit result validated by means of the postsurgical iEEG outcome: The blue spheres represent the postsurgical intracranial grid and stripe electrodes, the four orange spheres are the inferior parietal (IP) grid electrodes, which primarily received ictal spikes. The lesion is marked in red.

The location of the presurgical rotating dipole fit from Section 3.2 is shown together with the postsurgical iEEG electrodes and stripes in Figure 7. According to the clinical information, the 4 iEEG electrodes which primarily received ictal spikes, are shown in orange. A possible source for the ictal activity might be either located right beneath these electrodes with a mainly radial orientation or it might be located at the posterior lateral border of the electrodes with an increased tangential orientation component so that it only projects one of its poles to the iEEG electrodes. The latter scenario better fits to the presurgical rotating dipole fit result. In summary, the non-invasively localized dipole is located very close to the intracranial electrodes which primarily received ictal spikes, which validates the source analysis result.

4 Discussion

To the best of the authors knowledge, this is the first study using high-resolution (1mm) anisotropic finite element (FE) volume conductor modeling for a non-invasive surface electroencephalography (sEEG) based source analysis in presurgical epilepsy diagnosis. Five different inverse source analysis algorithms, a goal function scan (GFS) [22, 16], a minimum norm least squares (MNLS) [11, 16], a moving and a rotating dipole fit [35, 22, 16] and a standardized low resolution electromagnetic tomography (sLORETA) [26, 7] approach were based on a hexahedra FE model with about 3.1 Million unknowns to analyse the peak of 9 averaged delta spikes of a residivous patient suffering from medically-intractable epilepsy. With only small differences in location, i.e., a maximal difference of 2.6mm between GFS, sLORETA, moving and rotating dipole fit and 6.6mm between the MNLS and the other approaches, the FE-based sEEG inverse algorithms localized a single center of activity at the posterior lateral border of the lesion. While the MNLS localized about 6mm posterior to the other inverse methods, the GFS and the sLORETA localization results were identical. This might corroborate the result of [26], i.e., that, despite of all weighting efforts, former linear solutions such as MNLS produced images with non-zero localization errors, while, in a large series of single test source simulations at arbitrary positions and depths in the volume conductor, sLORETA was shown to produce zero-localization error [26]. Source orientation was mainly in posterior direction, i.e., away from the lesion towards the epileptogenic tissue. This source orientation result is in agreement with a recent study which showed that in central and interhemispheric spikes, the epileptogenic side cortex was gross surface negative through the sulcal wall to the adjacent gyrus [33].

The presurgical sEEG source analysis result was validated with post-surgical intra-cranial EEG (iEEG) measurements and it was found that the reconstructed rotating dipole was close to the iEEG electrodes which primarily received ictal spikes. The small differences might be due to the deformations of soft brain tissue occurring after craniotomy through the so-called brain shift [37] or through the implantation of the iEEG grids and stripes, the use of standard in contrast to the individual sEEG electrode locations, sEEG and iEEG data noise, segmentation inaccuracies and the general modeling errors of the bioelectric forward and inverse problem.

An essential requirement is a correctly triggered dataset. In this study, qualified persons supervised the long term monitoring, marked seizures at the moment they appeared and a clinical expert identified and averaged the corresponding spikes. Several algorithms also exist for automatic offline spike detection [47] but the accuracy is assumed to be inferior. The challenge of offline spike detection is known: even two experts often do not mark the same events as spikes. Spike morphology and background varies widely between patients, hence the differences between candidate spike events and actual spike events might be very large.

Sensitivity studies showed that brain conductivity anisotropy should be taken into account for accurate source reconstruction [12, 49, 10]. In [10] it was found that especially dipole orientation and strength are significantly influenced by brain anisotropy. As reported in [25, 33], dipole orientations might even be more important than absolute dipole localizations in attributing epileptic activity to subcompartments of the respective brain area. In [49] it was shown that the more the source is surrounded by anisotropic tissue, the more it is important to model the anisotropy. It is furthermore known that the high conductivity of the CSF [28, 49] and local conductivity changes in the vicinity of the primary source [4] have a non-negligible effect on source analysis. In light of those considerations, the modeling of head tissue conductivity inhomogeneities and anisotropies might be crucial in certain cases of presurgical epilepsy source analysis.

A former argument against FE head volume conductor modeling in source analysis was the complexity of the 3D mesh generation [18] and the heavy computational load and thus long waiting time [5, 4, 42, 27]. Because of computational complexity, FE models were restricted to low numbers of nodes such as, e.g., 10,731 (5mm edge length) in a study for the localization of epileptiform activity [42] and 18,322 for the setup of a lead field matrix with 8,742 unknown dipole components which still took roughly a week of computation time [5]. Rough restrictions to the number of FE nodes cause unacceptable numerical errors especially for eccentric sources [4, 5, 50, 51] and limit the possibilities of inhomogeneity and anisotropy modeling. The presented EEG FE transfer matrix approach (a similar approach is also possible for the MEG [48]) in combination with the algebraic multigrid preconditioned conjugate gradient (AMG-CG) solver method [48] allowed us to use 1mm edge length leading to about 3.1 Million FE nodes, a resolution, which seemed impossible before [5, 4, 42]. After transfer matrix setup computations in a preprocessing step, which only has to be carried out once per headmodel and which took less than an hour on a standard one-processor Linux machine, an FE forward computation in the 1mm anisotropic hexahedra FE model could be performed in just 37 Milliseconds, which allowed us to setup a lead field matrix with 517,098 unknown dipole components for the discrete inverse methods. The generation of the 1mm hexahedra FE mesh is performed in some seconds, the 3D meshing problem is reduced to just a conversion of the segmentation result into the corresponding hexahedra mesh. In [27] it was speculated that for three isotropic compartment (skin, skull, brain) head volume conductor models, the BEM approach is less computationally intensive compared to the FE approach, while providing improved computational accuracy relative to simple analytical models. However, in a recent three isotropic compartment study [20], the FE outperformed a BE approach (collocation method using the isolated skull and the vertex approach) with regard to both accuracy for eccentric sources and computational complexity.

The following limitations of the presented work are important. The data of a single case with obviously unilateral and unifocal expression of the epileptiform activity is not representative for all cases of localization-related epilepsy. Further studies including more unselected patients with multifocal epilepsy patterns have to be performed and results of non-invasive source analysis have to be validated with invasive recordings. Electrode positions should be recorded with a digitizer or a photogrammetry device and a larger number of electrodes should be used [44]. Our results are based on isotropic skull conductivity. A recent study reported that the skull's three-layeredness (outer compacta, spongiosa, inner compacta) should be modeled [32], which can easily be done in the presented 1mm hexahedra FE approach as long as a segmentation of the spongiosa is available. To map the diffusion tensors to conductivity tensors, a linear relationship with a scaling of 0.736 was established [40, 41]. In our study, this value would have led to a much higher mean conductivity of brain tissues than generally assumed [29], so that a scaling of 0.210 was determined using a volume constraint approach. Further studies have to be performed to validate the scaling parameter, examine its inter- and intra-individual variance and to overall further validate the proposed conductivity tensor imaging method.

In conclusion, the presented study indicates the feasibility of non-invasively localizing an epileptogenic focus by means of sEEG based inverse source analysis approaches using 1mm anisotropic FE volume conductor modeling. Our result may give new impulse to EEG based source analysis in epilepsy patients and might contribute to clinical presurgical evaluation.

Acknowledgment

This work was supported by the IST-program of the European Community, project SimBio (http://www.simbio.de), by the Deutsche Forschungsgemeinschaft (Wo1425/1-1), by a research grant from CIMIT, by NSF ITR 0426558, and by NIH grants R03 CA126466, R01 RR021885, R01 GM074068 and R01 EB008015. The authors would like to thank D. Güllmar and C. Kellinghaus for their help within the project and for proofreading the manuscript, respectively.

References

[1] P.J. Basser and J. Mattiello and D. LeBihan, *MR Diffusion Tensor Spectroscopy and Imaging*, Biophys J., 66:259-267, 1994.

[2] C. Baumgartner, G. Lindinger, A. Ebner, S. Aull, W. Serles, A. Olbrich, S. Lurger, T. Czech, R. Burgess and H. Luders, *Propagation of interictal epileptic activity in temporal lobe epilepsy*, Neurology, 45(1):118-22, 1995.

[3] S.B. Baumann, D.R. Wozny, S.K. Kelly and F.M. Meno, *The Electrical Conductivity of Human Cerebrospinal Fluid at Body Temperature*, IEEE Trans.Biomed.Eng., 44(3):220-23, 1997.

[4] S.P. van den Broek, *Volume Conduction Effects in EEG and MEG*, Proefschrift Universiteit Twente Enschede, The Netherlands, ISBN 90-365-0919-x, 1997.

[5] H. Buchner, G. Knoll, M. Fuchs, A. Rienäcker, R. Beckmann, M. Wagner, J. Silny and J. Pesch, *Inverse Localization of Electric Dipole Current Sources in Finite Element Models of the Human Head*, Electroenc.Clin.Neurophysiol., 102:267-278, 1997.

[6] B. Cuffin, *EEG localization accuracy improvements using realistically shaped head models*. IEEE Trans Biomed. Eng., 43:299-303, 1996.

[7] M. Dannhaur,*EEG/MEG source reconstruction with the sLORETA algorithm*, diploma thesis, Faculty of Mathematics and Computer Science, Universität Leipzig, 2007.

[8] J.S. Ebersole, *Noninvasive localization of epileptogenic foci by EEG source modeling*, Epilepsia, 41, Suppl.3:S24-S33, 2000.

[9] M. Fuchs, H.A. Wischmann and M. Wagner, *Generalized minimum norm least squares reconstruction algorithms*, ISBET Newsletter, 5: 8-11, 1994.

[10] D. Güllmar, J. Haueisen, M. Eiselt, F. Gießler, L. Flemming, A. Anwander, T. R. Knösche, C. H. Wolters and M. Dümpelmann, D.S. Tuch and J. R. Reichenbach, *Influence of Anisotropic Conductivity on EEG Source Reconstruction: Investigations in a Rabbit Model*, IEEE Trans. Biomed. Eng.,53(9):1841-50, 2006.

[11] M.S. Hämäläinen and R.J. Ilmoniemi, *Interpreting measured magnetic fields of the brain: Estimates of current distributions*, Helsinki University of Technology, Techn.Rep., TKK-F-A559", 1984.

[12] Haueisen J, Tuch DS, Ramon C, Schimpf PH, Wedeen VJ, George JS, Belliveau JW, *The Influence of Brain Tissue Anisotropy on Human EEG and MEG*, NeuroImage, Vol. 15:159-166, 2002.

[13] G. Huiskamp, J. Maintz, G. Wieneke, M.Viergever and A.C. van Huffelen, *The influence of the use of realistic head geometry in the dipole localization of interictal spike activity in MTLE patients*. Biomedizinische Technik, 42:84-87, 1997.

[14] G. Huiskamp, M. Vroeijenstijn, R. van Dijk, G. Wieneke and A. van Huffelen. *The need for correct realistic geometry in the inverse EEG problem*. IEEE Trans Biomed. Eng., 46(11):1281-1287, 1999.

[15] M. Jenkinson and S.M. Smith, *A global optimisation method for robust affine registration of brain images*, Medical Image Analysis, 5(2):143-156, June 2001.

[16] T.R. Knösche, *Solutions of the neuroelectromagnetic inverse problem*, PhD thesis, University of Twente, The Netherlands, 1997.

[17] K. Kobayashi, I. Merlet and J. Gotman, *Separation of spikes from background by independent component analysis with dipole modeling and comparison to intracranial recordings*, Clin. Neurophysiol., 112(3):405-13, 2001.

[18] J. Kybic, M. Clerc, T. Abboud, O. Faugeras, R. Keriven and T. Papadopoulo, *A common formalism for the integral formulations of the forward EEG problem*, IEEE Trans.Med.Imag., 24(1):12-18, 2005.

[19] G.Lantz, M.R. Grave de Peralta, A.S. Gonzalez, C.M. Michel, *Noninvasive localization of electromagnetic epileptic activity. II. Demonstration of sublobar accuracy in patients with simultaneous surface and depth recordings*, Brain Topography, 14(2):139-47, 2001.

[20] B. Lanfer, C.H. Wolters, A. Anwander, M. Dümpelmann, F. Zanow and T.R.Knösche, *Comparison of FEM and BEM in EEG source analysis with regard to accuracy and computational speed*, submitted to Phys. Med. Biol., 2007.

[21] I. Merlet and J. Gotman, *Reliability of dipole models of epileptic spikes*, Clin. Neurophysiol., 110(6):1013-28, 1999.

[22] Mosher JC, Lewis PS, Leahy RM, *Multiple dipole modeling and localization from spatio-temporal MEG data*, IEEE Transactions on Biomedical Engineering., Vol. 39(6):541-57, 1992.

[23] S. Murakami and Y.C. Okada, *Contributions of principal neocortical neurons to magnetoencephalography and electroencephalography signals*, J.Physiol., 575(3):925-936, 2006.

[24] P.W. Nicholson, *Specific impedance of cerebral white matter*, Exp.Neurol., 13:386-401, 1965.

[25] E. Pataraia, G. Lindinger, L. Deecke, D. Mayer and C. Baumgartner, *Combined MEG/EEG analysis of the interictal spike complex in mesial temporal lobe epilepsy*, NeuroImage, 24:607-14, 2005.

[26] R.D. Pascual-Marqui, *Standardized low resolution brain electromagnetic tomography (sLORETA): technical details*, Methods & Findings in Experimental & Clinical Pharmacology, 24D:5-12, 2002.

[27] S.M. Plis, J.S. George, S.C. Jun, D.M. Ranken, P.L. Volegov and D. M. Schmidt, *Probabilistic forward model for electroencephalography*, Phys.Med.Biol., 52:5309-27, 2007.

[28] C. Ramon, P.H. Schimpf, J, Haueisen, M. Holmes and A. Ishimaru, *Role of Soft Bone, CSF and Gray Matter in EEG Simulations*, Brain Topography, 16:245-248, 2004.

[29] C. Ramon, J. Haueisen and P.H. Schimpf, *Influence of head models on EEG simulations and inverse source localizations*, BioMedical Engineering OnLine, 5:55, 2006.

[30] F. Rosenow and H. Luders, *Presurgical evaluation of epilepsy*, Brain, 124(9):1683-1700, 2001.

[31] B.J. Roth, D. Ko, I.R. von Albertini-Carletti, D. Scaffidi and S. Sato, *Dipole Localization in Patients with Epilepsy using the Realistically shaped head model*, Electroenc.Clin.Neurophysiol., 102:159-66, 1997.

[32] R.J. Sadleir and A. Argibay, *Modeling Skull Electrical Properties*, Ann.Biomed.Eng., 35(10), 2007.

[33] K.A.Salayev, N. Nakasato, M. Ishitobi, H. Shamoto, A. Kanno and K. Iinuma, *Spike orientation may predict epileptogenic side across cerebral sulci containing the estimated equivalent dipole*, Clin. Neurophysiol., 117: 1836-43, 2006.

[34] J. Sarvas, *Basic Mathematical and Electromagnetic Concepts of the Biomagnetic Inverse Problem*, Phys.Med.Biol., 32(1): 11-22, 1987.

[35] M. Scherg and D. von Cramon, *Two bilateral sources of the late AEP as identified by a spatio-temporal dipole model*, Electroenc. Clin. Neurophysiol., 62, 32-44, 1985.

[36] S. M. Smith, *Fast robust automated brain extraction*, Human Brain Mapping, 17(3), 143-155, 2002.

[37] G. Soza, *Registration and Simulation for the Analysis of Intraoperative Brain Shift*, PhD thesis in Computer Science, Friedrich-Alexander-Universität Erlangen-Nürnberg, 2005.

[38] H. Stefan, C. Hummel, G. Scheler, A. Genow, K. Druschky, C. Tilz, M. Kaltenhauser, R. Hopfengärtner, M. Buchfelder and J. Romstock, *Magnetic brain source imaging of focal epileptic activity: a synopsis of 455 cases.*, Brain, 126(Pt 11):2396-405, 2003.

[39] J.P. Thirion, *Image matching as a diffusion process: an analogy with Maxwells demon*, Medical Image Analysis, Vol.2(3):243-260, 1998.

[40] D.S. Tuch, V.J. Wedeen, A.M. Dale, J.S. George, J.W. Belliveau, *Conductivity Mapping of Biological Tissue Using Diffusion MRI*, Ann N Y Acad Sci, vol. 888:314-6, 1999.

[41] D.S. Tuch, V.J. Wedeen, A.M. Dale, J.S. George, J.W. Belliveau, *Conductivity tensor mapping of the human brain using diffusion tensor MRI*, Proc Nat Acad Sci USA, Vol. 98:11697-11701, 2001.

[42] T.D. Waberski, H. Buchner, K. Lehnertz, A. Hufnagel, M. Fuchs, R. Beckmann and A. Rienäcker, *Properties of Advanced Headmodelling and Source Reconstruction for the Localization of Epileptiform Activity.*, Brain Topography,10 (4):283-290, 1998.

[43] T.D. Waberski, R. Gobbele, G. Herrendorf, B.J. Steinhoff, R. Kolle, M. Fuchs, W. Paulus and H. Buchner, *Source Reconstruction of Mesial-Temporal Epileptiform Activity: Comparison of Inverse Techniques*, Epilepsia, 41(12):1574-583, 2000.

[44] Wang Y, Gotman J, *The influence of electrode localization errors on EEG dipole source localization with a realistic head model*, Clinical Neurophysiology, Vol. 112:1777-1780, 2001.

[45] D. Weinstein, L. Zhukov and C. Johnson, *Lead-field bases for Electroencephalography source imaging*, Annals of Biomed.Eng., 28(9):1059-1066, 2000.

[46] Wiebe S, Blume WT, Girvin JP, Eliasziw M, *A randomized, controlled trial of surgery for temporal-lobe epilepsy*, The New England journal of medicine, 345(5):311-318, 2001.

[47] Wilson SB, Emerson R, *Spike detection: a review and comparison of algorithms*, Clinical Neurophysiology, Vol. 113(12):1873-1881, 2002.

[48] C.H. Wolters, L. Grasedyck and W. Hackbusch, *Efficient Computation of Lead Field Bases and Influence Matrix for the FEM-based EEG and MEG Inverse Problem*, Inverse Problems, Vol. 20:1099-1116, 2004.

[49] C.H. Wolters, A. Anwander, X. Tricoche, D. Weinstein, M.A. Koch, R.S. MacLeod, *Influence of Tissue Conductivity Anisotropy on EEG/MEG Field and Return Current Computation in a Realistic Head Model: A Simulation and Visualization Study using High-Resolution Finite Element Modeling*, NeuroImage, Vol. 30(3):813-826, 2006.

[50] C.H. Wolters, H. Köstler, C. Möller, J. Härtlein, L. Grasedyck and W. Hackbusch, *Numerical mathematics of the subtraction method for the modeling of a current dipole in EEG source reconstruction using finite element head models*, SIAM J. on Sci. Comp., 30(1):24-45, 2007.

[51] C.H. Wolters, H. Köstler, C. Möller, J. Härdtlein and A. Anwander, *Numerical approaches for dipole modeling in finite element method based source analysis*, International Congress Series, 1300:189-192, 2007.

[52] F. Zanow, *Realistically shaped models of the head and their application to EEG and MEG.*, PhD thesis, University of Twente, The Netherlands, 1997.

[53] Y. Zhang, L. Ding, W. van Drongelen, K. Hecox, D. Frim, B. He, *A Cortical Potential Imaging Study from Simultaneous Extra- and Intra-cranial Electrical Recordings by Means of the Finite Element Method*, NeuroImage, 31(4):1513-1524, 2006.

2.17.2 Multiscale modeling of neuronal activity from simultaneous intra-cranial and surface EEG data in presurgical epilepsy diagnosis

Project:
Unpublished results from
C.H. Wolters, IBB, University of Münster
Cooperation partners:
Scott Makeig, Swartz Center for Computational Neuroscience, Institute for Neural Computation, University of California San Diego, USA
Gregory A. Worrell, Mayo Clinic, Rochester, USA.
Chris Johnson, Scientific Computing and Imaging Institute, University of Utah, Salt Lake City, USA

and

Unpublished results from
C. Röer, Source analysis of simultaneous sEEG and iEEG measurements in presurgical epilepsy diagnosis. Diploma thesis in Physics, Institute for Biomagnetism and Biosignalanalysis (IBB), University of Münster, 2008.
Supervisors:
C.H. Wolters, IBB, University of Münster
R. Friedrich, Institute for Theoretical Physics, University of Münster.

Project aims

Because of the physics of volume conduction, brain electrical fields on the scalp are broad and only synchronous activity across relatively large cortical areas can account for them. Local field potential (LFP) recordings from the cortical surface, meanwhile, may be dominated by local field activity very near to the electrodes. Thus, the relationship of scalp and cortical surface fields is spatially a multiscale problem. Besides the recent studies of Lai et al. [2005] and Zhang et al. [2006], so far as the author knows, no previous study has reported on relationships between concurrently collected high-density scalp EEG (sEEG) and intracranial EEG (iEEG) data in humans. In large part, such data have not been recorded because productive methods for their analysis have not been available. Relatively little is known about the quantitative spatiotemporal relationship between field potentials recorded non-invasively from the scalp and LFP data recorded invasively from the cortical surface and/or depth electrodes. This project wants to assess this relationship based on data collected from a clinically important subject population, epilepsy patients whose seizures are not controlled by medications and are candidates for neurosurgery. The data will allow us to estimate and model volume conduction based relationships between noninvasive and invasive human electrical brain data. The use of methods will be explored for localizing seizure foci and modeling the activity of networks responsible for spontaneous seizures in neocortical and mesial temporal lobe epilepsies. The novelty of iEEG and sEEG recording appears to be based in part on a doubt frequently raised by neurologists, i.e., that volume conduction patterns are strongly altered by skull incisions involved in implanting the electrodes and especially the strongly resisting Silastic material of the iEEG grid, thus standard methods of reading and analyzing the scalp EEG data should be highly inaccurate or inapplicable.

Independent component analysis based source reconstruction using an FE head model

Equivalent dipole modeling of cortical EEG sources is often justified as representing the net far-field scalp projection of a likely EEG source configuration, a compact oriented cortex patch (Scherg and von Cramon [1985]). Independent component analysis (ICA) has not only proven to be an effective method for removing eye and muscle activity artifacts from sEEG and thus increasing the effective signal-to-noise ratio of subsequent analysis (Jung et al. [2000]), but can also identify and separate functionally independent components, which for normal sEEG prove to be most often associated with scalp maps matching the projection of a single equivalent current dipole (or two time-correlated sources located near symmetrically across the brain midline, possibly supported by dense connections via the corpus callosum) (Kobayashi et al. [2001]; Makeig et al. [2002]). This result thus strongly suggests that ICA isolates partially coherent LFP activities occurring within compact cortical regions of unknown size and curvature. Under the assumption that ICA is able to disentangle the sources, it is then desirable to estimate the location and extent of the involved cortical region. While, in general, sEEG source localization is an under-determined inverse problem, the localization of a single current dipole using data from a reasonable number of measurement electrodes is overdetermined. In this case, the linear inverse problem is much simpler, given an adequate volume conductor model of the patients head. The head model especially has to reflect the surgical skull defects and the impact of the Silastic pads in which the iEEG electrodes are embedded.

Former studies showed that the influence of a post-surgical skull incision on the forward problem cannot be neglected (van den Broek [1997]). Additionally, the electrical conductivity of the CSF is well known (Baumann et al. [1997]), though standard spherical or BE head models do not take this layer into account. Post-surgical incisions and fissures in skull and brain compartments are mainly filled with CSF, so an exact representation of these conductance anomalies is of high importance to accurate source estimation during implantation.

In the following computations, for the representation of a dipolar current source in an FE volume conductor model, linear basis functions and a Venant potential approach were chosen.

Data recording and volume conductor modeling

An array of 29 channel sEEG and 78 channel iEEG were measured simultaneously during implantation from a patient of the Mayo Clinic (Rochester, Minn.) with medically intractable epilepsy. Four approximately 15-minute recordings from the subject were subjected to ICA decomposition. Each decomposition returned 107 maximally independent components across the data, which were continuously recorded while the subject was drowsing. A pre-surgical T1-MRI was recorded with a resolution of 256 slices in axial, 256 in sagittal and 120 in coronal direction and a voxel-size of 0.86 x 1.6 x 0.86mm. Furthermore, post-surgically, a CT was taken with a resolution of 68 slices in axial, 512 in sagittal and 635 in coronal and a voxel-size of 0.49 x 0.49 x 2.65mm.

A voxel-based affine registration using mutual information from the ITK-toolbox was used to register the pre-surgical T1-MRI onto the post-surgical CT. An acceptable registration accuracy was observed. The registered dataset was then segmented into 4 tissue classes (skin, skull, CSF and brain) using an adaptive fuzzy C-means algorithm (Wolters [2003]) as well as manual segmentation approaches. Skin, skull, the CSF in the surgery opening and iEEG electrode locations were extracted from the CT while the remaining part of the CSF compart-

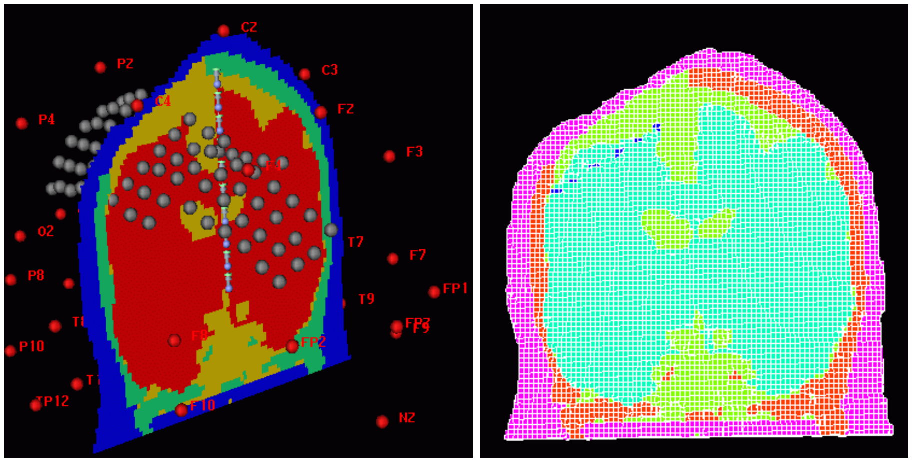

Figure 2.10: Cross-section of the segmented head model of the epilepsy patient, locations of iEEG and sEEG electrodes and test dipoles for the validation studies (left). 2mm geometry-adapted hexahedral model (right). Visualization was carried out using BioPSE [2002].

ment and the brain were segmented out of the T1-MRI.

A 2mm geometry-adapted hexahedral FE-mesh with 431K nodes and 410K elements was generated from the segmented dataset. A cross-section of the segmented head model of the epilepsy patient and the locations of iEEG and sEEG electrodes (left), as well as the geometry-adapted hexahedral model are shown in Figure 2.10.

Influence of the skull incision from trepanation

In order to study the influence of a skull incision from trepanation on the forward problem, a second four-tissue-model was created where the trepanation hole was manually closed. Both segmented datasets were tesselated into tetrahedral FE models of about 140K nodes and 850K elements using an ordinary Delaunay tetrahedralization (ODT) approach. Figure 2.11 (top row) shows sagittal slices of the conductivity tensor ellipsoids in the barycenters of the tetrahedral elements when modeling the tissues as isotropic (therefore, all tensors are spherical). The tensors were normalized and colored by trace. The highest trace values could be found in the CSF compartment (red) and the lowest in the skull compartment (dark blue). In order to show the impact of the skull hole on the forward problem, electric potential computations were performed in both FE models for dipole sources with strengths of 100 nAm as shown by the yellow cones in Figure 2.11 (top row). The resulting distributions of the electric potentials at the surfaces of

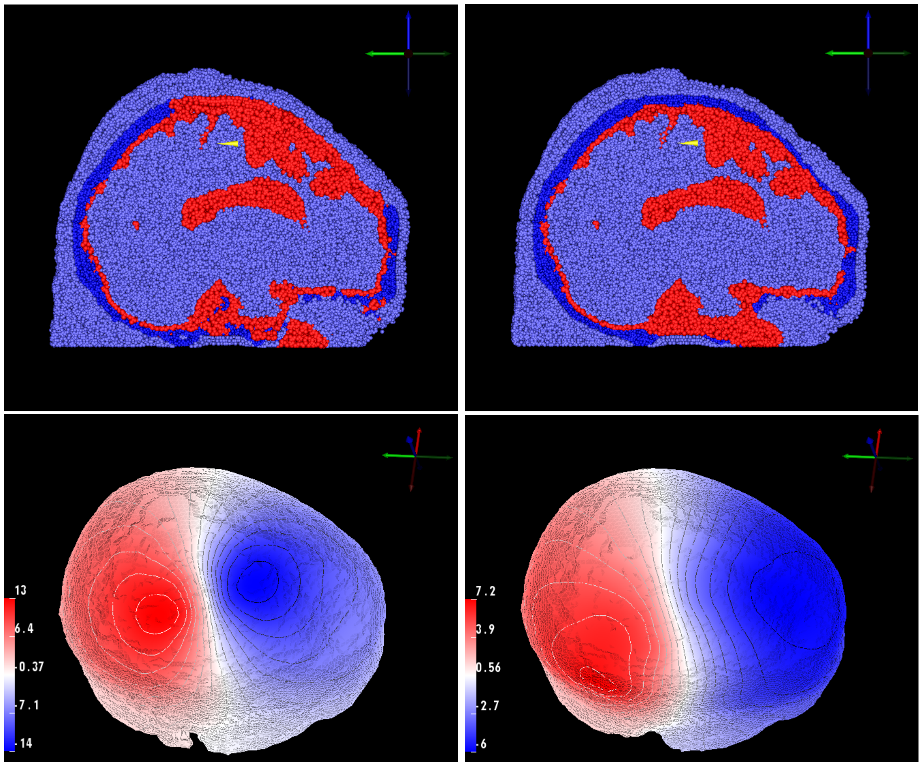

Figure 2.11: Influence of skull incision from trepanation on the sEEG forward problem: Dipole source used for field simulation (yellow) and sagittal slice of the conductivity tensor ellipsoids of the tetrahedral model from the epilepsy patient with skull incision (top, left) and with a manually closed skull incision (top, right) and the corresponding surface isopotential distributions (bottom row) (scale in μV). Tensor validation and visualization was carried out using BioPSE [2002].

both head models are shown in Figure 2.11 (bottom row). As it is well visible, neglecting the modeling of the skull opening results in a much blurred potential distribution, corroborating the importance of patient-specific volume conductor modeling.

Dipole fit validation

The inverse single dipole fit method in the 2mm geometry-adapted hexahedral model with skull hole was first validated by performing single dipole fits for simulated sEEG and iEEG data at known reference sources. The 10 reference source positions are shown in Figure 2.10 (left). This reference potential distribution was then used as the input data to an inverse single dipole fit approach as described in Section 1.4.2 based on the same FE model using a Nelder-Mead simplex optimization. For all dipole eccentricities, the seed-point was positioned in the approximate midpoint of the volume conductor model. Using the fast transfer matrix approach (Chapter 2.2), the inverse optimization results were achieved in acceptable computation times. For example, the computation of the combined sEEG/iEEG transfer matrix, which has to be carried out just once per head model, required about 10 minutes of computation time on a standard Linux PC (3.2GHz, Pentium 4). Each forward computation within the inverse optimization process was then reduced to only some few milliseconds for the multiplication of the sEEG/iEEG transfer matrix to an FE right-hand side. The reconstruction errors were measured for dipole fits by means of combined sEEG/iEEG and single sEEG and iEEG modalities. Results were computed for 10 mainly tangentially oriented sources and 10 mainly radially oriented sources (Figure 2.10) with varying z-coordinates. As expected, localization errors were in the sub-millimeter range for all tested configurations. However, the validation results for the tangential reference sources showed a further expected advantage of the sEEG/iEEG combined measurements: The more distant the source is from the iEEG grid, the less accurate the iEEG grid was able to reflect both poles of the dipole and the larger the stabilizing effect of the additional scalp EEG sensors on the reconstruction. With actual (not simulated, noise-free) data, this effect is assumed to be much more distinct.

Preliminary ICA-based source reconstruction results for a peri-ictal component of an epileptic seizure

The same iterative fitting methods were used to fit dipoles to either the sEEG or the iEEG map of a selected peri-ictal ICA component from the joint scalp and grid data ICA decomposition. Figure 2.12 shows representative results for a point-source like component principally projecting to a small neighborhood of the iEEG grid (left). FE model fitting successfully localized an equivalent current dipole for this activity in cortex directly below the affected area (right circle)–percent grid-map variance accounted for was high (96%). The scalp map associated by ICA with this source was weakly but broadly distributed over the scalp EEG recording array. The same equivalent dipole fitting method applied to this scalp map found it also to be highly dipolar (percent variance accounted for, 94%), confirming that ICA isolates sources with a simple biophysical structure, without use of any biophysical constraints. The location of the equivalent dipole for the scalp map activity was (left circle), however, much deeper than the computed source of the iEEG map activity (right circle). The orientation of the scalp-map dipole was close to the center of the grid map excitation, as expected

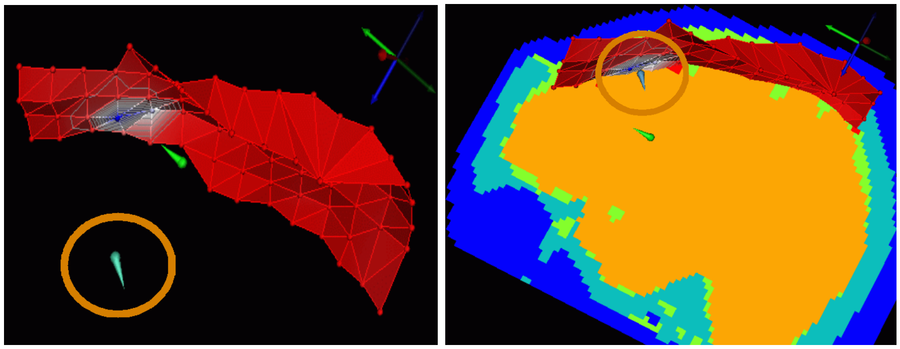

Figure 2.12: Inverse dipole fit results (encircled, in blue) for a peri-ictal ICA component: iEEG map fit just under the affected electrode (right circle; variance accounted for, 96%) and much deeper sEEG map fit (left circle; variance accounted for, 94%). The seed points for the inverse fits are shown in light green in both figures.

for a coherent source. However, the difference in depths of the equivalent dipoles was unexpected and points to the need for further research.

Preliminary CDT meshing results for the modeling of the iEEG silastic pads

The probably most obvious idea for the remaining difference in depths between sEEG and iEEG dipole fits in the last section is the modeling of the highly resisting iEEG Silastic grids.The Silastic pad is a kind of insulator and Zhang et al. [2006] used a conductivity of only $3.3 \cdot 10^{-11}$ S/m for it. An accurate modeling might thus be of high importance. While Zhang et al. [2006] used an ordinary Delaunay tetrahedralization (ODT) FE meshing approach for the Silastic pad, we are working towards an appropriate constrained Delaunay tetrahedralization. The preliminary CDT meshing results are shown in Figures 2.13 and 2.14.

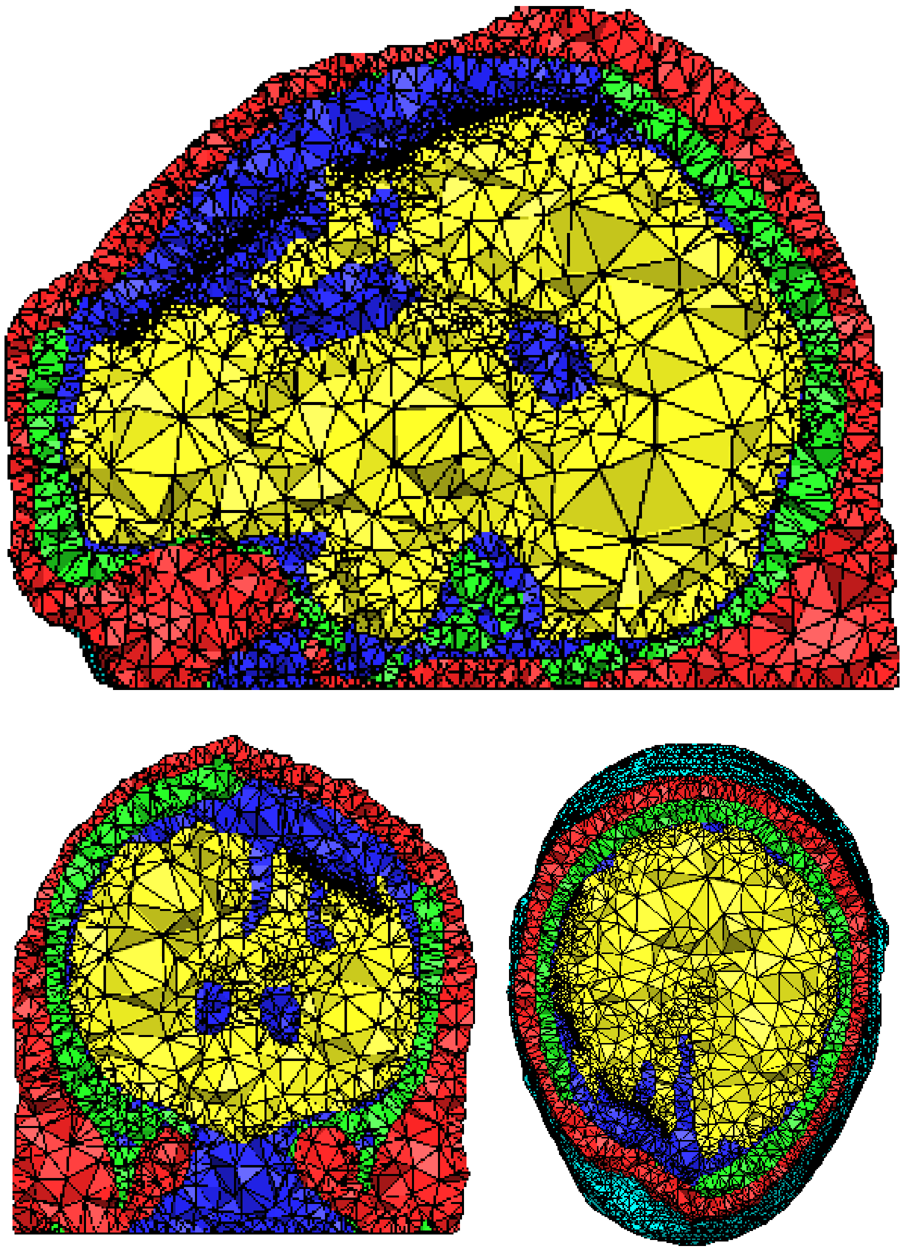

Figure 2.13: Röer [2008]: Constrained Delaunay tetrahedralization FE mesh of the epilepsy patient with a special focus on the modeling of the high resisting iEEG Silastic pads and the skull incision from trepanation. Visualization was carried out using Tetview (Si [2007]).

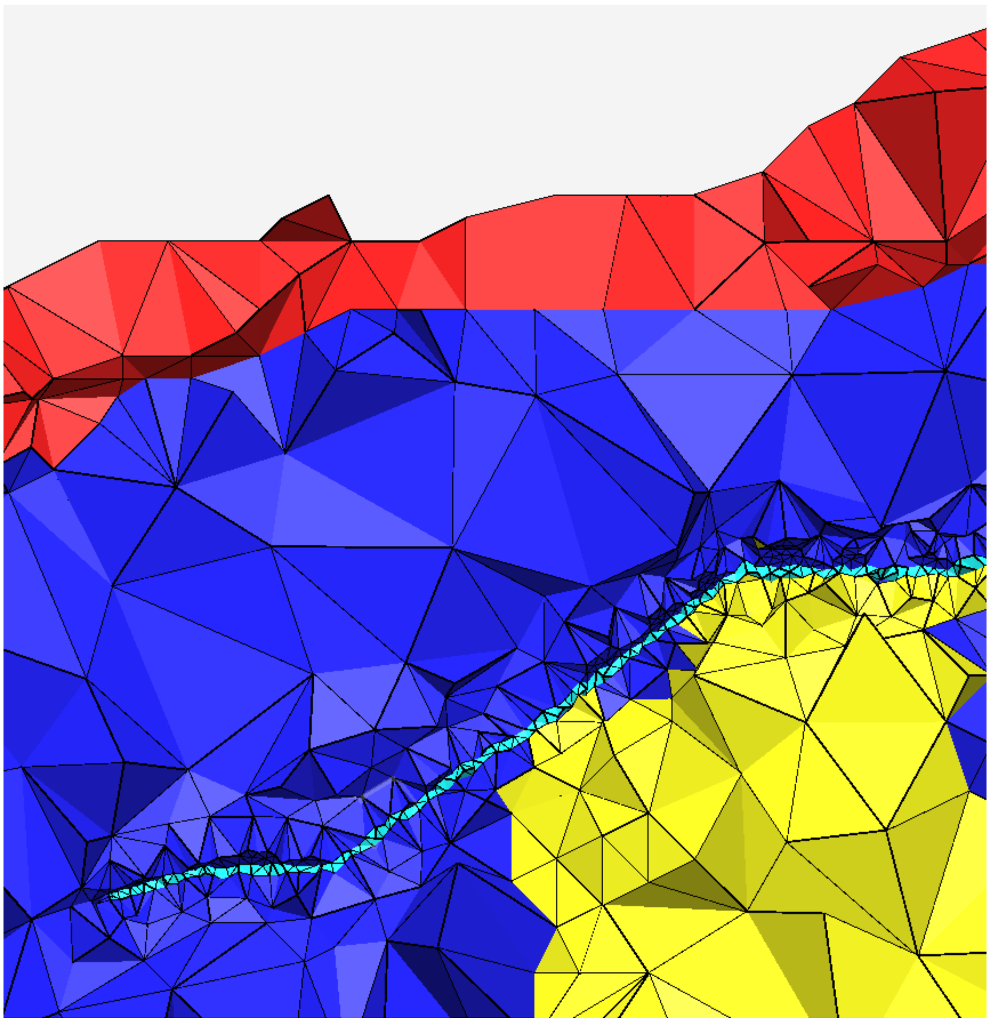

Figure 2.14: Röer [2008]: Same FE mesh as in Figure 2.13, but zoomed into the area of the thin insulating iEEG Silastic grid. Visualization was carried out using Tetview (Si [2007]).

Chapter 3

Discussion and conclusion

Accuracy and time play an important role in medical diagnostics and research as well as in the field of neuroscience. The presented work examined advanced numerical algorithms for a more accurate and fast source analysis of electroencephalography (EEG) and magnetoencephalography (MEG) data. A strong focus was on an improved solution to the EEG and MEG forward problem used within the inverse source analysis by means of a more realistic representation of the geometry and conductivity inhomogeneity and anisotropy of the head tissues using the finite element (FE) method. The improved forward modeling was applied in modern EEG and MEG inverse approaches such as the standardized low resolution electromagnetic tomography (sLORETA) method (Pascual-Marqui [2002]), the minimum norm least squares (MNLS) (Hämäläinen and Ilmoniemi [1984]; Knösche [1997]; Fuchs et al. [1994]), the scanning (Mosher et al. [1992]; Knösche [1997]) and the spatio-temporal dipole fit (Scherg and von Cramon [1985]; Mosher et al. [1992]; Knösche [1997]; Wolters et al. [1999]) approaches. Additionally, a new and especially fast spatio-temporal current density reconstruction (STR) method (Schmitt et al. [2002]) was shown to yield superior reconstruction results when compared to temporally uncoupled MNLS approaches and was applied for the first time to the field of source analysis using a realistic high-resolution FE forward approach in Chapter 2.12. Two medical application fields were considered, namely presurgical diagnosis of localization-related medically-intractable epilepsy in Chapter 2.17 and the field of evoked responses, or, more specifically, tactile somatosensory evoked potentials (SEP) and fields (SEF) in Chapters 2.11 and 2.16. A major motivation of this work was the special need in the medical diagnostic field of EEG and MEG source analysis to achieve high accuracy, which might provide substantial progress to the field, with acceptable computation costs in order to implement it in a clinical day-to-day business. The promising results of the new methodological source analysis developments in those application fields are addressed again in more detail in Section 3.3 of this chapter.

3.1 The FEM based EEG and MEG forward problem

3.1.1 Accuracy of the singularity treatment approaches

The numerical treatment of the singularity introduced into the differential equation by means of the mathematical point current dipole and the interplay with the conductivity inhomogeneity and anisotropy of the complex head tissues and with the FE meshing aspects was expatiated in the presented work. The subtraction approach is well-known in FE-based source analysis for the treatment of the singularity (Bertrand et al. [1991]; van den Broek [1997]; Awada et al. [1997]; Marin et al. [1998]; Schimpf et al. [2002]), but a satisfying FE theory was not yet derived and presented accuracies were not yet satisfactory. Therefore, in Chapter 2.1, a mathematical theory was developed for the subtraction approach, which contained a proof for existence and uniqueness of the weak solution in the function space of zero-mean potential functions and convergence statements of the FE method for the numerical solution of the electric potential. It was shown that the constant in the convergence proof largely depends on the distance of the source to the next conductivity discontinuity, i.e., a theoretical reasoning for the numerical finding that accuracy of the subtraction approach decreases with increasing source eccentricity in sphere model validation studies as reported in (Bertrand et al. [1991]; van den Broek [1997]; Awada et al. [1997]; Marin et al. [1998]; Schimpf et al. [2002]) and also in this work. A projected subtraction approach was implemented, validated in an EEG study in ordinary Delaunay tetrahedralization (ODT) and regular and geometry-adapted hexahedral meshes of a three compartment sphere model (skin, skull, brain) with anisotropic skull layer for sources with maximal eccentricities of 95%, i.e., 4mm distance to the inner skull, and applied in a realistic three-compartment head model with anisotropic skull compartment. The method was shown to yield satisfactory results for both the EEG in Chapter 2.1 as well as for the MEG evaluations in Chapter 2.5 in three-compartment sphere models. However, the validation and comparison of the projected subtraction approach with two direct potential methods, the partial integration (Yan et al. [1991]; Awada et al. [1997]) and the Venant (Buchner et al. [1997]) approach, were ambiguous in Chapter 2.5 (EEG, ODT and regular hexahedral meshes, three compartment isotropic sphere model with source eccentricities up to 95%, i.e., 4mm distance to the inner skull), Chapter 2.6 (EEG, regular hexahedral mesh, four compartment isotropic sphere model with source eccentricities up to 97%, i.e., 2mm distance to the CSF compartment) and Chapter 2.7 (setup like in Chapter 2.6, with additionally geometry-adapted hexahedral FE meshes). For the MEG, the projected subtraction approach was shown to yield consistently better validation results than the Venant approach for tangentially oriented MEG sensors, while for radially oriented MEG sensors, both methods were nearly identical because of the low contribution of the secondary compared to the primary currents in a sphere model (Chapter 2.5). Furthermore, for the EEG and for tangentially oriented sources, the projected subtraction approach was also shown to be consistently superior to the Venant and partial integration direct potential approaches (Chapters 2.6 and 2.7). However, for the EEG and eccentric dipoles with radial orientations, the Venant and partial integration methods outperformed the projected subtraction approach (Chapters 2.5, 2.6 and 2.7).

Because of these shortcomings of the projected subtraction approach, a full subtraction method was mathematically derived, implemented and validated in four-layer sphere models with anisotropic skull compartment (Chapter 2.8). Additionally to those developments, instead of the above ODT meshes, constrained Delaunay tetrahedralization (CDT) meshing approaches were applied, so far as the author knows, for the first time to the field of source analysis. The advantage of CDT in comparison with ODT meshing is described in detail in (Si and Gärtner [2005],Si [2004]). With a maximal relative Euclidian error (maxRE) of 0.71%, a maximal relative difference measure (maxRDM) of 0.34% and a maximal magnification factor (maxMAG) of 0.3% with regard to the forward problem (Chapter 2.8) and with maximal single source reconstruction errors of 0.3mm (localization), 0.03 degree (orientation) and 0.21% (magnitude) (Chapter 2.9.2) for sources with high eccentricities of up to 98.7%, i.e., up to 1mm below the CSF compartment, the combination of the full subtraction approach in a high quality CDT FE mesh with only 360K nodes led to accuracies that, to the best of the authors knowledge, have not yet been presented before. In a direct comparison with the projected subtraction approach from Chapter 2.1, it was found that the full subtraction approach was by an order of magnitude more accurate for dipole sources close to the next conductivity discontinuity. The fact that, in a realistic head model, most sources of interest have eccentricities between 50% and 98% shows the importance of those results. Papadopoulo and Vallaghé [2007] investigated a partial integration FE approach in a three layer sphere model with anisotropic skull and sources up to 3.5mm below the inner skull surface. In their article, a 1mm hexahedral approach (thus a much higher FE resolution than the above CDT mesh with 360K nodes) with smoothed tissue boundaries using an improved stiffness matrix integration by means of a levelset segmentation approach was used and a maxRDM of 2% was reported (maxMAG was not shown). Schimpf et al. [2002] investigated an FE subtraction approach in a four layer sphere model with isotropic skull and sources up to 1mm below the CSF compartment. In their article, a regular 1mm cube model was used and a maxRDM of 7% and a maxMAG of 25% was achieved. In a locally refined (around the source singularity) tetrahedral mesh with 13K nodes of a four layer sphere model with anisotropic skull, Bertrand et al. [1991] reported numerical accuracies up to a maximal eccentricity of 97.6%. A maxRE of above 20% and a maxMAG up to 70% were documented for the most eccentric source. van den Broek [1997] also used a locally refined (around the source singularity) tetrahedral mesh with 3,073 nodes of a three layer sphere model with anisotropic skull. The author mentioned in the conclusion that in some cases the accuracy could not further be improved by adding points globally as the numerical stability of the matrix equation that had to be solved was reduced. Marin et al. [1998] restricted their finest tetrahedral mesh of 88K nodes to eccentricities of 81% in order to reach a sufficient accuracy for radial dipole forward solutions in a three compartment sphere model with anisotropic skull. Awada et al. [1997] implemented a 2D subtraction approach and compared its numerical accuracy with a direct potential method in a 2D sphere model. A direct comparison with the above results is therefore difficult, but the authors concluded that the subtraction method was generally more accurate than the direct approach. Finally, in Chapter 2.9, the full subtraction approach was compared to the Venant and the partial integration direct approaches and was shown to perform consistently better in a quality CDT mesh of a four layer sphere model with anisotropic skull compartment and eccentricities up to 98.7%. While error curves oscillated on a low level for both direct approaches, they were smooth for the subtraction approaches. The oscillations do not have to be a disadvantage because, as shown in Chapter 2.9.3, the minimum Venant error for tetrahedral meshes was achieved for sources on FE nodes, so that a lead field interpolation technique (Yvert et al. [2001]) can be used to avoid oscillations and further decrease the numerical error of the direct potential approaches.

Plis et al. [2007] speculated that boundary element (BE) forward approaches are less computationally intensive compared to FE models, while providing improved computational accuracy relative to simple analytical models. In Chapter 2.10, the Venant FE approach was compared with the ISA vertex collocation BE method, i.e., a collocation BE method (Barnard et al. [1967]) using the isolated skull approach (ISA) (Meijs et al. [1989]; Hämäläinen and Sarvas [1989]; Zanow [1997]) and linear basis functions with analytically integrated elements (de Munck [1992]; Zanow [1997]) in an isotropic three layer sphere model. Both numerical approaches were combined with transfer matrices for a fast BE and FE forward modeling. For a 2mm geometry-adapted hexahedral FE model, the maximal RDM (MAG) of the FEM approach of 1% (5%) was about two (four) times lower than the maximal RDM (MAG) of the BEM approach. At the same time, with 0.7 milliseconds, the FE forward computation was more than four times faster than the BE forward computation. As recent investigations showed, the BE method can still be improved through the use of a Galerkin approach (Mosher et al. [1999]; Kybic et al. [2005]), a symmetric BE approach (Kybic et al. [2005]), or virtual mesh refinement (Fuchs et al. [1998]). However, as shown in Chapter 2.8 using a full subtraction approach, this is also true for the FE method.

As a final note, instead of trying to reduce numerical errors for the probably "over-singular" mathematical point dipole, it is important to reconsider other and especially smoother source models, taking into account the fact that the primary current sources are continuous throughout the cortical tissue (Tanzer et al. [2005]). This is where the FE-based subtraction method might provide a further important contribution to EEG and MEG source analysis.

3.1.2 Computational speed

With regard to computational speed, the state-of-the-art approach in FE based source analysis was to solve one FE equation system for each source (Bertrand et al. [1991]; Buchner et al. [1997]; Awada et al. [1997]; van den Broek [1997]; Waberski et al. [1998]; Schimpf et al. [2002]; Wolters et al. [2002]; Wolters [2003]). Because of the non-uniqueness of the EEG and MEG inverse problem, in most applications (see for example Chapter 2.17.1), a variety of inverse approaches with different a-priori constraints are examined and compared which leads to a huge amount of necessary forward solutions for tens or even hundreds of thousands of different sources. The excessive computational burden created by such an approach often forced the examiner to use sub-optimal numbers of FE nodes and sub-optimal numbers of possible sources in the brain (Bertrand et al. [1991]; Buchner et al. [1997]; van den Broek [1997]; Waberski et al. [1998]). For example, in Buchner et al. [1997], the setup of a lead field matrix which is needed for inverse current density reconstruction (CDR) methods with 8,742 unknown dipole components in a tetrahedral FE approach with 18,322 nodes took roughly a week of computation time. In Waberski et al. [1998], an FE model with 10,731 nodes was used for the localization of epileptiform activity and it was concluded that, for a general clinical use of FE source analysis, a finer FE discretization and parallel computing is needed. Parallelized source analysis techniques were investigated to alleviate the problem of the immense computational costs (Buchner et al. [2000]; Zhukov et al. [2000]; Wolters et al. [2002]; Wolters [2003]), but such approaches need specific computer systems and often have the disadvantage of more complex software structures which might limit a broader use in the application fields. In Chapter 2.2 of this work, the concept of EEG and MEG transfer matrices for the FE approach was derived and evaluated in Chapter 2.4

in a comparison with the state-of-the-art approach. The transfer matrix concept was already known to the BEM community for a longer time (Mosher and Leahy [1999]). However, in BEM applications, because of the far lower dimensions of only some thousand nodes, the geometry matrix can be directly inverted, while this is not possible for high-resolution three-dimensional approaches. Therefore, for the EEG, Helmholtz' principle of reciprocity was used and similar reductions of computational complexity were achieved for a Finite Difference (FD) (Vanrumste et al. [1998]; Mohr [2004]) and for an FE approach (Weinstein et al. [2000]). In Chapter 2.2, it was, so far as the author knows, for the first time shown how the concept of FE transfer matrices can be derived for both EEG and MEG by just using operations from linear algebra and avoiding the complex reciprocity theory. A similar development was presented simultaneously in (Gencer and Acar [2004]). Using this concept, for each head model, one only has to solve one large sparse FE system of equations for each of the possible EEG or MEG sensor locations in order to compute the full transfer matrix. Each forward solution is then reduced to multiplication of the transfer matrix by an FE right-hand side (RHS) vector containing the source load. Exploiting the fact that the number of sensors (currently up to about 600) is much smaller than the number of reasonable dipolar sources, the transfer matrix approach is substantially faster than the state-of-the-art forward approach and can be applied to inverse reconstruction algorithms in both continuous and discrete source parameter space for EEG and MEG. In Chapter 2.17.1, the speedup factor amounted to more than 20,000, showing the immense reduction of computational costs.

Still, the solution of hundreds of large linear FE equation systems for the construction of the EEG and MEG transfer matrices is a major time consuming part within FE-based source analysis. The state-of-the-art is the use of iterative FE solver techniques such as the successive over-relaxation method (Schimpf et al. [2002]) or the conjugate gradient (CG) method without preconditioning (Bertrand et al. [1991]) or with standard preconditioners like Jacobi (Jacobi-CG, Zhukov et al. [2000]) or incomplete Cholesky without fill-in (IC(0)-CG, Buchner et al. [1997]). In the mathematical community it is well known that multigrid (MG) methods are optimal preconditioners for the CG method (Jung and Langer [1991]; Hackbusch [1994]; Haase and Langer [1998]; Stüben [1999]) and recently, such iterative solver techniques were also applied to the problem of source analysis (Wolters et al. [2000]; Johnson et al. [2001]; Wolters et al. [2002]; Mohr and Vamrunste [2003]; Mohr [2004]). As shown in Chapter 2.9, the algebraic multigrid preconditioned CG (AMG-CG) (Ruge and Stüben [1986]; Haase and Langer [1998]; Stüben [1999]) iterative FE solver technique achieved an order of magnitude higher computational speed than IC(0)-CG and Jacobi-CG with an increasing gain factor when decreasing mesh size. The examination was performed in a four-compartment sphere model with anisotropic skull layer, where quasi-analytical solutions allowed for an exact quantification of computational speed versus numerical error, while former examinations (Wolters [2003]; Mohr [2004]) just considered the relative error in the solution of the FE equation system in the $KC^{-1}K$-energy norm (K: stiffness matrix; C: preconditioner). It was furthermore shown in Chapter 2.3, that a multiple right-hand side (RHS) AMG-CG approach can further speedup the computation of the transfer matrices by more than a factor of 2.

In summary, the combination of the transfer matrix approach with the multi-RHS-AMG-CG leads to highly efficient FE-based forward solutions and enables resolutions which seemed to be impracticable before. It allows to just convert a segmented MR image into a 1mm hexahedral model so that tedious FE meshing procedures are avoided. The developed code can be run on a standard 64bit single processor Linux machine, as shown for a 1mm hexahedral FE mesh with 3.1 Million FE nodes and 517 thousand unknown dipole components in Chapter 2.17.1, where the computation of the transfer matrix was carried out in less than an hour (only once per head model) and each forward computation was then performed in only 37 Milliseconds. The time for transfer matrix setup can be further reduced using the parallel solver approach if a cluster of PC's is available (Haase and Langer [1998]; Wolters et al. [2002]).

3.1.3 Meshing aspects

An essential prerequisite for FE modeling is the generation of a mesh which represents the geometric and electric properties of the volume conductor. The difficult construction of the volume discretization is often seen to be a major disadvantage of the FEM compared to the BEM which only requires the use of surface triangulation meshes Kybic et al. [2005].

So far, ordinary Delaunay tetrahedralizations (ODT) were mainly used in FE-based source analysis (Buchner et al. [1997]; Waberski et al. [1998]; Wagner et al. [2000]; Wolters [2003]; Zhang et al. [2006]). The ODT exploits a set of vertices in the three-dimensional head domain and does not take into account faces between compartments of different conductivity. As described in detail in (Wagner et al. [2000]; Si [2004]; Wolters [2003]), in a first step of the ODT meshing, the vertices are distributed on the segmented tissue boundaries (skin, skull, brain) and on auxiliary surfaces which are generated by eroding the innermost segmented boundary (brain gray or white matter). From this set of vertices and under the constraint that the Delaunay criterion is fulfilled, tetrahedral elements are constructed. The Delaunay criterion demands that no vertex lies inside the circumsphere of a tetrahedron. The ODT does not guarantee that tetrahedra only contain one type of head tissue and in certain rare cases, tetrahedra were found that crossed a tissue boundary. Such elements spoil the accuracy of the FE forward modeling.

As discussed in detail in (Si [2004]), a constrained Delaunay tetrahedralization (CDT) is a variation of the ODT that is additionally constrained to respect the boundaries between different head tissues, i.e., the input to a CDT are the surface meshes which describe the boundaries of the head tissues. As discussed in Section 3.1.1, the high-quality CDT meshes (Si and Gärtner [2005],Si [2004]) could significantly contribute to an improvement of numerical accuracy when compared to ODT approaches. For the FE modeling of the 2mm thin highly resistant silastic pads of the iEEG electrodes for the epilepsy patient in Chapter 2.17.2, the use of CDT approaches is considered to be of especially high importance, because ODT or hexahedralization approaches might definitely produce unrealistic holes in the silastic pads.

Only few studies examined regular hexahedral elements exploiting the spatial discretization inherent in medical tomographic data (Schimpf et al. [2002]). While the construction of CDT meshes can be tedious and time-consuming in topologically difficult situations, high-resolution hexahedral meshes can always easily and fastly be generated from segmented medical datasets and will in most situations (except the modeling of volume conductor anomalies such as the silastic pad in Chapter 2.17.2) be highly accurate, as shown in Chapters 2.1, 2.7, 2.10 and 2.17.1. Especially geometry-adapted hexahedral meshes have been shown to achieve high accuracies with RDM and MAG errors that were reduced by factors of between 1.5 (radial sources) and 2 (tangential sources) when compared to regular hexahedral elements (Chapter 2.7). Furthermore, as shown in Chapter 2.10, a 2mm geometry-adapted hexahedral Venant FE approach outperformed a BE forward approach with regard to both accuracy and computational speed.

Finally, as a future goal, the promising approach of combining the segmentation result of levelset segmentation approaches with FE-based forward modeling (Papadopoulo and Vallaghé [2007]) should be mentioned, which might help to further increase numerical accuracy for the EEG and MEG forward problem.

3.1.4 Sensitivity to tissue geometries and conductivities

The spatial resolution of especially EEG, but to a lesser extent also MEG, is dependent on the degree of modeling accuracy of the different head tissue geometries and conductivities.

With regard to the geometries, CT was used in the presented clinical studies for the extraction of the skull (Chapter 2.17.2) and for the identification of intra-cranial electrode locations (Chapters 2.17.1 and 2.17.2). CT is not justified for routine physiological studies in healthy human subjects. Therefore, a combination of T1-weighted MRI, which is well suited for the identification of soft tissues (scalp, brain) and proton-density (PD) weighted MRI, enabling the segmentation of the inner skull surface, was proposed in Chapters 2.11, 2.13 and 2.17.1. This approach leads to an improved modeling of the skull thickness over standard T1-MRI based approaches as shown in Chapter 2.11, an important parameter for EEG source analysis. An improved modeling of the inner skull surface also increases accuracy with regard to MEG source analysis. The presented FE volume conductor models consisted of the individually and accurately shaped compartments scalp, skull, CSF, and brain gray and white matter, which were segmented with quasi-automatic algorithms (Chapters 2.11, 2.13, 2.14, 2.15 and 2.17.2) or more or less manually (Chapter 2.17.1) from registered T1-MRI/PD-MRI or T1-MRI/PD-MRI/CT datasets, respectively. The importance of modeling the CSF has been shown in Chapter 2.13 and also by others (Ramon et al. [2004]). In most BEM based studies, only three isotropically conducting head tissue compartments are considered: skin, skull and brain (Meijs et al. [1989]; Hämäläinen and Sarvas [1989]; Zanow [1997]; Fuchs et al. [1998]; Mosher et al. [1999]; Kybic et al. [2005]). Even if it would be theoretically possible to also model, e.g., the isotropic CSF compartment, it is practically difficult with the BEM. Because of the cortical convolutions and because of BE accuracy reasons, the inner CSF surface mesh (identical to the outer gray matter surface) would need a high resolution of possibly some tens of thousands of BE nodes. Since in most BE approaches, the geometry (or stiffness) matrix is densely populated [1], the computational amount of work is quadratically increasing and would thus be huge. However, while most conductivities of the head tissues vary across individuals and within the same individual due to variations in age, disease state and environmental factors as shown by (Haueisen [1996]; Oostendorp et al. [2000]; Latikka et al. [2001]; Baysal and Haueisen [2004]; Gonçalves et al. [2003b,a]), the CSF was measured by Baumann et al. [1997] and is considered to be less variable. When using the presented fast and accurate FE approaches, the computational amount of work with the FEM is only increasing linearly with the number of nodes and it is therefore possible to take a further tissue compartment such as, e.g., the highly conducting CSF compartment, into account, as validated in the spherical studies in Chapters 2.8 and 2.9 and evaluated and applied to realistic geometries in Chapters 2.11–2.17.

As described above, there is a large inter-individual variability of skull and brain conductivities that were measured with regard to the EEG inverse problem. Assuming wrong conductivity values especially in the EEG inverse problem can lead to severe localization errors, there is thus an obvious need to incorporate individual conductivity values.

[1] except within the recently presented symmetric BE approach of Kybic et al. [2005], where it has a block structure

The first proposed approach, the low resolution conductivity estimation (LRCE) in Chapter 2.11 is to simultaneously estimate skull and brain conductivity and source location based on high signal-to-noise (SNR) focal SEP data in combination with a geometrically realistic FE model based on combined T1- and PD-MRI data. A similar approach was examined by Vallaghé et al. [2007]. The LRCE simulation studies showed that for realistic SNR SEP data, both the brain and the skull conductivity together with the underlying dipole source in somatosensory cortex could simultaneously be reconstructed and provided an improved source analysis result. When applied to measured SEP data, the LRCE estimated a skull conductivity of 0.004S/m, which is in the range of the commonly used value, while the reconstructed brain conductivity was 0.48S/m, which is higher than the commonly used value of 0.33S/m. With these results, the viability of an approach was shown that computes its own conductivity values and thus reduces the dependence on assigning values from the literature and likely produces a more robust estimate of source location. Using the LRCE method, the individually optimized (with regard to both geometry and conductivity) volume conductor model can in a second step be used for the analysis of clinical or cognitive data acquired from the same subject. However, there is a trade off between the number of independent parameters that can be determined and the complexity of the assumed source model. The specific trade off point is also strongly influenced by the quality of the measured electric potentials. Thus the number of parameters that can be dependably estimated is a function of both the signal quality and the number and quality of a priori knowledge about, for example, the source location or orientation through a combination with other modalities or anatomical and/or functional arguments (e.g., a strong restriction of the source location to anatomically and physiologically reasonable areas close to the somatosensory SI area). In this context, Gonçalves et al. [2003a] and Huang et al. [2007] have suggested that by including MEG data in the scheme, it will be possible to improve stability considerably. As described in Chapter 2.16.3, this is also our future goal.

The second approach is based on the determination of electrical conductivity data of brain tissue through the water diffusion tensor as measured by diffusion tensor MRI (DT-MRI) (Basser et al. [1994]; Tuch et al. [1999, 2001]). Furthermore, because of its three-layeredness into soft bone (spongiosa) and hard bone (compacta), the skull was described by an effective anisotropic conductivity with a ratio of up to 1 to 10 radially to tangentially to its surface (Rush and Driscoll [1968]; van den Broek [1997]; Marin et al. [1998]; Akhtari et al. [2002]). The importance of modeling anisotropies and the feasibility to do so using the presented FE approaches was shown in the anisotropic multilayer sphere studies in Chapters 2.8 and 2.9. The influence of skull and white matter anisotropy on EEG and MEG source analysis was then studied in high-resolution FE models in Chapters 2.13–2.15 and in 2.17.1. For the MEG, the importance of correctly modeling the return currents, which are dependent on tissue conductivity, was shown in (Haueisen et al. [1995]; Uitert et al. [2003]). In this work, it was found that anisotropic white matter conductivity causes return currents to flow in directions parallel to the white matter fiber tracts (Chapter 2.13). Especially local anisotropies around the sources with regard to both EEG and MEG (Chapter 2.14 and Haueisen et al. [2000]), but also remote anisotropies between the sensors and the sources with regard to especially the EEG (Chapter 2.13) have a larger influence on the forward problem. The deeper a source lies and the more it is surrounded by anisotropic tissue, the larger the influence of this anisotropy on the resulting electric and magnetic fields. With regard to the EEG inverse problem, white matter anisotropy mainly seems to effect source orientation and strength parameters (see Güllmar et al. [2006] and Chapter 2.13). However, as reported by Salayev et al. [2006] and Pataraia et al. [2005], dipole orientations might even be more important than absolute dipole localizations in attributing epileptic activity to subcompartments of the respective brain area. Skull anisotropy was shown to have a smearing effect on the forward potential computation and thus mainly leads to a localization error in depth (see Chapters 2.13 and 2.16.3). In Chapter 2.15, the anisotropy of especially skull and to a lesser extent also white matter substantially compromised the EEG restoration ability of an L1-norm current density reconstruction approach, the centers of activity of the early left anterior negativity (ELAN) in language processing were strongly shifted along the Sylvian fissure in the anterior direction. In contrast, the L1-approach using the MEG data successfully reconstructed the main features of the ELAN. In summary, it was found that for the EEG, the presence of tissue anisotropy both for the skull and white matter compartment substantially compromises the forward computation and the inverse source reconstruction. In contrast, for the MEG, only the anisotropy of the white matter compartment has a significant effect on source analysis.

Sadleir and Argibay [2007] recently reported that the approximation of the skull's three-layered conductivity (inner compacta, spongiosa, outer compacta) through a radial to tangential conductivity anisotropy is not sufficient. As long as the individual isotropic conductivity values of the three skull tissues and a segmentation of the spongiosa are available, the three-layeredness can easily be incorporated in a 1mm hexahedral FE approach. It is therefore a future goal to combine the DT-MRI method for the determination of anisotropic brain tissue conductivities with the LRCE parameter estimation approach in combined SEP and SEF source analysis scenarios based on geometrically realistic 1mm FE models to estimate the inter-individually varying skull compacta and spongiosa conductivity parameters as well as the inter-individually varying linear scaling factors between the diffusion tensor and the conductivity tensor as discussed in Chapter 2.17.1.

3.2 The EEG and MEG inverse problem

EEG and MEG source analysis is an ill-posed inverse problem. There are an infinite number of solutions that explain the measured data due to the existence of silent sources, i.e., source configurations that produce no external magnetic or electric field. Those ghost sources can thus be added to any estimate without affecting the data fit (v. Helmholtz [1853]; Sarvas [1987]). This non-uniqueness is handled by making assumptions about the nature of the sources, e.g.,

- number of sources in the spatio-temporal dipole fit: Scherg and von Cramon [1985]; Mosher et al. [1992]; Knösche [1997]; Wolters et al. [1999]

- anatomical and neurophysiological constraints, i.e., dipole sources should be localized in brain gray matter and their orientation should be perpendicular to the cortical surface: Dale and Sereno [1993]; Murakami and Okada [2006]

- norms, spatial extent constraints and smoothness in spatial current density reconstruction (CDR) methods such as

  - minimum norm least squares (MNLS) or L2-norm CDR: Hämäläinen and Ilmoniemi [1984]; Knösche [1997]; Wagner [1998]; Fuchs et al. [1999]; Wolters [2003]
  - L1-CDR: Wagner [1998]; Fuchs et al. [1999]; Wolters [2003]
  - sLORETA: Pascual-Marqui [2002]; Dannhaur [2007]

- smoothness constraints in spatio-temporal reconstruction (STR) methods: Schmitt [2001]; Schmitt and Louis [2002]; Schmitt et al. [2002]

- correlation: In the MUSIC (Mosher et al. [1992]) and adaptive spatial filtering (beamforming) (Veen et al. [1997]; Sekihara et al. [2005]) algorithms, only sources can be reconstructed which are not temporally correlated. Furthermore, the independent component analysis (ICA) can only disentangle sources which are not temporally correlated: Kobayashi et al. [2001]; Makeig et al. [2002].

Thus, the accuracy and validity of the source analysis result depends much on the biological correctness of the assumptions and priors adopted in the model. This is why priors should not only be informed by neurophysiology domain knowledge, but should also be flexible and adaptive to particular data sets. Since the experimenter often does not feel certain about the prior, it is common practice to compare results of inverse approaches with different priors. This is why computational speed of the forward problem solutions is so important.

Besides of the results of the above inverse EEG and MEG source reconstruction methods based on realistic FE forward approaches that are discussed in the next section, a new and fast spatio-temporal current density approach (STR) was developed and applied to EEG source analysis in Chapter 2.12. STR is new to the EEG and MEG source analysis domain, since it interweaves spatial and temporal a-priori information to a new regularization approach and cannot be obtained by applying known spatial regularization methods to temporally filtered data. In a statistical evaluation and comparison of STR with MNLS applied to temporally-filtered data, STR proved to be more stable with regard to both spatial localization error and temporal source waveform deviation in the presence of noise in a simple volume conductor model. STR was furthermore implemented in the SimBio [2000] code and a first reconstruction of two simulated simultaneously active auditory sources was successfully carried out in a realistic FE head model. In the future, STR will be statistically evaluated in realistic scenarios with regard to both volume conductor modeling as well as realistic EEG and MEG data. STR will furthermore have to be combined with appropriate standardization approaches for improving its depth localization properties.

3.3 Application of FE-based source analysis

3.3.1 Reconstruction of SEP and SEF sources

Chapter 2.16 first introduced into the active noise cancellation system of the MEG machine at the Institute for Biomagnetism and Biosignalanalysis of the University of Münster, since its understanding and modeling is necessary for correct MEG forward simulations. The early component of tactile somatosensory evoked potentials (SEP) and fields (SEF) from a stimulation of the right index finger were then analyzed.

As generally accepted in the EEG and MEG domain (Sarvas [1987]; Hämäläinen et al. [1993]; M.S.Gazzaniga et al. [2002]; Andrä and Nowak [2002]) and also shown in this work in Chapters 2.5, 2.13 and 2.16, the EEG is stronger dependent on accuracy aspects of volume conductor modeling than the MEG, especially with regard to the compartments skull and skin. Moreover, Chapter 2.16 corroborated the finding that the MEG is more sensitive to eccentric tangentially-oriented sources than the EEG, since the averaging over about a three times higher number of trials was necessary to achieve a similar signal-to-noise ratio for the SEP than for the SEF. Besides of the need for a correct modeling of the inner skull surface, the thickness, the three-layeredness and the accurate conductivity values of the skull tissues are not important for MEG source analysis (Chapter 2.13) as long as there are no skull anomalies such as, e.g., incisions from trepanation (van den Broek [1997]).

For SEP and SEF source analysis of the early component around 35 Milliseconds post-stimulus, a five compartment (skin, skull, CSF, brain gray and white matter) FE volume conductor model with a 1 to 10 (radially to tangentially to the skull surface) anisotropically conducting skull compartment was used. A single equivalent current dipole fit was performed and the resulting dipoles for both SEP and SEF were localized in the left primary somatosensory cortex. As shown by (Mertens and Lütkenhöner [2000]; Hari and Forss [1999]), the single dipole model is adequate for source analysis because the measured SEP/SEF data arise from area 3b of the primary somatosensory cortex (SI) contralateral to the side of stimulation. An explained variance of about 98% in the presented study further corroborated this model. With a difference in location of less than 4mm, EEG and MEG reconstructed at nearby positions. Since this difference was shown to be mainly a difference in source depth, it might be due to an erroneous choice of the skull anisotropy (see Chapter 2.13). A recent study reported that the skull's three-layeredness (outer compacta, spongiosa, inner compacta) should be modeled as a three-layeredness and not indirectly by means of the anisotropy (Sadleir and Argibay [2007]), which might also be a reason for the small location difference. It will be examined in the future if the SEP/SEF-combined LRCE approach might contribute to the solution of this problem.

3.3.2 Presurgical epilepsy diagnosis

The precise localization of the epileptogenic foci in medically-intractable epilepsy patients with focal seizures, preferably with non-invasive methods, is the major goal of the presurgical diagnosis (Rosenow and Luders [2001]). In addition to evaluation by video and EEG long-term monitoring, MRI, single photon emission computed tomography (SPECT) and neuropsychological examination, EEG and MEG source analysis has risen to a promising tool (Roth et al. [1997]; Huiskamp et al. [1997]; Waberski et al. [1998]; Merlet and Gotman [1999]; Huiskamp et al. [1999]; Waberski et al. [2000]; Kobayashi et al. [2001]; Stefan et al. [2003]; Salayev et al. [2006]).

sEEG source analysis of epileptiform activity using high resolution FE head modeling

In Chapter 2.17.1, a goal function scan (GFS) (Mosher et al. [1992]; Knösche [1997]), an MNLS approach, a moving and a rotating dipole fit and an sLORETA approach were based on a 1mm anisotropic hexahedral FE model with about 3.1 Million unknowns to analyze the peak of 9 averaged ictal surface EEG (sEEG) delta spikes of a medically-intractable residivous epilepsy patient. The FE head model was constructed using non-linearly registered T1-, T2- and DT-MRI. Brain tissue conductivity anisotropy was derived from the measured DT-MRI using the methods proposed by Tuch et al. [1999, 2001]. To the best of the authors knowledge, this level of accuracy in head volume conductor modeling has not yet been applied to source analysis in presurgical epilepsy diagnosis before. GFS, MNLS and sLORETA clearly showed a single center of activity. Moving and rotating single dipole fits resulted in an explained variance of more than 97%, corroborating the source model of a single focal center of activity. With only small differences in location, i.e., a maximal difference of 2.6mm between GFS, sLORETA, moving and rotating dipole fit and 6.6mm between the MNLS and the other approaches, the FE-based surface EEG inverse algorithms localized a single center of activity at the posterior lateral border of the brain tumor. This non-invasive current estimate was successfully validated with post-surgical intra-cranial EEG (iEEG) measurements. While the MNLS localized about 6mm posterior to the other inverse methods, the GFS and the sLORETA localization results were identical. This might corroborate the result of Pascual-Marqui [2002], who carried out a large series of single test source simulations at arbitrary positions and depths in the volume conductor and showed that sLORETA produced zero-localization error, while, despite of all weighting efforts (Fuchs et al. [1999]; Dale et al. [2000]), former linear solutions such as MNLS produced images with systematic non-zero localization errors.

In summary, non-invasive surface EEG source analysis based on realistic head models can contribute to clinical presurgical evaluation in epilepsy patients.

ICA-based source modeling of combined iEEG/sEEG epileptic seizure data using a realistic head model

ICA was shown to be able to disentangle functionally independent components, which are not correlated in time and which were shown to arise from a single or a pair of focal activated cortical areas (Kobayashi et al. [2001]; Makeig et al. [2002]). The remaining localization problem is then broken down to the fit of a single or a pair of dipoles to the spatial ICA topographies of interest. This localization subproblem has a unique solution and the quality of the source analysis result is mainly dependent on the accuracy of the volume conductor model.

In Chapter 2.17.2, concurrently collected sEEG and intracranial EEG (iEEG) data of an epilepsy patient whose seizures were not controlled by medications and who underwent neurosurgery, were evaluated using an ICA-based source analysis approach. The overall goal of this project is to estimate and model volume conduction based relationships between noninvasive and invasive human electrical brain data and to explore the use of FE-based ICA source analysis methods for localizing seizure foci and modeling the activity of networks responsible for spontaneous seizures in neocortical and mesial temporal lobe epilepsies. One of the major challenges of the study is the volume conductor modeling, which has to take into account the skull incision from trepanation and the highly resisting Silastic pads of the iEEG.

In a first approach, a 2mm geometry-adapted hexahedral FE model was used, which was generated from a pair of T1-MRI and CT datasets of the patients head. The CT dataset also allowed the identification of the iEEG electrode locations. The four compartment (skin, skull, CSF, brain) FE model accounted for the skull incision, but geometry-adapted hexahedral elements were found to be inappropriate for the modeling of the highly resisting thin iEEG Silastic pads which were therefore initially ignored. In a simulation study, it was shown that ignoring the trepanation hole would lead to a much blurred sEEG potential distribution. Single dipole fits were then carried out for either the iEEG or the sEEG map of a selected peri-ictal ICA component from the joint scalp and grid data decomposition. An explained variance of 96% for the iEEG dipole and 94% for the sEEG dipole corroborated the single dipole source model. However, while the iEEG dipole was reconstructed directly beneath the iEEG grid, the dipole for the scalp map activity was localized much deeper. It was concluded that the modeling of the Silastic grid is a key point in the analysis of combined iEEG/sEEG data, as also recently shown by Zhang et al. [2006].

As a future perspective, while Zhang et al. [2006] used an ordinary Delaunay tetrahedralization FE meshing approach for the Silastic pad, we are working towards an appropriate constrained Delaunay tetrahedralization. First meshing results were shown in Figures 2.13 and 2.14.

Appendix A

Further publications

Publications (invited, peer-reviewed)

1. Wolters C.H., de Munck, J.C. Volume conduction, *Encyclopedia of Computational Neuroscience, Scholarpedia* (2007).

2. Wolters C.H. The Finite Element Method in EEG/MEG Source Analysis. *SIAM News*, Volume 40, Number 2 (2007).

Publications (peer-reviewed)

1. R.J. Huster, C.H. Wolters, A. Wollbrink, E. Schweiger, W. Wittling, C. Pantev and M. Junghöfer, Effects of anterior cingulate fissurization on cognitive control during Stroop interference. submitted to *Human Brain Mapping*, 2007.

2. Okamoto, H, Stracke, H., Wolters, C.H., Schmael, F., and Pantev, C.. Attention improves population-level frequency tuning in human auditory cortex. *The Journal of Neuroscience*, Vol.27, No.39, pp.10383-10390 (2007).

3. Lew, S., Wolters C.H., Anwander, A., Makeig, S. and MacLeod, R.S.. Low resolution conductivity estimation to improve source localization. *International Congress Series, ICS-07008*, Vol.1300, pp.149-152 (June 2007).

4. Güllmar, D., Haueisen, J., Eiselt, M., Giessler, F., Flemming, L., Anwander, A., Knösche, T., Wolters, C.H., Dümpelmann, M., Tuch, D.S. and Reichenbach, J.R. Influence of Anisotropic Conductivity on EEG source reconstruction: Investigations in a rabbit model. *IEEE Trans. Biomed. Eng.*, Vol. 53, No. 9, pp. 1841-1850, 2006.

5. Güllmar, D, Reichenbach, J.R., Anwander, A., Knösche, T., Wolters, C.H., Eiselt, M. and Haueisen, J., Influence of Anisotropic Conductivity of the White Matter Tissue on EEG Source Reconstruction - a FEM Simulation Study, *Int. Journal of Bioelectromagnetism*, Vol. 7, No.1, pp.108-110, (2005).

6. Fingberg, J., Berti, G., Hartmann, H., Basermann, A., Wolters, C.H., Anwander, A., McCarthy, A. and Woods, S., Bio-numerical simulations with SimBio, *NEC Research and Development* **44**(1), pp. 140–145, (2003).

7. Wolters, C.H., Kuhn, M., Anwander, A. and Reitzinger, S., A parallel algebraic multigrid solver for finite element method based source localization in the human brain. *Computing and Visualization in Science* **5**(3), pp.165–177 (2002).

8. Schmitt, U., Louis, A.K., Wolters, C.H. and Vauhkonen, M., Efficient algorithms for the regularization of dynamic inverse problems: II. Applications. *Inverse Problems* **18**(3), pp. 659–676 (2002).

9. Wolters, C.H., Beckmann, R.F., Rienäcker, A. and Buchner, H., Comparing regularized and non-regularized nonlinear dipole fit methods: A study in a simulated sulcus structure. *Brain Topography* **12**(1), pp. 3–18 (1999).

Proceedings (peer-reviewed)

1. Wolters,C.H., Lew,S., Drechsler, F., Dierkes, T. and Grasedyck, L. Improved EEG/MEG forward modeling using conductivity fitting in realistic finite element volume conductor models. In: Proc. 16th German EEG/EP Mapping Meeting, Schloss Rauischholzhausen, Giessen, Germany, DMM, October 20-21, (2007).

2. Dierkes, T., Drechsler, F.,Grasedyck, L., de Munck, J.C. and Wolters, C.H., Anisotropy in M/EEG Source Reconstruction Using the Finite Element Method. In: Proc. 16th German EEG/EP Mapping Meeting, Schloss Rauischholzhausen, Giessen, Germany, DMM, October 20-21, (2007).

3. Haueisen, J., Güllmar, D., Flemming, L., Eiselt, M., Reichenbach, J.R., Anwander, A., Dümpelmann, M., Knösche, T. and Wolters, C.H., Validation of the new SimBio Electromagnetic Source Localization Environment in an Animal Model. In *Y.Okada, C.Wood, C.Aine & C.Osborn (eds.): 14th Conf. of the Int. Soc. for Brain Electromag. Top., Santa Fe, New Mexico, USA*, http://hsc.unm.edu/som/cobre/ISBET2003, (2003).

4. Fingberg, J., Berti, G., Hartmann, U., Basermann, A., Wolters, C.H., Anwander, A., McCarthy, A. and Woods, S., Bio-numerical simulations with SimBio. In *Buzug, T.M., Hartmann, U., Hülster, A., Kohl-Bareis, M. & Wilhein, T. (eds): Physikalische Methoden der Laser- und Medizintechnik*, VDI Verlag, pp. 114-120 (2003).

5. Wolters, C.H., Kuhn, M., Anwander, A. and Reitzinger, S., Fast anisotropic high resolution finite element head modeling in EEG/MEG-source localization. In *Nowak, H., Haueisen, J., Giessler, F. and Huonker, R. (eds.): Proc. of the 13th Int. Conf. on Biomagnetism, University of Jena, Jena, Germany*, VDE Verlag GmbH, Berlin, Offenbach, http://biomag2002.uni-jena.de, pp. 670–672 (2002).

6. Anwander, A., Wolters, C.H., Dümpelmann, M., and Knösche, T.R., Influence of realistic skull and white matter anisotropy on the inverse problem in EEG/MEG-source localization. In *Nowak, H., Haueisen, J., Giessler, F. and Huonker, R. (eds.): Proc. of the 13th Int. Conf. on Biomagnetism, University of Jena, Jena, Germany*, VDE Verlag GmbH, Berlin, Offenbach, http://biomag2002.uni-jena.de, pp. 679–681 (2002).

7. Dümpelmann, M., Knösche, T.R., Anwander, A. and Wolters, C.H., Sensitivity of inverse source reconstruction results towards forward model inaccuracies: Application of a universal sensitivity analysis software framework on different tissue conductivity ratios. In *Nowak, H., Haueisen, J., Giessler, F. and Huonker, R. (eds.): Proc. of the 13th Int. Conf. on Biomagnetism, University of Jena, Jena, Germany*, VDE Verlag GmbH, Berlin, Offenbach, http://biomag2002.uni-jena.de, pp. 694–696 (2002).

8. Burkhardt, S., Kruggel, F., Saupe, D. and Wolters, C.H., Segmentierung des Knochens aus T1- und PD-gewichteten Kernspinbildern vom Kopf. In *Handels, H., Horsch, A., Lehmann, T. & Meinzer, H.-P. (eds.): "Bildverarbeitung für die Medizin"*, Springer-Verlag, Berlin, pp. 187–191 (2001).

9. Wolters, C.H., Reitzinger, S., Basermann, A., Burkhardt, S., Hartmann, U., Kruggel, F. and Anwander, A., Improved tissue modeling and fast solver methods for high resolution FE-modeling in EEG/MEG-source localization. In *Nenonen, J., Ilmoniemi, R.J. & Katila, T. (eds.): Proc. of the 12th Int. Conf. on Biomagnetism, Helsinki Univ. of Tech., Espoo, Finland*, http://biomag2000.hut.fi, pp. 655–658 (2000).

10. Lonsdale, G., Grebe, R., Hartmann, U., Hose, D.R., Kruggel, F., Penrose, J.M.T. and Wolters, C.H., Bio-numerical simulations with SimBio: project

aims and objectives. In *RIKEN, Symposium on Computational Biomechanics Simulation, May, 24-25*, pp. 187–196 (2000).

11. Wolters, C.H., Hartmann, U., Koch, M., Kruggel, F., Burkhardt, S., Basermann, A., Tuch, D.S. and Haueisen, J., New methods for improved and accelerated FE-volume-conductor modelling in EEG/MEG-source reconstruction. In *Middleton, J., Jones, M., Shrive, N. & Pande, G. (eds.): "4th Symp. on Comp. Meth. in Biomech. and Biomed.Eng.", Lisboa, Portugal, Okt.31-Nov.3*, Gordon & Breach, ISBN: 9056993216, pp. 489–494 (1999).

12. Wolters, C.H., Beckmann, R.F., Rienäcker, A. and Buchner, H., New regularization method for nonlinear and constrained dipole fit. *NeuroImage* **9**(6), S177 (1999).

13. Wolters, C.H., Rienäcker, A., Beckmann, R., Jarausch, H., Buchner, H., Grebe, R. and Louis, A.K., Stable inverse current reconstruction in real anatomy using combinatorial optimization techniques combined with regularization methods. In *Witte, H., Zwiener, U., Schack, B. & Doering, A. (eds.): "Quantitative and Topological EEG and MEG Analysis"*, Druckhaus Mayer Verlag GmbH Jena-Erlangen, pp. 484–486 (1997).

Books and book chapters

1. Wolters, C. H., Influence of Tissue Conductivity Inhomogeneity and Anisotropy on EEG/MEG based Source Localization in the Human Brain, In *MPI of Cognitive Neuroscience Leipzig, MPI Series in Cognitive Neuroscience*, **39**, ISBN 3-936816-11-5, also: Leipzig, Univ., Diss., http://dol.uni-leipzig.de/pub/2003-33, (2003).

2. Wolters, C.H., Anwander, A., Koch, M., Reitzinger, S., Kuhn, M. and Svensén, M., Influence of head tissue conductivity anisotropy on human EEG and MEG using fast high resolution finite element modeling, based on a parallel algebraic multigrid solver. In *T.Plesser & V.Macho (eds.): "Forschung und wissenschaftliches Rechnen" Contributions to the Heinz-Billing Award, Gesellschaft für wissenschaftliche Datenverarbeitung mbH Göttingen*, **58**, ISSN: 0176-2516, pp. 111–157, http:// www.billingpreis.-mpg.de, (2001).

Appendix B

Curriculum Vitae

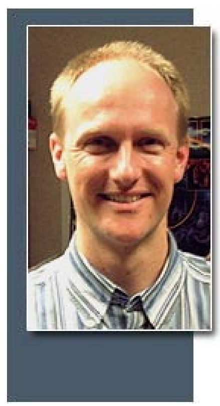

Personal data

Name:	Dr.rer.nat. Carsten Hermann Wolters
Date of birth:	June 10, 1967
Place of birth:	Emsdetten, Westfalia, Germany
Family status:	Married with Dr. Heidi Yppärilä-Wolters from Oulainen/Finland
Children:	Lina Maria Wolters (30.06.2006)
Nationality:	German

Scientific experience

since 03/2005	Research associate at the Institute for Biomagnetism and Biosignalanalysis, IBB (C. Pantev), University of Münster, http://biomag.uni-muenster.de.
02/2004–02/2005	Research associate at the Scientific Computing and Imaging Institute, SCI (C. Johnson, R. MacLeod), University of Utah, Salt Lake City, USA, http://www.sci.utah.edu.
11/2000–01/2004	Research associate at the Max Planck Institute for Mathematics in the Sciences Leipzig, MPI-MIS (W. Hackbusch, E. Zeidler), http://www.mis.mpg.de, in cooperation with the MPI for Human Cognitive and Brain Science Leipzig, MPI-CBS (A.D. Friederici, Y. von Cramon), http://www.cbs.mpg.de.
11/1997–10/2000	Research associate in the MEG-group of the MPI-CBS in cooperation with the MPI-MIS.
02/1995–04/1995	Research work (with F. Frouin, H. Benali and R. di Paola), “Faktoranalysis einer Bildsequenz von enddiastolisch-endsystolischen Herzszintigraphiebildern”, INSERM-Unité 494, Paris, France.
08/1993–12/1993	Student assistant at the Institute of Physiology, RWTH Aachen.
09/1992–06/1993	Research work at the INSERM-Unité 280 (F. Perrin, O. Bertrand, J. Pernier), Lyon, France: “La méthode des éléments de surface en utilisant une interpolation linéaire du potentiel afin de résoudre le problème direct”.

Scientific education

07/2003	Dissertation in Mathematics at the Fac. for Mathematics and Computer Science, University of Leipzig (magna cum laude, 1.0), http://lips.informatik.uni-leipzig.de/pub/2003-33.
10/1997	Diploma in Mathematics, Minor in Medicine, RWTH Aachen (with distinction, 1.0). Masters thesis at the In-

	stitute for Geometry and Applied Mathematics in cooperation with the Institute of Physiology, RWTH Aachen.
09/1992–06/1993	DAAD scholarship for the INSA de Lyon (http://www.insa-lyon.fr) and studies at the Université Claude Bernard Lyon I (http://www.univ-lyon1.fr), Lyon, France.

Teaching experience

since 04/2008	Seminar ”Numerical methods in EEG and MEG source analysis”, Faculty of Mathematics and Computer Science, University of Münster.
since 04/2005	Seminar ”Modern Investigation Methods in Human Neuroscience”, IBB, University of Münster.
11/1997–12/2004	Interdisciplinary lectures in EEG and MEG, MPI-CBS, MPI-MIS, University of Leipzig.
08/1994–08/1996	Student lecturer in numerical analysis for students in Mathematics, Institute for Geometry and Applied Mathematics, RWTH Aachen

Student education

since 2008	S. Sillekens, diploma thesis in Mathematics, together with Prof.M.Burger, Institut für Numerische und Angewandte Mathematik, Universität Münster. ”Beamforming in realistic FEM head models”.
since 2008	F. Gigengack, diploma thesis in Mathematics, together with Prof.X.Jiang, Institut für Informatik, Universität Münster. ”Registration and segmentation of multimodal MRI with regard to EEG/MEG source analysis”.
since 2007	C. Röer, diploma thesis in Physics, together with Prof.R.Friedrich, Institut für Theoretische Physik, Universität Münster. ”Mesh generation techniques for realistic volume conductor modeling in presurgical epilepsy diagnosis”.

09/2006–09/2007	B. Lanfer, diploma thesis in Physics, together with Prof.S.Demokritov, Institut für Angewandte Physik, Universität Münster. ”Validation and comparison of realistic head modeling techniques and application to combined somatosensory EMEG data”.
04/2005–10/2005	C. Möller, diploma thesis in Computer Science, together with Prof.U.Rüde, Lehrstuhl für Informatik 10, Universität Erlangen. ”Dipole models for Finite Element Method based Source Reconstruction.”.
since 2004	S.Lew, PhD in Biomedicine, together with Prof.R.S.MacLeod, SCI Institute, University of Utah, USA. ”Low resolution conductivity estimation from surface and internal EEG and MEG.”.
10/1999–10/2000	S.Burkhardt, diploma thesis in Computer Science, together with Prof.D.Saupe, Institut für Informatik, Universität Leipzig. ”Registration and segmentation of the human skull from multimodal MRI.”.

Professional experience and education

07/1996–12/1996	Coupling an Anaesthesia Work Station to the HP Viridia CMS, Patient Monitoring Division, Hewlett-Packard Medical Products Group, Böblingen.
02/1991–04/1991	Interface programming, Kolvenbach KG, electrofluid technology, Aachen.
08/1986–08/1989	Education for “Mathematisch technischer Assistent”, comparable to studies in Informatics (FH, Fach-Hochschule), Computer center, University of Münster, Examination at the Chamber of Industry and Commerce, Cologne.

Military service

10/1989–10/1990	Military service, Navy.

School education

1977–07/1986	High school education at “Privates Arnold-Janssen Gymnasium”, St.Arnold near Neuenkirchen.
1973–1977	Primary school education at “Buckhoff-Grundschule”, Emsdetten.

Münster, 17th of January 2008

Appendix C

Miscellaneous

Reviewer for

since 12/2006	Scholarpedia, Encyclopedia of Computational Neuroscience
since 04/2006	SIAM Computational Science and Engineering Book Series
since 04/2006	Journal of Applied Electromagnetics and Mechanics
since 11/2005	Enzy.Biomed.Eng.
since 10/2005	NeuroImage
since 11/2004	Journal of Neurology and Clinical Neurophysiology
since 05/2005	IEEE Transactions on Circuits and Systems
since 07/2004	Journal of Applied Numerical Mathematics
since 07/2004	IEEE Transactions on Biomedical Engineering
since 11/2000	IEEE Transactions on Medical Imaging.

Awards

11/2007	Paper evaluated for Faculty of 1000 Biology: http://www.f1000biology.com/article/id/1030531/evaluation Wolters et al., *NeuroImage*, Vol.30, No.3, pp.813-826 (2006).
08/2002	Anwander, A., Wolters, C.H., Dümpelmann, M. and Knösche, T.R. Young Investigators Award, 13^{th} Int.Conf. on Biomagnetism, Jena, http://biomag2002.uni-jena.de.

06/1998 Wolters, C.H., Friedrich Springorum Medaille, RWTH Aachen.

Projects

11/07–10/09 Cooperation project with MEGIS Software GmbH, München (C.H. Wolters, M.Scherg).

01/07–12/09 DFG project EmoBeamFem, JU445/5-1 (M. Junghöfer, C.H. Wolters, C. Pantev).

01/07–12/09 DFG project FemInvers, WO1425/1-1 (C.H. Wolters, L. Grasedyck, T. Knösche, J. Haueisen).

Since 2005 NCRR-NIH Center for Bioelectric Field Modeling, Simulation and Visualization (CIBC) (C.Johnson, R.S. MacLeod, SCI Institute, University of Utah, USA). Own status: NCRR collaborator, http://www.sci.utah.edu/cibc/collab/wolters.html.

04/00–07/03 SimBio-A generic environment for bionumerical simulation, European Commission, Information Society Technologies (IST) Programme, Framework V, Project IST-1999-10378, http://www.simbio.de.

Software SimBio

01/02/2008 Our software SimBio has 45 users worldwide.

Conference organization

07/2003 Organization of the SimBio project meeting at MPI-CBS in Leipzig.

11/2000 Wolters, C.H. & Anwander, A. (org.): Models to Generate Individual Anisotropic Conductivity Maps of Head Tissues from Multimodal MR and Influence on EEG/MEG Source Localization, MPI-CBS, Leipzig. Invited speakers from Europa and the USA.

07/2000 Organization of the SimBio project meeting at MPI-CBS in Leipzig.

References

Akhtari, M., Bryant, H., Marmelak, A., Flynn, E., Heller, L., Shih, J., Mandelkern, M., Matlachov, A., Ranken, D., Best, E., DiMauro, M., Lee, R., Sutherling, W., 2002. Conductivities of three-layer live human skull. Brain Top. 14 (3), 151–167.

Andrä, W., Nowak, H., 2002. Magnetism in Medicine – A Handbook, second edition Edition. Wiley–VCH, Weinheim.

Awada, K., Jackson, D., Williams, J., Wilton, D., Baumann, S., Papanicolaou, A., 1997. Computational aspects of finite element modeling in EEG source localization. IEEE Trans Biomed. Eng. 44 (8), 736–751.

Barnard, A., Duck, J., Lynn, M., Timlake, W., 1967. The application of electromagnetic theory to electrocardiology ii. Biophys.J. 7, 463–491.

Basser, P., Mattiello, J., LeBihan, D., 1994. MR diffusion tensor spectroscopy and imaging. Biophys. J. 66, 259–267.

Baumann, S., Wozny, D., Kelly, S., Meno, F., 1997. The electrical conductivity of human cerebrospinal fluid at body temperature. IEEE Trans Biomed. Eng. 44 (3), 220–223.

Baysal, U., Haueisen, J., 2004. Use of a priori information in estimating tissue resistivities-application to human data in vivo. Physiol. Meas. 25, 737–48.

Berger, H., 1929. Über das Elektrenkephalogramm des Menschen. Arch.Psychiat.Nervenkr. 87, 527–570.

Bertrand, O., Thévenet, M., Perrin, F., 1991. 3D finite element method in brain electrical activity studies. In: Nenonen, J., Rajala, H., Katila, T. (Eds.), Biomagnetic Localization and 3D Modelling. Report of the Dep. of Tech.Physics, Helsinki University of Technology, pp. 154–171.

BioPSE, 2002. Problem Solving Environment for modeling, simulation, and visualization of bioelectric fields. Scientific Computing and Imaging Institute (SCI), http://software.sci.utah.edu/biopse.html.

Brazier, M., 1949. A study of the electric field at the surface of the head. Electroenc. Clin. Neurophysiol. 2, 38–52.

Buchner, H., Darvas, F., Friedrich, V., Fuchs, M., Knepper, A., Knoll, G., Meyer-Ebrecht, D., Rienäcker, A., Sloot, P., Wassmuth, K., 2000. Localisation of the electromagnetic activity of the brain in its individual anatomy. In: Image processing and parallel computing in medical applications. Future Generation Computer Systems.

Buchner, H., Knoll, G., Fuchs, M., Rienäcker, A., Beckmann, R., Wagner, M., Silny, J., Pesch, J., 1997. Inverse localization of electric dipole current sources in finite element models of the human head. Electroenc. Clin. Neurophysiol. 102, 267–278.

Buchner, H., Waberski, T., Fuchs, M., Wischmann, H.-A., Wagner, M., Drenckhahn, R., 1996. Comparison of realistically shaped boundary element and spherical head models in source localization of early somatosensory evoked potentials. Brain Top. 8, 137–143.

Camacho, D., Hopper, R., Lin, G., Myers, B., 1997. An improved method for finite element mesh generation of geometrically complex structures with application to the skullbase. J. Biomech. 30 (10), 1067–1070.

Cohen, D., 1968. Magnetoencephalography: Evidence of magnetic field produced by alpha-rythm currents. Science 161, 784–786.

Cohen, D., 1972. Magnetoencephalography: Detection of the brain's electrical activity with a superconducting magnetometer. Science 175, 664–666.

Cook, M., Koles, Z., 2006. A high-resolution anisotropic finite-volume head model for eeg source analysis. In: Proc. of the 28th Annual Int. Conf. of the IEEE Engineering in Medicine and Biology Society. pp. 4536–4539.

Dale, A., Liu, A., Fischl, B., Buckner, R., Belliveau, J., Lewine, J., Halgren, E., 2000. Dynamic statistical parametric mapping: combining fMRI and MEG for high-resolution imaging of cortical activity. Neuron 26, 55–67.

Dale, A., Sereno, M., 1993. Improved localization of cortical activity by combining EEG and MEG with cortical surface reconstruction: a linear approach. Journal of Cognitive Neuroscience 5, 162–176.

Dannhaur, M., 2007. EEG/MEG source reconstruction with the sLORETA algorithm. Faculty of Computer Science. Universität Leipzig, diploma thesis.

de Munck, J., 1988. The potential distribution in a layered anisotropic spheroidal volume conductor. J. Appl. Phys. 64, 465–469.

de Munck, J., 1992. A linear discretization of the volume conductor boundary integral equation using analytically integrated elements. IEEE Trans Biomed. Eng. 39 (9), 986–990.

de Munck, J., Peters, M., 1993. A fast method to compute the potential in the multi sphere model. IEEE Trans Biomed. Eng. 40 (11), 1166–1174.

de Munck, J., van Dijk, B., Spekreijse, H., 1988. Mathematical dipoles are adequate to describe realistic generators of human brain activity. IEEE Trans Biomed. Eng. 35 (11), 960–966.

Friederici, A., Wang, Y., Herrmann, C., Maess, B., Oertel, U., 2000. Localization of early syntactic processes in frontal and temporal cortical areas: An MEG study. Human Brain Map. 11, 1–11.

Frijns, J., de Loo, S., Schoonhoven, R., 2000. Improving accuracy of the boundary element method by the use of second-order interpolation function. IEEE Trans. Biomed. Eng. 47 (10), 1336–1346.

Fuchs, M., Drenckhahn, R., Wischmann, H., Wagner, M., 1998. An improved boundary element method for realistical volume conductor modeling. IEEE Trans Biomed. Eng. 45 (8), 980–997.

Fuchs, M., Wagner, M., Köhler, T., Wischmann, H., 1999. Linear and nonlinear current density reconstructions. Jour.Clin.Neurophysiol. 16 (3), 267–295.

Fuchs, M., Wischmann, H., Wagner, M., 1994. Generalized minimum norm least squares reconstruction algorithms. ISBET Newsletter 5, 8–11.

Geddes, L., Baker, L., 1967. The specific resistance of biological material. A compendium of data for the biomedical engineer and physiologist. Med.Biol.Eng. 5, 271–293.

Gencer, N., Acar, C., 2004. Sensitivity of EEG and MEG measurements to tissue conductivity. Phys.Med.Biol. 49, 701–717.

Gerson, J., Cardenas, V., Fein, G., 1994. Equivalent dipole parameter estimation using simulated annealing. Electroenc. Clin. Neurophysiol. 92, 161–168.

Gonçalves, S., de Munck, J., Verbunt, J., Bijma, F., Heethaar, R., da Silva, F. L., 2003a. In vivo measurement of the brain and skull resistivities using an EIT-based method and realistic models for the head. IEEE Trans.Biomed.Eng. 50 (6), 754–767.

Gonçalves, S., de Munck, J., Verbunt, J., Heethaar, R., da Silva, F. L., 2003b. In vivo measurement of brain and skull resistivities using an EIT based method and the combined analysis of SEP/SEF data. IEEE Trans.Biomed.Eng. 50 (9), 1124–1127.

Güllmar, D., Haueisen, J., Eiselt, M., Gießler, F., Flemming, L., Anwander, A., Knösche, T. R., Wolters, C. H., Dümpelmann, M., Tuch, D., Reichenbach, J. R., 2006. Influence of anisotropic conductivity on EEG source reconstruction: Investigations in a rabbit model. IEEE Trans Biomed Eng.

Gutierrez, D., Nehorai, A., Muravchik, C., 2004. Estimating brain conductivities and dipole source signals with EEG arrays. IEEE Trans. Biomed. Eng. 51 (12), 2113–2122.

Haase, G., Langer, U., 1998. Multigrid-Methoden, vorlesungsskriptum, http://www.numa.uni-linz.ac.at/.

Hackbusch, W., 1994. Iterative solution of large sparse systems of equations. Springer Verlag, Applied Mathematical Sciences 95.

Hallez, H., Vanrumste, B., Hese, P. V., D'Asseler, Y., Lemahieu, I., de Walle, R. V., 2005. A finite difference method with reciprocity used to incorporate anisotropy in electroencephalogram dipole source localization. Phys.Med.Biol. 50, 3787–3806.

Hämäläinen, M., Hari, R., R.Ilmoniemi, Knuutila, J., O.Lounasmaa, 1993. Magnetoencephalography: theory, instrumentation, and applications to noninvasive studies of the working human brain. Rev.Mod.Phys. 65 (2), 413–497.

Hämäläinen, M., Ilmoniemi, R., 1984. Interpreting measured magnetic fields of the brain: Estimates of current distributions. Techn. Report TKK-F-A559, Helsinki University of Technology.

Hämäläinen, M., Sarvas, J., 1989. Realistic conductivity geometry model of the human head for interpretation of neuromagnetic data. IEEE Trans Biomed. Eng. 36, 165–171.

Haneishi, H., Ohyama, N., Sekihara, K., Honda, T., 1994. Multiple current dipole estimation using simulated annealing. IEEE Trans Biomed. Eng. 41, 1004–1009.

Hari, R., Forss, N., 1999. Magnetoencephalography in the study of human somatosensory cortical processing. Phil. Trans. R. Soc. Lond. 354 (Ser. B), 1145–1154.

Haueisen, J., 1996. Methods of numerical field calculation for neuromagnetic source localization. Ph.D. thesis, Shaker-Verlag Aachen, ISBN 3-8265-1691-5.

Haueisen, J., Ramon, C., Brauer, H., Nowak, H., 2000. The influence of local conductivity changes on MEG and EEG. Biomedizinische Technik 45 (7-8), 211–214.

Haueisen, J., Ramon, C., Czapski, P., Eiselt, M., 1995. On the influence of volume currents and extended sources on neuromagnetic fields: A simulation study. Annal. Biomed. Eng. 23, 728–739.

Haueisen, J., Tuch, D., Ramon, C., Schimpf, P., Wedeen, V., George, J., Belliveau, J., 2002. The influence of brain tissue anisotropy on human EEG and MEG. NeuroImage 15, 159–166.

Huang, M., Aine, C., Supek, S., Best, E., Ranken, D., Flynn, E., 1998. Multistart downhill simplex method for spatio-temporal source localization in MEG. Electroenc. Clin. Neurophysiol. 108, 32–44.

Huang, M., Song, T., Hagler, D., Podgorny, I., Jousmaki, V., L.Cui, K.Gaa, D.L.Harrington, Dale, A., R.R.Lee, J.Elman, E.Hargren, 2007. A novel integrated MEG and EEG analysis method for dipolar sources. NeuroImage 37, 731–748.

Huiskamp, G., Maintz, J., Wieneke, G., Viergever, M., van Huffelen, A., 1997. The influence of the use of realistic head geometry in the dipole localization of interictal spike activity in MTLE patients. Biomedizinische Technik 42, 84–87.

Huiskamp, G., Vroeijenstijn, M., van Dijk, R., Wieneke, G., van Huffelen, A., 1999. The need for correct realistic geometry in the inverse EEG problem. IEEE Trans Biomed. Eng. 46 (11), 1281–1287.

Johnson, C., Mohr, M., Rüde, U., Samsonov, A., Zyp, K., 2001. Multilevel methods for inverse bioelectric field problems. In: Barth, T., Chan, T., Haimes, R. (Eds.), Multiscale and Multiresolution Methods. Lecture Notes in Computational Science and Engineering. Vol. 20. Springer, pp. 331–346.

Jung, M., Langer, U., 1991. Applications of multilevel methods to practical problems. Surv.Math.Ind. 1, 217–257.

Jung, T.-P., Makeig, S., Humphries, C., Lee, T., Mckeown, M., Iraqui, V., Sejnowski, T., 2000. Removing electroencephalographic artifacts by blind source separation. Psychophysiology 37, 163–178.

Knösche, T., 1997. Solutions of the neuroelectromagnetic inverse problem. Ph.D. thesis, University of Twente, The Netherlands.

Kobayashi, K., Merlet, I., Gotman, J., 2001. Separation of spikes from background by independent component analysis with dipole modeling and comparison to intracranial recordings. Clin. Neurophysiol. 112 (3), 405–413.

Kybic, J., Clerc, M., Abboud, T., Faugeras, O., Keriven, R., Papadopoulo, T., 2005. A common formalism for the integral formulations of the forward eeg problem. IEEE Trans. Med. Imag. 24 (1), 12–18.

Lai, Y., van Drongelen, W., Ding, L., Hecox, K., Towle, V., Frim, D., He, B., 2005. Estimation of in vivo human brain-to-skull conductivity ratio from simultaneous extra- and intra-cranial electrical potential recordings. Clin.Neurophysiol. 116, 456–465.

Lanfer, B., 2007. Validation and comparison of realistic head modeling techniques and application to tactile somatosensory evoked EEG and MEG data. Master thesis in Physics, Institut für Biomagnetismus und Biosignalanalyse, Westfälische Wilhelms-Universität Münster.

Latikka, J., Kuume, T., Eskola, H., 2001. Conductivity of living intracranial tissues. Phys. Med. Biol. 46, 1611–1616.

Makeig, S., Westerfield, M., Jung, T.-P., Enghoff, S., Townsend, J., Courchesne, E., 2002. Dynamic brain sources of visual evoked responses. Science 295, 690–694.

Marin, G., Guerin, C., Baillet, S., Garnero, L., G., M., 1998. Influence of skull anisotropy for the forward and inverse problem in EEG: simulation studies using the FEM on realistic head models. Human Brain Mapping 6, 250–269.

Meijs, J., Weier, O., Peters, M., van Oosterom, A., 1989. On the numerical accuracy of the boundary element method. IEEE Trans Biomed. Eng. 36, 1038–1049.

Menon, V., Ford, J., Lim, K., Glover, G., Pfefferbaum, A., 1997. Combined event-related fMRI and EEG evidence for temporal-parietal cortex activation during target detection. Neuro Report 8, 3029–3037.

Merlet, I., Gotman, J., 1999. Reliability of dipole models of epileptic spikes. Clinical Neurophysiol. 110 (6), 1013–1028.

Mertens, M., Lütkenhöner, B., 2000. Efficient neuromagnetic determination of landmarks in the somatosensory cortex. Clinical Neurophysiol. 111, 1478–1487.

Mohr, M., 2004. Simulation of Bioelectric Fields: The Forward and Inverse Problem of Electroencephalographic Source Analysis. Vol. Band 37 of Arbeitsberichte des Instituts für Informatik. Friedrich-Alexander-Universität Erlangen-Nürnberg, iSSN 1611-4205.

Mohr, M., Vamrunste, B., 2003. Comparing iterative solvers for linear systems associated with the finite difference discretisation of the forward problem in electro-encephalographic source analysis. Med. Biol. Eng. Comp. 41, 75–84.

Mosher, J., Leahy, R., 1999. Source localization using recursively applied and projected (RAP) MUSIC. IEEE Trans. Sig. Proc. 47 (2), 332–340.

Mosher, J., Leahy, R., Lewis, P., 1999. Eeg and meg: Forward solutions for inverse methods. IEEE Trans. Biomed. Eng. 46 (3), 245–259.

Mosher, J., Lewis, P., Leahy, R., 1992. Multiple dipole modeling and localization from spatio-temporal MEG data. IEEE Trans Biomed. Eng. 39 (6), 541–557.

M.S.Gazzaniga, Ivry, R., Mangin, G. R., 2002. Cognitive Neuroscience: The Biology of the Mind, second edition Edition. W. W. Norton & Company, Inc., New York and London.

Murakami, S., Okada, Y., 2006. Contributions of principal neocortical neurons to magnetoencephalography and electroencephalography signals. J.Physiol. 575 (3), 925–936.

Nelder, J., Mead, R., 1965. A simplex method for function minimization. Comp.J. 7, 308–313.

Nenonen, J., Ilmoniemi, R., Katila, T. (Eds.), 2000. BIOMAG2000, Proc. of the 12th Int. Conf. on Biomagnetism. Helsinki Univ. of Tech., Finland, Aug.13-17, http://biomag2000.hut.fi.

Nicholson, P., 1965. Specific impedance of cerebral white matter. Exp.Neurol. 13, 386–401.

Ollikainen, J., Vauhkonen, M., Karjalainen, P., Kaipio, J., 1999. Effects of local skull inhomogeneities on EEG source estimation. Med.Eng.Phys. 21, 143–154.

Oostendorp, T. F., Delbeke, J., Stegeman, D. F., 2000. The conductivity of the human skull: Results of in vivo and in vitro measurements. IEEE Trans Biomed. Eng. 47, 1487–1492.

Opitz, B., Mecklinger, A., von Cramon, D., Kruggel, F., 1999. Combining electrophysiological and hemodynamic measures of the auditory oddball. Psychophysiology 36, 142–147.

Pantev, C., Hoke, M., Lütkenhöner, B., Lehnertz, K., 1989. Tonotopic organization of the auditory cortex: Pitch versus frequency representation. Science 246, 486–488.

Papadopoulo, T., Vallaghé, S., 2007. Implicit meshing for finite element methods using levelsets. In: Proceedings of MMBIA 07.

Pascual-Marqui, R., 2002. Standardized low resolution brain electromagnetic tomography (sloreta): technical details. Methods & Findings in Experimental & Clinical Pharmacology 24D, 5–12.

Pataraia, E., Lindinger, G., Deecke, L., Mayer, D., Baumgartner, C., 2005. Combined meg/eeg analysis of the interictal spike complex in mesial temporal lobe epilepsy. NeuroImage 24, 607–14.

Pham, D., Prince, J., 1999. An adaptive fuzzy C-means algorithm for image segmentation in the presence of intensity inhomogeneities. Pat. Rec. Let. 20, 57–68.

P.Kwan, M.J.Brodie, 2000. Early identification of refractory epilepsy. N.Engl.J.Med. 342 (5), 314–319.

Plis, S. M., George, J. S., Jun, S. C., Ranken, D. M., Volegov, P. L., Schmidt, D. M., 2007. Probabilistic forward model for electroencephalography. Phys.Med.Biol. 52, 5309–5327.

Pohlmeier, R., Buchner, H., Knoll, G., Rienäcker, A., Beckmann, R., Pesch, J., 1997. The influence of skull-conductivity misspecification on inverse source localization in realistically shaped finite element head models. Brain Top. 9 (3), 157–162.

Ramon, C., Schimpf, P., Haueisen, J., Holmes, M., Ishimaru, A., 2004. Role of soft bone, CSF and gray matter in EEG simulations. Brain Topography 16 (4), 245–248.

Roberts, T., Poeppel, D., Rowley, H., 1998. Magnetoencephalography and magnetic source imaging. Neuropsychiatry Neuropsych.Behav.Neurol. 11, 49–64.

Röer, C., 2008. Source analysis of simultaneous surface and internal EEG measurements in presurgical epilepsy diagnosis. Diploma thesis in Physics, Institut für Biomagnetismus und Biosignalanalyse, Westfälische-Wilhelms Universität Münster.

Rosenow, F., Luders, H., 2001. Presurgical evaluation of epilepsy. Brain 124 (Pt 9), 1683–1700.

Roth, B., Ko, D., von Albertini-Carletti, I., Scaffidi, D., Sato, S., 1997. Dipole localization in patients with epilepsy using the realistically shaped head model. Electroenc. Clin. Neurophysiol. 102, 159–166.

Ruge, J., Stüben, K., 1986. Algebraic multigrid (AMG). In: McCormick, S. (Ed.), Multigrid Methods. Vol. 5 of Frontiers in Applied Mathematics. SIAM, Philadelphia, pp. 73–130.

Rush, S., Driscoll, D., 1968. Current distribution in the brain from surface electrodes. Anesthesia and analgetica 47 (6), 717–723.

Sadleir, R., Argibay, A., 2007. Modeling skull electrical properties. Ann.Biomed.Eng. 35 (10).

Salayev, K., Nakasato, N., Ishitobi, M., Shamoto, H., Kanno, A., Iinuma, K., 2006. Spike orientation may predict epileptogenic side across cerebral sulci containing the estimated equivalent dipole. Clin. Neurophysiol. 117, 1836–43.

Saleheen, H., Kwong, T., 1997. New finite difference formulations for general inhomogeneous anisotropic bioelectric problems. IEEE Trans.Biomed.Eng. 44, 800–809.

Sarvas, J., 1987. Basic mathematical and electromagnetic concepts of the biomagnetic inverse problem. Phys.Med.Biol. 32 (1), 11–22.

Scherg, M., von Cramon, D., 1985. Two bilateral sources of the late AEP as identified by a spatio-temporal dipole model. Electroenc. Clin. Neurophysiol. 62, 32–44.

Schimpf, P., Ramon, C., Haueisen, J., 2002. Dipole models for the EEG and MEG. IEEE Trans Biomed. Eng. 49 (5), 409–418.

Schmitt, U., 2001. Effiziente Verfahren zur Regularisierung dynamischer inverser Probleme. Ph.D. thesis, Mathematisch-Naturwiss. Fakultät, Universität des Saarlandes.

Schmitt, U., Louis, A., 2002. Efficient algorithms for the regularization of dynamic inverse problems: I.Theory. Inverse Problems 18 (3), 645–658.

Schmitt, U., Louis, A., Wolters, C., Vauhkonen, M., 2002. Efficient algorithms for the regularization of dynamic inverse problems: II.Applications. Inverse Problems 18 (3), 659–676.

Sekihara, K., Sahani, M., Nagarajan, S., 2005. Localization bias and spatial resolution of adaptive and non-adaptive spatial filters for MEG source reconstruction. NeuroImage 25, 1056–1067.

Si, H., 2004. TetGen, a quality tetrahedral mesh generator and three-dimensional delaunay triangulator, v1.3, user's manual. Tech. Rep. 9, Weierstrass Institute for Applied Analysis and Stochastics.

Si, H., 2007. TetView. http://tetgen.berlios.de/tetview.html.

Si, H., Gärtner, K., 2005. Meshing piecewise linear complexes by constrained Delaunay tetrahedralizations. In: Proc. 14th International Meshing Roundtable. Sandia National Laboratories, pp. 147–163.

SimBio, 2000. SimBio: A Generic Environment for Bio-Numerical Simulation, SimBio software development started with the funding by the IST-Program of the European Commission, Project No.10378, http://www.simbio.de.

Somersalo, E., Cheney, M., Isaacson, D., 1992. Existence and uniqueness for electrode models for electric current computed tomography. SIAM J.Appl.Math. 52, 1023–1040.

Stefan, H., Hummel, C., Scheler, G., Genow, A., Druschky, K., Tilz, C., Kaltenhauser, M., Hopfengartner, R., Buchfelder, M., Romstock, J., 2003. Magnetic brain source imaging of focal epileptic activity: a synopsis of 455 cases. Brain 126 (Pt 11), 2396–2405.

Stüben, K., Nov. 1999. A review of algebraic multigrid. Techn. Report 69, GMD, http://www.gmd.de.

Tanzer, O., Järvenpää, S., Nenonen, J., E.Somersalo, 2005. Representation of bioelectric current sources using whitney elements in finite element method. Phys.Med.Biol. 50, 3023–3039.

Tuch, D., Wedeen, V., Dale, A., George, J., Belliveau, J., 1999. Conductivity mapping of biological tissue using diffusion MRI. Ann. NYAS 888, 314–316.

Tuch, D., Wedeen, V., Dale, A., George, J., Belliveau, J., 2001. Conductivity tensor mapping of the human brain using diffusion tensor MRI. Proc.Natl.Acad.Sci.USA 98 (20), 11697–11701.

Uitert, R. V., Weinstein, D., Johnson, C., 2003. Volume currents in forward and inverse magnetoencephalographic simulations using realistic head models. Annals of Biomedical Engineering 31, 21–31.

v. Helmholtz, H., 1853. Über einige Gesetze der Vertheilung elektrischer Ströme in körperlichen Leitern, mit Anwendung auf die thierisch-elektrischen Versuche. Ann Phys Chem 89, 211–233,353–377.

Vallaghé, S., Clerc, M., J.-M.Badier, 2007. In vivo conductivity estimation using somatosensory evoked potentials and cortical constraint on the source. In: 4th IEEE Int. Symp. on Biomedical Imaging. pp. 1036–9.

van den Broek, S., 1997. Volume conduction effects in EEG and MEG. Ph.D. thesis, Proefschrift Universiteit Twente Enschede, The Netherlands.

Vanrumste, B., Hoey, G. V., Boon, P., D'Havé, M., Lemahieu, I., 1998. Inverse calculations in EEG source analysis applying the finite difference method, reciprocity and lead fields. In: Proc. 20th Ann.Int.Conf. of the IEEE Eng. in Med. and Biol. Soc., Hong Kong. Vol. 20, part 4/6.

Veen, B. V., van Drongelen, W., Yuchtman, M., A.Suzuki, 1997. Localization of brain electrical activity via linearly constrained minimum variance spatial filtering. IEEE Trans Biomed. Eng. 44 (9), 867–880.

Vrba, J., 2000. Multichannel SQUID biomagnetic systems. In: Weinstock, H. (Ed.), Applications of Superconductivity. Kluwer Academic Publishers, Dordrecht, pp. 61–138.

Vrba, J., Robinson, S. E., October 2001. Signal processing in magnetoencephalography. Methods 25 (2), 249–271.

Waberski, T., Buchner, H., Lehnertz, K., Hufnagel, A., Fuchs, M., Beckmann, R., Rienäcker, A., 1998. The properties of source localization of epileptiform activity using advanced headmodelling and source reconstruction. Brain Top. 10 (4), 283–290.

Waberski, T., Gobbele, R., Herrendorf, G., Steinhoff, B., Kolle, R., Fuchs, M., Paulus, W., Buchner, H., 2000. Source reconstruction of mesial-temporal epileptiform activity: Comparison of inverse techniques. Epilepsia 41 (12), 1574–583.

Wagner, M., 1998. Rekonstruktion neuronaler Ströme aus bioelektrischen und biomagnetischen Messungen auf der aus MR-Bildern segmentierten Hirnrinde. Ph.D. thesis, Shaker-Verlag Aachen, ISBN 3-8265-4293-2.

Wagner, M., Fuchs, M., Drenckhahn, R., Wischmann, H.-A., Köhler, T., Theißen, A., 2000. Automatic generation of BEM and FEM meshes from 3D MR data. Neuroimage 3, S168.

Wagner, M., Fuchs, M., Wischmann, H.-A., Drenckhahn, R., Köhler, T., 1996. Current density reconstructions using the L1-norm. In: Proceedings of The 10th International Conference on Biomagnetism. Biomag96, pp. 158–207.

Weinstein, D., Zhukov, L., Johnson, C., 2000. Lead-field bases for electroencephalography source imaging. Annals of Biomed.Eng. 28 (9), 1059–1066.

Wiebe, S., Blume, W., Girvin, J., Eliasziw, M., 2001. A randomized, controlled trial of surgery for temporal-lobe epilepsy. The New England Journal of Medicine 345 (5), 311–318.

Wolters, C., 2003. Influence of Tissue Conductivity Inhomogeneity and Anisotropy on EEG/MEG based Source Localization in the Human Brain. No. 39 in MPI Series in Cognitive Neuroscience. MPI of Cognitive Neuroscience Leipzig, iSBN 3-936816-11-5 (also: Leipzig, Univ., Diss., http://lips.informatik.uni-leipzig.de/pub/2003-33/en).

Wolters, C., Beckmann, R., Rienäcker, A., Buchner, H., 1999. Comparing regularized and non-regularized nonlinear dipole fit methods: A study in a simulated sulcus structure. Brain Top. 12 (1), 3–18.

Wolters, C., Kuhn, M., Anwander, A., Reitzinger, S., 2002. A parallel algebraic multigrid solver for finite element method based source localization in the human brain. Comp.Vis.Sci. 5 (3), 165–177.

Wolters, C., Reitzinger, S., Basermann, A., Burkhardt, S., Hartmann, U., Kruggel, F., Anwander, A., 2000. Improved tissue modeling and fast solver methods for high resolution FE-modeling in EEG/MEG-source localization. In: Nenonen et al. [2000]. pp. 655–658.

Yan, Y., Nunez, P., Hart, R., 1991. Finite-element model of the human head: Scalp potentials due to dipole sources. Med.Biol.Eng.Comput. 29, 475–481.

Yvert, B., Bertrand, O., Echallier, J., Pernier, J., 1995. Improved forward EEG calculations using local mesh refinement of realistic head geometries. Electroenc. Clin. Neurophysiol. 95, 381–392.

Yvert, B., Crouzeix-Cheylus, A., Pernier, J., 2001. Fast realistic modeling in bioelectromagnetism using lead-field interpolation. Human Brain Mapping 14, 48–63.

Zanow, F., 1997. Realistically shaped models of the head and their application to EEG and MEG. Ph.D. thesis, University of Twente, The Netherlands.

Zanow, F., Peters, M., 1995. Individually shaped volume conductor models of the head in EEG source localisation. Med. & Biol. Eng. & Comp. 7, 151–161.

Zhang, Y., Ding, L., van Drongelen, W., Hecox, K., Frim, D., He, B., 2006. A cortical potential imaging study from simultaneous extra- and intra-cranial electrical recordings by means of the finite element method. NeuroImage 31 (4), 1513–1524.

Zhukov, L., Weinstein, D., Johnson, C., 2000. Independent component analysis for eeg source localization in realistic head model. IEEE Eng.Med.Biol. 19, 87–96.